Towards the total landscape of H-bonds in organic electronics : diketopyrrolopyrrole as a model system

Nelson Ricardo Ávila Rovelo

UNIVERSITÉ DE STRASBOURG

ÉCOLE DOCTORALE DE PHYSIQUE ET CHIMIE PHYSIQUE (ED182)

Institut Charles Sadron (ICS) - CNRS-UPR22

THÈSE présentée par :

Nelson Ricardo ÁVILA ROVELO

soutenue le : **16 décembre 2021**

pour obtenir le grade de : **Docteur de l'université de Strasbourg**

Discipline/ Spécialité : Chimie des matériaux

Vers une vision globale des liaisons hydrogène dans l'organique électronique : le dicétopyrrolopyrrole comme système modèle.

Towards the total landscape of H-bonds in organic electronics: Diketopyrrolopyrrole as a model system.

THÈSE dirigée par :

Dr. COLLIN Dominique	Chargé de Recherche, ICS, Université de Strasbourg

RAPPORTEURS :

Dr. SCHMALTZ Bruno	Maître de Conférence, PCM2E, Université de Tours
Dr. HERRERO CHAMORRO María	Prof. des Universités, Universidad de Castilla-La Mancha

AUTRES MEMBRES DU JURY :

Dr. LECLERC Nicolas	Directeur de Recherche, ICPEES, Université de Strasbourg

---

MEMBRES INVITÉS DU JURY :

Dr. RUIZ CARRETERO Amparo	Chargée de Recherche, ICS, Université de Strasbourg

Acknowledgements

"What we know is a drop, what we don't know is an ocean."

-Sir Isaac Newton

First, I would like to thank God for all his blessings and for having accompanied me throughout my career, for being my strength in my weakest moments and providing me a life full of learning.

I thank both of my parents, **Nelson Ávila** and **Lourdes Rovelo**, for supporting me every moment of my life, for the instilled values and principles, for the opportunity of having an excellent education throughout my life and foremost, for all of the love I have received from them.

In the same way I want to thank both of my sisters, first to the elder one, **Nielsen**, who has been a professional development example, and to my youngest sister, **Nelbeth**, for always believing in me and motivating me to do my best. To both, for being an important part of my life, filling it with happiness, good moments and laughs.

I want to thank my thesis directors, **Dr. Dominique Collin** and **Dr. Amparo Ruiz Carretero**, for their help and support throughout this thesis. I want to express my deepest gratitude to **Amparo**, for her patience, advices, guidance and responsiveness. Thank you not only for believing in me, but for all your support, the opportunity of growing as a professional, for teaching me something new everyday, and for all the time you dedicated while working together during the past four years! Thank you for sharing all your knowledge and experience with me and for always pushing me to reach my highest potential. I wish nothing but the best for your future projects, both professionally and personally.

I would also like to thank **Dr. Martin Brinkmann** and **Dr. Philippe Mésini** for fruitful discussions and their guidance in the interpretation of the obtained results, your contributions helped me a lot.

A huge thanks to **Dr. Jean-Philippe Lamps** for providing help daily during the entirety of the PhD. Thank you for always being helpful, for sharing tips and advice so that when setting up a reaction everything went smoothly. Thank you for making sure that we are always well-equipped and that we have enough reagents and solvents to perform reactions in the best way possible. Thank you for your support, contributions, and goodwill. You're an essential part of the **SYCOMMOR** team.

I would like to thank my friends and colleagues in the lab, **Dr. Ana García** and **MSc. Gabriel Martínez** for sharing their insight, knowledge, and time. Thank you for allowing me to speak in Spanish daily and providing the Hispanic vibe in the lab. **Ana**, I wish you success in your professional career and that you manage to achieve your goal of becoming a researcher for CNRS. **Gabriel**, good luck in the rest of the PhD, keep up the good work and motivation.

Many thanks to my peers, colleagues, and friends in the team: **Duncan Schwaller**, **Quentin Weinbach**, and **Marion Brosset**. Thank you for all the support, for helping me improving my French language and culture, and for the funny conversations during lunch, you guys helped a lot during stressing times. I wish the best for each one of you during the final line of the PhD and that you achieve your goals. **Duncan**, thank you for always providing feedback, correcting me, and criticizing when I was wrong, it helped a lot to improve myself. It is by learning from our mistakes that we can truly flourish and grow, and for that I will always be grateful.

Thanks to **Swapneel Thakkar** for his goodwill and advice during the past months, best wishes for you in your projects.

I thank the entirety of the **SYCOMMOR** team for welcoming me and making me feel a part of the team, for your direct and indirect help and support throughout this thesis. In the same regard, I would like to thank all the people from **ICS** who contributed in this work, from the characterization platform, to the administration.

A special thanks to my first friend in **ICS**, **Eirini Skoufa**. Thank you for being a good friend, in good and bad times. I will always be thankful for the moments where you helped me by cheering me up, listening to my complaints and providing life advice. I wish nothing but the best for you during the final stretch of your thesis, and I'm sure you will succeed with no problems in your professional career and that all your struggles and effort will be rewarded.

I want to thank my colleague and flat mate, **Vaibhav Sharma** who has had the patience to tolerate me during the past three years. Thanks for the shared time, the exquisite Indian food you prepare, for the beers and all the jokes along our masters and PhD journey. Good luck in your future projects!

Thanks to all my friends all around the world: **Gioconda Mejía**, **Christian Girón**, **Nahúm Valladares**, **Elvira Toro**, **Madelin Cáceres**, **Laura Barrientos**, **Daniela Velasco**, **Andrés Padilla**, and **Marie-Charlotte Sánchez**. Thank you for your friendship and for always sharing good moments, funny stories, and unforgettable memories. Thanks a bunch for believing in me and for feeling proud of my achievements whenever we talk. Your friendship has an incalculable value to me, and I feel so happy to have met each one of you at different stages of my life.

Finally, I want to thank all the professors that allowed me to reach this far in my life, especially **Mr. Eric Vendramini**, who saw my potential and pushed me to become a chemical engineer when I was in high school. In the same way, I want to thank my professor, colleague, and friend, **MSc. David Pineda**, who was always willing to help during my time as an engineering student and taught me how important it is to follow and fight for your dreams, too bad you're not among us anymore, but I am sure you would be proud of what I have achieved.

This is for you guys! Once again, thanks a million to everyone!!!

Ricardo

Table of contents

BRIEF SUMMARY

This thesis has been divided into five different chapters.

Chapter I

A general introduction giving the context leading to this PhD work is presented and has been divided into four main sections. The first part describes the current situation concerning the world's energetic consumption and its forecast. The different sources of energy are briefly presented to finally talk about sustainability.

The second part addresses the evolution of organic electronics, reviewing the different type of materials that can be used, their properties, and the importance of their design and morphology.

The third part introduces how supramolecular chemistry in organic electronics has been used by first describing what supramolecular systems are, and then discussing what approaches have been employed in organic electronics. A special emphasis is given to hydrogen-bonded (H-bonded) systems towards the end of this section.

The fourth and final part presents the history, reactivity, properties and the role of the diketopyrrolopyrrole (**DPP**) molecule in this thesis. Particularly, how and why this compound will be used to perform a systematic study is presented, as well as the different families that have been synthesized so far by our group. Among them, three of these families are encompassed throughout the succeeding chapters.

Chapter II

In this chapter, special focus is put on H-bonded **DPP** derivatives containing amide bonds coupled to the π-conjugated core through a flexible six carbon linker. In this part of the thesis, new molecules were designed, where the functionalization with H-bonded group was done on the lactam rings separating them through a flexible linker. In addition, chirality was added as a parameter, introducing a chiral center next to the H-bonding group.

The synthesis and characterization of three amide containing **DPP** derivatives is presented. The study on the aggregation behavior of all three derivatives to form J-type aggregates, where H-bonds and chirality are involved is discussed. Photoconductivity measurements were performed, and the importance of H-bonding is highlighted.

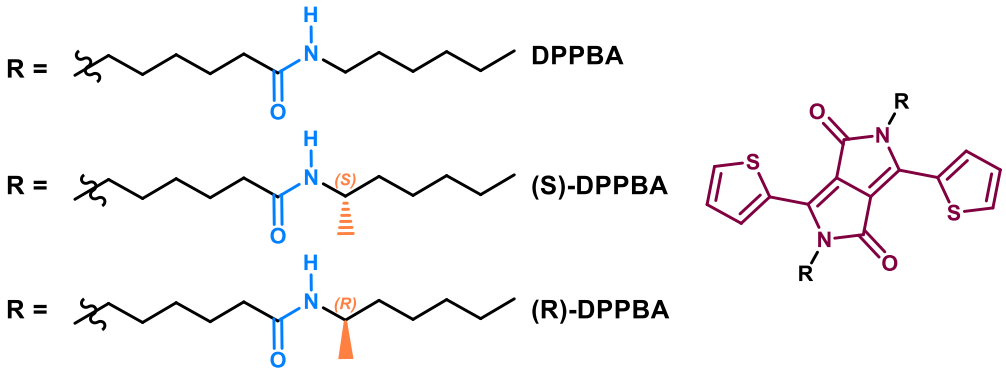

Chapter III

Following the design of H-bonded derivatives to expand the **DPP** library, the study of other parameters that impact the formation of H-bonds was continued. In this case, the solubility of the bisamide derivatives presented in Chapter II was improved and additionally, the impact of amide topology on the self-assembly and electrical properties was explored.

In this chapter, the thiophene rings on the **DPP** were functionalized with hexyl chains, while keeping the same amide branch in the lactam rings. Additionally, amide topology, either N- or C-centered was explored. These derivatives were compared to the derivatives shown in chapter II.

Together with the two H-bonded derivatives, a control **DPP** molecule bearing no H-bonds was synthesized having only hexyl alkyl tails attached to the core. The self-assembly processes of the N- and C-centered amide-containing **DPP** derivatives were once again followed by different spectroscopy and microscopy techniques, and the charge transport properties were also studied. The results are compared to the control molecule, finding a positive result in the case of the H-bonded derivatives.

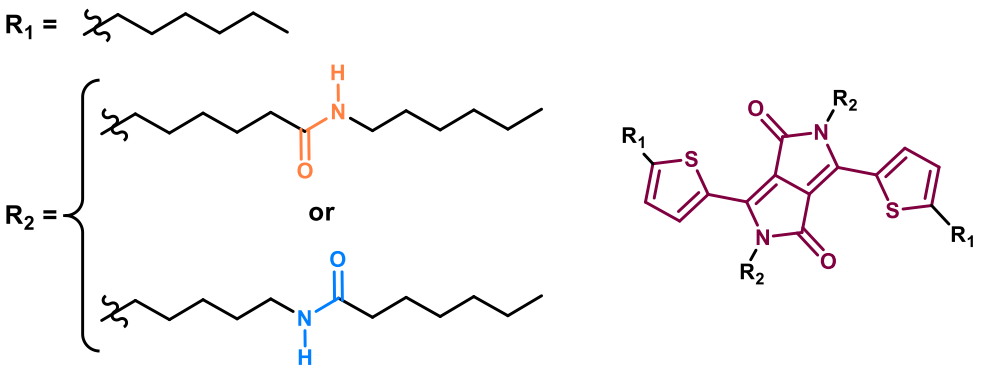

Chapter IV

In this chapter, the main objective is to explore and evaluate the effect of the position of the H-bond within the main **DPP** core. Apart from studying the influence of the position of the H-bond moiety, the topology of the amide was evaluated once again. In this new family, the position of the H-bonding units has been changed to the thiophene rings.

In this chapter a very detailed synthetic approach of two **DPP** derivatives with different topology and functionalized in the thiophene rings is presented. The synthesis of said derivatives was attempted by two different methods, the first one was a succinic cyclization approach, while the second one is a direct functionalization of the **DPP** cycle. All the difficulties encountered for achieving these products are discussed.

The self-assembly processes of the N- and C-centered amide-containing **DPP** derivatives were also followed with different spectroscopy and microscopy techniques. The results are also compared to the derivatives described in Chapter III.

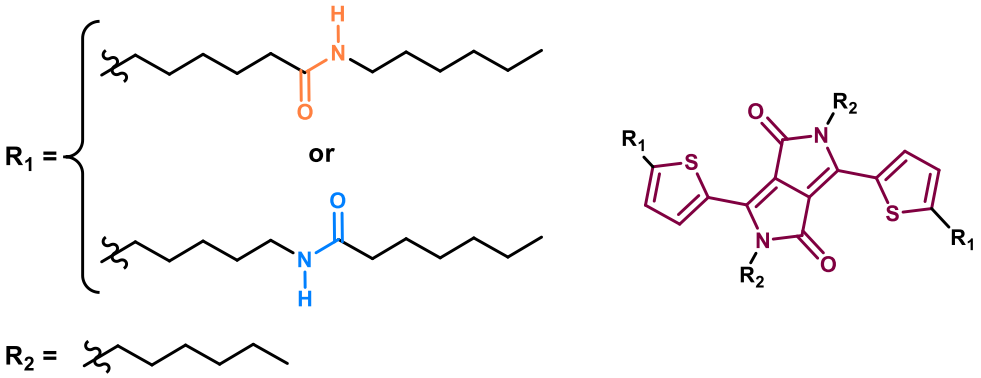

Chapter V

In the previous chapters the beginning of the comparative and systematic studies done on H-bonded π-conjugated materials based on **DPP** was shown. So far, we have found that even subtle differences in the molecular structure among **DPP** families and the different self-assembly properties can impact optoelectronic properties.

Furthermore, other parameters such as sample preparation, solvent chosen, concentration and temperature can influence the H-bonding ability, making the optimization process very complex. In this sense, we are starting to work on the *in-situ* control over the morphology and electric properties to gather as much information as possible and build up a screening protocol.

In this regard, our intention is to upgrade an existing setup by adding a properties analyser and choose an electronic parameter of interest. Nevertheless, before moving to our studies using said setup, we have studied several H-bonded **DPP** systems individually before and after exposure to solvent vapour and temperature. The work shown in this chapter explores the alignment techniques that can be used for these systems. Particularly, this has been done with the **DPP** derivatives presented in chapter III.

RÉSUMÉ EN FRANÇAIS

Cette thèse a été divisée en cinq chapitres et chacun d'eux est résumé dans ce document.

Chapitre I : Introduction

L'énergie est l'approvisionnement le plus important de l'humanité pour le bon fonctionnement de la société telle qu'on la connaît. Les activités comme la production, la distribution, le stockage et la consommation ne seraient pas possibles sans énergie. Son utilisation et ses applications sont si profondément enracinées dans la vie quotidienne, que la plupart des personnes l'ont considéré comme acquis.

Comme nous le constatons, notre consommation énergétique n'a fait que croitre de façon drastique au cours du temps. Depuis les temps préhistoriques avec la découverte du feu, elle n'a cessé d'augmenter progressivement au cours des siècles pour s'intensifier avec la révolution industrielle et s'accroitre de façon exponentielle depuis, le tout considéré comme une conséquence logique de la modernisation des activités économiques.

Pendant les trois dernières décennies, l'utilisation de l'énergie a dramatiquement augmenté partout dans le monde, en passant de 8,6 milliards de tonnes d'équivalent de pétrole (Gtep) en 1995 à 13,2 Gtep en 2015,[1] et ne va pas cesser d'augmenter tant dans les pays dits « développés » que dans les pays considérés comme émergents. Si l'on considère le besoin énergétique actuel de la Chine, son développement économique l'a amené à consommer la plus importante part de matières premières énergivores produites dans le monde.[1] La Chine est actuellement le pays avec la plus grande consommation énergétique, doublant presque celle des États-Unis, qui se place en deuxième place comme le montre la *Figure 1*.

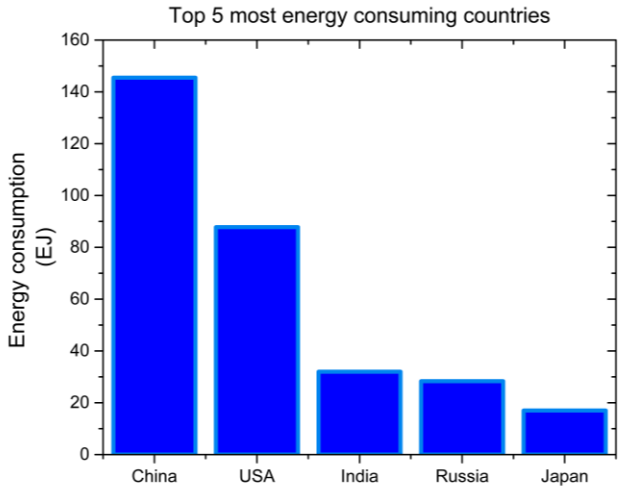

*Figure 1 La Chine en tête de la consommation énergétique mondiale avec 145,46 exajoules (EJ).*Adaptée.*[2]

La consommation énergétique mondiale repose sur les sources primaires d'énergie, qui peuvent prendre plusieurs formes et avoir différentes origines. En revanche, ces sources primaires d'énergie sont transformées en une source secondaire, l'électricité, qui peut être distribuée par des lignes électriques ou autres infrastructures de transport afin d'assurer la demande énergétique d'un complexe industriel voire d'un pays en entier. Trois sources

principales d'énergie pour la production d'électricité existent : fossile, nucléaire et renouvelable.

Les énergies non renouvelables ont longtemps été privilégiées, en raison d'un cout moins élevé que celles issues de sources renouvelables. L'importance croissante des problèmes environnementaux et le changement climatique provoqué par la production d'énergie à partir de combustibles fossiles sont devenus un problème mondial majeur, ce qui a fait que les technologies liées à la production d'énergie renouvelable sont considérées comme une solution pour réduire et atténuer les émissions de gaz à effet de serre dans l'atmosphère grâce à la production d'énergie propre.

L'énergie solaire fournit une source d'électricité ayant le taux de croissance le plus élevé et le plus abordable. Le soleil produit constamment de l'énergie et est donc considéré comme la source d'énergie renouvelable disponible la plus abondante. À travers l'histoire, elle a été utilisée comme énergie thermique pour cuisiner ou pour chauffer des fluides de travail comme l'eau pour des applications domestiques ou industrielles, mais plus récemment, elle a commencé à être utilisée pour transformer les rayons solaires en électricité à travers l'utilisation de dispositifs photovoltaïques (PV).

Les dispositifs PV sont des appareils électriques qui transforment la lumière du soleil directement en électricité en utilisant l'effet photovoltaïque. Elles sont traditionnellement faites à base de silicium et fonctionnent comme montré sur la *Figure 2*.

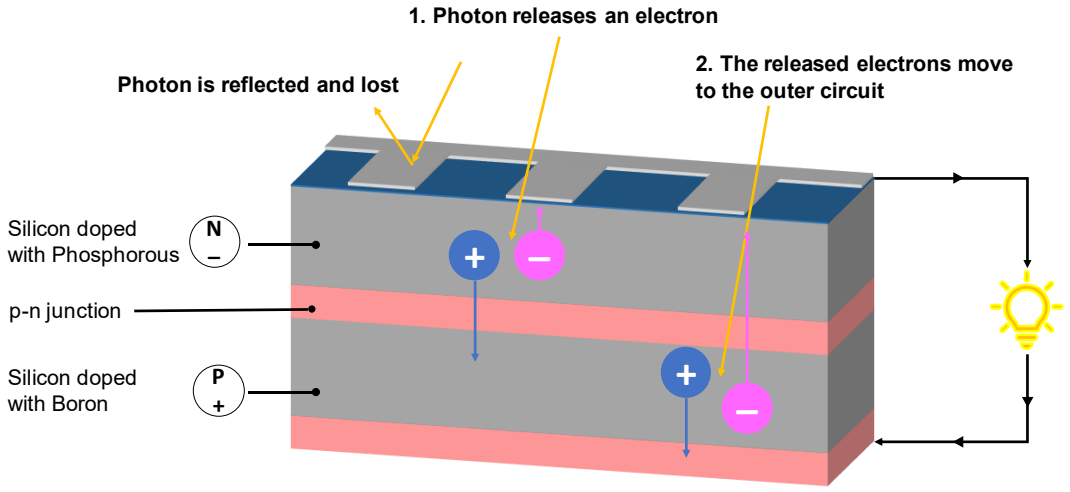

*Figure 2 Structure et principe de fonctionnement d'un dispositif photovoltaïque à silicium.*Adaptée.*[3]

L'évolution de l'industrie PV est remarquable à la vue des succès technologiques obtenus au niveau de la mise en forme, de l'installation, et des réductions des coûts. Par suite, les dispositifs solaires PV ont réussi à dominer l'industrie des énergies renouvelables. En outre, la dynamique de cette industrie permet régulièrement d'apporter des innovations intégrées rapidement dans la chaîne de production.

Le principal moteur de ces innovations a été la recherche d'une plus grande efficacité, ce qui est essentiel pour une fabrication compétitive de modules, car elle diminue directement les

coûts de traitement des cellules solaires en réduisant les quantités requises pour une puissance électrique donnée. La croissance future de l'industrie solaire PV dépend en grande partie de la réduction des coûts en utilisant des matériaux adéquats et c'est là que tous les développements de l'électronique organique deviennent pertinents.

Les semi-conducteurs organiques sont principalement faits à partir de carbone et hydrogène, avec quelques hétéroatomes comme le soufre, l'oxygène et l'azote. Ils sont souvent dotés d'un système d'électrons libres, cela est dû à l'exceptionnelle nature de l'atome de carbone, qui peut former différents types de structures à travers des liaisons covalentes σ et π.

Les liaisons σ sont formées par l'hybridation des orbitaux moléculaires entre atomes de carbone adjacents, tandis que les liaisons π sont formées par le chevauchement d'orbitaux d'atomes de carbone qui ne participent pas à la formation de liaison σ (*Figure 3*). Les liaisons σ sont relativement fortes et les électrons sont plus facilement localisables. En revanche, les électrons π sont largement délocalisés, ce qui rend les liaisons π plus faibles que les liaisons σ. Des molécules qui contiennent plusieurs électrons délocalisés sont connues comme systèmes conjuguées, cette délocalisation des électrons dote les semi-conducteurs organiques de propriétés remarquables.

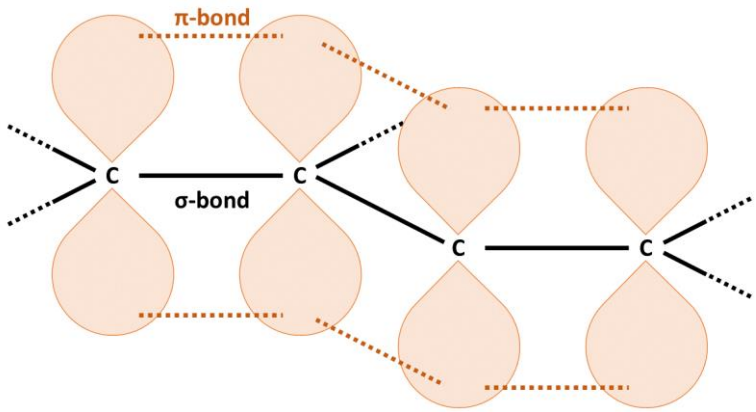

Figure 3 Représentation simplifiée d'une chaîne carbonée linéaire connectée par des liaisons σ et π.

Les semi-conducteurs organiques combinent les bénéfices chimiques et mécaniques des composés organiques avec les avantages des matériaux semi-conducteurs ; ce qui rend possible l'obtention de structures versatiles qui peuvent être modifiés par synthèse chimique pour améliorer leur capacité d'absorption de lumière ou leur conductivité électrique.

L'utilisation de composés organiques comme matériaux actifs dans des dispositifs électroniques et optoélectroniques a mené au développement de méthodes à bas prix pour fabriquer des structures qui soient utiles mais inaccessibles lorsqu'on utilise des semi-conducteurs traditionnels. Ils sont souvent utilisés en couche mince dans diverses applications comme l'affichage des écrans ou les cellules solaires.

Les qualités prometteuses des dispositifs organiques photovoltaïques (OPV) leur ont valu beaucoup d'attention, car ils ont la facilité de traitement en solution, des propriétés

électroniques modifiables, une basse température de fabrication et ils sont aussi relativement peu chers à produire et moins nocifs sur l'environnement.

Il existe plusieurs paramètres qui peuvent influencer la morphologie et la distribution spatiale moléculaire des semi-conducteurs organiques en couche mince, ce qui crée des opportunités pour ajuster les propriétés de transport. En plus, des changements de paramètres de traitement comme la vitesse de dépôt, le type de solvant utilisé ou la procédure de recuit peuvent entraîner des changements des propriétés du système.

La combinaison de tous ces paramètres gouverne donc la morphologie et la distribution spatiale moléculaire des semi-conducteurs organiques en couche mince, ce qui est essentiel pour obtenir une bonne performance électronique d'un système moléculaire.[4]

De plus, la morphologie des matériaux semi-conducteurs organiques peut aussi être modifiée par d'assemblages supramoléculaires. C'est le cas des systèmes π conjugués, qui ont tendance à former des agrégats et parfois même des grandes cristallites en fonction des conditions de traitement.[5]

En général, l'agrégation peut être contrôlée dès la conception moléculaire, le choix du solvant et les étapes du traitement thermique. Dans le cas de systèmes π conjugués comme les polymères, l'alignement des chaînes mène à une organisation au niveau microscopique ou mésoscopique, permettant la réalisation de structures supramoléculaires.

Les composés supramoléculaires sont considérés comme un groupe de molécules où chaque élément individuel confère à la globalité de l'assemblage de propriétés par des interactions non covalentes. Pendant les trente dernières années, l'auto-organisation des molécules utilisant des nombreuses interactions supramoléculaires a suscité beaucoup d'intérêt en raison du nombre important d'assemblages pouvant être réalisés, ayant des propriétés ajustables[6] parfois exceptionnelles.

Parmi les différentes interactions non covalentes utilisées en chimie supramoléculaire, les liaisons hydrogène (liaisons-H) présentent l'avantage de guider de manière efficace l'auto-assemblage des matériaux organiques rendant possible la modification des propriétés dans les procédés d'agrégation.

Une liaison-H est une interaction où un atome d'hydrogène est attiré par deux autres atomes, et pas par un seul atome comme habituellement, il agît donc comme un pont qui connecte les deux atomes comme montré sur la *Figure 4*, où l'espèce X–H est souvent connue comme le donneur, tandis que Y–Z est connue comme l'accepteur. La liaison-H est souvent décrite comme une interaction d'attraction dans laquelle un atome d'hydrogène électropositif intervient entre deux espèces électronégatives X et Y pour les rapprocher.

La liaison-H est assez forte pour maintenir ensemble les molécules XH et YZ à des températures normales et agît aussi dans une direction donnée pour que leurs associations soient spécifique à l'orientation. Malgré tout, selon la nature des espèces X et Y, elle peut s'affaiblir suffisamment pour permettre aux molécules de se séparer, ce qui entraîne une perte de la spécificité de l'orientation dans l'association de XH et YZ, comme c'est le cas des interactions hydrophobiques.[7]

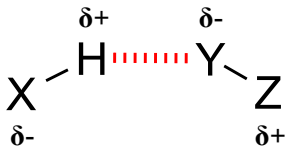

Figure 4 Représentation schématique des 4 espèces atomiques engagées dans une liaison-H.

Les liaisons-H peuvent déterminer la conformation moléculaire, l'agrégation et la fonctionnalité d'un grand nombre de systèmes chimiques, sans elles, les structures en bois collapseraient, le ciment s'émietterait, les océans s'évaporeraient et les êtres humains se désintègreraient en matière inerte.

Les éléments constitutifs des acides nucléiques naturels sont un des exemples les plus connus illustrant l'importance de la liaison hydrogène. Ces liaisons ont toujours été considérées très pertinentes dans les procédés biologiques, comme dans la reconnaissance entre la purine et la pyrimidine dans l'acide désoxyribonucléique (ADN) (*Figure 5*), ou dans la catalyse enzymatique et la formation des hélices α et β.[8]

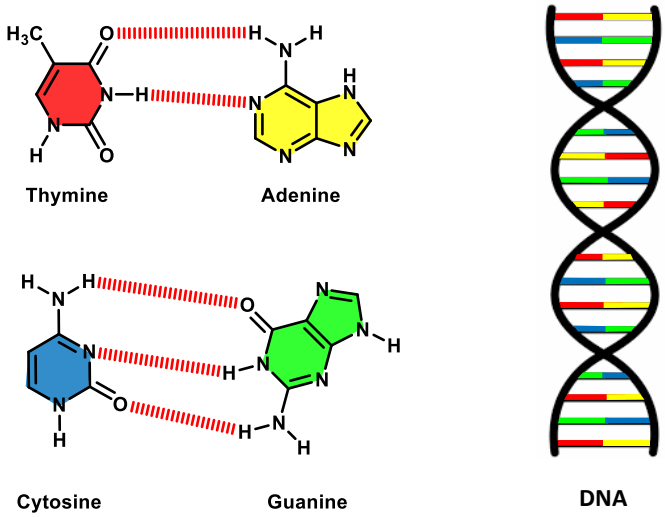

Figure 5 Reconnaissance moléculaire entre la purine et la pyrimidine qui créent les bases de l'ADN à travers la formation sélective des liaisons-H.

Étant donné que les interactions des liaisons-H sont si répandues dans la nature, il n'est pas surprenant qu'elles puissent également être exploitées comme outil de conception moléculaire pour obtenir des matériaux organiques semi-conducteurs et conducteurs. Par exemple, la liaison-H est cruciale pour les interactions supramoléculaires qui permettent la création de nombreux ensembles donneurs/accepteurs photo actifs.[9]

Il est possible de trouver dans la littérature plusieurs exemples où les liaisons-H sont utilisées pour des applications photovoltaïques, la *Figure 6* résume les cas les plus courants utilisés pour la fabrication de cellules solaires organiques, même si des exemples de transistors existent.[10]

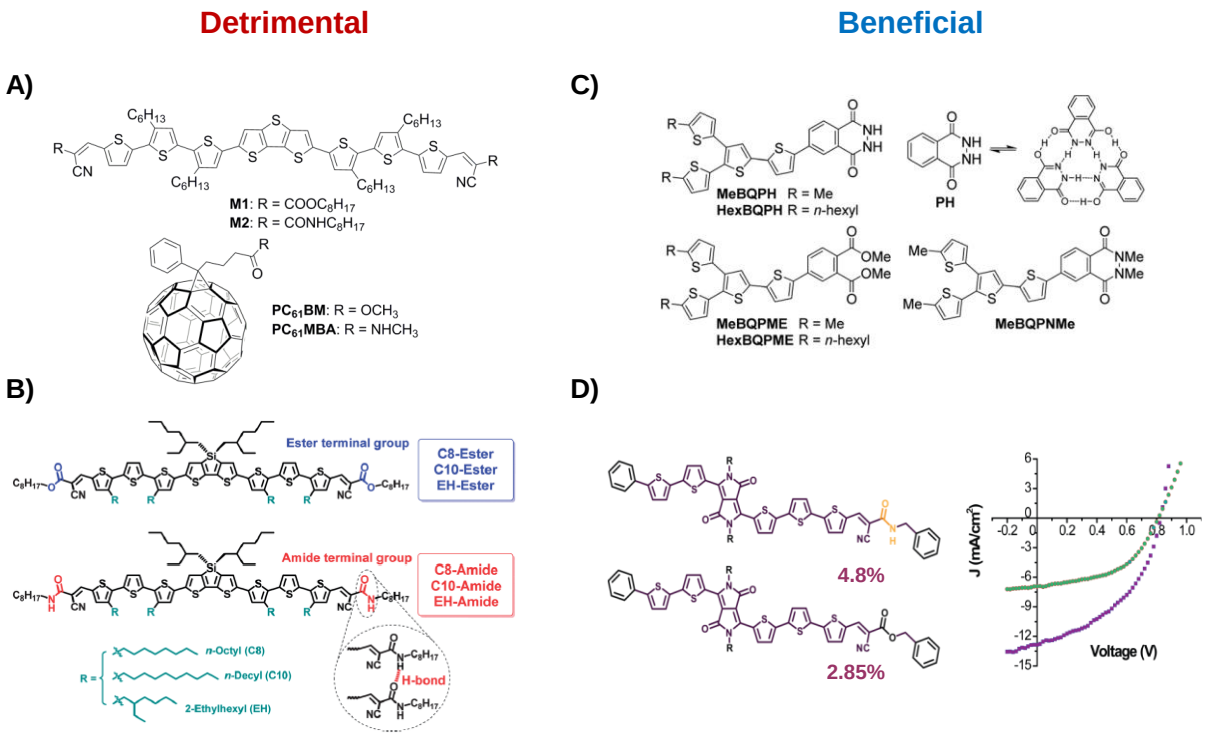

Figure 6 Exemples où des matériaux utilisés pour la fabrication des cellules solaires organiques portant de liaisons-H sont nuisibles (A et B) ou bénéfiques (C et D).

Néanmoins, des résultats contradictoires sont souvent décrits pour les cas où des matériaux donneurs et accepteurs portent des groupes capables de former des liaisons-H et aussi pour des cas où seulement un des éléments a la capacité de les former. Les *Figure 6*A et *Figure 6*B montrent deux cas où des oligo-thiophènes ont été modifiés pour porter des groupes amides ou ester à la périphérie.[11,12]

Dans les deux cas, du chloroforme a été utilisé pour préparer le mélange de matériaux d'accepteur et donneur, ce qui d'un point de vue supramoléculaire n'est pas le meilleur choix car il est souvent utilisé comme « un bon solvant » pour éviter l'agrégation. Par ailleurs, dans ces deux travaux de recherche, l'efficacité de la cellule solaire est inférieure lorsque les mélanges sont faits avec des dérivés capables de former des liaisons-H.

Par ailleurs, même si les structures moléculaires des exemples montrés sur la *Figure 6*C et la *Figure 6*D sont différentes, en comparaison à la similarité qui existe entre les deux exemples présentés précédemment, des résultats contradictoires sont obtenus. En l'occurrence, dans le cas de la *Figure 6*C, les auteurs démontrent que la molécule sans capacité de former des liaisons-H a besoin du double de concentration pour obtenir une efficacité semblable à celle de sa contrepartie qui peut former des liaisons-H, mais qui a majoritairement pour désavantage un faible courant de court-circuit.[13] En outre, dans l'exemple de la *Figure 6*D, une efficacité plus grande est obtenue pour le dérivé du dicétopyrrolopyrrole (**DPP**) portant des groupes amides.[14]

Il est évident qu'il n'existe pas de consensus sur l'impact positif ou négatif des matériaux portant des liaisons-H sur les dispositifs solaires. Cependant, il est important de remarquer qu'il n'est pas possible de comparer tous les différents paramètres entre ces études. La différence entre les divers paramètres présentés comme : le type de système π conjugué, le type d'unité qui peut former des liaisons-H, le solvant choisi et la proportion de

donneur/accepteur utilisé, parmi d'autres, est trop vaste. Ce qui rend difficile la tâche de faire une comparaison significative. De plus, le manque d'études de l'auto-assemblage dans la plupart des cas, néglige l'information concernant le type de structures formées par les systèmes à liaisons-H, ce qui est essentiel pour comprendre la performance des dispositifs.

Pour cette raison, le but de cette thèse est de déterminer l'impact des liaisons-H sur les propriétés optoélectroniques des semi-conducteurs organiques en faisant des études systématiques et comparatives en utilisant le **DPP** comme système modèle. En plus, cette étude systématique vise à identifier les conditions nécessaires pour pouvoir fabriquer des dispositifs électroniques efficaces.

Les **DPPs** sont des molécules qui ont été largement étudiées et sont parmi les meilleurs éléments électro-actifs utilisés pour des applications dans le domaine des semi-conducteurs[15,16] depuis leur découverte par Farnum dans les années 70, lorsqu'il essayait d'obtenir une azetinone.[17] Le **DPP** est un des pigments le plus utilisé pour des applications industrielles et dans la recherche de nouveaux matériaux. Plusieurs exemples de polymères et d'oligomères peuvent être trouvés pour la fabrication de cellules organique solaires[18], de transistors organiques[19,20], et de capteurs.[21,22]

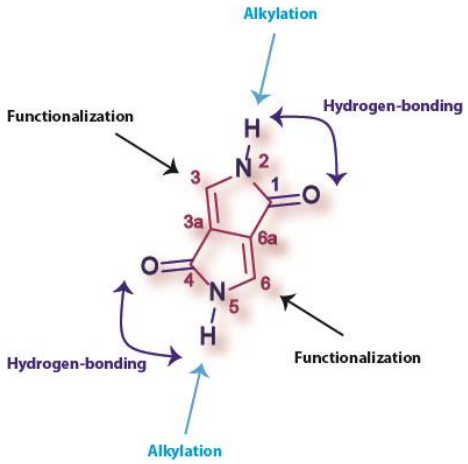

*Figure 7 Structure chimique détaillée d'un **DPP** avec la numération correspondante de ses atomes, des groupes capables de former des liaisons-H et de ses principales positions de fonctionnalisation.*

La structure chimique d'une molécule de 2,5-Dihydropyrrolo[4,3-c] pyrrolo-1,4-dione est présentée sur la *Figure 7*, et jusqu'à présent il n'existe pas des rapports de la synthèse de cette structure. Les dérivés de **DPP** les plus connus portent souvent des substituants aromatiques sur les positions -3 et -6, bien qu'il existe aussi des composés avec des groupes aliphatiques.[23,24]

Le **DPP** étant déjà une molécule possédant déjà des liaisons-H, à cause de son insolubilité, on peut l'employer dans les techniques de dépôt sous vide ou l'utiliser comme un pigment latent après un traitement thermique ou acide. Mais grâce à la possibilité de fonctionnalisation du noyau **DPP**, il est possible d'introduire plusieurs types de groupes capables de former des liaisons-H, ce qui rend possible l'étude de son agrégation en solution et son utilisation pour la fabrication de dispositifs.

Une stratégie très utilisée pour rajouter des liaisons-H dans la structure moléculaire du **DPP** consiste à rattacher des groupes amides à la périphérie des groupes aromatiques qui sont liés au noyau central du **DPP**.

Cette thèse porte sur une étude systématique utilisant comme système modèle un élément électro actif de **DPP** portant des thiophènes rattachés au noyau. Plusieurs paramètres en rapport aux liaisons-H seront testés, puis cette étude sera étendue aux semi-conducteurs de pointe comme les rhodanines[25,26] ou l'isoindigo[27,28]. Finalement, l'étude sera étendue à des molécules d'accepteurs et des mélanges donneur-accepteur y compris les fullerènes et accepteur non basés sur les fullerènes.[29,30]

Dans cette thèse, l'influence de différents paramètres sera évaluée, en l'occurrence :

- ✓ **Le type de groupe capable de former la liaison-H :** Amides, urées, systèmes auto-complémentaires et autres.
- ✓ **La position des liaisons-H** dans la structure moléculaire : en périphérie ou intégrée dans les chaînes.
- ✓ **La solubilité** : différentes longueurs et ramifications des chaînes alkylées.
- ✓ **La topologie** des liaisons-H dans les bras amide.
- ✓ **La chiralité** dans les bras attachés au noyau **DPP**.

Le **DPP** a été choisi comme système modèle en raison de ses grandes propriétés optoélectroniques et sa versatilité de fonctionnalisation, ainsi que de la possibilité qu'il fournisse une vision globale de l'influence des liaisons-H dans l'organique électronique et pour explorer la généralité des résultats, lorsqu'ils sont transposés à tout autre semi-conducteur.

Jusqu'à présent, plusieurs familles de **DPP** portant des liaisons-H ont été étudiées et sont présentées sur la *Figure 8*. Cette thèse abordera l'étude de trois de ces familles, en particulier le chapitre II couvrira la famille des bisamides[31] (*Figure 8*b). Le chapitre III abordera l'étude de l'expansion de la famille des bisamides avec une solubilité améliorée et des changements en topologie (*Figure 8*d). Ensuite, dans le chapitre IV l'impact de garder le même type de chaîne alkyle, alors que la position et la topologie des groupes amides change sera discuté (*Figure 8*e). Enfin, dans le chapitre V des résultats préliminaires sur l'impact des changements du solvant sur la morphologie et l'orientation des agrégats formés par les dérivés décrits dans le chapitre III seront présentés.

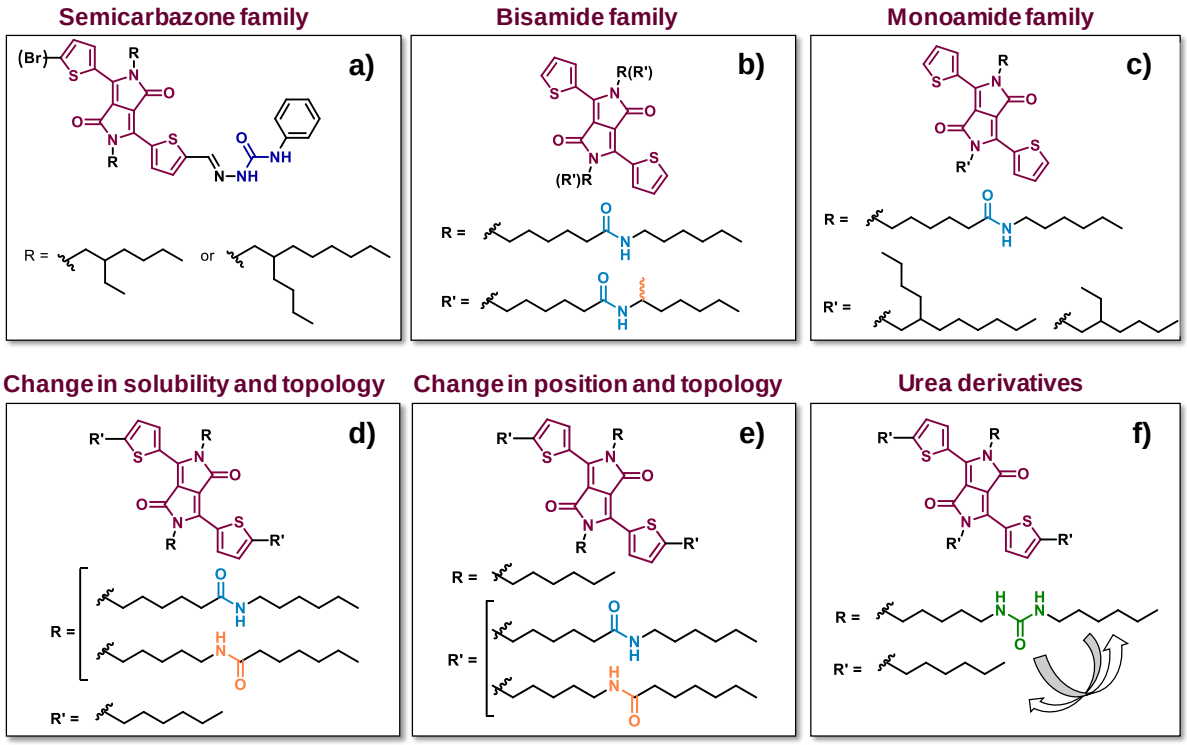

*Figure 8 Familles de **DPPs** portant des liaisons-H synthétisés jusqu'à présent dans l'étude systématique des **DPPs** comme système modèle.*

Chapitre II : Exploration de la fonction amide

Pour ce chapitre, une attention particulière est accordée aux dérivés de **DPP** capables de former des liaisons-H, en utilisant des groupes amides couplés et rattachés au noyau π conjugué par une chaîne flexible à six carbones. Cette conception a été choisie parce que notre groupe a commencé des études systématiques avec des dérivés contenant des semicarbazones directement rattachées au noyau **DPP**.[32]

Les dérivés de semicarbazone donnent des molécules très rigides avec une solubilité limitée et avec une dynamique de recombinaison rapide lorsque leurs propriétés de photoconductivité ont été criblées. Néanmoins, leurs propriétés d'auto-assemblage et morphologiques fournissent des informations très utiles pour poursuivre la conception de nouvelles familles de **DPP** portant des liaisons-H.

Dans cette partie de la thèse, des molécules complètement différentes ont été conçues, leur fonctionnalisation a été faite sur le lactame et non pas sur le thiophène, comme pour les dérivés de semicarbazone (Figure 9). La liaison-H a aussi été espacée à travers une chaîne flexible, pour comparer les processus d'auto-assemblage. Enfin, la chiralité a été introduite comme paramètre d'étude et un centre chiral à côté de la fonction amide a été rajouté.

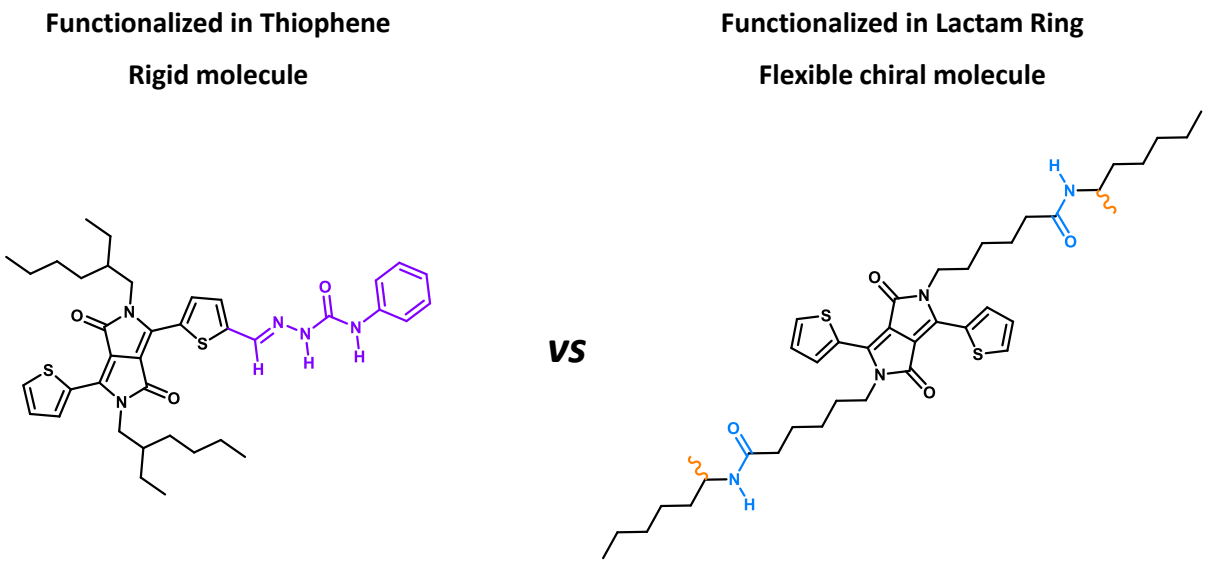

Figure 9 Comparaison structurelle entre la famille semicarbazone et la famille des bisamides.

Le groupe amide a été choisi, car il s'agit de l'un des groupes de liaisons-H le plus exploré historiquement et qui peut être retrouvé dans tous les domaines de la chimie.[33] Il est un candidat parfait pour étudier les processus d'auto-assemblage dans lequel l'agrégation H et J sont impliquées grâce à leurs procédures de synthèse, bien connues pour leur capacité d'être rajoutés dans tout type de molécules et aussi à leur facilité de caractérisation par des techniques de spectroscopie, telles que la spectroscopie infrarouge.

L'autre paramètre qui a été évalué pour cette famille de **DPPs** est la chiralité, qui peut aussi avoir un impact sur les propriétés d'autoassemblage et dans le cas des semiconducteurs, sur les propriétés optoélectroniques.[34,35] La chiralité a déjà été évaluée dans des dérivés du **DPP**, principalement en rajoutant des chaînes alkyle chirales comme le 2-ethylhexyl[36–39], des molécules d'hélicène,[40] ou en rajoutant des dérivés du myrtenal.[41]

Ici, la synthèse des dérivés fonctionnalisés sur le lactame (comme montré sur la Figure 9) est décrite, ainsi que la caractérisation de leurs propriétés optiques et d'autoassemblage, ce qui aidera dans la compréhension des propriétés de transport de charge qui ont été mesurées à l'aide d'une technique sans électrodes basée sur la conductivité de micro-onde.

Le noyau de **DPP** a été synthétisé par la réaction de cyclisation entre le 2-thiophènecarbonitrile et le diéthyl succinate, en suivant un protocole déjà décrit.[42] Trois molécules finales, **DPPBA, (S)-DPPBA** et **(R)-DPPBA**, ont été obtenues via des réactions d'alkylation avec des bras amides contenant un mésilate (*Schéma 1*). Ces bras amides ont été obtenus en faisant réagir la ε-caprolactone avec des dérivés d'amine (achiraux et chiraux) et en rajoutant le groupe mésilate par la suite. La **DPP** a été N-alkylé en utilisant le carbonate de césium comme base pour déprotoner et la DMF a été utilisée comme solvant, comme mentionné dans d'autres alkylations de **DPP**.[43,44] Les rendements sont faibles (10%) en raison de réactions additionnelles qui conduisent à des sous-produits isolés et identifiés, comme les isomères O-alkylés.

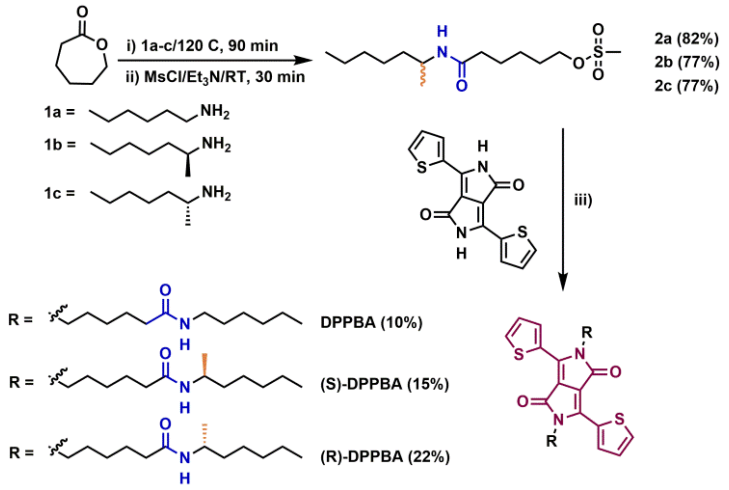

*Schéma 1 Approche synthétique pour produire **DPPBA**, **(S)-DPPBA** et **(R)-DPPBA**. iii) Irradiation par micro-onde (P = 150 W, DMF, 2 h, 120 ºC pour **(S)-DPPBA** et P = 150 W, DMF, 2h, 70 ºC pour **(R)-DPPBA**).*

Une fois les molécules synthétisées, on a procédé à l'étude des propriétés optiques et d'autoassemblage. En particulier, on a utilisé les techniques spectroscopiques d'absorption d'UV/vis, d'infrarouge et de dichroïsme circulaire, en solution et à l'état solide, pour comprendre les processus d'assemblage des trois dérivés. La microscopie électronique en transmission (MET) a aussi été utilisée pour étudier la formation des structures supramoléculaires.

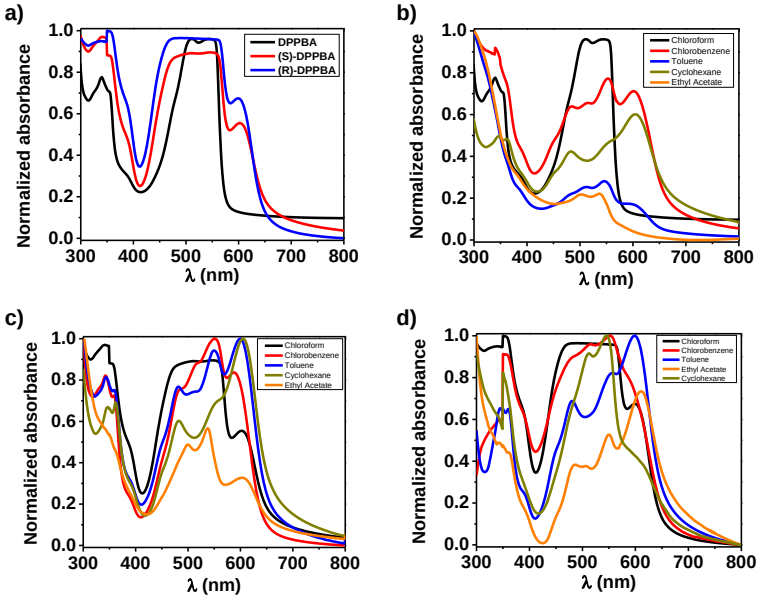

*Figure 10 a) Spectre d'absorption en chloroforme pour **DPPBA**, **(S)-DPPBA** et **(R)-DPPBA**. La concentration est de 2,5 mg/ml dans tous les trois cas. Spectres d'absorption dans différents solvants pour b) **DPPBA** ; c) **(S)-DPPBA** ; et d) **(R)-DPPBA**, la concentration est de 2,5 mg/ml pour tous les solvants, sauf pour le chloroforme (1.6 mg/ml) dans les figures c) et d).*

Au début les trois composés dissouts dans le chloroforme (2,5 mg/ml) ont été étudiés. Il a été observé que les spectres des trois dérivés présentent des larges bandes d'absorption entre 415 et 600 nm à 20 °C (*Figure 10*a). Les dérivés chiraux présentent eux une bande

d'absorption additionnelle à des énergies plus basses, vers 600 nm (*Figure 10*a, lignes rouge et bleue).

Cette bande n'est pas observée pour **DPPBA**, même dans des solutions très concentrées. Cette bande peut être attribuée à la formation d'agrégats de type J, comme pour des dérivés de **DPP** portant des liaisons-H, y compris les dérivés de **DPP** semicarbazone reportés par notre équipe.[32,45,46] Ce signal est lié à la formation des liaisons-H, puisqu'il disparaît lorsqu'on rajoute du méthanol (un solvant qui rentre en compétition avec les liaisons-H) à des solutions de **(S)-DPPBA** et **(R)-DPPBA**.

Les propriétés optiques ont aussi été mesurées dans différents solvants : toluène, chlorobenzène, cyclohexane et acétate d'éthyle. Dans ces solvants, pour les trois dérivés, les bandes d'agrégats J deviennent encore plus intenses que pour le cas du chloroforme (*Figure 10*b à d). Un épaulement se produit vers 480 nm dans plusieurs solvants, ce qui est attribué à la formation d'agrégats de type H.

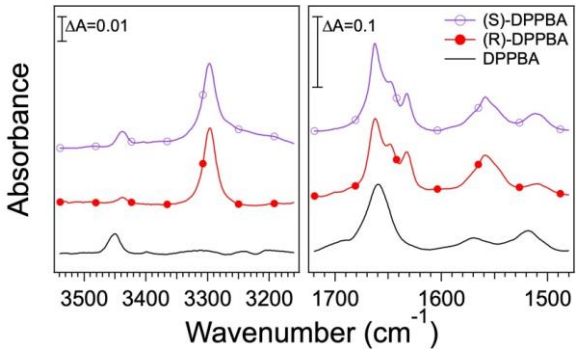

Figure 11 Spectre IRTF à température ambiante dans du chloroforme deutéré pour ***(S)-DPPBA****,* ***(R)-DPPBA*** *et* ***DPPBA****.*

Des spectres IRTF en solution utilisant du chloroforme deutéré comme solvant prouvent l'existence de liaisons-H dans ces dérivés bisamides (*Figure 11*). **DPPBA** présente une bande à 3450 cm^{-1} pour l'élongation de la liaison NH, ce qui est caractéristique des groupements amides libres. Cela prouve que **DPPBA** ne forme pas des liaisons-H dans le chloroforme. Un autre signal est vu vers 1659 cm^{-1}, ce qui correspond aussi à des amides libres.

D'un autre côté, à température ambiante, **(S)-DPPBA** et **(R)-DPPBA** présentent de bandes vers 3439 cm^{-1} et 3297 cm^{-1} dans la région de l'élongation de la liaison NH. La première bande est attribuée à un groupe amide libre comme pour le cas précèdent, la deuxième bande correspond à des groupes amides engagés dans des liaisons-H. Par conséquent, **(S)-DPPBA** et **(R)-DPPBA** forment partiellement des liaisons-H en solution.

Dans le domaine situé entre 1600 cm^{-1} et 1700 cm^{-1}, **(S)-DPPBA** et **(R)-DPPBA** présentent trois pics vers 1632 cm^{-1}, 1648 cm^{-1} et 1663 cm^{-1}. Les deux premiers pics correspondent à des groupes amide engagés dans des liaisons-H fortes et faibles respectivement[47], tandis que le troisième pic correspond à un groupe amide libre, comme observé pour **DPPBA**.

Des mesures en diluant la concentration et en faisant varier la température ont aussi été faites pour continuer à explorer le processus d'agrégation. Les bandes d'agrégats J sont observées après dilution, même à des concentrations faibles dans les solvants qui favorisent la formation des liaisons-H. Lorsque la température augmente, les bandes d'agrégats J sont toujours

présentes, ce qui met l'accent sur la formation d'agrégats, même à haute température (*Figure 12*).

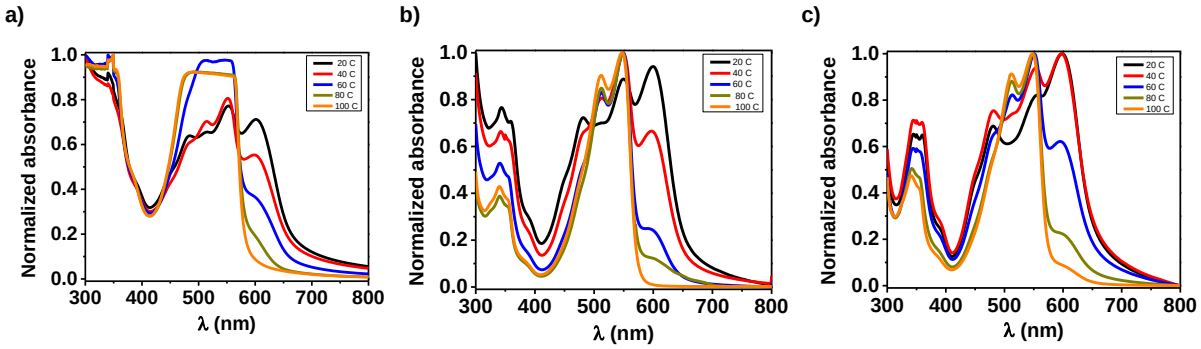

*Figure 12 Spectres d'absorption pour **DPPBA** dans le chlorobenzène, et pour **(S)-DPPBA** et **(R)-DPPBA** dans le toluène, lors de l'augmentation en température. La concentration dans tous les cas est de 2,5 mg/ml.*

Cette tendance a été observée pour les trois dérivés, mais pour les dérivés chiraux, la bande d'agrégats J disparaît à très hautes températures et à des faibles concentrations lorsqu'on les compare avec le dérivé achiral. Ce qui prouve que les dérivés chiraux forment des agrégats plus stables que le dérivé achiral correspondant.

Pour étudier les dérivés chiraux, des mesures de dichroïsme circulaire en solution ont été faites, et des signaux avec un fort effet Cotton sont retrouvés pour les dérivés chiraux, mais pas de signal pour **DPPBA**, même dans des conditions d'agrégation.

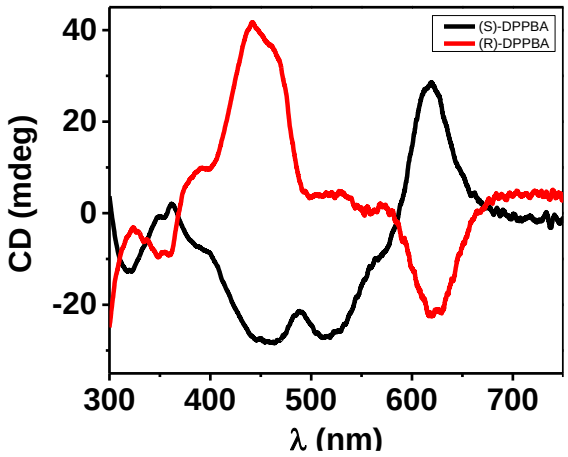

*Figure 13 Spectre de dichroïsme circulaire pour **(S)-DPPBA** et **(R)-DPPBA** dans une solution de toluène. [**(S)-DPPBA**] = [**(R)-DPPBA**] = 2,5 mg/ml.*

La *Figure 13* montre un spectre de dichroïsme circulaire pour **(S)-DPPBA** et **(R)-DPPBA** à température ambiante. Des forts signaux ont été trouvés, spécialement à la longueur d'onde de l'agrégat J, indiquant un transfert de chiralité à travers les agrégats.

Des études morphologiques ont été faites par MET en déposant des solutions de ces dérivés dans les différents solvants utilisés précédemment. Dans chaque solvant, des clichés avec des structures ayant des rapports d'aspect différent ont été obtenus pour les trois dérivés. Les dérivés chiraux présentent des structures hélicoïdales dans presque tous les solvants, tandis que **DPPBA** présente différentes structures unidimensionnelles (*Figure 14*).

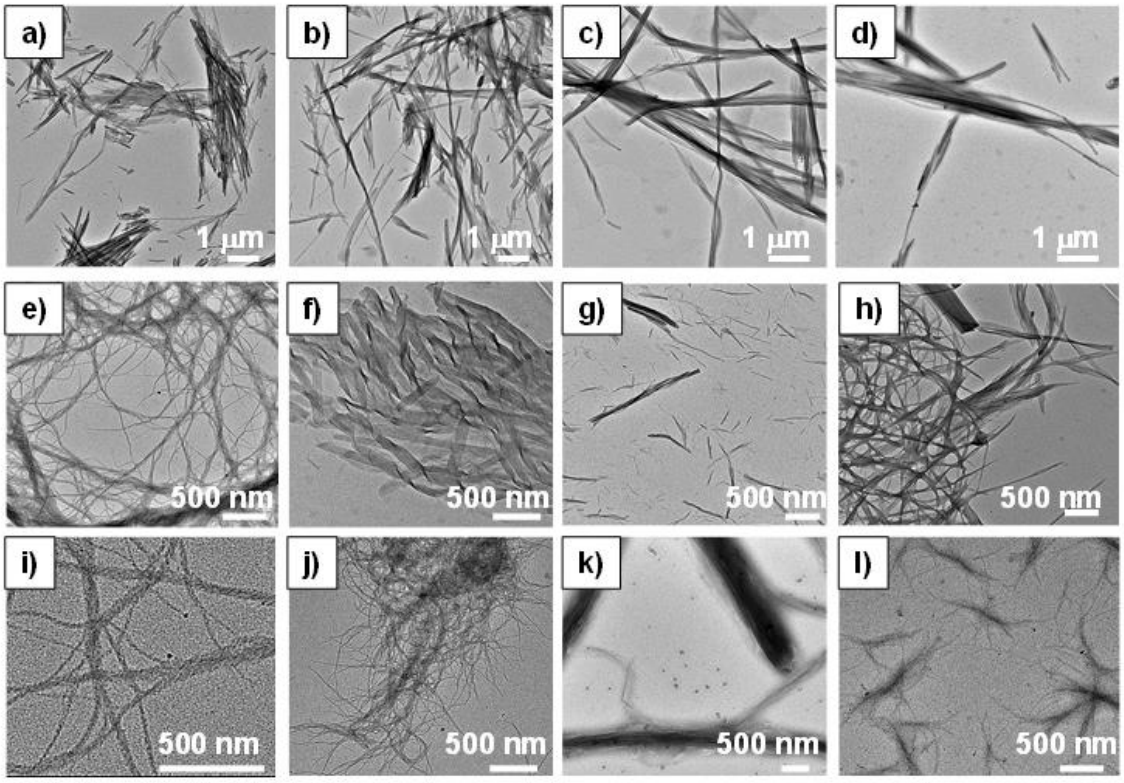

Figure 14 Clichés de MET pour ***DPPBA*** *(a-d),* ***(S)-DPPBA*** *(e-h) et* ***(R)-DPPBA*** *(i-l) dans chlorobenzène, toluène, cyclohexane et acétate d'éthyle respectivement.*

Après avoir exploré la capacité d'agrégation de ces molécules, leurs propriétés électriques ont été examinées. Les propriétés de photoconductivité ont été explorées en utilisant une technique sans électrodes basée sur la conductivité de micro-ondes (FP-TRMC). Ces mesures indiquent que **DPPBA** possède des valeurs supérieures de photoconductivité, ainsi qu'un temps de recombinaison des transporteurs de charge plus lent. Les mesures cinétiques de photoconductivité sont représentées sur la *Figure 15* et les valeurs de la photoconductivité déduite sont reportées dans le *Tableau 1*.

L'importance des liaisons-H a été mise en évidence lorsque des échantillons ont été mis en présence de vapeurs des solvants. Cette exposition favorise l'auto-assemblage, ce qui a été confirmé par l'augmentation de la photoconductivité.

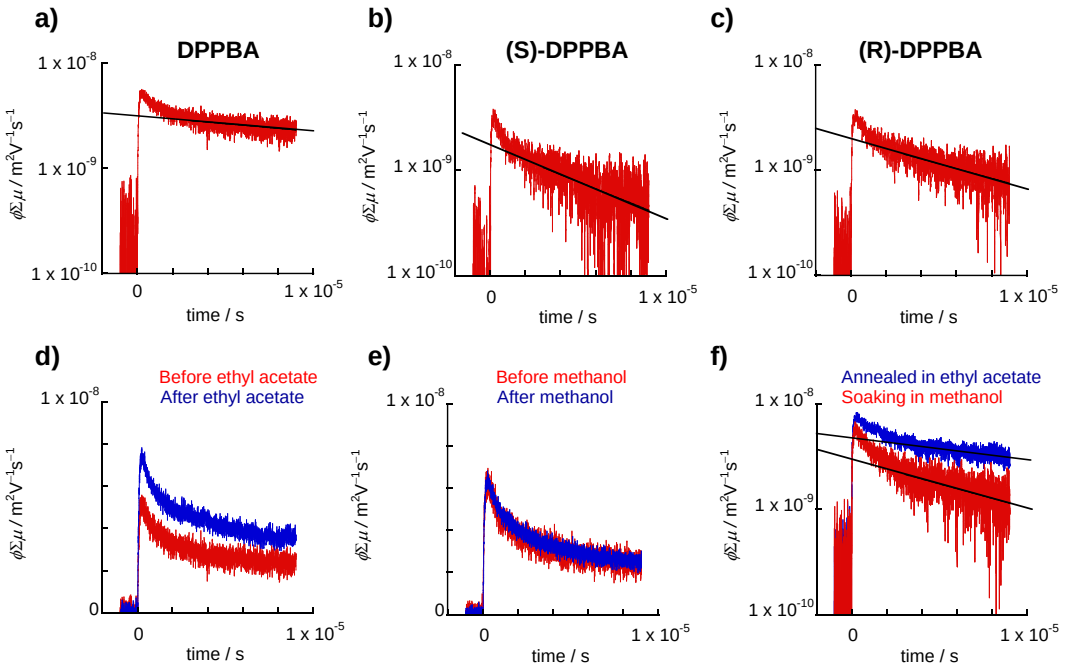

*Figure 15 Cinétiques de la photoconductivité pour **DPPBA** (a), **(S)-DPPBA** (b) et **(R)-DPPBA** (c) échantillons déposés à partir du chloroforme. Cinétiques de photoconductivité pour **DPPBA** avant et après recuit en présence de vapeur d'acétate d'éthyle (d), avant et après recuit en présence de vapeur de méthanol (e) et après l'avoir immergé dans du méthanol (f).*

Tableau 1 Valeurs de photoconductivité des trois dérivés avant et après recuit en présence de vapeur de solvant.

Composé	$\Phi\Sigma\mu$ ($cm^2V^{-1}s^{-1}$) Avant recuit au solvant	Type de solvant	$\Phi\Sigma\mu$ ($cm^2V^{-1}s^{-1}$) Après recuit au solvant
DPPBA	5×10^{-5}	Acetate d'éthyle	7×10^{-5}
DPPBA	6×10^{-5}	Méthanol	7×10^{-5}
(S)-DPPBA	3×10^{-5}	Acetate d'éthyle	3×10^{-5}
(S)-DPPBA	3×10^{-5}	Méthanol	2×10^{-5}
(R)-DPPBA	3×10^{-5}	Acetate d'éthyle	3×10^{-5}
(R)-DPPBA	4×10^{-5}	Méthanol	4×10^{-5}

En revanche, les valeurs de photoconductivités ont beaucoup diminué lorsque les échantillons ont été immergés dans des solvants en compétition avec les liaisons-H. Cet effet n'a pas été observé pour les dérivés chiraux, ce qui indique que le centre chiral à côté de la liaison-H encombre le transport de charges. Ces résultats ont aidé à la conception des prochains composés **DPPs** qui seront étudiés par la suite.

Chapitre III : Expansion de la famille bisamide : influence de la topologie et de la solubilité

Pour optimiser la conception de dérivés à liaisons-H et compléter notre bibliothèque, nous avons testé d'autres paramètres ayant un impact sur la formation de liaisons-H. Pour cela, nous avons d'abord choisi d'augmenter la solubilité des dérivés présentés au chapitre II. Nous avons également examiné l'impact de la topologie des amides sur l'auto-assemblage et sur les propriétés électroniques.

Pour améliorer la solubilité des **DPPs**, les thiophènes du noyau ont été fonctionnalisés avec des chaînes hexyl et les bras amides ont été placés sur les lactames (*Figure 16*).

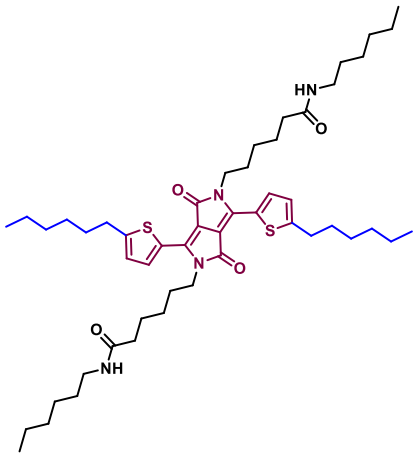

*Figure 16 Structure chimique d'un **DPP** bisamide alkylé sur les thiophènes.*

Deux dérivés de **DPP** contenant des groupes amide attachés aux lactames, avec une topologie centrée sur l'azote (centré-N) ou le carbone (centré-C), et portant des chaînes alkyles sur les thiophènes ont été synthétisés. Une comparaison entre ces deux nouvelles molécules a été réalisée, ainsi qu'une comparaison de cette nouvelle famille à la famille présentée au chapitre II. Avec ces deux nouveaux dérivés, une molécule de **DPP** ne portant que des chaînes hexyle, sur les lactames et les thiophènes, a également été synthétisée comme une molécule de contrôle qui ne peut pas former des liaisons-H.

Les processus d'auto-assemblage des **DPPs** centré-N et centré-C ont été suivis à nouveau par des techniques de spectroscopie et de microscopie. Les propriétés de transport de charges ont été étudiées par FP-TRMC et les résultats ont été comparés aux résultats obtenus avec la molécule de contrôle, ce qui met en évidence l'impact positif des liaisons-H sur les propriétés électroniques.

Dans ce cas, une approche de cyclisation succinique a été conçue, elle consiste à alkyler un thiophène et le fonctionnaliser pour enfin réaliser la réaction de cyclisation normalement utilisée lorsqu'on obtient un noyau de **DPP**.

Les molécules **HDPPBA-C** et **HDPPBA-N** ont été synthétisées *via* l'approche de cyclisation succinique (*Schéma 2*). Un thiophène est d'abord alkylé avec du bromure d'hexyle pour produire le dérivé **1** avec un rendement de 82%, puis, un atome de brome est introduit en position 5 pour produire **2**. Ensuite, le brome est remplacé par un nitrile, pour produire le 5-

hexylthiophene-2-carbonitrile (**3**), qui en présence de diéthyl succinate et t-butoxide de potassium réagi pour produire un **DPP** fonctionnalisé sur les thiophènes, le dérivé **4**, avec un rendement de 72%. Dans l'étape finale, les lactames sont alkylés avec des groupes amides, qui ont été synthétisés en parallèle et qui présentent des topologies différentes.

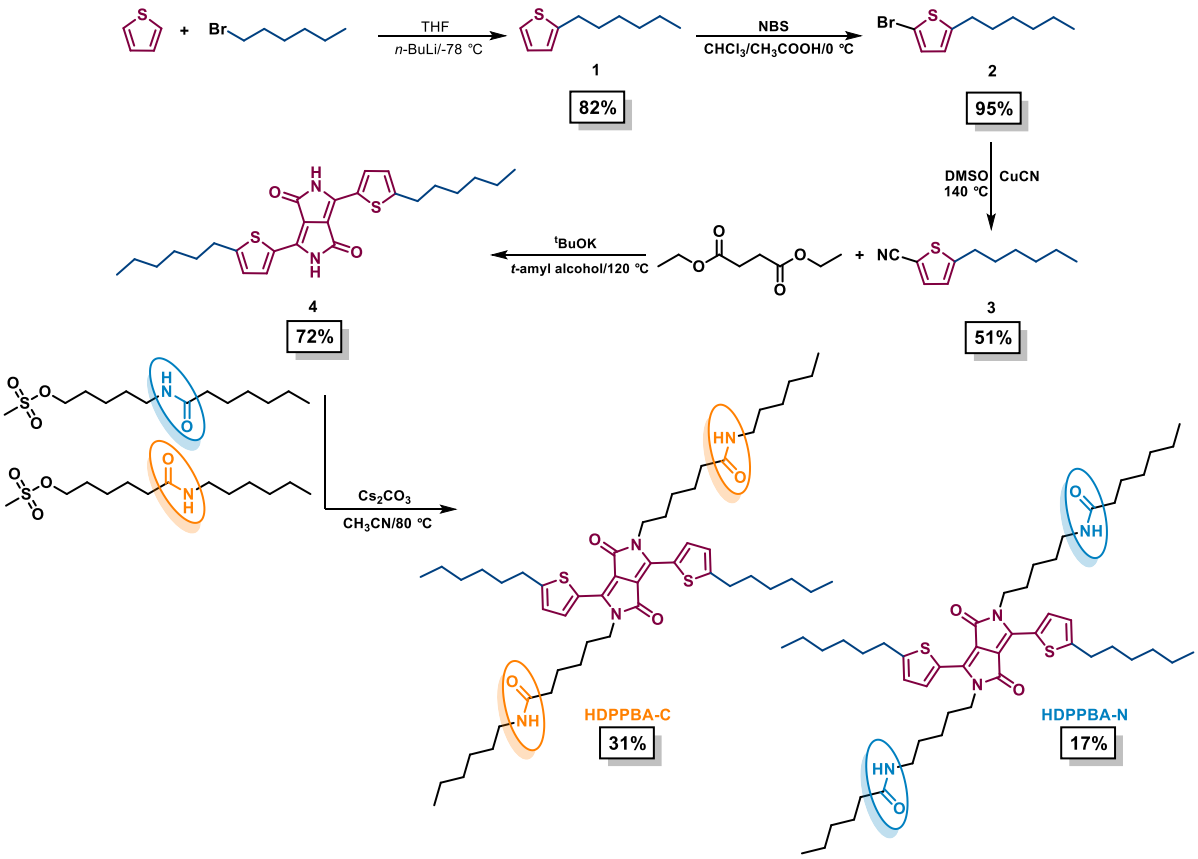

*Schéma 2 Approche synthétique pour obtenir **HDPPBA-C** et **HDPPBA-N.***

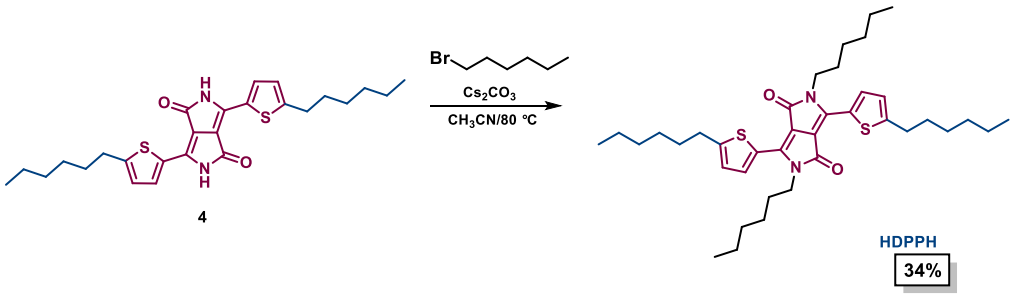

*Schéma 3 Alkylation de **4** pour obtenir **HDPPH**.*

La molécule de contrôle **HDPPH** a été synthétisée en suivant la même stratégie, mais les lactames sont ici alkylés avec du bromure d'hexyle (*Schéma 3*).

Les propriétés optiques et d'autoassemblage de **HDPPBA-C**, **HDPPBA-N** et **HDPPH** ont été suivies par spectroscopie d'absorption UV-vis, en solution et en couche mince, à température variable pour différents solvants en fonction de la concentration, ainsi que par IRTF. En

présence de chloroforme, les deux dérivés amide et la molécule de contrôle absorbent entre 400 et 600 nm à 20 °C.

Les trois molécules ne montrent aucun signal d'agrégation dans le chloroforme à 20 °C et les bandes d'absorption ne changent pas lorsque la solution est chauffée, ou lorsque sa concentration est modifiée (*Figure 17*). Des bandes supplémentaires apparaissent pour des énergies plus basses lorsque les mesures de **HDPPBA-C** et **HDPPBA-N** sont réalisées dans des solvants différents comme le chlorobenzène, le toluène et l'acétate d'éthyle (*Figure 18* a et b). On remarque que la bande située vers 620 nm n'est pas présente pour la molécule **HDPPH**, qui présente un spectre similaire dans tous les autres solvants (*Figure 18*c).

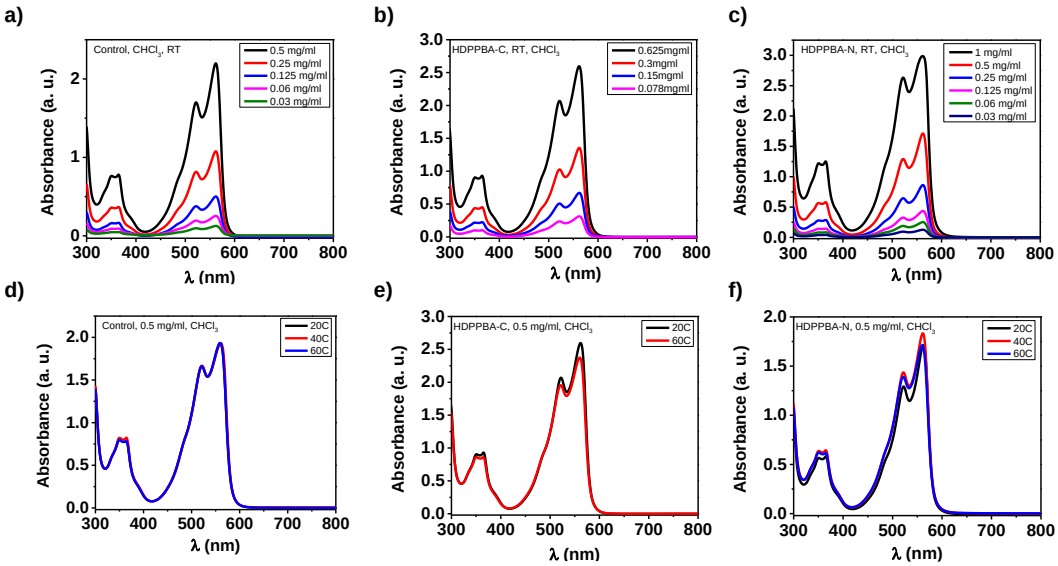

Figure 17 Spectres d'absorption en chloroforme à différentes concentrations et températures pour a), d) ***HDPPBA-C*** *; b), e)* ***HDPPBA-N*** *et c), f)* ***HDPPB****.*

Cette bande peut être attribuée à la formation d'agrégats J, comme cela est observé pour la famille de DPP décrite au chapitre II et dans la littérature.[31,48–50] En outre, les différences entre les dérivés amide et la molécule de contrôle, suggèrent que les liaisons-H sont impliquées dans la formation de ce type d'agrégat. Cette interprétation est confirmée par les spectres UV-vis lors de l'ajout de méthanol, où on observe que la bande d'agrégats J disparaît comme pour la famille précédente.

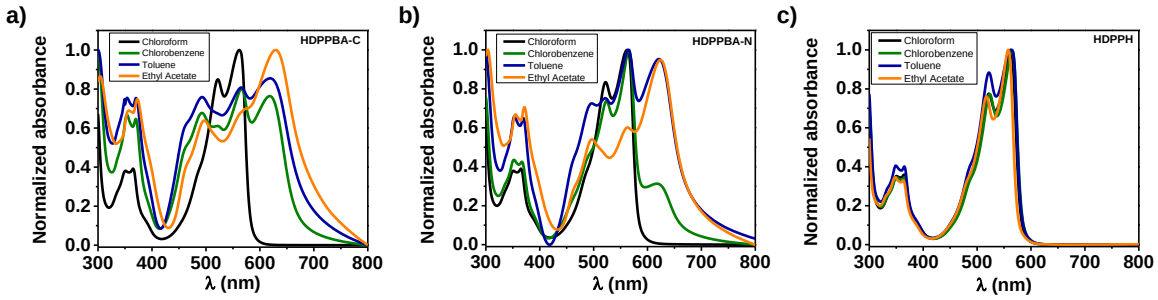

*Figure 18 Spectres d'absorption pour a) **HDPPBA-C**, b) **HDPPBA-N** et c) **HDPPH** à température ambiante dans différents solvants (chloroforme, chlorobenzène, toluène et acétate d'éthyle).*

Le spectre IRTF en poudre à température ambiante prouve l'existence des liaisons-H pour les dérivés amide. **HDPPBA-C** et **HDPPBA-N** présentent une bande vers 3303 cm^{-1}, attribué à l'élongation des groupes NH des amides. Cette fréquence révèle que les amides forment des liaisons-H (*Figure 19* à gauche). Dans la région entre 1600 cm^{-1} et 1700 cm^{-1}, les composés amide et la molécule de contrôle, présentent un pic vers 1655 cm^{-1}, ce qui correspond à la bande amide I des lactames du noyau **DPP**. Dans cette même région, les pics vers 1641 cm^{-1} et 1637 cm^{-1} pour **HDPPBA-C** et **HDPPBA-N** respectivement, correspondent à des groupes amide engagés dans des liaisons-H (*Figure 19* à droite). Les bandes amide II se trouvent vers 1550 cm^{-1} et 1548 cm^{-1} pour **HDPPBA-C** et **HDPPBA-N** respectivement, ce qui démontre également que les groupes amide forment des liaisons-H. Ces bandes chevauchent la bande amide II du lactame, visible vers 1553 cm^{-1} pour **HDPPH**. La différence de 4 cm^{-1} entre les dérivés amide indique une légère différence dans la force des liaisons-H, ce qui peut induire de faibles différences d'agrégation.

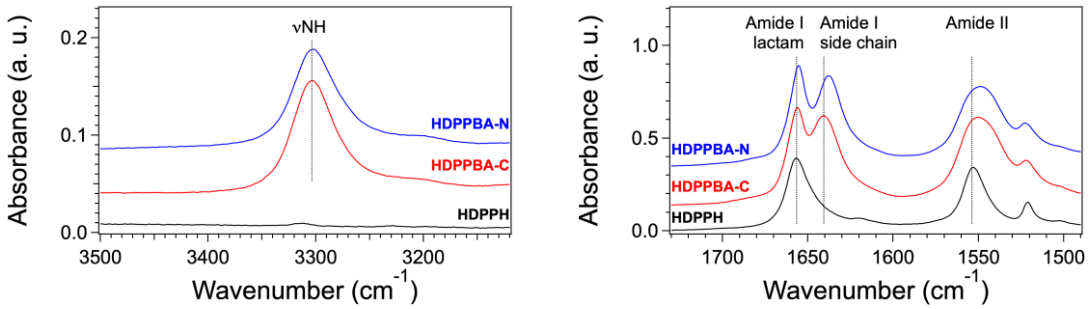

*Figure 19 Spectre IFTR en poudre de **HDPPBA-C**, **HDPPBA-N** et **HDPPH**.*

La morphologie de **HDPPBA-C**, **HDPPBA-N** et **HDPPH** a été étudiée par MET dans différents solvants (Figure III. 12). Des différences significatives sont observées lorsqu'on compare les dérivés capables de former des liaisons-H avec la molécule de contrôle. Tandis que **HDPPBA-C** et **HDPPBA-N** s'auto-assemblent dans des structures à haut rapport d'aspect, **HDPPH** forme des cristallites courtes d'approximativement 2 μm en longueur, en se chevauchant les uns aux autres pour tous les solvants utilisés, sauf dans le cas du cyclohexane, où les structures sont plus étroites et élongées.

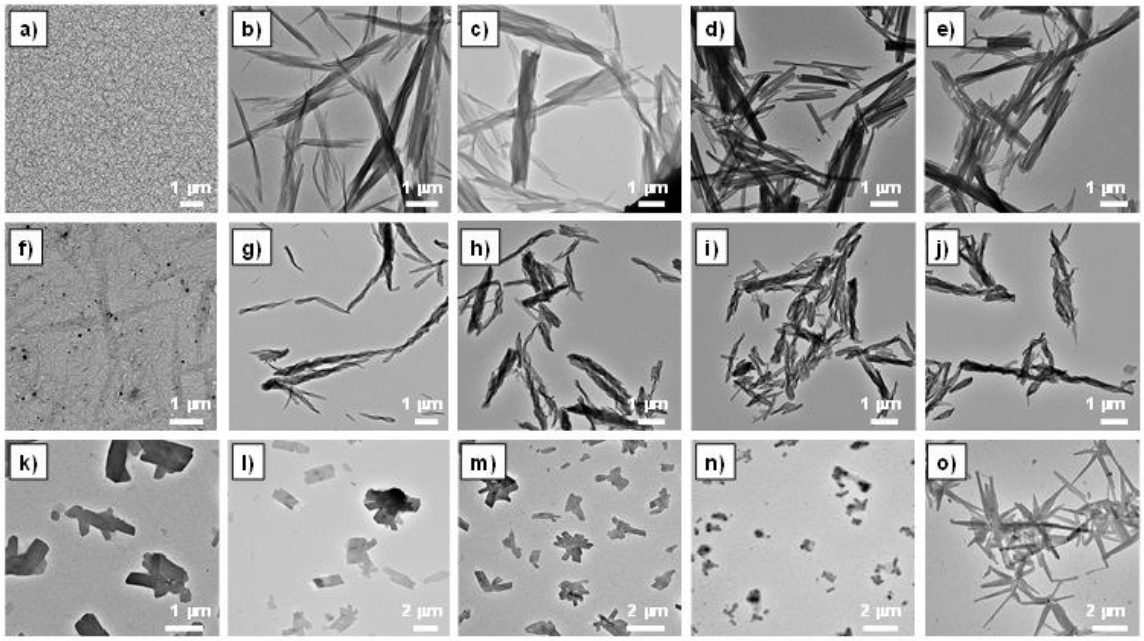

*Figure 20 Clichés de MET pour **HDPPBA-C (a-e), HDPPBA-N (f-j)** et **HDPPH (k-o)** dans le chloroforme, chlorobenzène, toluène, acétate d'éthyle et cyclohexane, respectivement. Les échantillons ont été préparés par déposition d'une goutte à partir de solutions à une concentration de 2,5 mg/ml, sur des grilles de carbone puis en absorbant à l'aide d'un buvard l'excès de solvant pour éviter des effets de séchage.*

Les propriétés électroniques de **HDPPBA-C** et **HDPPBA-N** ont été explorées en mesurant la photoconductivité par FP-TRMC, comme pour la famille précédente et ont été comparées avec les mesures de la molécule de contrôle **HDPPH**. Des films en couche mince avec ces composés ont été préparés par déposition par goutte depuis des solutions de chloroforme/toluène, et leurs photoconductivités ont été analysées directement. Les cinétiques de conductivité sont représentées sur la *Figure 21* .

Les valeurs de photoconductivité pour **HDPPBA-C** et **HDPPBA-N** sont très similaires, étant respectivement de 2.0 x 10^{-5} $cm^{-2}V^{-1}s^{-1}$ et 1.6 x 10^{-5} $cm^{-2}V^{-1}s^{-1}$. Ces valeurs sont nettement plus grandes que la valeur trouvée pour **HDPPH**, 5.8 x 10^{-6} $cm^{-2}V^{-1}s^{-1}$, un ordre de grandeur plus petit que pour les dérivés capables de former des liaisons-H.

Ces résultats mettent en évidence le rôle bénéfique des liaisons-H dans cette famille en particulier, et par extension au reste des familles examinées jusqu'à présent. A ce stade de l'étude, les résultats pour **HDPPBA-C** et **HDPPBA-N** sont très proches en raison de la technique utilisée, car la photoconductivité est mesurée à l'échelle nanoscopique.

Des mesures complémentaires sont toujours en cours avec nos collaborateurs pour élucider l'effet des réarrangements dans la disposition spatiale moléculaire après l'exposition au solvant. Elles permettront également de comparer les valeurs trouvées à celles des familles précédemment étudiées dans les mêmes conditions.

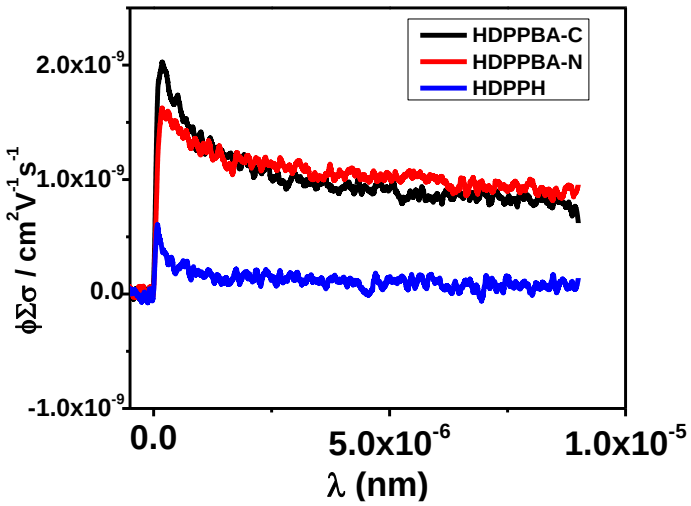

*Figure 21 Cinétique de photoconductivité pour **HDPPBA-C**, **HDPPBA-N** et **HDPPH** déposés à partir de solutions de chloroforme/toluène.*

Chapitre IV : Expansion de la famille bisamide : influence de la position et de la topologie

Dans ce chapitre, l'objectif principal est de tester l'influence de la position de la liaison-H par rapport au noyau principal, ainsi que l'effet de topologie de l'amide. Dans cette nouvelle famille, la position de la liaison-H dans les molécules thiophènes a été changée (*Figure 22*). Les thiophènes sur le noyau **DPP** ont été fonctionnalisés avec des bras amide, tandis que des chaînes alkyles sont placées sur les lactames.

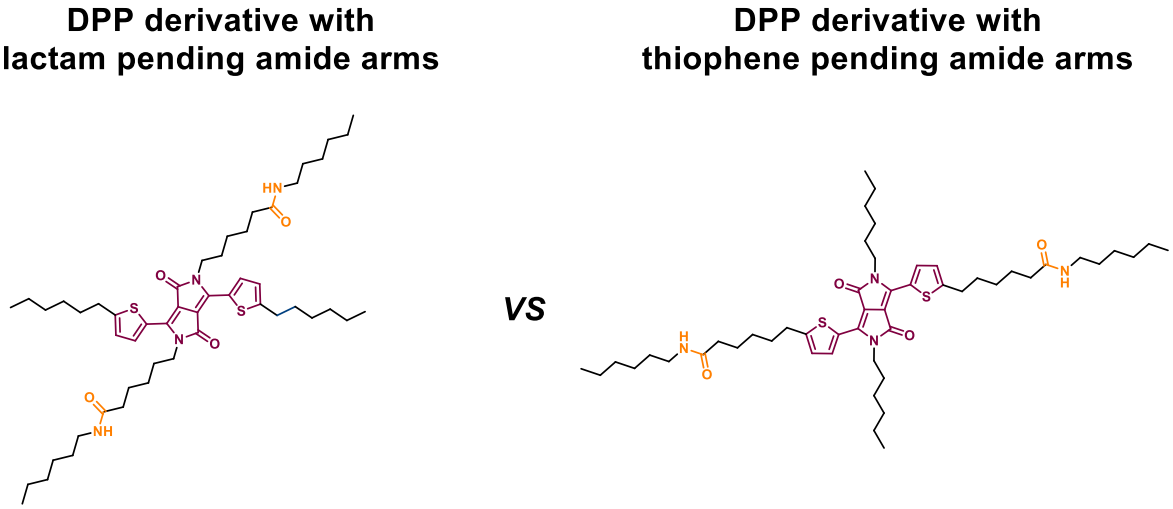

*Figure 22 Comparaison structurale pour le changement de la position du groupe amide dans les dérivés de **DPP**.*

En général, les dérivés de **DPP** portant des thiophènes sont souvent fonctionnalisés pour servir comme produit de départ pour les réactions de couplage croisé, réalisées en présence de Palladium.[51]

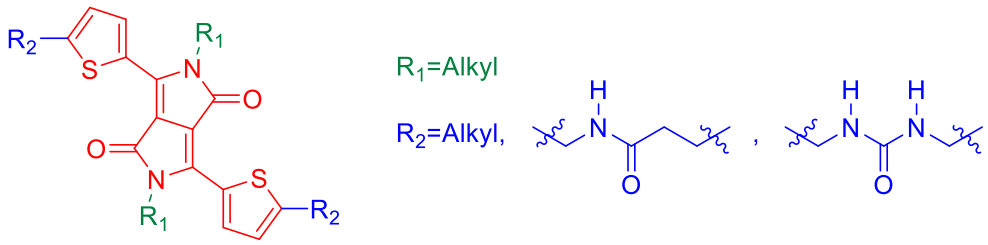

*Figure 23 Structure d'un noyau **DPP** portant des chaînes alkyles fonctionnalisées directement attachées sur les thiophènes du noyau.*

Plusieurs exemples où la fonctionnalisation est effectuée sur les thiophènes du noyau **DPP** existent dans la littérature, cependant, la majorité de ces approches sont généralement utilisées pour étendre le noyau conjugué de **DPP**, en rajoutant plus de thiophènes, tandis que le cas où l'unité **DPP** de base porte des thiophènes alkylés et fonctionnalisés (*Figure 23*) n'est pas mentionné dans la littérature.

Cependant, dans le chapitre III, la synthèse de dérivés de **DPP** avec des chaînes alkyles sur les thiophènes, avec des bons rendements, a été mis en évidence. Par conséquent, il a été décidé d'utiliser la même approche de cyclisation succinique pour produire un **DPP** qui porte des chaînes alkyl non-fonctionnalisées sur les lactames et portant des amides sur les thiophènes.

Dans ce chapitre, une approche synthétique détaillée de deux dérivés de **DPP**, avec différentes topologies et fonctionnalités sur les thiophènes, est présentée. La synthèse de ces composés a été envisagée selon deux voies différentes.

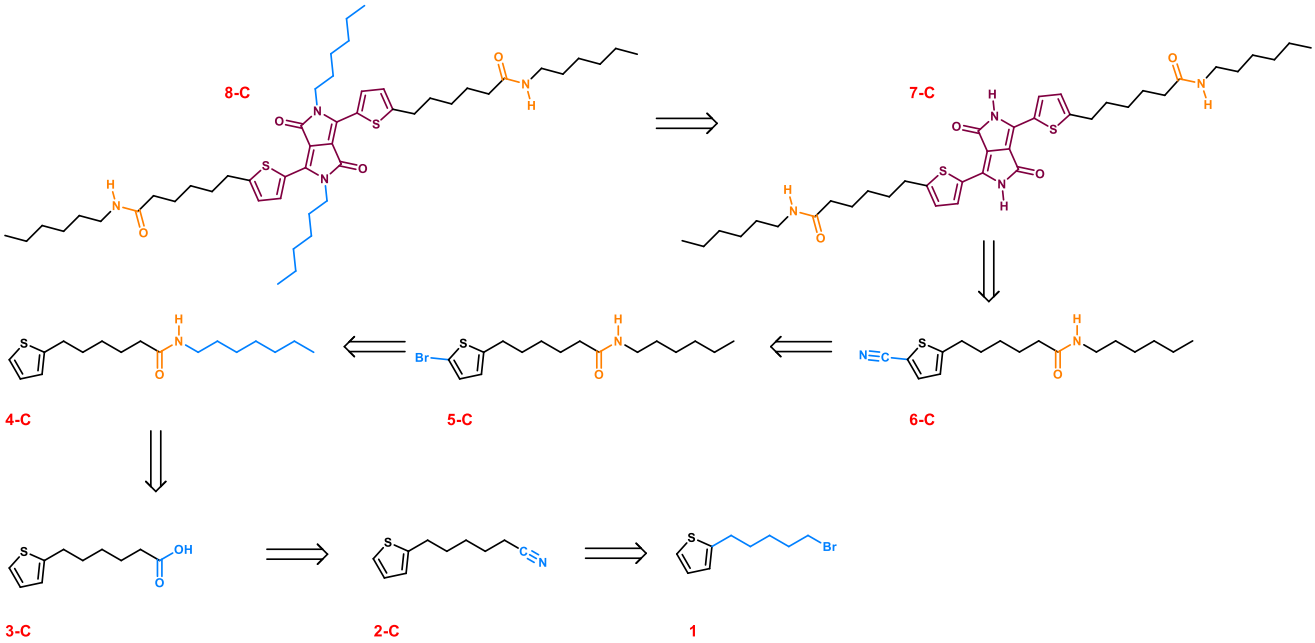

*Schéma 4 Retro synthèse pour obtenir le composé **8-C**.*

Ce chapitre porte sur la synthèse de dérivés centrés-C. Dans le manuscrit final, cette synthèse a été comparée à la synthèse des analogues centrés-N, effectuées au laboratoire. Elle ne sera pas évoquée dans ce qui suit. Cette comparaison synthétique a été faite pour avoir une meilleure compréhension des résultats.

Une rétro-synthèse a été faite (*Schéma 4*). En principe, ce schéma versatile est applicable à la synthèse des dérivés de **DPP** avec une topologie inversée, la clé se trouvant sur le précurseur **1**. La synthèse des précurseurs avec différentes topologies est la même à partir des produits **4-C** jusqu'à **6-C** et pour **4-N** jusqu'à **6-N**, dans ce cas seulement la route du produit centré-C est montrée sur le *Schéma 5*.

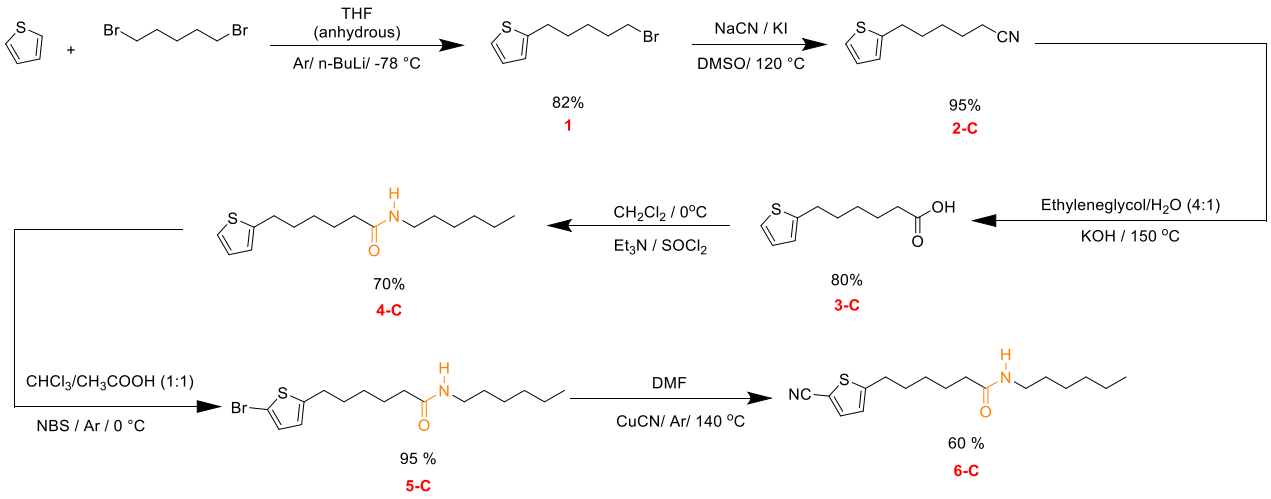

Schéma 5 Route synthétique pour le thiophène portant une amide C-centré.

L'étape suivante est la réaction de cyclisation où les composés **6-C** et **6-N** sont engagés, cependant des rendements bas ont été obtenus (*Schéma 6*). Par conséquent, cette approche a été considéré comme inadéquate pour obtenir ce type de produit, ce qui a entraîné à la proposition de routes alternatives pour obtenir un **DPP** avec des thiophènes portant des chaînes amides. Therefore, this approach was considered not suitable to obtain this type of products, leading to the proposal of alternative routes to obtain the **DPP** functionalized with an amide chain in the thiophene rings.

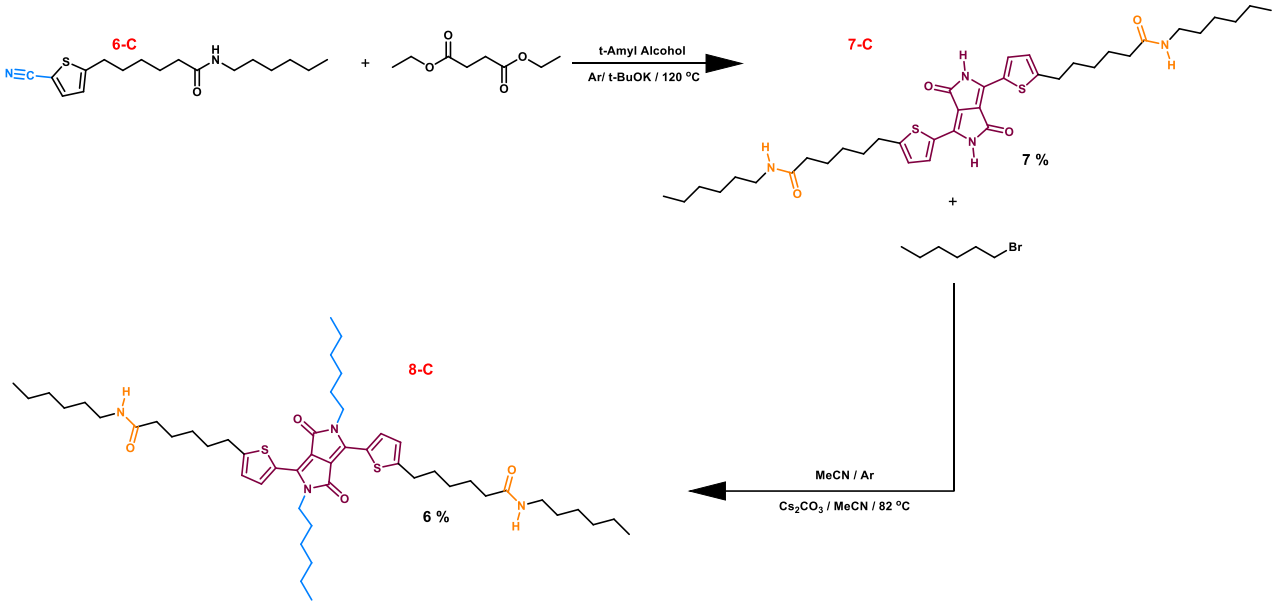

Schéma 6 Étapes finales dans l'approche synthétique par cyclisation succinique pour obtenir le produit **8-C**.

Plusieurs modifications ont été essayées pour essayer d'améliorer le rendement de cette réaction. En l'absence de rendement élevé, il a été décidé de changer la stratégie de synthèse, étant donné que l'obtention du composé **8-C** par cette voie était trop difficile.

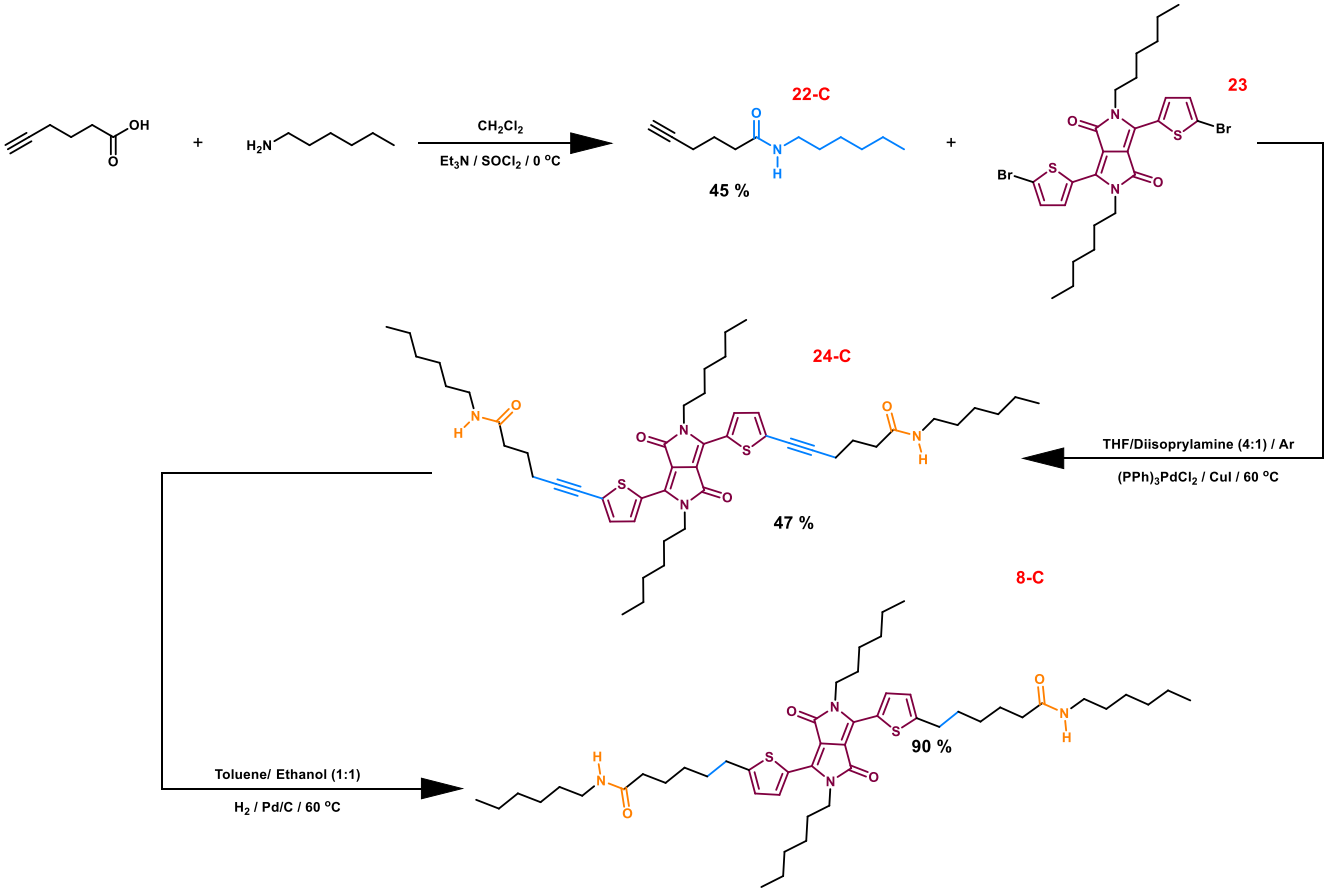

Schéma 7 Approche synthétique finale et fiable pour obtenir **8-C**.

La possibilité d'un couplage de Sonogashira avec un **DPP**[52,53] n'avait pas encore été testé et un essai en utilisant un dérivé **DPP** dibromé (produit **23**) comme produit de départ a été effectué (*Schéma 7*). Le composé **8-C** a été obtenu par hydrogénation à 60 °C en utilisant un mélange de solvant.

De la même façon, le produit N-centré a été obtenu *via* cette approche, qui est très directe et a prouvé sa versatilité. Elle servira dans la synthèse de nouveaux dérivés de **DPP** portant des chaînes alkyl fonctionnalisées sur le thiophène.

Les propriétés optiques et d'autoassemblage de **8-C** et **24-C** ont été suivies par spectroscopie d'absorption UV-Vis en solution, à température variable pour différents solvants et concentrations, et par IRTF. Comme d'habitude pour ces dérivés, le composé **8-C** présente des larges bandes d'absorption entre 400 et 600 nm à 20 °C dans le chloroforme, avec un maximum d'absorption vers λ= 562 nm (*Figure 24*, tracée bleue). Il ne présente pas cependant des signaux d'agrégation et les bandes d'absorption ne changent pas lorsque la concentration de la solution est augmentée (*Figure 25*a).

Des bandes d'absorption supplémentaires sont observées à des énergies plus faibles lorsque les spectres de **8-C** sont mesurés dans différents solvants, comme le chlorobenzène, le toluène et l'acétate d'éthyle. Dans le chlorobenzène, la valeur de λ_{max} est de 621 nm dans le toluène, vers 622 nm dans le chlorobenzène, et vers 629 nm dans l'acétate d'éthyle (*Figure 24*).

Cette bande a été attribuée à la formation d'agrégats J et son intensité diminue lorsqu'on chauffe ou on dilue la concentration de la solution, comme pour les familles de **DPPs** décrites précédemment (*Figure 25*b-d et *Figure 26*, respectivement). La formation de ces agrégats a été confirmé à nouveau en réalisant des mesures lorsqu'on rajoute du méthanol.

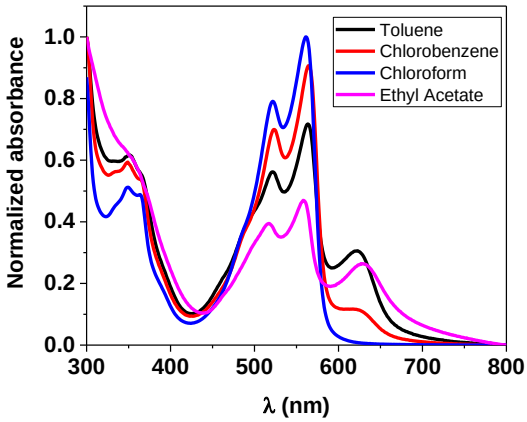

*Figure 24 Spectres d'absorption de **8-C** à température ambiante dans différents solvants. [**8-C**] = 0,5 mg/ml pour tous les solvants.*

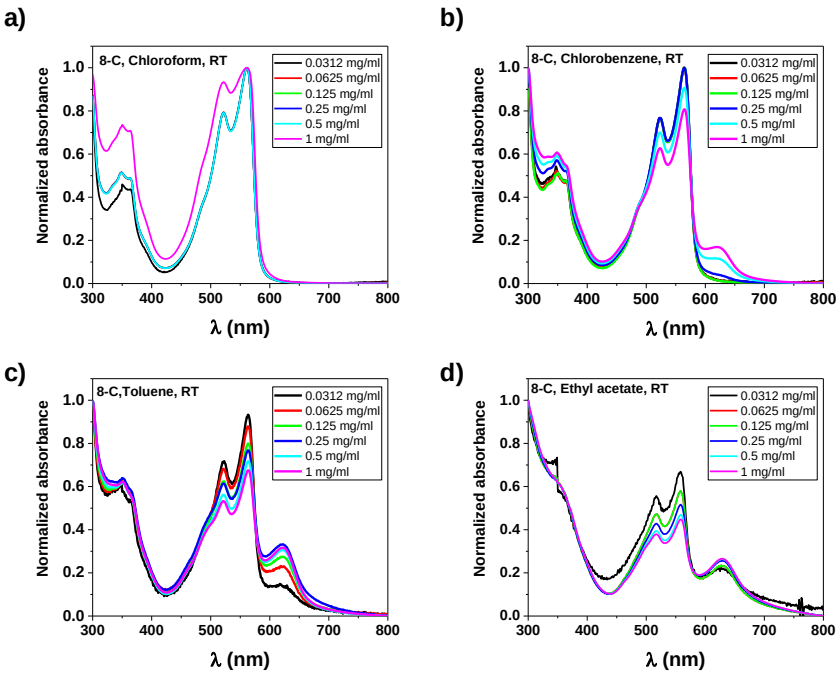

*Figure 25 Spectres d'absorption pour **8-C** réalisées à température ambiante pour différentes concentrations dans a) le chloroforme, b) le chlorobenzène, c) le toluène et d) l'acétate d'éthyle.*

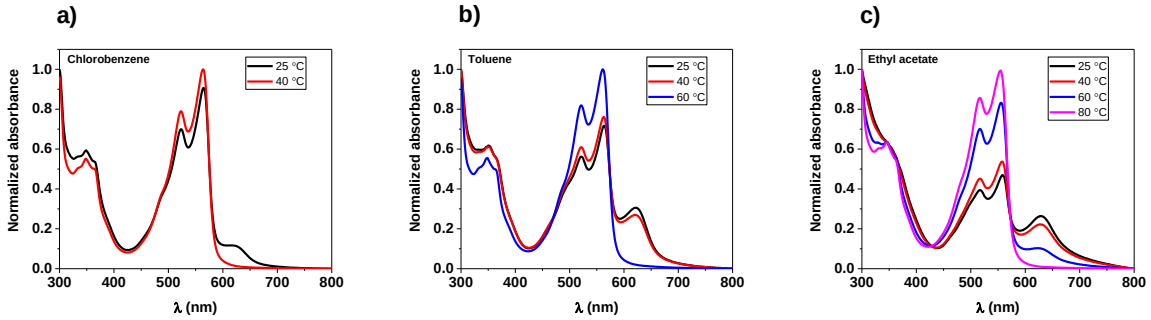

*Figure 26 Spectres d'absorption pour **8-C** pour lesquels la bande d'agrégats J disparaît lorsqu'on chauffe dans a) le chlorobenzène, b) le toluène et c) l'acétate d'éthyle. **[8-C]** = 0,5 mg/ml pour tous les solvants.*

A ce stade, bien que la caractérisation des molécules **8-C** et **8-N** ne soit pas complète, il ressort de la comparaison des résultats obtenus avec le dérivé **HDPPBA-C** (chapitre III) et la molécule **8-C**, que la position de l'amide dans la structure moléculaire est fortement modifiée. Il a été observé également que les molécules ont un comportement différent pour la spectroscopie d'absorption UV-Vis, ainsi que pour la morphologie. Bien que les propriétés optiques du produit **8-C** suivent un comportement similaire par rapport au reste des **DPPs** déjà étudiés, en présentant notamment des bandes d'agrégats de type J dans les solvants comme le chlorobenzène et le toluène (*Figure 27*, ligne bleue), il a été observé que **8-C** est plus soluble que **HDPPBA-C** dans tous les solvants utilisés.

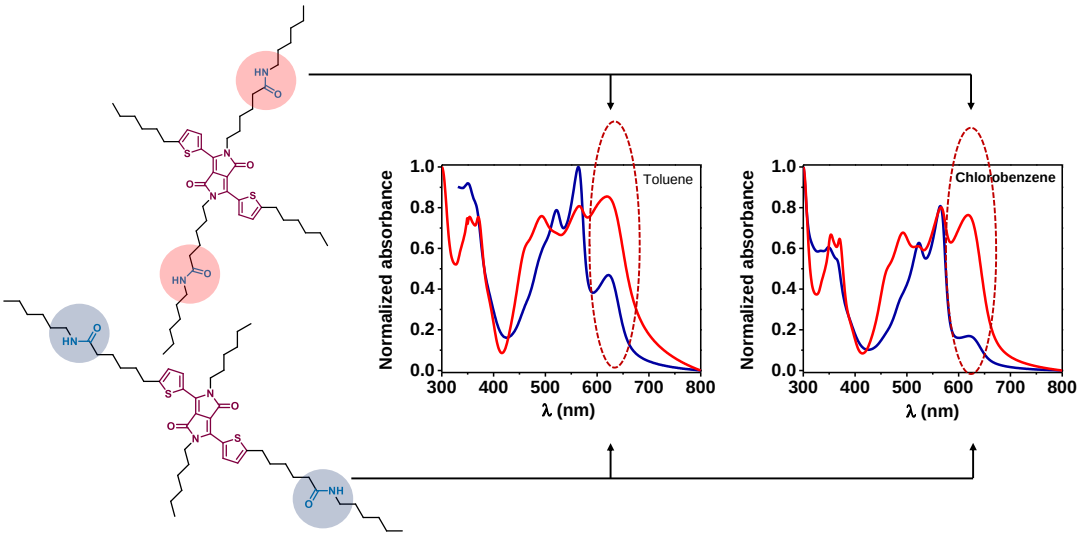

*Figure 27 Spectres d'absorption pour **HDPPBA-C** et **8-C** dans le toluène et dans le chlorobenzène aux mêmes concentrations et à température ambiante.*

Ce comportement est concordant avec les résultats issus du spectre d'absorption UV-Vis, qui présente des bandes d'agrégats J plus petites que pour **HDPPBA-C** (*Figure 27*) à la même concentration. Lorsque la morphologie des agrégats formés par **8-C** a été étudiée (*Figure 28*d-f), des structures bien définies à haut rapport d'aspect n'ont pas été observées comme dans le cas de **HDPPBA-C** (*Figure 28*a-c), en revanche, du matériel amorphe qui n'était pas assemblé dans des structures bien définies a été observé. Il semble donc que changer la position du groupe amide change dramatiquement les processus d'auto-assemblage, ainsi que les propriétés optoélectroniques.

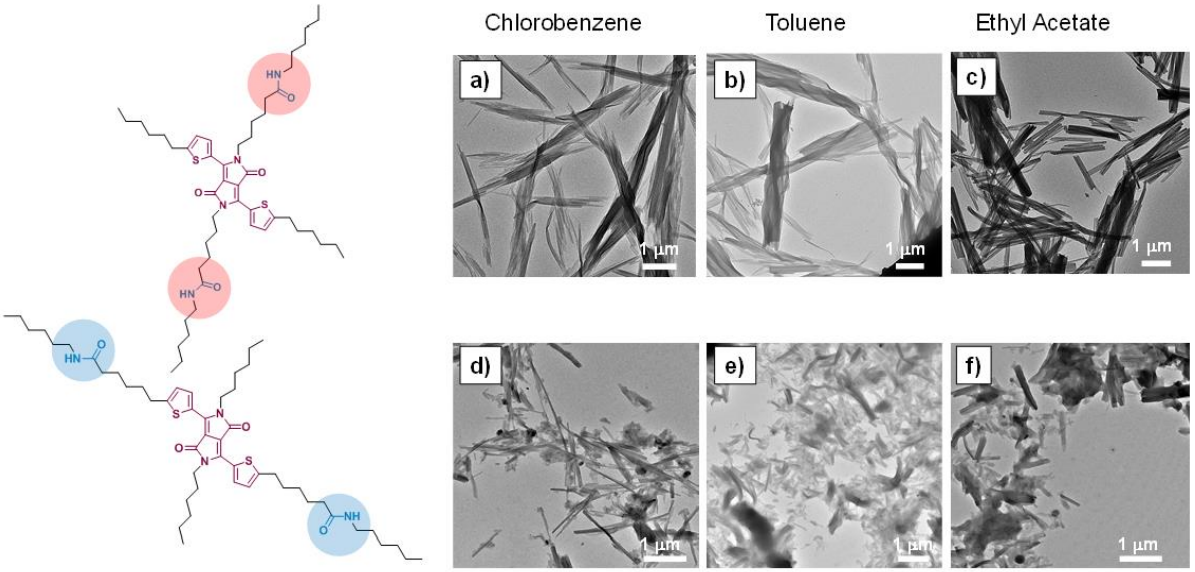

*Figure 28 Clichés par MET dans différent solvants pour **HDPPBA-C** (a-c) et **8-C** (d-f).*

Les précurseurs alcynes **24-C** et **24-N** sont encore en cours d'étude, parce que la présence de la triple liaison change le processus d'auto-assemblage, même si la structure moléculaire est pratiquement la même.

Des spectres IRTF en poudre à température ambiante prouvent également l'existence des liaisons-H dans **8-C** et **24-C**.

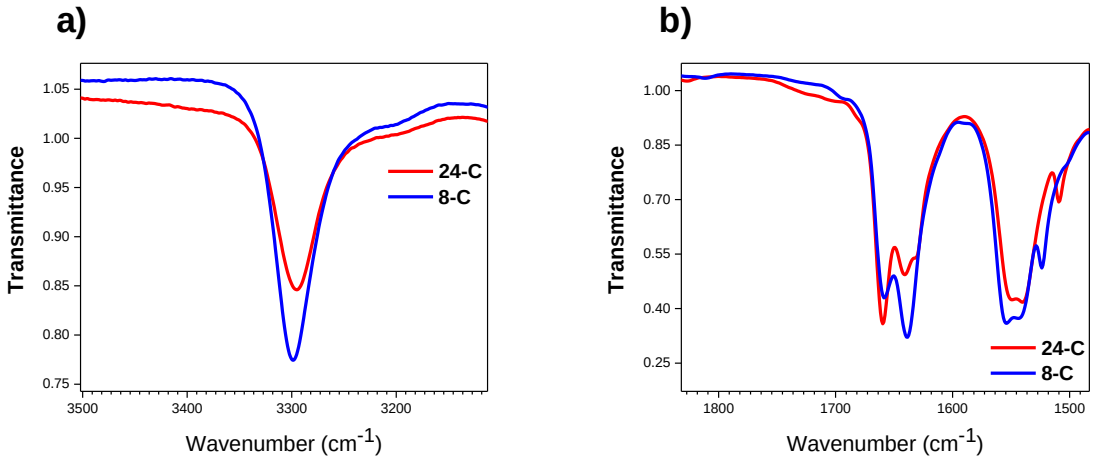

*Figure 29 Spectres IRTF en poudre pour **8-C** et **24-C**.*

Une comparaison des spectres IRTF en poudre entre **8-C** et **HDPPBA-C** a aussi été faite, mais aucune différence majeure n'a été observée. Toutefois, ces résultats ont été obtenus sur des poudres, pour lesquelles les différences d'agrégation ne sont pas trop évidentes. La comparaison de ces dérivés est toujours en cours. Des mesures de spectres dans différents solvants et à différentes concentrations devraient conduire à des informations plus détaillées sur les processus d'auto-assemblage.

La caractérisation complète de cette famille est très importante. En particulier, les mesures de photoconductivité et une comparaison plus complète de l'influence de la topologie devraient fournir des données essentielles pour les futures conceptions moléculaires envisagées et également pour élucider l'impact de la position de la liaison-H par rapport au noyau conjugué.

Chapitre V : Perspectives : Ouvrir la voie à un processus de criblage en temps-réel pour des dispositifs électroniques organiques

Dans les chapitres précédents, on a montré le début d'études comparatives et systématiques faites sur des matériaux π conjugués portant des liaisons-H basées sur le **DPP**. Ce travail devait permettre d'aider à la conception moléculaire de nouveaux composants. Jusqu'à présent, il avait été observé que des faibles différences dans la structure moléculaire des **DPPs** ou des différences dans le processus d'auto-assemblage pouvaient avoir un impact majeur les propriétés optoélectroniques. En plus, d'autres paramètres comme la méthode de préparation de l'échantillon, le solvant choisi, la concentration et la température pouvaient influer la capacité de formation des liaisons-H, compliquant par suite leur optimisation. C'est pourquoi nous avons commencé à travailler sur le contrôle *in situ* de la morphologie et des propriétés électroniques, pour recueillir un maximum d'information et créer un protocole de criblage.

Le travail qui suit a eu précisément pour but d'examiner les propriétés de différents systèmes de **DPP** portant des liaisons-H, avant puis après exposition à une vapeur de solvant ou/et à des traitements thermiques. Cette étude a été effectuée pour les dérivés **DPP** présentés au chapitre III : **HDPPH**, **HDPPBA-C** et **HDPPBA-N.**

Au départ, ces études ont porté sur la caractérisation thermique de ces dérivés pour connaître leur température de dégradation et leur stabilité thermique. Il a été est possible ainsi d'évaluer le domaine de température compatible avec un processus de recuit. L'analyse thermogravimétrique (ATG), a été réalisée en chauffant des échantillons à partir de 25 °C jusqu'à 300 °C à une vitesse de 5 °C/min sous atmosphère d'azote.

Les résultats obtenus montrent que **HDPPBA-C** (*Figure 30*a) et **HDPPBA-N** (*Figure 30*b) sont thermiquement stables dans ce domaine de température, car ils n'ont pas perdu plus de 1% en masse. D'autre part, **HDPPH** (*Figure 30*c) subit une perte de 2% en masse aux alentours de 230 °C et une perte massique de presque 10% vers 300 °C. Cette différence a été attribuée au fait que **HDPPH** ne possède pas la capacité de former des liaisons-H, ainsi qu'au caractère de donneur d'électrons des chaînes alkyles. En fait, l'introduction des groupes hexyles sur les atomes d'azote modifie la structure plate de la molécule, ce qui provoque une défragmentation plus facile de celle-ci lorsqu'on la chauffe.[54,55]

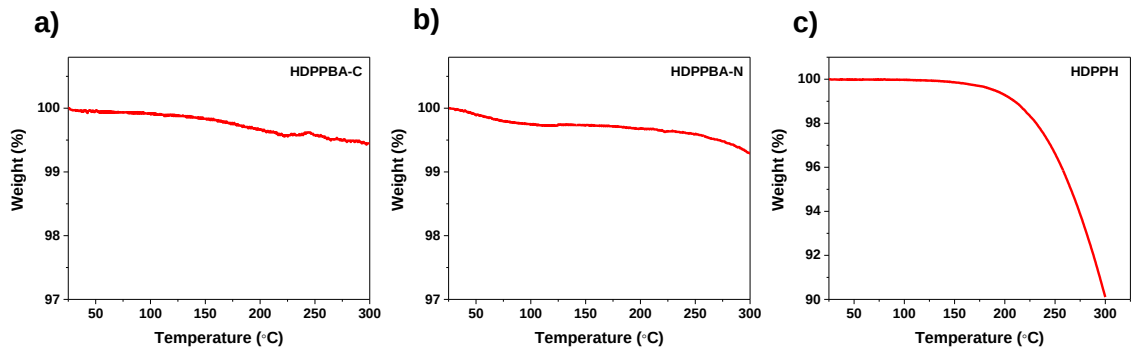

Figure 30 ATG pour a) ***HDPPBA-C*** *b)* ***HDPPBA-N*** *et c)* ***HDPPH****.*

À partir de ces données expérimentales, il a été possible de déterminer les conditions nécessaires pour réaliser une calorimétrie différentielle à balayage (DSC). Ces mesures visaient à comprendre le comportement de fusion de ces composés. Les résultats de DSCs de **HDPPBA-C**, **HDPPBA-N** et **HDPPH** sont présentés sur la *Figure 31*, les deux premiers composés ont des points de fusion de 218 °C (*Figure 31*a) et 204 °C (*Figure 31*b), respectivement, tandis que **HDPPH** a un point de fusion substantiellement plus bas, 159 °C (*Figure 31*c).

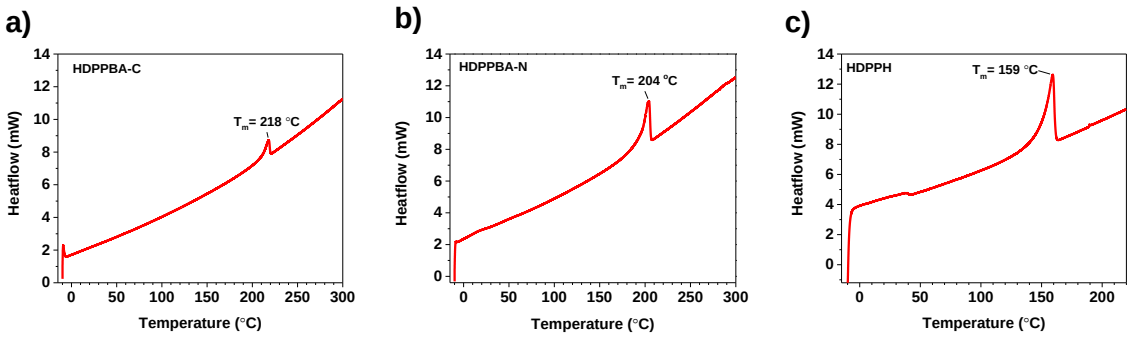

*Figure 31 DSC pour a) **HDPPBA-C** b) **HDPPBA-N** et c) **HDPPH**.*

Pour avoir une meilleure compréhension des assemblages formés par ces composés, des films à couche mince ont été étudiés. En particulier, l'orientation structurelle de molécules auto-assemblées a été suivie par diffraction d'électrons (DE) en préparant des films sur différents substrats. Le premier groupe d'expériences sur substrat a consisté à réaliser un dépôt d'une goutte de chacun des composés en solution dans du chlorobenzène (concentration de 2,5 mg/ml). Ce dépôt a été fait sur des grilles en carbone pour MET, l'excès de solvant étant retiré à l'aide d'un buvard.

Le premier composé analysé est **HDPPBA-C**, pour lequel la direction de l'empilement des molécules de **DPP** est trouvée parallèle à l'axe des fibres (Figure V. 6). En plus, les molécules forment des colonnes qui sont penchées par rapport à l'axe de la fibre. Le diffractogramme montre la périodicité des amides portant des liaisons-H avec la distance charactéristique de 4.9 Angstroms (Å).

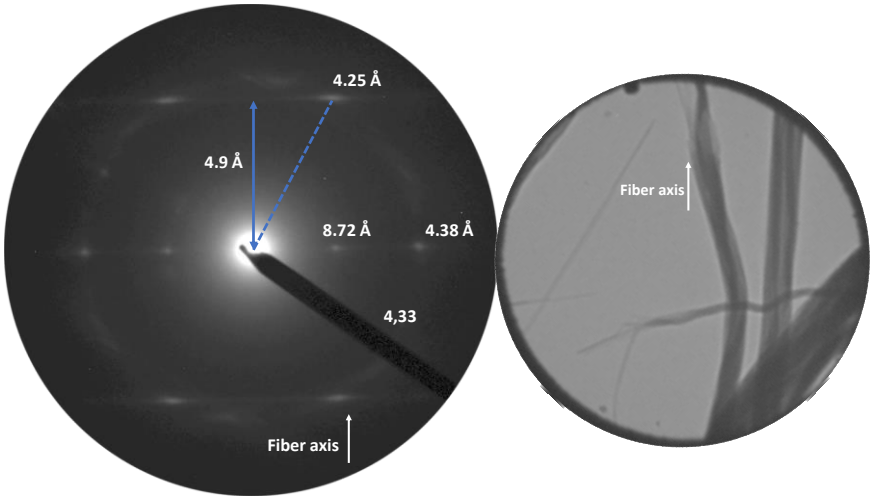

*Figure 32 À gauche : Cliché de DE d'un film de **HDPPBA-C** déposé par goutte, à partir d'une solution de chlorobenzène, sur une grille de carbone pour MET. À droite : Cliché MET du film étudié.*

L'impact de la fonte et de la recristallisation sur l'orientation des agrégats induits par les liaisons-H a également été examiné pour ce composé. Pour cela, le film a été préparé sur un

substrat de polytetrafluoroethylène (PTFE) en faisant un dépôt par goutte comme précédemment, mais en chauffant ensuite le film à 240 °C, température bien au-delà de celle de fusion de **HDPPBA-C**. La température de l'échantillon a ensuite été amenée à température ambiante pour qu'il cristallise.

Les résultats précédents ont montré qu'il est possible de contrôler l'orientation d'agrégats en faisant fondre le film. L'impact de la vapeur de solvant a aussi été évalué. Des films préparés par dépôt de goutte ont également été soumis à un recuit d'une heure en présence de vapeur de chloroforme. La température de recuit était située au-delà de la température de fusion de l'échantillon. Les résultats obtenus montrent que **HDPPBA-C** présente la même structure que les échantillons qui ont été préparés par dépôt de goutte sans recuit thermique, mais avec des réflexions plus fortes indiquant une meilleure cristallisation et orientation, sans stries des réflexions (*Figure 33*).

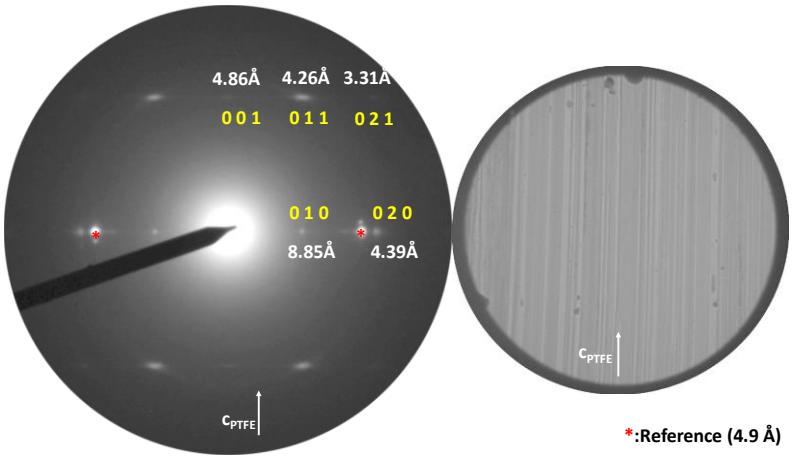

*Figure 33 À gauche : Cliché de DE d'un film de **HDPPBA-C** qui a été recuit en présence de vapeur de chloroforme sur un substrat de PTFE. À droite : Cliché MET du film étudié.*

En utilisant les clichés de DE, il a été possible de construire un modèle simple des structures formées par ces agrégats (*Figure 34*). Les réflexions peuvent être indexées sur une cellule unitaire orthorhombique simple.

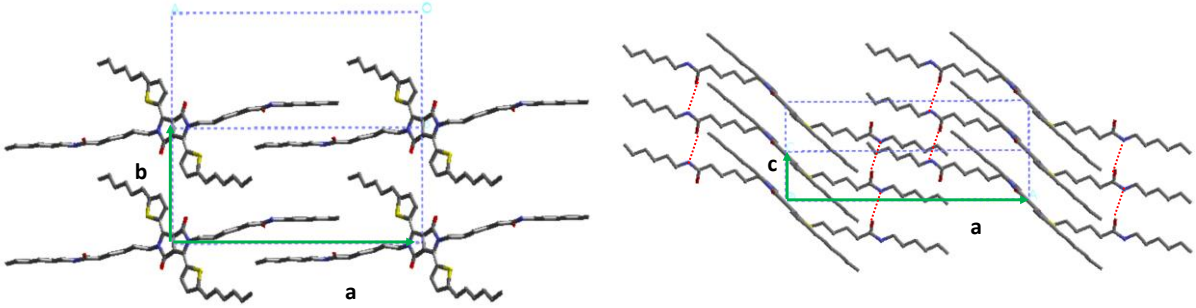

Figure 34 Structure générée par modélisation en utilisant les données obtenues des clichés de DE.

Par ailleurs, les clichés de DE pour ce modèle ont été indexés pour les plans [100] et [010], et sont en accord avec les données expérimentales. Les mêmes expériences ont été réalisées pour **HDPPBA-N** et **HDPPH**.

Dans l'étape suivante, l'orientation des agrégats sur des films à couche mince a été étudiée par microscopie optique polarisé (MOP). Les trois composés ont été utilisés pour préparer des films sur des substrats de PTFE, les échantillons de **HDPPBA-C** et **HDPPBA-N** ont été préparés en partant d'une solution de chlorobenzène à 2,5 mg/ml.

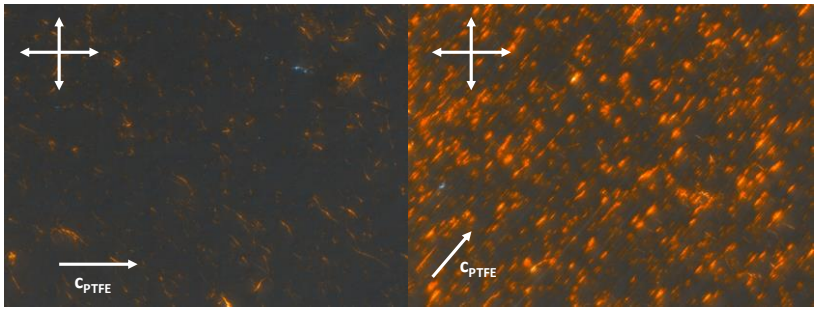

*Figure 35 Clichés d'un film de **HDPPBA-N** orienté sur du PTFE observé par MOP.*

Après un processus de fonte-recristallisation, les films ont été étudiés par DE à 4°C. Pour le film préparé sur du PTFE à 4°C, les clichés de DE présentent une diffraction étroite sur le plan (010), ce qui indique un degré d'alignement très élevé (*Figure 36*). En plus, les films présentent des fibres orientées le long de la direction des chaînes du PTFE, ce qui signifie que la direction de l'empilement de **HDPPBA-N** est parallèle à C_{PTFE}.

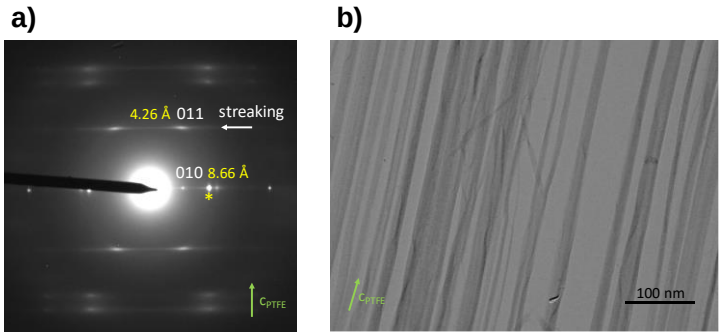

*Figure 36 a) Cliché de DE d'un film de **HDPPBA-N** formé sur du PTFE à 4°C et b) cliché obtenu par MET du film étudié.*

Après un recuit thermique, l'orientation est maintenue, et il n'y a pas de changement observé sur le plan de contact (Figure 37). Les stries sur la couche de la ligne l=1 sont fortement réduites après le recuit. En outre, des réflexions plus nettes sont observées, ce qui implique une organisation des colonnes moléculaires adjacentes ainsi que les changements des spectres UV-Vis. La même séquence d'expériences a été réalisée pour **HDPPBA-C** et **HDPPH**.

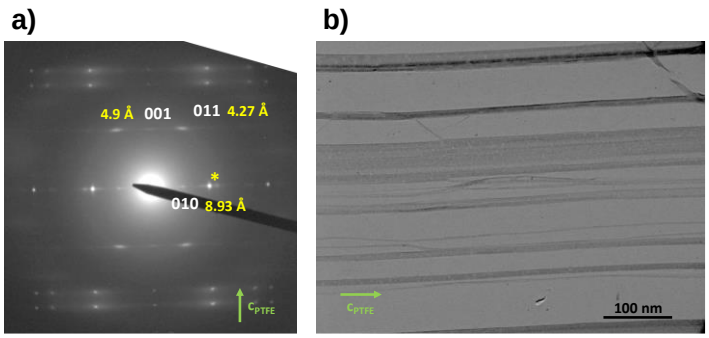

*Figure 37 a) Cliché de DE d'un film de **HDPPBA-N** après un recuit thermique et b) cliché MET du film étudié.*

Les spectres UV-Vis des trois dérivés sont similaires lorsque les échantillons sont recuits. Cependant, des différences entre les films préparés par solution et les films recuits sont observées pour **HDPPBA-N**, qui est le dérivé qui s'oriente sur le PTFE. Les clichés DE montrent que le recuit des films de **HDPPBA-N** améliore l'ordre des colonnes en raison de la perte des stries, ce qui signifie que les agrégats subissent une possible transformation des colonnes unidimensionnelles vers un ordre plus tridimensionnelle. Par ailleurs, les films préparés avec **HDPPBA-C** ne changent pas leurs structures entre les films préparés par solution et les films recuits, ce qui indique un caractère moins dynamique des agrégats formés par ce dérivé.

Ces études préliminaires ont fourni un aperçu des moyens pour contrôler la morphologie des assemblages formés par les dérivés de **DPP**, ce qui devrait maintenant ouvrir la voie à la conception d'un processus de criblage en temps réel des dispositifs électroniques organiques.

Références

[1] K. Dong, X. Dong, Q. Jiang, *World Econ* **2020**, *43*, 1665–1698.

[2] "• Primary energy consumption by country 2020 | Statista," can be found under https://www.statista.com/statistics/263455/primary-energy-consumption-of-selected-countries/, **n.d.**

[3] "Photovoltaic Cell – Definition and How It Works | Planète Énergies," can be found under https://www.planete-energies.com/en/medias/close/how-does-photovoltaic-cell-work, **n.d.**

[4] M. M. Ling, Z. Bao, *Chem. Mater.* **2004**, *16*, 4824–4840.

[5] A. Köhler, H. Bässler, *Electronic Processes in Organic Semiconductors: An Introduction*, Wiley-VCH Verlag GmbH & Co. KGaA, Weinheim, Germany, **2015**.

[6] G. M. Whitesides, *Science* **2002**, *295*, 2418–2421.

[7] G. R. Desiraju, *Angew. Chem. Int. Ed.* **2011**, *50*, 52–59.

[8] G. A. Jeffrey, W. Saenger, *Hydrogen Bonding in Biological Structures*, Springer Berlin Heidelberg, Berlin, Heidelberg, **1991**.

[9] C.-C. Chu, D. M. Bassani, *Photochem. Photobiol. Sci.* **2008**, *7*, 521.

[10] M. Irimia-Vladu, Y. Kanbur, F. Camaioni, M. E. Coppola, C. Yumusak, C. V. Irimia, A. Vlad, A. Operamolla, G. M. Farinola, G. P. Suranna, N. González-Benitez, M. C. Molina,

L. F. Bautista, H. Langhals, B. Stadlober, E. D. Głowacki, N. S. Sariciftci, *Chem. Mater.* **2019**, *31*, 6315–6346.
[11] Z. Xiao, K. Sun, J. Subbiah, S. Ji, D. J. Jones, W. W. H. Wong, *Sci Rep* **2015**, *4*, 5701.
[12] K.-H. Kim, H. Yu, H. Kang, D. J. Kang, C.-H. Cho, H.-H. Cho, J. H. Oh, B. J. Kim, *Journal of Materials Chemistry A* **2013**, *1*, 14538.
[13] R. J. Kumar, J. Subbiah, A. B. Holmes, *Beilstein Journal of Organic Chemistry* **2013**, *9*, 1102–1110.
[14] T. Aytun, L. Barreda, A. Ruiz-Carretero, J. A. Lehrman, S. I. Stupp, *Chemistry of Materials* **2015**, *27*, 1201–1209.
[15] A. D. Hendsbee, J.-P. Sun, L. R. Rutledge, I. G. Hill, G. C. Welch, *J. Mater. Chem. A* **2014**, *2*, 4198–4207.
[16] E. D. Głowacki, H. Coskun, M. A. Blood-Forsythe, U. Monkowius, L. Leonat, M. Grzybowski, D. Gryko, M. S. White, A. Aspuru-Guzik, N. S. Sariciftci, *Organic Electronics* **2014**, *15*, 3521–3528.
[17] D. G. Farnum, G. Mehta, G. G. I. Moore, F. P. Siegal, *Tetrahedron Letters* **1974**, *15*, 2549–2552.
[18] W. Li, K. H. Hendriks, M. M. Wienk, R. A. J. Janssen, *Acc. Chem. Res.* **2016**, *49*, 78–85.
[19] J. C. Bijleveld, A. P. Zoombelt, S. G. J. Mathijssen, M. M. Wienk, M. Turbiez, D. M. de Leeuw, R. A. J. Janssen, *Journal of the American Chemical Society* **2009**, *131*, 16616–16617.
[20] M. Stolte, S.-L. Suraru, P. Diemer, T. He, C. Burschka, U. Zschieschang, H. Klauk, F. Würthner, *Advanced Functional Materials* **2016**, *26*, 7415–7422.
[21] X. Yang, L. Zheng, L. Xie, Z. Liu, Y. Li, R. Ning, G. Zhang, X. Gong, B. Gao, C. Liu, Y. Cui, G. Sun, G. Zhang, *Sensors and Actuators B: Chemical* **2015**, *207*, 9–24.
[22] X. Yang, L. Xie, R. Ning, X. Gong, Z. Liu, Y. Li, L. Zheng, G. Zhang, B. Gao, Y. Cui, G. Sun, G. Zhang, *Sensors and Actuators B: Chemical* **2015**, *210*, 784–794.
[23] C. J. H. Morton, R. Gilmour, D. M. Smith, P. Lightfoot, A. M. Z. Slawin, E. J. MacLean, *Tetrahedron* **2002**, *58*, 5547–5565.
[24] D. Feng, G. Barton, C. N. Scott, *Organic Letters* **2019**, *21*, 1973–1978.
[25] B. Kan, M. Li, Q. Zhang, F. Liu, X. Wan, Y. Wang, W. Ni, G. Long, X. Yang, H. Feng, Y. Zuo, M. Zhang, F. Huang, Y. Cao, T. P. Russell, Y. Chen, *Journal of the American Chemical Society* **2015**, *137*, 3886–3893.
[26] B. Kan, Q. Zhang, M. Li, X. Wan, W. Ni, G. Long, Y. Wang, X. Yang, H. Feng, Y. Chen, *Journal of the American Chemical Society* **2014**, *136*, 15529–15532.
[27] N. M. Randell, T. L. Kelly, *The Chemical Record* **2019**, *19*, 973–988.
[28] X. Wei, W. Zhang, G. Yu, *Advanced Functional Materials* **2021**, *31*, 2010979.
[29] Y. Cui, H. Yao, J. Zhang, T. Zhang, Y. Wang, L. Hong, K. Xian, B. Xu, S. Zhang, J. Peng, Z. Wei, F. Gao, J. Hou, *Nat Commun* **2019**, *10*, 1–8.
[30] J. Yuan, Y. Zhang, L. Zhou, G. Zhang, H.-L. Yip, T.-K. Lau, X. Lu, C. Zhu, H. Peng, P. A. Johnson, M. Leclerc, Y. Cao, J. Ulanski, Y. Li, Y. Zou, *Joule* **2019**, *3*, 1140–1151.
[31] S. Militzer, N. Nishimura, N. R. Ávila-Rovelo, W. Matsuda, D. Schwaller, P. J. Mésini, S. Seki, A. Ruiz-Carretero, *Chem. Eur. J.* **2020**, chem.202001540.
[32] S. Militzer, T. M. P. Tran, P. J. Mésini, A. Ruiz-Carretero, *ChemNanoMat* **2018**, *4*, 790–795.
[33] “Hydrogen bonding ability of the amide group,” DOI 10.1021/ja00819a013can be found under https://pubs.acs.org/doi/pdf/10.1021/ja00819a013, **n.d.**

[34] G. Ghosh, M. Paul, T. Sakurai, W. Matsuda, S. Seki, S. Ghosh, *Chem. Eur. J.* **2018**, *24*, 1938–1946.
[35] M. Liu, L. Zhang, T. Wang, *Chem. Rev.* **2015**, *115*, 7304–7397.
[36] J. Liu, Y. Zhang, H. Phan, A. Sharenko, P. Moonsin, B. Walker, V. Promarak, T.-Q. Nguyen, *Adv. Mater.* **2013**, *25*, 3645–3650.
[37] R. B. Zerdan, N. T. Shewmon, Y. Zhu, J. P. Mudrick, K. J. Chesney, J. Xue, R. K. Castellano, *Adv. Funct. Mater.* **2014**, *24*, 5993–6004.
[38] T. He, P. Leowanawat, C. Burschka, V. Stepanenko, M. Stolte, F. Würthner, *Adv. Mater.* **2018**, *30*, 1804032.
[39] M. Stolte, S.-L. Suraru, P. Diemer, T. He, C. Burschka, U. Zschieschang, H. Klauk, F. Würthner, *Adv. Funct. Mater.* **2016**, *26*, 7415–7422.
[40] K. Dhbaibi, L. Favereau, M. Srebro-Hooper, M. Jean, N. Vanthuyne, F. Zinna, B. Jamoussi, L. Di Bari, J. Autschbach, J. Crassous, *Chem. Sci.* **2018**, *9*, 735–742.
[41] P. A. Hume, J. P. Monks, F. Pop, E. S. Davies, R. C. I. MacKenzie, D. B. Amabilino, *Chem. Eur. J.* **2018**, *24*, 14461–14469.
[42] A. Iqbal, M. Jost, R. Kirchmayr, J. Pfenninger, A. Rochat, O. Wallquist, *Bulletin des Societes Chimiques Belges* **1988**, *97*, 615–644.
[43] A. Ruiz-Carretero, T. Aytun, C. J. Bruns, C. J. Newcomb, W.-W. Tsai, S. I. Stupp, *J. Mater. Chem. A* **2013**, *1*, 11674–11681.
[44] S. Loser, C. J. Bruns, H. Miyauchi, R. P. Ortiz, A. Facchetti, S. I. Stupp, T. J. Marks, *J. Am. Chem. Soc.* **2011**, *133*, 8142–8145.
[45] J. Mizuguchi, A. C. Rochat, G. Rihs, *Berichte der Bunsengesellschaft für physikalische Chemie* **1992**, *96*, 607–619.
[46] J. Mizuguchi, *Berichte der Bunsengesellschaft für physikalische Chemie* **1993**, *97*, 684–693.
[47] G. Eaton, M. C. R. Symons, P. P. Rastogi, *J. Chem. Soc., Faraday Trans. 1* **1989**, *85*, 3257.
[48] M. Kirkus, L. Wang, S. Mothy, D. Beljonne, J. Cornil, R. A. J. Janssen, S. C. J. Meskers, *J. Phys. Chem. A* **2012**, *116*, 7927–7936.
[49] W.-W. Tsai, I. D. Tevis, A. S. Tayi, H. Cui, S. I. Stupp, *J. Phys. Chem. B* **2010**, *114*, 14778–14786.
[50] Y. Zhou, C. X. Guzman, L. C. Helguero-Kelley, C. Liu, S. R. Peurifoy, B. Captain, A. B. Braunschweig, *Journal of Physical Organic Chemistry* **2016**, *29*, 689–699.
[51] M. Grzybowski, D. T. Gryko, *Advanced Optical Materials* **2015**, *3*, 280–320.
[52] M. Takahashi, K. Masui, H. Sekiguchi, N. Kobayashi, A. Mori, M. Funahashi, N. Tamaoki, *J. Am. Chem. Soc.* **2006**, *128*, 10930–10933.
[53] Y.-Z. Wu, Y.-C. Zhang, J.-J. Chen, L.-J. Fan, *Chin J Polym Sci* **2019**, *37*, 1092–1098.
[54] M. Vala, M. Weiter, J. Vyňuchal, P. Toman, S. Luňák, *J Fluoresc* **2008**, *18*, 1181.
[55] J. David, M. Weiter, M. Vala, J. Vyňuchal, J. Kučerík, *Dyes and Pigments* **2011**, *89*, 137–143.

List of abbreviations

2

2D ..... two dimension

3

3D .....three dimension

A

Å .....Angstroms
AFM ..... atomic force microscopy
anti-DBTP .....anti-dibenzothienopyrrole

B

BBBT..... benzo[1,2-b:4,5-b′]bis[b]benzothiophene
BHJ ..... bulk heterojunction
Boc ..... tert-Butyloxycarbonyl

C

CD ..... circular dichroism
ClT 5-chlorotetracene
CNnitriles
CO_2 ..... carbon dioxide
Covid-19..... corona virus disease

D

D/A..... donor–acceptor
DACH..... trans-1,2-diamidocyclohexane
DAP .....diamidopyridine
DBTDT ..... dibenzo[d,d′]thieno[3,2-b;4,5-b′]dithiophene
DClT..... 5,11-dichlorotetracene
D-HD ..... hydrogen-donor dye
dithienyl-DPP DPP3T
DMF .....N,N-dimethylformamide
DMSO..... dimethyl sulfoxide
DPC .....droplet-pinned crystallization
DPP ..... Diketopyrrolopyrrole
DR .....dichroic ratio
DSC.....differential scanning calorimetry

E

ED .....electron diffraction
EIA..... Energy Information Administration
EJ .....exajoules
Eq. ..... equivalents
ETL.....electron-transporting layer
eV ..... electronvolt

F

FF ..... fill factor
FP-TRMC .....Flash-photolysis time resolved microwave conductivity

G

GIWAXS .... grazing incidence wide-angle X-ray scattering
GIXD ..... grazing incidence X-ray diffraction
GW .....Gigawatts

H

H-bonded ..... hydrogen bonded
H-bonding ..... hydrogen bonding
H-bonds.....hydrogen bonds
HTL .....hole-transporting layer

I

ICZ ..... indo[3,2-b]carbozole
IR .....infrared
ITO.....Indium Tin Oxide

L

LDA.....diisopropylAmide

M

m .....meter
MD .....molecular dynamics
Mtoe ..... million tonnes of oil equivalent
MW .....Megawatts

N

NBS..... N-Bromosuccinimide
NFAs..... non-fullerene acceptors
NMP ..... N-methylpyrrolidone

O

OFETs .....organic field transistor devices
OLED ..... organic light emitting diodes
OPVs..... organic photovoltaic devices
OTFTs .....organic thin film transistors

P

P3HT.....poly (3-hexylthiophene)
PBI.....perylene bisimides
$PC_{71}BM$..... phenyl [6,6]-Phenyl C71 butyric acid methyl ester
PCBM ..... [6,6]-phenyl-C61-butyric acid methyl ester
PCE.....power conversion efficiency
p-ClDPP ..... "Ferrari red" pigment
PCPDTBT .....poly{[4,4-bis-alkyl-cyclopenta-(2,1-b;3,4-b')dithiophen]-2,6-diyl-alt-(2,1,3-benzo-thiadiazole)-4,7-diyl}
PDMS .....polydimethylsiloxane
PEDOT PSS .....Poly(3,4-ethylenedioxythiophene) polystyrene sulfonate
P-HA..... hydrogen acceptor polymer
POM.....polarized optical microscope
PSCs ..... polymer solar cells
PTFE ..... polytetrafluoroethylene
PV .....photovoltaic
PWR ..... Pressurized Water Reactor

S

SDS..... Sustainable Development Scenario
SEM..... scanning electron microscopy
SF ..... singlet fission
STEPS.....Stated Policies Scenario
STM..... scanning tunneling microscopy
SVA..... solvent vapor annealing
syn-DBTP .....syn-dibenzothieno[b,d]pyrrole

T

TAT ..... triazatruxene
t-Boc.....tert-butoxycarbonyl
TClT 5,6,11,12-tetrachlorotetracene
TFA .....trifluroacetic acid
TGA ..... thermogravimetric analysis
TPA..... triphenylamine
TTF .....tetrathiofulvalene

U

USA .....United States of America

V

V_{OC}..... open circuit voltage
VT .....variable temperature

X

XRD .....X-ray diffraction

INTRODUCTION

CHAPTER I

I. World's Energetic consumption

II.1) Current situation and forecast

Energy is humanity's most essential supply for the correct functioning of society as we know it; activities such as production, distribution, stockage and consumption are not possible without energy. Its uses and applications are so deeply ingrained in our daily lives, that most people have taken it for granted. In fact, our energy consumption has been increasing since prehistoric times with the discovery of fire, considerably enlarged during industrial revolution and has nowadays exponentially augmented since then; all being a consequence of the modernization of economic activities.

In the past three decades, energy use has dramatically risen all around the world, fluctuating from 8 588.9 million tonnes of oil equivalent (Mtoe) in 1995 to 13 147.3 Mtoe in 2015.[1] As more countries start to develop, energy demand will also increase, for instance China's growth has raised the proportion of energy-intensive commodities produced globally.[1] China is currently the country leading energy consumption, almost doubling the consumption of the United States of America (USA), which is the second most energy consuming country as presented in Figure I. 1.

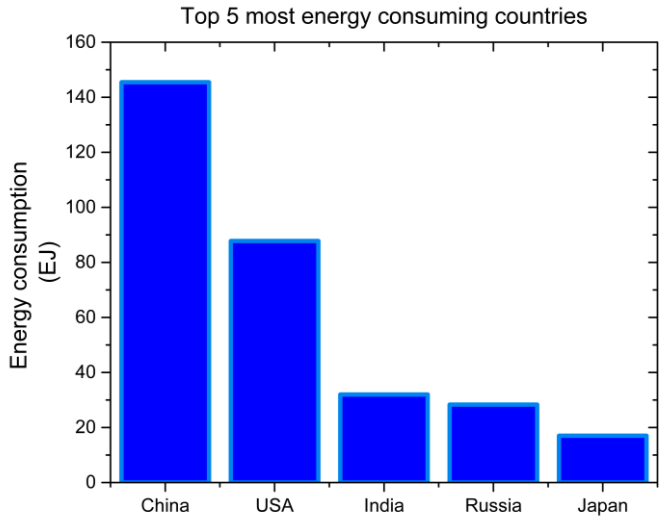

*Figure I. 1 China leads the energy consumption with 145.46 exajoules (EJ).*Adapted.*[2]

It has been projected by the Energy Information Administration (EIA) that the world energy consumption will augment by approximately 50% in the next 30 years.[3] Most of this growth is expected to come from the industrial sector, accounting for the largest share of energy consumption compared to other sectors, such as transportation and building.

On the other hand, energy consumption does not only depend on industrial activity, the corona virus disease (Covid-19) pandemic has affected the global energy demand, which is set to rise by 4.6% in 2021.[4] The pandemic has produced more disturbance to the energy sector than any other recent historical event, and its impact and consequences will be felt for years. It is still difficult to assess if the Covid-19 pandemic portrays a setback to all the efforts towards ensuring a more sustainable energy system or if it could be considered as a catalyst that will

hasten the pace towards a change. What is certain is that this crisis has brought back the fact that crucial changes in energy policy must be taken worldwide.

Trends in the global emissions of carbon dioxide (CO_2) and other air pollutants continue to warn about the rapid climate change and underline that strong coordinated action is needed urgently to reduce these gas emissions; that result in the rise of temperatures of the planet. For this reason, different scenarios have been projected such as the Stated Policies Scenario (STEPS), in which Covid-19 is gradually brought under control and the global economy returns to pre-crisis levels within one year.[5] Another envisioned scenario is the Sustainable Development Scenario (SDS), where clean energy policies and investments emerge setting the energy system on track to achieve sustainable energy objectives in full, including the Paris Agreement, energy access and air quality goals.[6]

Addressing all this thematic would go beyond the purpose of this work, although it is important to briefly discuss it, as it gives context on the role of energy in our society and thus, highlights the importance to know how we are currently satisfying this crucial need.

II.2) Sources of energy

The world's energy consumption relies on primary energy sources, which can take many forms and origins. In turn, these primary sources are converted into a secondary energy source, electricity, which is distributed through power lines and other transmission infrastructures; to satiate the energy demand of an industrial complex or even an entire country. There are three main sources of energy for electricity generation and they will be briefly discussed in this section.

a) Fossil fuels

Before the Industrial Revolution, mankind depended on very rudimentary forms of energy: human and animal muscle, as well as burning materials such as wood. Since then, fossil fuels have been an essential driver of economic, social and technological development. Currently, at the global scale electricity is mostly produced from fossil fuels and its share was estimated to be around 64% in 2019.[7]

Fossil fuels include coal, oil and gas, all of which have an important role in global energy systems; although they possess several negative impacts as once they are burned, they produce CO_2 and become the largest driver of global climate change. Additionally, they contribute to local air pollution, which has been linked to millions of premature deaths every year.[8]

Almost one third of global electricity generation is supplied by coal[9], which has been classified into four main ranks: anthracite, bituminous, subbituminous, and lignite. The ranking depends on the types and amounts of carbon contained in the coal and on the amount of heat energy it releases when burned.[10]

On the other hand, we have crude oil, which has remained dominant in the world energy supply over the past half century, and finds most of its applications in heating and

transportation. It is particularly useful as source of energy because of its high energy density when it is burned in the presence of oxygen. Crude oil is composed of mixtures of hydrocarbons that formed from the remains of animals and plants that lived millions of years ago in a marine environment. Over thousands of millennia, these remains were covered by layers of sand, silt, and rock; which in unison with the heat from the Earth's core and the pressure from these layers, turned into what we now call petroleum.[11] It is found in underground reservoirs and once it is extracted, it is sent to a refinery, where it is separated into a wide variety of derivatives. These petroleum derivatives include gasoline, jet fuel, waxes, lubricating oils, and even asphalt.

Although the use of oil is still increasing and focused in industries such as petrochemicals and transportation, where its substitution is difficult, it is still used to produce electricity to a small extent. There are three major ways to convert oil into electricity:[12]

- Conventional steam, where oil is burned to heat water, creating steam which is used to propel a turbine and generate electricity.
- Combustion turbine, where oil is burned under pressure, producing hot exhaust gases that spin a turbine which then generates electricity.
- Combined-cycle technology, where oil is first combusted in a combustion turbine, using the heated exhaust gases to generate electricity. After these exhaust gases are recovered, they heat water in a boiler, creating steam to drive a second turbine.

It is estimated that oil will at least continue to play the leading role in satisfying global energy needs for the following 20 years, even though the future supply of crude oil may be severely limited.[13]

Finally, natural gas is considered the cleanest burning and fastest growing fossil fuel, accounting for roughly one third of total energy demand growth through the last decade.[14] Natural gas is a combustible mixture of hydrocarbon gases, formed primarily of methane and its composition can differ extensively as it is produced in a similar process as crude oil. It is formed from organic particles that were covered in mud and other sediment, which accumulated over time, exerting high pressure on the organic matter, which ended up compressing it. This compression, combined with high temperatures found deep underneath the Earth, breaks down the carbon bonds in the organic matter. As one gets deeper in these layers, temperature increases. At lower temperatures, more oil is produced whereas at higher temperatures, more natural gas is created. Since natural gas has a low density, once it has formed, it will rise toward the surface of the Earth through loose, shale type rock and other materials, where it will rise up until it gets in a geological formation that is able to trap the gas under the ground and form a reservoir and is later extracted.

Natural gas is deployed as a major source of electricity generation in gas turbines and steam turbines. It does not have as many environmental disadvantages compared to the previously mentioned fossil fuels, particularly in terms of air quality and greenhouse gas emissions as it has been estimated that it emits 50% less environmental pollution than other fossil fuels.[15] Additionally, its ease of storability and the operational flexibility of gas-fired power plants allows it to respond to both seasonal and short-term demand fluctuations, as well as enhancing electricity supply security in power systems with a growing share of variable renewables. It also finds several applications in areas such as the industrial, residential, commercial and transportation sectors.[16]

b) Nuclear energy

In the 1930s, the idea of nuclear power began to flourish when the physicist Enrico Fermi demonstrated that neutrons were able to split atoms. Fermi led a team that achieved the first nuclear chain reaction in 1942 at the University of Chicago.[17] Nuclear energy originates from a process called fission where uranium atoms are split, generating heat that is used to produce steam, which is further used by a turbine generator to produce electricity.

It is often produced using a Pressurized Water Reactor (PWR) as shown in Figure I. 2, its function is to store and control the nuclear fission using uranium as nuclear fuel. The uranium is processed into small ceramic pellets and stacked together into sealed metal tubes known as fuel rods. Inside the reactor vessel, the fuel rods are submerged in water that has a dual purpose, functioning as a coolant and as moderator. The moderator aids in slowing down the neutrons produced by fission, which in turn helps to sustain the chain reaction.

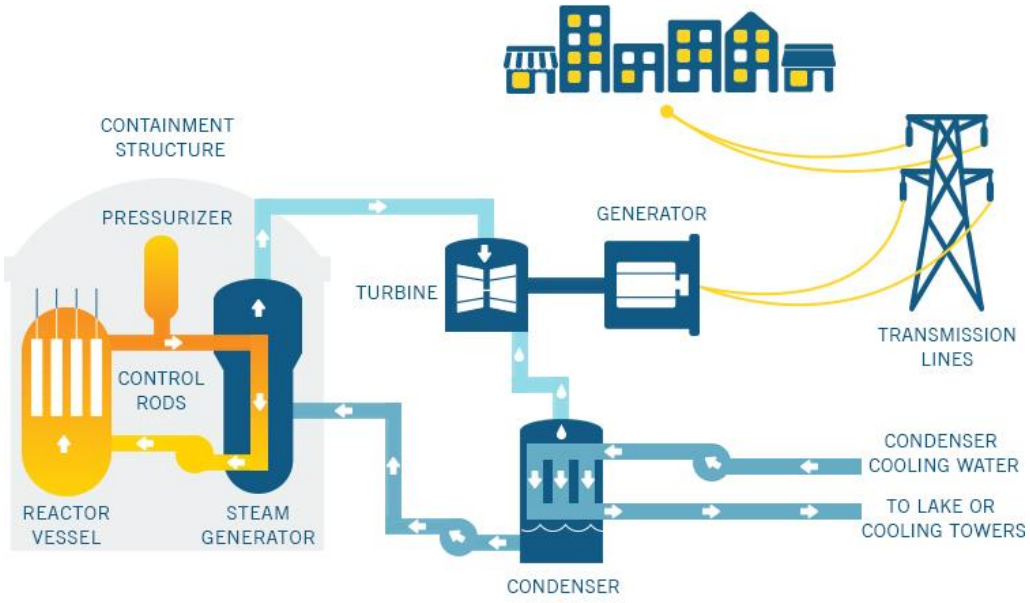

Figure I. 2 Simplified process flow chart of a typical PWR used to produce nuclear energy into electricity. Reproduced.[18]

As a mean to reduce or increase the rate of the chain reaction, control rods can be inserted or withdrawn into the reactor core. The reaction heats water in a primary coolant loop by thermal conduction, which is then pumped into a heat exchanger called the steam generator, where it flows through small tubes. Energy is transferred through the walls of these tubes, exchanging heat with a secondary coolant stream at lower pressure located on the sheet side of the heat exchanger, where the secondary coolant evaporates to pressurized steam. This energy transfer is performed without mixing the two fluids to prevent the secondary coolant from becoming radioactive. The generated steam is then fed to a turbine, which finally converts it into electricity and is eventually distributed to cities.

Nowadays, nuclear energy is the second-largest source of low-carbon electricity, with 452 operating reactors worldwide, and in 2018 it was estimated they provide 10% of global

electricity supply.[19] The countries that lead nuclear power generation are the USA, France, China, Russia, and South Korea.[20]

Despite its lower carbon emission footprint, electricity generation from nuclear reactors possesses several disadvantages and is not considered as renewable energy, given its dependence on a finite resource that requires mining of uraninite. But the most prominent problem is the potential risk of a reactor meltdown, as its devastating consequences have been shown by the nuclear accident at Chernobyl in 1986.[21] More recently, the accident at Fukushima Daiichi in 2011 caused by a huge earthquake and tsunami essentially highlighted the flaws in the design of this type of reactors.[22]

Other issues related to nuclear power include the produced nuclear waste, which remains dangerously radioactive for thousands of years making it difficult to store. Many nuclear plants are located near coasts because of the proximity to water for cooling, where due to climate change they face risk of more extreme storms and rising sea levels.

c) Renewable energy sources

It is unequivocal that the growing significance of environmental problems and climate change is a direct consequence of the world energy reliance on fossil fuels. Non-renewable energy sources took over because they seemed much cheaper than the renewable sources. Nevertheless, environmental problems have risen awareness, making renewable energy technologies considered as a solution to reduce and mitigate greenhouse gas emissions in the atmosphere through clean energy generation.

Although, their most prominent feature is that they are often considered as virtually infinite and that once facilities are operational, energy investments are spent on materials and personnel to expand and maintain the facilities. The share of renewable energy in global electricity generation jumped to 29% in 2020 as demand for all other fuels declined.[23] Similarly to fossil fuels, there are multiple types of renewable energy, but they can be divided into 5 major categories: hydropower, wind, bioenergy, geothermal and solar.

Currently, hydropower is the leading renewable energy in the world, supplying roughly 17% of total global electricity in over 160 countries.[24] Hydropower consists on using the kinetic energy of flowing water to move a turbine and generate electricity, which is then fed into the electrical grid. The endless nature of the cycle of water makes this process a reliable and clean way of producing electricity. Based on the way they function they can be classified into three types:

- Impoundment: Using a dam to store river water in a reservoir, the water is then released from the reservoir flowing through a turbine, activating a generator to produce electricity. The amount of released water depends on electricity needs or the level of water in the reservoir.
- Diversion: Also known as run-of-river, this facility channels a portion of a river through a canal to then power a turbine. Sometimes it might not require the use of a dam.
- Pumped storage: It functions as a battery by storing the electricity for later use. Water is pumped from a reservoir at a lower elevation to a reservoir at higher elevation and

in periods of high electrical demand, the water is released back to the lower reservoir, turning a turbine and generating electricity.

The size of the installed capacity determines if hydropower stations are expressed as small, medium or large as depicted in Table I. 1, and the size of the installed plant has to be done according to the environment in which they will be implemented. For instance, major disadvantages of large hydropower plants are energy loss due to long transmission lines, which end up harming the surrounding ecology and the subsequent deforestation and waste of underground resources to build the facilities.

*Table I. 1 Typical classification of hydropower stations.*Adapted.*[24]

Type	Capacity in Megawatts (MW)
Small	<10 MW
Medium	10 to 300 MW
Large	>300 MW

Some advantages of the small-scale hydropower plants are the reliable and flexible operation, as well as the ease of maintenance. In addition, small power plants have gained attention because they have the highest potential for electrification in rural and remote areas in which grid connection is not available.[25]

Despite being a renewable source of energy, hydropower can still be responsible for environmental problems disrupting aquatic ecosystems, which is why new projects are required to go through an Environmental and Social Impact Assessment.[26]

Taking the second spot in renewable energy supply, wind power has grown at a fast pace over the last two decades. Global wind power capacity was estimated to be above 740 Gigawatts (GW) in 2020, which has grown more than double since 2014.[27] China and the USA, currently lead and continue to grow in wind power output, together representing more than half of global wind output.[23]

In the same spirit as hydropower, wind power transforms kinetic energy from the wind by using a turbine that converts it into electricity by using the aerodynamic force from rotor blades. As wind flows across the blade, the air pressure on one of its side decreases, and this difference in air pressure across the two sides of the blade creates lift and drag. Since the force of the lift is stronger than the drag, the rotor spins powering a generator, thus transforming the aerodynamic force into electricity. A simplified chart of this process is shown on Figure I. 3.

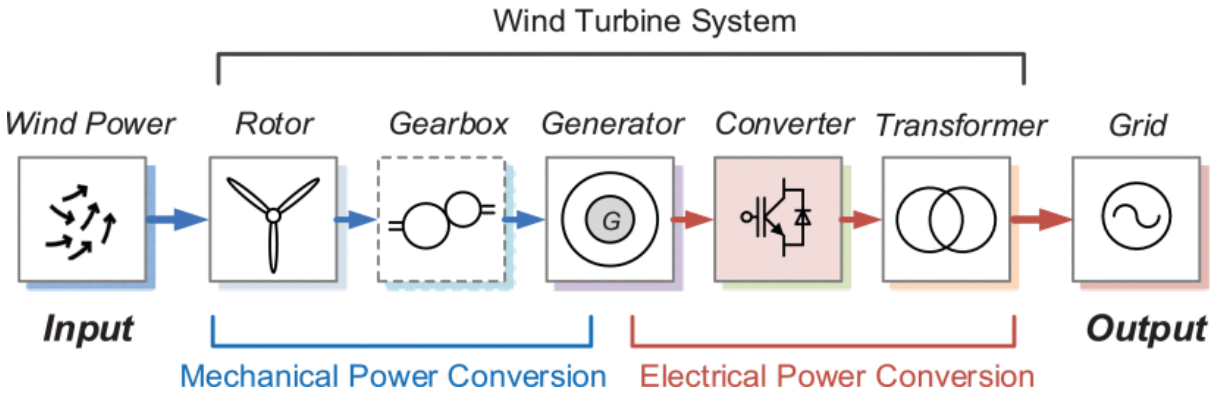

*Figure I. 3 The different stages of transformation of wind force into electricity in a typical wind turbine system.*Reproduced.*[28]

The design and installation of the turbines depends on the wind flow speed and its patterns, which can fluctuate and be modified by bodies of water, vegetation, and differences in terrain. The size of the rotor has also an influence in the power output, the larger the blade, the more electricity it can generate.

Two major types of wind turbines exist:

- Horizontal axis turbines: Endowed with three blades that face into the wind's direction, with the turbine pivoting at the top of the tower, usually known as "upwind" operation.
- Vertical axis turbines: These turbines are omnidirectional, and hence do not required to be adjusted to point into the wind to operate.

Wind power is often classified into two major categories, land based and offshore based. Land based wind power groups together several turbines what is known as a wind farm. Offshore wind turbines are installed in the ocean, they tend to be bigger than their land counterparts, generating vast amounts of energy. For a comparison, in 2015 the average rating of wind turbines installed in Europe was 2.7 MW for onshore and 4.2 MW for offshore, nowadays 8 MW wind turbines with a diameter of 164 meters (m) are installed offshore.[28]

Wind power has yet many challenges to overcome, such as being able to compete economically with conventional electricity generation sources and some locations may not be windy enough to be cost competitive. On the other hand, good land-based wind sites are often located in remote locations, thus increasing the cost of transmission lines as they must be built to bring the electricity from the wind farm to the city. It also faces a competition between land that is suitable for wind-turbine installation *vs* alternative uses such as agriculture or livestock, which might be more highly valued than electricity generation. Last but not least, turbines might cause noise and aesthetic pollution, as well as impact local wildlife since birds have been killed by flying into spinning turbine blades.[29]

Similarly, another renewable source that is currently helping us to meet our energy demand is bioenergy, which is derived from recently living organic materials usually referred to as biomass. It can be used to produce transportation fuels, heat, electricity, and even other type of products such as plastics. Biomass is often derived from organic materials that include:

- Crop wastes
- Forest residues

- Purpose-grown grasses
- Woody energy crops
- Microalgae
- Urban waste
- Food waste

The USA and Brazil, are currently leading the production of biofuels and account for around 80% of global production.[27] In 2018, bioenergy was the third largest renewable electricity generating source with a share of 9% of global production.[30]

Energy from biomass plays an important role in the global energy system, as it can significantly reduce carbon emissions, especially in sectors like manufacturing and transportation, where it is difficult to decarbonize.

In the same way as for fossil fuel, bioenergy technologies convert renewable biomass fuels into heat and electricity, for instance dry combustible feedstocks such as wood pellets are burnt in boilers or furnaces. This heat is used to boil water, producing steam which then powers a turbine to generate electricity. Biomass can also substitute a portion of coal in an existing power plant furnace, combusting both materials at the same time in a process called co-firing.[31]

For wet feedstocks, like food waste for example, biogas can be produced by putting the waste into sealed tanks where they rot and produce methane gas. Inside these oxygen-free tanks, often called digesters, matter gets decomposed by anaerobic bacteria that produce methane and other byproducts to form biogas. The gas is captured and purified to be further burnt to generate electricity or distributed to be used for cooking and heating purposes.

Biomass can also be converted to a gaseous or liquid fuel through gasification and pyrolysis.[32] In the gasification process, solid biomass materials are exposed to high temperatures with very little oxygen present, producing synthesis gas. This gas mixture consists mostly of carbon monoxide and hydrogen, which can then be burned in a conventional boiler to produce electricity or used to replace natural gas in a combined-cycle gas turbine. On the other hand, pyrolysis uses a similar process to gasification but under different operating conditions, lower temperatures and in the absence of oxygen, producing a crude bio-oil. This bio-oil is then substituted for fuel used in engines used for electricity production.

While biopower possesses advantages such as being a widely available renewable source of energy, being less expensive than traditional fuels and considered as a carbon neutral emitting source, reducing the overreliance of fossil fuels, there are also some intrinsic disadvantages.

Biomass energy is not as efficient as fossil fuels and is sometimes fortified with fossil fuels to increase its efficiency.[33] Furthermore, it is not entirely clean, as the use of animal and human waste increases the amount of methane gases, which damages the environment. Additionally, the pollution created from burning natural materials can be considered as bad as burning coal and other types of energy resources.

An additional disadvantage is that wood is often considered as the principal source of biomass energy, and vast amounts must be burned to produce the desired amount of power, potentially leading to deforestation as energetic demand will continue to grow. Lastly, bioenergy requires the utilization of vast amounts of land, a resource that is limited in supply. Even though there

are some downsides to biopower, it is considered as a necessary transitional element of global energy generation, that will play an important role over the next few decades.[34]

Another renewable energy that uses heating principles to produce electricity is geothermal power. Thermal energy produces underground reservoirs of hot water that exist in a wide range of temperatures, depending on the depth. This thermal energy originates from the formation of the planet and the slow decay of radioactive particles in the Earth's core. As presented on Figure I. 4, the earth's interior can be divided into four main layers: the inner core made of solid iron, an outer core of hot molten rock called magma, a mantle of magma and rock surrounding the outer core and finally a crust of solid rock that forms the continents and ocean floors.

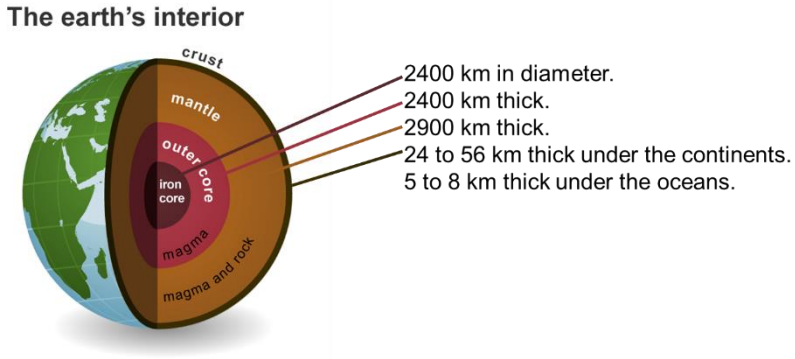

*Figure I. 4 Cross section of the Earth's interior describing each layer.*Adapted.*[35]

The heat that stems from the core travels through the layers, all the way to the crust where rocks and water absorb the heat from deep underground. This thermal energy is accessed by drilling water or steam wells in a process like drilling for oil and geothermal power plants use turbines and generators to convert this heat into electricity. There are three main types of geothermal power plants[36]:

- Dry Steam: They draw power from underground resources of steam, which is piped directly from underground wells to the power plant where it is directed into a turbine.
- Flash Steam: These are the most common and use geothermal reservoirs of water with temperatures greater than 182°C. This very hot water flows up through wells in the ground under its own pressure, which decreases as it flows upward inducing the hot water to boil into steam. The steam is then separated from the water and used to power a turbine. The leftover water and condensed steam are injected back into the reservoir, making this a sustainable resource.
- Binary Steam: They operate with water at temperatures ranging between 107-182°C, using the heat from the hot water to boil a secondary fluid that has a low boiling point. Both fluids are kept separated during the whole process, since the secondary fluid is vaporized in a heat exchanger and used to turn a turbine. The water is then injected back into the ground to be reheated.

The USA is the world's largest electric geothermal producer, although geothermal energy finds applications in other fields, mostly for thermal applications in bathing, house heating and industry. The direct use of geothermal energy for thermal applications continues to grow worldwide, roughly 8% every year, but the market remains geographically concentrated, with

only four countries (China, Turkey, Iceland and Japan), representing three-quarters of all direct geothermal use.[27]

One of the biggest advantages of geothermal energy is that it is a very predictable and reliable source of energy, having no restrictions in terms of weather conditions especially in comparison to other renewable energy resources like wind energy. Moreover, geothermal power plants have a small land footprint since the energy comes from within the earth, and large land surface to harness it is not required.[37]

On the other hand, the greatest disadvantage of geothermal energy is that geothermal power plants can only be built at specific sites, since reservoirs above 100°C are necessary for most geothermal plants, and these reservoirs are only found near tectonic plate boundaries or volcanoes. Additionally, the geothermal facilities have a high upfront construction cost, most of it is associated with the difficulty and cost of drilling deep into the Earth to access the geothermal reservoirs. Finally, geothermal plants can cause earthquakes as drilling deep underground is known to cause instability, which can lead to earthquakes at the surface of the Earth; for instance, a promising geothermal project in the Alsace region of France was suspended in late 2020, after a series of earthquakes that were attributed to geothermal drilling and well stimulation on the northern outskirts of Strasbourg.[38,39]

Finally, being the fastest growing and most affordable source of electricity, solar power is the last renewable source of energy that will be discussed. The sun has produced energy for billions of years and is so considered as the most abundant renewable energy source available. Throughout history, solar energy has been used as thermal energy to cook or to heat working fluids like water for domestic or industrial use, but more recently it started to be used to convert sunlight into electricity through photovoltaic (PV) devices.

A solar PV cell is an electrical device that converts the energy of sunlight directly into electricity by using the photovoltaic effect. Edmond Becquerel discovered the photovoltaic effect in 1839, while performing experiments with an electrolytic cell composed of two metal electrodes, concluding that some of them produced small amounts of electric current when exposed to sunlight.[40] In 1873, the British engineer Willoughby Smith discovered the photoconductivity of selenium, which varies its electrical conductivity upon illumination of its surface. Ten years later, Charles Fritts invented the first solar cell by using selenium, although too low for practical applications, this cell showed a power conversion efficiency (PCE) of roughly 1%.[41]

It was not until 1941, that Russel Ohl produced and patented the first silicon cell, more efficient than the selenium one, and within few years silicon-based photovoltaic cells reached PCE of 15%; this made them suitable for practical applications and even to start being deployed to power space satellites.[42,43]

Many solar cells and PV modules have been developed since the 1950s and are still intensively studied and improved to this day. The basic functioning of a traditional silicon PV cell is described in Figure I. 5. Nowadays a PV cell is made of semiconducting materials that absorb the photons emitted by the sun and as the photons are absorbed by the semiconducting material, they release the electrons from its atoms; leaving an unoccupied space that can be filled by other randomly moving electrons looking for another “hole” to be occupied.

Although, to produce an electric current, the electrons must flow in the same direction and this is achieved by using two different layers. In the case of silicon-based PV, the first layer is doped with atoms of phosphorus, which has one more electron than silicon, while the second layer is doped with atoms of boron, which has one less electron. When exposed to the sun, the resulting "sandwich" functions like a battery: the layer with an excess of electrons becomes the negative terminal (n-side) and the side that has a deficit of electrons becomes the positive terminal (p-side), generating an electric field at the junction between the two layers. This electric field sweeps electrons to the n-side, while the holes drift to the p-side, in turn the electrons and holes are directed to the electrical contacts applied to both sides, flowing to the external circuit as electricity. To minimize photon loss due to surface reflection an anti-reflective coating is added to the top of the cell.

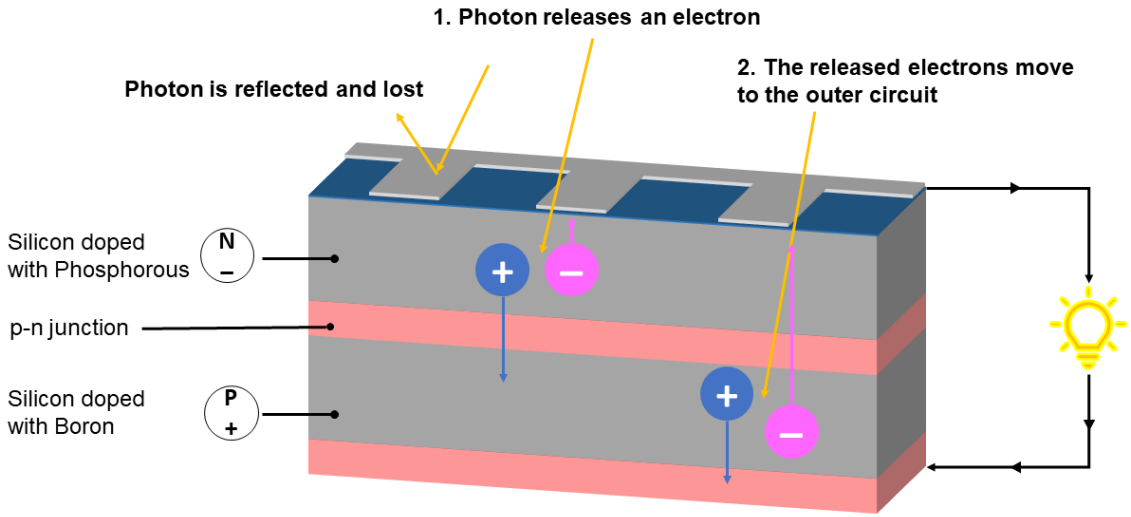

*Figure I. 5 How a silicon based photovoltaic cell works.*Adapted.*[44]

The operation of PV cells is based on 3 basic principles: the first one being the absorption of light, to generate the electron-hole pairs; the second is the separation of charge carriers of opposite types and finally the extraction of those carriers to an external circuit. In this sense, three main types of PV cells can be found:

- Crystalline Silicon Cells: Accounting for more than 95% of the solar cell market. In commercial applications, with efficiencies up to 27%.[45]
- Perovskites: These solar cells are made from hybrid materials, containing both organic and inorganic parts. Their PCEs at the laboratory scale has reached values of 25.2%.[46] Although a lot of research still needs to be done before the cells can be mass produced, due to instability problems, perovskites have many advantages such as being lightweight and flexible. Moreover, they are cheap to produce.[47,48]
- Organic Cells: They use organic molecules or polymers instead of semiconducting minerals. The cells continue to have a low conversion efficiency (compared to the previous ones) and a short lifetime, but they are potentially a low-cost alternative in terms of production.[49]

Demand for solar PV is thriving as it becomes the most competitive option for electricity generation, both for residential and commercial applications; this growth is shown on Figure I.

6, where global capacity reached roughly 760 GW in 2020.[27] Additionally, the price of silicon cells has dropped in recent years, making PVs very competitive compared to other sources of electricity.[50]

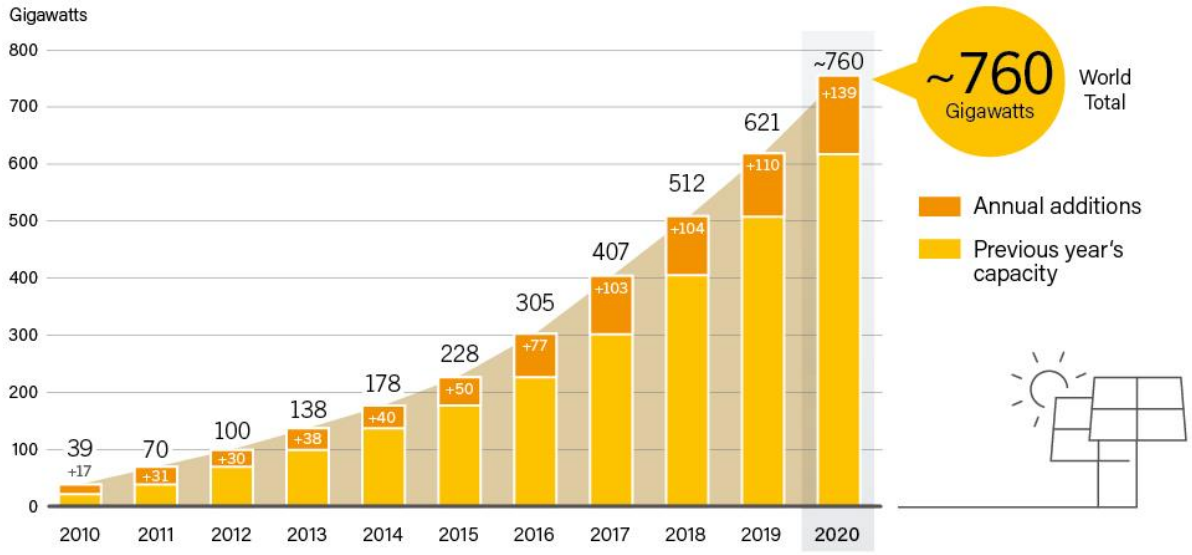

*Figure I. 6 Solar PV Global Capacity and Annual Additions in the last decade.*Reproduced.*[27]

Solar PV has an important role in electricity generation in a growing number of countries, and by the end of 2020, at least 15 countries had enough capacity in operation to meet at least 5% of their electricity demand with solar PV. For instance, solar PV accounted for around 11.2% of annual generation in Honduras and for notable shares in Germany (10.5%) and Greece (10.4%) just to mention a few.[27]

The use of solar energy has two main benefits: these systems do not produce air pollutants and they can be installed on buildings, having minimal effects on the environment. Nevertheless, despite its rapid growth, it still possesses some limitations, the main one being that the amount of sunlight that arrives at the earth's surface is not constant. It can vary depending on location, time of the day, season of the year, and weather conditions. Additionally, the amount of sunlight reaching a square meter of the earth's surface is relatively small, hence a large surface area is necessary to collect a good amount of energy; requiring a lot of space and increasing the amount of solar panels necessary to meet the energy demand.

Although pollution related to solar energy systems is far less compared to other sources of energy, there are also some toxic materials and hazardous products used during the manufacturing process of PV systems, which can indirectly affect the environment, particularly in the case of perovskites.

Additionally, contrary to fossil fuels, it is not easy to store energy from renewable sources. The electricity produced from PV is direct current, which is used to charge the batteries; thus, requiring battery replacement on a regular basis.

Finally, even though there has been a rapid decline in solar technology costs in the last decade, the overall costs to generate solar power remain high. Hence researchers are

focusing on improving the competitiveness of solar power and towards PV technologies to enhance their efficiency, stability, manufacturability, and availability.

To summarize, renewable energy is helping us to meet our current energy demand, although they also present a variety of obstacles such as the irregularity of weather, wind, and solar cycles, which hinder that the electric generation of a country can solely rely on them. Lastly, the high cost of the initial investment to install these technologies is not always affordable.

II.3) Sustainability

Worldwide, environmental pollution is a considerable concern and furthermore, the demand and prices of fossil fuels and its derived products continue to rise; and so renewable forms of energy are becoming more attractive. The current energy system has environmental impacts that extend beyond the by-products of combustion, such as climate change, biodiversity loss, the release of hazardous chemicals into the environment, and water scarcity.

These aspects have increased the focus on sustainable energy resources derived from wind power, hydro power, solar power, biomass, and geothermal power. This sustainability aims to meet the energy needs of the present without compromising the ability of future generations to meet their own needs, meaning that sustainable energy must become a power which can be replenished within a human lifetime and causes no long-term damage to the environment.

Actions have already been taken to mitigate these environmental impacts, for instance, the Paris Agreement has the objective of holding the increase in the global average temperature to well below 2 °C.[51] The physical impacts of climate change are among the challenges that renewable energies will have to face, as they have implications for the reliability and performance of energy generation. Furthermore, in order to meet the 2 °C climate goal, the share of renewable energy in the final energy consumption must increase above 65% by 2050.[52]

Meeting the current and future energy demand in a sustainable way is a critical challenge in the global ambition to reduce the impact of climate change, while maintaining economic growth. Additionally, electricity is essential for health care, education, and economic development and improving energy access in the least-developed countries and making energy cleaner are essential to achieve most of the United Nations 2030 Sustainable Development Goals.[53]

While renewable energy is plentiful, most of the environmental impact is related to the manufacturing of the equipment required to harness energy. In this regard, due to its less harmful impacts on the environment, solar energy is often considered as the best and most attractive candidate to ensure a sustainable way to produce energy in future. Being practically inexhaustible, almost pollution-free, silent, and having no mechanical involved parts, solar power will clearly continue to be essential in the upcoming decades.

The evolution of the solar PV industry so far has been remarkable, with several milestones achieved in recent years in terms of installations, cost reductions and technological advancements; as a result, solar PV power installations have been dominating the renewables industry in the past years.

Moreover, the solar PV industry is changing rapidly, with innovations occurring along the entire chain of production. The major driver for innovation has been the push for higher efficiency, which is essential for competitive module manufacturing, since it directly decreases cell processing costs by reducing quantities required for a given output. The further growth of the solar PV industry largely depends on reducing the costs by using adequate materials and this is where all the developments in organic electronics become important.

II. Organic Electronics

Organic semiconductors combine the chemical and mechanical benefits of organic compounds with the electronic advantages of semiconducting materials; obtaining versatile structures that can be altered through chemical synthesis to improve their ability to absorb light or conduct electricity. The use of organic compounds as active materials in electronic and optoelectronic devices has led to low-cost methods for fabricating useful structures that are inaccessible when using conventional semiconductors.

Hence, organic electronics has been studied in the fields of physics and chemistry for more than 70 years, with its main attraction being the ability to modify chemical structure in ways that could directly impact the properties of the materials when deposited in thin films. Being the first person to observe electroluminescence in organic materials, André Bernanose is often considered the father of organic light emitting diodes (OLEDs), although it was not until 1987 that Ching W. Tang reported the fabrication of a practical OLED device.[54] This OLED incorporated a double-layer structure motif composed of copper phthalocyanine and a derivative of perylenetetracarboxylic dianhydride.

Since that first demonstration, organic thin films have proven useful for several applications, and are nowadays used to create digital displays in devices such as televisions, computer monitors, smartphones, and even handheld game consoles. Furthermore, the charge carrier transport properties of molecular organic materials have been investigated extensively, which has led to the development of semiconducting materials that are used for electricity applications.

II.1) Organic semiconducting materials

Organic semiconductors are mostly made up by carbon and hydrogen atoms, with a few heteroatoms such as sulfur, oxygen, and nitrogen. These materials combine the electronic advantages of semiconducting materials with the chemical and mechanical benefits of organic compounds, like polymers.

In this sense, these materials are capable of absorbing light, conduct electricity, and emit light; these properties are all linked to the material's structure, which can easily be modified on the chemical synthesis. Chemical modification not only permits tuning of electronic properties but can also help to improve solubility or modify the material to make it mechanically robust, lightweight, and/or flexible.

Furthermore, a semiconductor is a material whose resistivity lies between the values of a conductor and an insulator (10^{-4} – 0.5 Ω·m).[55] However, the resistance of a semiconductor

material decreases with an increase in temperature, as the energy gap between conduction and valence band is narrow for semiconductors when compared to insulators. The energy gap is the energy required to promote a valence electron bound to an atom to become a conduction electron, which serves as a charge carrier to conduct an electric current as it is free to move within the crystal lattice of a solid material. The valence band of a semiconductor is almost filled by electrons, whereas the conduction band is nearly empty. The forbidden energy gap is small, close to 1 electronvolt (eV), therefore, a small amount of energy is required for valence electrons to move into the conduction band. And so, a rise in temperature allows electrons in the valence band to gain energy and jump to the conduction band. As a result, semiconductors can change from insulators to conductors due to variations in temperature.

While they show semiconducting properties, inorganic and organic materials have strongly different “semiconducting” nature and so, semiconductors can be classified in two categories:

- Intrinsic: Commonly known as a pure semiconductor, having the ability to create electron–hole pairs at room temperature. When a potential is applied across it, conduction is induced through free electrons and holes that are generated by the breaking of covalent bonds through thermal energy. Consequently, the current flow in the intrinsic semiconductor is a combination of electron and hole. They are often attributed to inorganic materials.
- Extrinsic: Also called impure semiconductor and often associated to organic materials. It consists of a mixture of an intrinsic semiconductor with impurities. At room temperature, the intrinsic semiconductor has small conduction, so in order to improve its conductivity, a small amount of impurity is added. This process is called doping and when performed, either the number of electrons increases, or the number of holes increases depending on the dopant. Addition of pentavalent impurities produces free electrons (n-type semiconductor), while in the case of trivalent impurities, additional holes are generated (p-type semiconductor).

The differences between intrinsic and extrinsic semiconductors are compiled in Table I. 2. These differences between organic and inorganic semiconductors show that deep understanding on their electronic structure is needed in order to understand their photophysical properties, as well as useful when designing and improving semiconductor devices.

*Table I. 2 Differences between intrinsic and extrinsic semiconductors.*Adapted.*[55]

Factors	Intrinsic semiconductor	Extrinsic semiconductor
Purity of semiconductor	Pure semiconductor	Impure semiconductor
Density of electrons	Equal to density of holes	Not equal to density of holes
Electrical conductivity	Low	High
Effect of temperature	Only depends on temperature	Temperature dependent and on the amount of impurities
Type of impurities	No impurities	Trivalent, pentavalent

In addition, organic semiconductors can be used in three ways: amorphous molecular films, molecular crystals and polymer films. As the name implies it, in the first application, organic

molecules are deposited as an amorphous film through evaporation or spin-coating, forming thin films; which can then be used for device applications such as OLEDs.

In the second method, molecular crystals are formed using organic molecules such as naphthalene. A crystal consists of a lattice and a basis, for instance atoms like silicon can form a crystal through covalent bonding. In the same way, organic molecules are also able to form the basis of a crystal that is held together via van der Waals interactions. The charge mobilities that can be obtained in molecular crystals are high compared to those in non-crystalline organic materials, which makes them very suitable for transistor applications.[56]

Lastly, polymer films are applied through several deposition techniques including simple spin-coating or ink-jet deposition. Polymers are molecules that have been covalently coupled together, bearing repeating units that form a chain like structure. They are more suitable to blending than small molecules since polymer blends are thermodynamically more stable and less susceptible to crystallization.

Furthermore, organic semiconductors are quite unique since their solid-state properties are attributed to a hierarchical structure of atom–molecule–solid. Atoms link together by covalent bonds, composing molecules, which in turn are held together by van der Waals interactions and create the solid material. This hierarchy is possible due to π-electrons, which are the source for all the functional electronic properties of organic semiconductors.

II.2) Properties of organic semiconductors

Organic molecular materials used as semiconductors are endowed of a free electron system, this is due to the exceptional nature of the carbon atom, which can form several types of structures through stable covalent σ- and π-bonds. The σ-bonds are formed by hybrid orbitals between the adjacent carbon atoms, whereas the π-bonds are formed by the overlap between orbitals of adjacent carbon atoms that do not participate in the formation of σ-bonds, a simplified scheme is shown in Figure I. 7. The σ-bonds are relatively strong and the electrons in the σ-bonds are likely to be localized. In contrast, the π-electrons are widely delocalized making π-bonds weaker than σ-bonds. Molecules containing several delocalized electrons are known as conjugated systems, this delocalization of electrons bestows organic semiconductors with special properties.

One of said properties is that these materials can show strong colors, in contrast to usual organic or plastic materials that are formed only by the σ-bonds and do not possess colors. Since σ-bonds are so strong in non-conjugated molecules, the electronic excitation energy becomes high and the optical gap energy is much larger than the visible photon energy range, which is between 1.6–3.3 eV. On the other hand, when the π-electrons are delocalized across a molecule, the electronic excitation energy considerably decreases, making the materials to become colored due to the absorption of visible light.

Another property these materials possess is that they tend to have large dipolar moments, and hence are able to strongly couple with electromagnetic waves. This is once again due to the electronic π-system, which typically delocalizes electrons within the molecule; furthermore,

the gap between binding and anti-binding can be manipulated by controlling the size of the π-system (degree of conjugation).[57]

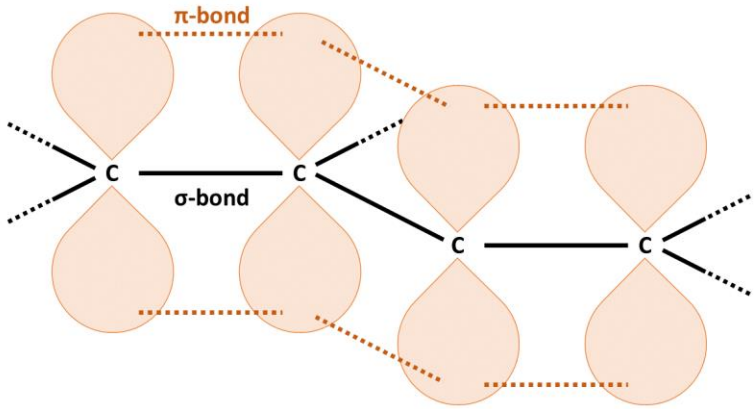

Figure I. 7 Simplified schematic for a linear carbon chain connected with σ- and π-bonds.

Finally, molecules containing aromatic groups can self-organize to form crystals when they gather; furthermore, if the molecular shapes have relatively high symmetry, molecules can be packed densely. This phenomenon is known as π-stacking and will be further discussed in detail throughout this chapter. In the crystals composed of densely packed molecules, molecular orbitals of π-electrons, can overlap and interact with those of the adjacent molecules. Consequently, the electronic states of the π-electrons are extended widely over the crystals. These intermolecular interactions between the combination of adjacent molecules play an important role in the charge carrier transportation of organic semiconductors.

An essential tool to determine the π-electronic states of organic semiconductors is molecular orbital (MO) theory, which is based on the concept that the electrons are not assigned to the individual bonds between atoms, but to the molecular orbital that is extended to the whole molecule.[58] In the simplest MO calculations, empirical values are used to describe electronic states in the molecules. In the same regard, calculations using density functional theory (DFT) are more frequently used to calculate ground states of many π-electron systems; the method is based on the calculation of distribution function of electron density and the effective potential.[59]

Moreover, predicting what kind of crystal structure can be formed by a molecule before it is synthesized and crystallized is a difficult task. However, the stability of molecular packing in the crystals can be studied using molecular dynamics (MD) simulations, which simulate the motion of atoms and molecules while assuming an interatomic potential. Although, it is still compulsory to synthesize the materials and to conduct the crystal structure analyses for the proper development and design of organic semiconducting devices.

II.3) Design of molecules for organic semiconductors

As previously mentioned, the rate of charge transport in organic semiconductors is ruled by electron–electron, as well as by electron–vibration interactions. However, factors such as defects, impurities, charge carrier densities, electrical fields, temperature and pressure can also have an influence. The inability to predict the extent of the previously mentioned factors makes virtually impossible to accurately predict the charge transport properties of small molecules or polymers from their individual molecular structures. Nevertheless, molecular design has proven to be a useful tool in development of promising organic semiconductors.

The molecular design of these materials can be divided into four main constituting components, as depicted in Figure I. 8. Such a structure can be a single molecule or a repeating unit in a conjugated polymer. The conjugated core (backbone) and alkyl chains govern a big part of the electronic properties, like energy bandgap and solubility, as well as they influence the molecular packing.

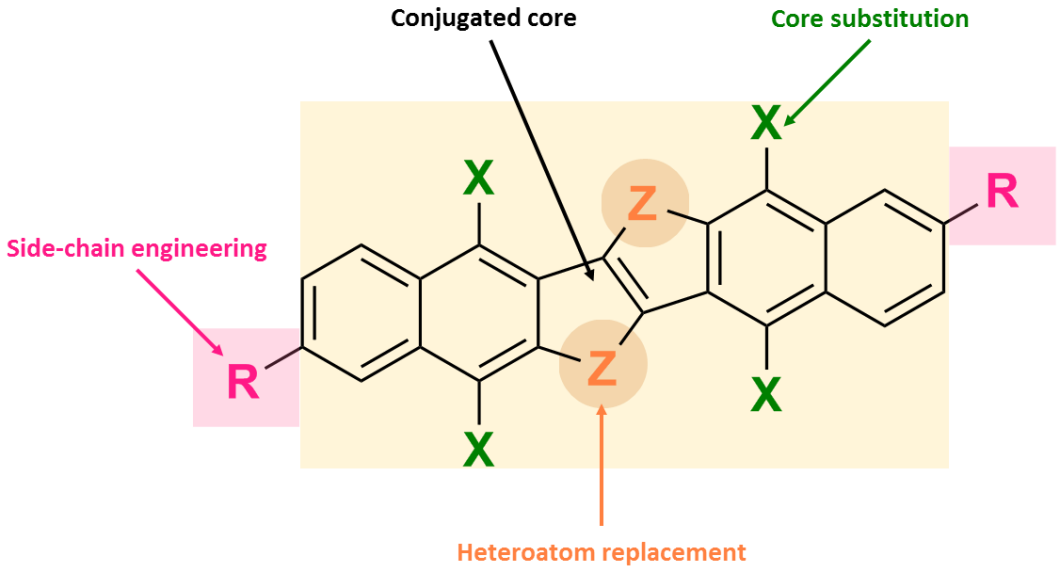

*Figure I. 8 Representation of a typical π-conjugated system.*Adapted.*[60]

Another effective way to tune electronic properties, solubility and molecular packing is by the addition of heteroatoms, for instance thiophene rings are known to be an extremely important unit to obtain high-performance organic semiconductors. In the same spirit, core substitution affects electronic properties, solubility and molecular arrangements, this is done by changing the carbon/hydrogen ratio or by introducing halogen atoms, which modifies the dipolar moment of the structure.

The incorporation of side chains is commonly done to improve the solubility, while they may also impact electronic properties in the solid state by changing molecular packing structures or altering the torsion conformation of the conjugated backbone. Side chains are typically insulating, as a result, if an excessive amount of side chains is present, the mass percentage of conjugated segments decreases. The importance of each constituting component in the design of semiconductors is briefly highlighted below.

a) Effect of conjugation extension and aromaticity

There are many studies confirming that conjugation extension in small molecules is a viable approach to improve charge mobility, particularly for the linear acene family.[61–63] As can be seen in Figure I. 9, linear acenes are aromatic hydrocarbons composed of fused benzene rings. From a theoretical point of view, as well as performance wise, they have been of great interest; for instance, anthracene is one member of the acene family with reported transistor characteristics, showing a mobility of 0.02 $cm^2/(V \cdot s)$ when measured at low temperature.[61]

In practical applications, the selection of the acene core length is a combination of the theoretical performance limit, chemical stability and ease of processing. The thin film morphology is also strongly dependent on the molecular size: smaller acenes have a tendency to give more three-dimensional growth, while larger acenes lead to small grains due to lower diffusivity at a given temperature.[64]

Moreover, with increasing number of rings, solubility is tough to achieve and hence, requires the addition of solubilizing groups, which may ultimately reduce the mobility of the soluble derivatives due to the insulating nature of alkyl chains. To circumvent these issues, several approaches have been reported, including replacement of some benzene rings with other heteroaromatic rings to lower the aromaticity, attaching bulky substituents, and substitution with electron-withdrawing groups.[60]

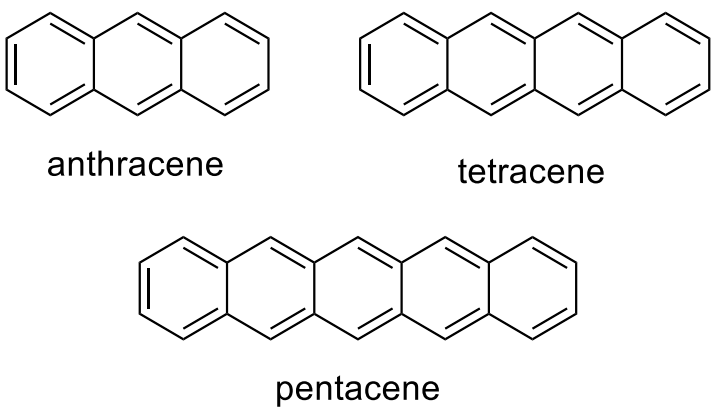

Figure I. 9 A few members of the linear acene family.

Ultimately, it is possible to say that the combination of conjugation extension and proper lowering of aromaticity is an effective way to achieve high charge mobilities for fused ring systems with good stability. In fact, there are additional examples which have used the above design principles and resulted in stable high-performance organic semiconductors.[65,66]

b) Heteroatom replacement

The addition of a heteroatom can have a big impact on the electronic structure and crystal packing of a conjugated system, and most commonly, heteroatom replacement ranges from chalcogen atoms to nitrogen. For instance, in the quaterchalcogenophene family presented in

Figure I. 10, switching from sulfur to selenium has a slight effect in the mobility.[67,68] However, in 2,6-diphenylbenzodichalcogenophenes, replacing sulfur by selenium had a great effect on the charge mobility, almost doubling in value.[69] Surprisingly, the trend did not continue when selenium was replaced by tellurium, and the mobility dropped about 2 orders of magnitude compared to the sulfur derivative. On the other hand, the chemistry of sulfur is more versatile when compared to that of selenium and tellurium, coupled with the higher toxicity and environmental impact of selenium and tellurium, their use in practical applications has been discouraged.

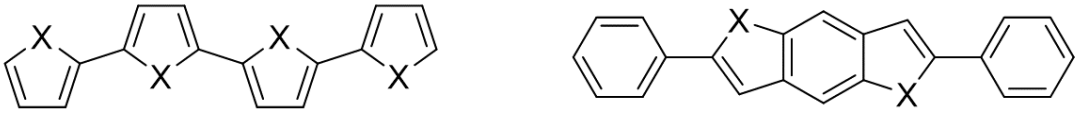

Quaterchalcogenophene

X=S μ_h**=0.0025 cm²/V·s**

X=Se μ_h**=0.0036 cm²/V·s**

Diphenylbenzodichalcogenophene

X=S μ_h**=0.081** **cm²/V·s**

X=Se μ_h**=0.17** **cm²/V·s**

X=Te μ_h**=0.0073** **cm²/V·s**

*Figure I. 10 Influence of heteroatom replacement in mobility values for two different molecules used for organic semiconductors. Mobilities were measured for vacuum deposited films of the materials.*Adapted.*[60]

The heteroatom effect between sulfur and nitrogen has been explored in other families, such as the ones depicted on Figure I. 11. The anti-dibenzothienopyrrole (anti-DBTP) showed a 50 fold decrease in mobility in vacuum deposited organic field transistor devices (OFETs) when compared to its sulfur counterpart, dibenzo[d,d′]thieno[3,2-b;4,5-b′]dithiophene (DBTDT); although this was measured in single crystal OFETs.[70,71]

Conversely, the syn-dibenzothieno[b,d]pyrrole (syn-DBTP) exhibit no field effect properties, while its sulfur counterpart (BBTT) exhibited a mobility of 0.5 $cm^2/(V·s)$.[72] However, the introduction of N–H···π interactions is not always detrimental, for instance in indo[3,2-b]carbozole (ICZ), extremely favorable bidirectional electronic coupling in crystals has been observed. OFETs of ICZ gave satisfying mobility values, whereas its sulfur counterpart, benzo[1,2-b:4,5-b′]bis[b]benzothiophene (BBBT), had 10 times smaller mobility values.[73]

Furthermore, an increase in charge mobility in OFET devices was often reported in linear acenes, when some of the carbons are replaced with nitrogen atoms.[74] Nevertheless, more experiments are needed to further extend and study this phenomenon to other systems.

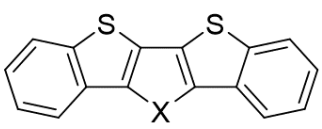

Dibenzothienodithiophene (DBTDT)

X=S μ_h=0.6 $cm^2/V{\cdot}s^{\pm}$

anti-Dibenzothienodithiophene (anti-DBTP)

X=NH μ_h=0.012 $cm^2/V{\cdot}s$

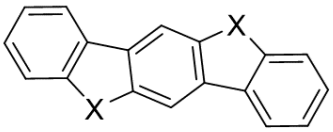

Benzobisbenzothiophene (BBBT)

X=S μ_h=0.01 $cm^2/V{\cdot}s$

Indolocarbozole (ICZ)

X=NH μ_h=0.1 $cm^2/V{\cdot}s$

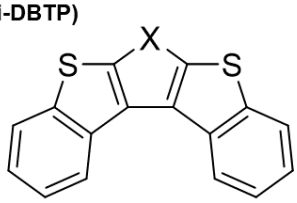

Bisbenzothienothiophene (BBTT)

X=S μ_h=0.5 $cm^2/V{\cdot}s$

syn-Dibenzothienopyrrole (syn-DBTP)

X=NH No FET properties

*Figure I. 11 Effect of N–H···π interactions on the mobilities of different families. ±All mobilities were measured for vacuum deposited films except for DBTDT.*Adapted.*[60]

c) Core Substitution with Electron Withdrawing Groups

The substitution on a conjugated core with electron withdrawing groups, such as halogens or nitriles (CN), usually enhances stability against oxidation, leads to changes in molecular packing and can potentially induce a transition from p-type materials to ambipolar or n-type materials. Electron withdrawing groups are capable of pulling electron density away from a π-conjugated system, either through an inductive effect or by resonance. On the contrary, electron donating groups, such as alkoxy or alkyl thioether, typically increase oxidation potential and reduce stability.

The development and stability of n-type organic semiconductors that can operate under ambient conditions, to complement high performance p-type materials for making organic integrated circuits, has been one of the obstacles that the organic electronic community has had the most issues with.

In this regard, MO theory plays an important role, as most often in π-conjugated systems, the highest occupied molecular orbital (HOMO) and the lowest unoccupied molecular orbital (LUMO) are respectively the binding π-state and the anti-binding π*-state. This means that the HOMO can be related with the valence band and the LUMO with the conduction band of a semiconductor. It has been reported that to achieve operational stability in air, organic semiconductors must be designed with low lying LUMO levels, since electron affinity needs to be at least 3.0 eV but should not be much greater than 4.0 eV.[75]

The most common way to achieve air-stable n-type organic semiconductors is through perfluorination. For instance, replacing all hydrogen by fluorine (F) atoms in pentacene leads

to perfluoropentacene; for which ionization energy increased roughly by 0.6 eV with respect to pentacene. Furthermore, electron affinity increased by 0.7 eV, translating into better air stability and ease of electron injection.[76]

Finally, perfluoropentacene has different crystal packing from pentacene, suggesting the intrinsic hole and electron mobilities might be lower in perfluoropentacene.[77] Furthermore, the importance of fluorination in the backbone of conjugated polymers has recently been reviewed[78], where a general understanding of the impact of fluorination on the device performances has been discussed. Additionally, atomic substitution of the polymer backbone with fluorine atoms has attracted a lot of attention, since, fluorine atoms impact positively some of the key features of such polymers including the lowering of the energy levels.[79] It is worth mentioning that in the case of partial fluorination, ambipolar materials are obtained.[80]

Besides fluorination, chlorination has proven to be more effective at dropping the LUMO level of the resulting molecules, this has been attributed to the fact that a chlorine (Cl) atom contains empty 3d orbitals able to accept π-electrons from the conjugated core, whereas F does not possess empty orbitals for such delocalization.

On the other hand, the position of the substitution plays an important role on charge transport properties and crystal packing. For instance, chlorinated derivatives such as 5-chlorotetracene (ClT), 5,11-dichlorotetracene (DClT) and 5,6,11,12-tetrachlorotetracene (TClT) were obtained and tested in OFETs, as shown in Figure I. 12. [81,82]

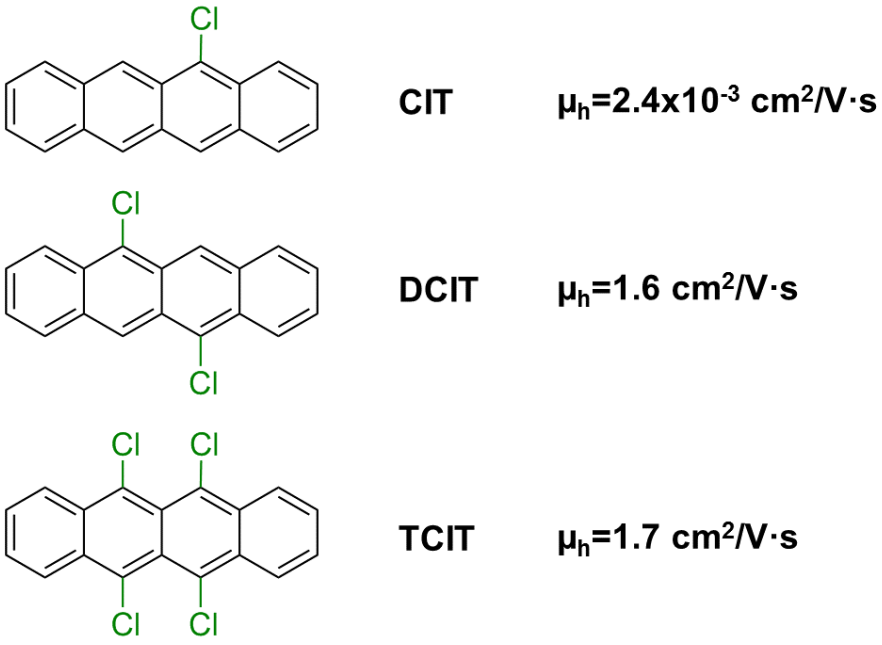

Figure I. 12 Representative acene chlorinated derivatives along with their respective hole mobility values. All mobilities were measured for single crystals.[60]

Yet, none of these molecules presented n-type charge transport properties; but both DClT and TClT displayed rather good hole mobilities. In contrast, halogenation altered the crystal packings from a herringbone-type structure for ClT to a face-to-face slipped π-stacking motif for DClT and TClT, which is what might explain the difference in their charge transport

properties. Further studies of the effects of halogenation on the properties of organic semiconductors have been broadly done and summarized.[83]

Possibly, perylene diimide and naphthalene diimide derivatives are the most studied air-stable n-channel (hole-transporting) organic semiconductors, and upon addition of electron withdrawing groups, numerous high mobility air-stable materials have been reported.[84]

d) Incorporation of side chains

As it was briefly mentioned before, the inclusion of side chains on conjugated cores is principally done to add solubilizing groups that ease solution-processability of organic semiconductors. Alkyl chains are considered insulating materials; hence, they do not contribute to charge transport directly. However, these side chains can considerably impact the charge transport properties by affecting molecular packing and the thin film morphology.[85,86]

For instance, to prevent dimerization and improve their stability against oxidation, alkylation or arylation of peri-positions have been performed in acene derivatives. Furthermore, this also changed their packing motifs from a herringbone pattern to a face-to-face π-stacking, by diminishing the C–H···π interactions.[87,88] In the same way as for halogen substitution, the packing of the crystals is susceptible to the position of alkylation.[89] Additionally, other reports have found that the size of the alkyl chain plays a significant role in two dimension (2D) and three dimension (3D) polycrystallite formation, which ultimately impacts the charge mobility.[90]

In addition, the attachment of alkyl chains is not only limited to carbon atoms, N-alkylation introduces solubilizing groups when the conjugated core has nitrogen atoms. Nevertheless, this can block N–H···π interactions, which in turn can possibly change the molecular packing. Such an example was mentioned before, where the synergy of N–H···π interactions in ICZ crystals resulted in strong bidirectional electronic coupling, enhancing the charge transport.[73]

Moreover, hydrophilic triglyme chains and other oligo ethers have also been used as side chains in conjugated molecules.[91] Unique features can be obtained when both hydrophilic triglyme and hydrophobic alkyl chains are substituted on the same conjugated core, resulting in amphiphilic molecular design, which can sometimes be advantageous on charge transport.[60]

Another type of substituents are branched side chains, since linear side chains usually do not impart enough solubility for various printing techniques; unfortunately, they have a tendency to disrupt crystal packing, which results in poor mobilities. In an attempt to solve these issues, thermally cleavable aliphatic carbonyloxy substituents have been introduced onto conjugated cores such as sexithiophene. The carbonyloxy group is volatilized upon thermal treatment, and two short hydrocarbon chains remain at the terminal thiophene rings.[92]

Finally, another unique side chain that can be used is the cyclohexyl group, which has been frequently known to add steric bulkiness at the periphery of the core, providing improved solubility without having a detrimental consequence on the molecular packing in the thin film phase.[93]

II.4) Importance of Morphology

The promising qualities of organic photovoltaic devices (OPVs) have made them receive a lot of attention, as they have the ease of solution processability, tunable electronic properties, low manufacturing temperature, as well as being relatively cheap and less environmental impactful. They have exceeded certified efficiencies of 17% to date, close to efficiency values obtained by low-cost commercial silicon solar cells.[94,95]

The operation of OPVs can be summarized in five steps (Figure I. 13). First, the absorption of incident light excites electrons and when light with high enough energy levels is absorbed, electrons excited from the HOMO to the LUMO generate an exciton. If the energy of the absorbed light is greater than the band gap, the electron will move to a higher energy level than the LUMO and decay down in a process known as thermalization, which results in an energy loss in the form of heat.

Secondly, the diffusion of the exciton occurs between the donor-acceptor interface and the organic semiconductor component, where the offset between LUMO levels will drive exciton dissociation. Although, this must occur within a certain amount of time otherwise the excited electron will return to the empty energy state (leaving a hole), this process is often referred as recombination. The time taken is known as the exciton lifetime, which is often represented as the distance that the exciton can diffuse in this time (usually about 10nm).

Thirdly, a dissociation of the exciton across this interface ensues, the electron moves to the acceptor material and the hole will remain on the donor. The charge carriers will still be attracted, and charge-transfer state happens. When the distance between the pair increases, the attraction decreases. Ultimately, a charge-separated state is formed as the binding energy between them is surpassed by thermal energy. While the electron-hole pair is still attracted in the charge-transfer state, recombination can take place across the interface between both materials.

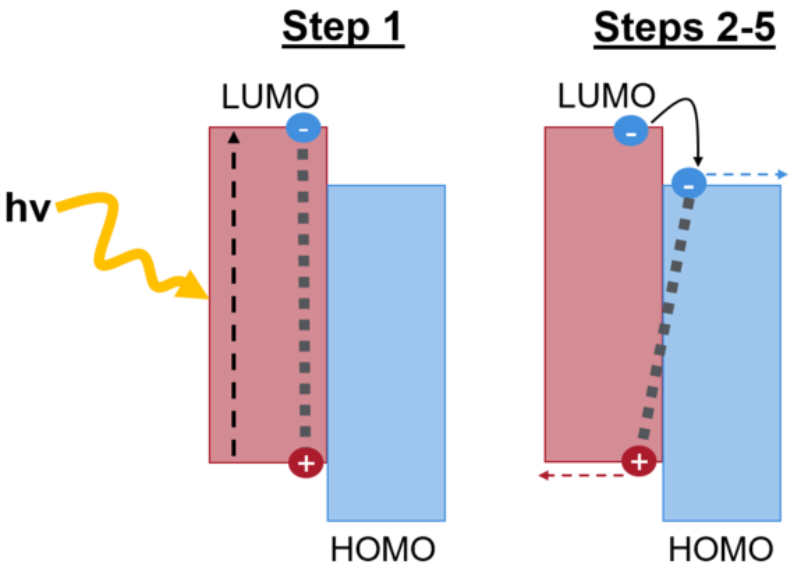

*Figure I. 13 An approximation of the basic steps that govern OPV function under light illumination.*Reproduced.*[96]

Next, the charge-carriers will diffuse to the appropriate electrodes through the relevant interfacial layers; for instance, the holes will travel to the anode and the electrons to the cathode. Finally, a charge-carrier collection process arises at the electrodes and the charge carriers are used to do work in the external circuit of the cell to generate an electric current.

It is important to consider that at several stages, the electron and hole can recombine, wasting the absorbed energy used for initial excitation. Furthermore, recombination can be categorized as either geminate, were the initially produced electron-hole pair recombines before exciton dissociation; or as non-geminate, where the free electrons and holes can recombine, regardless of their source. Both processes can be radiative, which is when a photon is released or non-radiative, meaning that no photon is released.[97]

The first two-component OPV was proposed by Tang et al in 1986[98], but efficiencies remained low for several years as they relied on bilayer cells. The main issue being that excitons are only able to dissociate at the interface between donor and acceptor, generally diffusing around 10 nm before decaying back to the ground state.[99] Although, the total active layer required to efficiently absorb light usually has a thickness of more than 100 nm, this means that bilayer cells are either too thin to properly absorb, or too thick for efficient exciton dissociation.

The solution to this is known as the bulk heterojunction (BHJ) cell and it was conceived in 1995.[100,100] In this type of device, instead of a strict two-layer system, the donor and acceptor materials are intimately mixed at the nanoscale level, which allows the interfaces to be dispersed across the active layer, while preserving the required thickness for absorption. There have been countless refinements in morphology control[101,102], development of new donors and acceptors[103], and technical expertise, which all together has led to modern BHJ OPVs reach efficiencies over 17%.[94]

Most OPVs used in modern research are solution-processed BHJ cells, where depending on the orientation of the electrodes, the architecture can be considered as conventional or inverted (Figure I. 14). The hole-and electron-transporting at the interfacial layers facilitates the charge-carrier transport on either side of the active layer. Typically, the hole-transporting layer (HTL) in a conventional stack is made from Poly(3,4-ethylenedioxythiophene) polystyrene sulfonate (PEDOT:PSS) and is often paired with an Indium Tin Oxide (ITO) anode. Whilst a typical electron-transporting layer (ETL) is calcium, often paired with an aluminum cathode. These layers promote the transport of one type of charge carrier through favorable energy level positioning, while hindering the transport of the other carrier. As result, the HTL is frequently known as the electron-blocking layer, and vice versa.

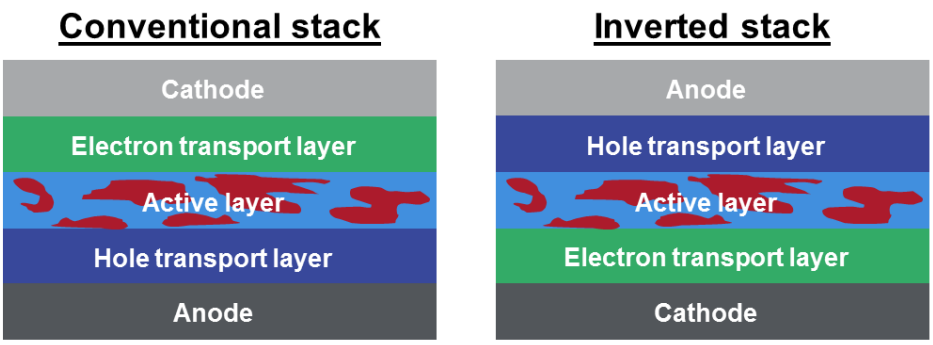

*Figure I. 14 The stacks used in a conventional and inverted OPV cell, where the layers are not given to scale.*Adapted.*[96]

Noteworthy advances in high-performance and air-stable organic semiconductors have been achieved through molecular design. However, charge carrier mobility is usually determined by the strength of electronic coupling between the hopping sites, their disorder, and their geometric reorganization energy. Therefore, by increasing structural order, charge transport can be improved. For instance, for small molecules this can be achieved through self-assembly, whereas in the case of conjugated polymers, chain alignment is used.

Although, these procedures have a major disadvantage, as for polymer films, structural ordering can only be established at a microscopic or mesoscopic level and achieving macroscopic ordering with films made from small molecules can also be challenging. Consequently, local ordering can give rise to defect-containing regions, such as grain boundaries and domain walls between ordered domains, which can then act as traps for charge carriers and compensate the local mobility enhancement due to microscopic ordering.

Furthermore, there are several parameters that can influence the morphology and molecular packing of organic semiconductor thin films, leading to opportunities for tuning charge transport properties. Moreover, changes of processing parameters like the rate of deposition, the type of solvent used and even annealing treatment, can lead to a range of field-effect mobilities with different orders of magnitude within the same material system.[104] The principal causes of this phenomenon are the complexity of the crystal growth and the nucleation processes involved in the thin film formation.

Additionally, in solution processing methods such as spin coating or drop casting, crystal formation happens in a multiphase environment, where solvent vapor, the solution's layer and the substrate have interactions. The nucleation and crystal growth are heavily affected by the exchanges between solute, solvent, and substrate, as well as by the presence of phase boundaries, and by mass and heat transport processes.[85]

The combination of all these parameters governs the morphology and molecular packing of organic semiconductor thin films, which are critical to achieve high electronic performance in a given molecular system.[105] For instance molecular packing can be tuned by non-synthetic approaches, some studies have even shown that a small displacement between adjacent molecules leads to a significant change in charge carrier mobility.[106]

On the other hand, varying the processing conditions can modify the molecular packing due to the multiple crystal structures (polymorphs) that can be formed. Since organic crystals are

characterized by weak intermolecular interactions, like π–π stacking, they can adopt several polymorphic forms.[107] In spite of the importance of molecular packing on charge transport properties, controlling polymorphism has not been deeply explored, and most studies have been performed on pentacene polymorphs deposited from the vapor phase. These approaches contain the tuning of film thickness[108],the chemistry of the used substrate[109], and temperature among a plethora of different parameters.[110,111]

Another equally important way to achieve high electrical performance is through single crystal devices, where controlling crystal morphology is essential. High performance organic thin film transistors (OTFTs) can be produced from vapor phase or solution, to then form polycrystalline thin films, aligned micro crystals or single crystals. Single-crystalline thin films are preferred for multiple reasons, the first one being the scarcity of grain boundaries, leading to an absence of molecular disorder in single-crystalline domains, which is essential for achieving high electrical performance.[112] The second reason is the reduction of structural defects and chemical impurities, making single crystals suitable for fundamental studies of intrinsic charge carrier mobility. Lastly, the ability to directly pattern OTFTs during film formation ensures a high quality dielectric-semiconductor interface, leading to outstanding device performance.[113] Furthermore, direct patterning also permits high device density over a large area, which is valuable for industrial scale production.

In the same spirit, different techniques to produce aligned single-crystalline ribbons over a large area have been developed, one such example is the droplet-pinned crystallization method (DPC).[114] This approach has allowed well-aligned C_{60} single-crystal needles and ribbons, along with electron mobility values of 11 $cm^2/(V \cdot s)$. In this process, the nucleation density is adjusted by changing the concentration in solution as shown in Figure I. 15, with the help of a small piece of silicon wafer, the droplet is pinned, yielding to a steady receding contact line. It has been inferred that the reason why such high device performance is obtained through this method is in part due to the intimate crystal interface with the dielectric during in situ growth of single crystals on the device substrates. However, the main drawback of DPC is its applicability to high-throughput industrial manufacturing, because of the somewhat long processing time.

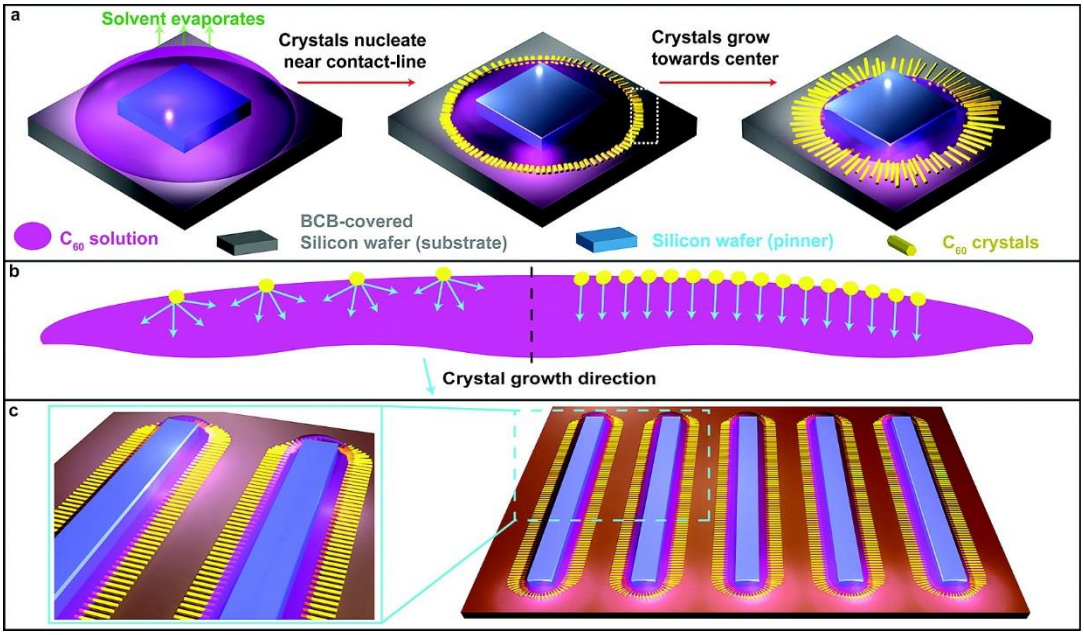

*Figure I. 15 Schematic representations of the DPC method. (a) An organic semiconductor droplet pinned by a silicon wafer. As the solvent evaporates slowly, the crystals of the organic semiconductors nucleate near the contact line of the droplet. Subsequently, the nuclei grow along the receding direction (toward the center) of the droplet. (b) A magnified view of a white-marked area in (a), highlighting the contact line where a high nucleation density (right side) leads to unidirectional crystallization along the receding direction of the droplet, while a low nucleation density (left side) results in nondirectional crystallization. (c) DPC can be scaled up by using multiple pinners with larger sizes. Elongation of the pinner leads to unidirectional parallel alignment of the crystals.*Reproduced.*[114]

These examples demonstrate the challenges and opportunities in fabricating aligned, patterned, single-crystal arrays; moreover, they have shown that to successfully develop organic semiconductors, controlling the processing techniques is also important, as they have an impact in device morphology. However, as it was previously mentioned another way in which the morphology of organic semiconductor materials can be tuned is through supramolecular assemblies; as π-conjugated materials tend to form aggregates, and sometimes even larger crystallites depending on processing conditions.[115] In general, the aggregation can be controlled by molecular design, the choice of solvent and thermal treatment steps. In the case of π-conjugated polymers, alignment of the chains leads to ordering on a microscopic or mesoscopic level, creating supramolecular structures. Therefore, it is essential to address the role of supramolecular chemistry in organic electronics.

III. Supramolecular Chemistry in Organic Electronics

III.1) What are supramolecular systems?

First, it is important to define what supramolecular chemistry is. In words of one of its founding fathers, Jean-Marie Lehn, it has been described as “the chemistry beyond the molecule”, since it comprises the study of molecular assemblies and of intermolecular bonds.[116] A supramolecular compound is considered as a group of molecular components endowed with

properties from each individual element to the entirety of the assembly, by non-covalent interactions.

For the past three decades, self-organization of molecules using various supramolecular interactions has gained a lot of attention, due to the large number of versatile assemblies that can be obtained with tunable and exceptional properties.[117] Hence, it has become vital to study the various aspects of supramolecular chemistry, since crucial and deciding factors of assembling molecules depend on the incorporation of suitable functional moieties. In this sense, molecules can self-organize in a programmed manner gathering amended properties and the reversibility of functional properties, through monomer-aggregate transitions, has served as inspiration to design new functional assemblies.

Undoubtedly, the control over the self-organization remains a challenging task, although morphologies with defined size and shape can also be tuned. This has led the majority of recent work to focus on the expansion of self-assembling synthetic pathways towards supramolecular materials that often self-assemble using a plethora of cooperatively working interactions, ranging from Van der Waals forces, to electrostatic interaction, to metal coordination, hydrophobicity and even hydrogen bonding (H-bonding).[118]

In general, research in modern supramolecular chemistry covers host-guest systems, but also molecular devices and machines, molecular recognition, as well as self-assembly and self-organization. This rapid expansion in supramolecular chemistry has resulted in an enormous diversity of chemical systems, with applications in many fields. Although, in the next sections special emphasis will be given to organic electronics applications.

For instance, supramolecular electronics has been proposed as a promising intermediary-scale approach that rests on the design of electronic components, with sizes between micrometers for plastic electronics and nanometers for molecular electronics. Supramolecular engineering controls the self-assembly processes through thermodynamic processes and non-covalent forces.[117,119] This represents a crucial bottom-up strategy to build and process relatively soft functional objects while introducing “pseudo-crystalline” electroactive domains corresponding to this typical intermediate length, therefore a deeper discussion in this field follows.

III.2) Semiconducting polymers and small semiconducting molecules

Semiconducting polymers are a special class of materials that have been designed for an extensive range of electronic applications due to their semiconducting, conducting, electrochemical, and/or optical properties. For instance, polymer solar cells (PSCs) are very attractive as they possess some advantageous features[120] including:

- Thin-film architecture
- Low material consumption
- Utilization of efficient solution processes
- Low manufacturing energy requirements
- Low specific weight and mechanical flexibility
- Tunable material properties

– High transparency

All of the above allow the electronic and physical properties of conjugated polymers to be extensively optimized, which in turn has permitted them to find effective application in devices, such as OPVs, OFETs, and OLEDs.[60,121–123]. Moreover, their synthetic flexibility and tunability have allowed them to be applied in other fields, such as electrochromic devices, chemical sensors, organic lasers, and biological applications.[124–127]

Despite that initially the main goal of studying conjugated polymers was the comprehension of fundamental properties such as conductivity, electrochemistry, and photophysical properties, it subsequently evolved through the years into understanding how small changes in the structure can influence the performance for a given application. Therefore, throughout the decades the progression and development of conjugated polymers has gone from simple repeating units, such as polyacetylene, to poly (3-hexylthiophene) (P3HT), and to PM6 (Figure I. 16).[128]

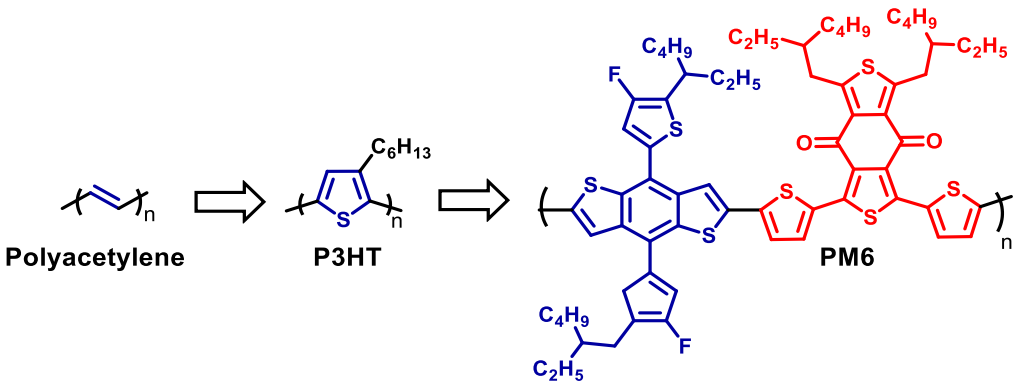

*Figure I. 16 Evolution of semiconducting polymers throughout the recent decades.*Adapted.*[129]

One of the most important structural developments in the field of conjugated polymers has been the improvement of polymerization conditions to prepare polymers with high structural fidelity, such as regio-regular P3HT and donor-acceptor copolymers (PM6). Furthermore, the ability to tune the electronic and physical properties through the addition heteroatoms along the π-conjugated backbone, the introduction of sidechains for improving solubility or tailoring physical properties have also impacted their development.[129]

Moreover, their evolution can be tracked since the early 2000's, when an enormous amount of research was performed using P3HT to improve solar cells, with the first P3HT:PCBM cells possessing a PCE of 2.8%[130],for which by 2010 the average PCE had only slightly increased up to 3%[131]; all the way to non-fullerene acceptors blended with PM6 which have recently reported PCEs over 18%.[132]

Even though OPVs are still not comparable to silicon cells in peak efficiency, since the latter tend to perform better under the low light intensities and elevated temperatures usually experienced in real world conditions, they have the potential for use in utility-scale applications.[133] Additionally, OPVs can be prepared using high-throughput manufacturing processes on flexible substrates, due to the compatibility of organic semiconductors with solution processing, diversifying their applicability, which is something most inorganic solar cells cannot do.

Whereas polymer OPVs receive more attention, solar cells created from solution-processed small molecule donor materials have rapidly grown in the last decade, with systems that have reached PCEs over 10%.[134,135] Their continued improvement is essential because they offer multiple advantages over polymer donors.

The individuality of small molecules is an advantage that is not present in the case of conjugated polymers, which always consist of mixtures of components with different molecular weights. The preparation of polymers itself is a complicated task, and their purification is even harder, as traditional methods such as chromatography on silica, or distillation are not useful. Hence, controlling the quality of conjugated polymers is difficult and frequently leads to a strong variation between each batch, utterly impacting their physical and electronic properties. In contrast, small molecules can be widely purified and have fully reproducible physical and electronic properties, making the latest research to strongly focus on small molecules.

Small molecules can also evade defects like chain kinks and chain-end defects, which are usually present in polymers and can lead to structural disorder and to low-lying trap states.[136,137] Furthermore, even when compared to polymers that require fewer synthetic steps or that obtain higher PCEs, small molecules can compete with them when a simpler work-up and purification protocol helps them keeping the estimated module cost at similar values.[138]

It is important that small molecules at the active layer of organic solar cells are well ordered, allowing for efficient generation of charges and their transport to the electrodes. Controlling the morphology of small molecular solar cells is considered a major holdup, since well-ordered self-assembling small molecular donor/acceptor composites must be designed to obtain high performance in organic solar cells.

Throughout the years, most of the used acceptors were derived from fullerene, normally in the form of [6,6]-phenyl-C61-butyric acid methyl ester (PCBM); however, there has recently been a significant movement towards non-fullerene acceptors (NFAs), particularly those that are built from small molecules. In contrast to typical fullerene acceptors, which have poor absorption of light in the visible spectrum, NFAs are often designed to have high absorbance, which allows generation of excitons at both, the donor and acceptor components of the active layer. In this sense, bilayer and diffusion bilayer devices have been designed and these dye-sensitized organic solar cells rely on the supramolecular interactions between the layers of the photon absorbing organic dye, the donors/acceptors, and the substrate.

In the same way as for polymers, small molecule organic semiconductors have constantly been evolving from simple to very complex structures (Figure I. 17). Since the 1960s, anthracene derivatives have been intensively studied as an interesting building block and starting material in OLEDs,[139] due to their unusual photoluminescence and electroluminescence properties, as well as their excellent electrochemical properties and ease of modification.[140] They can be classified into several categories according to the different substituent groups: non-heteroaryl substituted anthracene derivatives; silyl-substituted anthracene derivatives; electron-rich groups substituted anthracene derivatives; electron-deficient groups substituted anthracene derivatives; bipolar anthracene derivatives and large π-conjugation substituted anthracene derivatives.[141] Furthermore, as it was previously

discussed in section II, their conjugation can be extended to obtain acene derivatives, which highlights how they have played a key role in the development and applications of OLEDs materials.

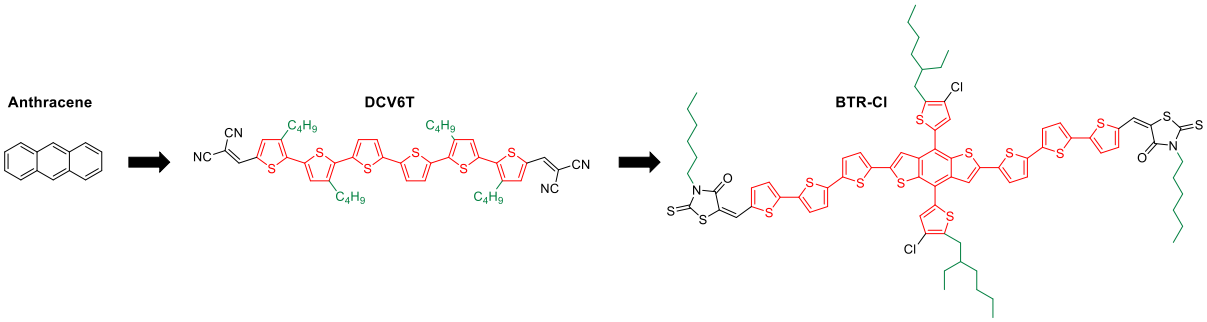

Figure I. 17 Evolution of small semiconducting molecules throughout the recent decades.

For instance, tetracene and pentacene are the most widely investigated p-type conjugated materials in OFETs with high carrier mobilities of up to 0.1 and 3 $cm^2/(V \cdot s)$, respectively.[142,143] Due to their planar π-conjugated structure, they have a relatively low band gap of 1.7 eV and these materials were as well investigated as p-type semiconductors in photovoltaics. Additionally, OSCs fabricated using tetracene/C_{60}-heterojunctions as photoactive layer resulted have reported PCEs of 2.3 %.[144]

Development of organic semiconductor materials has thrived in the past decades and in 1989, an oligothiophene called α-sexithiophene was implemented as an active semiconductor material in OFETs.[145] Later on, Sakai *et al*. prepared an OSC device using α-sexithiophene as donor and C_{60} as an acceptor, which exhibited a PCE close to 0.8 %.[146] The structure eventually evolved to α,ω-bis-(dicyanovinylene)-sexithiophene (DCV6T), shown in (Figure I. 17), and BHJ solar cells were prepared along with C_{60}.[147] The device was prepared on a heated substrate at 90 °C and gave an excellent PCE of 4.9 %. In comparison, devices prepared without substrate heating showed a PCE of only 2.1 %. The increased performance of devices prepared on heated substrates was due to a large increase in short circuit current and fill factor (FF), which was attributed to a change in mixed-layer morphology induced when heating the substrate. Hence, a strong phase separation is facilitated and leads to a better charge transport within the percolation pathways of the mixed layer.

Finally, a liquid crystalline molecule based on benzodithiophene terthiophene rhodanine with two small electronegative chlorine atoms (BTR-Cl) was recently developed (Figure I. 17),[148] and a 14.7% PCE was obtained when using a BTR-Cl:Y6 system.[149] These performance enhancements are mainly attributed to the precise morphology control, which yields to enhanced absorption, improved crystallinity, reduced trap-assistant recombination and suppressed energetic disorder.

Despite all this progress in small molecule organic semiconductors, one of the disadvantages they still have is their poor device stability under various operation conditions, such as light soaking and damp heat. This is one of the issues that should be addressed before starting their mass production and industrial applications, while several studies on the stability of small molecule OPVs have recently been conducted, deeper research is required to settle this matter.[150–153] Another significant problem is the fast drop in solar cell parameters at the

beginning of device operation, principally the rapid drop in the open circuit voltage (V_{OC}).[154] It is believed that one of the possible causes of this phenomenon is the trap formation in the photoactive layer during light soaking.[151,155,156]

Compared to polymers, small molecules are reorganized more readily, and their local morphology is altered in the presence of external stress, such as heat or light, which can lead to divergence from the optimized BHJ and result in FF and V_{OC} losses. One example of a bulk morphology change is the phase separation of small molecules and fullerenes in small molecule BHJ blends, which would result in the formation of large pure donor and acceptor phase crystallites.[157,158]

It has been shown that both types of semiconducting materials have different virtues and limitations, but supramolecular chemistry has the potential to combine the best characteristics of polymers and small molecules. In this sense, the performance of OPVs can be influenced by using supramolecular interactions such as H-bonding and/or π–π stacking and it will now be presented.

III.3) Supramolecular approaches in organic electronics

In general, supramolecular structures are formed by rational design,[159,160] allowing the molecules to interact without any additional treatment. Thanks to such control, it is possible to build semiconducting systems where the electroactive motifs are precisely organized by non-covalent interactions, into functional supramolecular polymers[119]. In this sense, by functionalizing very simple electroactive segments, the optical and self-assembly properties can be tuned while controlling the interplay between non-covalent interactions.

As it has been discussed before, a lot of effort has been made toward the development of conducting organic materials during the past decades. In addition to films of conducting polymers and single molecules, the emergence of supramolecular electronics is a promising field of investigation.[162,163] For instance, Giuseppone and co-workers have reported the synthesis of nanostructures based on triarylamine stacks, along with their addressable self-construction between two electrodes, representing a major progress in the control of supramolecular electroactive materials at the 100 nm length scale (Figure I. 18).[164–166]

Triarylamine-type molecules are very effective functional units that are extensively used as photoconductors and charge carriers, since they display high hole-transport mobility, being possible to incorporate them in OLEDs.[164]

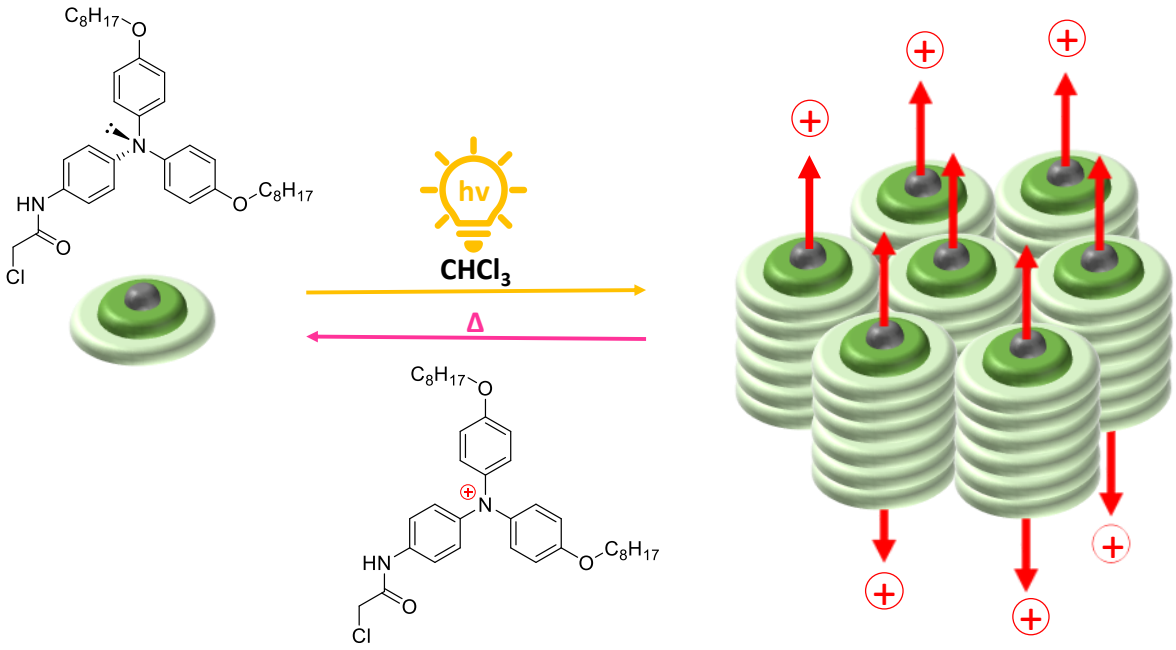

*Figure I. 18 Light-triggered self-construction of supramolecular organic nanowires as metallic interconnects.*Adapted.*[164]

In their work, supramolecular triarylamine nanowires were created by simple light irradiation of solution prepared in chloroform, this allowed the production of a catalytic amount of triarylammonium radicals that piled with their neutral counterparts along nucleation–growth and self-replication processes. Additionally, the stimuli-responsive supramolecular scaffolds were reversibly broken up by heating. By using these principles and by applying an electric field directly between the electrodes, the localization and directionality of the elongation of fibers were addressed and exceptional channel conductivity were measured for these self-constructing devices, exceeding 5×10^3 S/m.[167]

Another exciting example of supramolecular structures applied to organic electronics are thiophene derivatives, in particular in their oligomer form, finding applications in OFETs.[168] For instance, the group of Barbarella combined a wet lithographic technique with the non-solvent vapor-induced crystallization of octathiophene derivatives to form aligned fibers with precise control over density and size in OFETs (Figure I. 19).[169] These compounds are able to self-assemble into thermodynamically stable supramolecular crystalline fibers when exposed to vapor of a non-solvent.

The procedure consisted of taking an airtight container saturated with non-solvent vapor, an elastomeric stamp, consisting of parallel lines, which was then placed in contact with a solution containing one of the compounds. The film was spread on a SiO_2/Si substrate with or without gold electrode. A confinement effect is produced due to the capillary forces that pin the solution under stamp protrusions, while the self-assembly process induced by non-solvent vapor takes place and leads to the formation of a well-oriented array of fibers imposed by the motif of the stamp protrusions.

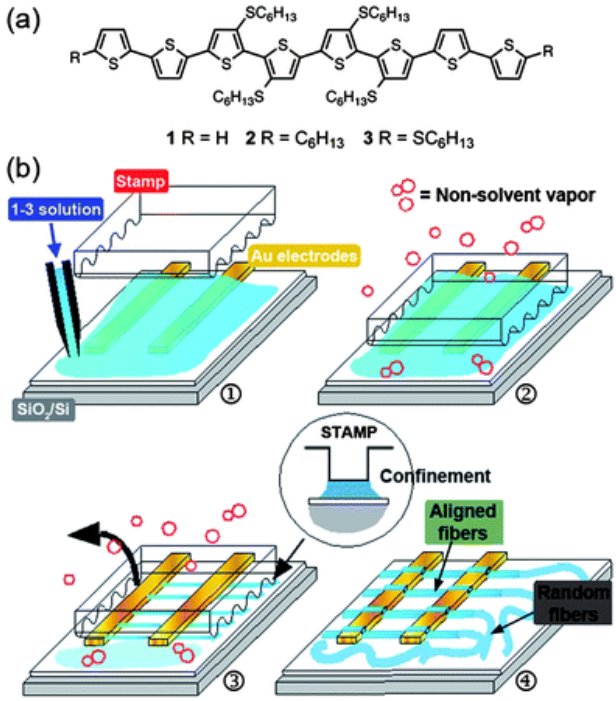

*Figure I. 19 a) Molecular structures of oligothiophenes. b) Schematic representation of non-solvent vapor-induced crystallization in combination with lithographically controlled wetting.*Reproduced.*[169]

The combination of thioalkyl substituents and head-to-head substitution, induced aggregation mainly via S–S non-covalent interactions and a high degree of control of the supramolecular self-assembly was also achieved through the non-covalent interaction of the π-conjugated structure. This is critical for applications in flexible electronic devices of organic charge-transport materials, because their electronic properties depend on both, the chemical structure and the molecular packing/orientation.[170] In particular, fibers can facilitate charge carrier mobility through long-range molecular orientation with respect to device electrodes.[171]

Furthermore, this strategy allowed precise control over density, orientation, and size of supramolecular semiconducting fibers in OFETs and proved that well-aligned fibers exhibit a substantial enhancement of electrical performances. Devices made of all aligned fibers showed saturated charge mobilities increased by about three orders of magnitude when compared to randomly distributed fibers and a strong decrease of the threshold voltages. These results show that supramolecular alignment of fibers through confinement effect is an attractive technique in fabrication of OFETs and could be applied for many other known supramolecular fibers.

Examples of supramolecular polymer strategies in organic electronics can also be found, for instance in perylene bisimide incorporating H-bonding motifs that co-polymerize with ditopic building blocks into millimeter-long fibers (Figure I. 20).[172] Remarkably, the stacking of perylene units was not the driving force of the polymerization along the long axis of the fibers, but contributed to the height of the nanostructure.

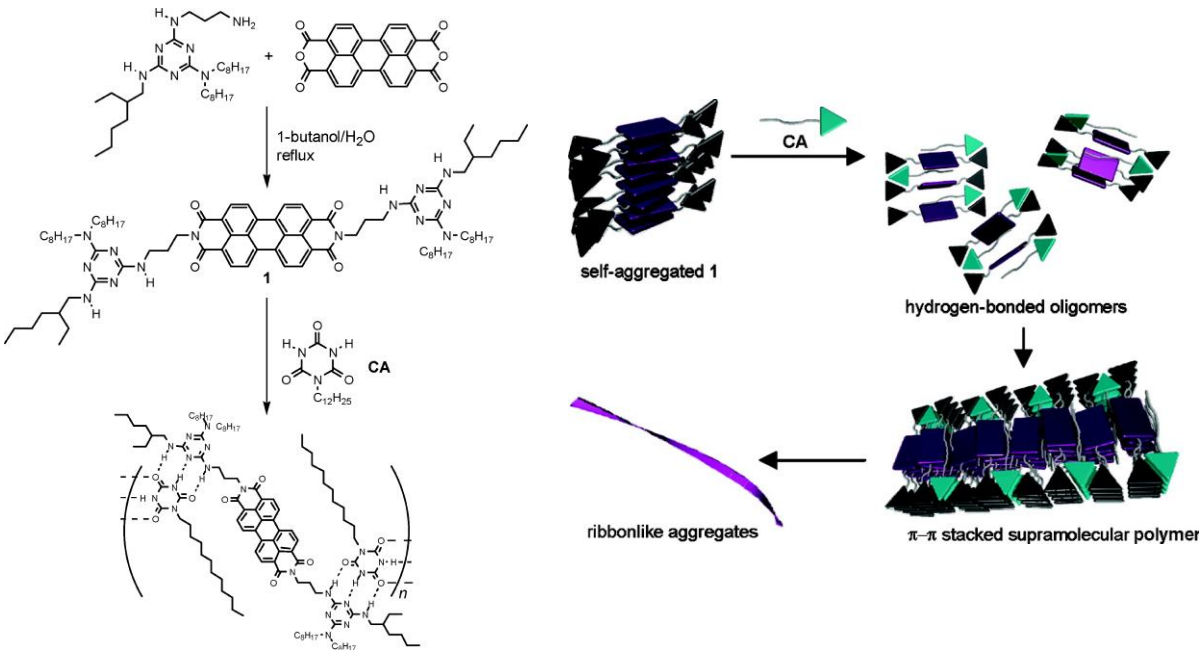

Figure I. 20 Formation of discrete 1D elongated nanoobjects from a flexible hydrogen bonded supramolecular polymer containing perylene bis-imide chromophores in the main chain. Adapted.[172]

The extremely long perylene bis-imide nanofibers were formed through complexation between complementary triple H-bonding modules. Moreover, the intrinsic 1D electron mobility observed for these nanofibers competed at the time with the highest mobilities of columnar stacks of other fluorescent dyes with high thermal and photo-stability, which were usually employed to explore 1D self-assemblies as photon- and electron-carriers in optoelectronic nanodevices.[173] This structural transition which arises from a molecular rearrangement from rosette to linear type, is associated with a remarkable increase in transient photoconductivity.

They also showed that hydrogen bonded (H-bonded) networks incorporating perylene units can be structurally rearranged from fibrillar assemblies to lamellar structures in the bulk upon heating.[174] This last example showed that hydrogen bonds (H-bonds) can efficiently guide the self-assembly of organic materials, which also enables the tuning of the properties in aggregation processes, hence the next section will review them in more detail.

III.4) H-bonded supramolecular electronic materials

The first question one might ask is: why are H-bonds so special? It turns out that a hydrogen bond is an interaction where a hydrogen atom is attracted to two atoms, rather than just one, acting like a bridge between them and can usually be represented as shown in Figure I. 21, where species X–H is often referred as donor, whereas Y–Z is known as the acceptor. It is often described as an attractive interaction in which an electropositive hydrogen atom mediates between two electronegative species X and Y, bringing them closer together.

The hydrogen bond is strong enough to hold molecules such as XH and YZ together at normal temperatures, and it is also directional enough so that this association is orientationally

specific. Nevertheless, and depending on the nature of X and Y, it can also weaken enough to allow these molecules to come apart, permitting loss of orientational specificity in the association of XH and YZ, like a hydrophobic interaction.[175]

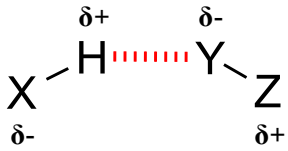

Figure I. 21 Typical representation of the 4 atomic species involved in H-bonds.

Usually, H-bonds are formed when a hydrogen atom is covalently bonded to a highly electronegative atom such as N, O, Cl or F, hence it presents a partial positive charge and can be strongly attracted by another electronegative atom in another or in the same molecule, respectively forming an intermolecular or an intramolecular hydrogen bond.

In this sense, the hydrogen bond can play a crucial role both in stabilizing static structures and in mediating dynamic processes, giving it its importance as a structure-defining element in supramolecular chemistry and as a major facilitator of biological reactions.[176] Depending on the nature of X, Y, and Z, the energy of a hydrogen bond is between 0.5 to 40 kcal·mol^{-1}.[175] The strongest H-bonds are as strong as the weakest of covalent bonds, while the weakest H-bonds are practically indistinguishable, and it is this intermediate energy range what makes them able to quickly associate and dissociate at ambient temperatures.

Over the years, the concept of the hydrogen bond has become more relaxed to include weaker and more dispersive interactions, provided that some electrostatic character remains. The hydrogen bond is a complex interaction that has at least four chemical characteristics[177]:

- Electrostatic (acid/base)
- Polarization (hard/soft)
- Van der Waals (dispersion/repulsion);
- Covalency (charge transfer).

H-bonds can determine the molecular conformation, molecular aggregation, and the function of an immense number of chemical systems, having a huge impact on our daily life. Without them, wooden structures would collapse, concrete would crumble, oceans would evaporate, and human beings would disintegrate into random pieces or into inert matter. Furthermore, the surprising properties of water, such as its high boiling point (100 ºC vs -60,7 ºC for H_2S), the contraction of solid water upon melting and its maximum density in the solid state at 3.98 ºC, are based on the network formation of H-bonds.[178]

There are some strongly donating and accepting groups, such as -COOH, -OH, -$CONH_2$ and -CONHR that form the same type of H-bonds when they are included in an organic aggregate or when they behave as ligands in metallic complexes. The energy of the H-bonds with these groups are usually at least one order of magnitude higher than for the rest of non-covalent interactions and in solution, the thermodynamic stability of hydrogen-bonded species strongly depends on the solvent. They are usually more stable and unable to form H-bonds in apolar solvents like alkanes. On the other hand, the stability is lower in solvents with donor or acceptor hydrogen-bonding ability.

The most know example of H-bonds are the natural building blocks of nucleic acids; therefore, H-bonds have always been considered very relevant interactions in biological processes, as molecular recognition between purine and pyrimidine bases in deoxyribonucleic acid (DNA) (Figure I. 22), enzymatic catalysis and the formation of α and β helixes.[179]

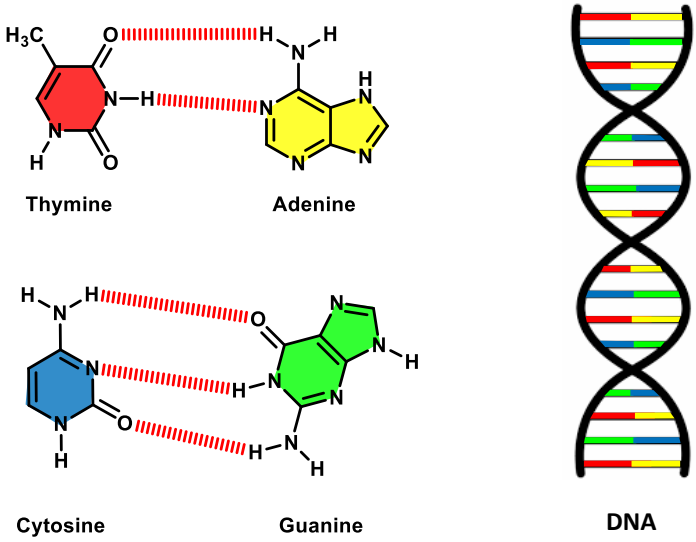

Figure I. 22 Molecular recognition between purine and pyrimidine creating the bases of DNA through the selective formation of H-bonds

Since H-bonding interactions are so prevalent in nature, it is not surprising that H-bonds can also be exploited as a molecular design tool for obtaining organic semiconducting and conducing materials. For instance, H-bonding is crucial for supramolecular interactions that permit the creation of numerous photoactive donor/acceptor assemblies.[180]

An example of these type of materials can be found in a fullerene derivative attached to a barbituric acid framework (FBA in Figure I. 23), which has been applied as a building block for the development of a variety of H-bonded supramolecular ensembles.[181,182] Additionally, a similar photophysical study was performed in another H-bonded fullerene–oligophenylenevinylene system, providing comparable results.[183] The self-assembling of FBA with the complementary oligothiophene donor (Figure I. 23) permitted the fabrication of photoelectrochemical devices that provided clear photocurrent response under white light irradiation.

An interesting approach to design light-harvesting electron donor materials for organic solar cells was presented by Cheng *et al*.[184], it consisted on a conjugated thiophene–fluorene copolymer that was tweaked with chelating terpyridyl units (PTPy), which are known for their strong affinity for complex formation. This work resulted in organic solar cells which exhibited PCE of 0.12% and EQE of 12%. Hence, a similar approach was explored by Liang *et al*. who applied H-bonding to construct supramolecular donor supramolecular polymers as it can be seen in Figure I. 23.[185]

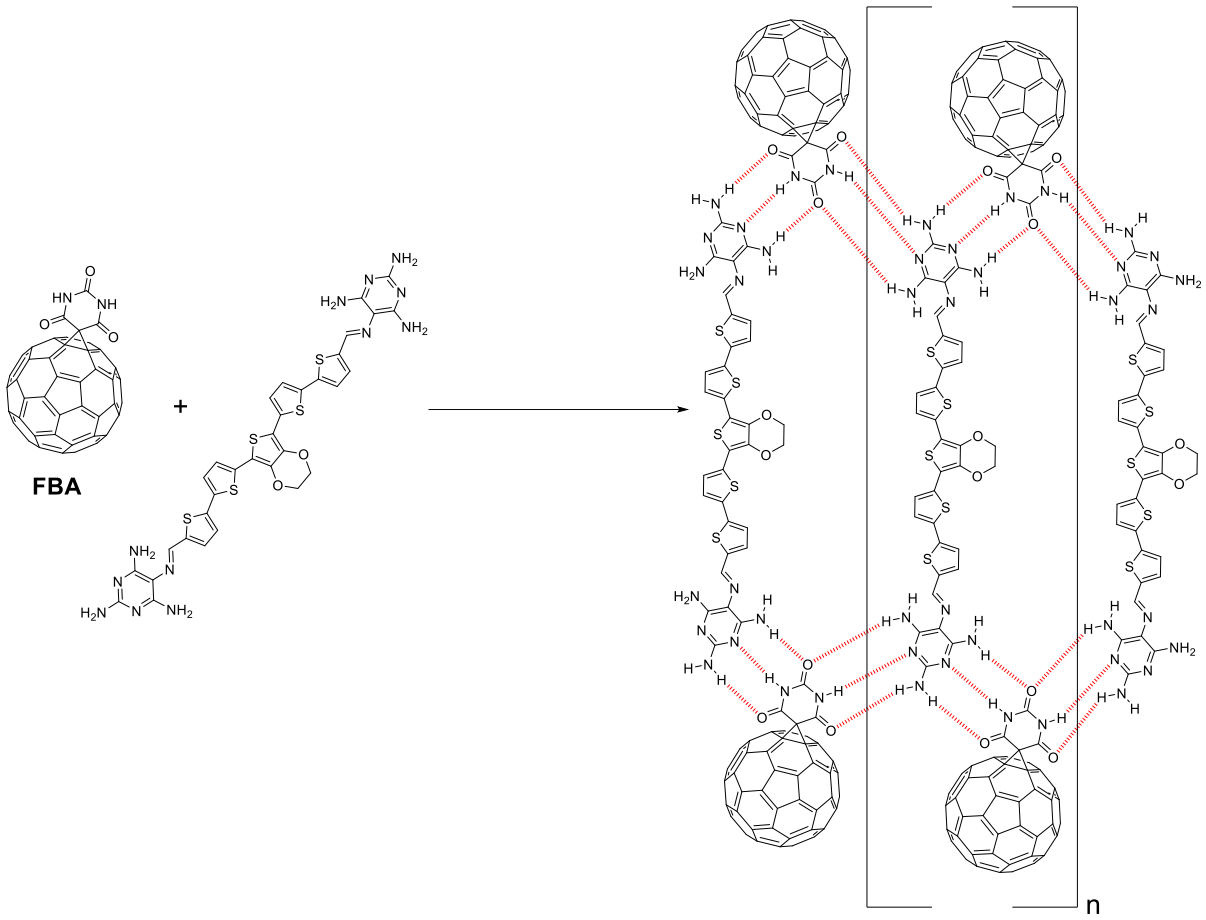

Figure I. 23 The formation of a hydrogen-bonded supramolecular system based on the fullerene derivative FBA and oligothiophene derivative.[186]

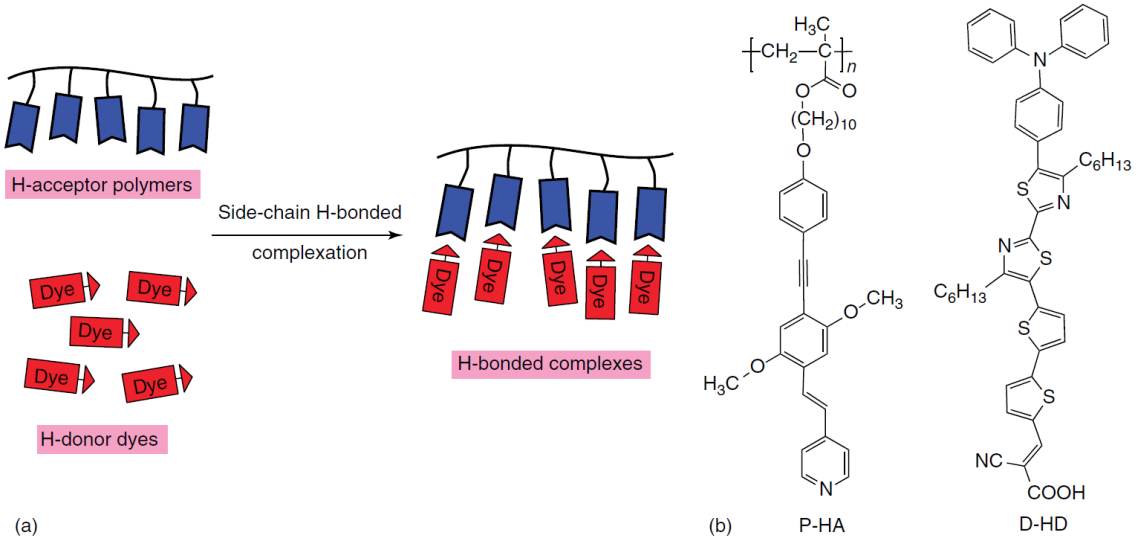

*Figure I. 24 a) The formation of supramolecular electron donor polymer via hydrogen-bonding complexation of nonconjugated polymer with small molecular organic dye and b) molecular structures of the best performing polymer (P-HA) and dye (D-HD) combination.*Reproduced.*[186]

For instance, a PMMA-based polymer was modified with an electron donor block bearing pyridyl end groups, producing a hydrogen-bonding acceptor polymer (P-HA). The pyridyl unit of P-HA can form H-bonds with the carboxyl group of a small molecular hydrogen-donor dye (D-HD). Consequentially, the supramolecular polymer yielded PCE of 0.5% in BHJSCs with PCBM, an impressive considering the relatively simple molecular structures of the applied materials.

Other examples of H-bonded systems with photovoltaic applications have been reported in literature and Figure I. 25 shows the most representative cases regarding the fabrication of organic solar cells, even though many examples of organic transistors can be found.[187]

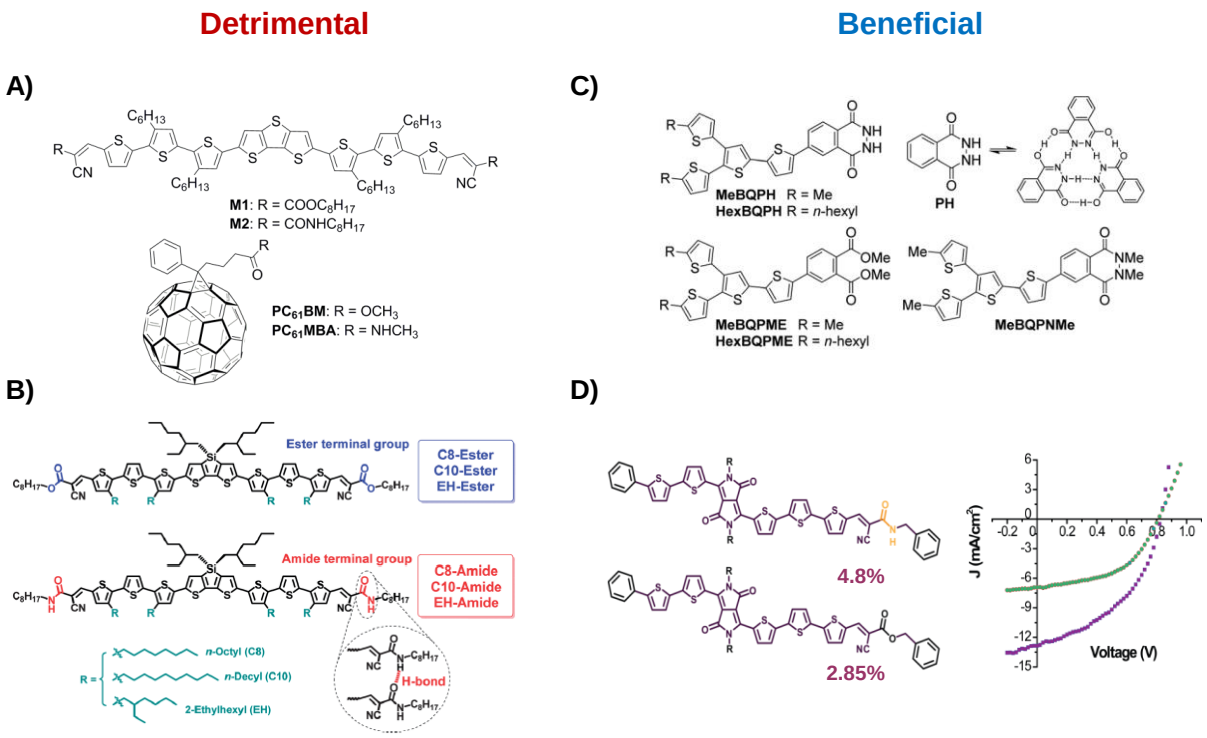

Figure I. 25 Example of detrimental (A and B) and beneficial (C and D) cases of H-bonded materials in the fabrication of organic solar cells.

Nevertheless, contradictory results have been described in cases where both, donor and acceptor materials had hydrogen-bonding units, and when only one of the components had hydrogen-bonding ability. Figure I. 25A and Figure I. 25B show two cases of oligothiophene small molecules symmetrically modified with amides or ester groups in the periphery.[188,189]

In both cases, chloroform was used as the solvent to blend donor and acceptor materials, which from a supramolecular point of view is not the best choice since it is commonly used as a “good solvent” to avoid aggregation. Furthermore, in these two works the solar cell efficiency was lower for all the blends where the H-bonding derivatives were involved.

On the other hand, although the molecular structures of the examples shown in Figure I. 25C and Figure I. 25D are very different from the similar design of the previous two examples,

contradictory results were found. For instance, in the case depicted in Figure I. 25C, the authors found out that the molecule without the ability to form H-bonds needed double the concentration to achieve similar efficiency as the hydrogen-bonded donor, the main drawback being its low short circuit current.[190] When the donor molecules were well interconnected thanks to H-bonding, the current was much higher, which also increased the FF.
Furthermore, in the example shown in Figure I. 25D, higher efficiency was found for the amide-containing a diketopyrrolopyrrole (**DPP**) donor molecule, even in the most optimized conditions for both donor molecules.[191] In this case, several solvents were tested and it was found out that the best solvent was chlorobenzene for solubility issues.

As it has just been discussed, the results with H-bonded materials do not seem to agree on its positive or negative role on solar cell devices. Nevertheless, it is important to remark that it is not possible to compare all the parameters previously shown. The type of π-conjugated segment, type of hydrogen-bonding unit, solvent utilized and the donor/acceptor ratio among other parameters are different in all the cases, making very difficult to make a fair comparison. Furthermore, the lack of self-assembly studies in most of the cases, neglects the information regarding the type of structures formed by the H-bonded systems, which is something crucial to understand the device performance.

Since the aim of this PhD is to elucidate the impact of H-bonds in the optoelectronic properties of organic semiconductors, systematic and comparative studies have been done using **DPP** as a model system. In addition, this systematic study aims to help screening the required conditions needed to fabricate efficient electronic devices.

DPPs are extensively studied molecules and are among the best electroactive segments used in semiconductors,[192,193] since their discovery by Farnum[194] in the 70's while trying to synthesize azetinone, **DPP** has been one of the most used pigments in industrial applications and in the search of new materials. Multiple examples of polymers and small molecules can be found for the fabrication of organic solar cells,[195] OFETs,[196,197] and sensors.[198,199]

While H-bonding is the principal and strongest stabilizing interaction within these assemblies, their structures vary dramatically depending on the nature of the pendant heteroaromatic substituents.[200] It was proven that co-assembly can be achieved through H-bonding of the **DPP** lactam group with a carboxylic acid, which persists in both single crystals and interfacial layers. This work suggests that there is an unexpected tendency of **DPP** derivatives to assemble on graphite in a twisted conformation, providing stronger intermolecular interactions and higher molecular density. Therefore, these materials have proven to be interesting and will be discussed in more detail.

IV. The Diketopyrrolopyrrole pigment

IV.1) History and synthesis

DPP derivatives were first reported in 1974 as one of the products of a modified Reformatsky reaction that aimed and failed to produce azetinone derivatives as shown in Scheme I. *1*.[194] Farnum *et al*. attempted to optimize the reaction conditions to increase the yield of phenyl-functionalized **DPP** (**DPP**-Ph, Scheme I. *1*), while additionally looking for an elucidation of its

formation. Nonetheless, the yield never exceeded 20%, stopping their work on the subject and publishing the results as “the discovery of a pigment chromophore.”[194]

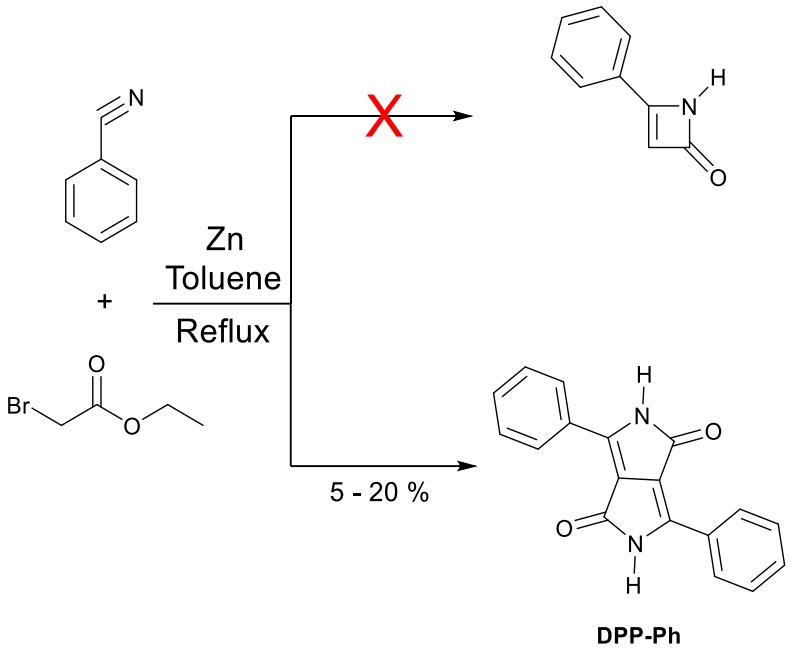

DPP-Ph

Scheme I. 1 First and accidental synthesis of **DPP**-Ph.

The chemical structure of a 2,5-Dihydropyrrolo[4,3-c] pyrrolo-1,4-dione molecule is shown in Figure I. 26 and up to now, this structure has not been reported to be synthesized. The most commonly known **DPP** derivatives generally have aromatic substituents at the -3 and -6 positions, although compounds with aliphatic groups are also known.[201,202] Their physical properties such as their high melting point (>350 °C), high insolubility and prominent red color would have been most probably forgotten, if it had not appealed the attention of researchers from Ciba-Geigy AG (currently part of BASF), who came across a compilation of interesting reactions published by Ranganathan in 1980.

Afterwards, the chemistry along with the applications were developed, and in 1986 the first **DPP** pigment was introduced to the market.[203,204] Since then, several other **DPP** pigments have been presented to the market for conventional pigment applications such as fibers, inks, paints and plastics.[205] The interest in their high tech applications has grown increasingly in recent years, as **DPP** derivatives exhibit remarkable resistance against chemical, heat, light and climate stimuli, resulting in more than 9000 patents in different areas.[206]

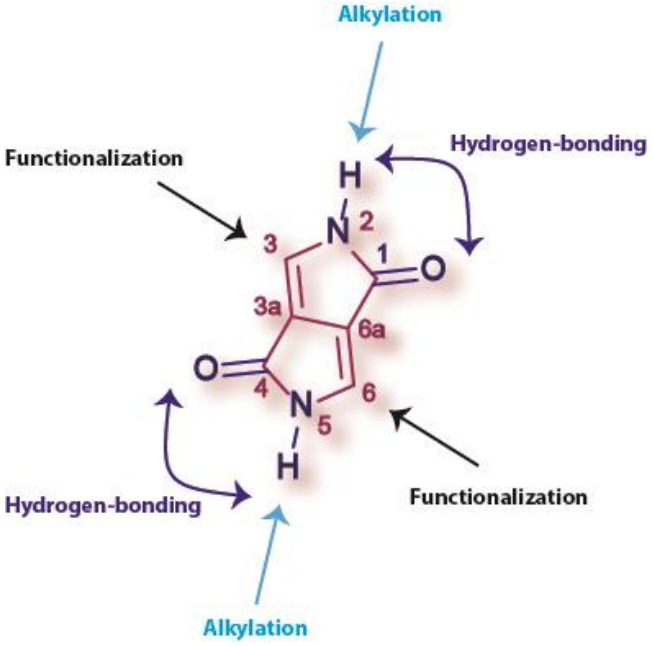

*Figure I. 26 Chemical structure of the **DPP** core with its corresponding atom numeration, hydrogen-bonding groups, and main functionalization positions.*

While used in many fields, the majority of **DPP** articles comprehend the use of **DPP** derivatives in semiconductor electronic devices, such as solar cells,[195,207] OFETs[197,208] and OLEDs.[123,209–211]

IV.2) Reactivity of **DPPs**

DPP derivatives contain several reactive groups within their structure susceptible to electrophilic attack, such as oxygen and nitrogen atoms in the amide group, in addition to the double bonds in the **DPP** core and the aryl groups at the -3 and -6 positions. Conversely, the carbonyl carbon atom or the α, β -unsaturated system within the bicyclic **DPP** unit are prone to nucleophilic attack through Michael addition. Furthermore, reactions with nucleophiles can also be performed in the aromatic substituents. In this section, the main chemical reactions that **DPP** derivatives can undergo will be summarized. For a deeper and extended comprehension, the reader is once again referred to the work of Grzybowski *et al*.[212]

a) Nucleophilic alkylation of the amide groups of **DPPs**

While the **DPPs** with hydrogen atoms at the -2 and -5 positions (Figure I. 26 and Figure I. 27) are quite insoluble, alkylation of the nitrogen atom results in very soluble materials. However, **DPP** derivatives can be alkylated in different positions as shown in Figure I. 27, depending on the reaction conditions.[213]

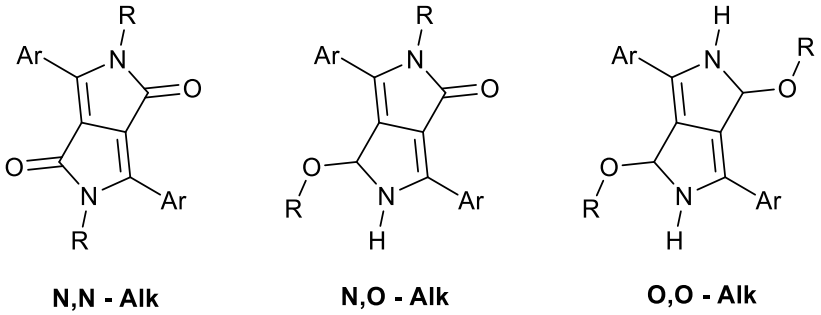

*Figure I. 27 The possible product structures in the alkylation of **DPPs**.*

The O-alkylation is favored in neutral conditions and at low temperature, since the product is kinetically more stable, whereas the N-alkylation is predominantly observed at high temperatures. Thermal rearrangement is also possible when the reaction is performed over long reaction times with excess of alkylation reagents at high temperatures, yielding both alkylated derivatives.[214] On the other hand, **DPPs** are deprotonated to give anions under basic conditions, distributing the charges amid the two heteroatoms and promoting the alkylation at either or both N- and O-atoms.[215,216] The most common solvents for alkylation are N,N-dimethylformamide (DMF) [217,218] and N-methylpyrrolidone (NMP),[219] even though the use of acetonitrile, a greener solvent, has been recently reported,[214] being possible to run the reaction at room temperature and with shorter reaction times.

b) Reactions of the aromatic substituents at the -3 and -6 positions of **DPP**

Most **DPP** derivatives possess aromatic substituents at the -3 and -6 position. Therefore, they may experience the typical reactions of aromatic compounds, especially electrophilic aromatic substitution.[203–205] The sulfonation of **DPPs** is widely used to produce salts used as thermal stabilizer surfactants, improving the rheological properties of **DPP** paint formulations.[203–205,220] One of the main reactions performed is the halogenation of heteroaromatic substituents in **DPPs**, such as thiophene, furan, and selenophene.[221–223] Bromination can be performed by exposing **DPPs** derivatives to gaseous bromine, but is most frequently done by using N-bromosuccinimide (NBS), as illustrated on Scheme I. 2.

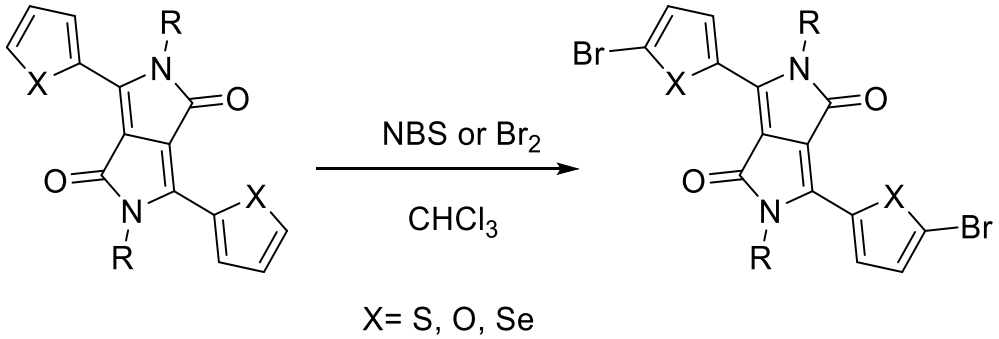

*Scheme I. 2 Bromination of heteroaromatic substituents in **DPPs**.*

DPPs can also be copolymerized to generate biaryl compounds with electron-rich aromatic compounds, due to the electron-accepting character of the **DPP** unit. Suzuki and Stille

couplings are effective procedures for the synthesis of biaryl derivatives[224,225] The produced copolymers are of the donor–acceptor (D/A) type, having high charge mobility and low-energy bandgap; allowing the material to be applied in semiconducting devices.[209,211,226,227]

Finally, thiophene **DPP** derivatives can experience reactions with lithium diisopropylAmide (LDA) at the -5 positions of thienyl groups, which can be used to introduce new substituents that can lead to further reactions. [228,229] A common example of such substitution is shown in Scheme I. 3, where the formylation leads to dialdehyde **DPP** derivatives when the reaction is performed with DMF.

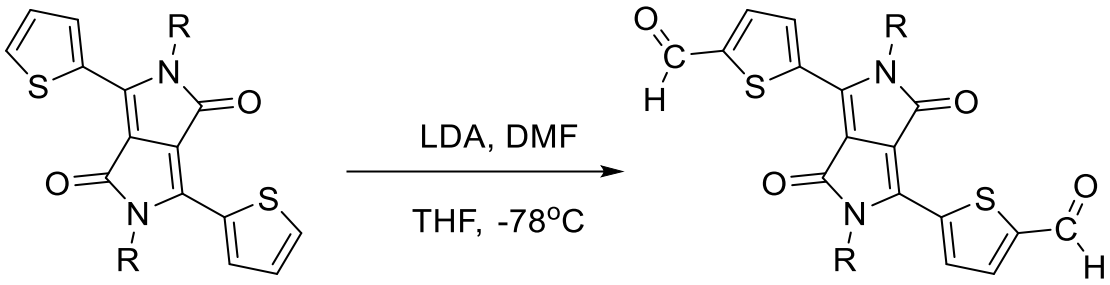

*Scheme I. 3 Formylation of thiophene-**DPP** derivatives.*

IV.3) H-bonding in **DPP**

IV.3.1) Hydrogen-bonded **DPP** with unsubstituted lactam rings

a) Structural characterization, crystallization, and optical properties

1,4-diketo-3,6-diaryl-pyrrolo–[3,4-c]-pyrrole as synthesized contains two unsubstituted lactams with ability to form H-bonds (Figure I. 26). In the solid state, there are chains of NH···O intermolecular H-bonds between the NH group of one molecule and the O atom of the neighboring molecule forming linear chains. These H-bonds are necessary to align the transition dipole in a “head-to-tail” mode that results in a bathochromic shift of the absorption band when transitioning from the solution state to the solid state.

Besides, the NH···O H-bonds connect the **DPP** molecules to achieve stability similar to those of polymers. The linear chains are parallel to each other and to the plane, while brick wall-pattern π-π stacking is found perpendicular to the plane (Figure I. 28).[230–232] This same structural behavior is seen in other H-bonded pigments, such as indigo,[233,234] perylene bisimides,[235] quinacridone[236,237] or epindolidione,[236] yet the H-bonding distances were found to be shorter in **DPP**.[238] Even though many authors have claimed that amine and carbonyl groups should be avoided in the molecular structures of semiconductors due to a possible disruption of the conjugation,[239] it has been demonstrated that maximizing the charge transfer integrals through neighboring molecules can enhance the mobility.[238] In this sense, crystal engineering through H-bonding has been one of the main strategies applied in device fabrication.

Early investigations by Mizuguchi[240–247] at the end of the 80's and early 90's show the crystal and electronic structures of several small H-bonded **DPP** molecules, starting from 1,4-diketo-3,6-diphenyl-pyrrolo-[4,4-c]-pyrrole[240–242] and extending it to the dithioketo,[248] pyridine-containing[249,250] and halogenated analogues.[243] The conclusions of these studies showed that the intermolecular NH···O H-bonds result in a bathochromic shift in the absorption maxima upon crystallization with respect to solutions (Figure I. 29), and that the spectral shape in solid state differs substantially from the one in solution mainly depending on the extent of the molecular overlap along the stacking axis. When the molecular overlap is insignificant, the solid state and solution absorption spectra are quite similar and when the molecular overlap increases along the stacking axis, the absorption maximum shows a hypsochromic shift, making the color more yellow.

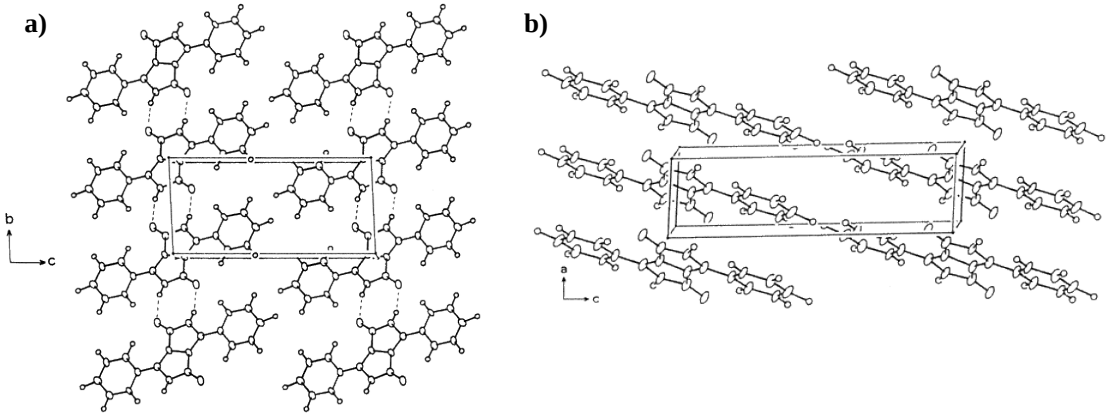

Figure I. 28 Projection of the crystal structure of **DPP** a) onto the plane (b,c), b) onto the (a,c) plane.*Reproduced.[230]

The authors concluded that the "head-to-tail" arrangement caused by H-bonding is found to displace the absorption maximum towards longer wavelengths, while the stack pair or parallel arrangement significantly contributes to the hypsochromic shift.[230] In this work, the exciton coupling model based on the interaction between transition dipoles was used to qualitatively interpret the correlation between the crystal and electronic structures in **DPP** derivatives. This way, it could be understood why the famous "Ferrari red" pigment (***p*-ClDPP**) shows bright red color mainly due to the formation of the "head-to-tail" arrangement thanks to H-bonding *vs* the yellowish color in *m*-substituted derivatives, where the stack pair contribution (hypsochromic shift) overpowers the H-bonding. These initial findings led to the study of different applications, such as H_2 gas sensors,[250] information storage[244] and the study of photoconductivity.[246]

Still until very recently the supramolecular ordering of H-bonded **DPP** pigments have continued to be studied. Perepichka *et al*,[200] used scanning tunneling microscopy (STM) combined with X-ray crystallographic analysis to demonstrate how the interactions of heteroatoms in the aromatic substituents of the **DPP** core interplay with hydrogen-bonding and the final influence on charge transport properties. The authors studied the supramolecular order of H-bonded difuran, dithiophene and diphenyl **DPP** derivatives in monolayers at the solid-liquid interface and in bulk crystalline solids. This study demonstrated that even though H-bonding is the main and strongest interaction in the supramolecular assemblies of the **DPP** derivatives described, their structures change radically depending on the nature of the aromatic substituents (furan, phenyl or thiophene). The diphenyl derivative was found to form exclusively H-bonded homoassemblies; the difuran **DPP** preferentially co-assembles with

alkanoic acids (used to create the solid-liquid interface), and the dithiophene substituted **DPP** either co-assembles with alkanoic acids or self-assembles in one of two H-bonded polymorphs depending on the conditions.

Remarkably, one of these two polymorphs shows an out-of-place (in graphite) twist of the thiophene rings that provides for stronger intermolecular interactions and higher molecular density. This was the first case reported of a planar molecule reorganizing into a less favorable twisted geometry and it could help for example in OFET applications, where the interfacial layer plays a crucial role in the device properties.

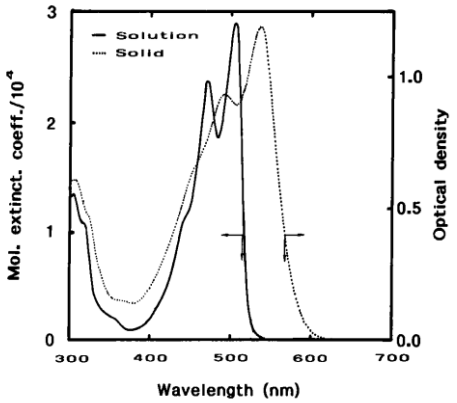

Figure I. 29 Absorption spectra of **DPP**-Ph in dimethyl sulfoxide (DMSO) solution and on evaporated thin film.*Reproduced.[230]

b) Vacuum deposited thin films and the use of the latent pigment strategy

In 1997, Iqbal *et* al[251] showed a method to achieve soluble **DPP** derivatives by introducing *tert*-butoxycarbonyl (*t*-Boc) protecting groups, synthesizing the so-called “latent pigments” that render the final dye after thermal cleavage of the *t*-Boc groups, which decomposes into isobutene and CO_2 at approximately 180 ºC (Figure I. 30).

Later on, this technique has been widely used for the fabrication of thin films cast from solution, which is an easier and cheaper method than vacuum deposition techniques, even though several parameters such as removal rate, the nucleation and growth mechanism of the thermally converted derivatives and the role of the volatilized molecules needed to be explored. Several studies have been reported on the influence of the solubilizing group removal on the morphology and properties of H-bonded **DPPs**.

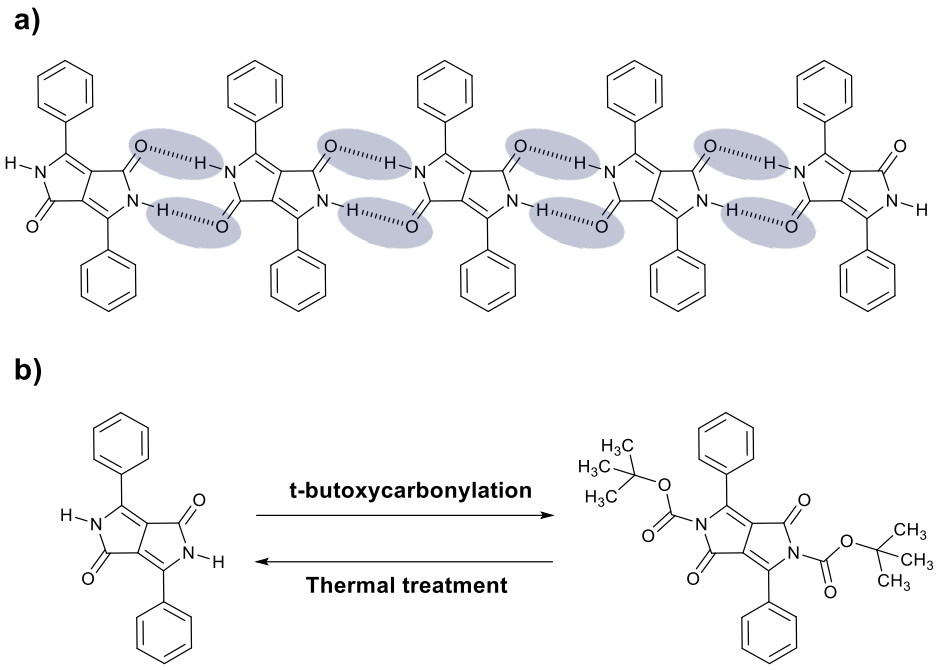

*Figure I. 30 a) Schematic illustration of the H-bonding network of **DPP**. b) Insoluble parent **DPP** pigment and soluble latent pigment.*Adapted.*[251]

For instance, Salammal *et al*[252] studied the role of the solubilizing group removal rate on the grain size and crystallinity of **DPP-4T** (Figure I. 31). The authors studied the use of different heating rates ranging from 0.1 to 50 ºC/min until reaching 225 ºC, and the isothermal decarboxylation of the **DPP-4T** precursor at different temperatures. In this case, it was found that the crystallite size increased from 344 to 976 nm when the precursor film was heated up to 225 ºC increasing the heating rate from 0.1 to 50 ºC/min, while improving the crystallinity as well. This result could be explained due the formation of H-bonding between decarboxylated molecules during the removal process. If the heating rate is too low, the *t*-Boc groups not cleaved can hinder the formation of H-bonds (N-H···O) with neighboring molecules, decreasing the crystallite size and crystallinity due to the disruption in growth in one dimension and trapping of *t*-Boc in the network. On the other hand, when the heating rate or the isothermal deprotection temperature increase, the volatilized isobutene and CO_2 can scape easily from the network, and the growth of crystallites is facilitated by the simultaneous decarboxylation of both *t*-Boc groups that results in the formation of H-bonds.

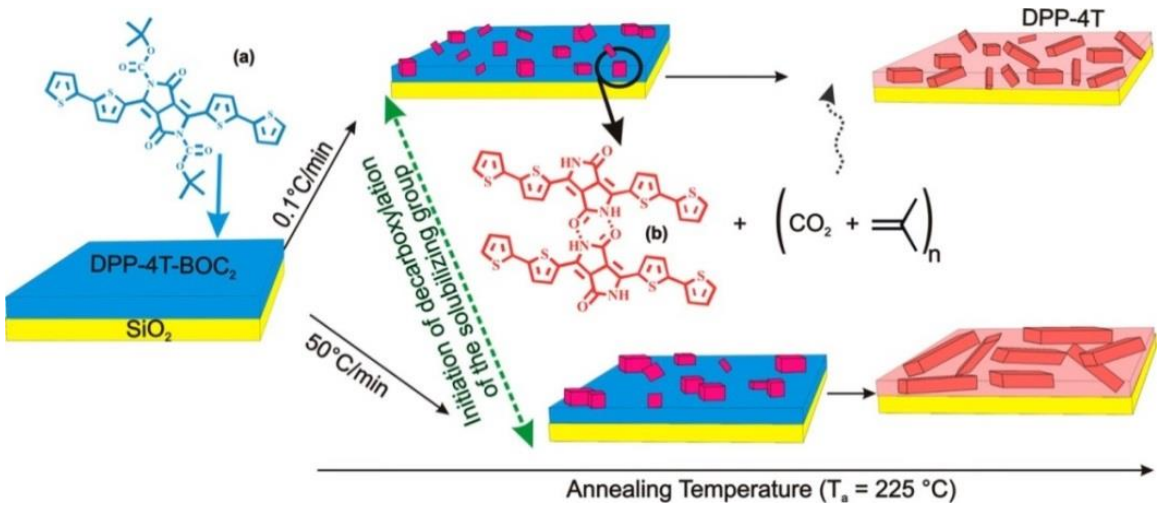

*Figure I. 31 Schematic representation of the impact of the heating rate on morphology and final grain size.*Reproduced.*[252]

One of the first examples of electronic devices using thermal removal of solubilizing groups was reported by Sakai *et al* in 2008.[237] This work reports the use of phenyl substituted **DPP** using the *t*-Boc-protected latent pigment that is soluble in common organic solvents. OFETs were fabricated by spin coating the latent pigment and by thermally annealing at 180 ºC-200 ºC for 15 minutes, to yield the deprotected **DPP** able to form H-bonds. Mobility values in the order of 10^{-6}. $cm^2/(V \cdot s)$ were obtained, which were similar (10^{-5} $cm^2/(V \cdot s)$) to the ones obtained by vacuum depositing the same type of material. The authors reported a difference in morphology when films were spin coated from solution and then the H-bonds were thermally regenerated, and when the H-bonded pigments were vacuum deposited. In the first case, the films studied by scanning electron microscopy (SEM) showed a rough and uneven surface with needle-like structures *vs* a very smooth surface when the **DPP** derivatives were vacuum deposited.

The authors demonstrated the simplicity of the preparation method but later, Yamashita *et al*[253] reported that the mobility values in the work of Sakai could be due to the production of CO_2 and isobutene released during the thermal annealing process, which negatively impacted the morphology of the spin coated film. The work of Yamashita shows larger **DPP** derivatives (Figure I. 32a) for the fabrication of OFETs using the same strategy. In this case, OFETs that showed ambipolar charge-carrier transfer with field effect mobility values of μ_h of 6.7 x 10^{-3} $cm^2/(V \cdot s)$ and μ_e of 5.6 x 10^{-3} $cm^2/(V \cdot s)$ were fabricated. The optical properties of **NH BTTDPP**1 and **NH BTTDPP**2 change dramatically when comparing solution to thin films (Figure I. 32b and c), initially just by spin coating and subsequently, by thermally annealing and cleaving the *t*-Boc groups. A bathochromic shift of 80 nm is observed in the absorption onset of **NH BTTDPP**1, while in **NH BTTDPP**2 the absorption onset red-shifts more than 200 nm.

In both cases, a shoulder band at lower energy appears, that dramatically increases after thermal treatment and that is related to the formation of H-bonds. The authors use infrared (IR) measurements to confirm the appearance of H-bonds on the thermally treated films, being this technique fundamental in these types of studies. OFET devices were fabricated and field-

effect mobility values were measured in devices made with the latent pigments and with H-bonded films. In the first case, hole mobility values in the order of 10^{-6} and 10^{-5} $cm^2/(V \cdot s)$ were found (similar to the studies of Sakai years before) and that were enhanced by two orders of magnitude after thermal cleavage of the *t*-Boc groups. Interestingly, derivative **NH BTTDPP2** containing two **DPP** moieties in the structure, exhibited well-balanced hole and electron mobilities in the order of 10^{-3} $cm^2/(V \cdot s)$.

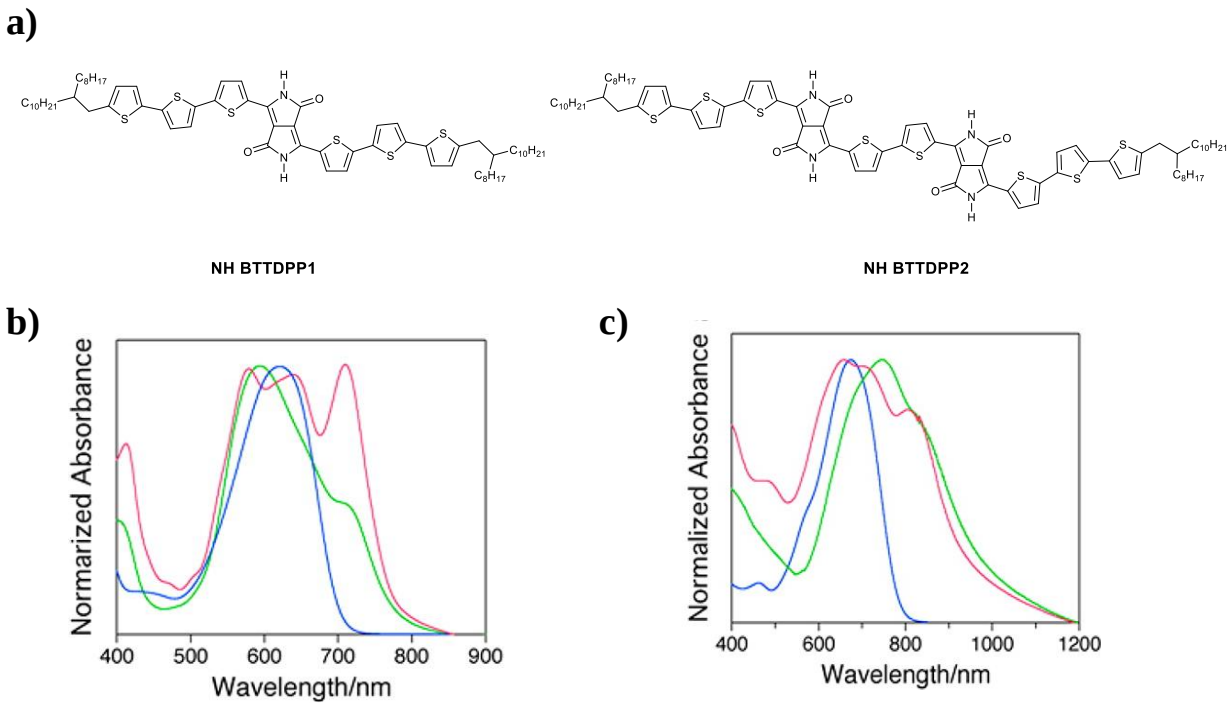

*Figure I. 32 a) Molecular structures of **NH BTTDPP1** and **NH BTTDPP2**. b) UV-Vis spectra of Boc-proteted **NH BTTDPP1** in solution (green trace), thin film (blue trace), and **NH BTTDPP1** (red trace). c) UV-Vis spectra of Boc-protected **NH BTTDPP2** in solution (green trace), thin film (blue trace), and **NH BTTDPP2** (red trace).*Reproduced.*[253]

Previously, a H-bonded **DPP** system containing electron withdrawing $-CF_3$ groups in *para*-position used as n-channel semiconductors with electron mobility values of 2.9×10^{-2} $cm^2/(V \cdot s)$ were reported by this group.[254] In this case, the devices were fabricated by vacuum deposition directly from the H-bonded pigment, while the latter study was the first one finding ambipolar behavior using hydrogen-bonded **DPP** molecules and processing the devices from solution.

Other reports using vacuum deposition techniques of H-bonded **DPPs** present archetypical derivatives (Figure I. 33a) containing in this case halogen (-Cl and –Br) substituents in the -*para* position of the phenyl rings that decorate the **DPP** core.[238] In this work, the results are complemented with DFT calculations to better understand the charge transport studies. The authors used anodically-grown AlO_x passivated with tetratetracontane ($C_{44}H_{90}$) as a composite low surface-energy dielectric to fabricate OFET devices because they found out in previous works on indigo dyes that low surface-energy dielectrics were crucial to enhance high mobility in H-bonded small molecule devices.[255] The final mobility values were enhanced several

orders of magnitude with respect to the initial report by Sakai *et al*,[237] who used phenyl-substituted **DPP** as well.

Furthermore, ambipolar behavior was reported for the three hydrogen-bonded **DPP** derivatives shown, being $\mu_h = \mu_e = 0.01$ cm^2/(V·s) for **DPP-Ph**, μ_h of 0.03 and μ_e of 0.01 for the ***p*-Cl DPP** and μ_h of 0.06 and μ_e of 0.02 for *p*-Br **DPP**. The crystalline structures obtained are very important to understand the differences in mobility values. While in the phenyl derivative, the H-bonded chains are parallel to one another (Figure I. 33b) and parallel to the plane, which was the same for the *para*-halogenated **DPPs** but the chains were staggered relative to each other making two linear H-bonded chains run along the [001] plane, and other two chains run along the [002] plane, with a tilt with respect to the first chain (Figure I. 33c). The crystal structures were described as pseudo brick-wall π-π stacking. While no discrepancies in charge transport were expected for the three derivatives described, a difference in crystallite size was found. **DPP-Ph** formed crystal grains between 100-200 nm with clearly defined boundaries, ***p*-Cl DPP** had similar crystallites but oblong in shape, and ***p*-Br DPP** had smaller grains making very smooth films and more continuous. The higher mobility values found for ***p*-Br DPP** might be explained according to this morphology.

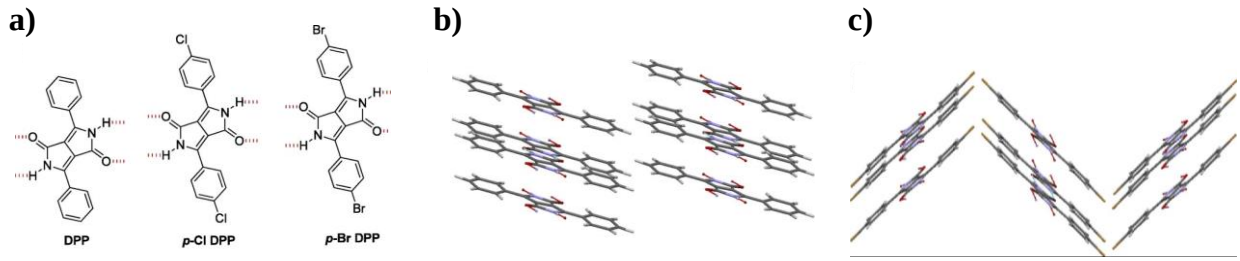

*Figure I. 33 Molecular structures of a) **DPP**, b) p-Cl **DPP** and c) p-Br **DPP**.*[238]

To demonstrate the strength of this strategy, more sophisticated oligomers have been reported recently, as for example the work of Zhu *et al*.,[256] where two **DPP** oligomers with different number of phenyl and thiophene rings were attached to the central **DPP** core, which was functionalized with thermo labile groups were based on 2-methylhexyl-2-oxylcarbonyl. In this case, field effect behavior was only found for the derivative containing thiophene rings (**HTBT**), including its latent pigment. Other examples as the work of Mula *et al.*[257] showing thiophene-capped **DPP** coupled to triazatruxene (**TAT**) derivatives (Figure I. *34*) with μ_h of 4.2 x 10^{-4} cm^2/(V·s). Interestingly, the charge transport properties were unaffected when blends of NH-**TATDPP** and phenyl [6,6]-Phenyl C_{71} butyric acid methyl ester (**PC$_{71}$BM**) were studied, emphasizing the robustness of the morphology when **NH-TATDPP** was used as donor material.

The use of thermo-cleavable side chains has been applied in semiconductors containing longer solubilizing chains, especially when using polymers. Sun *et al*[258] reported a **DPP**-based polymer containing 2-octyldodecanoyl side chains that can be thermally removed at 200 °C to generate a side chain-free conjugated polymer. X-ray diffraction (XRD) measurements and atomic force microscopy (AFM) images show the thin film progress upon thermal decomposition of the side chains. The as-spun films showed a diffraction peak at 2θ

of 4.40°, which corresponds to a *d*-spacing of 20.1 Å and that was attributed to the inter-lamellar distance. Upon raising the temperature, the primary peak of the thin film became more intense as a result of the improved molecular ordering by thermal annealing. When reaching 200 °C for 3 hours, the main diffraction peak disappeared as a result of the total elimination of the side chains, which resulted in the shortening of the interlayer distance.

AFM images showed that at 150 °C the films were quite smooth, while at 200 °C for 3 hours, the nanograins initially formed evolved into connected nanofibers with higher roughness and large gaps between domains. When the charge transport properties were studied, the hole mobility values when annealing at 150 °C (μ_h = 0.096 $cm^2/(V \cdot s)$) were one order of magnitude lower than the mobility of the polymer with solubilizing alkyl chains previously reported.[259] Still at 200 °C, the mobility values (μ_h = 0.078 $cm^2/(V \cdot s)$) were lower than at 150 °C. The authors concluded that the amorphous nature of the decarboxylated polymer needs to be taken into account, being in this case an efficient material for charge transport.

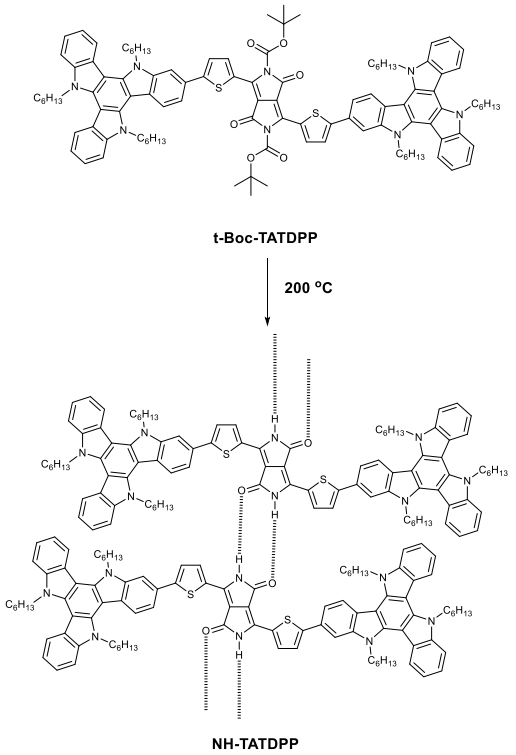

Figure I. 34 Synthesis of compound NH-TAT**DPP**.*Reproduced.[257]

Other **DPP** polymers with thermo-cleavable groups can be found in literature. Lee *et al*[260] for example, reported inversion of the dominant polarity in H-bonded **DPP** derivatives upon thermal treatment using low bandgap polymers (**Boc-PTDPP**, Figure I. 35a) in this case. In this work, OFET devices were fabricated applying a solution-sheared deposition technique, where a volume of the H-bonded **DPP** was placed between two preheated silicon wafers that move relative to each other at a specific rate (Figure I. 35b). This way, the semiconductor molecules can form highly crystalline and elongated grains along the shearing direction. The authors compared drop cast and solution-sheared films using IR spectroscopy before and after thermal annealing. The C=O stretching signal disappears after thermal treatment with a

concomitant appearance of the N-H band as a consequence of the carbamate deprotection. As an indication of the formation of H-bonds, the $\upsilon_{C=O}$ (amide) shifted to lower energies. Remarkably, the solution-sheared films showed further shift of the $\upsilon_{C=O}$ (amide) compared to the drop cast films, probably due to stronger H-bonding in the solid state in these types of films.

The ambipolar **Boc-PTDPP** was integrated into transistors and showed p-channel dominant characteristics, resulting in μ_h and μ_e of 1.32 x 10^{-2} $cm^2/(V \cdot s)$ and 2.3 x 10^{-3} $cm^2/(V \cdot s)$, respectively. These values are one order of magnitude higher than the values found in devices made by drop-casting the polymer. After decarboxylation at 200 ºC the dominant polarity of charge carriers changed from positive to negative in devices fabricated by solution-shearing, reaching μ_e of 4.6 x 10^{-2} $cm^2/(V \cdot s)$ and decreasing μ_h in one order of magnitude. DFT studies suggest that the LUMO orbitals of the deprotected polymer become much more delocalized than the protected polymer, which is favorable for *n*-channel conduction. Furthermore, the downshift of the HOMO-LUMO levels after thermal treatment could decrease the injection barrier for holes. The authors also suggest that the removal of *t*-Boc groups could act as electron traps and facilitate electron transport.

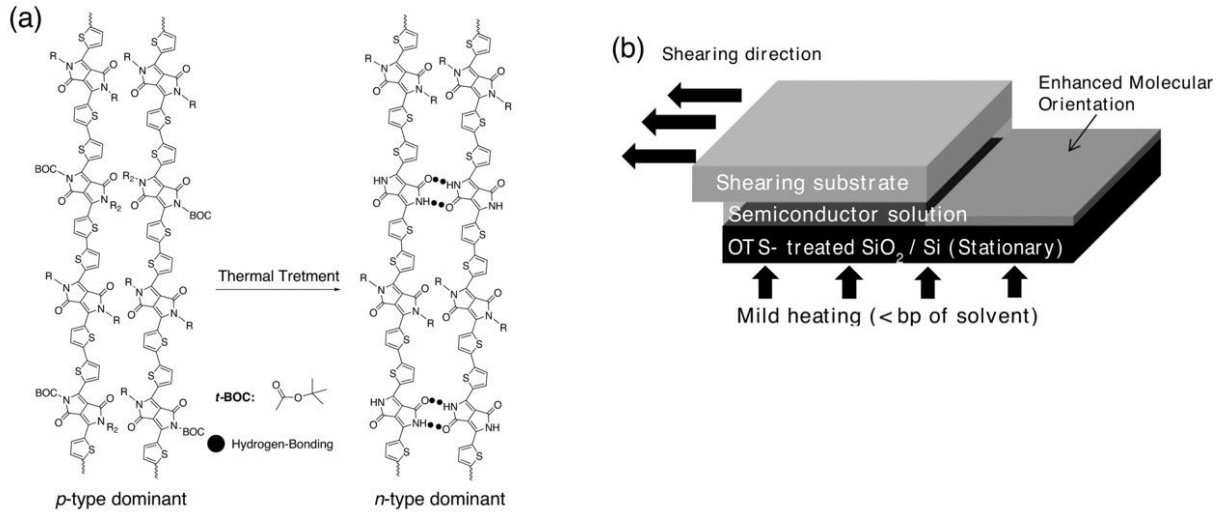

*Figure I. 35 a) Thermo-cleavable polymer based on **DPP**. (b) Schematic illustration of solution-shearing technique.*Reproduced.*[260]

Even though most of the examples report the fabrication of OFET devices, some reports can be found on the fabrication of BHJSCs. Brovelli *et al*.[261] used this strategy to optimize the charge separation efficiency at the donor/acceptor interface in an attempt to form interpenetrated phase separated percolation pathways. Proof-of-principle devices consisting of 100 nm blends of *t*-Boc protected **DPP**-Ph and PCBM were fabricated and the performance was followed at different thermal treatment times. While the V_{OC} showed no dependence on increasing the thermal treatment time from 0 to 300 s, the short circuit current showed a 30-fold increase (reaching its maximum at 270 s of treatment time), resulting in a 20-fold enhancement of efficiency with respect to the pristine device.

The morphology of the devices was followed by AFM and XRD during the thermal treatment and it was observed that the films changed from being uniform with roughness below 1 nm at

the initial state, to an increase in crystallinity and formation of 10-20 nm three-dimensional crystalline domains at 270 s of thermal treatment. The blends were stored in air under ambient illumination for up to 6 months, finding the same morphological features and emphasizing the strength of this strategy to stabilize the nanoarchitecture of the blend. Control experiments were carried out using a **DPP** containing alkyl tails (ethylhexyl) and interestingly, the efficiency values were lower emphasizing the effect of the hydrogen-bonding strategy.

c) Mono-alkylated **DPPs**

Even though the **DPP** with unsubstituted amides lack solubility and should be processed via vacuum deposition or by the latent pigment technology, the mono-alkylated **DPP** derivatives show very interesting properties while combining solubility and ability to form H-bonds. Patil *et al*,[262] reported mono-hexyl phenyl and mono-hexyl thiophene **DPP** derivatives (**PDPP-MH** and **TDPP-MH**, Figure I. 36a) and studied their properties by single crystal X-ray analysis and correlated the results to the charge transport properties in both, mono and di-alkylated analogues. The authors found that while the di-alkylated analogues show herringbone packing arrangements, the mono-alkylated derivatives crystallize in a co-facial layered structure thanks to the formation of intermolecular H-bonding between the free amide groups. Charge carrier mobility values (p-type) two orders of magnitude higher were found for the mono-alkylated derivatives compared to the di-alkylated analogues. The authors explain that according to the crystal structures and theoretical calculations, charge transport occurs in two or three directions while it happens in only one direction for the di-alkylated derivatives.

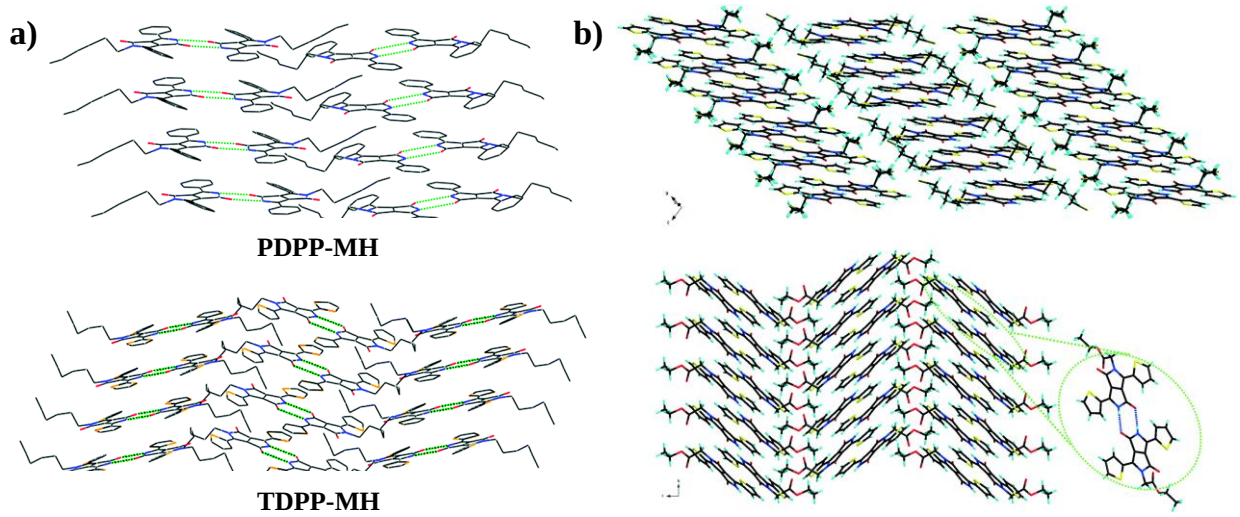

*Figure I. 36 a) Co-facial packing via H-bonding in **PDPP-MH** and **TDPP-MH**. b) Molecular packing of two of the studied mono-alkylated **DPP** derivatives, one showing anisotropy of the p-stacking along the a axis (top) and another one showing co-facial herringbone arrangement (bottom).*

Pop and Amabilino showed similar results extending their study to a larger variety of di- and mono-alkylated thiophene-capped **DPPs**.[263] In this case, the authors found out herringbone structures in some of the mono-alkylated **DPP** derivatives. Particularly, the authors observed that the mono-substituted **DPPs** with hexyl and ethyl acetate substituents were less distorted

than the other derivatives of the series, causing stronger intermolecular H-bonding that increases the molecular overlap and planarity of the **DPP** cores (Figure I. 36b). More specifically, the mono-substituted **DPP** with ethyl acetate showed high potential for optimizing the charge transport properties in be applied in organic electronic devices.

Other examples of mono-alkylated **DPP** derivatives have been reported in literature but most of them have been applied as anion sensors thanks to the binding of anions by H-bonding with the free amide in one of the lactam rings.[264–266]

IV.3.2) **DPPs** with H-bonding groups in different positions: polymers and small molecules

Even though the **DPP** molecule is considered an H-bonded pigment as shown in the previous section, it can only be processed by vacuum deposition or using the latent pigment technology after applying thermal or acid treatment. Due to the possibility of functionalization of the **DPP** core, it is possible to introduce different types of H-bonding motifs in soluble derivatives, making possible to study the aggregation in solution as well as device fabrication.

a) Amide-functionalized **DPP** systems

One common strategy for introducing H-bonds into the molecular structure of **DPP** derivatives is attaching amide groups at the periphery of the aromatic rings attached to the central **DPP** core. This strategy is usually based on introducing an aldehyde group that can react subsequently with electron-deficient acetamides via Knoevenagel condensation. In this sense, most of the examples found in literature are based on linear molecules, even though some cases of hairpin-shaped **DPP** derivatives are also reported. An example of the latter approach was reported by Stupp *et al*,[267] where a hydrogen-bonded small molecule containing *trans*-1,2-diamidocyclohexane and two **DPP** conjugated arms (Figure I. 37), were fabricated with the hairpin derivative **DPP**HP as the donor material, and **$PC_{71}BM$** as the acceptor, finding that a stepwise self-assembly process was needed to achieve functional devices (Figure I. 37). When both components were mixed in solution in an attempt to simultaneously assemble them into organized structures, non-working devices were found (Figure I. 37, top).

On the other hand, a slow cooling process starting from the molecularly dissolved state of the hairpin-shaped derivative (Figure I. 37, bottom), yielded robust supramolecular wires that were not disrupted when **$PC_{71}BM$** was added, resulting in well-defined heterostructures with improved efficiency. The self-assembly processes were followed by cryogenic transmission electron microscopy (cryo-TEM) and AFM, observing the presence of nanofibers in solution that were still present after the addition of **$PC_{71}BM$** and visible on the solar cell active layer (Figure I. 37A to C).

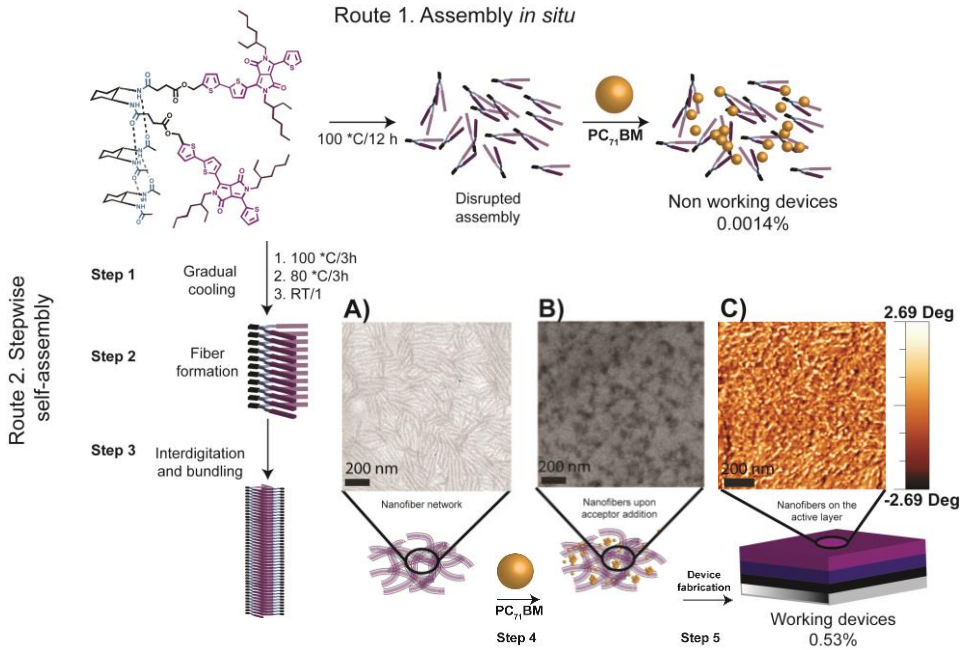

*Figure I. 37 Schematic representation of the preparation pathways used for device fabrication. Pathway 1 (top) shows the single step self-assembly of **DPPPHP** and **$PC_{71}BM$**. Route 2 (bottom) shows the stepwise self-assembly of **DPP**HP prior to the addition of $PC_{71}BM$. Cryo-TEM image of a **DPP**HP solution in toluene prepared following the stepwise self-assembly pathway. [**DPPHP**] = 7 mg ml^{-1} a). Cryo-TEM image of a DPPHP:$PC_{71}BM$ blend in a 1 : 1 ratio mixed for 30 seconds. [**DPP**HP] = 7 mg ml^{-1} and [**$PC_{71}BM$**] = 27 mg ml^{-1} b). AFM image of the active layer of a device fabricated by the stepwise self-assembly pathway c).*Reproduced.*[188]

Despite the proof-of-concept strategy used by Stupp *et al*.,[191] the solar cell efficiency obtained was too low. Therefore, the same group proposed the use of linear H-bonded **DPPs** (A-Amide) containing terminal amide groups (Figure I. 38) for the fabrication of BHJSCs. In this case, symmetric and asymmetric H-bonded **DPP** derivatives were studied, finding that the asymmetric derivatives showed improved solubility and more efficient devices.

The authors synthesized control molecules containing ester functional groups instead of amides (A-Ester). Both, A-Amide and A-Ester, showed very similar optoelectronic properties but different morphologies on thin film. While A-Ester active layers revealed greater crystallinity and π-π stacking analyzed by grazing incidence X-ray diffraction (GIXD), the active layers of devices made with A-Amide presented short fiber-like supramolecular aggregates with much smaller domain sizes and less ordered than the A-Ester active layers.

Interestingly, the devices fabricated in blends with **$PC_{71}BM$** show PCE 50% higher for A-Amide than for A-Ester. All the results point out that the H-bonds compete with long-range π-π stacking interactions, resulting in interconnected and nanoscale smaller donor domains *vs* highly crystalline larger domains obtained with A-Ester. Such morphology seems to nearly double the device efficiency when the H-bonded donors are present. The authors showed that with a good compromise between solubility and the formation of the appropriate nanostructures, this general strategy could be used to optimize function. Remarkably, there

were simultaneous studies reported by other groups where H-bonded semiconductors different to **DPP** were functionalized with terminal amides. In this case, the presence of H-bonding resulted to be detrimental for device performance.[268] However, only one solvent was used to prepare the devices and it is possible that poor solubility played an important role in that case.

The terminal amide strategy has been reported by other groups, finding very interesting results and applications. For example, Ghosh et al.[269] reported a **DPP**-based small molecule (**DPP**-Amide) with terminal amide groups that formed a black colored gel in toluene (Figure I. 39a and b). In this case, the derivative reported was symmetric, containing dodecyl branches as solubilizing alkyl tails, vs butyloctyl alkyl tails in the previous example. Figure I. 39c shows the absorption spectra of **DPP**-Amide in monomeric state using chloroform as a good solvent and in aggregated state in toluene. It can be observed that the spectrum in aggregated state is very different from the spectrum in the molecularly dissolved state, appearing typical bands corresponding to the formation of H- and J-aggregates, a behavior previously observed in other **DPP**[270,271] and H-bonded systems.[272]

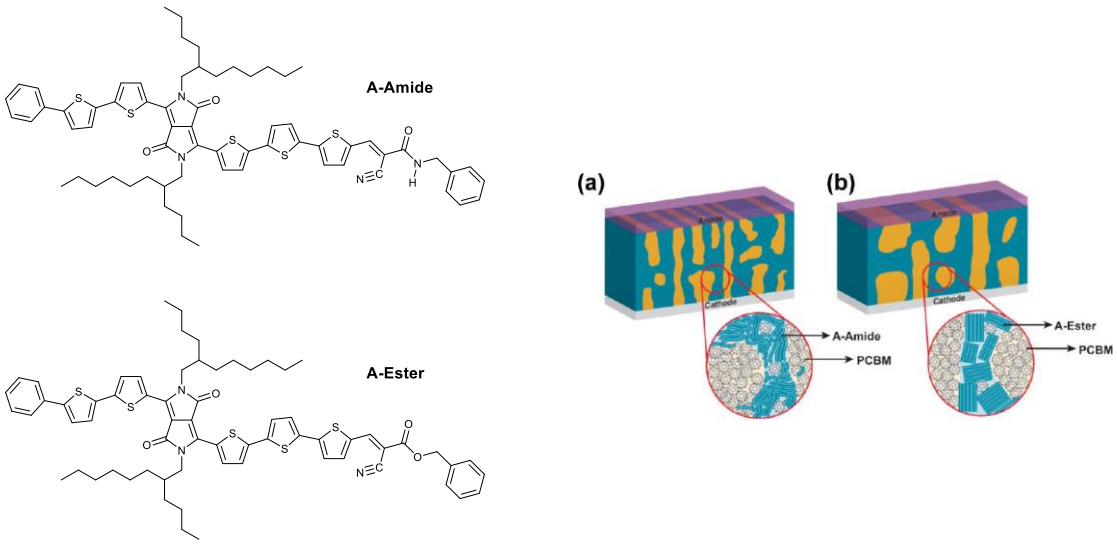

*Figure I. 38 Structures of **A-Amide** and **A-Ester** and schematic illustration of active layer morphology for **A-Amide** (a) and **A-Ester** devices (b).*Adapted.[191]*

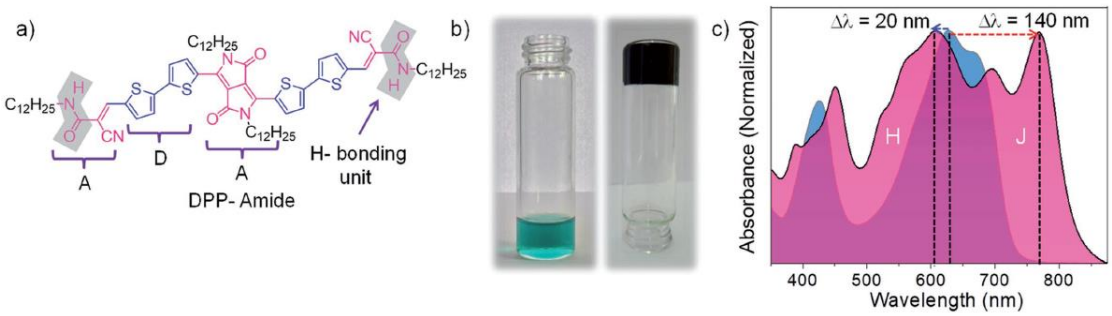

*Figure I. 39 a) Molecular structure of **DPP-Amide**. b) Photograph of a dilute solution of **DPP-Amide** in chloroform and the gel formed in toluene (inverted vial). c) UV-Vis spectra of **DPP**-Amide in monomeric state and aggregated state.*Adapted.[269]*

DPP-Amide was successfully employed to fabricate a composite material together with polydimethylsiloxane (**PDMS**). A small amount of the self-assembled fibers formed by **DPP-Amide** were incorporated into the **PDMS** matrix, obtaining a self-standing filter. Thanks to its absorption properties, covering the visible region and being transparent in the near IR region could be employed in anti-counterfeiting, infrared photography and forensic applications.

Furthermore, **DPP-Amide** was employed to fabricate a hybrid system with **$PC_{71}BM$**, resulting in the formation of a hybrid gel under certain conditions (Figure I. 40).[273] In this case, a self-sorted p-n heterojunctions with broad absorption and low band, which was not possible with other hybrid systems especially the ones based on perylene bisimides.[274] The importance of the self-assembled state by H-bonding was observed by measuring emission quenching upon the addition of **$PC_{71}BM$**. While the addition of **$PC_{71}BM$** to solutions of **DPP-Amide** or **DPP**-Ester in their molecularly dissolved state (chloroform) no emission quenching was observed, indicating the absence of electron transfer processes, finding the same effect in toluene solutions of **DPP**-Ester. In contrast, when different ratios of **$PC_{71}BM$** were added to toluene solutions of **DPP**-Amide (aggregated conditions), attenuation in the emission signal of **DPP**-Amide was observed with increasing weight ratio of **$PC_{71}BM$** (Figure I. 40b). Such attenuation was not due to ground state charge transfer since the absorption spectrum of the **DPP-Amide**: **$PC_{71}BM$** mixture did not show any additional bands, being the sum of the spectral features of both components (Figure I. 40a). These results indicate that the self-assembled structures of **DPP-Amide** are necessary to immobilize **$PC_{71}BM$** aggregates and to facilitate the electron transfer process.

Flash-photolysis time resolved microwave conductivity (FP-TRMC) was used to study charge carrier mobility and photovoltaic performance, which can be predicted by plotting transient photoconductivity vs different blending ratios of acceptor material. FP-TRMC measurements were performed on assembled (toluene) and disassembled samples (chloroform) of **DPP-Amide** using different ratios of $PC_{71}BM$, finding a 5-fold increase in intrinsic conductivity for self-assembled films of **DPP-Amide:$PC_{71}BM$** in 1.5:1-1:1.5 ratio (Figure I. 40c). No enhancement in conductivity was observed in DPP-Ester: $PC_{71}BM$ films.

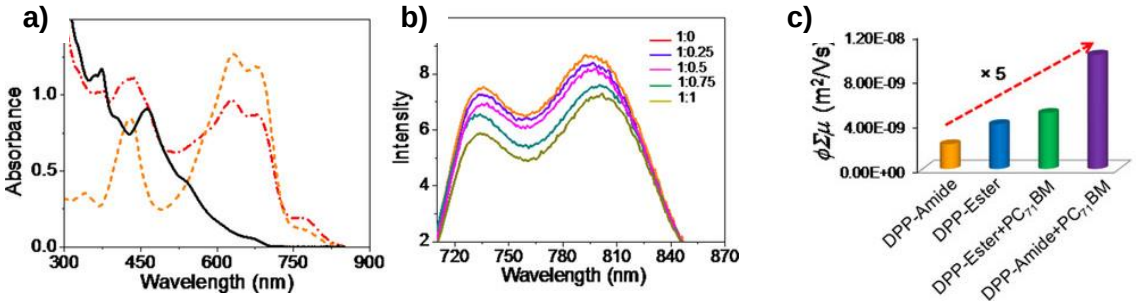

*Figure I. 40 a) Absorption spectra of **DPP-Amide** aggregates (orange, dash), **$PC_{71}BM$** (black, solid) and **DPP-Amide : $PC_{71}BM$** (1 : 1 wt. ratio) hybrid assembly (red, dash-dot). b) Emission spectra of **DPP-Amide** in toluene (λ_{ex}=680 nm) with different blend ratio of $PC_{71}BM$. c) The plot showing increase in photoconductivity of **DPP-Amide** and **DPP-Ester** upon addition of **$PC_{71}BM$** (1 : 1 wt. ratio).*Adapted.*[273]

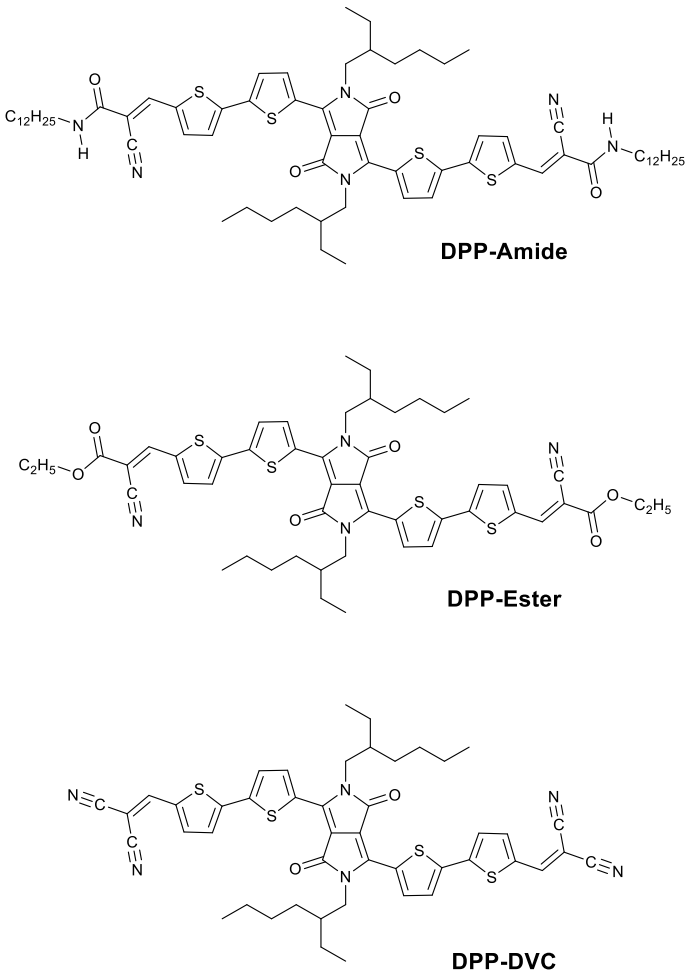

*Figure I. 41 Structures of the three diphenyl-**DPP** derivatives used to modulate charger carrier polarity.*Adapted.*[275]

More recently, the terminal functionalization of **DPP** semiconductors has been used to modulate charge carrier polarity. Ghosh *et al*.,[275] reported three **DPP** derivatives with the same π-conjugated backbone symmetrically functionalized with amide, ester and cyano groups (Figure I. 41). The authors used FP-TRMC as well to confirm that the n-type charge carrier mobility increased with higher acceptor strength and OFET devices were fabricated to confirm the change of polarity from p- to n-type.

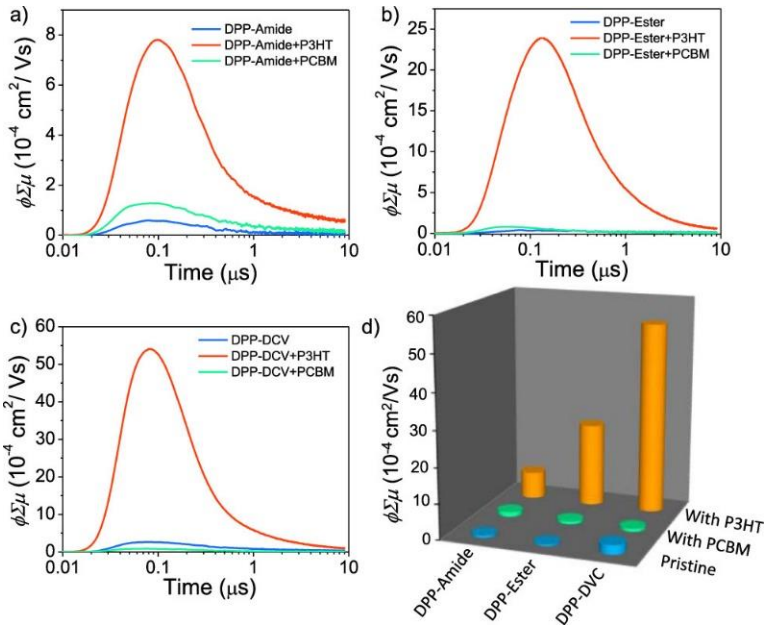

*Figure I. 42 FP-TRMC transients of a) **DPP−Amide**, **DPP−Amide:P3HT**, and **DPP−amide:PC$_{71}$BM**; b) **DPP−Ester**, **DPP− Ester:P3HT**, and **DPP−Ester:PC$_{71}$BM**; and c) **DPP−DCV**, **DPP−DCV:P3HT**, and **DPP−DCV:PC$_{71}$BM**. d) Comparison of ϕΣμ values of all the **DPP** derivatives in the absence and presence of **P3HT** and **PC$_{71}$BM**.*Reproduced.*[275]

The photoconductivity of the three derivatives on thin film was measured either in their pristine state or by mixing them with **PC$_{71}$BM** to analyze the p-type charge mobility. When the amide-functionalized derivative was spin-coated from toluene solutions, an enhancement in photoconductivity was observed in comparison to the chloroform films. This was a clear indication of the importance of the H-bonding formation. Interestingly, in blends with **PC$_{71}$BM** (Figure I. 42b) the amide-functionalized derivative showed enhanced photoconductivity related to the pristine film. On the other hand, the blends made with the ester-functionalized **DPP** exhibited much lower photoconductivity enhancement with respect to the pristine film and a decrease in photoconductivity in blends made with the dicyano derivative.

These results indicate a transition from p-type character of the amide derivative to n-type character in the cyano derivative. Inversely, the three derivatives were blended with **P3HT** (Figure I. 42a to c) to evaluate the n-type character, finding in this case the opposite trend. However, the solvent used in this case was chlorobenzene instead of chloroform, which could yield different supramolecular structures with different electronic properties, especially in the case of the H-bonded derivative. The mobility values were calculated by fabricating FET devices, finding μ_h of 1.3 x 10^{-2} $cm^2/(V{\cdot}s)$ for the amide derivative, while μ_e of 1.5 x 10^{-2} $cm^2/(V{\cdot}s)$ for the ester derivative and of 1 x 10^{-2} $cm^2/(V{\cdot}s)$ for the dicyano **DPP**. With these results the authors offered an alternative strategy to modulate charge transport properties.

b) Complementary H-bonding groups incorporated in **DPPs**

Complementary H-bonding between two conjugated species to form hetero-aggregates is a great strategy to achieve hierarchical structures, being p-n heterojunctions in the case of

semiconductors. In this sense, H-bonding motifs able to form multiple and complementary bonds with other conjugated systems have been incorporated into **DPP** derivatives. Braunschweig *et al*.,[276,277] studied systems composed of **DPP** donors with chiral and achiral side chains. These systems can form triple H-bonds with PDI acceptors and assemble into superstructures (Figure I. 43a to c). They discovered that by heating solutions containing both type of molecules, achiral PDIs bind to disordered **DPP** stacks upon cooling, this then leads to the development of chiral superstructures.

Additionally, a model was developed to elucidate the structural cues that induce the transition from a disordered aggregate into a chiral helix. The major breakthrough of this model is that it allowed the quantitative determination of all the thermodynamic parameters, while also establishing that the H-bonding and the subsequent helix formation process are enthalpically favored but entropically disfavored.[276] Recently, this same group has explored six superstructures featuring different geometries, resulting in subtle changes in the solid-state packing of the **DPPs**.[278] They achieved this by performing combinations of two **DPPs** and three rylenes to form six hierarchical superstructures that assemble as a result of orthogonal H-bonding and π···π stacking (Figure I. 43d to f). The changes in inter-**DPP** stacking that are templated by the neighboring rylenes have a subtle effect on the excited-state dynamics and on the activation of new pathways such as singlet fission (SF).

The exclusive benefits of combinatorial supramolecular assembly demonstrated the impact of the structure on advanced light management in the form of SF, affording triplet quantum yields as high as 65% for a correlated pair of triplets and 15% for an uncorrelated pair of triplets.[278]

The changes in the molecular structures of the components resulted in various 1D and 2D morphologies, whose long-range order and geometric differences have an influence on the management of light. Further studies of these supramolecular scaffoldings will be important to understand the morphology dependence on the photophysics of the supramolecular heterojunctions in order to maximize the junction area to achieve efficient charge separation and transport.[278]

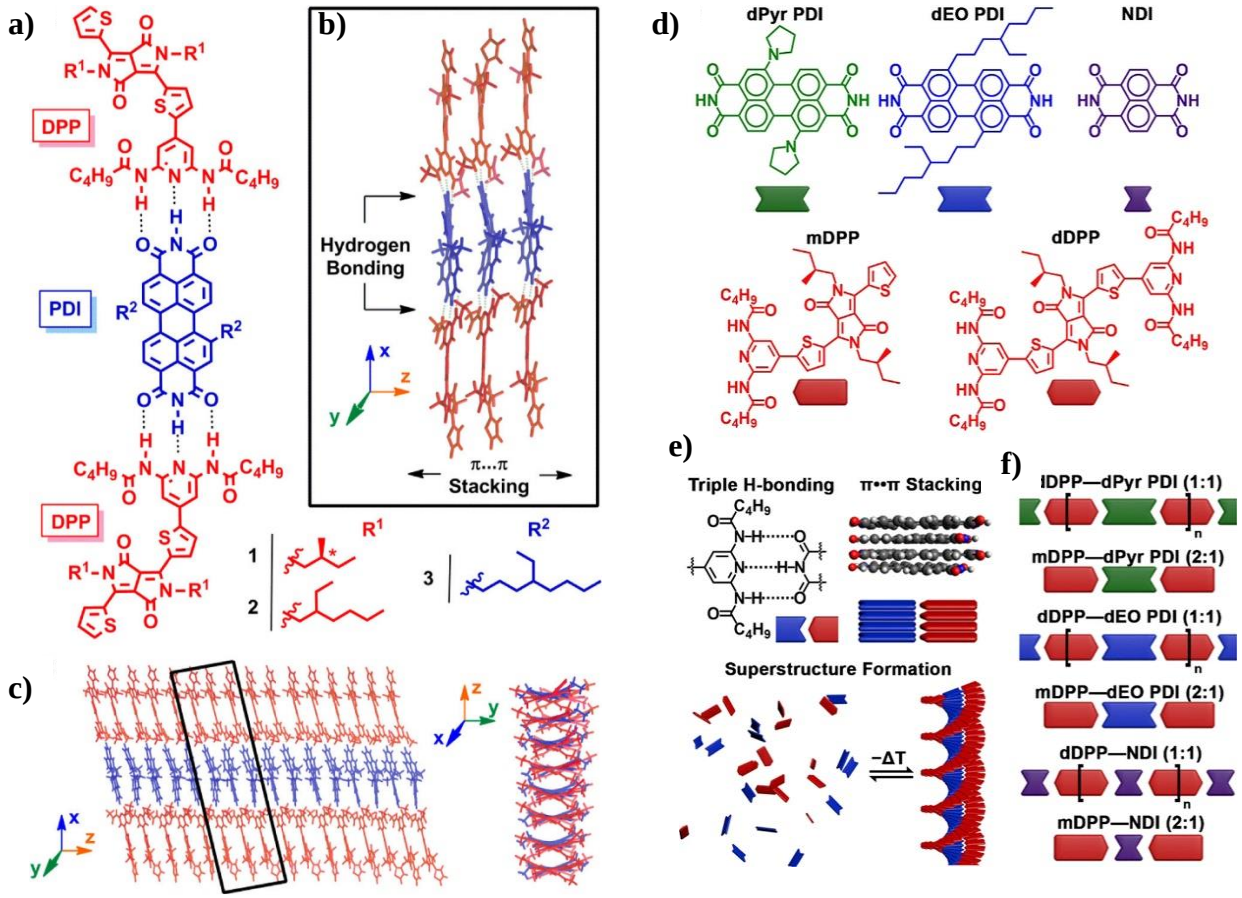

Figure I. 43 a) ***DPP*** *donor (red) and* ***PDI*** *acceptor (blue) molecules 1−3 are capable of b) heteroaggregation through a combination of H-bonding and π–π stacking, resulting in c) well-ordered superstructures.*Adapted.*[276] *d) Library composed of three rylenes and two diketopyrrolopyrroles, e) supramolecular assembly via triple H-bonding and π–π stacking results in* ***DPP−rylene*** *superstructures, and f) superstructures vary in the* ***DPP*** *and rylene components and* ***DPP/rylene*** *stoichiometry.*Adapted.*[278]

Braunschweig *et al*., have also performed studies to determine how solubilizing side chains, the conjugation length and the type of H-bonding groups affect the homo-assembly of **DPPs** into J-aggregates.[279] These studies were performed by variable temperature (VT) UV-Vis titrations in toluene on multiple thiophene **DPP** derivatives (Figure I. 44). They reported that the presence of diamidopyridine (**DAP**) groups and their ability to form H-bonds improved considerably the driving force for assembly into larger clusters compared to those without the **DAP** group. According to their findings, the interplay of π–π stacking, H-bonding, van der Waals forces, solvent, concentration and temperature is responsible for the size, structure, stability and spectroscopic attributes of the resulting superstructures.

Moreover, the main discovery in this work was that these molecules assemble into slip-stacked geometries, described as J-aggregates. They also managed to derive two equations for the calculation of the size of aggregated stacks and its average mole fraction.[279] These findings are very important since the structure and properties of supramolecular assemblies are intimately linked, and small changes in the relative orientations of stacks can have great impact on their optoelectronic properties and device performance.[280,281]

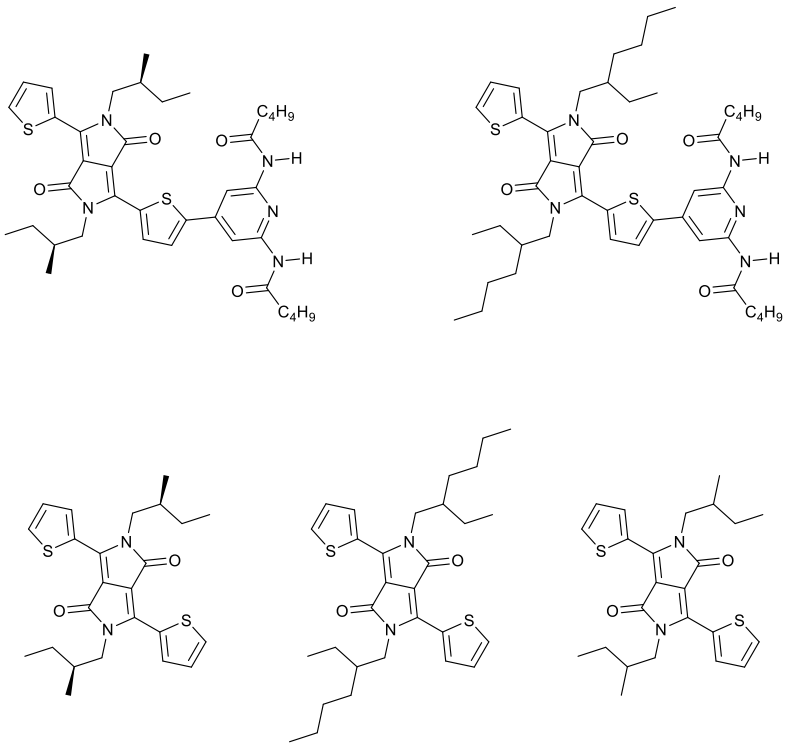

Figure I. 44 ***DPP*** *derivatives whose aggregation was studied by Braunschweig* et al.[282]

c) Other H-bonding motifs present in **DPP** derivatives

Our group has shown for example the introduction of semicarbazone functionalities into the simple thiophene-capped **DPP** core.[283] Two **DPP** derivatives were synthesized (Figure I. 45a and b) and the appearance of J-aggregates due to H-bonding formation was observed. We observed the increase of the J-aggregate band in solvents that promote the formation of H-bonds *vs* chloroform, which was used as a good solvent. The addition of methanol, a solvent that competes with the formation of H-bonds, resulted in the disappearance of the J-aggregate bands, putting in evidence the participation of H-bonds in the formation of such kinds of aggregates (Figure I. 45c and d). Furthermore, by tuning the aggregation state of these simple derivatives using different solvents, concentrations and temperature, it was possible to tune the energy bandgaps and cover large regions of the solar spectrum even reaching the near IR region. Different 1D structures were found, which presented different optical properties, making these small molecules very interesting to compare the different aggregation conditions on device efficiency.

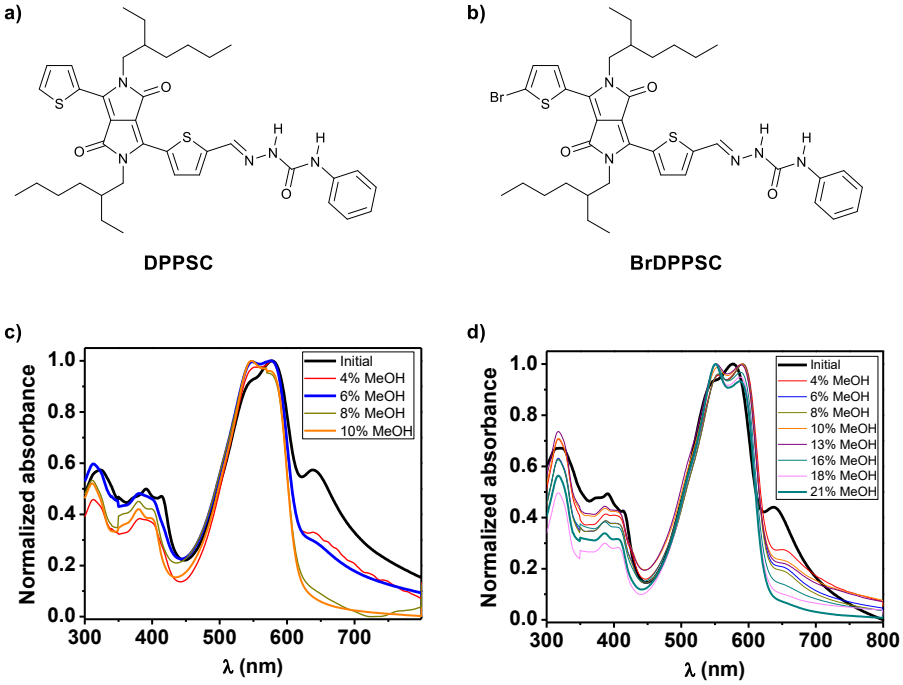

*Figure I. 45 Structures of **DPPSC** (a) and Br **DPPSC** (b). Normalized absorption spectra in solution of **DPPSC** (c) and (d) **BrDPPC** upon the addition of methanol.*Adadpted.*[283]

The presence of semicarbazone groups has also been found in other **DPP** derivatives that were used as colorimetric chemosensors for fluoride ions.[198] This same group reported another chemosensor for fluoride ions using phenylhydrazone[199] as the H-bonding unit. In these cases, the H-bonding groups were employed to bind the fluoride ions and the supramolecular structures formed by them were not studied.

An example of a bola-amphiphilic **DPP** derivative has also been reported[284] to obtain supramolecular nanofibers by combination of H-bonding and π-π stacking (Figure I. 46b). Two carboxylic acids were attached to the **DPP** core through a C_{10} alkyl linker to obtain the bola-amphiphile compound that resulted to form nanofibers in aqueous solution. The self-assembly properties of **DPP-11a** were studied by UV-Vis spectroscopy in different solvents, using tetrahydrofuran (THF) as a good solvent and water as a bad solvent and probing the absorption spectra at different times (Figure I. 46d). In this case, the evolution of the bands and the appearance of aggregate bands (J-aggregate) manifest the important role of H-bonds to tune the formation of different morphologies. In this case, THF solutions drop cast on mica showed the formation of nanoparticles, while the aqueous solutions presented the formation of nanofibers.

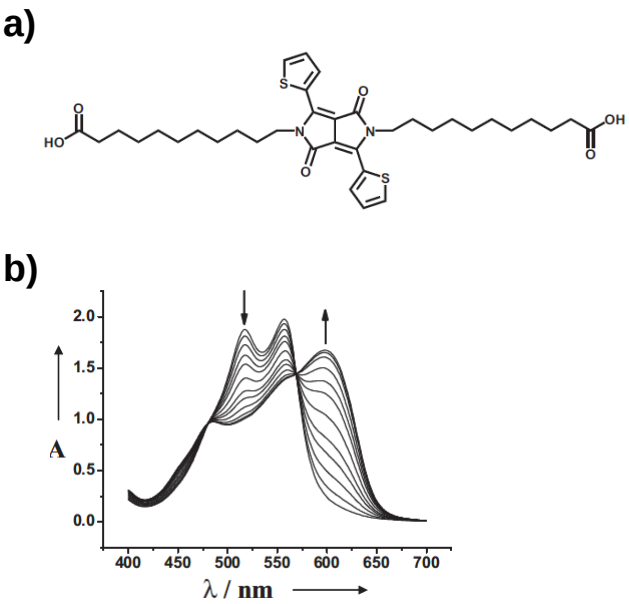

*Figure I. 46 a) Molecular structure of **DPP**-11a. b) Time-dependent absorption spectra of **DPP**-11a.*Adapted.*[284]

d) H-bonds incorporated into **DPP**-based polymers

H-bonding groups have also been integrated into the structure of semiconducting polymers to achieve enhanced charge transport and expand the applications into sensing devices. Zhang *et al*[285] incorporated thymine groups in the side chains of a thiophene-functionalized **DPP** polymer (**PDPP4T-6**) (Figure I. 47a). Thymine is one of the four nucleobases in DNA and has been demonstrated to bind with certain metal ions, such as Pd(II) and Hg(II).[286] FET devices were fabricated by spin-coating solutions of **DPP4T-T** and controls molecule **PDPP4T-A** (with branched alkyl tails) and **PDPP4T-B** (with branched and linear alkyl tails), finding μ_h values higher for the polymer containing thymine. This result was rationalized considering the enhancement of the film crystallinity due to H-bonding in comparison with the conjugated polymers containing only alkyl chains. This was demonstrated with grazing incidence wide-angle X-ray scattering (GIWAXS) measurements, which showed improved lamellar stacking than the films made with the control molecules.

Furthermore, the FET devices made with the thymine-containing polymer were used as sensors for CO and H_2S. The incorporation of Pd(II) and Hg(II) was achieved through the air-water interface coordination. After the metallic ion coordination, FETs were fabricated and exposed to different gaseous analytes and solvent vapors. The polymer containing Pd(II) could detect CO in concentrations as low as 10 ppb, while devices made with Hg(II) coordinated ions could sense S_2Hg down to 1 ppb. In this case, the introduction of H-bonding functionalities in semiconducting polymers resulted not only in a mobility enhancement, but also in additional applications and properties.

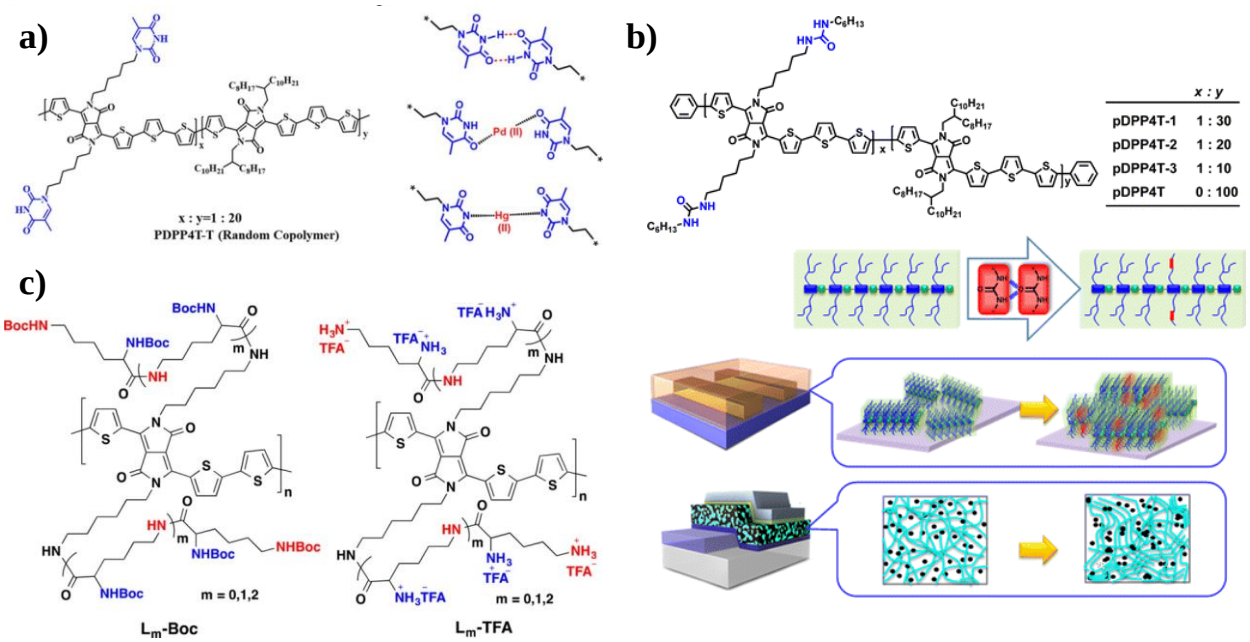

*Figure I. 47 a) Chemical Structure of **PDPP4T-T**; Thymine groups are randomly connected to the conjugated backbone and the illustration of T−T Intermolecular H-bonding and the coordination with Pd(II) and Hg(II).*Reproduced.*[285] *b) Chemical Structures of **pDPP4T-1**, **pDPP4T-2**, **pDPP4T-3**, and **pDPP4T**, and illustration of the design rationale for the incorporation of urea groups in the side chains of conjugated D–A polymers.*Reproduced.*[287] *c) Chemical structures of **DPP** polymers containing lysine residues.*Reproduced.*[288]

Urea groups have also been introduced in the pending chains of **DPP** polymers. Zhang *et al*,[287] reported three **DPP**-based polymers containing different ratios of urea groups and branched alkyl chains (Figure I. 47b). OFETS and BHJSCs were fabricated with these polymers and the control **DPP** polymer without urea units. The authors found out that the polymer containing the lowest ratio (1:30) of urea groups, showed the highest hole mobility (μ_h = 13.1 $cm^2/(V \cdot s)$). The influence of the presence of urea groups in **DPP** polymers was also studied in BHJSCs, finding in this case that the polymer with the highest ratio of urea groups (1:30) presented the best efficiency of all (6.8%), including the control devices made with polymers without urea groups.

The high mobility values found were attributed to the enhancement of lamellar packing order of the alkyl said chains on the thin films prepared thanks to the H-bonding interactions led by the urea groups and the appearance of inter-chain π-π stacking after thermal annealing at 100 ºC. Regarding the solar cell devices, the presence of urea groups was found to guide the assembly of the polymers into nanofibers and direct the ordered aggregation of the acceptor material, resulting in micro-phase separation in the blends were charge separation can be enhanced, compared to the control polymers without urea groups.

The use of H-bonds in **DPP** polymers has also interesting applications in bioelectronics. Du *et al*,[288] reported a **DPP** polymer containing lysine side chains (Figure I. 47c) that was applied in neural cell adhesion and growth. This way, it was not necessary to use other biological coating steps on electrical devices, making them promising materials for applications in

bioelectronics. **DPP** polymers based on **DPP3T** (dithienyl-**DPP**) containing different number of lysine derivatives (Figure I. 47c) were synthesized. However, the strong H-bonding ability of lysine resulted in very strong intermolecular aggregation and lack of solubility. The lysine groups were protected with *t*-Boc groups to provide solubility and deprotected subsequently with trifluroacetic acid (TFA) to render protonated lysine units, which increased the surface charge and improved cell adhesion.

Of course everything that has been presented is just the tip of the iceberg, more information on **DPPs** can be found in literature[289]. Nevertheless, now that the current state of the art regarding H-bonded **DPP** systems has been discussed, it is finally time to discuss about their role in this thesis.

IV.4) Role of **DPP** in this thesis

As it was previously mentioned, this PhD work consists of a systematic study based on a simple thiophene-capped **DPP** electroactive segment as a model system, several H-bonding parameters will be explored and subsequently, the results will be extended to state of the art semiconductors, such as rhodanine-containing systems[134,290] or isoindigo-based[291,292] semiconductors (Figure I. 48). Finally, the study will be extended to acceptor molecules and donor-acceptor blends, including fullerene and NFAs (Figure I. 48).[293,294]

In this thesis, the effect of varying several parameters has been evaluated, for instance:

- ✓ **Type of H-bonding functionality:** Amide, urea, self-complementary systems, and others.
- ✓ **Position of the H-bonds** in the molecular structure: peripheral or embedded in the solubilizing alkyl tails.
- ✓ **Solubility**: different lengths and branching of alkyl tails.
- ✓ **Topology** of the H-bonds in amides arms.
- ✓ **Chirality** within the pending arms attached to the **DPP** core.

Regarding supramolecular electronic systems, the optoelectronic properties and the structural aspects of these systems must be optimized to reach good performance in the final applications.

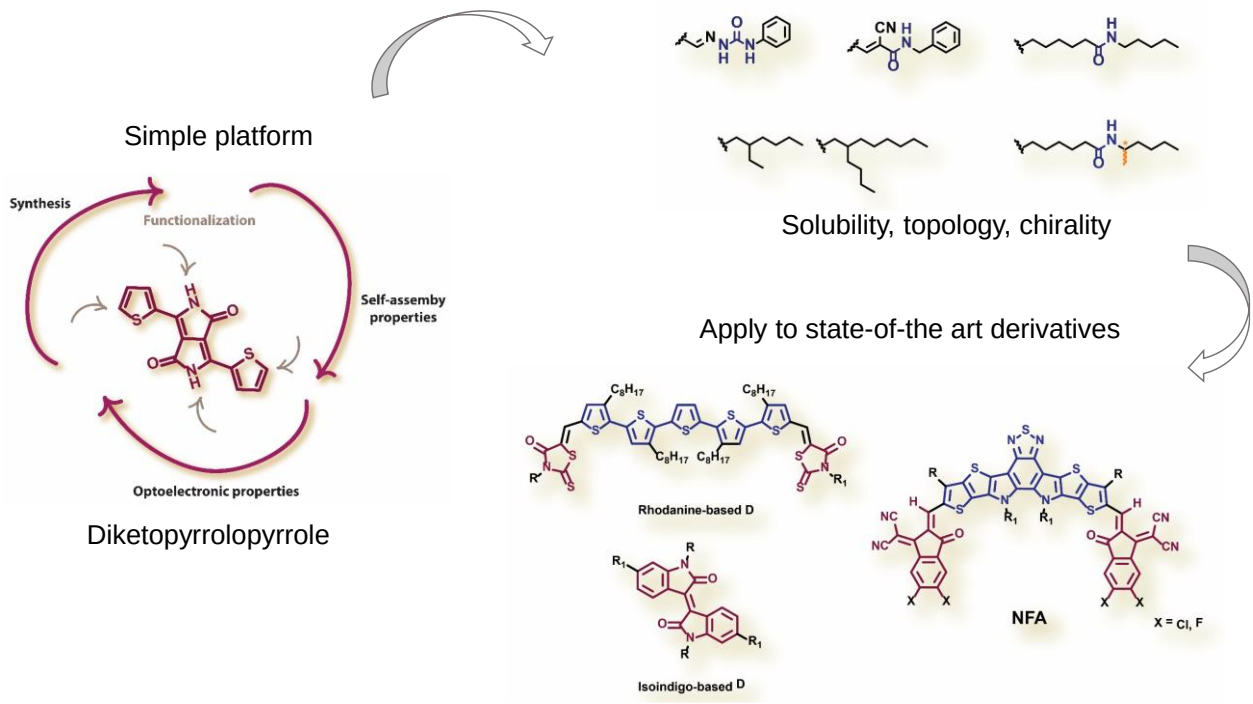

*Figure I. 48 Thiophene-capped **DPP** main structure, parameters to study and state-of-the-art semiconductors.*

DPP has been chosen as the model system due to its great electronic properties and functionalization versatility, as well as the possibility that it will provide an overview of the influence of H-bonding and explore how general the results are when translated to any other semiconductor.

The simple **DPP** derivative having two thiophene rings is one of the most used starting materials to synthesize semiconducting polymers and oligomers.[295] The optoelectronic and self-assembly properties of **DPP** derivatives mainly depend on the aromatic groups attached to the **DPP** core, and in many studies they are modified with electron-donating(withdrawing) groups.[195,296–298] Interestingly, H-bonding is a great tool to tune the optoelectronic and self-assembly properties of small **DPP** derivatives without enlarging the thiophene **DPP** core. The examples of hydrogen-bonded **DPP** found in literature usually utilize the non-alkylated version of the pyrrole rings,[237,238] which normally are vacuum deposited due to insolubility as shown in the previous paragraphs or **DPP** oligomers modified in the peripheral positions with amide bonds.[191,269,299]

So far, several H-bonded **DPP** families have been studied and can be seen in Figure I. 49. This thesis will address the study of three of these families, in particular chapter II will cover the bisamide familiy[300] (Figure I. 49b). Chapter III will cover the study of the expansion of the bisamide family with enhanced solubility and amide topology changes (Figure I. 49d). Next, in chapter IV the impact of keeping the same solubilizing alkyl chains, while changing the position and topology of the amide bonds (Figure I. 49e) is discussed. Finally, in chapter V preliminary results on the impact of solvent in changes in morphology of some of the derivatives described in chapter III will be presented.

In this thesis, I have worked on families with very different designs from the previously studied families in our group.[283] This way, very different parameters can be compared at the same time along with their optimization.

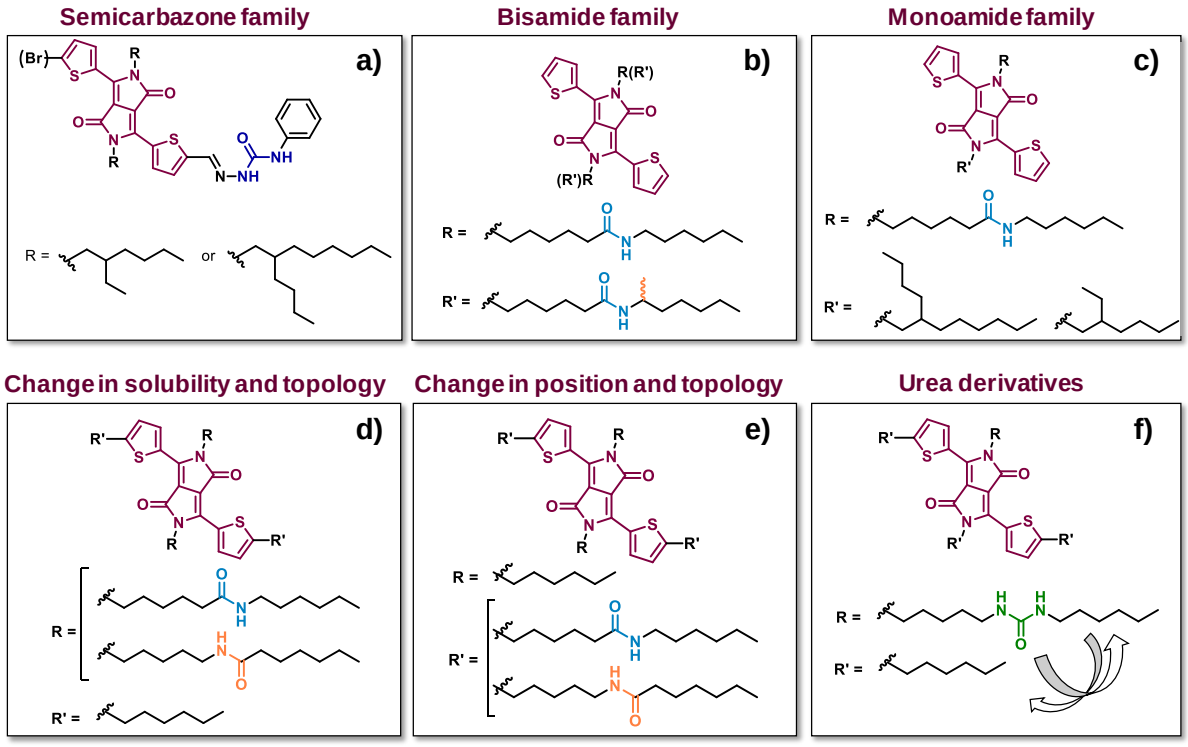

*Figure I. 49 H-bonded **DPP** families synthesized so far in the **DPP** model system study.*

IV.5) References

[1] K. Dong, X. Dong, Q. Jiang, *World Econ* **2020**, *43*, 1665–1698.

[2] "• Primary energy consumption by country 2020 | Statista," can be found under https://www.statista.com/statistics/263455/primary-energy-consumption-of-selected-countries/, **n.d.**

[3] "EIA projects nearly 50% increase in world energy usage by 2050, led by growth in Asia - Today in Energy - U.S. Energy Information Administration (EIA)," can be found under https://www.eia.gov/todayinenergy/detail.php?id=41433, **n.d.**

[4] "Global Energy Review 2021 – Analysis - IEA," can be found under https://www.iea.org/reports/global-energy-review-2021?mode=overview, **n.d.**

[5] "Stated Policies Scenario – World Energy Model – Analysis - IEA," can be found under https://www.iea.org/reports/world-energy-model/stated-policies-scenario, **n.d.**

[6] "Sustainable Development Scenario – World Energy Model – Analysis - IEA," can be found under https://www.iea.org/reports/world-energy-model/sustainable-development-scenario, **n.d.**

[7] "Fossil Fuels - Our World in Data," can be found under https://ourworldindata.org/fossil-fuels#citation, **n.d.**

[8] “Air pollution,” can be found under https://www.who.int/health-topics/air-pollution#tab=tab_1, **n.d.**
[9] “Coal - Fuels & Technologies - IEA,” can be found under https://www.iea.org/fuels-and-technologies/coal, **n.d.**
[10] “Coal explained - U.S. Energy Information Administration (EIA),” can be found under https://www.eia.gov/energyexplained/coal/, **n.d.**
[11] “Oil and petroleum products explained - U.S. Energy Information Administration (EIA),” can be found under https://www.eia.gov/energyexplained/oil-and-petroleum-products/, **n.d.**
[12] “Electricity from Oil,” can be found under http://powerscorecard.org/tech_detail.cfm?resource_id=8, **n.d.**
[13] X. F. Wu, G. Q. Chen, *Energy Policy* **2019**, *128*, 476–486.
[14] “Gas - Fuels & Technologies - IEA,” can be found under https://www.iea.org/fuels-and-technologies/gas, **n.d.**
[15] K. Dong, R. Sun, G. Hochman, X. Zeng, H. Li, H. Jiang, *Journal of Cleaner Production* **2017**, *162*, 400–410.
[16] “Use of natural gas - U.S. Energy Information Administration (EIA),” can be found under https://www.eia.gov/energyexplained/natural-gas/use-of-natural-gas.php, **n.d.**
[17] A. Wellerstein, *Bulletin of the Atomic Scientists* **2008**, *64*, 26–31.
[18] “Nuclear Energy - How Energy Works - Duke Energy,” can be found under https://www.duke-energy.com/Energy-Education/How-Energy-Works/Nuclear-Power#tab-1973b216-dd36-401f-9959-96cac246cc61, **n.d.**
[19] “Nuclear Power in a Clean Energy System – Analysis - IEA,” can be found under https://www.iea.org/reports/nuclear-power-in-a-clean-energy-system, **n.d.**
[20] “Top 15 Nuclear Generating Countries,” can be found under https://www.nei.org/resources/statistics/top-15-nuclear-generating-countries, **n.d.**
[21] V. Kortov, Yu. Ustyantsev, *Radiation Measurements* **2013**, *55*, 12–16.
[22] M. Baba, *Radiation Measurements* **2013**, *55*, 17–21.
[23] “Renewables – Global Energy Review 2021 – Analysis - IEA,” can be found under https://www.iea.org/reports/global-energy-review-2021/renewables, **n.d.**
[24] M. Bilgili, H. Bilirgen, A. Ozbek, F. Ekinci, T. Demirdelen, *Renewable Energy* **2018**, *126*, 755–764.
[25] J. A. Laghari, H. Mokhlis, A. H. A. Bakar, H. Mohammad, *Renewable and Sustainable Energy Reviews* **2013**, *20*, 279–293.
[26] E. F. Moran, M. C. Lopez, N. Moore, N. Müller, D. W. Hyndman, *Proc Natl Acad Sci USA* **2018**, *115*, 11891–11898.
[27] “Renewables Global Status Report - REN21,” can be found under https://www.ren21.net/reports/global-status-report/, **n.d.**
[28] J.-Y. Son, K. Ma, *Proc. IEEE* **2017**, *105*, 2116–2131.
[29] R. Saidur, N. A. Rahim, M. R. Islam, K. H. Solangi, *Renewable and Sustainable Energy Reviews* **2011**, *15*, 2423–2430.
[30] “Global bioenergy statistics - Worldbioenergy,” can be found under http://www.worldbioenergy.org/global-bioenergy-statistics/, **n.d.**
[31] M. Sami, K. Annamalai, M. Wooldridge, *Progress in Energy and Combustion Science* **2001**, *27*, 171–214.
[32] C.-L. Jin, Z.-M. Wu, S.-W. Wang, Z.-Q. Cai, T. Chen, M. R. Farahani, D.-X. Li, *Energy Sources, Part B: Economics, Planning, and Policy* **2017**, *12*, 1030–1035.

[33] S. T. Coelho, J. Goldemberg, O. Lucon, P. Guardabassi, *Energy for Sustainable Development* **2006**, *10*, 26–39.
[34] W. V. Reid, M. K. Ali, C. B. Field, *Glob Chang Biol* **2020**, *26*, 274–286.
[35] “Geothermal explained - U.S. Energy Information Administration (EIA),” can be found under https://www.eia.gov/energyexplained/geothermal/, **n.d.**
[36] “Geothermal Electricity Production Basics | NREL,” can be found under https://www.nrel.gov/research/re-geo-elec-production.html, **n.d.**
[37] “Geothermal Energy | National Geographic Society,” can be found under https://www.nationalgeographic.org/encyclopedia/geothermal-energy/, **n.d.**
[38] “Vendenheim-Reichstett. Chronique d’une aventure industrielle mise en suspens,” can be found under https://www.dna.fr/environnement/2020/12/04/chronique-d-une-aventure-industrielle-mise-en-suspens, **n.d.**
[39] “Environnement. Après les séismes, les autres projets de géothermie suspendus autour de Strasbourg,” can be found under https://www.dna.fr/economie/2020/12/09/la-prefecture-suspend-les-autres-projets-de-geothermie, **n.d.**
[40] M. N. K. Kuber, B. N. Chaudhari, *Resincap Journal of Science & Engineering* **2017**, *1*, 7.
[41] A. Bosio, S. Pasini, N. Romeo, *Coatings* **2020**, *10*, 344.
[42] “US2402662A - Light-sensitive electric device - Google Patents,” can be found under https://patents.google.com/patent/US2402662/en, **n.d.**
[43] R. L. Easton, M. J. Votaw, *Review of Scientific Instruments* **1959**, *30*, 70–75.
[44] “Photovoltaic Cell – Definition and How It Works | Planète Énergies,” can be found under https://www.planete-energies.com/en/medias/close/how-does-photovoltaic-cell-work, **n.d.**
[45] M. Green, E. Dunlop, J. Hohl-Ebinger, M. Yoshita, N. Kopidakis, X. Hao, *Prog Photovolt Res Appl* **2021**, *29*, 3–15.
[46] J. Jeong, M. Kim, J. Seo, H. Lu, P. Ahlawat, A. Mishra, Y. Yang, M. A. Hope, F. T. Eickemeyer, M. Kim, Y. J. Yoon, I. W. Choi, B. P. Darwich, S. J. Choi, Y. Jo, J. H. Lee, B. Walker, S. M. Zakeeruddin, L. Emsley, U. Rothlisberger, A. Hagfeldt, D. S. Kim, M. Grätzel, J. Y. Kim, *Nature* **2021**, *592*, 381–385.
[47] M. Grätzel, *Nature Mater* **2014**, *13*, 838–842.
[48] M. Saliba, J.-P. Correa-Baena, M. Grätzel, A. Hagfeldt, A. Abate, *Angew. Chem. Int. Ed.* **2018**, *57*, 2554–2569.
[49] M. Benghanem, A. Almohammedi, in *A Practical Guide for Advanced Methods in Solar Photovoltaic Systems* (Eds.: A. Mellit, M. Benghanem), Springer International Publishing, Cham, **2020**, pp. 81–106.
[50] E. Kabir, P. Kumar, S. Kumar, A. A. Adelodun, K.-H. Kim, *Renewable and Sustainable Energy Reviews* **2018**, *82*, 894–900.
[51] “Paris Agreement - Wikisource, the free online library,” can be found under https://en.wikisource.org/wiki/Paris_Agreement, **n.d.**
[52] “Global energy transformation: A roadmap to 2050 (2019 edition),” can be found under https://www.irena.org/publications/2019/Apr/Global-energy-transformation-A-roadmap-to-2050-2019Edition, **n.d.**
[53] “Transforming our world: the 2030 Agenda for Sustainable Development | Department of Economic and Social Affairs,” can be found under https://sdgs.un.org/2030agenda, **n.d.**
[54] C. W. Tang, S. A. VanSlyke, *Appl. Phys. Lett.* **1987**, *51*, 913–915.

[55] A. Kumar, G. Richhariya, A. Sharma, in *Energy Sustainability Through Green Energy* (Eds.: A. Sharma, S.K. Kar), Springer India, New Delhi, **2015**, pp. 3–25.
[56] C. Wang, H. Dong, L. Jiang, W. Hu, *Chem. Soc. Rev.* **2018**, *47*, 422–500.
[57] M. Riede, B. Lüssem, K. Leo, A. Z. M. S. Rahman, in *Reference Module in Materials Science and Materials Engineering*, Elsevier, **2018**, p. B9780128035818105000.
[58] G. H. Wagnière, *Introduction to Elementary Molecular Orbital Theory and to Semiempirical Methods*, Springer Berlin Heidelberg, Berlin, Heidelberg, **1976**.
[59] T. Hasegawa, in *Organic Electronics Materials and Devices* (Ed.: S. Ogawa), Springer Japan, Tokyo, **2015**, pp. 1–41.
[60] J. Mei, Y. Diao, A. L. Appleton, L. Fang, Z. Bao, *J. Am. Chem. Soc.* **2013**, *135*, 6724–6746.
[61] A. L. Briseno, J. Aizenberg, Y.-Jin. Han, R. A. Penkala, H. Moon, A. J. Lovinger, C. Kloc, Z. Bao, *J. Am. Chem. Soc.* **2005**, *127*, 12164–12165.
[62] Y. Takeyama, S. Ono, Y. Matsumoto, *Appl. Phys. Lett.* **2012**, *101*, 083303.
[63] M. Watanabe, Y. J. Chang, S.-W. Liu, T.-H. Chao, K. Goto, Md. M. Islam, C.-H. Yuan, Y.-T. Tao, T. Shinmyozu, T. J. Chow, *Nature Chem* **2012**, *4*, 574–578.
[64] S. Verlaak, S. Steudel, P. Heremans, D. Janssen, M. S. Deleuze, *Phys. Rev. B* **2003**, *68*, 195409.
[65] T. Okamoto, K. Kudoh, A. Wakamiya, S. Yamaguchi, *Org. Lett.* **2005**, *7*, 5301–5304.
[66] T. V. Pho, J. D. Yuen, J. A. Kurzman, B. G. Smith, M. Miao, W. T. Walker, R. Seshadri, F. Wudl, *J. Am. Chem. Soc.* **2012**, *134*, 18185–18188.
[67] F. Garnier, R. Hajlaoui, A. El Kassmi, G. Horowitz, L. Laigre, W. Porzio, M. Armanini, F. Provasoli, *Chem. Mater.* **1998**, *10*, 3334–3339.
[68] Y. Kunugi, K. Takimiya, K. Yamane, K. Yamashita, Y. Aso, T. Otsubo, *Chem. Mater.* **2003**, *15*, 6–7.
[69] K. Takimiya, Y. Kunugi, Y. Konda, N. Niihara, T. Otsubo, *J. Am. Chem. Soc.* **2004**, *126*, 5084–5085.
[70] T. Qi, Y. Guo, Y. Liu, H. Xi, H. Zhang, X. Gao, Y. Liu, K. Lu, C. Du, G. Yu, D. Zhu, *Chem. Commun.* **2008**, 6227.
[71] J. H. Gao, R. J. Li, L. Q. Li, Q. Meng, H. Jiang, H. X. Li, W. P. Hu, *Adv. Mater.* **2007**, *19*, 3008–3011.
[72] R. Li, H. Dong, X. Zhan, Y. He, H. Li, W. Hu, *J. Mater. Chem.* **2010**, *20*, 6014.
[73] H. Zhao, L. Jiang, H. Dong, H. Li, W. Hu, B. S. Ong, *ChemPhysChem* **2009**, *10*, 2345–2348.
[74] Z. Liang, Q. Tang, R. Mao, D. Liu, J. Xu, Q. Miao, *Adv. Mater.* **2011**, *23*, 5514–5518.
[75] C. R. Newman, C. D. Frisbie, D. A. da Silva Filho, J.-L. Brédas, P. C. Ewbank, K. R. Mann, *Chem. Mater.* **2004**, *16*, 4436–4451.
[76] Y. Sakamoto, T. Suzuki, M. Kobayashi, Y. Gao, Y. Fukai, Y. Inoue, F. Sato, S. Tokito, *J. Am. Chem. Soc.* **2004**, *126*, 8138–8140.
[77] M. C. R. Delgado, K. R. Pigg, D. A. da Silva Filho, N. E. Gruhn, Y. Sakamoto, T. Suzuki, R. M. Osuna, J. Casado, V. Hernández, J. T. L. Navarrete, N. G. Martinelli, J. Cornil, R. S. Sánchez-Carrera, V. Coropceanu, J.-L. Brédas, *J. Am. Chem. Soc.* **2009**, *131*, 1502–1512.
[78] N. Leclerc, P. Chávez, O. Ibraikulov, T. Heiser, P. Lévêque, *Polymers* **2016**, *8*, 11.
[79] E. Tatsi, M. Spanos, A. Katsouras, B. M. Squeo, O. A. Ibraikulov, N. Zimmermann, T. Heiser, P. Lévêque, V. G. Gregoriou, A. Avgeropoulos, N. Leclerc, C. L. Chochos, *Macromol. Chem. Phys.* **2019**, *220*, 1800418.

[80] H. Sirringhaus, T. Sakanoue, J.-F. Chang, *Phys. Status Solidi B* **2012**, *249*, 1655–1676.
[81] H. Moon, R. Zeis, E.-J. Borkent, C. Besnard, A. J. Lovinger, T. Siegrist, C. Kloc, Z. Bao, *J. Am. Chem. Soc.* **2004**, *126*, 15322–15323.
[82] X. Chi, D. Li, H. Zhang, Y. Chen, V. Garcia, C. Garcia, T. Siegrist, *Organic Electronics* **2008**, *9*, 234–240.
[83] M. L. Tang, Z. Bao, *Chem. Mater.* **2011**, *23*, 446–455.
[84] H. Usta, A. Facchetti, T. J. Marks, *Acc. Chem. Res.* **2011**, *44*, 501–510.
[85] A. A. Virkar, S. Mannsfeld, Z. Bao, N. Stingelin, *Adv. Mater.* **2010**, *22*, 3857–3875.
[86] J. E. Anthony, *Chem. Rev.* **2006**, *106*, 5028–5048.
[87] J. E. Anthony, J. S. Brooks, D. L. Eaton, S. R. Parkin, *J. Am. Chem. Soc.* **2001**, *123*, 9482–9483.
[88] J. E. Anthony, D. L. Eaton, S. R. Parkin, *Org. Lett.* **2002**, *4*, 15–18.
[89] M. J. Kang, T. Yamamoto, S. Shinamura, E. Miyazaki, K. Takimiya, *Chem. Sci.* **2010**, *1*, 179.
[90] Q. Yuan, S. C. B. Mannsfeld, M. L. Tang, M. Roberts, M. F. Toney, D. M. DeLongchamp, Z. Bao, *Chem. Mater.* **2008**, *20*, 2763–2772.
[91] J. Mei, K. R. Graham, R. Stalder, S. P. Tiwari, H. Cheun, J. Shim, M. Yoshio, C. Nuckolls, B. Kippelen, R. K. Castellano, J. R. Reynolds, *Chem. Mater.* **2011**, *23*, 2285–2288.
[92] A. R. Murphy, J. M. J. Fréchet, P. Chang, J. Lee, V. Subramanian, *J. Am. Chem. Soc.* **2004**, *126*, 1596–1597.
[93] J. Locklin, D. Li, S. C. B. Mannsfeld, E.-J. Borkent, H. Meng, R. Advincula, Z. Bao, *Chem. Mater.* **2005**, *17*, 3366–3374.
[94] Y. Cui, H. Yao, J. Zhang, K. Xian, T. Zhang, L. Hong, Y. Wang, Y. Xu, K. Ma, C. An, C. He, Z. Wei, F. Gao, J. Hou, *Adv. Mater.* **2020**, *32*, 1908205.
[95] S. Wang, Y. Tao, S. Li, X. Xia, Z. Chen, M. Shi, L. Zuo, H. Zhu, X. Lu, H. Chen, *Macromolecules* **2021**, *54*, 7862–7869.
[96] "Organic Photovoltaic (OPV) Cells | How Organic Solar Cells Work | Ossila," can be found under https://www.ossila.com/pages/organic-photovoltaics-introduction, **n.d.**
[97] S. M. Menke, N. A. Ran, G. C. Bazan, R. H. Friend, *Joule* **2018**, *2*, 25–35.
[98] C. W. Tang, *Appl. Phys. Lett.* **1986**, *48*, 183–185.
[99] G. Dennler, M. C. Scharber, C. J. Brabec, *Adv. Mater.* **2009**, *21*, 1323–1338.
[100] J. J. M. Halls, C. A. Walsh, N. C. Greenham, E. A. Marseglia, R. H. Friend, S. C. Moratti, A. B. Holmes, *Nature* **1995**, *376*, 498–500.
[101] S. E. Shaheen, C. J. Brabec, N. S. Sariciftci, F. Padinger, T. Fromherz, J. C. Hummelen, *Appl. Phys. Lett.* **2001**, *78*, 841–843.
[102] Y. Huang, E. J. Kramer, A. J. Heeger, G. C. Bazan, *Chem. Rev.* **2014**, *114*, 7006–7043.
[103] S. Holliday, Y. Li, C. K. Luscombe, *Progress in Polymer Science* **2017**, *70*, 34–51.
[104] J. Rivnay, L. H. Jimison, J. E. Northrup, M. F. Toney, R. Noriega, S. Lu, T. J. Marks, A. Facchetti, A. Salleo, *Nature Mater* **2009**, *8*, 952–958.
[105] M. M. Ling, Z. Bao, *Chem. Mater.* **2004**, *16*, 4824–4840.
[106] D. A. da Silva Filho, E.-G. Kim, J.-L. Brédas, *Adv. Mater.* **2005**, *17*, 1072–1076.
[107] C. A. Hunter, J. K. M. Sanders, *J. Am. Chem. Soc.* **1990**, *112*, 5525–5534.
[108] H.-L. Cheng, Y.-S. Mai, W.-Y. Chou, L.-R. Chang, X.-W. Liang, *Adv. Funct. Mater.* **2007**, *17*, 3639–3649.
[109] G.-C. Yuan, Z. Lu, Z. Xu, C. Gong, Q.-L. Song, S.-L. Zhao, F.-J. Zhang, N. Xu, Y. Gan, H.-B. Yang, C. M. Li, *Organic Electronics* **2009**, *10*, 1388–1395.

[110] A. Virkar, S. Mannsfeld, J. H. Oh, M. F. Toney, Y. H. Tan, G. Liu, J. C. Scott, R. Miller, Z. Bao, *Adv. Funct. Mater.* **2009**, *19*, 1962–1970.
[111] H.-L. Cheng, J.-W. Lin, *Crystal Growth & Design* **2010**, *10*, 4501–4508.
[112] V. Podzorov, E. Menard, A. Borissov, V. Kiryukhin, J. A. Rogers, M. E. Gershenson, *Phys. Rev. Lett.* **2004**, *93*, 086602.
[113] S. Wo, R. L. Headrick, J. E. Anthony, *Journal of Applied Physics* **2012**, *111*, 073716.
[114] H. Li, B. C.-K. Tee, J. J. Cha, Y. Cui, J. W. Chung, S. Y. Lee, Z. Bao, *J. Am. Chem. Soc.* **2012**, *134*, 2760–2765.
[115] A. Köhler, H. Bässler, *Electronic Processes in Organic Semiconductors: An Introduction*, Wiley-VCH Verlag GmbH & Co. KGaA, Weinheim, Germany, **2015**.
[116] J.-M. Lehn, *Angew. Chem. Int. Ed. Engl.* **1988**, *27*, 89–112.
[117] G. M. Whitesides, *Science* **2002**, *295*, 2418–2421.
[118] D. B. Amabilino, D. K. Smith, J. W. Steed, *Chem. Soc. Rev.* **2017**, *46*, 2404–2420.
[119] T. Aida, E. W. Meijer, S. I. Stupp, *Science* **2012**, *335*, 813–817.
[120] R. R. Søndergaard, M. Hösel, F. C. Krebs, *J. Polym. Sci. B Polym. Phys.* **2013**, *51*, 16–34.
[121] G. Luo, X. Ren, S. Zhang, H. Wu, W. C. H. Choy, Z. He, Y. Cao, *Small* **2016**, *12*, 1547–1571.
[122] S. Günes, H. Neugebauer, N. S. Sariciftci, *Chem. Rev.* **2007**, *107*, 1324–1338.
[123] O. Ostroverkhova, *Chemical Reviews* **2016**, *116*, 13279–13412.
[124] P. M. Beaujuge, J. R. Reynolds, *Chem. Rev.* **2010**, *110*, 268–320.
[125] D. T. McQuade, A. E. Pullen, T. M. Swager, *Chem. Rev.* **2000**, *100*, 2537–2574.
[126] P. Lin, F. Yan, *Adv. Mater.* **2012**, *24*, 34–51.
[127] M. D. McGehee, A. J. Heeger, *Advanced Materials* **2000**, *12*, 1655–1668.
[128] J. R. Reynolds, B. C. Thompson, T. A. Skotheim, *Conjugated Polymers: Perspective, Theory, and New Materials*, CRC Press, **2019**.
[129] R. M. Pankow, B. C. Thompson, *Polymer* **2020**, *207*, 122874.
[130] P. Schilinsky, C. Waldauf, C. J. Brabec, *Appl. Phys. Lett.* **2002**, *81*, 3885–3887.
[131] M. T. Dang, L. Hirsch, G. Wantz, *Adv. Mater.* **2011**, *23*, 3597–3602.
[132] C. Li, J. Zhou, J. Song, J. Xu, H. Zhang, X. Zhang, J. Guo, L. Zhu, D. Wei, G. Han, J. Min, Y. Zhang, Z. Xie, Y. Yi, H. Yan, F. Gao, F. Liu, Y. Sun, *Nat Energy* **2021**, *6*, 605–613.
[133] F. C. Krebs, Ed. , *Stability and Degradation of Organic and Polymer Solar Cells: Krebs/Stability and Degradation of Organic and Polymer Solar Cells*, John Wiley & Sons, Ltd, Chichester, UK, **2012**.
[134] B. Kan, Q. Zhang, M. Li, X. Wan, W. Ni, G. Long, Y. Wang, X. Yang, H. Feng, Y. Chen, *Journal of the American Chemical Society* **2014**, *136*, 15529–15532.
[135] B. Kan, M. Li, Q. Zhang, F. Liu, X. Wan, Y. Wang, W. Ni, G. Long, X. Yang, H. Feng, Y. Zuo, M. Zhang, F. Huang, Y. Cao, T. P. Russell, Y. Chen, *J. Am. Chem. Soc.* **2015**, *137*, 3886–3893.
[136] D. Venkateshvaran, M. Nikolka, A. Sadhanala, V. Lemaur, M. Zelazny, M. Kepa, M. Hurhangee, A. J. Kronemeijer, V. Pecunia, I. Nasrallah, I. Romanov, K. Broch, I. McCulloch, D. Emin, Y. Olivier, J. Cornil, D. Beljonne, H. Sirringhaus, *Nature* **2014**, *515*, 384–388.
[137] S. M. Tuladhar, M. Azzouzi, F. Delval, J. Yao, A. A. Y. Guilbert, T. Kirchartz, N. F. Montcada, R. Dominguez, F. Langa, E. Palomares, J. Nelson, *ACS Energy Lett.* **2016**, *1*, 302–308.

[138] T. P. Osedach, T. L. Andrew, V. Bulović, *Energy Environ. Sci.* **2013**, *6*, 711.
[139] M. Pope, H. P. Kallmann, P. Magnante, *The Journal of Chemical Physics* **1963**, *38*, 2042–2043.
[140] J. Huang, J.-H. Su, X. Li, M.-K. Lam, K.-M. Fung, H.-H. Fan, K.-W. Cheah, C. H. Chen, H. Tian, *J. Mater. Chem.* **2011**, *21*, 2957.
[141] J. Huang, J.-H. Su, H. Tian, *J. Mater. Chem.* **2012**, *22*, 10977.
[142] M. Pope, C. E. Swenberg, P. D. C. E. Swenberg, *Electronic Processes in Organic Crystals and Polymers*, Oxford University Press, **1999**.
[143] G. Horowitz, *Advanced Materials* **1998**, *10*, 365–377.
[144] C.-W. Chu, Y. Shao, V. Shrotriya, Y. Yang, *Appl. Phys. Lett.* **2005**, *86*, 243506.
[145] G. Horowitz, D. Fichou, X. Peng, Z. Xu, F. Garnier, *Solid State Communications* **1989**, *72*, 381–384.
[146] J. Sakai, T. Taima, K. Saito, *Organic Electronics* **2008**, *9*, 582–590.
[147] D. Wynands, M. Levichkova, K. Leo, C. Uhrich, G. Schwartz, D. Hildebrandt, M. Pfeiffer, M. Riede, *Appl. Phys. Lett.* **2010**, *97*, 073503.
[148] H. Chen, D. Hu, Q. Yang, J. Gao, J. Fu, K. Yang, H. He, S. Chen, Z. Kan, T. Duan, C. Yang, J. Ouyang, Z. Xiao, K. Sun, S. Lu, *Joule* **2019**, *3*, 3034–3047.
[149] H. Tang, H. Chen, C. Yan, J. Huang, P. W. K. Fong, J. Lv, D. Hu, R. Singh, M. Kumar, Z. Xiao, Z. Kan, S. Lu, G. Li, *Adv. Energy Mater.* **2020**, *10*, 2001076.
[150] S. Engmann, F. A. Bokel, A. A. Herzing, H. W. Ro, C. Girotto, B. Caputo, C. V. Hoven, E. Schaible, A. Hexemer, D. M. DeLongchamp, L. J. Richter, *J. Mater. Chem. A* **2015**, *3*, 8764–8771.
[151] X. Hao, S. Wang, T. Sakurai, S. Masuda, K. Akimoto, *ACS Appl. Mater. Interfaces* **2015**, *7*, 18379–18386.
[152] F. J. Lim, A. Krishnamoorthy, G. W. Ho, *Solar Energy Materials and Solar Cells* **2016**, *150*, 19–31.
[153] P. Cheng, H. Wang, Y. Zhu, R. Zheng, T. Li, C. Chen, T. Huang, Y. Zhao, R. Wang, D. Meng, Y. Li, C. Zhu, K. Wei, X. Zhan, Y. Yang, *Adv. Mater.* **2020**, *32*, 2003891.
[154] M. Jørgensen, K. Norrman, S. A. Gevorgyan, T. Tromholt, B. Andreasen, F. C. Krebs, *Adv. Mater.* **2012**, *24*, 580–612.
[155] C. H. Peters, I. T. Sachs-Quintana, W. R. Mateker, T. Heumueller, J. Rivnay, R. Noriega, Z. M. Beiley, E. T. Hoke, A. Salleo, M. D. McGehee, *Adv. Mater.* **2012**, *24*, 663–668.
[156] J. Kong, S. Song, M. Yoo, G. Y. Lee, O. Kwon, J. K. Park, H. Back, G. Kim, S. H. Lee, H. Suh, K. Lee, *Nat Commun* **2014**, *5*, 5688.
[157] A. Sharenko, M. Kuik, M. F. Toney, T.-Q. Nguyen, *Adv. Funct. Mater.* **2014**, *24*, 3543–3550.
[158] Y. Sun, G. C. Welch, W. L. Leong, C. J. Takacs, G. C. Bazan, A. J. Heeger, *Nature Mater* **2012**, *11*, 44–48.
[159] B. McDearmon, Z. A. Page, M. L. Chabinyc, C. J. Hawker, *J. Mater. Chem. C* **2018**, *6*, 3564–3572.
[160] J. Roncali, P. Leriche, P. Blanchard, *Advanced Materials* **2014**, *26*, 3821–3838.
[161] L. Brunsveld, B. J. B. Folmer, E. W. Meijer, R. P. Sijbesma, *Chemical Reviews* **2001**, *101*, 4071–4098.
[162] Y. Yamamoto, *Science and Technology of Advanced Materials* **2012**, *13*, 033001.
[163] M. Hasegawa, M. Iyoda, *Chem. Soc. Rev.* **2010**, *39*, 2420.

[164] E. Moulin, F. Niess, M. Maaloum, E. Buhler, I. Nyrkova, N. Giuseppone, *Angewandte Chemie International Edition* **2010**, *49*, 6974–6978.
[165] V. Faramarzi, F. Niess, E. Moulin, M. Maaloum, J.-F. Dayen, J.-B. Beaufrand, S. Zanettini, B. Doudin, N. Giuseppone, *Nature Chem* **2012**, *4*, 485–490.
[166] E. Moulin, F. Niess, G. Fuks, N. Jouault, E. Buhler, N. Giuseppone, *Nanoscale* **2012**, *4*, 6748.
[167] N. Giuseppone, *Acc. Chem. Res.* **2012**, *45*, 2178–2188.
[168] I. F. Perepichka, D. F. Perepichka, *Handbook of Thiophene-Based Materials: Applications in Organic Electronics and Photonics, 2 Volume Set | Wiley*, **2009**.
[169] D. Gentili, F. Di Maria, F. Liscio, L. Ferlauto, F. Leonardi, L. Maini, M. Gazzano, S. Milita, G. Barbarella, M. Cavallini, *J. Mater. Chem.* **2012**, *22*, 20852.
[170] H. Sirringhaus, P. J. Brown, R. H. Friend, M. M. Nielsen, K. Bechgaard, B. M. W. Langeveld-Voss, A. J. H. Spiering, R. A. J. Janssen, E. W. Meijer, P. Herwig, D. M. de Leeuw, *Nature* **1999**, *401*, 685–688.
[171] I. D. Tevis, L. C. Palmer, D. J. Herman, I. P. Murray, D. A. Stone, S. I. Stupp, *J. Am. Chem. Soc.* **2011**, *133*, 16486–16494.
[172] S. Yagai, T. Seki, H. Murayama, Y. Wakikawa, T. Ikoma, Y. Kikkawa, T. Karatsu, A. Kitamura, Y. Honsho, S. Seki, *Small* **2010**, *6*, 2731–2740.
[173] L. Zang, Y. Che, J. S. Moore, *Acc. Chem. Res.* **2008**, *41*, 1596–1608.
[174] S. Yagai, M. Usui, T. Seki, H. Murayama, Y. Kikkawa, S. Uemura, T. Karatsu, A. Kitamura, A. Asano, S. Seki, *J. Am. Chem. Soc.* **2012**, *134*, 7983–7994.
[175] G. R. Desiraju, *Angew. Chem. Int. Ed.* **2011**, *50*, 52–59.
[176] N. Nandi, K. Bhattacharyya, B. Bagchi, *Chem. Rev.* **2000**, *100*, 2013–2046.
[177] G. R. Desiraju, *Acc. Chem. Res.* **2002**, *35*, 565–573.
[178] D. Hadzi, *Theoretical Treatments of Hydrogen Bonding*, John Wiley & Sons Chichester, **1997**.
[179] G. A. Jeffrey, W. Saenger, *Hydrogen Bonding in Biological Structures*, Springer Berlin Heidelberg, Berlin, Heidelberg, **1991**.
[180] C.-C. Chu, D. M. Bassani, *Photochem. Photobiol. Sci.* **2008**, *7*, 521.
[181] N. D. McClenaghan, Z. Grote, K. Darriet, M. Zimine, R. M. Williams, L. De Cola, D. M. Bassani, *Org. Lett.* **2005**, *7*, 807–810.
[182] C.-H. Huang, N. D. McClenaghan, A. Kuhn, J. W. Hofstraat, D. M. Bassani, *Org. Lett.* **2005**, *7*, 3409–3412.
[183] E. H. A. Beckers, P. A. van Hal, A. P. H. J. Schenning, A. El-ghayoury, E. Peeters, M. T. Rispens, J. C. Hummelen, E. W. Meijer, R. A. J. Janssen, *J. Mater. Chem.* **2002**, *12*, 2054–2060.
[184] K. W. Cheng, C. S. C. Mak, W. K. Chan, A. M. Ching Ng, A. B. Djurišić, *J. Polym. Sci. A Polym. Chem.* **2008**, *46*, 1305–1317.
[185] T.-C. Liang, I.-H. Chiang, P.-J. Yang, D. Kekuda, C.-W. Chu, H.-C. Lin, *J. Polym. Sci. A Polym. Chem.* **2009**, *47*, 5998–6013.
[186] K.-M. Park, L. Lindoy, *From Molecules to Nanomaterials* **n.d.**
[187] M. Irimia-Vladu, Y. Kanbur, F. Camaioni, M. E. Coppola, C. Yumusak, C. V. Irimia, A. Vlad, A. Operamolla, G. M. Farinola, G. P. Suranna, N. González-Benitez, M. C. Molina, L. F. Bautista, H. Langhals, B. Stadlober, E. D. Głowacki, N. S. Sariciftci, *Chem. Mater.* **2019**, *31*, 6315–6346.
[188] Z. Xiao, K. Sun, J. Subbiah, S. Ji, D. J. Jones, W. W. H. Wong, *Sci Rep* **2015**, *4*, 5701.

[189] K.-H. Kim, H. Yu, H. Kang, D. J. Kang, C.-H. Cho, H.-H. Cho, J. H. Oh, B. J. Kim, *Journal of Materials Chemistry A* **2013**, *1*, 14538.
[190] R. J. Kumar, J. Subbiah, A. B. Holmes, *Beilstein Journal of Organic Chemistry* **2013**, *9*, 1102–1110.
[191] T. Aytun, L. Barreda, A. Ruiz-Carretero, J. A. Lehrman, S. I. Stupp, *Chemistry of Materials* **2015**, *27*, 1201–1209.
[192] A. D. Hendsbee, J.-P. Sun, L. R. Rutledge, I. G. Hill, G. C. Welch, *J. Mater. Chem. A* **2014**, *2*, 4198–4207.
[193] E. D. Głowacki, H. Coskun, M. A. Blood-Forsythe, U. Monkowius, L. Leonat, M. Grzybowski, D. Gryko, M. S. White, A. Aspuru-Guzik, N. S. Sariciftci, *Organic Electronics* **2014**, *15*, 3521–3528.
[194] D. G. Farnum, G. Mehta, G. G. I. Moore, F. P. Siegal, *Tetrahedron Letters* **1974**, *15*, 2549–2552.
[195] W. Li, K. H. Hendriks, M. M. Wienk, R. A. J. Janssen, *Acc. Chem. Res.* **2016**, *49*, 78–85.
[196] J. C. Bijleveld, A. P. Zoombelt, S. G. J. Mathijssen, M. M. Wienk, M. Turbiez, D. M. de Leeuw, R. A. J. Janssen, *Journal of the American Chemical Society* **2009**, *131*, 16616–16617.
[197] M. Stolte, S.-L. Suraru, P. Diemer, T. He, C. Burschka, U. Zschieschang, H. Klauk, F. Würthner, *Advanced Functional Materials* **2016**, *26*, 7415–7422.
[198] X. Yang, L. Zheng, L. Xie, Z. Liu, Y. Li, R. Ning, G. Zhang, X. Gong, B. Gao, C. Liu, Y. Cui, G. Sun, G. Zhang, *Sensors and Actuators B: Chemical* **2015**, *207*, 9–24.
[199] X. Yang, L. Xie, R. Ning, X. Gong, Z. Liu, Y. Li, L. Zheng, G. Zhang, B. Gao, Y. Cui, G. Sun, G. Zhang, *Sensors and Actuators B: Chemical* **2015**, *210*, 784–794.
[200] C. Fu, P. J. Beldon, D. F. Perepichka, *Chem. Mater.* **2017**, *29*, 2979–2987.
[201] C. J. H. Morton, R. Gilmour, D. M. Smith, P. Lightfoot, A. M. Z. Slawin, E. J. MacLean, *Tetrahedron* **2002**, *58*, 5547–5565.
[202] D. Feng, G. Barton, C. N. Scott, *Organic Letters* **2019**, *21*, 1973–1978.
[203] A. C. Rochat, L. Cassar, A. Iqbal, *Preparation of Pyrrolo[3,4-c]Pyrroles*, **1986**, US4579949A.
[204] L. Cassar, A. Iqbal, A. C. Rochat, *Preparation of 1,4-Diketopyrrolo-[3,4-c]Pyrroles*, **1986**, US4613669A.
[205] E. B. Faulkner, R. J. Schwartz, Eds. , *High Performance Pigments*, Wiley-VCH Verlag GmbH & Co. KGaA, Weinheim, Germany, **2009**.
[206] Number of patents based on Google Patents database (https://www.google.com/patents), **2019**.
[207] A. Tang, C. Zhan, J. Yao, E. Zhou, *Advanced Materials* **2017**, *29*, 1600013.
[208] B. Lim, H. Sun, J. Lee, Y.-Y. Noh, *Scientific Reports* **2017**, *7*, 164.
[209] C. B. Nielsen, M. Turbiez, I. McCulloch, *Advanced Materials* **2013**, *25*, 1859–1880.
[210] M. Sassi, N. Buccheri, M. Rooney, C. Botta, F. Bruni, U. Giovanella, S. Brovelli, L. Beverina, *Scientific Reports* **2016**, *6*, 34096.
[211] D. Chandran, K.-S. Lee, *Macromolecular Research* **2013**, *21*, 272–283.
[212] M. Grzybowski, D. T. Gryko, *Advanced Optical Materials* **2015**, *3*, 280–320.
[213] J. Z. Zabicky, *The Chemistry of Amides*, Interscience Publishers, **1970**.
[214] F. Pop, J. Humphreys, J. Schwarz, L. Brown, A. van den Berg, D. B. Amabilino, *New Journal of Chemistry* **2019**, DOI 10.1039/C9NJ01074B.
[215] S. A. Shevelev, *Russ. Chem. Rev.* **1970**, *39*, 844–858.

[216] M. Grzybowski, D. T. Gryko, *Advanced Optical Materials* **2015**, *3*, 280–320.
[217] S. Stas, S. Sergeyev, Y. Geerts, *Tetrahedron* **2010**, *66*, 1837–1845.
[218] Š. Frebort, Z. Eliáš, A. Lyčka, S. Luňák, J. Vyňuchal, L. Kubáč, R. Hrdina, L. Burgert, *Tetrahedron Letters* **2011**, *52*, 5769–5773.
[219] S. Stas, J.-Y. Balandier, V. Lemaur, O. Fenwick, G. Tregnago, F. Quist, F. Cacialli, J. Cornil, Y. H. Geerts, *Dyes and Pigments* **2013**, *97*, 198–208.
[220] M. Jost, A. Iqbal, A. C. Rochat, *Pigment Compositions*, **1990**, US4914211A.
[221] C. H. Woo, P. M. Beaujuge, T. W. Holcombe, O. P. Lee, J. M. J. Fréchet, *J. Am. Chem. Soc.* **2010**, *132*, 15547–15549.
[222] A. B. Tamayo, M. Tantiwiwat, B. Walker, T.-Q. Nguyen, *The Journal of Physical Chemistry C* **2008**, *112*, 15543–15552.
[223] L. Dou, W.-H. Chang, J. Gao, C.-C. Chen, J. You, Y. Yang, *Advanced Materials* **2013**, *25*, 825–831.
[224] G. P. McGlacken, L. M. Bateman, *Chemical Society Reviews* **2009**, *38*, 2447.
[225] W. Han, A. Ofial, *Synlett* **2011**, *2011*, 1951–1955.
[226] Y. Li, P. Sonar, L. Murphy, W. Hong, *Energy & Environmental Science* **2013**, *6*, 1684-.
[227] S. Qu, H. Tian, *Chemical Communications* **2012**, *48*, 3039.
[228] B. P. Karsten, J. C. Bijleveld, R. A. J. Janssen, *Macromolecular Rapid Communications* **2010**, *31*, 1554–1559.
[229] W. Hong, B. Sun, H. Aziz, W.-T. Park, Y.-Y. Noh, Y. Li, *Chemical Communications* **2012**, *48*, 8413.
[230] J. Mizuguchi, *J. Phys. Chem. A* **2000**, *104*, 1817–1821.
[231] Z. Hao, A. Iqbal, *Chem. Soc. Rev.* **1997**, *26*, 203–213.
[232] G. R. Desiraju, *Journal of Molecular Structure* **2003**, *656*, 5–15.
[233] M. Irimia-Vladu, E. D. Głowacki, P. A. Troshin, G. Schwabegger, L. Leonat, D. K. Susarova, O. Krystal, M. Ullah, Y. Kanbur, M. A. Bodea, V. F. Razumov, H. Sitter, S. Bauer, N. S. Sariciftci, *Advanced Materials* **2012**, *24*, 375–380.
[234] E. D. G\lowacki, G. Voss, L. Leonat, M. Irimia-Vladu, S. Bauer, N. S. Sariciftci, *Israel Journal of Chemistry* **2012**, *52*, 540–551.
[235] D. Basak, D. S. Pal, T. Sakurai, S. Yoneda, S. Seki, S. Ghosh, *Physical Chemistry Chemical Physics* **2017**, *19*, 31024–31029.
[236] E. D. Głowacki, M. Irimia-Vladu, M. Kaltenbrunner, J. Gsiorowski, M. S. White, U. Monkowius, G. Romanazzi, G. P. Suranna, P. Mastrorilli, T. Sekitani, S. Bauer, T. Someya, L. Torsi, N. S. Sariciftci, *Advanced Materials* **2013**, *25*, 1563–1569.
[237] H. Yanagisawa, J. Mizuguchi, S. Aramaki, Y. Sakai, *Japanese Journal of Applied Physics* **2008**, *47*, 4728.
[238] E. D. Głowacki, H. Coskun, M. A. Blood-Forsythe, U. Monkowius, L. Leonat, M. Grzybowski, D. Gryko, M. S. White, A. Aspuru-Guzik, N. S. Sariciftci, *Organic Electronics* **2014**, *15*, 3521–3528.
[239] A. Facchetti, *Chem. Mater.* **2011**, *23*, 733–758.
[240] J. Mizuguchi, G. Wooden, *Berichte der Bunsengesellschaft für physikalische Chemie* **1991**, *95*, 1264–1274.
[241] J. Mizuguchi, G. Rihs, *Berichte der Bunsengesellschaft für physikalische Chemie* **1992**, *96*, 597–606.
[242] J. Mizuguchi, A. Grubenmann, G. Wooden, G. Rihs, *Acta Crystallographica Section B: Structural Science* **1992**, *48*, 696–700.

[243] J. Mizuguchi, A. Grubenmann, G. Rihs, *Acta Crystallographica Section B: Structural Science* **1993**, *49*, 1056–1060.
[244] J. Mizuguchi, G. Giller, E. Baeriswyl, *Journal of Applied Physics* **1994**, *75*, 514–518.
[245] J. Mizuguchi, A. Grubenmann, G. Wooden, G. Rihs, *Acta Cryst B* **1992**, *48*, 696–700.
[246] J. Mizuguchi, *Journal of Applied Physics* **1989**, *66*, 3111–3113.
[247] J. Mizuguchi, S. Homma, *Journal of Applied Physics* **1989**, *66*, 3104–3110.
[248] J. Mizuguchi, A. C. Rochat, G. Rihs, *Berichte der Bunsengesellschaft für physikalische Chemie* **1992**, *96*, 607–619.
[249] J. Mizuguchi, *Berichte der Bunsengesellschaft für physikalische Chemie* **1993**, *97*, 684–693.
[250] J. Mizuguchi, T. Imoda, H. Takahashi, H. Yamakami, *Dyes and Pigments* **2006**, *68*, 47–52.
[251] J. S. Zambounis, Z. Hao, A. Iqbal, *Nature* **1997**, *388*, 131.
[252] S. T. Salammal, J.-Y. Balandier, S. Kumar, E. Goormaghtigh, Y. H. Geerts, *Crystal Growth & Design* **2014**, *14*, 339–349.
[253] Y. Suna, J. Nishida, Y. Fujisaki, Y. Yamashita, *Organic Letters* **2012**, *14*, 3356–3359.
[254] SunaYuki, NishidaJun-ichi, FujisakiYoshihide, YamashitaYoshiro, *Chemistry Letters* **2011**, DOI 10.1246/cl.2011.822.
[255] E. Daniel Głowacki, M. Irimia-Vladu, S. Bauer, N. Serdar Sariciftci, *Journal of Materials Chemistry B* **2013**, *1*, 3742–3753.
[256] K. Yang, L. Xiang, Y. F. Huang, R. S. Bhatta, J. Liu, M. Tsige, C. L. Wang, S. Cheng, Y. Zhu, *Polymer* **2019**, 238–245.
[257] S. Mula, T. Han, T. Heiser, P. Lévêque, N. Leclerc, A. P. Srivastava, A. Ruiz-Carretero, G. Ulrich, *Chemistry – A European Journal* **n.d.**, *0*, DOI 10.1002/chem.201900689.
[258] B. Sun, W. Hong, H. Aziz, Y. Li, *J. Mater. Chem.* **2012**, *22*, 18950–18955.
[259] Y. Li, P. Sonar, S. P. Singh, M. S. Soh, M. van Meurs, J. Tan, *J. Am. Chem. Soc.* **2011**, *133*, 2198–2204.
[260] J. Lee, A.-R. Han, J. Hong, J. H. Seo, J. H. Oh, C. Yang, *Advanced Functional Materials* **2012**, *22*, 4128–4138.
[261] F. Bruni, M. Sassi, M. Campione, U. Giovanella, R. Ruffo, S. Luzzati, F. Meinardi, L. Beverina, S. Brovelli, *Advanced Functional Materials* **2014**, *24*, 7410–7419.
[262] J. Dhar, D. Prasad Karothu, S. Patil, *Chemical Communications* **2015**, *51*, 97–100.
[263] F. Pop, W. Lewis, D. B. Amabilino, *CrystEngComm* **2016**, *18*, 8933–8943.
[264] Y.-J. Zhang, X. Wang, Y. Zhou, C.-K. Wang, *Chemical Physics Letters* **2016**, *658*, 125–129.
[265] C. Yang, M. Zheng, Y. Li, B. Zhang, J. Li, L. Bu, W. Liu, M. Sun, H. Zhang, Y. Tao, S. Xue, W. Yang, *J. Mater. Chem. A* **2013**, *1*, 5172–5178.
[266] K. Nie, B. Dong, H. Shi, Z. Liu, B. Liang, *Sensors and Actuators B: Chemical* **2017**, *244*, 849–853.
[267] A. Ruiz-Carretero, T. Aytun, C. J. Bruns, C. J. Newcomb, W.-W. Tsai, S. I. Stupp, *Journal of Materials Chemistry A* **2013**, *1*, 11674.
[268] Z. Xiao, K. Sun, J. Subbiah, S. Ji, D. J. Jones, W. W. H. Wong, *Scientific Reports* **2014**, *4*, DOI 10.1038/srep05701.
[269] S. Ghosh, S. Cherumukkil, C. H. Suresh, A. Ajayaghosh, *Advanced Materials* **2017**, *29*, 1703783.
[270] M. Kirkus, L. Wang, S. Mothy, D. Beljonne, J. Cornil, R. A. J. Janssen, S. C. J. Meskers, *J. Phys. Chem. A* **2012**, *116*, 7927–7936.

[271] M. Más-Montoya, R. A. J. Janssen, *Advanced Functional Materials* **2017**, *27*, DOI 10.1002/adfm.201605779.
[272] W.-W. Tsai, I. D. Tevis, A. S. Tayi, H. Cui, S. I. Stupp, *The Journal of Physical Chemistry B* **2010**, *114*, 14778–14786.
[273] S. Ghosh, S. Das, A. Saeki, V. K. Praveen, S. Seki, A. Ajayaghosh, *ChemNanoMat* **2018**, *4*, 831–836.
[274] A. Mishra, P. Bäuerle, *Angewandte Chemie International Edition* **2012**, *51*, 2020–2067.
[275] S. Ghosh, R. Raveendran, A. Saeki, S. Seki, M. Namboothiry, A. Ajayaghosh, *ACS Appl. Mater. Interfaces* **2019**, *11*, 1088–1095.
[276] S. Rieth, Z. Li, C. E. Hinkle, C. X. Guzman, J. J. Lee, S. I. Nehme, A. B. Braunschweig, *The Journal of Physical Chemistry C* **2013**, *117*, 11347–11356.
[277] D. Ley, C. X. Guzman, K. H. Adolfsson, A. M. Scott, A. B. Braunschweig, *J. Am. Chem. Soc.* **2014**, *136*, 7809–7812.
[278] A. M. Levine, C. Schierl, B. S. Basel, M. Ahmed, B. A. Camargo, D. M. Guldi, A. B. Braunschweig, *The Journal of Physical Chemistry C* **2019**, *123*, 1587–1595.
[279] Y. Zhou, C. X. Guzman, L. C. Helguero-Kelley, C. Liu, S. R. Peurifoy, B. Captain, A. B. Braunschweig, *Journal of Physical Organic Chemistry* **2016**, *29*, 689–699.
[280] E. H. A. Beckers, S. C. J. Meskers, A. P. H. J. Schenning, Z. Chen, F. Würthner, P. Marsal, D. Beljonne, J. Cornil, R. A. J. Janssen, *Journal of the American Chemical Society* **2006**, *128*, 649–657.
[281] R. F. Fink, J. Seibt, V. Engel, M. Renz, M. Kaupp, S. Lochbrunner, H.-M. Zhao, J. Pfister, F. Würthner, B. Engels, *Journal of the American Chemical Society* **2008**, *130*, 12858–12859.
[282] Y. Zhou, C. X. Guzman, L. C. Helguero-Kelley, C. Liu, S. R. Peurifoy, B. Captain, A. B. Braunschweig, *Journal of Physical Organic Chemistry* **2016**, *29*, 689–699.
[283] S. Militzer, T. M. P. Tran, P. J. Mésini, A. Ruiz-Carretero, *ChemNanoMat* **2018**, *4*, 790–795.
[284] B. Song, H. Wei, Z. Wang, X. Zhang, M. Smet, W. Dehaen, *Advanced Materials* **2007**, *19*, 416–420.
[285] Y. Yang, Z. Liu, L. Chen, J. Yao, G. Lin, X. Zhang, G. Zhang, D. Zhang, *Chem. Mater.* **2019**, *31*, 1800–1807.
[286] J. Šebera, J. Burda, M. Straka, A. Ono, C. Kojima, Y. Tanaka, V. Sychrovský, *Chemistry – A European Journal* **2013**, *19*, 9884–9894.
[287] J. Yao, C. Yu, Z. Liu, H. Luo, Y. Yang, G. Zhang, D. Zhang, *Journal of the American Chemical Society* **2016**, *138*, 173–185.
[288] W. Du, D. Ohayon, C. Combe, L. Mottier, I. P. Maria, R. S. Ashraf, H. Fiumelli, S. Inal, I. McCulloch, *Chem. Mater.* **2018**, *30*, 6164–6172.
[289] A. Ruiz-Carretero, N. R. Á. Rovelo, S. Militzer, P. J. Mésini, *J. Mater. Chem. A* **2019**, *7*, 23451–23475.
[290] B. Kan, M. Li, Q. Zhang, F. Liu, X. Wan, Y. Wang, W. Ni, G. Long, X. Yang, H. Feng, Y. Zuo, M. Zhang, F. Huang, Y. Cao, T. P. Russell, Y. Chen, *Journal of the American Chemical Society* **2015**, *137*, 3886–3893.
[291] N. M. Randell, T. L. Kelly, *The Chemical Record* **2019**, *19*, 973–988.
[292] X. Wei, W. Zhang, G. Yu, *Advanced Functional Materials* **2021**, *31*, 2010979.
[293] Y. Cui, H. Yao, J. Zhang, T. Zhang, Y. Wang, L. Hong, K. Xian, B. Xu, S. Zhang, J. Peng, Z. Wei, F. Gao, J. Hou, *Nat Commun* **2019**, *10*, 1–8.

[294] J. Yuan, Y. Zhang, L. Zhou, G. Zhang, H.-L. Yip, T.-K. Lau, X. Lu, C. Zhu, H. Peng, P. A. Johnson, M. Leclerc, Y. Cao, J. Ulanski, Y. Li, Y. Zou, *Joule* **2019**, *3*, 1140–1151.
[295] A. B. Tamayo, M. Tantiwiwat, B. Walker, T. Q. Nguyen, *The Journal of Physical Chemistry C* **2008**, *112*, 15543–15552.
[296] H. Bürckstümmer, A. Weissenstein, D. Bialas, F. Würthner, *The Journal of Organic Chemistry* **2011**, *76*, 2426–2432.
[297] A. Tang, C. Zhan, J. Yao, E. Zhou, *Advanced Materials* **2017**, *29*, 1600013.
[298] N. Luo, G. Zhang, Z. Liu, *Org. Chem. Front.* **2021**, DOI 10.1039/D1QO00613D.
[299] G. S. Thool, K. Narayanaswamy, A. Venkateswararao, S. Naqvi, V. Gupta, S. Chand, V. Vivekananthan, R. R. Koner, V. Krishnan, S. P. Singh, *Langmuir* **2016**, *32*, 4346–4351.
[300] S. Militzer, N. Nishimura, N. R. Ávila-Rovelo, W. Matsuda, D. Schwaller, P. J. Mésini, S. Seki, A. Ruiz-Carretero, *Chem. Eur. J.* **2020**, chem.202001540.

EXPLORING THE AMIDE FUNCTION:

Impact of chirality and solubility

CHAPTER II

I. Introduction and main goal

As it has been shown in chapter I, supramolecular strategies have been applied in the field of organic electronics. [1–9] It was also discussed that the use of H-bonds is a topic still unexplored and without consensus on the results. In this chapter, special focus is put on H-bonded **DPP** derivatives containing amide bonds coupled to the π-conjugated core through a flexible six carbon linker. This design was chosen because our group started the systematic studies with derivatives containing semicarbazone units directly attached to the **DPP** core.[10] The semicarbazone derivatives resulted in very rigid molecules with limited solubility and with fast recombination dynamics when their photoconductivity properties were screened. Nevertheless, their self-assembly and morphological properties provided very useful information on how to continue designing other components of the H-bonded **DPP** family.

In this part of the thesis, totally different molecules were designed, where the functionalization was done on the lactam rings *vs* the thiophene rings as in the semicarbazone derivatives (Figure II. 1) and the H-bonding group was separated through a flexible linker to compare the self-assembly process. In addition, chirality was added as a parameter, so a chiral center next to the amide group (Figure II. 1) was introduced. Particularly, my task was synthesizing the (R)-enantiomer and perform the full characterization, while the (S)-enantiomer was made by a former PhD student of our group. Nevertheless, I synthesized all three derivatives to obtain enough amount of every compound to do a fair comparison for the results.

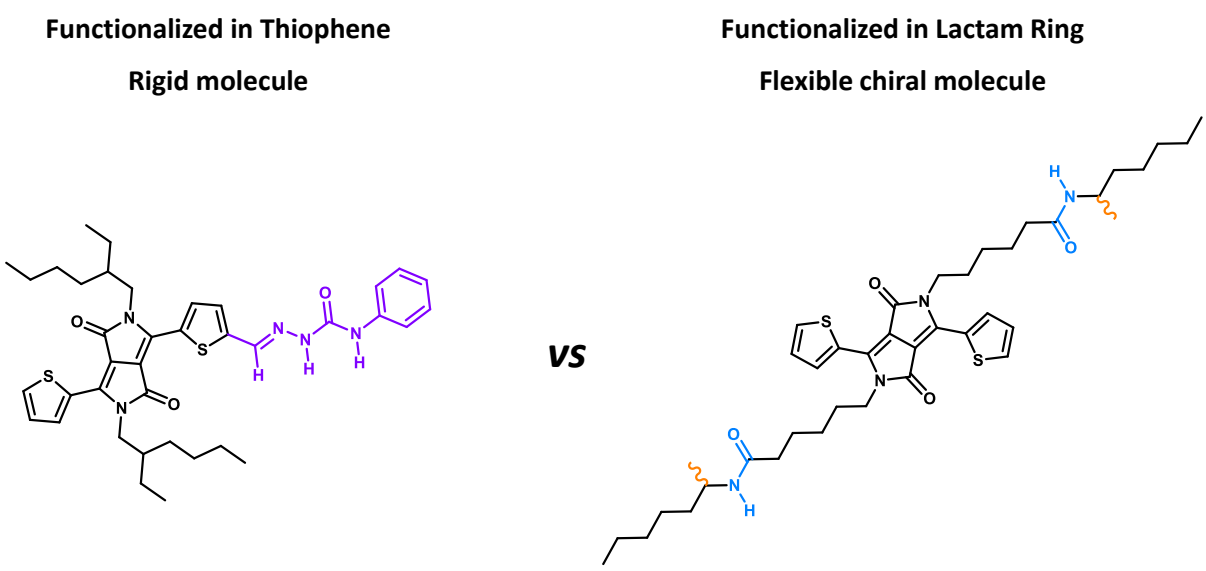

Figure II. 1 Structural comparison between the semicarbazone family and the bisamide family.

The amide group was chosen since it is one of the most explored H-bonding groups in history and found almost in all the fields of chemistry.[11] The well-known synthetic procedures to introduce them into any type of molecule, and their easy characterization by spectroscopy techniques, such as infrared spectroscopy, make them the perfect candidates to study self-assembly processes where H- and J-aggregation are involved and some of these examples are illustrated in Figure II. 2.

For instance, Stupp *et al*.[12] have shown a hairpin-shaped molecule containing a sexithiophene unit as the electroactive segment attached to a *trans*-1,2-diamidocyclohexane (**DACH**), as the self-assembly motif (Figure II. 2a). In this case, the coexistence of H- and J-aggregates results in the broadening of the wavelength spectral range of optical absorption, and in the formation of semiconducting nanowires.

Similar results were observed by Ghosh *et al*.[13] They found Davydov splitting[14] in a **DPP** system symmetrically functionalized with amide bonds (Figure II. 2b). The authors observed the presence of H- and J-type aggregates upon self-assembly conditions.[13] Dilute solutions in chloroform and toluene showed absorption spectra of the monomeric species. In contrast, under aggregation conditions, the absorption spectrum differs from the one at low concentration. In this case, new bands appear at higher and lower energies, being H- and J-type aggregates, respectively, and achieving spectral coverage in the visible region and transparency in the near infrared region.

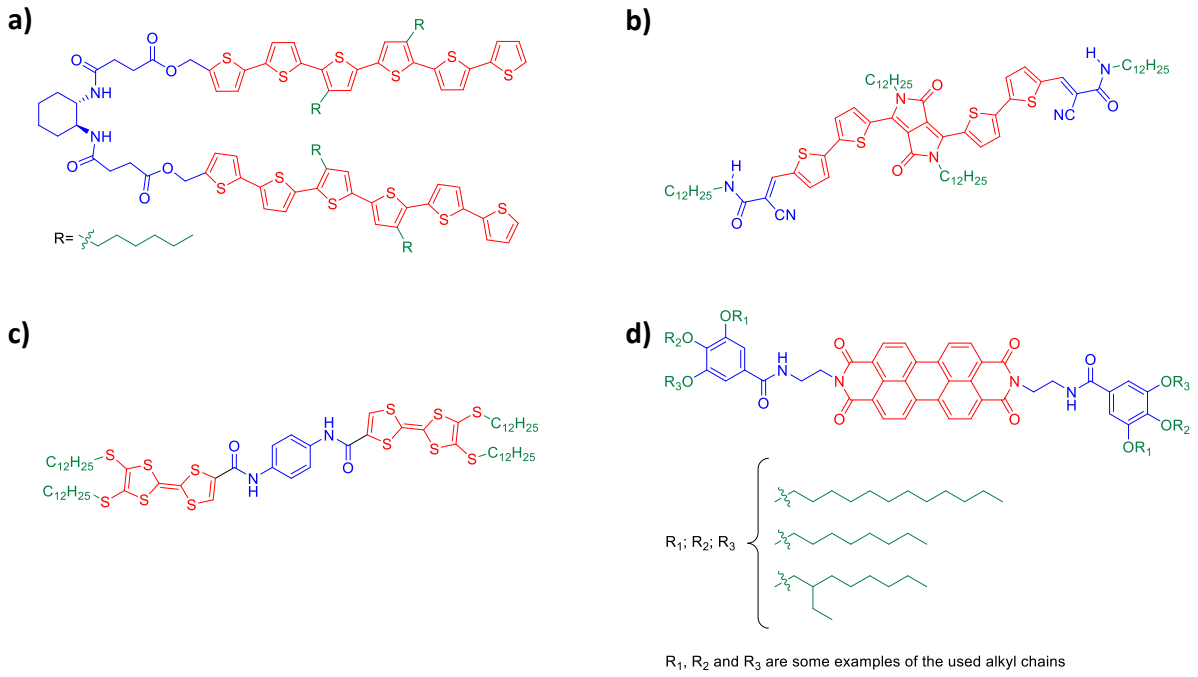

Figure II. 2 A few examples of previously explored π-conjugated systems containing amide functionalities and explored in the supramolecular field.

The field of perovskite photovoltaic devices has also benefitted from the presence of amides in materials showing J-aggregates. Kaneko *et al*.[15] have shown H-bonded tetrathiofulvalene (**TTF**) derivatives containing amide groups (Figure II. 2c) that have been used as dopant-free hole transport materials in perovskite solar cells. In this case, the H-bonded **TTF** derivatives had electrical conductivity values higher than **spiro-OMeTAD** (2,2',7,7'-Tetrakis[N,N-di(4-methoxyphenyl)amino]-9,9'-spirobifluorene, which is the most usual hole transport material.[16] J-type aggregates were found in H-bonded **TTF** thin films leading to the formation of nanofibers with enhanced mobility.

Finally, many examples with perylene bisimide (**PBI**) derivatives with pending amide groups exhibiting J-aggregates have been reported. The Würthner group has shown multiple examples of self-assembled **PBIs**[17] containing amide bonds as well as other self-assembly motifs. Back in 2008 they showed a study on how to control H- and J-type homo- and heteroaggregates in amide-containing **PBIs**. For this purpose, they synthesized several **PBI** derivatives (Figure II. 2d) with the same core and amide groups as H-bonding motifs and changed the alkyl chains.[18]

The authors found that the steric effects in the peripheral side chains dictated the self-assembly mode, going from the usually found H-type to the J-type aggregates. **PBIs** containing linear alkyl side chains, which are sterically less demanding, formed face-to-face H-type aggregates, while the **PBIs** having branched alkyl tails, formed slipped J-aggregates or did not aggregate.

As part of this study, the other parameter that was evaluated in this **DPP** family was chirality, which can impact the self-assembly properties as well, and in the case of semiconductors their optoelectronic properties.[19,20] For instance, molecular chirality plays an important role in chemistry in pharmaceutical applications[21], whereas in biology numerous chiral molecules with asymmetric arrangements of atoms exist widely in nature, such as in amino acids and sugars.[22]

As it has been discussed before, one of the most powerful methods for preparing different scales of functional materials is through self-assembly; in the same way, chiral information can also pass from single molecules to supramolecular assemblies and then to macroscopic superstructures.[23] Additionally, $\pi-\pi$ stacking interactions are frequently used as a preliminary driving force for the self-assembly of structures based on conjugated molecules.

Furthermore, a number of similarities have been observed between H-bonding and $\pi-\pi$ stacking interactions. Hence, supramolecular chirality has mainly been explored in organic semiconductors using $\pi-\pi$ stacking and H-bonding.[19,24–27]. In this sense, chirality is amplified when the molecular chirality is transferred to the supramolecular structures, making new properties emerge. Therefore, using conjugated molecules with one-handed chirality as building blocks to prepare hierarchical superstructures by mimicking the self-assembly behavior of biomolecules is a state-of-the-art strategy for designing novel functional nanomaterials.[28,29]

Palmans and Meijer reviewed chirality in supramolecular aggregates, making especial emphasis in non-covalent systems and on the factors that affect the amplification of chirality in dynamic supramolecular aggregates.[30] One very interesting example that utilizes H-bonding, $\pi-\pi$ stacking and chirality is the study of benzene-1,3,5-tricarboxamide derivatives (Figure II. 3a).[31] The aggregates formed by these derivatives demonstrated pronounced amplification of chirality and the energy for helical reversal and mismatch were on the order of magnitude of 1.2 $kJ \cdot mol^{-1}$.[32]

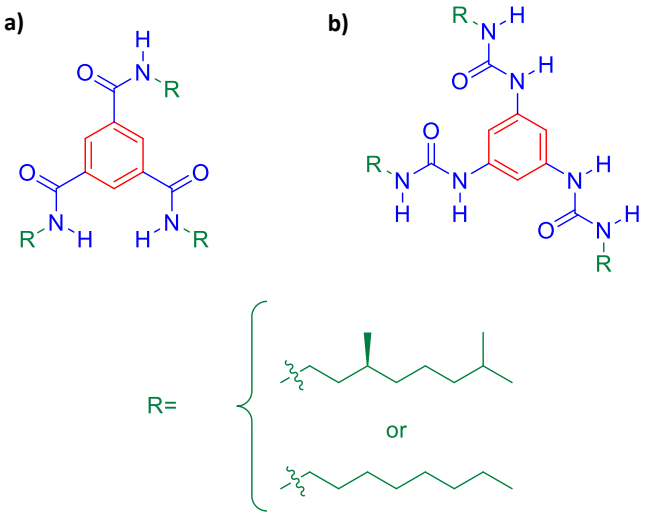

Figure II. 3 Structures of a) benzene-1,3,5-tricarboxamide derivatives and b) their urea derivatives counterparts.

Furthermore, the introduction of additional H-bonds by replacing the amide group by a urea group (Figure II. 3b) afforded compounds that showed slight circular dichroism (CD) effect in alkane solutions, which is indicative of the presence of ordered stacks. Mixing solutions of achiral urea with chiral amide illustrated the effect of a mismatch of the secondary H-bonding interactions in these systems; in particular, mixtures containing between 5-20% of chiral amide with achiral urea resulted in amplification of chirality.[33] However, when a mixture of 85% of achiral urea derivative and 15% of chiral amide was prepared, the CD effect present in the mixture disappeared over time.

Another example of supramolecular chirality is the one reported by Aida *et al*[34], where they reported an unprecedentedly high degree of chiral amplification of supramolecular helices in a system using triphenylamine (**TPA**), a propeller-shaped molecule (Figure II. 4a). This was achieved by using a strategy known as "the sergeants and soldiers experiment"[35], where few sergeants (chiral units) can control the movements of large numbers of cooperative soldiers (achiral units). In their work one sergeant controlled the handedness of 500 soldiers in supramolecular helices and they manage to demonstrate that a **TPA** derivative could switch its role from sergeant to soldier and vice versa depending on its partners.

They investigated their self-assembly behavior in cyclohexane finding that they formed supramolecular aggregates at room temperature. AFM measurements revealed that derivative **A** (Figure II. 4a) forms one-dimensional supramolecular polymers, possibly by connecting *via* intermolecular H-bonding and π–π interactions. The CD spectra of $\mathbf{C_3}$ derivatives (Figure II. 4b), showed the formation of one-handed supramolecular helices under the same conditions.

Finally they also found that one-handed helices of **A** could be obtained by mixing an unusually small fraction of $\mathbf{C_3(S)}$ with **A**, in other words, the chiral information of the side chains of $\mathbf{C_3(S)}$ was efficiently amplified into the handedness of the supramolecular helices of **A**. The study the proved that the handedness of the helices was fully controlled using a 0.2 mol% fraction of sergeants and provided valuable insights into the construction of helical structures and a novel design strategy for supramolecular chiral amplification.

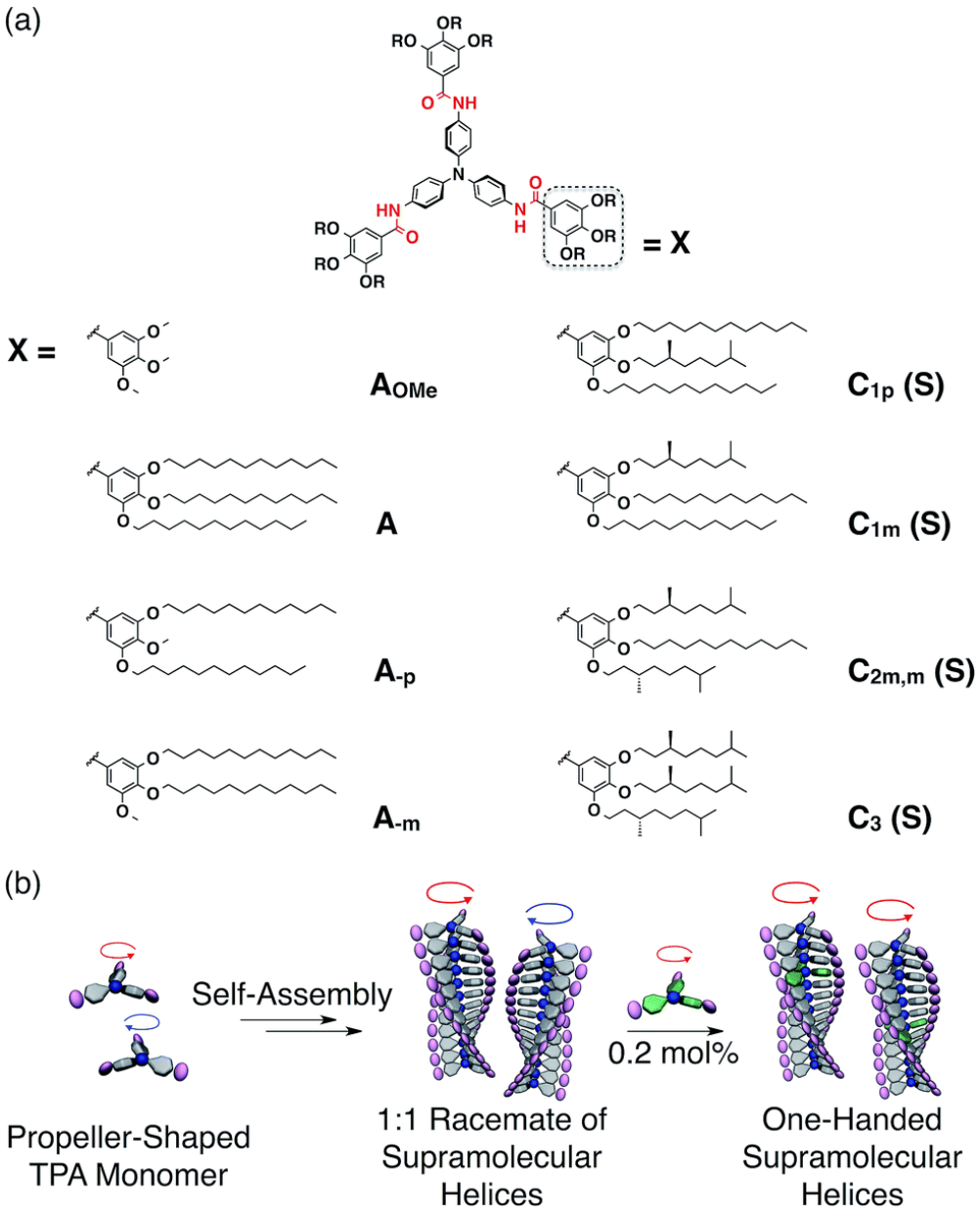

*Figure II. 4 a) Chemical structures of propeller-shaped **TPA** derivatives. (b) Schematic illustration of the self-assembly of **TPA** monomers into supramolecular helices and chiral amplification through the sergeants and soldiers experiment. The green **TPA** monomer corresponds to a sergeant.*

Chirality has been introduced in **DPP** derivatives mainly by linking them to chiral alkyl tails, usually 2-ethylhexyl[36–39], to helicene molecules,[40] or adding myrtenal derivatives.[41] For instance, when the effects of stereoisomerism of **DPP(TBFu)$_2$** derivatives (Figure II. 4) in their crystal structures and the optoelectrical properties were studied, they found that the crystal structures and FET mobilities were sensitive to stereoisomerism, whereas optical properties were not.[36] Additionally, isolated stereoisomers exhibit different FET mobilities correlated to their different crystal structures.

The crystallization of **DPP(TBFu)$_2$** derivatives was found to be dominated by the mesomere, which possessed the greatest crystallization tendency among the three. The *RR*-isomer

and *SS*-isomer which are enantiomers showed very similar crystal structures, thin-film morphologies and FET properties, while the mesomer exhibited different characteristics.

According to their single-crystal structures, the mesomer has a coplanar conjugated backbone favoring intermolecular π–π stacking and a shorter plan-to-plan distance; while the other two chiral compounds exhibited twisted conjugated backbone and therefore inferior intermolecular stacking.

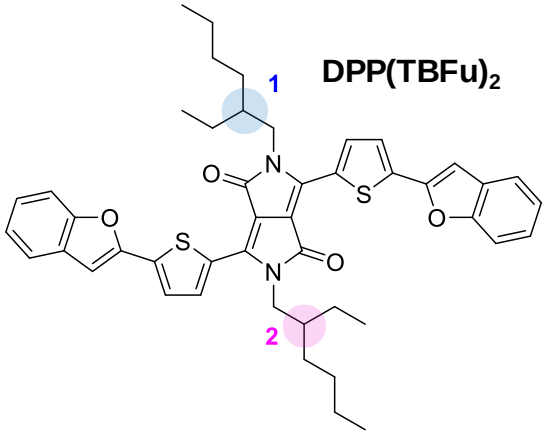

Stereoisomer	Chiral carbon	
	1	2
SS-isomer	S	S
RR-isomer	R	R
Mesomer	S (R)	R (S)

*Figure II. 5 Chemical structure of **DPP(TBFu)$_2$** with two chiral carbons highlighted, 1 and 2, and the resulting stereoisomers relating to the configurations of the two chiral carbons.*Adapted.*[36]

When **DPP** linked to helicene derivatives (Figure II. 6) were studied they found they showed intense electronic CD in the visible and near-IR region.[40] The UV-vis absorption spectra of mono, disubstututed and oligomers of these derivatives were recorded in dichloromethane solutions. The comparison with their corresponding precursors showed that the mono substituted derivative had red shifted bands with respect to both precursors (by about 20 nm relative to **DPPBr**), which clearly reflects an extension of the π-conjugation between the **DPP** dye and the helicene via the alkynyl bridge. Interestingly, going from one **DPP** substituent into two in **H6**(**DPP**)$_2$ (Figure II. 5), did not further red-shifted the absorption, which indicated lack of electronic conjugation through the whole helix. Accordingly, the high molar extinction coefficients in the visible part of the spectrum were approximately proportional to the number of **DPP** units within the molecule.

Furthermore, the association between enantiopure hexahelicene and **DPP** provided molecular and macromolecular helical π-conjugated molecules while also showing that chiral helicenes symmetrically functionalized by **DPP** units display an exciton coupling effect, which resulted in a strong synergy between the chiral helical π-conjugated core and the photophysical properties of the **DPP**.

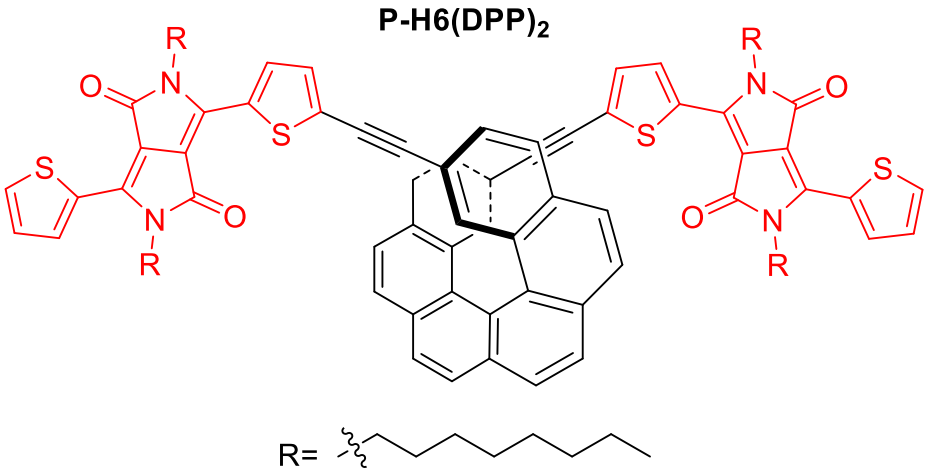

*Figure II. 6 Chemical structure of a triad **DPP**–helicene derivative.*

Lastly, for the **DPP** myrtenal derivatives (Figure II. 7) the attachment of one or two chiral units was done at the end positions (extremities) of the **DPP** core and its influence on self-assembly for was studied.[41] These derivatives showed how the chiral at-end strategy is a way to influence the organization of optically active aggregates of chromophores. In this case, chiral substitution at both extremities was necessary to create significant optical activity in solution. Additionally, the results demonstrated that CD is an extremely sensitive probe for the organization of these compounds, as very modest changes in the absorption spectra were observed, making the chiral structures useful for the understanding of related self-assembled structures in general.

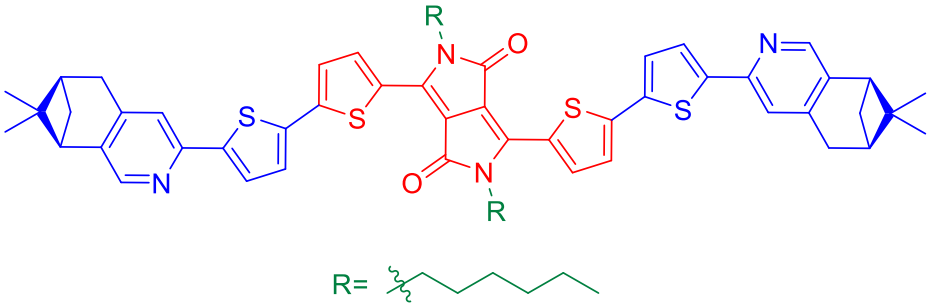

*Figure II. 7 Chemical structure of the disubstituted myrtenal **DPP** derivative.*

Although, OPV devices prepared using these myrtenal **DPP** derivatives as donors and PCBM as an acceptor gave very low PCE and short circuit current values, around an order of magnitude lower than devices made with **P3HT:PCBM** under similar conditions. They attributed the poor performance to be related to the low charge carrier mobility of the materials, as mobility in chiral materials is known to be extremely sensitive to supramolecular organization.[42] Finally, the morphological analysis revealed that the monosubstituted

derivative is more inclined to form ordered crystalline domains when spun-cast as a blend with $PC_{61}BM$.

Having briefly reviewed some examples containing amides, **DPP** derivatives and chiral groups, it is now appropriate to present what was performed for the new **DPP** family. In this chapter, the synthesis of the lactam functionalized derivatives shown in Figure II. 1 will be described, as well as their optical and self-assembly properties characterization, which will help in the understanding of the charge transport properties measured by electrodeless techniques based on microwave conductivity.

II. Results and Discussion

II.1) Synthesis

The main **DPP** core was synthesized by the cyclization reaction between 2-thiophenecarbonitrile and diethylsuccinate, following a reported protocol.[43] The final **DPPBA, (S)-DPPBA** and **(R)-DPPBA** were obtained via alkylation reactions with the mesylated amide-containing branches (Scheme II. 1). These branches were synthesized by reacting ε-caprolactone with the corresponding amine derivatives (chiral and achiral) and subsequently adding the mesylate activating group (Scheme II. 1). The **DPP** was N-alkylated with cesium carbonate as the base to deprotonate and DMF as the solvent like in similar **DPP** alkylation reactions reported.[44,45] The yields are low (10%) because of the produced sub-products isolated and identified, such as the O-alkylated isomers.

Different reaction conditions were tested to increase the N-alkylation yield. For instance, the reactions were performed under microwave irradiation as the heating source. In a first attempt, the reaction was carried out at room temperature to slow the formation of sub-products, since at high temperature and basic conditions, both N- and O-alkylation are favoured.[46] After one hour, only the mono N-alkylated product was obtained together with unreacted **DPP** and mesylate. When the reaction time increased, the O-alkylated isomer was already formed and the desired product was found at low yield (5-8%).

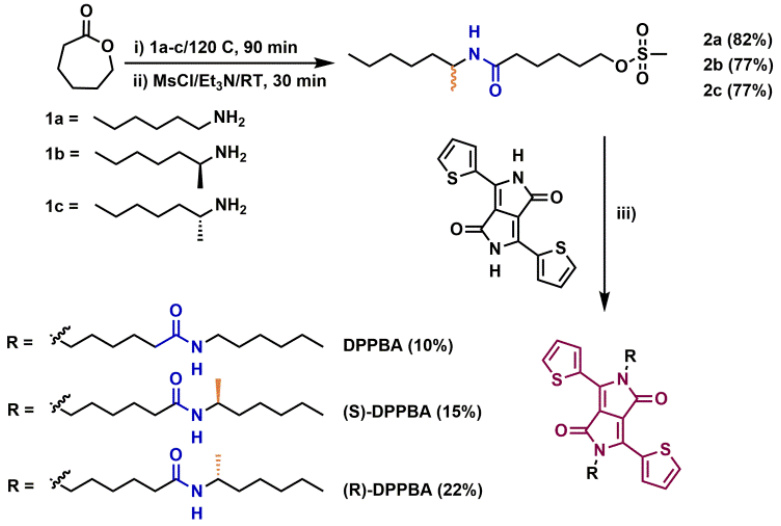

*Scheme II. 1 Synthetic pathway towards **DPPBA**, **(S)-DPPBA** and **(R)-DPPBA**. iii) Microwave irradiation (P = 150 W, DMF, 2 h, 120 ºC for **(S)-DPPBA** and P = 150 W, DMF, 2h, 70 ºC for **(R)-DPPBA**).*

In a second attempt, the reaction was performed at 120 ºC for one hour, adding a few drops of DMF to make a heterogeneous reaction mixture, demonstrated to work better for microwave reactions.[53,54] In this case, the major products were the N-alkylated derivative accompanied by the O-alkylated isomer. Both products were isolated by column chromatography, finding yields of 15% for the (S)-enantiomer, but not higher than 10% for the (R). The reactions were performed at lower temperatures (70-80 ºC) to achieve the bis-alkylated derivatives and try to avoid O-alkylated isomers. However, the (S)-enantiomer was obtained in 8% yield, and the (R) in yields of 15-22%. In acetonitrile, a greener solvent, the yields were even lower either with microwave irradiation or conventional heating.

II.2) Optical and self-assembly properties

After synthesizing the target compounds, we proceded to study the optical and self-assembly properties. Particularly, we used UV/Vis absorption, FTIR and CD spectroscopies in solution and in the solid state to shed light into the assembly processes of the three derivatives, and transmission electron microscopy (TEM) was used to study the formation of supramolecular structures.

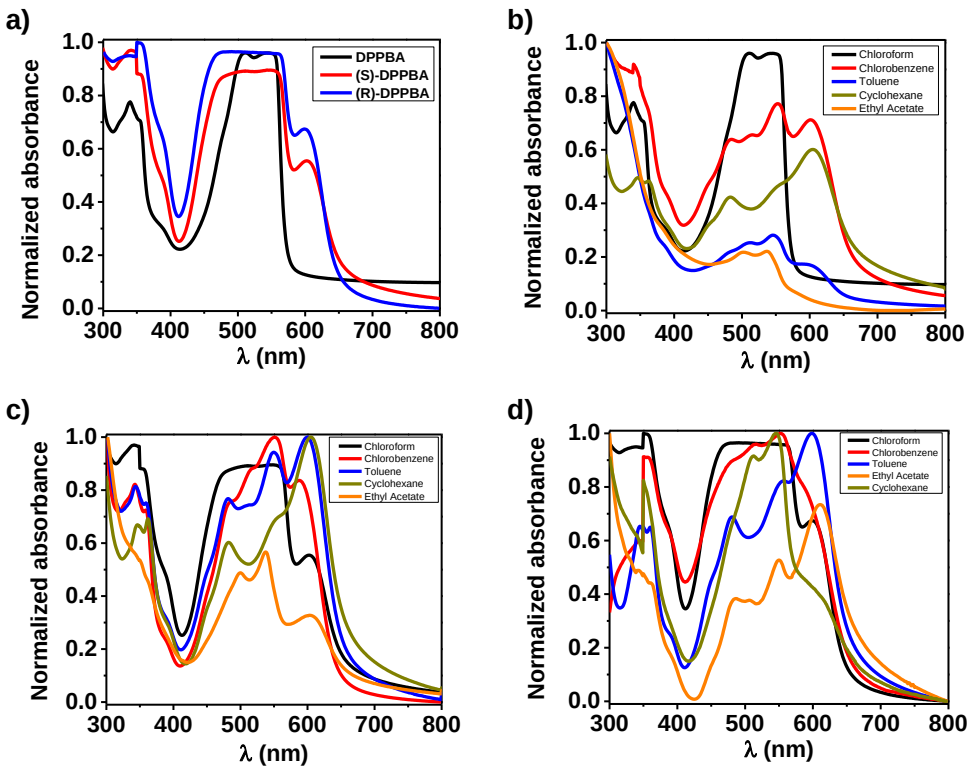

*Figure II. 8 a) Absorption spectra in chloroform of **DPPBA**, **(S)-DPPBA** and **(R)-DPPBA**. The concentration is 2.5 mg/ml in all cases. Absorption spectra in different solvents of b) **DPPBA**; c) **(S)-DPPBA**; and d) **(R)-DPPBA**. The concentration is 2.5 mg/ml for all solvents, except for chloroform (1.6 mg/ml).*

Initially we measured the compounds in chloroform (2.5 mg/mL), observing broad absorption bands ranging from 415 to 600 nm for the three derivatives at 20 °C (Figure II. 8a). The chiral derivatives showed an additional absorption band at lower energy at 600 nm (Figure II. 8a, traces red and blue). This band was not observed for **DPPBA**, even in saturated solutions (Figure II. 8a). This band could be attributed to the formation of J-type aggregates, as for other H-bonded **DPP** derivatives, including semicarbazone-containing **DPPs** reported earlier by our group.[10,47,48] This signal is related to the formation of H-bonds since it disappears when methanol, an H-bonding competing solvent, is added to **(S)-DPPBA** and **(R)-DPPBA** (Figure II. 9). So far, it was the first time that we observed aggregation bands in chloroform, which is normally a good solvent for the H-bonded DPP derivatives we have reported until the moment. The presence of such a band, already indicates the stronger aggregation tendency of the chiral derivatives in comparison to the achiral.

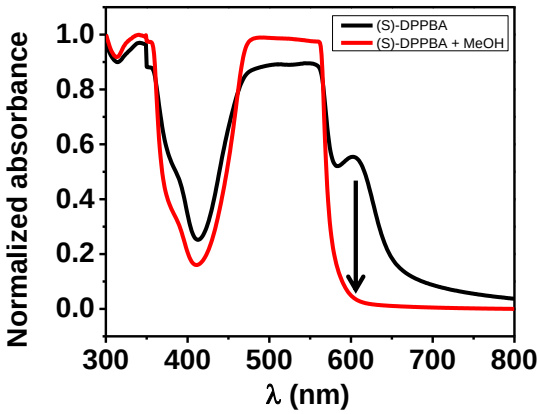

*Figure II. 9 Absorption spectra of **(S)-DPPBA** in chloroform (black trace) and after the addition of 4% volume of methanol (red trace).*

FTIR spectra of chloroform solutions at room temperature proved the existence of H-bonds in the bisamide derivatives (Figure II. 10a). **DPPBA** showed only one band at 3450 cm^{-1} in the NH stretching area, which is characteristic of the NH stretching mode (amide A) of free amide groups. This result points out that **DPPBA** is not H-bonded in chloroform.

The amide I mode is found at 1659 cm^{-1}, which also corresponds to free amide groups. On the other hand, **(S)-DPPBA** and **(R)-DPPBA** showed two bands at 3439 cm^{-1} and 3297 cm^{-1} in the NH stretching area at room temperature (Figure II. 10a). The first band can be attributed to the free amide, analogously to the band at 3450 cm^{-1} for **DPPBA**; the second band corresponds to H-bonded amide groups. Hence, **(S)-DPPBA** and **(R)-DPPBA** are partially H-bonded. In the region between 1600 cm^{-1} and 1700 cm^{-1}, **(S)-DPPBA** and **(R)-DPPBA** show three peaks at 1632 cm^{-1}, 1648 cm^{-1} and 1663 cm^{-1}. The peak at 1632 cm^{-1} corresponds to amide groups engaged in strong H-bonds[49], while the peak at 1648 cm^{-1} corresponds to weaker bonds. The peak at 1663 cm^{-1} matches with the peak for free amide observed with **DPPBA**.

When increasing gradually the temperature from 27 to 59 °C the spectra of **DPPBA** did not show significant evolution. In contrast, for the chiral derivatives, the peaks corresponding to H-bonded amides gradually decreased and fully disappear at 45 °C. At this temperature, the spectrum of **(S)-DPPBA** matches the one of **DPPBA** at room temperature (Figure II. 11).

The optical properties were measured in different solvents: toluene, chlorobenzene, cyclohexane and ethyl acetate. In these solvents, the J-aggregate band becomes more intense than in chloroform for the three derivatives (Figure II. 8 b to d). A shoulder band appears at approximately 480 nm in several solvents, attributed to the formation of H-type aggregates. It is particularly intense in chlorobenzene, toluene and cyclohexane. For **(S)-DPPBA** and **(R)-DPPBA**, the J-aggregate signal (λ = 600 nm) is the predominant one in toluene, cyclohexane and ethyl acetate, showing the strong formation of H-bonds in these conditions. In these solvents, like in the case of chloroform, the J-aggregate band disappears when methanol is added (Figure II. 12).

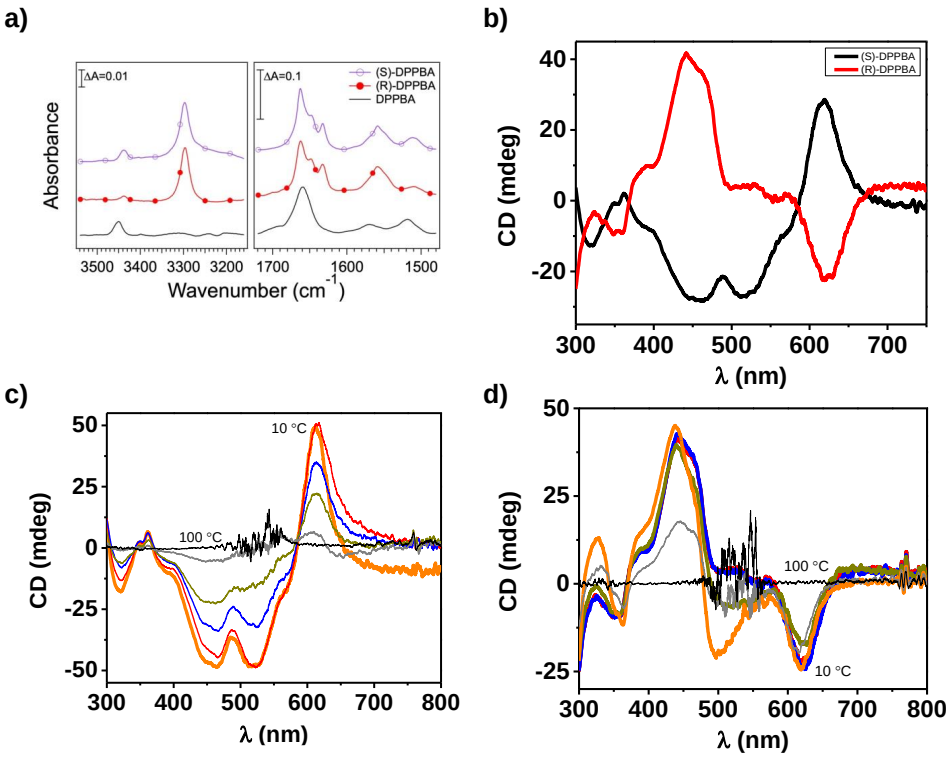

Figure II. 10 a) FTIR spectra in deuterated chloroform at room temperature of **(S)-DPPBA**, **(R)-DPPBA** and **DPPBA**. b) CD spectra **(S)-DPPBA** and **(R)-DPPBA** in toluene solution. [**(S)-DPPBA**] = [**(R)-DPPBA**] = 2.5 mg/ml. Variable temperature CD spectra in toluene of (c) **(S)-DPPBA** and (d) **(R)-DPPBA**. c = 2.5 mg/ml.

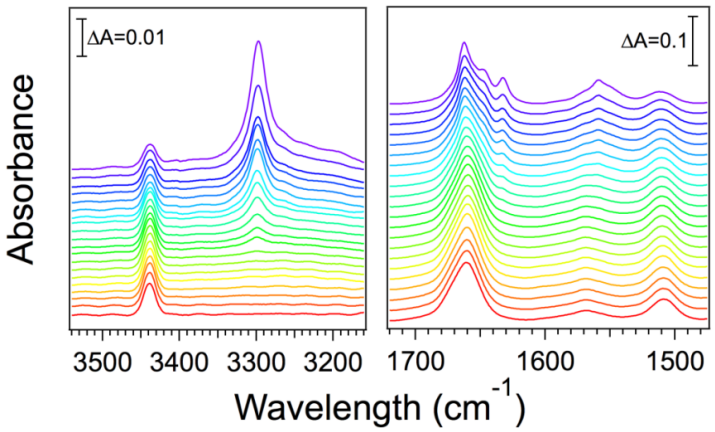

*Figure II. 11 FTIR spectra of **(S)-DPPBA** in deuterated chloroform at different temperatures. From 27 ºC to 59 ºC (red trace).*

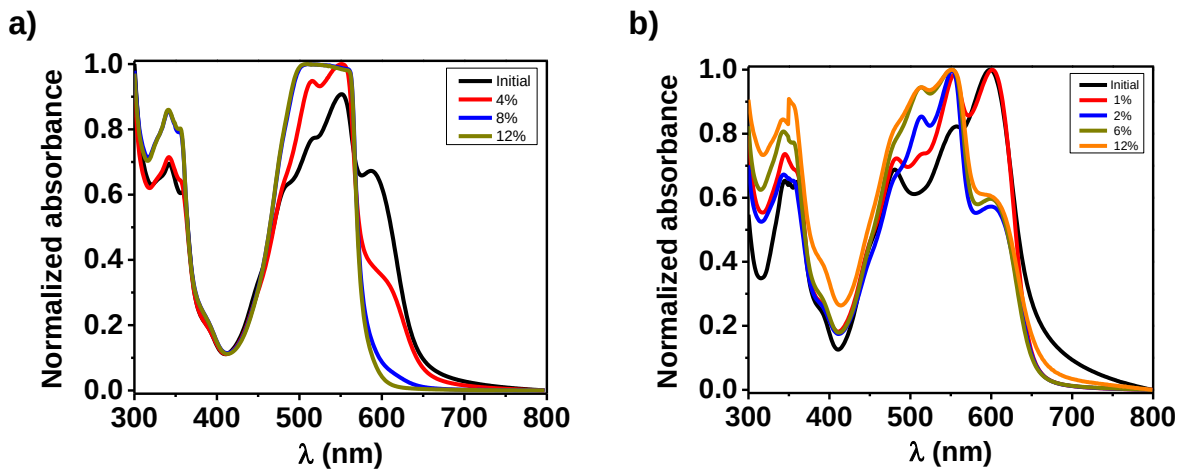

*Figure II. 12 Absorption spectra of **(S)-DPPBA** in chlorobenzene and **(R)-DPPBA** in toluene upon the addition of methanol (in vol %).*

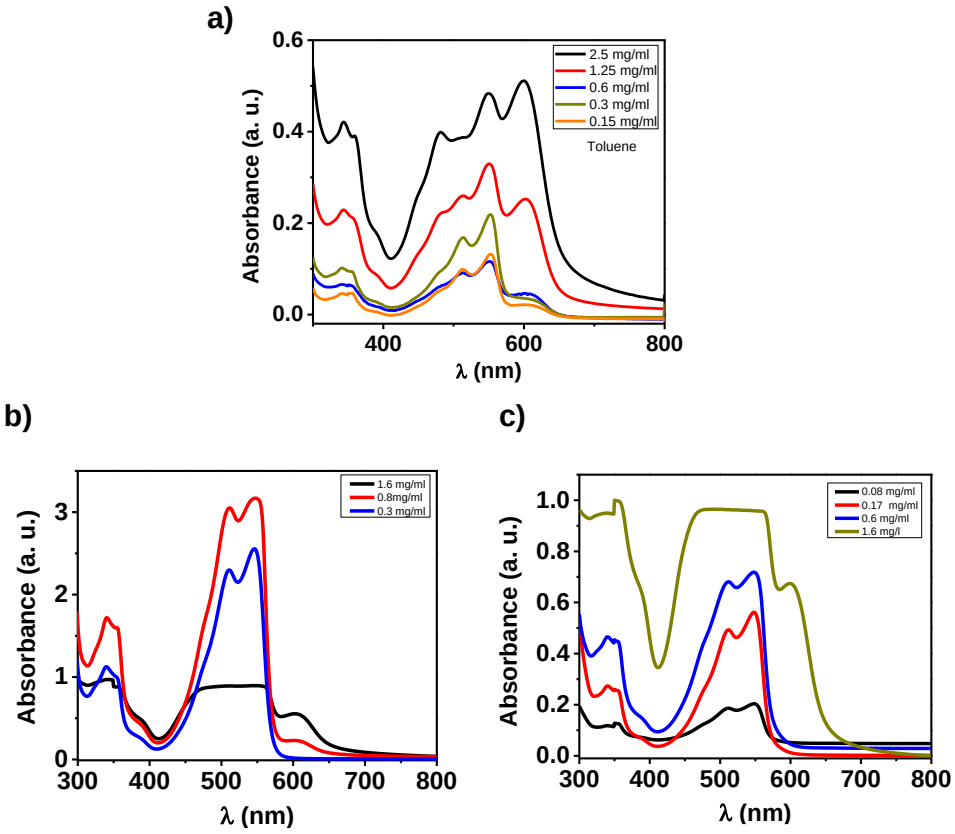

*Figure II. 13 a) Absorption spectra of **(S)-DPPBA** in toluene at different concentrations. b) Absorption spectra of **(S)-DPPBA** in chloroform at different concentrations. c) Absorption spectra of **(R)-DPPBA** in chloroform at different concentrations.*

Thanks to the formation of J-aggregates it is possible to cover a larger zone of the spectrum and to tune the energy band gap. This is very interesting since the optoelectronic properties can be modified by varying the aggregation state without modifying the molecule. Furthermore,

this strategy allows us, with very simple semiconducting segments, to control the properties through aggregation.

Dilution series and variable temperature measurements were performed to keep on exploring the aggregation process. The J-aggregate bands were observed upon diluting, still appearing at low concentrations in solvents that promote the formation of strong H-bonds (Figure II. 13). When the temperature increases, the J-aggregate band is still present, emphasizing the formation of aggregates even at high temperature (Figure II. 14).

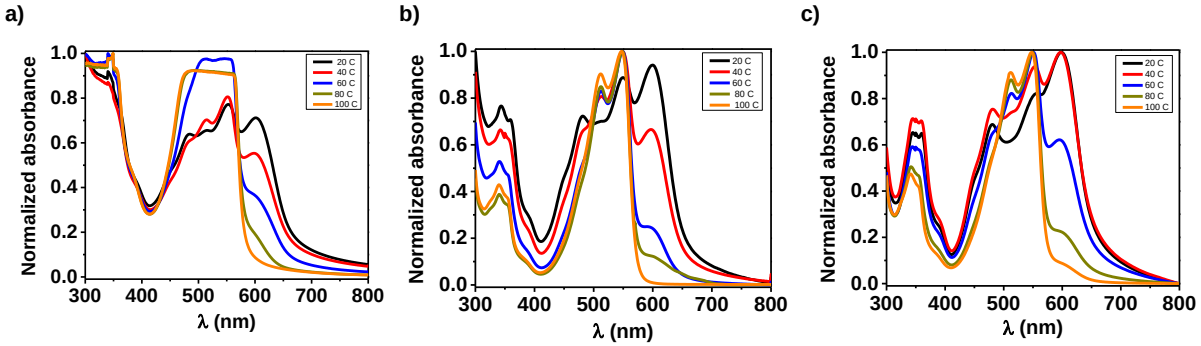

*Figure II. 14 Absorption spectra of **DPPBA** in chlorobenzene, **(S)-DPPBA** and **(R)-DPPBA** in toluene upon increasing the temperature. The concentration is of 2.5 mg/ml in all cases.*

This trend was also observed for the three derivatives, but the J-aggregate bands disappeared at higher temperatures and lower concentrations for the chiral derivatives compared to the achiral one. This proves that the chiral derivatives form more stable aggregates than the achiral one.

The absorption properties were also measured on cast thin films, showing a bathochromic shift with the appearance of a predominant J-aggregate band, as an effect of planarization with respect to the solutions. This result is independent from the casting solvent (Figure II. 15).

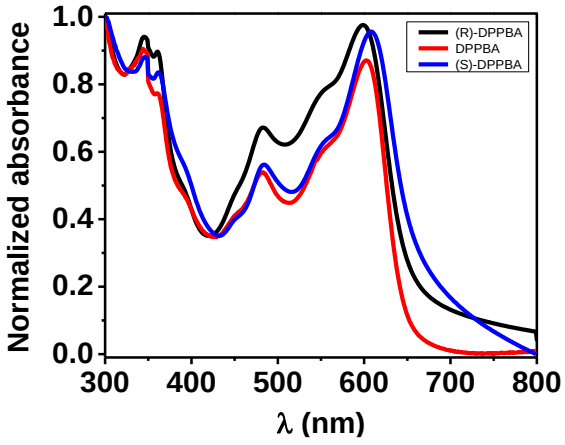

*Figure II. 15 Absorption spectra of thin films of **DPPBA, (S)-DPPBA** and **(R)-DPPBA** drop cast from chloroform solutions at room temperature.*

To explore the chiral derivatives, CD spectroscopy in solution was used, finding signals with strong Cotton effect for the chiral derivatives, while no signal was observed for **DPPBA** even in aggregation conditions (Figure II. 16). Figure II. 10b shows the CD spectra in toluene for **(S)-DPPBA** and **(R)-DPPBA** at room temperature, where strong signals are found, especially at the J-aggregate wavelength as a sign of chirality transfer through the aggregates. Variable temperature CD was performed in several solvents, finding strong signals at low temperature that gradually disappear upon heating. The CD signal can be observed up to high temperatures, reaching 60-80 ºC, as evidenced in Figure II. 10c and d and Figure II. 17, where the variable temperature spectra in toluene were recorded.

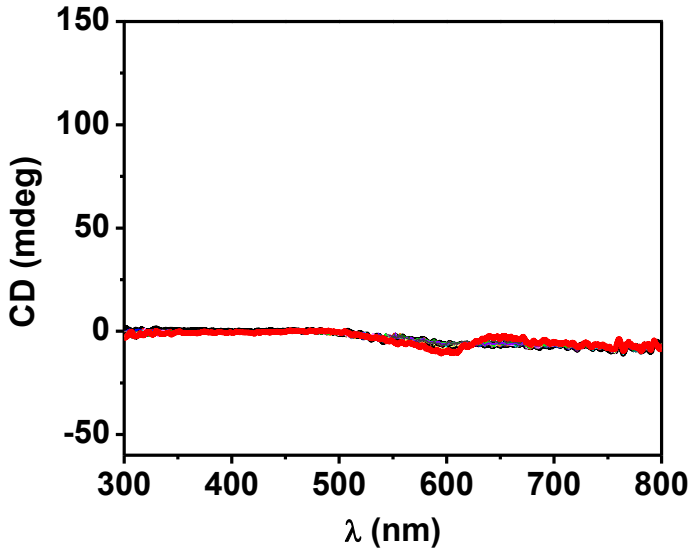

*Figure II. 16 CD spectrum of **DPPBA** in chloroform, chlorobenzene, toluene, ethyl acetate and cyclohexane. [**DPPBA**] = 2.5 mg/ml.*

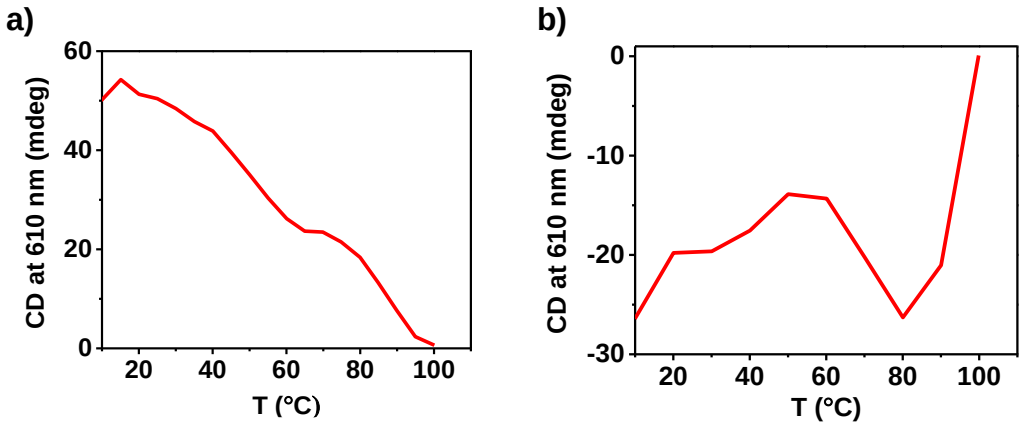

*Figure II. 17 Variable temperature CD signal followed at 610 nm for **(S)-DPPBA** and **(R)-DPPBA** in toluene. [**(S)-DPPBA**] = [**(R)-DPPBA] =** 2.5 mg/ml.*

Morphology studies were performed using transmission electron microscopy (TEM) by depositing solutions of the amide-based **DPPs** in the solvents used for UV-visible and CD spectroscopy. Different high aspect-ratio structures were observed for the three derivatives in each solvent. The chiral derivatives show helical structures in most of the solvents, while the **DPPBA** shows different one-dimensional structures. Thin films of **DPPBA** in chloroform showed the presence of fibres with an average length of 10 µm (Figure II. 18). In chlorobenzene and toluene, shorter structures were observed with an average length of 2 µm that regroup in ribbon-like structures with widths of several hundreds of nanometers. Stiff fibres were observed in ethyl acetate and cyclohexane samples (Figure II. 19a-d). Regarding **(S)-DPPBA** (Figure II. 19e-h) and **(R)-DPPBA** (Figure II. 19i-l) samples, twisted fibres and helical structures were found in all the solvents studied, being more flexible than the structures of **DPPBA**, which seem stiffer (Figure II. 19a-d). Nevertheless, less flexible structures were found for **(R)-DPPBA** and **(S)-DPPBA** in solvents like cyclohexane (Figure II. 19) and ethyl acetate (Figure II. 20).

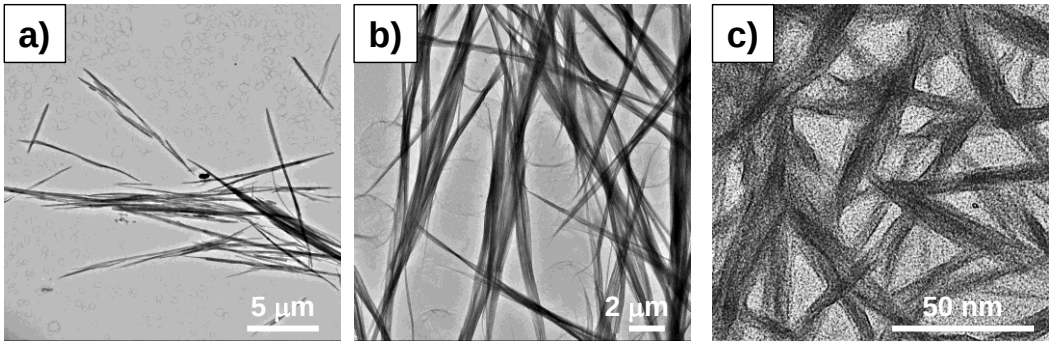

*Figure II. 18 TEM images of chloroform prepared samples of a) **DPPBA**, b) **(S)-DPPBA** and c) **(R)-DPPBA**.*

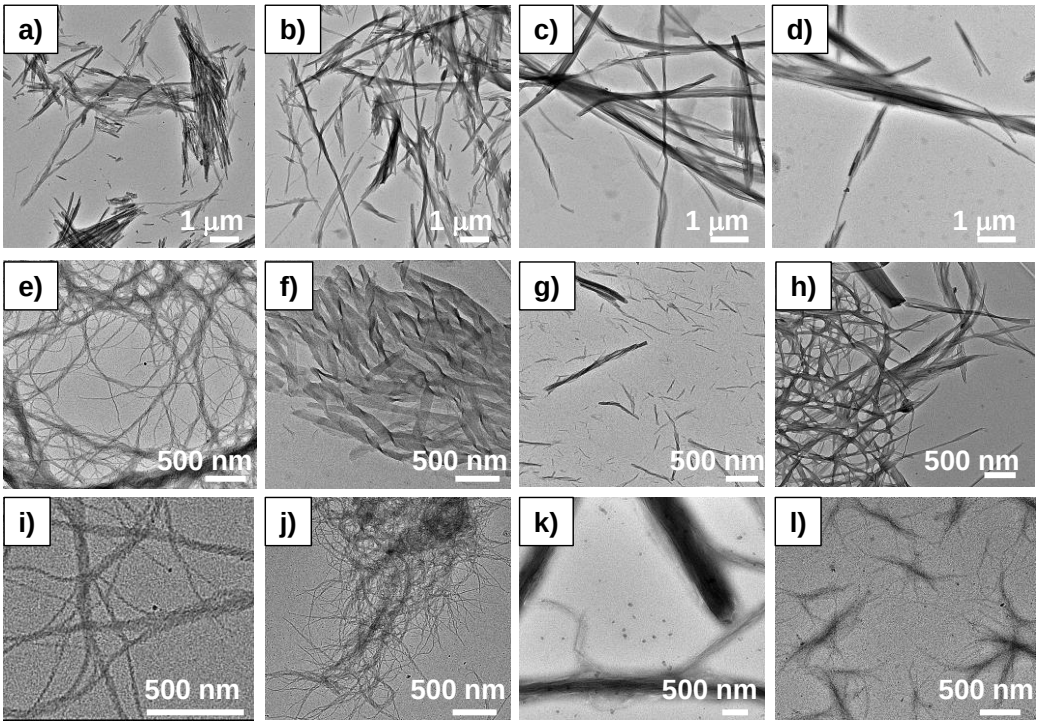

*Figure II. 19 TEM images of **DPPBA** (a-d), **(S)-DPPBA** (e-h) and **(R)-DPPBA** (i-l) in chlorobenzene, toluene, cyclohexane and ethyl acetate, respectively.*

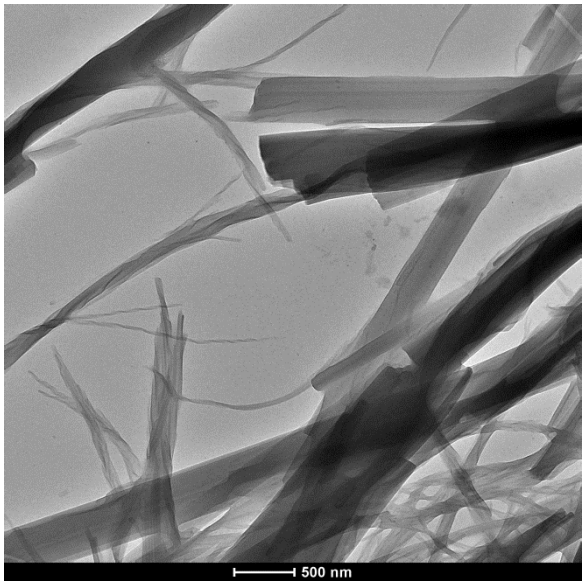

*Figure II. 20 TEM image of **(S)-DPPBA** in ethyl acetate.*

II.3) Electrical properties

After exploring the aggregation ability of the amide-containing molecules, knowing their electrical properties was the next topic of interest. The photoconductivity properties were explored using electrodeless techniques based on microwave conductivity. This part of the work was done in collaboration with the group of Prof. Shu Seki from the University of Kyoto (Japan). This group has pioneered contactless techniques to measure a wide variety of electronic properties. This means that the molecules can be explored simply by drop casting without the need of making an entire device. Particularly, they measured the photoconductivity of the two chiral molecules and the achiral one using Flash-Photolysis Time Resolved Microwave Conductivity (FP-TRMC). It is a technique that provides a measure of photoconductivity as $\Phi\Sigma\mu$ were Φ is the charge carrier generation quantum yield and $\Sigma\mu$ is the sum of charge carrier mobilities of electrons and holes.[50–52] The samples are drop cast onto quartz substrates and exposed to a 355 nm pulsed laser. Once the irradiation stops, the charge recombination lifetime is recorded.

For these compounds, films were prepared by drop casting them from chloroform solutions (Figure II. 21), and their photoconductivity was analysed before and after solvent vapor annealing and the solvent annealing protocol was:

1) To expose to ethyl acetate for 24 h
2) To methanol vapor for 24 h: ethyl acetate promotes efficiently aggregation of the molecules, and methanol disrupts H-bonds.

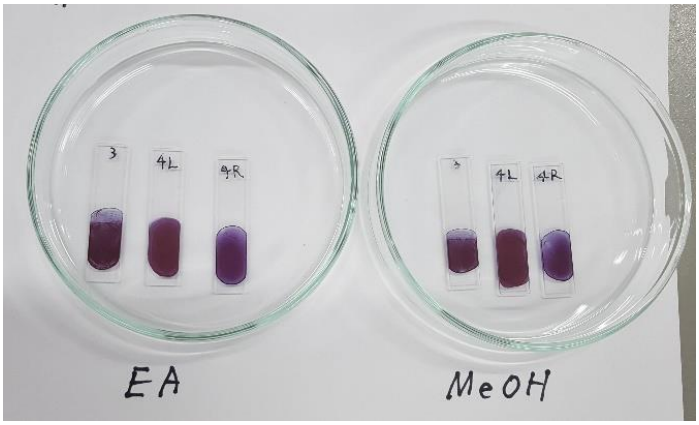

*Figure II. 21 Sample preparation for the **DPP** bisamide derivatives. All the films are drop cast from chloroform (at a concentration of 5 mg/ml) to be subsequently exposed to ethyl acetate and methanol.*

The observed kinetic traces of conductivity transients are shown on Figure II. 22. The photoconductivity of **DPPBA** is evidently larger than those of **(S)-** and **(R)-DPPBA** (the values can be found in Table II. 1), even though photoconductivity ($\Phi\Sigma\mu$) depends on the photo generation yield Φ. The kinetics decay of photoconductivity of **DPPBA** shows that the photo-generated free charge carriers are stable up to 10 µs. The recombination of charge carriers is slower in **DPPBA** than in **(S)-** and **(R)-DPPBA**, with one order of magnitude longer lifetime:

$t_{1/2}$ amounts 2 x 10^{-5} s for **DPPBA**, 5 x 10^{-6} s for **(S)-DPPBA**, and 7 x 10^{-6} s for **(R)-DPPBA** (Table II. 2). It seems that the lower solubility of the chiral **DPPs** and the presence of the methyl group next to the amide group are detrimental for the charge carrier pathways.

Table II. 1 Photoconductivity values for the three derivatives before and after solvent annealing.

Compound	$\Phi\Sigma\mu$ ($cm^2V^{-1}s^{-1}$) Before solvent annealing	Solvent vapor exposure	$\Phi\Sigma\mu$ ($cm^2V^{-1}s^{-1}$) After solvent annealing
DPPBA	5×10^{-5}	Ethyl acetate	7×10^{-5}
DPPBA	6×10^{-5}	Methanol	7×10^{-5}
(S)-DPPBA	3×10^{-5}	Ethyl acetate	3×10^{-5}
(S)-DPPBA	3×10^{-5}	Methanol	2×10^{-5}
(R)-DPPBA	3×10^{-5}	Ethyl acetate	3×10^{-5}
(R)-DPPBA	4×10^{-5}	Methanol	4×10^{-5}

To assess the impact of the self-assembled structure quantitatively on the charge carrier pathways, the photoconductivity signal was traced at each step of the solvent annealing protocol in an identical film of each compound. Interestingly, the highest photoconductivity (7.5 x 10^{-5} $cm^2V^{-1}s^{-1}$, Table II. 1) was recorded in **DPPBA** after solvent annealing in ethyl acetate (Figure II. 22d), suggesting an efficient promotion of aggregated states of the molecule.

The photoconductivity value increased up to 1.5 fold from the initial 5.0 x 10^{-5} $cm^2V^{-1}s^{-1}$, emphasizing the importance of promoting the H-bonding strength. On the other hand, methanol vapor annealing did not show any significant effect on photoconductivity (Figure II. 22e) in **DPPBA**. It seems that only methanol vapor is not enough to disrupt H-bonds in the condensed phase. However, when the film previously exposed to ethyl acetate was soaked in methanol, the photoconductivity decreased dramatically as well as the lifetime (Figure II. 22f, Table II. 3).

This result highlights the important role of H-bonding to facilitate the charge carrier pathways in the self-assembled structures. Regarding the chiral derivatives **(S)-** and **(R)-DPPBA**, no differences in photoconductivity were found during the solvent annealing protocols (Figure II. 23, Table II. 1). This would suggest that tightly-bound self-assembled structures were already formed in the solution phases, and the annealing is no longer efficient to cause significant rearrangements in the molecular packing structures of chiral substances. The presence of a methyl group next to the H-bonding (amide) motif and the lower solubility of both chiral isomers compared to **DPPBA**, might be supportive for the stability of the self-assembled structures.

Table II. 2 Rate constant (calculated after 3 µs after pulse excitation) and half lifetime values for the three derivatives.

	DPPBA	(S)-DPPBA	(R)-DPPBA
***k* (s^{-1})**	3×10^{4}	2×10^{5}	1×10^{5}
$t_{1/2}$ (s)	2×10^{-5}	5×10^{-6}	7×10^{-6}

*Table II. 3 Rate constant (calculated after 3 µs after pulse excitation) and half lifetime values for **DPPBA**.*

DPPBA	Anneal ethyl acetate	Soaking in methanol
***k* (s^{-1})**	4×10^{4}	1×10^{5}
$t_{1/2}$ / s	2×10^{-5}	7×10^{-6}

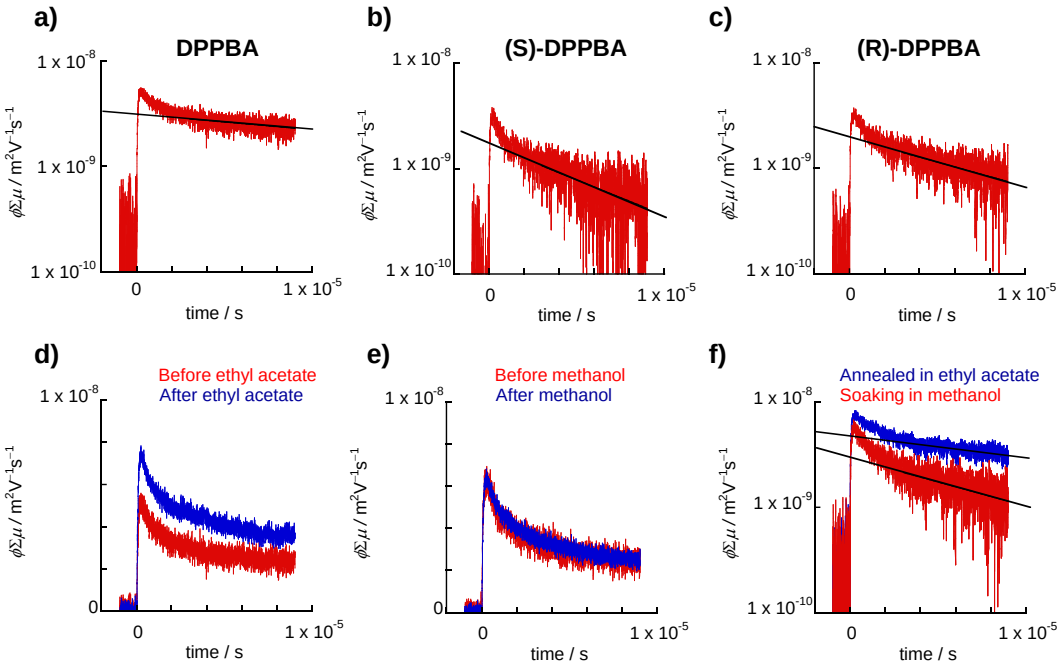

*Figure II. 22 Kinetic traces of photoconductivity transients of **DPPBA** (a), **(S)-DPPBA** (b) and **(R)-DPPBA** (c) cast from chloroform. Kinetic traces of photoconductivity traces of **DPPBA** before and after ethyl acetate vapor annealing (d), before and after methanol vapor annealing (e) and after soaking in methanol (f).*

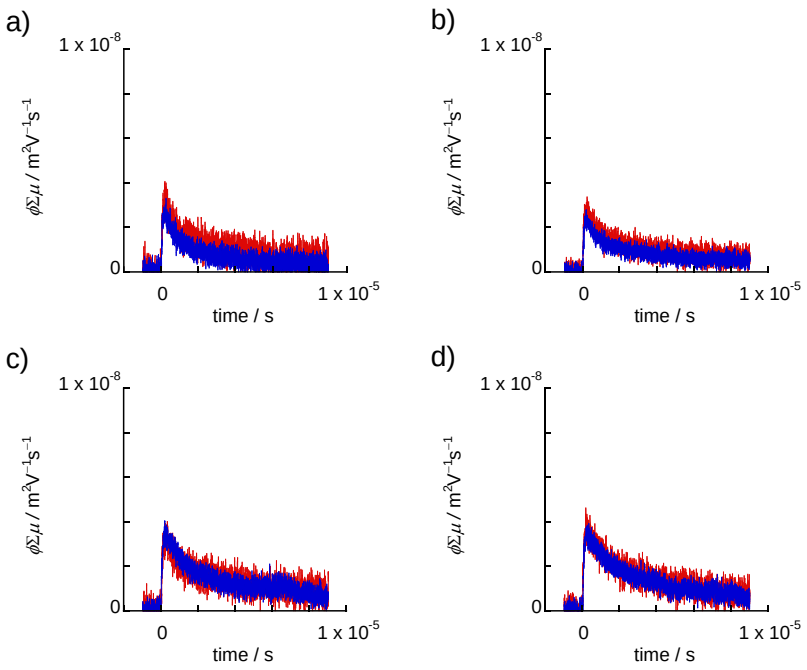

*Figure II. 23 Kinetic traces of photoconductivity transients of **(S)-DPPBA** (a) and (b) and **(R)-DPPBA** (c) and (d) before and after ethyl acetate (a) and (c) and methanol vapor annealing (b) and (d).*

II.4) Conclusions

In conclusion, three amide-containing **DPP** derivatives were synthesized and characterized, two of them bearing chiral centers. The three derivatives aggregate and form J-type aggregates, where H-bonds are involved. The aggregation is particularly strong in the chiral derivatives, which show aggregate signals in solvents where the achiral **DPP** is fully dissociated.

The photoconductivity measurements performed using FP-TRMC indicate that the achiral derivative has superior values of photoconductivity as well as slower recombination of the charge carriers. The importance of H-bonding is highlighted by annealing samples in solvents that promote self-assembly, where the photoconductivity values increased. In contrast, the photoconductivity values decreased dramatically when the samples were soaked in H-bonding competing solvents. This effect was not observed for the chiral derivatives, indicating that the chiral center next to the H-bonding functionality might hinder charge transport.

These results have helped in the design of the next H-bonded **DPP** families that will continue to be used in the systematic and comparative studies. In this regard, chapter III shows how the solubility of the derivatives described in this chapter can be increased by adding solubilizing alkyl tails in the thiophene rings. However, the incorporation of chirality while increasing solubility is being explored by another colleague in my group, while I have focused on drastically changing other H-bonding parameters that can influence the self-assembly properties, as for example the amide topology also described in chapter III.

The work of this chapter resulted in a publication and all the details can be found here:

Chemistry – A European Journal. **2020**, *26*, 9998–10004, 10.1002/chem.202001540.

III. Experimental

III.1) Materials and methods

All reagents and solvents were obtained from commercial suppliers and purified or dried according to standard procedures. Column chromatography was performed on silica gel (VWR Silica 60, particle size 0.040–0.063 mm). Solvents for spectroscopic studies were of spectroscopic grade and used as received. Elemental analysis was performed on a Thermofischer Scientific Flash 2000. Matrix-assisted laser desorption/ionisation-time of filght (MALDI) was performed in a Bruker Daltonics. ^{1}H and ^{13}C spectra were recorded in $CDCl_3$ on a Bruker Avance 400 MHz spectrometer and/or Bruker Avance III HD 500 MHz spectrometer. UV–vis measurements were performed in a conventional quartz cell (light pass 1 mm) on a Cary 5000 UV-Vis-NIR spectrophotometer. TEM measurements were done with a Technai G2 (FEI) microscope with an accelerating voltage of 200 kV. 5 µL of the sample solution were deposited onto a freshly glow discharged carbon-covered grid (400 mesh). The suspension was left for 2 min, and then, the grid was negatively stained with 5 µL of uranyl acetate (2% in water) for another 1 min and finally blotted using a filter paper.

FTIR spectra were recorded with a Vertex 70 from Bruker Optics, equipped with MCT detector and a black-body source. The spectra of the solids were measured by ATR on diamond. The solutions were studied in cells from Specac Pike with KBr NaCl windows. For the VT experiments the solutions were inserted in a home-made cell between two NaCl windows. The cell was inserted in a Linkam heating stage, hold in a horizontal measurement chamber. The spectra were measured with the built-in MCT detector of the Vertex 70. The spectra were compensated from CO_2 and moisture with OPUS from Bruker. The solvent intensities were measured separately and subtracted. The spin coated samples were prepared using a Spin 150 spin coater at 2000 rpm using 80 µl of solution on glass slides or silicon wafers.

Charge carrier mobilities were evaluated by FP-TRMC at room temperature.[48,53] The thin films of samples were fabricated by drop-cast method onto quartz substrates (9 × 40 mm^2, 1 mm thick). Charge carriers were injected into the materials via photo-ionization with a third harmonic generation (λ = 355 nm) of a Spectra Physics model INDI-HG Nd:YAG laser pulses at 10 Hz with a pulse duration of ca. 5 ns. The photon density of a 355 nm pulse was modulated from 4.5 × 10^{15} photons cm^{-2} $pulse^{-1}$. The microwave frequency and power were set at ~9.1 GHz and 3 mW, respectively, and guided into a microwave cavity. The *Q*-factor of the microwave cavity loaded with the sample was 2200, and the substrates with the compound films were set at the point of electric field maximum. The reflected power of the probing microwave, picked up by a diode (rise time < 1 ns), was monitored by a Tektronics model TDS3032B digital oscilloscope after an amplification by Ciao Electronics CA812-304 FET amplifier system. The observed change in the reflected microwave power (ΔP_r) was normalised with the steady reflection of the microwave from the cavity (P_r), and converted directly into the product of a photocarrier generation yield (Φ) and the sum of photo-generated electron/hole mobilities (Σµ),

$$\phi\Sigma\mu = 1/(\varepsilon I_0 F_{light}) \times (1/A) \times (\Delta P_r/P_r) \quad (1)$$

where ε, A, I_0, and F_{light} are elementary charge, sensitivity factor (S^{-1} cm), incident photon density of the excitation laser (photon cm^{-2}), and filling factor (cm^{-1}), respectively. The value of Flight was calculated based on the overlap of the area of photo-carrier injection (presumed to be proportional to the absorbance of excitation light by the sample film) with electric field strength distribution in the cavity derived from a calculation code of CST Microwave Studio from AET Inc.

III.2) Synthetic procedure

N-hexyl-6-hydroxyhexanamide:

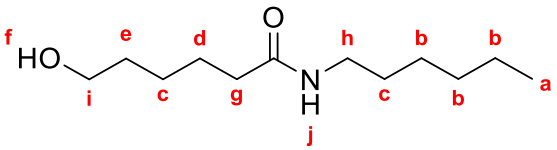

A solution of hexylamine (3.8 g, 37.3 mmol) in toluene was stirred at room temperature and ε-caprolactone (2.85 g, 24.7 mmol) was added dropwise. The mixture was then stirred for 90 min at 130 °C and cooled down to room temperature. The crude was extracted with DCM (50 ml) and washed with a 1 M solution of HCl, then with a solution of $NaHCO_3$ (aq). The organic phase was dried with $MgSO_4$, filtered, and concentrated under reduced pressure. The final product was purified by recrystallization (75% ethyl acetate/cyclohexane) and obtained as white crystals (2.82 g, 53%).

^{1}H-NMR (400 MHz, $CDCl_3$): δ [ppm] 5.6 (s, 1H_j), 3.64 (td, J= 6.5 Hz, 5.1 Hz, 2H_i), 3.22 (td, J= 7.3 Hz, 5.7 Hz, 2H_h), 2.17 (t, J=7.5 Hz, 2H_g), 1.95 (t, J= 5.1 Hz, H_f),1.66 (quint, J= 7.6 Hz, 2H_e), 1.58 (quint, J= 7.0 Hz, 2H_d), 1.53-1.35 (m, 4H_c), 1.34-1.21 (m, 6H_b), 0.88 (t, J= 6.6 Hz, 3H_a).

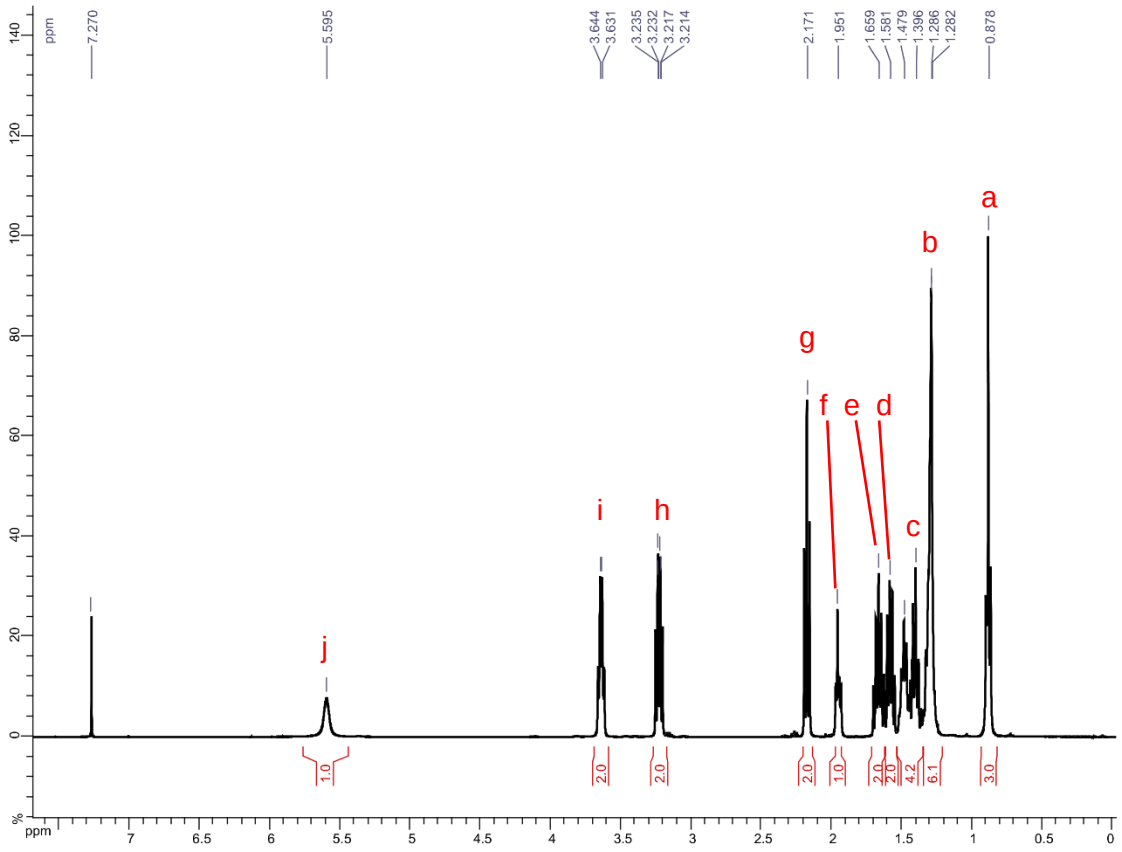

6-(hexylamino)-6-oxohexyl methanesulfonate:

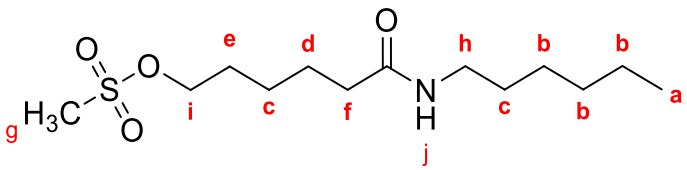

A solution of N-hexyl-6-hydroxyhexanamide (2.8 g, 13 mmol) and triethylamine (2.8 g, 28 mmol) in anhydrous THF (45 ml) was stirred under argon atmosphere at 0°C. Methanesulfonyl chloride (3.5 g, 28 mmol) was added dropwise. The mixture was stirred at room temperature for 30 min, poured in iced water (100 ml) and extracted with DCM. The organic phase was dried with $MgSO_4$, filtered and concentrated under reduced pressure. The desired compound was purified by column chromatography (ethyl acetate) and dried under reduced pressure as a white solid (3.1 g, 82%).

^{1}H-NMR (400 MHz, $CDCl_3$): δ [ppm] 5.48 (s, 1 H_j), 4.23 (t, J= 6.4 Hz, 3 H_i), 3.23 (td, J= 7,2 Hz, 5.8 Hz, 2H_h), 3.00 (s, 3 H_g), 2.17 (t, J= 7.4 Hz, 2 H_f), 1.78 (m, J= 7.1 Hz, 2H_e), 1.69 (m, J= 7.8 Hz, 2H_d), 1.47 (m, J= 7.4 Hz, 4H_c), 1.29 (m, 6 H_b) 0.89 (t, J= 6.5 Hz, 3H_a).

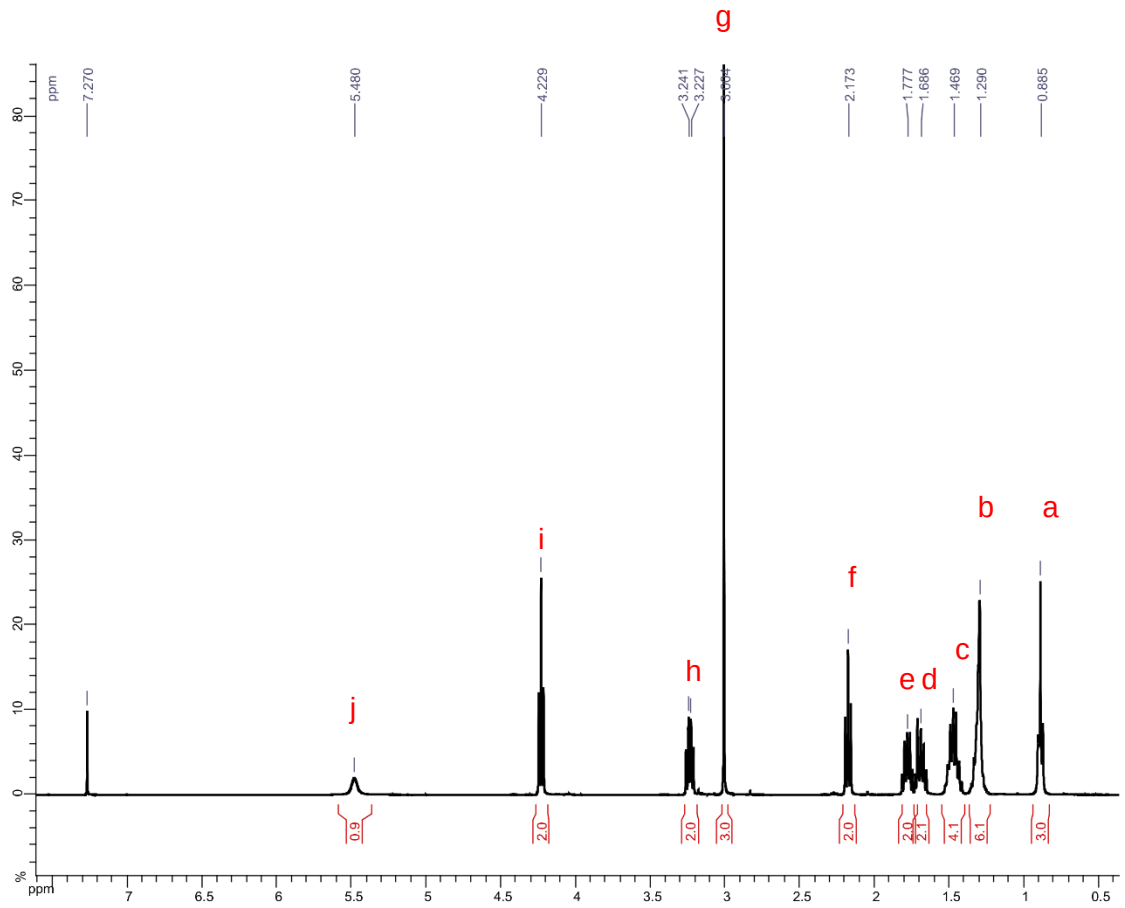

(S)-N-(heptan-2-yl)-6-hydroxyhexanamide:

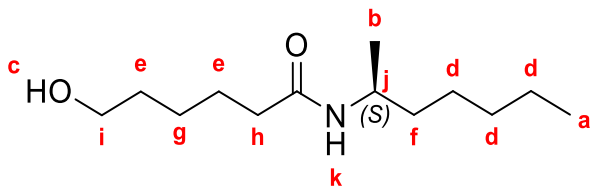

A solution of (S)-heptan-2-amine (11.34 g, 98.4 mmol) in toluene was stirred at room temperature and ε-caprolactone (7.49 g, 65.6 mmol) was added dropwise. The mixture was then stirred for 4 h at 130 °C and cooled down to room temperature. The crude was extracted with DCM (300 ml), washed with a 1 M solution of HCl, and with a solution of $NaHCO_3$ (aq). The organic phase was dried with $MgSO_4$, filtered, and concentrated under reduced pressure. The final product was obtained after washing (75% ethyl acetate/cyclohexane) as a pink oil (10.77 g, 61%).

^{1}H-NMR (400 MHz, $CDCl_3$): δ [ppm] 5.2 (d, 1H$_k$), 3.99 (ddm, *J* = 13.4 Hz, 8.6 Hz, 6.7 Hz, 1H$_j$), 3.66 (t, J= 6.5 Hz, 2H$_i$), , 2.16 (t, J= 7.3 Hz, 2H$_h$),1.67 (m, J= 7.2 Hz, 2H$_g$), 1.60 (m, J= 6.9 Hz, 2H$_f$), 1.41 (m, J= 6.7 Hz, 4H$_e$), 1.34-1.26 (m, 6H$_d$), 1.22 (d, J= 6.1 Hz, 1H$_c$), 1.12 (d, J= 6.5 Hz, 3H$_b$), 0.88 (t, J= 6.6 Hz, 3H$_a$).

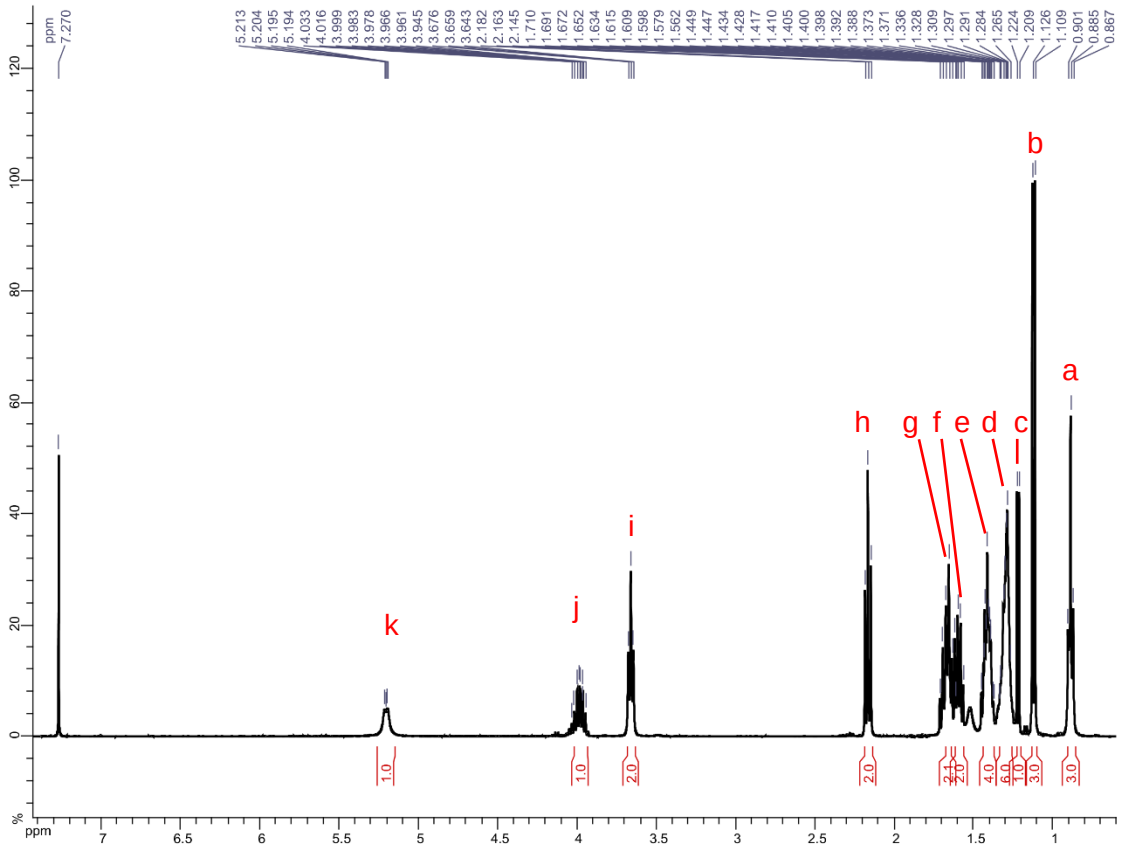

(S)-6-(heptan-2-ylamino)-6-oxohexyl methanesulfonate:

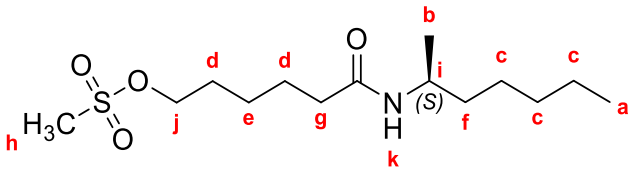

A solution of (S)-N-(heptan-2-yl)-6-hydroxyhexanamide (4 g, 17.4 mmol) and triethylamine (5.29 g, 52.3 mmol) in anhydrous THF (65 ml) was stirred under argon atmosphere at 0°C. Methanesulfonyl chloride (6 g, 52.3 mmol) was added dropwise. The mixture was stirred at room temperature overnight, poured in iced water (150 ml) and extracted in DCM. The organic phase was dried with $MgSO_4$, filtered and concentrated under reduced pressure. The desired compound was purified by column chromatography (ethyl acetate) and dried under reduced pressure and obtained as a white solid (5.18 g, 77%).

^{1}H-NMR (400 MHz, $CDCl_3$): δ [ppm] 5.21 (d, J= 7.9 Hz, 1H$_k$), 4.23 (t, J= 6.5 Hz, 2H$_g$), 3.97 (dtq, *J* = 8.6 Hz, 6.8 Hz, 6.4 Hz, 1H$_j$), 3.01 (s, 3H$_h$), 2.16 (t, J= 7.4 Hz, 2H$_g$), 1.78 (dq, J= 8.2 Hz, 6.5 Hz, 2H$_f$), 1.69 (t, J= 7.8 Hz, 2H$_e$), 1.44 (m, J= 7.3 Hz, 4H$_d$), 1.34-1.25 (m, 6H$_c$), 1.12 (d, J= 6.5 Hz, 3H$_b$), 0.88 (t, J= 6.6 Hz, 3H$_a$).

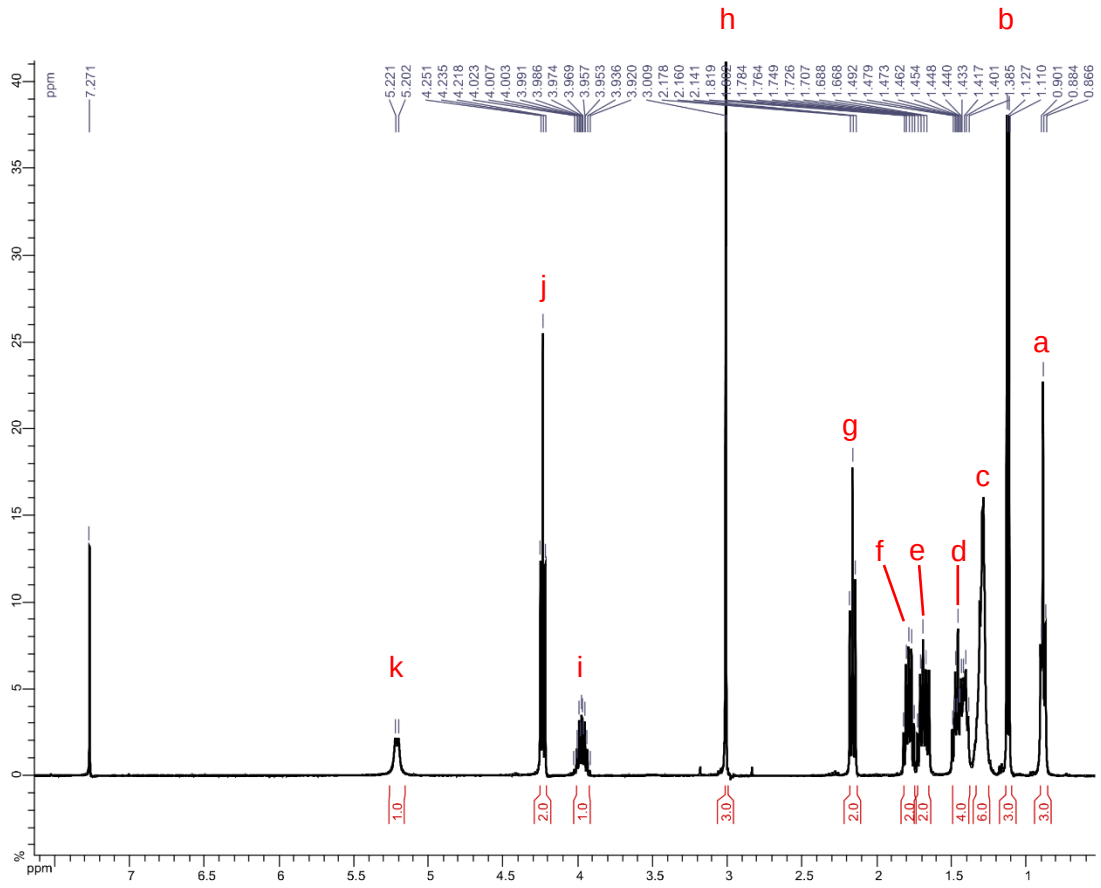

(R)-N-(heptan-2-yl)-6-hydroxyhexanamide:

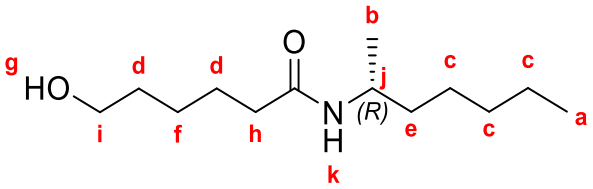

A solution of (R)-heptan-2-amine (11.34 g, 98.4 mmol) was stirred at room temperature. ε-caprolactone (7.49 g, 65.6 mmol) was added dropwise. The mixture was then stirred for 4 hours at 130°C and cooled down to room temperature. The crude was extracted with DCM (300 ml) and washed with a 1 M solution of HCl, then with a saturated solution of $NaHCO_3$ (aq). The organic phase was dried with $MgSO_4$, filtered and concentrated under reduced pressure. The final product was obtained after washing (75% ethyl acetate/cyclohexane) as a pink oil (8.88 g, 59%).

^{1}H-NMR (400 MHz, $CDCl_3$): δ [ppm] 5.39 (d, *J* = 7.3 Hz, 1H$_k$), 3.95 (ddm, *J* = 8.5 Hz, 7.3 Hz, 6.3 Hz, 1H$_j$), 3.62 (t, J=6.5 Hz, 2H$_i$), 2.14 (td, J=7.4 Hz, 3.8 Hz, 2H$_h$), 1.75 (d, J= 4.3 Hz, 1H$_g$), 1.64 (m, J= 7.4 Hz, 2H$_f$), 1.57 (m, J= 6.9 Hz, 2H$_e$), 1.39 (dqd, J= 9.6 Hz, 6.7 Hz, 2.7 Hz, 4H$_d$), 1.29-1.24 (m, 6H$_c$), 1.09 (d, J= 6.6 Hz, 3H$_b$), 0.86 (t, J= 6.6 Hz, 3H$_a$).

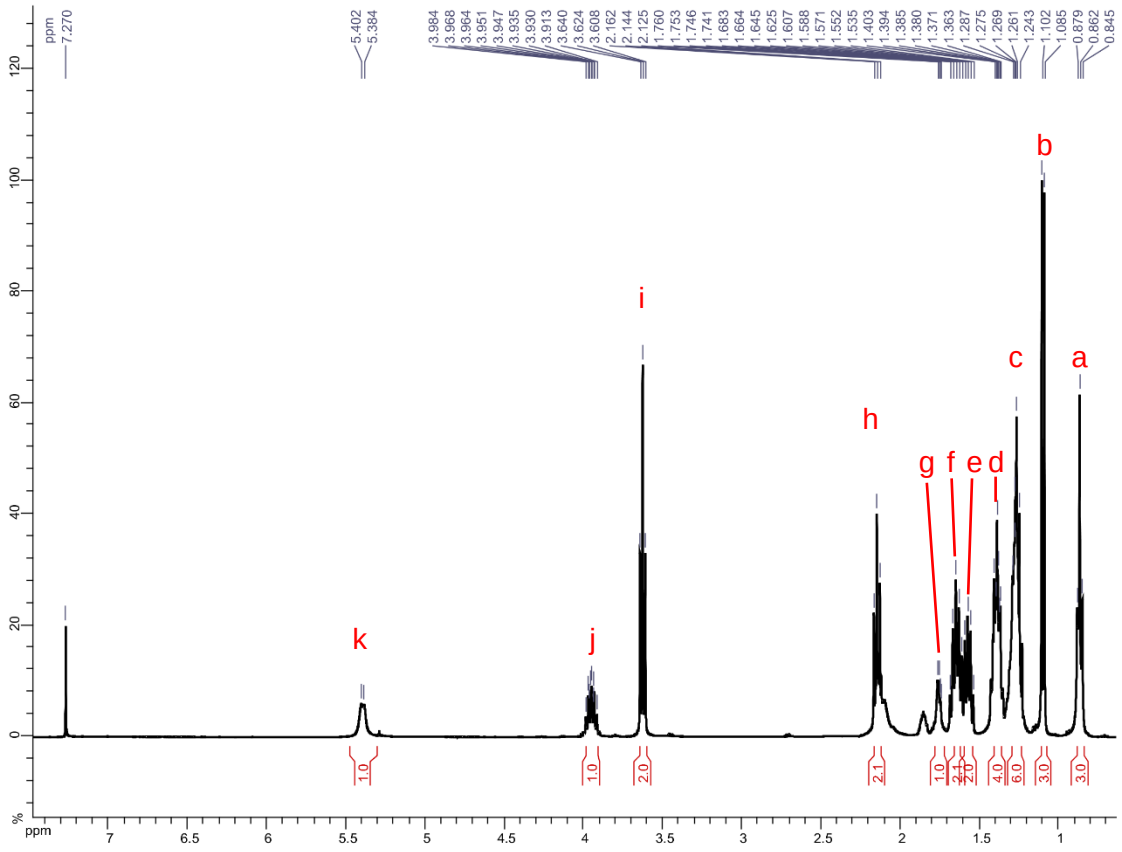

(R)-6-(heptan-2-ylamino)-6-oxohexyl methanesulfonate:

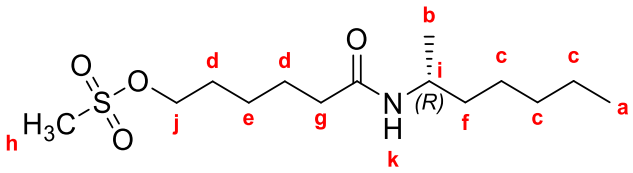

A solution of (R)-N-(heptan-2-yl)-6-hydroxyhexanamide (4 g, 17.4 mmol) and triethylamine (5.29 g, 52.3 mmol) in anhydrous THF (65 ml) was stirred under argon atmosphere at 0°C. Methanesulfonyl chloride (6 g, 52.3 mmol) was added dropwise. The mixture was stirred at room temperature overnight, poured in iced water (150 ml) and extracted in DCM. The organic phase was dried with $MgSO_4$, filtered and concentrated under reduced pressure. The desired compound was purified by column chromatography (ethyl acetate) and dried under reduced pressure and obtained as a white solid (4.12 g, 77%).

^{1}H-NMR (400 MHz, $CDCl_3$): δ [ppm] 5.21 (d, J= 7.9 Hz, 1H_k), 4.23 (t, J= 6.5 Hz, 2H_g), 3.97 (dtq, *J* = 8.6 Hz, 6.8 Hz, 6.4 Hz, 1H_j), 3.01 (s, 3H_h), 2.16 (t, J= 7.4 Hz, 2H_g), 1.78 (dq, J= 8.2 Hz, 6.5 Hz, 2H_f), 1.69 (t, J= 7.8 Hz, 2H_e), 1.44 (m, J= 7.3 Hz, 4H_d), 1.34-1.25 (m, 6H_c), 1.12 (d, J= 6.5 Hz, 3H_b), 0.88 (t, J= 6.6 Hz, 3H_a).

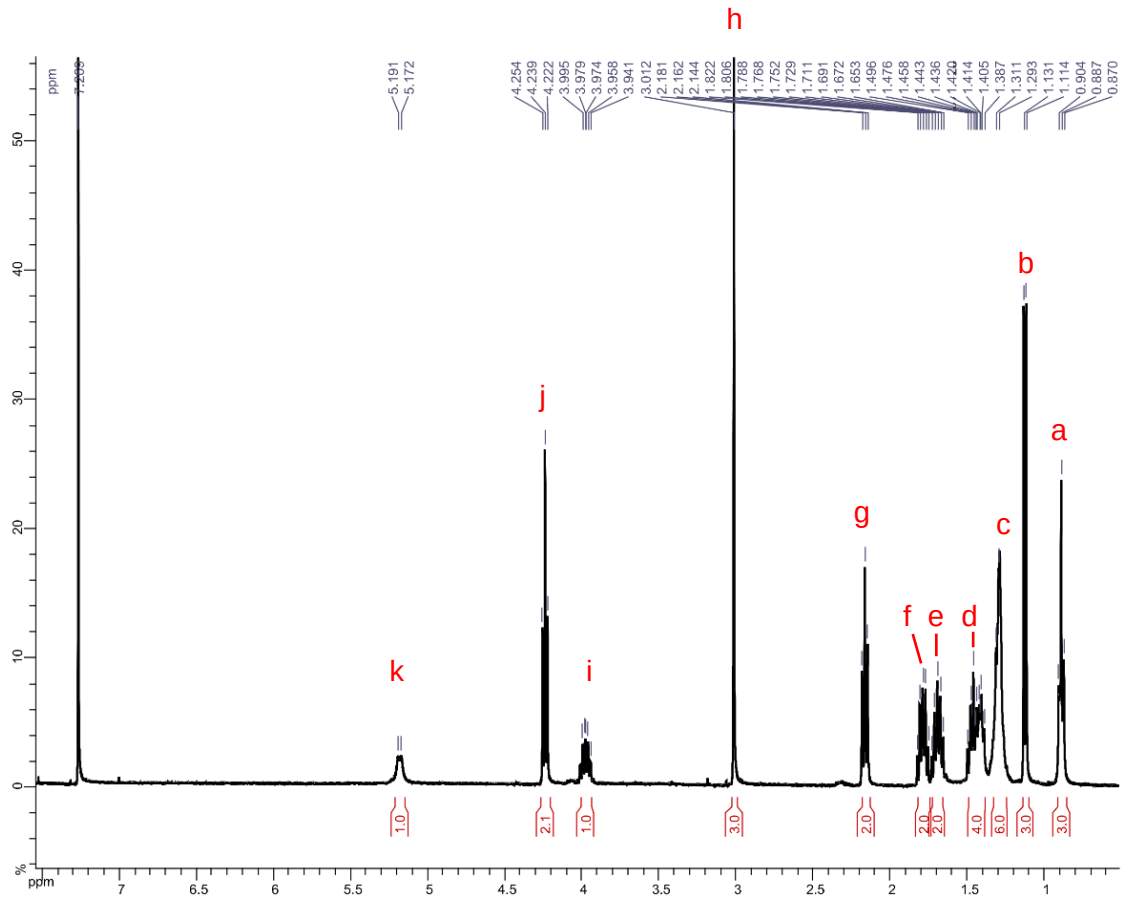

3,6-di(thiophen-2-yl)-2,5-dihydropyrrolo[3,4-c]pyrrole-1,4-dione (TDPP):

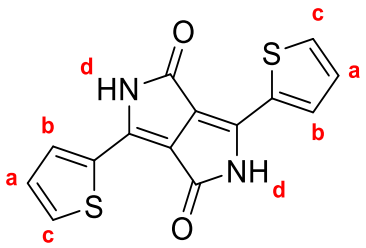

A solution of 2-thiophenecarbonitrile (10.4 g, 95 mmol) and potassium tert-butoxyde (12.3 g, 109 mmol) was stirred under argon in *tert*-amyl alcohol (200ml) at 120°C. Diethyl succinate (8.25g, 47mmol) was then added dropwise. The solution was stirred at 120 °C overnight and then cooled down to room temperature. The mixture was neutralized with 5 ml of concentrated acetic acid while being vigorously stirred for two hours at room temperature. The crude was filtered and washed several times with MeOH and dried to afford **TDPP** as a dark red solid (11.6 g, 82 %).

^{1}H-NMR (400 MHz, DMSO) δ [ppm]: 11.10 (s, 2H$_d$), 8.22 (d, J = 3.3 Hz, 2H$_c$); 7.88 (d, J = 4.7 Hz, 2H$_b$); 7.27 (t, J = 4.7 Hz, 2H$_a$).

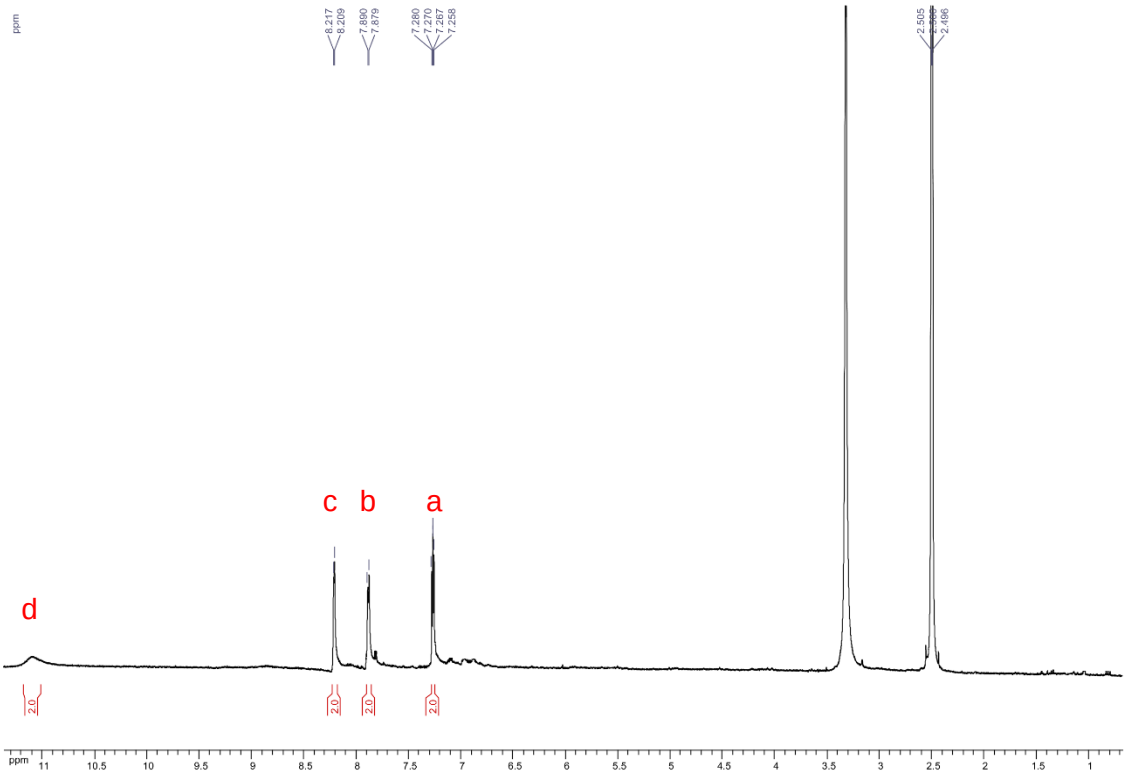

6,6'-(1,4-dioxo-3,6-di(thiophen-2-yl)pyrrolo[3,4-c]pyrrole-2,5(1H,4H)-diyl)bis(N-hexylhexanamide) (DPPBA):

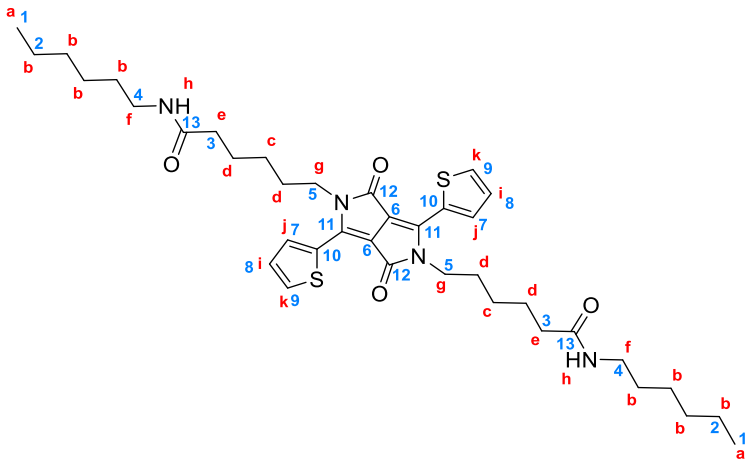

A suspension of **TDPP** (2 g, 6.8 mmol) in anhydrous DMF (150 ml) was stirred under argon atmosphere at 120°C. Cesium carbonate (5.4 g, 16.5 mmol) was added progressively. The mixture was stirred for 1h at 120°C then a solution of 6-(hexylamino)-6-oxohexyl methanesulfonate (12.24 g, 42 mmol) in anhydrous DMF was added dropwise. The solution was stirred overnight at 120°C and was cooled down to room temperature. The crude was

added to distilled water (600ml) and extracted with DCM. After collecting the organic phase, the solvent was removed under vacuum and the product was purified by column chromatography (DCM:Cyclohexane 50:50) to afford **DPPBA** as a purple solid (438 mg, 10%).

^{1}H-NMR (400 MHz, $CDCl_3$) δ [ppm]: 8.91 (dd, J = 4.0 Hz, 1.1Hz, $2H_k$), 7.66 (dd, J = 5.0 Hz, 1.1 Hz, $2H_j$), 7.29 (dd, J = 5.0 Hz, 4.0 Hz, $2H_i$), 5.48 (m, $2H_h$), 4.09 (t, J = 7.7 Hz, $4H_g$), 3.23 (q, J = 6.7 Hz, $4H_f$), 2.18 (t, J = 7.6 Hz, $4H_e$), 1.79-1.69 (m, $8H_d$), 1.48-1.45 (m, $4H_c$), 1.32-1.27 (m, $16H_b$), 0.89 (t, J = 6.9 Hz, $6H_a$).

^{13}C-NMR (400 MHz, $CDCl_3$) δ [ppm]: 172.8 ($2C_{13}$), 161.6 ($2C_{12}$), 140.2 ($2C_{11}$), 135.5 ($2C_{10}$), 131.1 ($2C_9$), 129.9 ($2C_8$), 128.8 ($2C_7$), 107.9 ($2C_6$), 42.0 ($2C_5$), 39.7 ($2C_4$), 36.7 ($2C_3$), 31.6, 29.8, 29.7, 26.7, 26.5, 25.4, 22.7 ($2C_2$), 14.2 ($2C_1$).

HRMS (ESI) m/z 695.3659 (MH^+)

Elemental analysis. Found: C, 64.88 %; H, 7.88 %; N, 8.06 %. Calculated: C, 65.67 %, H, 7.83 %; N, 8.06 %.

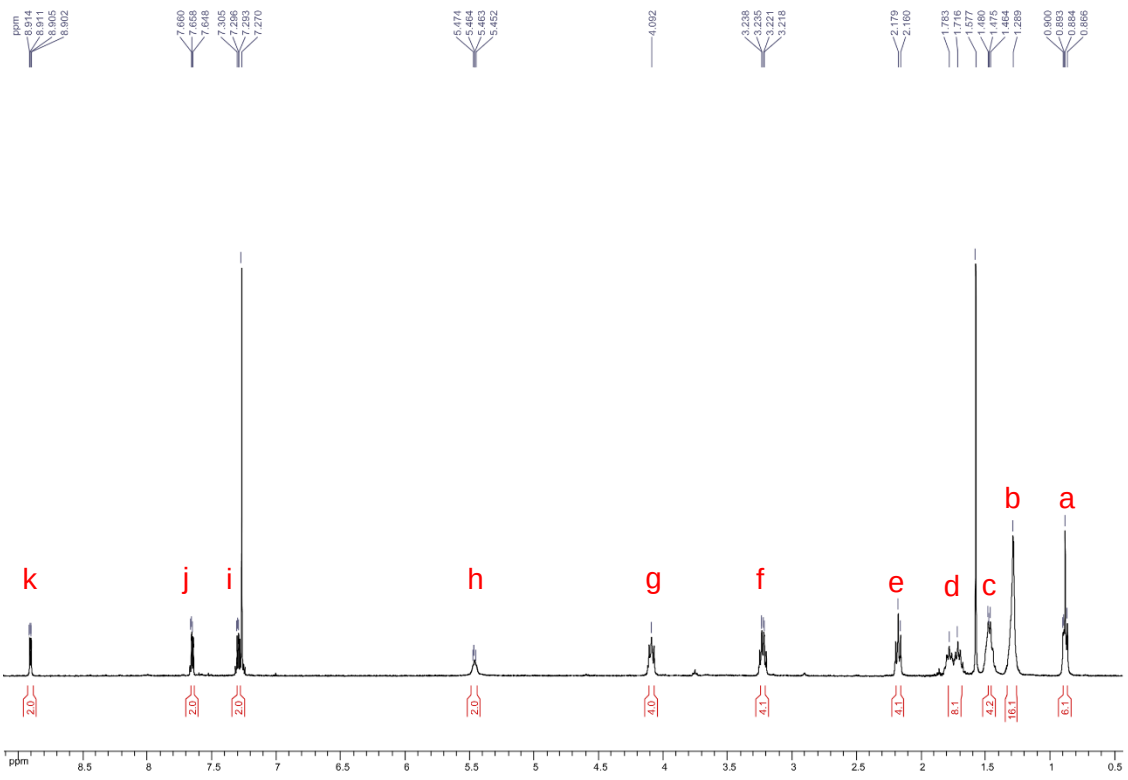

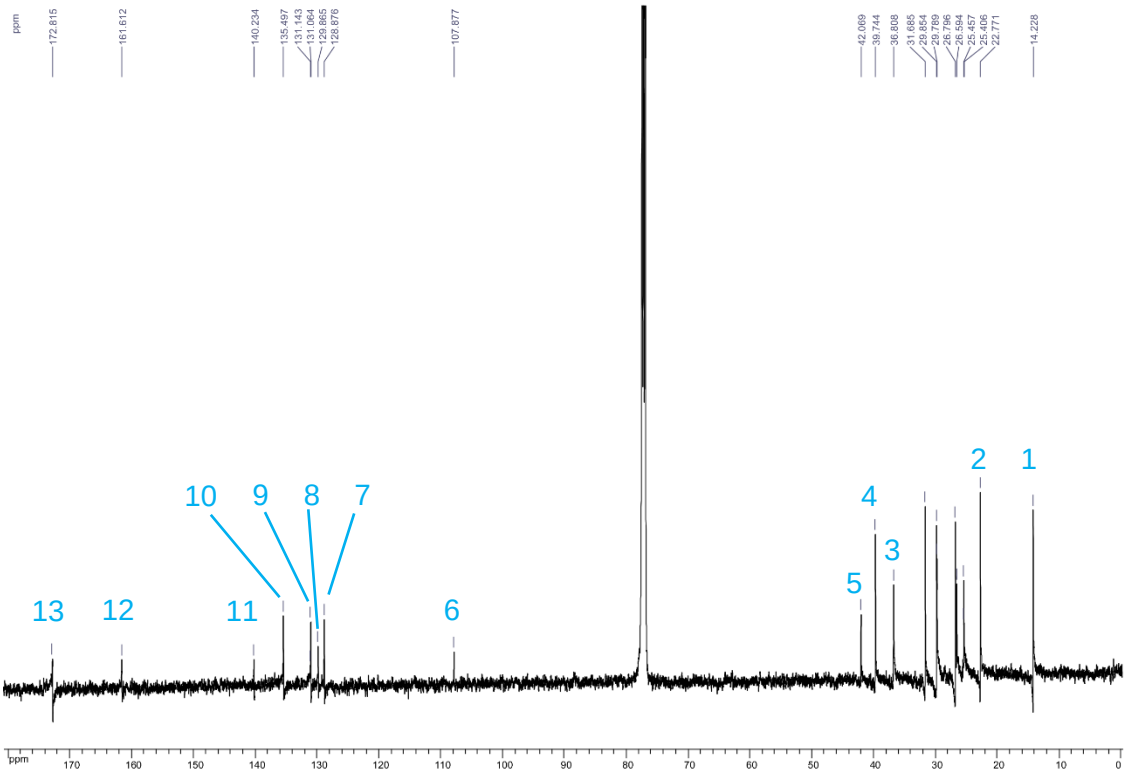

Mass Spectrum HR Report

Analysis Info

Analysis Name	D:\Data\SMasse\2017\12_Decembre2017\F01407SK.d	Acquisition Date	12/7/2017 11:22:37 AM
Method	Tune_pos_Mid.m	Operator	BDAL@DE
Sample Name	SM22 DPP Bisamide	Instrument	micrOTOF II 8213750.1045
Comment			1

Acquisition Parameter

Source Type	ESI	Ion Polarity	Positive	Set Corrector Fill	59.0 V
n/a	n/a	n/a	n/a	n/a	n/a
Scan Begin	50 m/z	n/a	n/a	Set Reflector	1800.0 V
Scan End	3000 m/z	n/a	n/a	Set Flight Tube	8600.0 V
		n/a	n/a	Set Detector TOF	1953.3 V

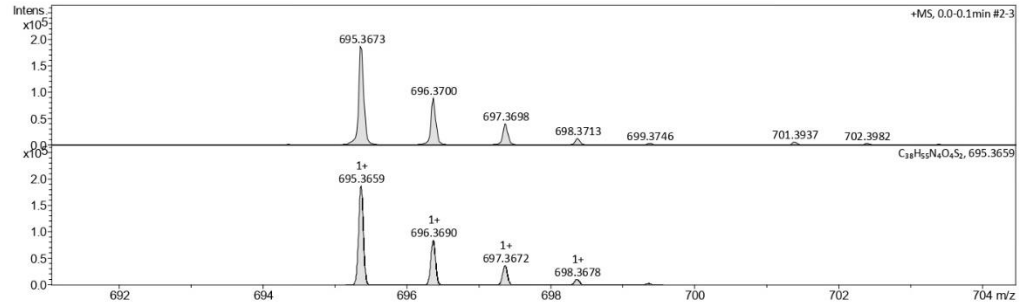

Meas. m/z	#	Ion	Formula	m/z err [ppm]	Mean err [ppm]	rdb	N-Rule	e⁻ Conf	mSigma	Std I	Std Mean m/z	Std I	VarNorm	Std m/z	Diff Std	Comb Dev
695.367300	1	C38H55N4O4S2	695.365925	-2.0	-3.6	13.5	ok	even	14.6	21.8	n.a.	n.a.	n.a.	n.a.		

6,6'-(1,4-dioxo-3,6-di(thiophen-2-yl)pyrrolo[3,4-c]pyrrole-2,5(1H,4H)-diyl)bis(N-((S)-heptan-2-yl)hexanamide) (S)-DPPBA:

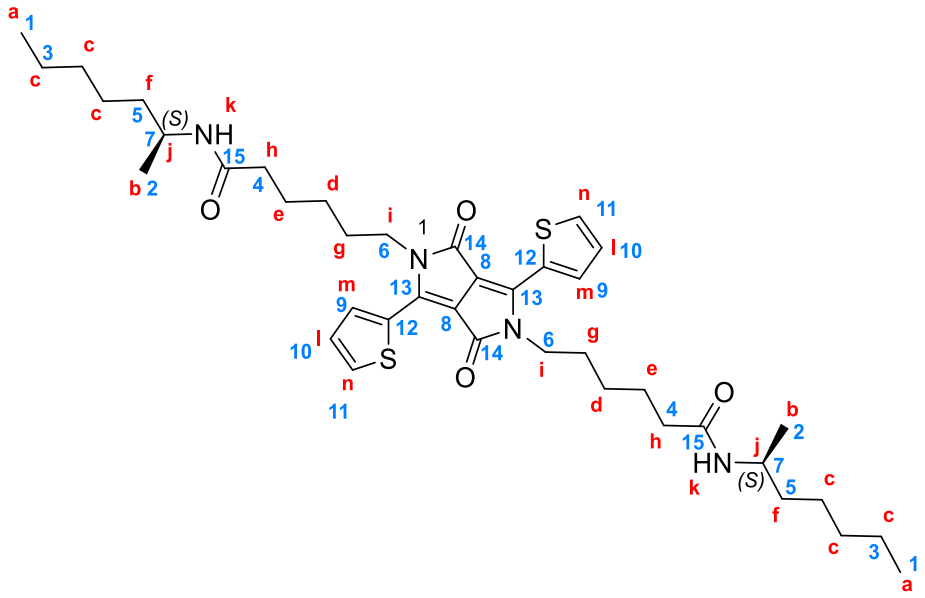

A suspension of **TDPP** (650 mg, 2 mmol) in anhydrous DMF (15 ml) was stirred under argon atmosphere at 120°C. Cesium carbonate (2.17 g, 6.62 mmol) was added progressively. The mixture was stirred for 1h at 120°C and then a solution of (S)-6-(heptan-2-ylamino)-6-oxohexyl methanesulfonate (2 g, 6.5 mmol) in anhydrous DMF was added dropwise. The solution was stirred overnight at 120°C and cooled down to room temperature to be then dropped in distilled water (600ml). The crude was extracted with DCM. After collecting the organic phase, the solvent was removed under vacuum and the product was purified by column chromatography (DCM:Cyclohexane 50:50) to afford **(S)-DPPBA** as a purple solid (150 mg, 9%).

^{1}H-NMR (400 MHz, $CDCl_3$) δ [ppm]: 8.91 (dd, J= 3.9 Hz, 1.0 Hz, 2 H_n), 7.65 (dd, J= 5.0 Hz, 1.0 Hz, 2H_m), 7.3 (t, J= 4.5 Hz, 2H_l), 5.23 (d, J= 8.6 Hz, 2H_k), 4.09 (t, J= 7.7 Hz, 4H_j), 3.97 (m, J=5.5 Hz, 2H_i), 2.16 (t, J= 7.6 Hz, 4H_h), 1.79 (m, J= 7.5 Hz, 4H_g), 1.71 (m, J= 7.5 Hz, 4H_f), 1.48 (m, J= 3.9 Hz, 4H_e), 1.42-1.38 (m, 4H_d), 1.33-1.27 (m, 12 H_c), 1.11 (d, J= 6.6 Hz, 6H_b), 0.88 (t, J= 6.7 Hz, 6H_a).

^{13}C-NMR (500 MHz, $CDCl_3$) δ [ppm]: 171.9 (2C_{15}), 161.4 (2C_{14}), 140.0 (2C_{13}), 135.3 (2C_{12}), 130.8 (2C_{11}), 129.7 (2C_{10}), 128.7 (2C_9), 107.7 (2C_8), 45.3 (2C_7), 42.0 (2C_6), 37.0 (2C_5), 36.8 (2C_4), 31.8, 29.7, 26.5, 25.9, 25.5, 22.6 (2C_3), 21.1 (2C_2), 14.1 (2C_1).

HRMS (ESI) m/z 723.3972 (MH^+)

Elemental analysis. Found: C, 66.01 %; H, 8.07 %; N, 7.63 %. Calculated: C, 66.45 %; H, 8.09 %; N, 7.75 %.

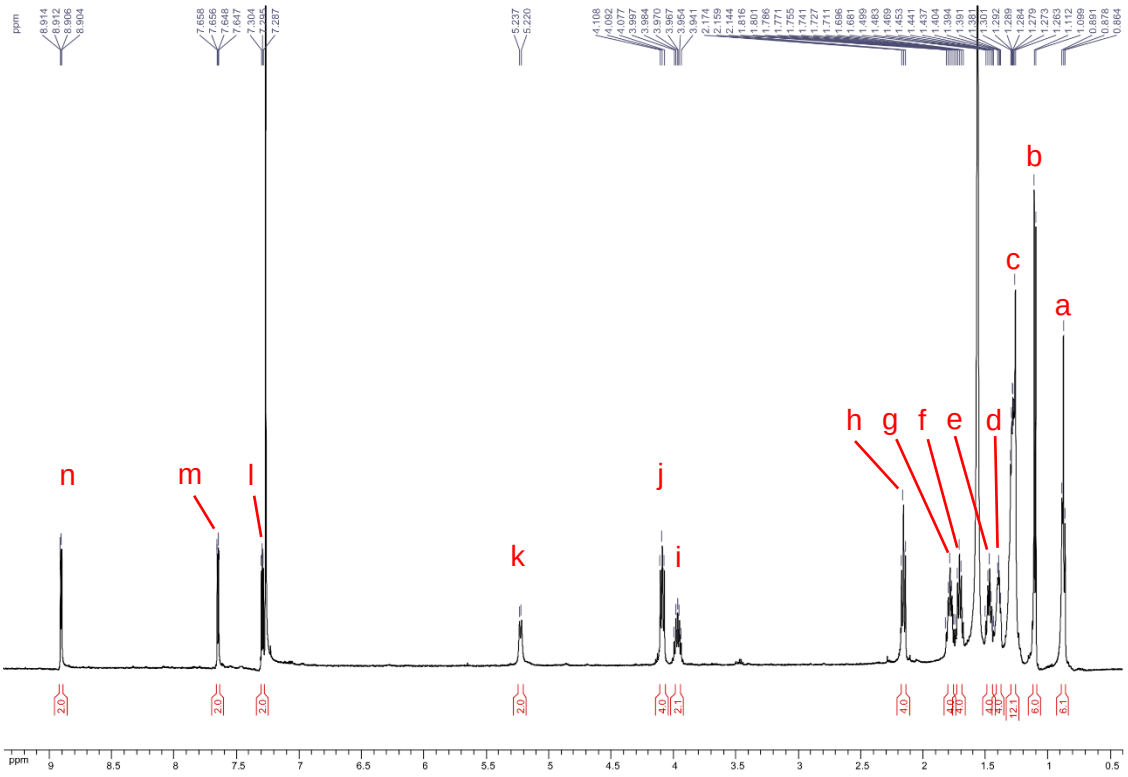
n
m
l
k
j
i
h
g
f
e
d
c
b
a

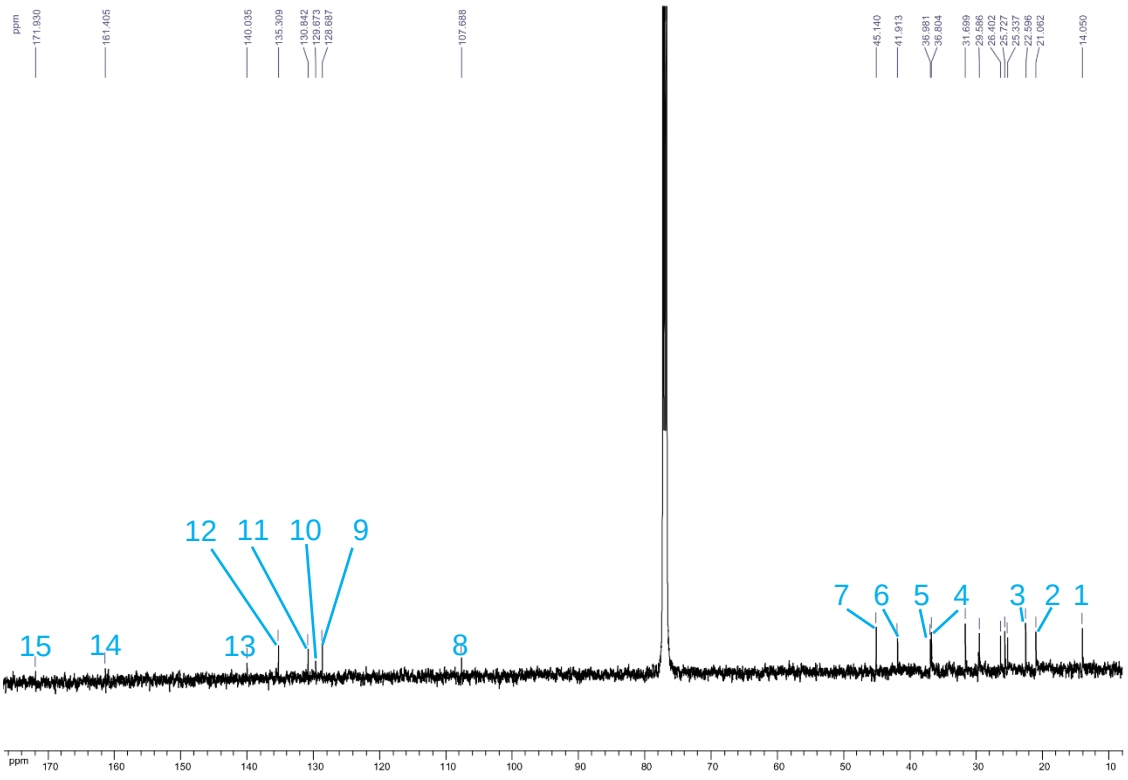
15
14
13
12
11
10
9
8
7
6
5
4
3
2
1

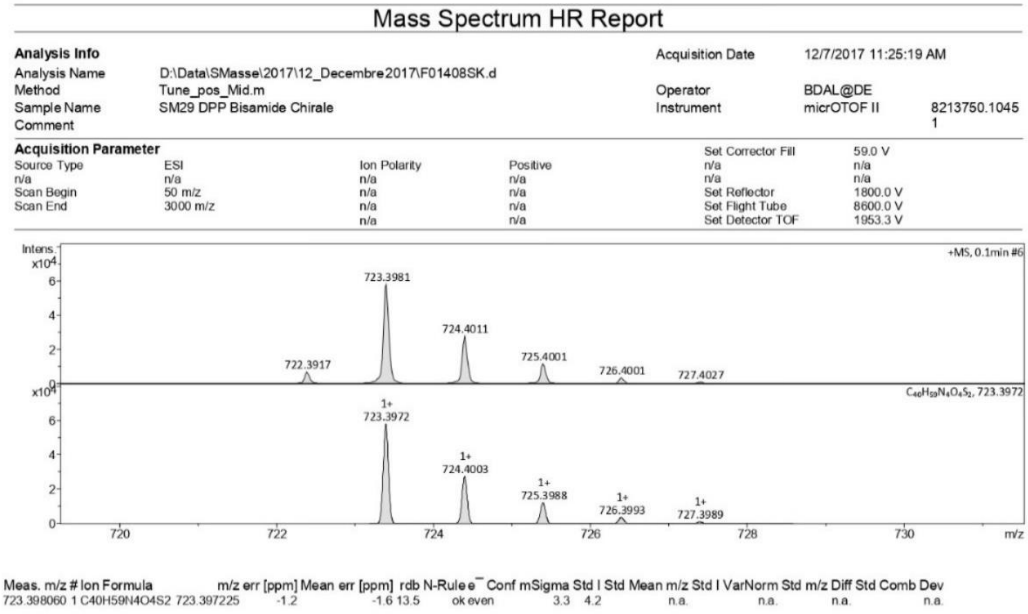

6,6'-(1,4-dioxo-3,6-di(thiophen-2-yl)pyrrolo[3,4-c]pyrrole-2,5(1H,4H)-diyl)bis(N-((R)-heptan-2-yl)hexanamide) (R)-DPPBA:

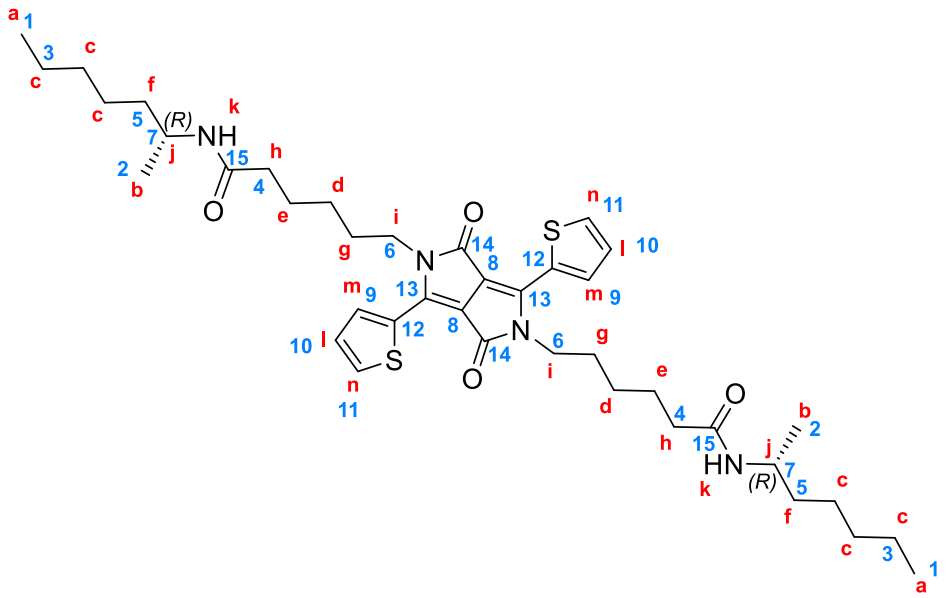

A suspension of **TDPP** (500 mg, 1.66 mmol), cesium carbonate (1.35 g, 4.15 mmol) and (R)-6-(heptan-2-ylamino)-6-oxohexyl methanesulfonate (0.95 g, 4.15 mmol) in anhydrous DMF (1 ml) under stirring was reacted in the microwave. The reaction was performed in two steps in the microwave at 150 W, first for 2h at 20°C and then for 0.5 h at 70°C. Once it was cooled down to room temperature, the mixture was dropped in distilled water (300ml) and the crude was extracted with DCM. After collecting the organic phase, the solvent was removed under

vacuum and the product was purified by column chromatography (DCM:Cyclohexane 50:50) to afford **(R)-DPPBA** as a purple solid (265 mg, 22%).

^{1}H-NMR (400 MHz, $CDCl_3$) δ [ppm]: 8.91 (dd, J= 3.9 Hz, 1.1 Hz, 2 H_n), 7.65 (dd, J= 5.0 Hz, 1.0 Hz, 2H_m), 7.3 (dd, J= 5.0 Hz, 4.0 Hz, 2H_l), 5.22 (d, J= 8.7 Hz, 2H_k), 4.09 (t, J= 7.7 Hz, 4H_j), 3.97 (m, J=7.1 Hz, 2H_i), 2.16 (t, J= 7.6 Hz, 4H_h), 1.79 (m, J= 6.2 Hz, 4H_g), 1.71 (m, J= 5.8 Hz, 4H_f), 1.48 (md, J= 7.8 Hz, 2.5 Hz, 4H_e), 1.43-1.37 (m, 4H_d), 1.33-1.23 (m, 12 H_c), 1.11 (d, J= 6.6 Hz, 6H_b), 0.88 (t, J= 6.6 Hz, 6H_a).

^{13}C-NMR (400 MHz, $CDCl_3$) δ [ppm]: 172.1 (2C_{15}), 161.4 (2C_{14}), 140.0 (2C_{13}), 135.4 (2C_{12}), 130.9 (2C_{11}), 129.7 (2C_{10}), 128.7 (2C_9), 107.7 (2C_8), 45.2 (2C_7), 41.9 (2C_6), 37.0 (2C_5), 36.8 (2C_4), 31.8, 29.7, 26.5, 25.9, 25.5, 22.6 (2C_3), 21.0 (2C_2), 14.1 (2C_1).

HRMS (ESI+) m/z: 723.3947 (MH+)

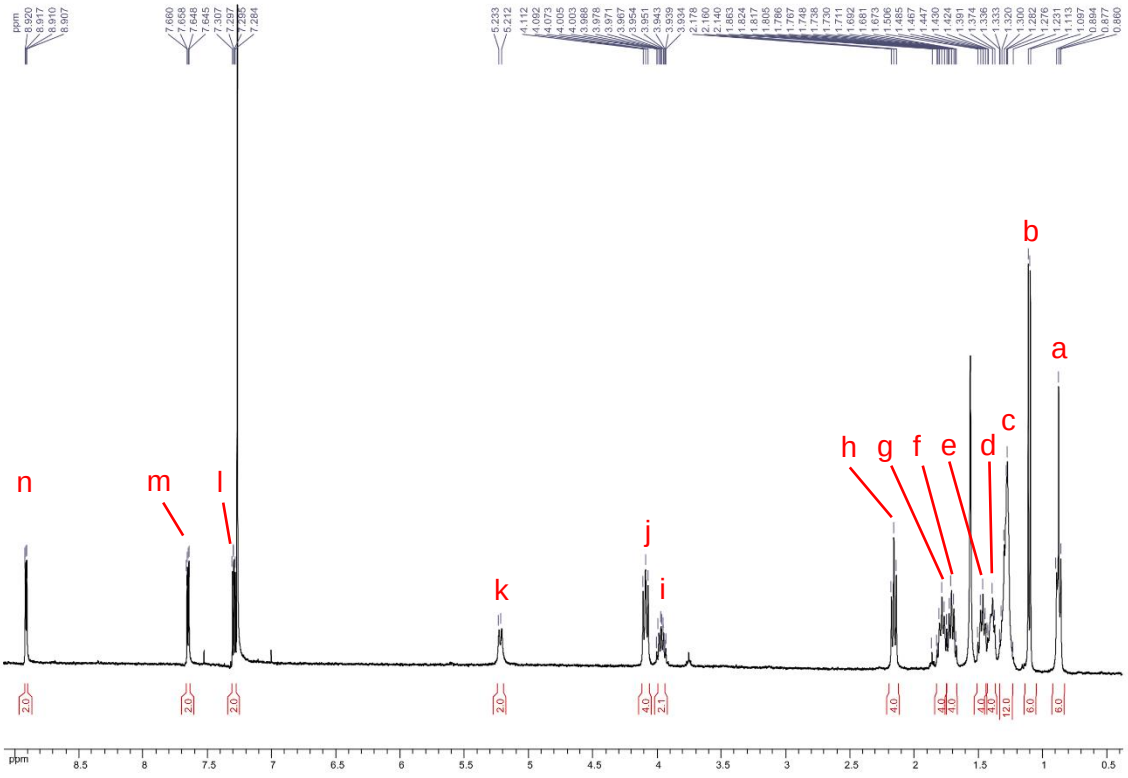

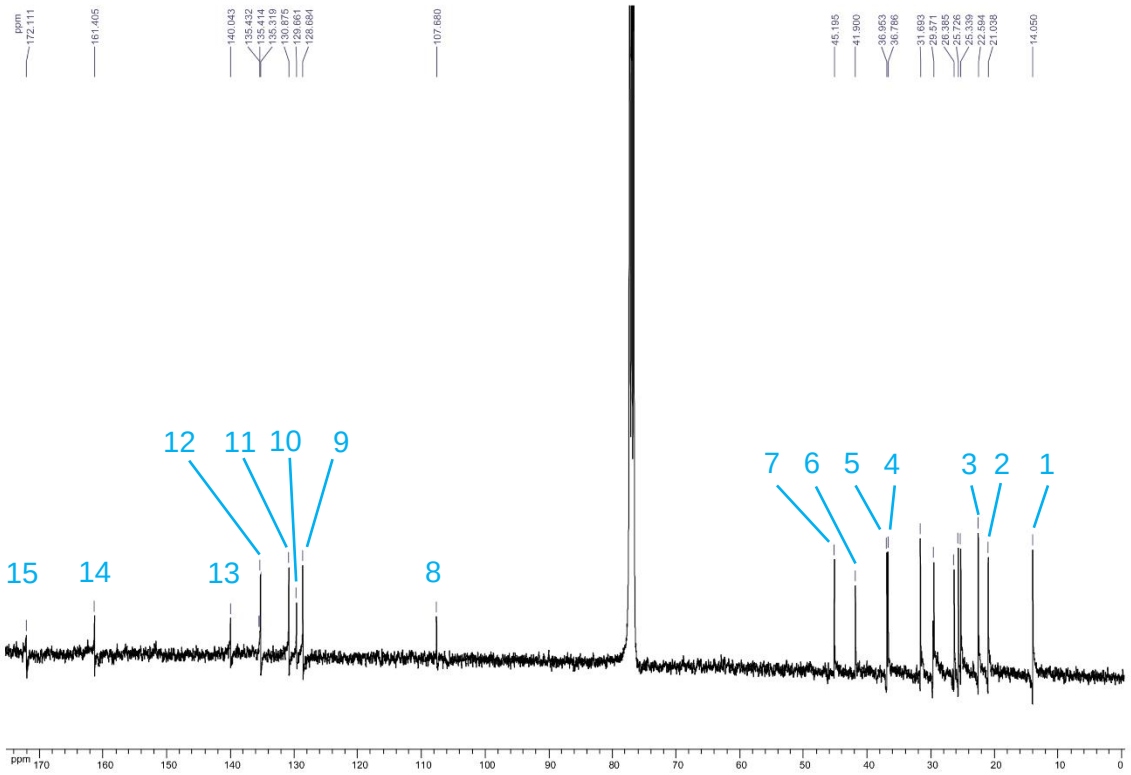

Mass Spectrum HR Report

Analysis Info

Analysis Name	D:\Data\SMasse\2018\1012_Septembre 2018\G01801SK.d	Acquisition Date	16/09/2018 09:57:26 AM
Method	Tune_pos_Mid.m		
Sample Name	RAR cDPPBA-R	Operator	BDAL@DE
Comment		Instrument	micrOTOF II 8213750.1045 1

Acquisition Parameter

Source Type	ESI	Ion Polarity	Positive	Set Corrector Fill	59.0 V
n/a	n/a	n/a	n/a	n/a	n/a
Scan Begin	50 m/z	n/a	n/a	Set Reflector	1800.0 V
Scan End	3000 m/z	n/a	n/a	Set Flight Tube	8600.0 V
		n/a	n/a	Set Detector TOF	1953.3 V

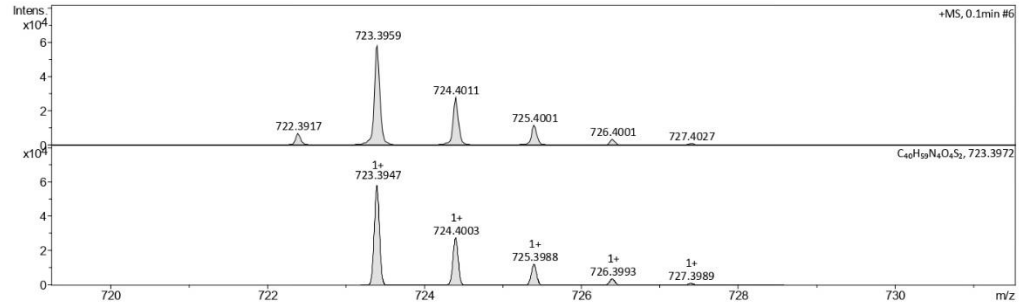

Meas. m/z	#	Ion Formula	m/z err [ppm]	Mean err [ppm]	rdb	N-Rule	e⁻ Conf	mSigma	Std I	Std Mean m/z	Std I	VarNorm Std m/z	Diff Std Comb	Dev
723.398060	1	C40H59N4O4S2	723.397225	-1.2	-1.6	13.5	ok	even	3.3	4.2	n.a.	n.a.	n.a.	n.a.

IV. References

[1] E. H. A. Beckers, P. A. van Hal, A. P. H. J. Schenning, A. El-ghayoury, E. Peeters, M. T. Rispens, J. C. Hummelen, E. W. Meijer, R. A. J. Janssen, *J. Mater. Chem.* **2002**, *12*, 2054–2060.

[2] K. W. Cheng, C. S. C. Mak, W. K. Chan, A. M. Ching Ng, A. B. Djurišić, *J. Polym. Sci. A Polym. Chem.* **2008**, *46*, 1305–1317.

[3] T.-C. Liang, I.-H. Chiang, P.-J. Yang, D. Kekuda, C.-W. Chu, H.-C. Lin, *J. Polym. Sci. A Polym. Chem.* **2009**, *47*, 5998–6013.

[4] K.-M. Park, L. Lindoy, *From Molecules to Nanomaterials* **n.d.**

[5] M. Irimia-Vladu, Y. Kanbur, F. Camaioni, M. E. Coppola, C. Yumusak, C. V. Irimia, A. Vlad, A. Operamolla, G. M. Farinola, G. P. Suranna, N. González-Benitez, M. C. Molina, L. F. Bautista, H. Langhals, B. Stadlober, E. D. Głowacki, N. S. Sariciftci, *Chem. Mater.* **2019**, *31*, 6315–6346.

[6] Z. Xiao, K. Sun, J. Subbiah, S. Ji, D. J. Jones, W. W. H. Wong, *Sci Rep* **2015**, *4*, 5701.

[7] K.-H. Kim, H. Yu, H. Kang, D. J. Kang, C.-H. Cho, H.-H. Cho, J. H. Oh, B. J. Kim, *Journal of Materials Chemistry A* **2013**, *1*, 14538.

[8] R. J. Kumar, J. Subbiah, A. B. Holmes, *Beilstein Journal of Organic Chemistry* **2013**, *9*, 1102–1110.

[9] T. Aytun, L. Barreda, A. Ruiz-Carretero, J. A. Lehrman, S. I. Stupp, *Chemistry of Materials* **2015**, *27*, 1201–1209.

[10] S. Militzer, T. M. P. Tran, P. J. Mésini, A. Ruiz-Carretero, *ChemNanoMat* **2018**, *4*, 790–795.

[11] “Hydrogen bonding ability of the amide group,” DOI 10.1021/ja00819a013can be found under https://pubs.acs.org/doi/pdf/10.1021/ja00819a013, **n.d.**

[12] W.-W. Tsai, I. D. Tevis, A. S. Tayi, H. Cui, S. I. Stupp, *The Journal of Physical Chemistry B* **2010**, *114*, 14778–14786.

[13] S. Ghosh, S. Cherumukkil, C. H. Suresh, A. Ajayaghosh, *Advanced Materials* **2017**, *29*, 1703783.

[14] P. N. Ghosh, *Solid State Communications* **1976**, *19*, 639–642.

[15] R. Kaneko, T. H. Chowdhury, K. Sugawa, J.-J. Lee, J. Otsuki, A. Islam, *Solar Energy* **2019**, *194*, 248–253.

[16] A. K. Jena, Y. Numata, M. Ikegami, T. Miyasaka, *J. Mater. Chem. A* **2018**, *6*, 2219–2230.

[17] F. Würthner, *Chem. Commun.* **2004**, 1564–1579.

[18] S. Ghosh, X.-Q. Li, V. Stepanenko, F. Würthner, *Chemistry – A European Journal* **2008**, *14*, 11343–11357.

[19] G. Ghosh, M. Paul, T. Sakurai, W. Matsuda, S. Seki, S. Ghosh, *Chem. Eur. J.* **2018**, *24*, 1938–1946.

[20] M. Liu, L. Zhang, T. Wang, *Chem. Rev.* **2015**, *115*, 7304–7397.

[21] N. M. Maier, P. Franco, W. Lindner, *Journal of Chromatography A* **2001**, *906*, 3–33.

[22] J. Gal, *Chirality* **2012**, *24*, 959–976.

[23] T. Aida, E. W. Meijer, S. I. Stupp, *Science* **2012**, *335*, 813–817.

[24] A. P. H. J. Schenning, P. Jonkheijm, E. Peeters, E. W. Meijer, *J. Am. Chem. Soc.* **2001**, *123*, 409–416.
[25] X. Shang, I. Song, H. Ohtsu, Y. H. Lee, T. Zhao, T. Kojima, J. H. Jung, M. Kawano, J. H. Oh, *Adv. Mater.* **2017**, *29*, 1605828.
[26] F. Würthner, Z. Chen, F. J. M. Hoeben, P. Osswald, C.-C. You, P. Jonkheijm, J. v. Herrikhuyzen, A. P. H. J. Schenning, P. P. A. M. van der Schoot, E. W. Meijer, E. H. A. Beckers, S. C. J. Meskers, R. A. J. Janssen, *J. Am. Chem. Soc.* **2004**, *126*, 10611–10618.
[27] A. Ruiz-Carretero, N. R. Ávila Rovelo, S. Militzer, P. J. Mésini, *J. Mater. Chem. A* **2019**, *7*, 23451–23475.
[28] Y. Yan, Y. Zhang, W. Hu, Z. Wei, *Chem. Eur. J.* **2010**, *16*, 8626–8630.
[29] Y. Yan, R. Wang, X. Qiu, Z. Wei, *J. Am. Chem. Soc.* **2010**, *132*, 12006–12012.
[30] A. R. A. Palmans, E. W. Meijer, *Angew. Chem. Int. Ed.* **2007**, *46*, 8948–8968.
[31] L. Brunsveld, A. P. H. J. Schenning, M. A. C. Broeren, H. M. Janssen, J. A. J. M. Vekemans, E. W. Meijer, *Chem. Lett.* **2000**, *29*, 292–293.
[32] A. J. Wilson, J. van Gestel, R. P. Sijbesma, E. W. Meijer, *Chem. Commun.* **2006**, 4404.
[33] J. J. van Gorp, J. A. J. M. Vekemans, E. W. Meijer, *J. Am. Chem. Soc.* **2002**, *124*, 14759–14769.
[34] T. Kim, T. Mori, T. Aida, D. Miyajima, *Chem. Sci.* **2016**, *7*, 6689–6694.
[35] M. M. Green, M. P. Reidy, R. D. Johnson, G. Darling, D. J. O'Leary, G. Willson, *J. Am. Chem. Soc.* **1989**, *111*, 6452–6454.
[36] J. Liu, Y. Zhang, H. Phan, A. Sharenko, P. Moonsin, B. Walker, V. Promarak, T.-Q. Nguyen, *Adv. Mater.* **2013**, *25*, 3645–3650.
[37] R. B. Zerdan, N. T. Shewmon, Y. Zhu, J. P. Mudrick, K. J. Chesney, J. Xue, R. K. Castellano, *Adv. Funct. Mater.* **2014**, *24*, 5993–6004.
[38] T. He, P. Leowanawat, C. Burschka, V. Stepanenko, M. Stolte, F. Würthner, *Adv. Mater.* **2018**, *30*, 1804032.
[39] M. Stolte, S.-L. Suraru, P. Diemer, T. He, C. Burschka, U. Zschieschang, H. Klauk, F. Würthner, *Adv. Funct. Mater.* **2016**, *26*, 7415–7422.
[40] K. Dhbaibi, L. Favereau, M. Srebro-Hooper, M. Jean, N. Vanthuyne, F. Zinna, B. Jamoussi, L. Di Bari, J. Autschbach, J. Crassous, *Chem. Sci.* **2018**, *9*, 735–742.
[41] P. A. Hume, J. P. Monks, F. Pop, E. S. Davies, R. C. I. MacKenzie, D. B. Amabilino, *Chem. Eur. J.* **2018**, *24*, 14461–14469.
[42] N. Avarvari, J. D. Wallis, *J. Mater. Chem.* **2009**, *19*, 4061.
[43] A. Iqbal, M. Jost, R. Kirchmayr, J. Pfenninger, A. Rochat, O. Wallquist, *Bulletin des Societes Chimiques Belges* **1988**, *97*, 615–644.
[44] A. Ruiz-Carretero, T. Aytun, C. J. Bruns, C. J. Newcomb, W.-W. Tsai, S. I. Stupp, *J. Mater. Chem. A* **2013**, *1*, 11674–11681.
[45] S. Loser, C. J. Bruns, H. Miyauchi, R. P. Ortiz, A. Facchetti, S. I. Stupp, T. J. Marks, *J. Am. Chem. Soc.* **2011**, *133*, 8142–8145.
[46] F. Pop, J. Humphreys, J. Schwarz, L. Brown, A. van den Berg, D. B. Amabilino, *New Journal of Chemistry* **2019**, DOI 10.1039/C9NJ01074B.
[47] J. Mizuguchi, A. C. Rochat, G. Rihs, *Berichte der Bunsengesellschaft für physikalische Chemie* **1992**, *96*, 607–619.
[48] J. Mizuguchi, *Berichte der Bunsengesellschaft für physikalische Chemie* **1993**, *97*, 684–693.

[49] G. Eaton, M. C. R. Symons, P. P. Rastogi, *J. Chem. Soc., Faraday Trans. 1* **1989**, *85*, 3257.
[50] S. Ghosh, R. Raveendran, A. Saeki, S. Seki, M. Namboothiry, A. Ajayaghosh, *ACS Appl. Mater. Interfaces* **2019**, *11*, 1088–1095.
[51] W. Matsuda, T. Sakurai, G. Ghosh, S. Ghosh, S. Seki, *J. Photopol. Sci. Technol.* **2018**, *31*, 91–99.
[52] Y. Tsutsui, H. Okamoto, D. Sakamaki, K. Sugiyasu, M. Takeuchi, S. Seki, *J. Phys. Chem. Lett.* **2018**, *9*, 3639–3645.
[53] S. Ghosh, S. Cherumukkil, C. H. Suresh, A. Ajayaghosh, *Adv. Mater.* **2017**, *29*, 1703783.

EXPANDING THE BISAMIDE FAMILY:

Influence of amide topology and increasing solubility

CHAPTER III

I. Introduction and objectives

Following the design of H-bonded derivatives to complete our library, we continued studying other parameters that impact the formation of H-bonds. In this case, we decided to increase solubility of the bisamide derivatives shown in Chapter II and additionally, we explored the amide topology impact on the self-assembly and electrical properties.

The bisamide **DPP** derivatives were designed containing additional alkyl chains to improve their solubility. In this chapter, the thiophene rings on the **DPP** were functionalized with hexyl chains, while keeping the same amide branch in the lactam rings (Figure III. 1).

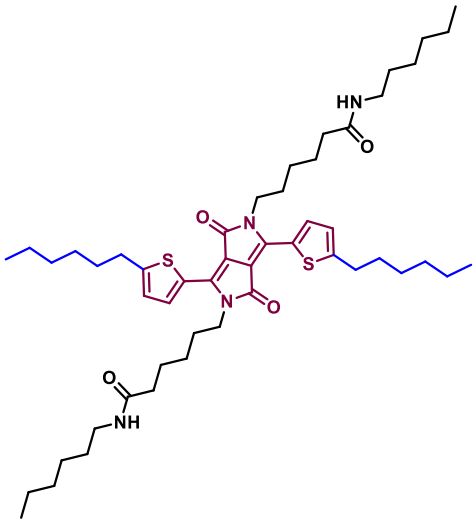

*Figure III. 1 Chemical structure of a bisamide **DPP** alkylated on the thiophenes.*

Additionally, a comparison of two **DPP** derivatives containing amide groups attached to the lactam rings through a six carbons alkyl linker with N- or C-centered topology, and hexyl alkyl tails in the thiophene rings (to provide solubility), with respect to the previously reported amide-containing **DPP** derivatives with unsubstituted thiophenes was performed.

Together with the two H-bonded derivatives, a **DPP** molecule having only hexyl alkyl tails as a control was also synthesized. The self-assembly processes of the N- and C-centered amide-containing **DPP** derivatives were once again followed with different spectroscopy and microscopy techniques, and the charge transport properties were studied with FP-TRMC. The results are compared to the control molecule and the positive role of H-bonds in the electronic properties was highlighted.

An important factor to consider when designing organic semiconductor devices is solubility, as they are often prepared through solution processing. Moreover, the solubility of the **DPP** derivatives previously synthesized by our group has frequently made difficult to perform experiments where high concentration in solution was required. Additionally, as discussed in chapter II, a lower solubility can be detrimental for the charge carrier pathways. Hence, improving their solubility became a necessity.

It was envisioned that one possible way to increase the solubility of the **DPP** core could be by adding alkyl chains to the thiophene rings. As one of the main objectives of using **DPP** as model system is to explore several derivatives and evaluate the effect of solubility in these compounds. Additionally, this step provided insight on how to synthesize **DPP** derivatives that bear flexible H-bonding groups that are not directly attached to the lactam ring (Figure III. 2).

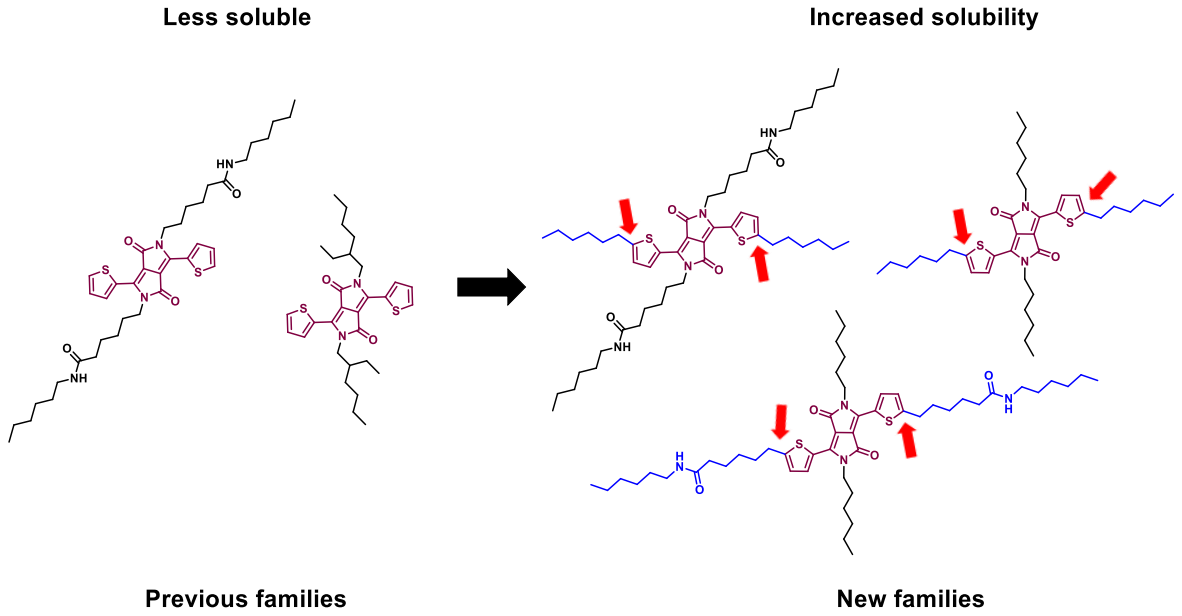

Figure III. 2 Structural comparison between previous and new envisioned **DPP** derivatives.

Apart from studying the influence of solubility, the topology of the amide (N- or C- centered) was evaluated; a subtle, but very important parameter able to change the self-assembly of a given system and hence, the properties.[1,2]

For instance, Philipps *et al* have compared the self-assembly behavior of a series of C_2- and C_3-symmetrical oligo(p-phenyleneethynylene)s (**OPEs**)[5], (Figure III. 3), differing only in the amide topology, N- or C-centered. They reported how the delicate interplay between H-bonding and preorganization determines the evolution and final outcome of supramolecular nanostructures. The investigations were first carried out on linear **OPEs** (1 and 2), and these results were then compared with those obtained for the C_3-symmetrical derivatives (3 and 4) to confirm the generalization of the trends found.

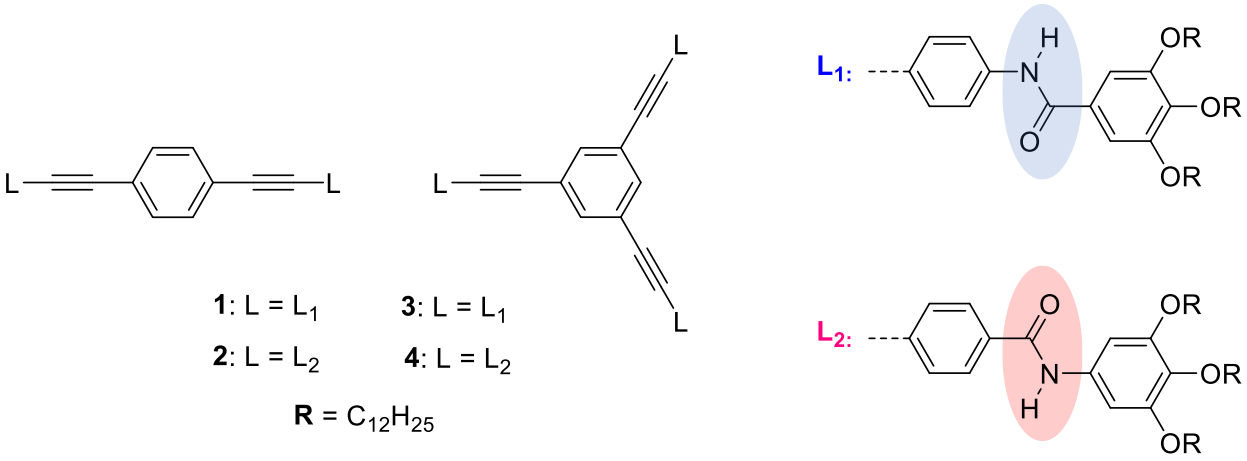

*Figure III. 3 Chemical structures of **OPEs 1–4**. The highlighted portions show the nature of amide connectivity, N-centered in blue and C-centered in pink.*Adapted.*[5]

The theory they presented along with the various experiments they performed, revealed how this subtle structural change brings about differences in their photophysical and supramolecular properties, such as molecular packing and aggregate morphology. One of their main findings was that a strong charge-transfer character for HOMO–LUMO excitations can significantly affect the emission characteristics in C-centered systems. Additionally, the N-centered molecules showed a much stronger HOMO–LUMO overlap than their C-centered counterparts, which is an indication of more allowed electronic transitions for the N-centered derivatives.

Furthermore, when variable-temperature UV/Vis studies were performed, significant differences in the optical properties caused by aggregation were observed for all molecules, especially when performed in a poor solvent such as methylcyclohexane. For instance, the emission studies of **OPE 1** showed a slight fluorescence enhancement when the temperature was decreased. Moreover, for both N-centered **OPEs 1** and **3**, a blue shift of the absorption maximum along with the appearance of a red-shifted shoulder was observed, which are in accordance with a face-to-face stacking of the **OPE** units with a slightly twisted arrangement to favor H-bonding interactions.

On the other hand, the measurements of the C-centered **OPEs** in MCH gave rather different observations, for instance, unlike **OPE 1**, **OPE 2** displays no increase in absorption. Additionally, AFM revealed a dissimilar interplay of non-covalent interactions, which resulted in distinct nanostructure morphologies for **OPE 1** and **OPE 2**. While **OPE 1** self-assembled into highly entangled fibers of several microns in length, **OPE 2** formed considerably smaller round-shaped discrete aggregates.

Another system where the effect of the amide topology was evaluated was in the local molecular packing of different benzene-1,3,5-tricarboxamides with either C-centered or N-centered amide groups (Figure III. 4).[2] It was shown that the ^{1}H-NMR spectra vary between the solution and the solid state due to the shielding impact of neighboring molecules and intramolecular polarization effects. This study also demonstrated that solid-state NMR in

combination with Car–Parrinello Molecular Dynamics simulations and DFT calculations of NMR chemical shift is highly suited to elucidate the geometry of supramolecular assemblies. Furthermore, solid-state NMR provided unique insight into the dynamics of the N-centered derivative.

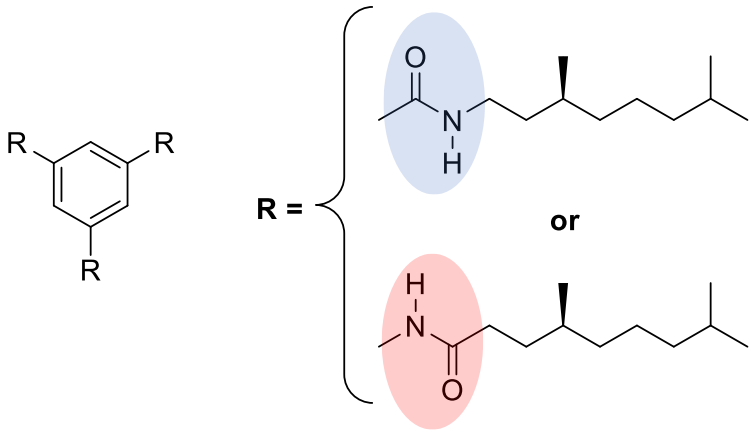

Figure III. 4 Chemical structure of the benzene-1,3,5-tricarboxamides derivatives with different amide topology.

These examples provided evidence on how changes in amide topology can influence the different properties of supramolecular assemblies. In the family described in this chapter, the position of the H-bonding units is maintained in the lactam rings while in the next chapter the impact of exchanging the H-bonding position within the conjugated structure will be explored.

In this sense, a succinic cyclization approach was envisioned, it consists of alkylating a thiophene ring and further functionalize it to finally perform the cyclization reaction that is normally used to obtain the **DPP** core. Particularly, I took care of the synthesis of the C-centered amide, while another PhD student involved in the project, synthesized the N-center analogue. Together we characterized the self-assembly and optical properties. This synthesis is discussed in the next section.

II. Results and Discussion

II.1) Synthesis

Molecules **HDPPBA-C** and **HDPPBA-N** were synthesized *via* a succinic cyclization approach (Scheme III. 1) starting with the functionalization of the thiophene ring and finalizing with a cyclization reaction to form the **DPP** core. Initially, the thiophene ring was alkylated with hexyl bromide (**1**) in high yield, and subsequently, a nitrile group was introduced in position 5 after replacement of a bromine atom obtaining (**2**) (Scheme III. 1). Then 5-hexylthiophene-2-carbonitrile (**3**) reacted with diethylsuccinate in the presence of potassium *t*-butoxide to form the hexyl-functionalized thiophene-capped **DPP** main core (**4**) in 72% yield. In a last step, the lactam rings of the **DPP** were alkylated with the amide-containing branches that were synthesized in parallel.

The mesylated carbon-centered amide (-CONH) branch was synthesized as described in chapter II. On the other hand, Schotten-Baumann conditions were followed to obtain the N-centered amide (-NHCO) branch (Scheme III. 2). In this case the acylation of 5-amino-1-pentanol with heptanoyl chloride was carried out in a biphasic system of dichloromethane and a basic aqueous solution. The use of base drives the equilibrium of the reaction towards the formation of the amide, obtained in high yield (91%). Next, the N-centered amide was treated with methanesulfonyl chloride to achieve the mesylated amide-containing branch (Scheme III. 2).

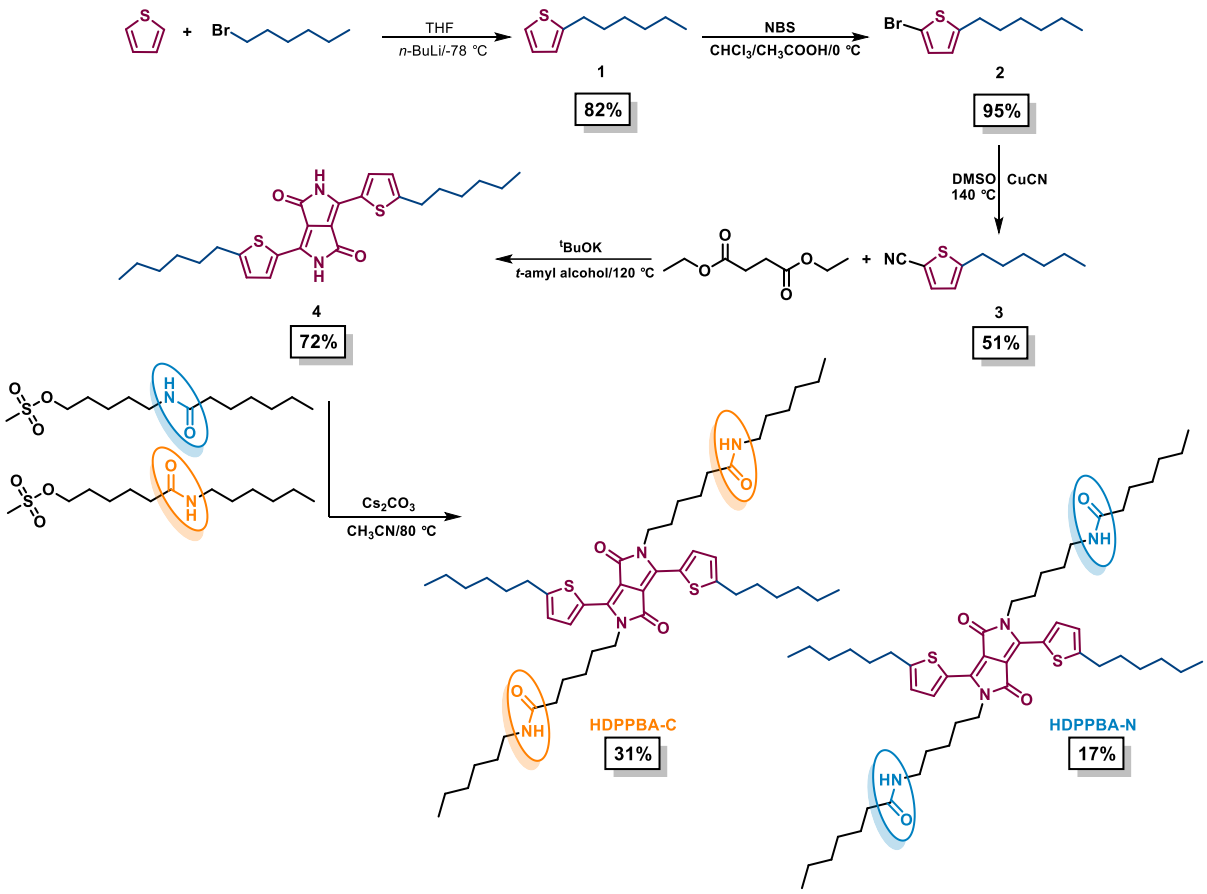

*Scheme III. 1 Synthetic route towards **HDPPBA-C** and **HDPPBA-N.***

The last step was the alkylation of the **DPP** core functionalized with hexyl tails in the thiophenes with the amide-containing branches. In this case, neither the *N*,*O*- and/or *O*,*O'*-alkylated isomers were obtained, which are common side products of this reaction. In this sense, the starting material (**4**) seems to provide higher regioselectivity towards the *N,N'*-alkylated products. It might be explained by the improved solubility of the starting material (introduction of hexyl groups in the thiophene *vs* previously reported **DPP** without functionalization in the thiophenes[6]), the steric hindrance provided by the hexyl chains with respect to the **DPP** carbonyl groups, the lower reaction temperature (80 ºC in CH_3CN *vs* 120 ºC in DMF) and the choice of base (cesium carbonate *vs* potassium carbonate).

The improved regioselectivity resulted in higher yields for the alkylation reactions in the lactams, reaching 30% in comparison to the same reaction using non-alkylated on the thiophene **DPP** derivatives reported in chapter II. The control molecule **HDPPH** was synthesized following the same strategy (Scheme III. 3) but the lactam rings were alkylated with hexyl bromide.

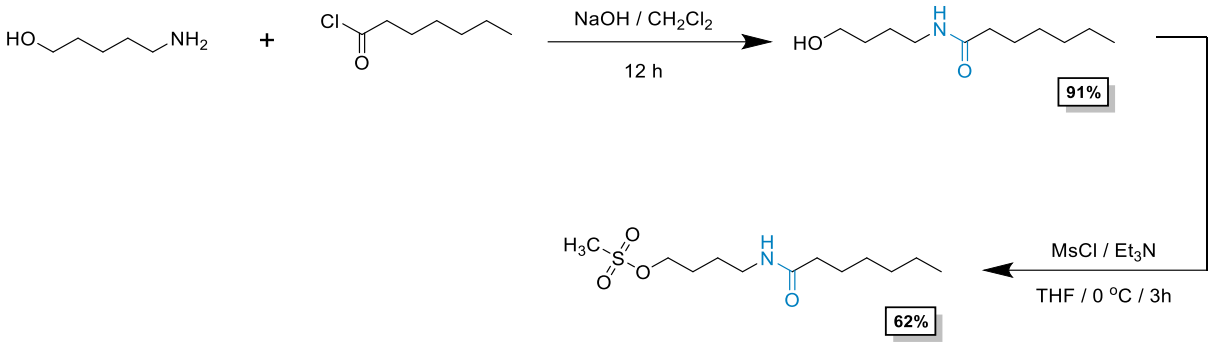

Scheme III. 2 Synthesis of the N-centered amide branch.

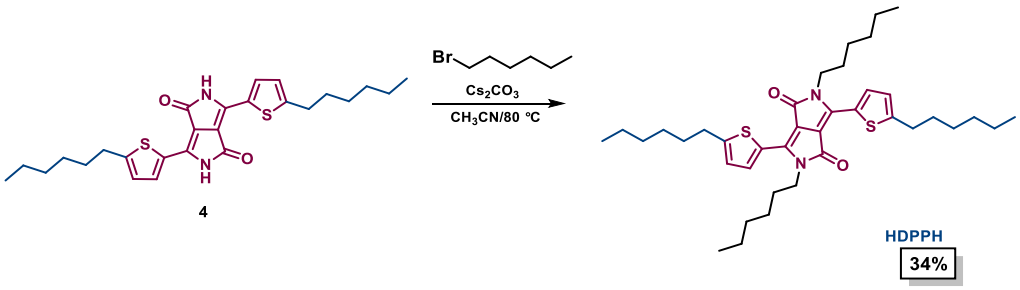

*Scheme III. 3 Alkylation of (4) to obtain **HDPPH**.*

II.2) Optical and self-assembly properties

The optical and self-assembly properties of **HDPPBA-C**, **HDPPBA-N** and **HDPPH** were followed with UV-Vis absorption in solution and on thin film at variable temperature in different solvents and concentrations, as well as by FTIR. The amide-containing derivatives and the control molecule display broad absorption bands ranging from 400 to 600 nm at 20 °C in chloroform with absorption maxima at λ = 521 nm and λ = 560 nm (Figure III. 5). The three derivatives do not show any sign of aggregation in chloroform at 20 °C and the absorption bands do not change upon heating or changing the concentration (Figure III. 6 a-f). Additional absorption bands appeared at lower energy when **HDPPBA-C** and **HDPPBA-N** were measured in different solvents, such as chlorobenzene, toluene and ethyl acetate (Figure III. 7a and b) with λ_{max} at 620 nm in chlorobenzene and toluene, and at 630 nm in ethyl acetate for **HDPPBA-C,** and λ_{max} at 617 nm in chlorobenzene, 620 nm in toluene and 624 nm in ethyl acetate for **HDPPBA-N**. Interestingly, this band at lower energy was not observed for the control molecule **HDPPH**, which displayed equal spectra in all the solvents (Figure III. 7c).

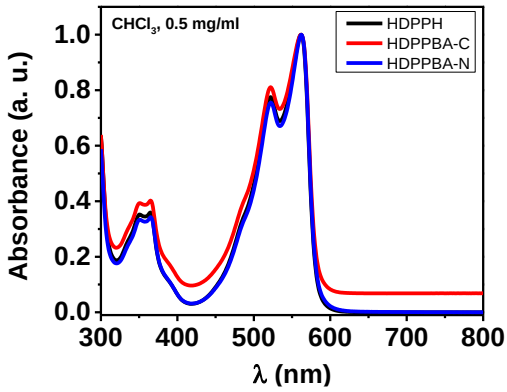

*Figure III. 5 Absorption spectra of **HDPPBA-C**, **HDPPBA-N** and **HDPPBH** in chloroform solution at room temperature.*

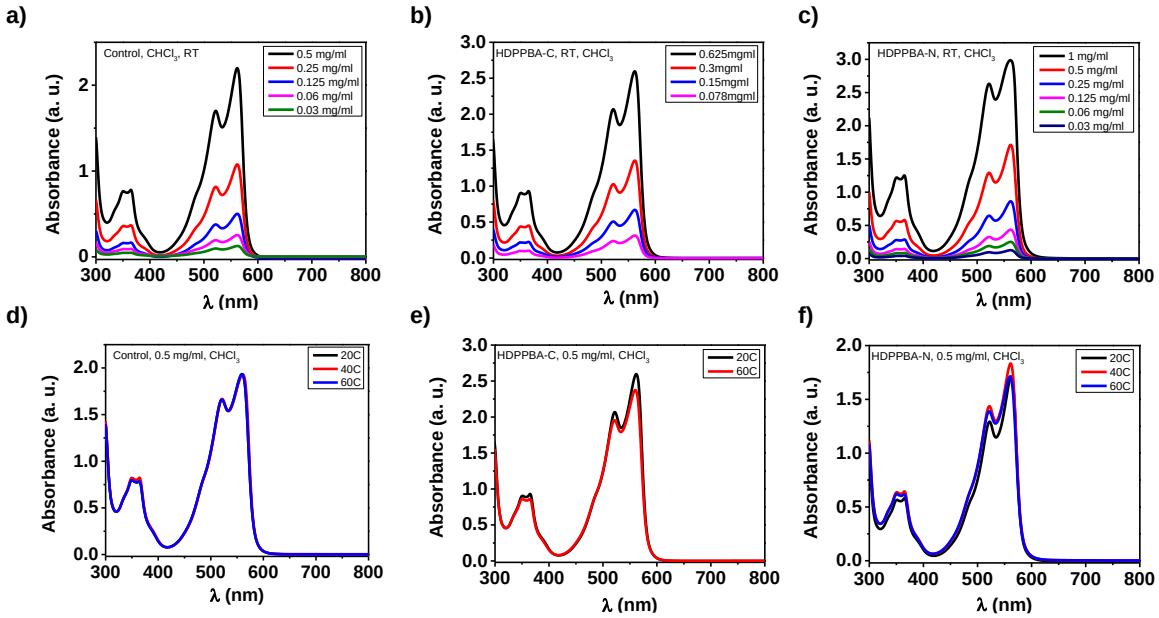

*Figure III. 6 Absorption spectra in chloroform at different concentrations and temperatures of **HDPPBA-C** ((a) & d)), **HDPPBA-N** ((b) & e)) and **HDPPBH** ((c) & (f)).*

This band could be attributed to the formation of J-type aggregates, as observed for the other families of H-bonded **DPPs** previously described in chapter II and in literature.[6–9] Furthermore, the differences found between the amide derivatives and the control suggest that H-bonds are involved in the formation of such type of aggregate. This hypothesis was confirmed by measuring spectra upon the addition of methanol, finding the disappearance of the J-aggregate band (Figure III. 8) in the same way as it occurred for the previous bisamide **DPP** family.

When comparing to the previously described amide-containing **DPPs** in chapter II, where the α-position of the thiophene was not functionalized with hexyl tails, a bathochromic shift of 10 nm of the J-aggregate band was observed. To explore this difference, preliminary results

obtained from electron diffraction will be presented in chapter V, showing the molecular packing of the different H-bonded **DPPs**.

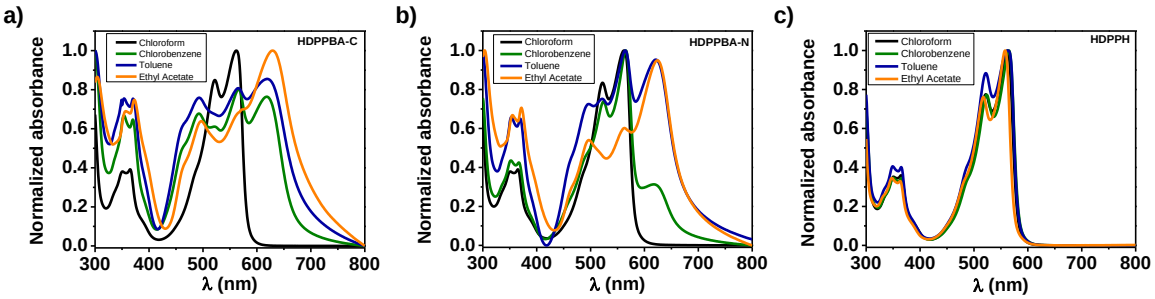

*Figure III. 7 Absorption spectra of a) **HDPPBA-C**, b) **HDPPBA-N** and c) **HDPPH** at room temperature in different solvents (chloroform, chlorobenzene, toluene and ethyl acetate).*

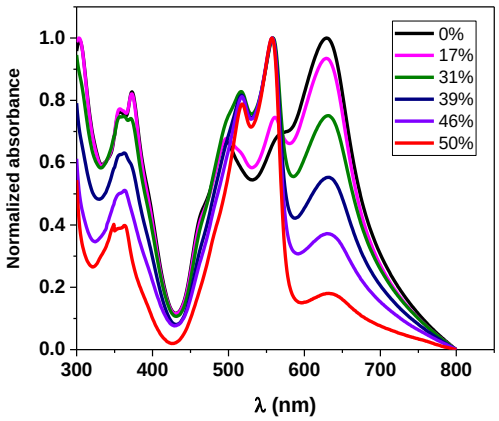

*Figure III. 8 Absorption spectra for **HDPPBA-C** showing disappearance of the J-aggregate band upon addition of methanol at room temperature. **[HDPPBA-C]** = 0.625 mg/ml.*

Even though **HDPPBA-C** and **HDPPBA-N** display aggregate bands, that are not present in the control molecule, differences between them could also be observed. **HDPPBA-C** presents a bathochromic shift in all the solvents compared to **HDPPBA-N**, and the J-aggregate is more pronounced in all the solvents tested, presumably as a sign of stronger aggregation in the C-centered amide than in the N-centered derivative. This effect could be observed by the naked eye since solutions of both amide derivatives in the same solvent and concentration, have different colors (Figure III. 9).

Furthermore, the disappearance of the J-aggregate band was observed as well upon diluting (Figure III. 10a and b) and heating in all the solvents studied (Figure III. 10c and d). For **HDPPBA-C**, the J-aggregate band was observed at lower concentrations than for **HDPPBA-N** and it was present at higher temperatures (Figure III. 10).

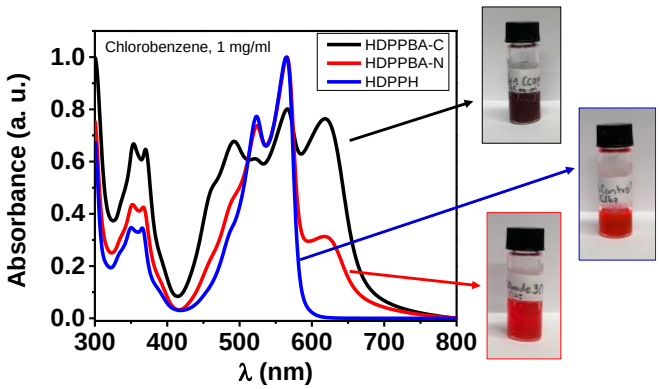

*Figure III. 9 Absorption spectra of **HDPPBA-C**, **HDPPBA-N** and **HDPPH** in chlorobenzene at room temperature and digital pictures of the solutions measured.*

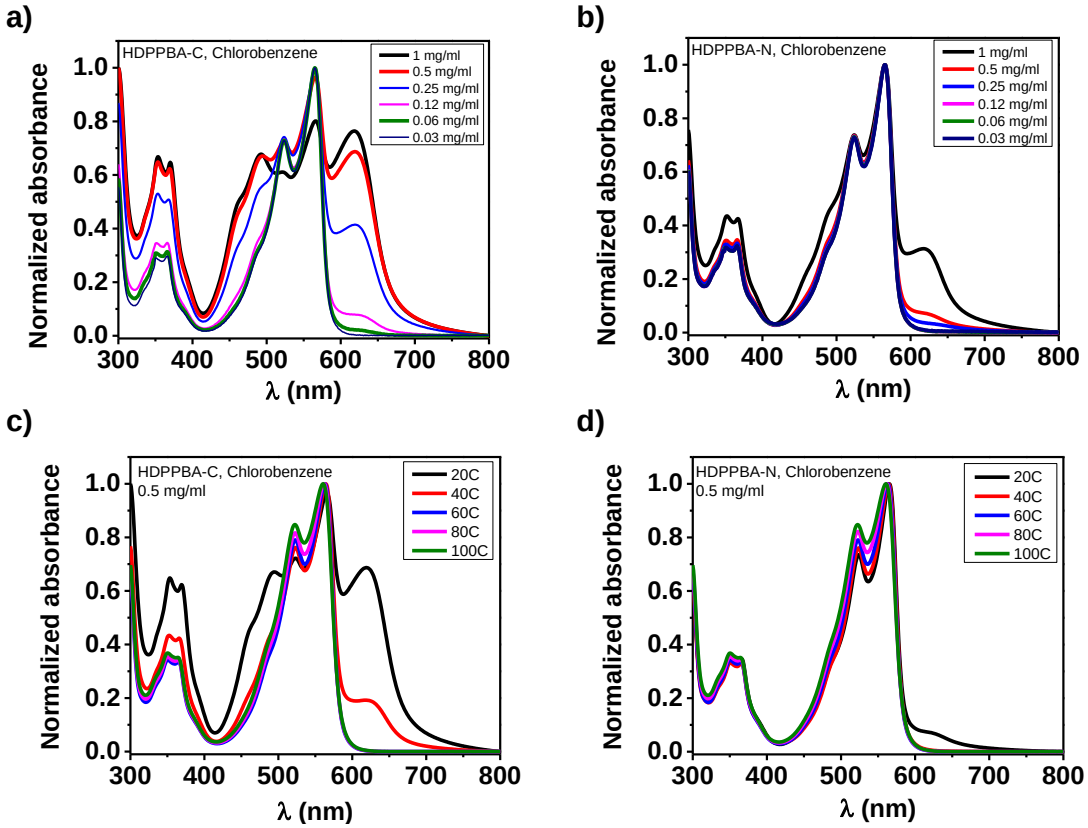

*Figure III. 10 Absorption spectra in chlorobenzene at different concentrations and temperatures of a) c) **HDPPBA-C** and b) d) **HDPPBA-N**.*

FTIR spectra of powders at room temperature proved the existence of H-bonds in the bisamide derivatives. **HDPPBA-C** and **HDPPBA-N** showed a band a 3303 cm^{-1} assigned to the NH stretching bands of the amides. This frequency shows the amides are H-bonded (Figure III. 11 left). In the region between 1600 cm^{-1} and 1700 cm^{-1}, the amide derivatives and the control show peaks at 1655 cm^{-1}, corresponding to the amide I bands of the lactam rings of the DPP core. In the same area, the other peaks at 1641 cm^{-1} and 1637 cm^{-1} for **HDPPBA-C** and **HDPPBA-N** respectively, correspond to amide groups engaged in H-bonding (Figure III. 11

right). The amide II bands are located at 1550 and 1548 cm^{-1} for **HDPPBA-C** and **HDPPBA-N** respectively, which also shows the amide groups are H-bonded. These large bands overlap with the amide II band of the lactam, visible at 1553 cm^{-1} for **HDPPH**. The difference of 4 cm^{-1} between the amide-containing derivatives indicates a slight difference in the strength of the H-bonds that can induce subtle differences in aggregation.

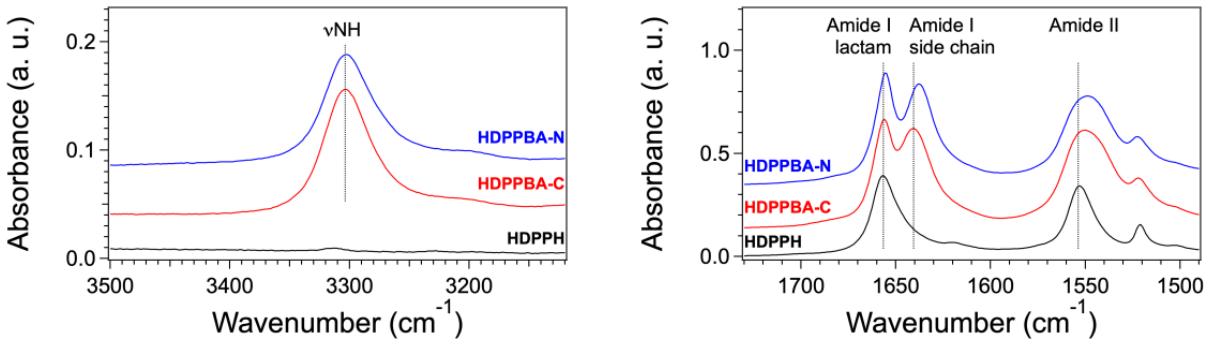

*Figure III. 11 FTIR powder spectra of **HDPPBA-C**, **HDPPBA-N** and **HDPPH**.*

The morphology of **HDPPBA-C**, **HDPPBA-N** and **HDPPH** was studied using TEM in different solvents (Figure III. 12). Clear differences were found when comparing the H-bonded derivatives to the control molecule. While **HDPPBA-C** and **HDPPBA-N** self-assemble into high aspect-ratio structures, **HDPPH** forms short tape-like crystallites of approximately 2 µm in length overlapping with each other in all the solvents tested except for cyclohexane, where the tape-like structures are narrower and longer (Figure III. 12k-o).

In the case of **HDPPBA-C**, a great disparity of fibers with different width and length were observed in toluene, ethyl acetate and cyclohexane (Figure III. 12a-e). The fibers are wavy, intertwined in bundles of rectangular size, and their length can exceed 15 mm. The structures in chlorobenzene are slightly different, finding elongated fibers as well, but narrower, less twisted than in the other solvents and with sharper edges. In chloroform, there are much smaller fibers that are straight and flat. These are the usual structures previously observed for the other **DPP** families studied in chloroform and it seems to be in part due to drying effects.

Regarding **HDPPBA-N** the structures observed are different from those of **HDPPBA-C**, finding very similar fibers in all the solvents except for chloroform (Figure III. 12f-j). Elongated fibers of up to 5 mm are found, but generally smaller than those of **HDPPBA-C**. They are wavy and twisted fibers, are very variable in size and they appear to be folded into several thin layers, well individualized. In the case of chloroform, the fibers are very different and in some areas of the sample, they resemble the fibers found in **HDPPBA-C**.

Taking into account the H-bonded **DPP** families previously described in chapter II, it can be seen that for this particular family there is less variety of morphologies than for the bisamides without functionalization in the thiophene rings or compared to the semicarbazone-based family[10], especially for **HDPPBA-N** that self-assembles in almost identical morphologies in all of the tested solvents.

A similar effect is observed regarding the UV-Vis absorption data, while J-aggregates are present in all the families studied so far, in solvents that promote self-assembly, this band is the predominant one in certain solvents for **HDPPBA**, **(S)-HDPPBA** and **(R)-DPPBA**, where the thiophene rings are not substituted. It has been hypothesized that the increase of solubility could be the responsible for the different behavior of **HDPPBA-C** and **HDPPBA-N**, as well as the change in amide topology in the case of the N-center derivative, which seems to guide the assembly towards smaller aggregates.

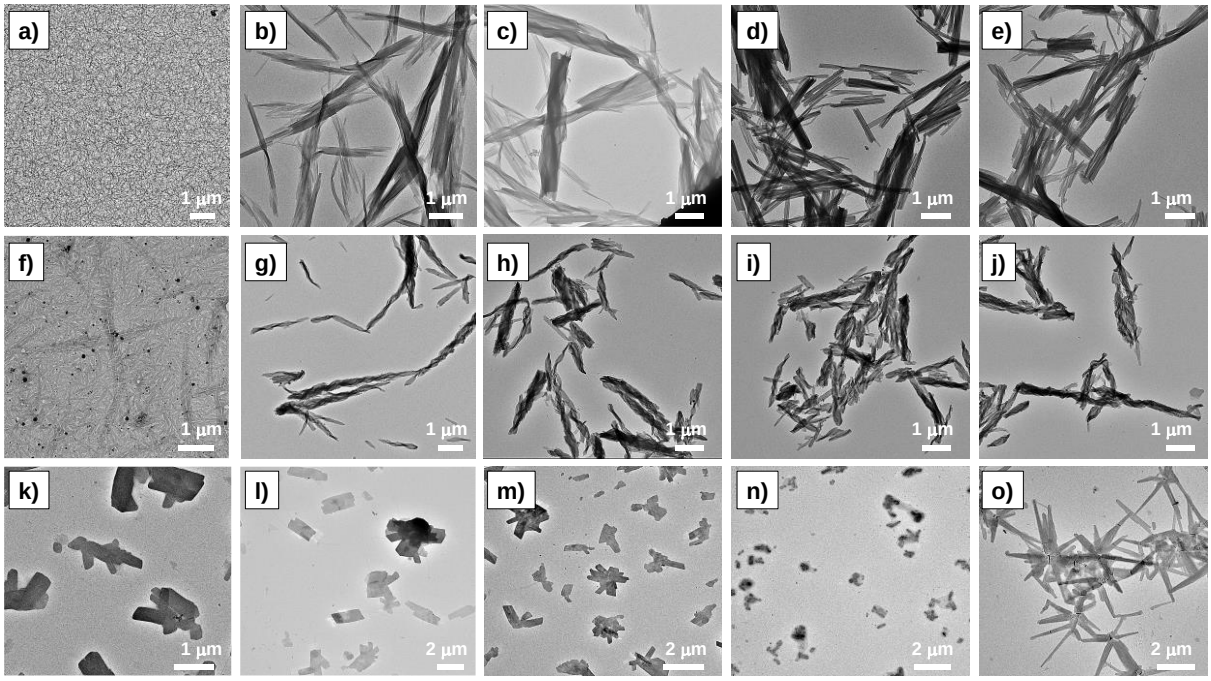

*Figure III. 12 TEM images of **HDPPBA-C (a-e), HDPPBA-N (f-j)** and **HDPPH (k-o)** in chloroform, chlorobenzene, toluene, ethyl acetate and cyclohexane, respectively. The samples were prepared by drop casting solutions at a 2.5 mg/ml onto carbon grids and blotting to eliminate the excess of solvent to avoid drying effects.*

Time dependent-DFT calculations were performed to rationalize the behavior of the amide-containing derivatives, showing that the dihedral angles of **HDPPBA-C** and **HDPPBA-N** are different, the N-centered derivative being more like the control molecule (Figure III. 13). The control molecule is quite planar, with angles between the **DPP** core and the thiophenes of 5° and 15°, **HDPPBA-N** is very dissymmetrical, with angles of 0° and 20°. In contrast, the C-centered derivative is the least planar of the three, with both angles of 20°. These results could rationalize the different molecular packing among these derivatives.

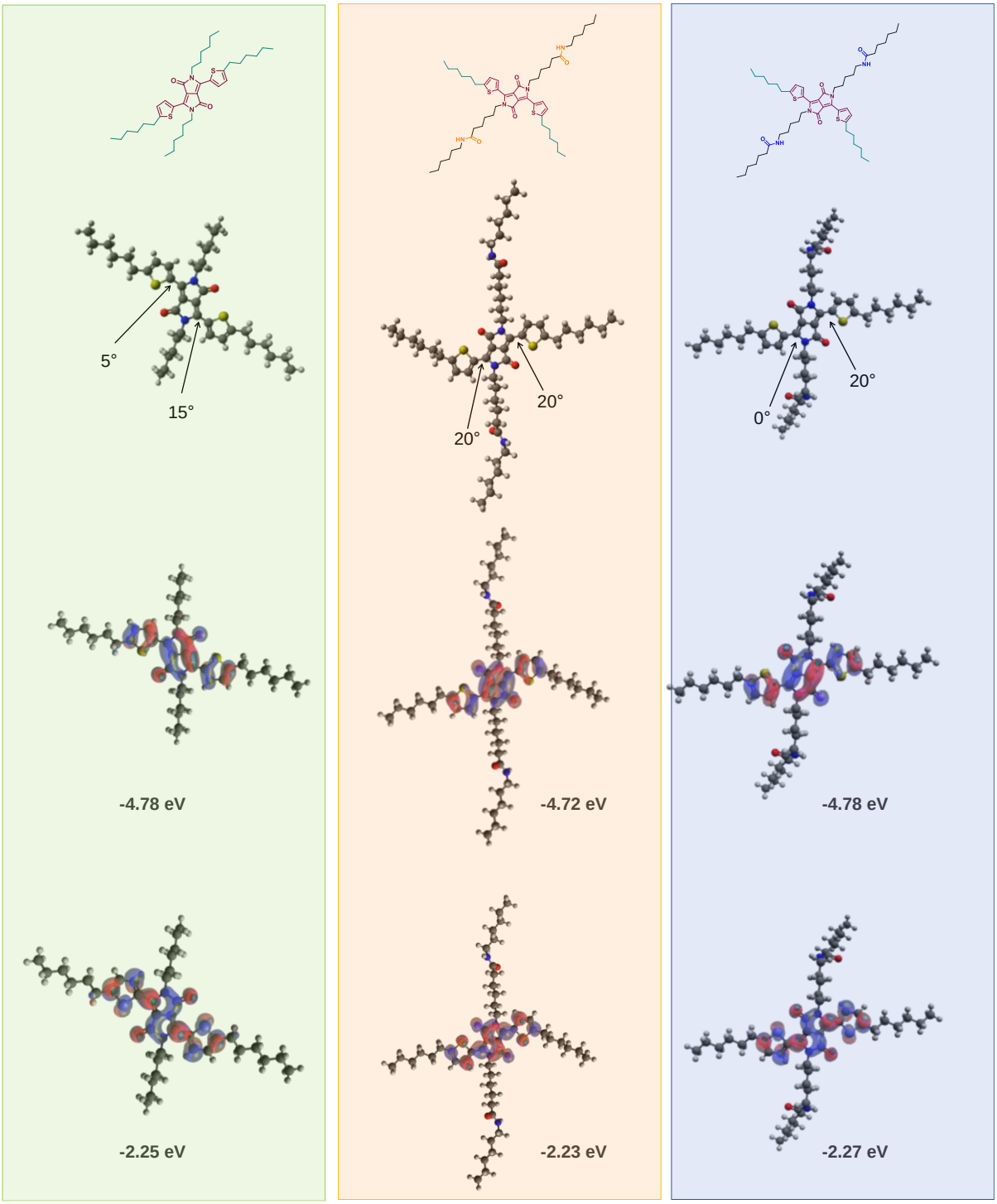

Figure III. 13 DFT calculations data. Minimized energy configurations and HOMO-LUMO topology.

II.3) Electrical properties

The electrical properties of **HDPPBA-C**, **HDPPBA-N** were screened by exploring the photoconductivity measured by FP-TRMC as for the previous families and comparing it to the control molecule **HDPPH**. Thin films of the compounds were prepared by drop casting from chloroform/toluene solutions, and their photoconductivity was directly analysed. The observed kinetic traces of conductivity transients can be seen in Figure III. 14.

The photoconductivity values of **HDPPBA-C** and **HDPPBA-N** are very similar, being of 2.0 x 10^{-5} $cm^{-2}V^{-1}s^{-1}$ and 1.6 x 10^{-5} $cm^{-2}V^{-1}s^{-1}$ (Table III. 1, entries 4 and 5), respectively. These values are clearly larger than the value found for **HDPPH**, being 5.8 x 10^{-6} $cm^{-2}V^{-1}s^{-1}$ (Table III. 1, entry 6), one order of magnitude smaller than for the H-bonded derivatives. The kinetics decay of photoconductivity of **HDPPBA-C** and **HDPPBA-N** show that the photo-generated free charge carriers are stable up to more than 10 μs. The recombination of charge carriers is slower for **HDPPBA-C** and **HDPPBA-N** than for the control molecule, with one order of magnitude longer lifetime: $t_{1/2}$ equals 2 x 10^{-5} s for **HDPPBA-C** and **HDPPBA-N**, and 8 x 10^{-6} s for **HDPPH** (Table III. 1, entries 4-6).

These results highlight the beneficial role of H-bonding in this particular family and in extension, to the rest of the families explored so far. For the moment, the results for **HDPPBA-C** and **HDPPBA-N** are very similar since this technique measures photoconductivity at the nanoscale. However, measurements after solvent vapour annealing are being carried out by our collaborators in Kyoto to shed light on the effect of rearrangements in molecular packing after solvent exposure to compare the values to the previously measured families under the same conditions. Simultaneously, the molecular packing is being studied in our group using electron diffraction in cast samples and after thermal and vapor annealing. Once all these results are obtained, it will be possible to rationalize and complete the photoconductivity results.

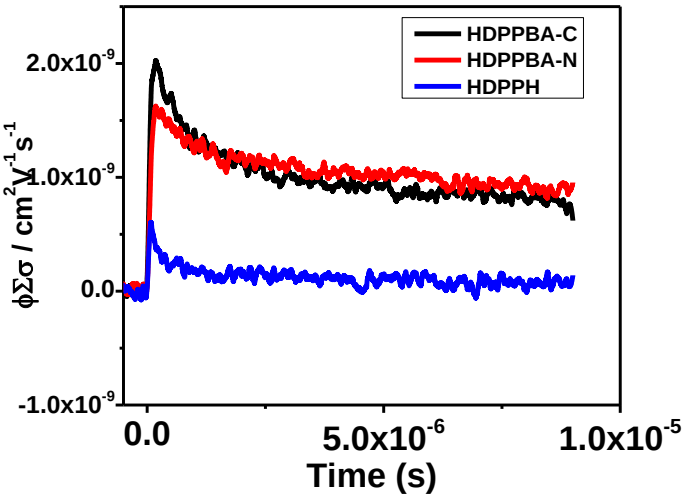

*Figure III. 14 Kinetic traces of photoconductivity transients of **HDPPBA-C**, **HDPPBA-N** and **HDPPH** cast from chloroform/toluene solutions.*

When comparing to the previously studied families, it can be observed that the recombination of charge carriers of **HDPPBA-C** and **HDPPBA-N** are comparable to **DPPBA** (Table III. 1, entry 1), the achiral derivative previously studied containing unfunctionalized thiophene rings, and that the photoconductivity values are lower (Table III. 1, entry 1 *vs* entries 4 and 5), but like those of the chiral compounds, **(S)-** and **(R)-DPPBA** (Table III. 1, entries 2 and 3 *vs* entries 4 and 5). The recombination of charge carriers is equal than **DPPBA** (entries 1, 4 and 5), being in this case one order of magnitude slower than the chiral derivatives **(S)-** and **(R)-DPPBA** previously studied (entries 2 and 3 vs entries 4 and 5). Interestingly, the recombination of charge carriers for **(S)-** and **(R)-DPPBA** is in the same order of magnitude as for the control molecule **HDPPH** not containing H-bonds in its structure. These results indicate how important is to finely-tune the molecular design of H-bonded π-conjugated materials, since the most subtle change can dramatically impact the electronic properties.

*Table III. 1 Photoconductivity ($\phi\Sigma\mu$) values for **HDPPBA-C**, **HDPPBA-N** and **HDPPH** and the comparison to the previously studied family. Rate constant (k, calculated after 3 ms after pulse excitation) and half lifetime ($t_{1/2}$) values for **HDPPBA-C**, **HDPPBA-N** and **HDPPH** and the comparison to the previously studied family.*

Entry	Derivative	$\phi\Sigma\mu$ ($cm^2V^{-1}s^{-1}$)	k (s^{-1})	$t_{1/2}$ (s)
1	**DPPBA**	5.0×10^{-5}	3×10^{4}	2×10^{-5}
2	**(S)-DPPBA**	3.1×10^{-5}	2×10^{5}	5×10^{-6}
3	**(R)-DPPBA**	3.2×10^{-5}	1×10^{5}	7×10^{-6}
4	**HDPPBA-C**	2.0×10^{-5}	4×10^{4}	2×10^{-5}
5	**HDPPBA-N**	1.6×10^{-5}	3×10^{4}	2×10^{-5}
6	**HDPPH**	5.8×10^{-6}	8×10^{5}	8×10^{-6}

II.4) Conclusions

In conclusion, three new **DPP** derivatives were synthesized and characterized, with two of them having mostly the same structure, but different amide topology. Furthermore, a very soluble **DPP** derivative that has no H-bond functionality was obtained and used as a control molecule for comparison. The two amide **DPP** derivatives aggregate and form J-type aggregates, where H-bonds are involved, whereas the control does not display J-aggregation.

Furthermore, the synthetic approach seems to provide higher regioselectivity towards the N,N'-alkylated products, as the typical isomers that are usually obtained in **DPP** alkylation were not present. This might be explained by the combination of multiple factors: improved solubility of the starting material, the steric hindrance provided by the hexyl chains with respect to the **DPP** carbonyl groups, the lower reaction temperature and the based used to deprotonate the lactam. The improved regioselectivity also resulted in higher yields for the alkylation reactions in the lactams, reaching 30%.

Slight differences were observed for changes in topology, the C-centered derivative presents a bathochromic shift in all the solvents compared to N-centered derivative, and the J-

aggregate is more pronounced in all the solvents tested, presumably as a sign of stronger aggregation.

In the case of morphology, for this family there is less variety when compared to previous **DPP** derivatives, especially for the N-centered derivative that self-assembles in almost identical morphologies in all the tested solvents. It has been hypothesized that the increase of solubility could be the responsible for the different behavior of **HDPPBA-C** and **HDPPBA-N**, as well as the change in amide topology in the case of the N-center derivative, which seems to guide the assembly towards smaller aggregates.

The photoconductivities of **HDPPBA-C** and **HDPPBA-N** are very similar, but clearly larger than the value found for **HDPPH**, highlighting the beneficial role of H-bonding in this family and in extension, to the rest of the families explored so far. When comparing to the previously studied families, it can be observed that the recombination of charge carriers is comparable and that the photoconductivity values are lower. Interestingly, the recombination of charge carriers for chiral **DPP** derivatives is in the same order of magnitude as for the control molecule **HDPPH** not containing H-bonds in its structure, which indicates how important is to finely-tune the molecular design of H-bonded π-conjugated materials, since the most subtle change can dramatically impact the electronic properties.

Now, the main focus is on further exploring the electrical properties of **HDPPBA-C** and **HDPPBA-N**. As shown previously, the photo-generated free charge carriers are stable up to more than 10 μs and therefore, our collaborators kept on increasing the measuring time, finding very interesting results (Figure III. 15):

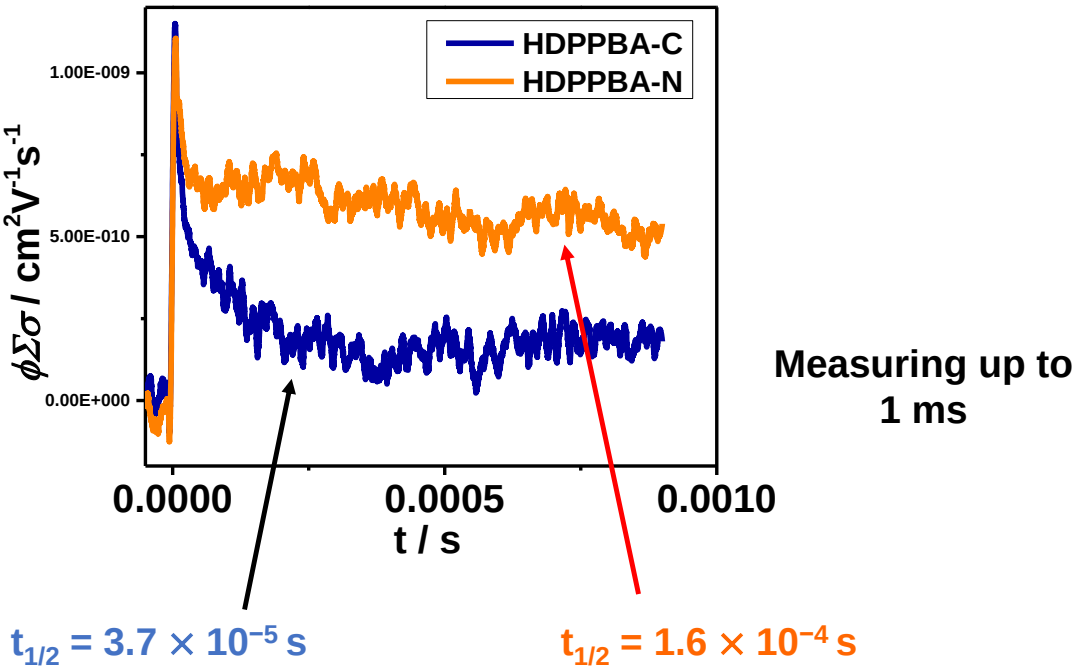

*Figure III. 15 Free charge carrier stability over time of **HDPPBA-C** and **HDPPBA-N**.*

Interestingly, the photo-generated free charge carriers are stable up to more than 1 ms and more importantly, the recombination of charge carriers for **HDPPBA-N** was one order of magnitude slower than for the C-centered analogue. For now, our collaborators are following up with these results and the comparison to the rest of the derivatives shown in Chapter II.

III. Experimental

III.1) Materials and methods

All reagents and solvents were obtained from commercial suppliers and purified or dried according to standard procedures. Column chromatography was performed on silica gel (VWR Silica 60, particle size 0.040–0.063 mm). Solvents for spectroscopic studies were of spectroscopic grade and used as received. Elemental analysis was performed on a Thermofischer Scientific Flash 2000. Matrix-assisted laser desorption/ionisation-time of filght (MALDI) was performed in a Bruker Daltonics. ^{1}H and ^{13}C spectra were recorded in $CDCl_3$ on a Bruker Avance 400 MHz spectrometer and/or Bruker Avance III HD 500 MHz spectrometer. UV–vis measurements were performed in a conventional quartz cell (light pass 1 mm) on a Cary 5000 UV-Vis-NIR spectrophotometer. TEM measurements were done with a Technai G2 (FEI) microscope with an accelerating voltage of 200 kV. 5 µL of the sample solution were deposited onto a freshly glow discharged carbon-covered grid (400 mesh). The suspension was left for 2 min, and then, the grid was negatively stained with 5 µL of uranyl acetate (2% in water) for another 1 min and finally blotted using a filter paper.

FTIR spectra were recorded with a Vertex 70 from Bruker Optics, equipped with MCT detector and a black-body source. The spectra of the solids were measured by ATR on diamond. The solutions were studied in cells from Specac Pike with KBr NaCl windows. For the VT experiments the solutions were inserted in a home-made cell between two NaCl windows. The cell was inserted in a Linkam heating stage, hold in a horizontal measurement chamber. The spectra were measured with the built-in MCT detector of the Vertex 70. The spectra were compensated from CO_2 and moisture with OPUS from Bruker. The solvent intensities were measured separately and subtracted. The spin coated samples were prepared using a Spin 150 spin coater at 2000 rpm using 80 ml of solution on glass slides or silicon wafers.

Charge carrier mobilities were evaluated by FP-TRMC at room temperature.[56, 57] The thin films of samples were fabricated by drop-cast method onto quartz substrates (9 × 40 mm^2, 1 mm thick). Charge carriers were injected into the materials via photo-ionization with a third harmonic generation (λ = 355 nm) of a Spectra Physics model INDI-HG Nd:YAG laser pulses at 10 Hz with a pulse duration of ca. 5 ns. The photon density of a 355 nm pulse was modulated from 4.5 × 10^{15} photons cm^{-2} $pulse^{-1}$. The microwave frequency and power were set at ~9.1 GHz and 3 mW, respectively, and guided into a microwave cavity. The *Q*-factor of the microwave cavity loaded with the sample was 2200, and the substrates with the compound films were set at the point of electric field maximum. The reflected power of the probing microwave, picked up by a diode (rise time < 1 ns), was monitored by a Tektronics model TDS3032B digital oscilloscope after an amplification by Ciao Electronics CA812-304 FET amplifier system. The observed change in the reflected microwave power (ΔP_r) was normalised with the steady reflection of the microwave from the cavity (P_r), and converted

directly into the product of a photocarrier generation yield (*f*) and the sum of photo-generated electron/hole mobilities (S*m*),

$$\phi\Sigma\mu = 1/(eI_0F_{light}) \times (1/A) \times (\Delta P_r/P_r) \qquad (1)$$

where *e*, *A*, I_0, and F_{light} are elementary charge, sensitivity factor (S^{-1} cm), incident photon density of the excitation laser (photon cm^{-2}), and filling factor (cm^{-1}), respectively. The value of Flight was calculated based on the overlap of the area of photo-carrier injection (presumed to be proportional to the absorbance of excitation light by the sample film) with electric field strength distribution in the cavity derived from a calculation code of CST Microwave Studio from AET Inc.

III.2) Synthetic procedure

2-hexylthiophene **(1)**

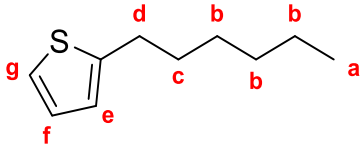

In a 2-neck round bottom flask under inert atmosphere, 400 ml of anhydrous Tetrahydrofuran were added along with a magnetic stirrer. The thiophene (200 mmol, 1 eq, 33.66 g) was then added to form a solution, which was then cooled down to -78 °C for 30 mins by using an isopropanol and dry ice bath. Mixture became white in color, then a 2.3 M solution of n-Buthyl Lithium in hexanes (220 mmol, 1.1 eq, 95.66 ml) was added dropwise while the mixture was still at -78 °C and it was allowed to react for 1h. Finally, 1-bromohexane (220 mmol, 1.1 eq, 72.62 g) was added dropwise and the mixture was allowed to gradually warm up to room temperature by changing to an ice bath that eventually warmed up to room temperature, since the reaction was allowed to occur for 24 h. The flask and the ice bath were covered in aluminum foil to avoid having decomposition products due to light (halides give the solution an orange color). After 24 h, the mixture was cooled down back to 0 °C, diluted and quenched by adding 400 ml of distilled water. Extraction was performed by using diethyl ether (3x300 ml) and the organic phase was washed with 200 ml of a brine solution, the resulting organic phase was dried over anhydrous $MgSO_4$ and filtered. Solvent was then evaporated, and a yellow oil remained as a mixture of 1-bromohexane and the product. Purification was performed by vacuum distillation at 0.4 mbar, a first distillate was recovered at 60 °C, 1-bromohexane, temperature was then increased to 100 °C and a second distillate was recovered, compound **1**. Yield: colorless oil (27.56 g, 82%).

^{1}H NMR (400 MHz, $CDCl_3$): δ 7.16 (dd, J=6.2 Hz, 3.0 Hz, 1H$_g$), 6.99 (t, 1H$_f$), 6.85 (dd, *J* = 3.9Hz, 3.7Hz, 1H$_e$), 2.90 (t, 2H$_d$), 1.75 (m, 2H$_c$), 1.4 (m, 6 H$_b$), 0.98 (t, 3H$_a$).

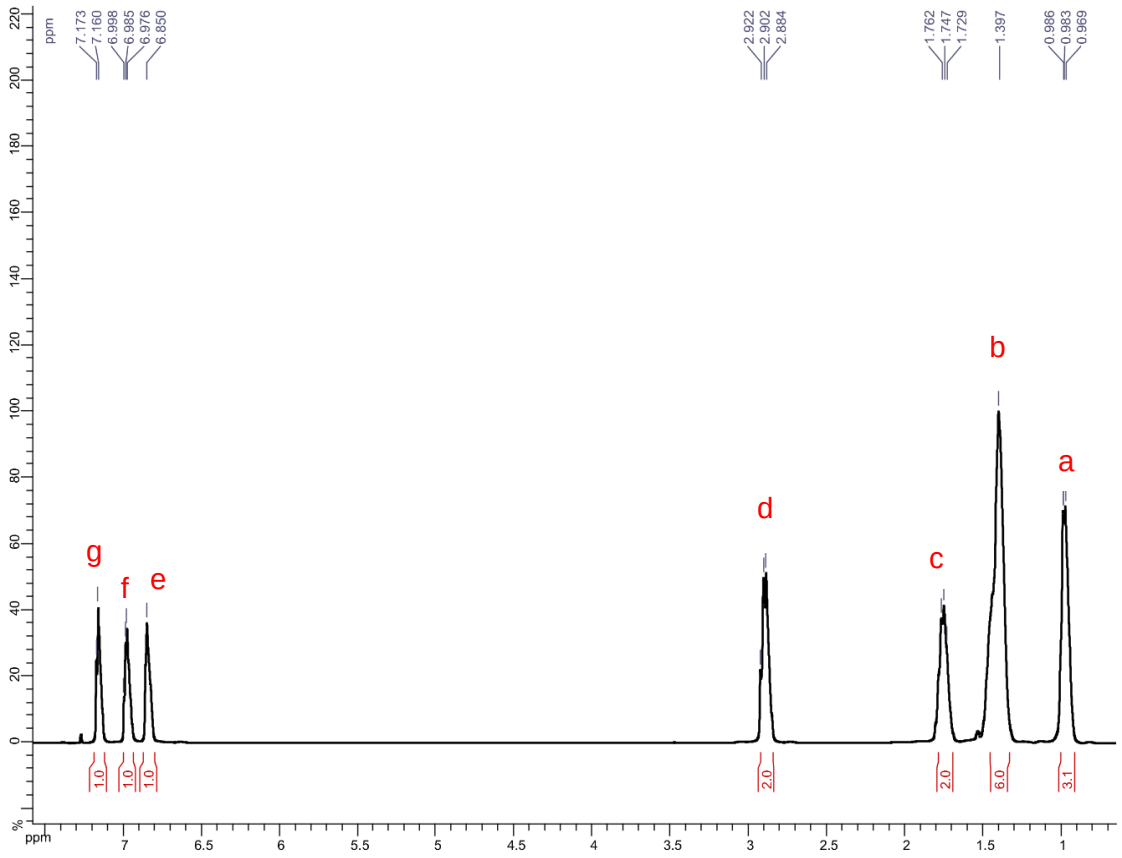

2-bromo-5-hexylthiophene **(2)**

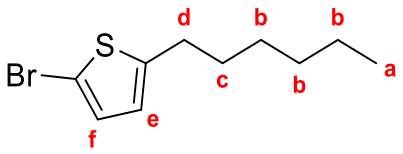

In a 2-neck round bottom flask under inert atmosphere, 150 ml of a mixture of chloroform and acetic acid (1:1, v/v) were added along with a magnetic stirrer. N-bromosuccinimide (180 mmol, 1.1 eq, 32.7 g) was then added to form a solution, which was then cooled down to 0 °C for 30 mins by using an ice bath. Compound **1** (163 mmol, 1 eq, 27.56 g) was so added dropwise while the mixture was at 0 °C and it was allowed to gradually warm up to room temperature, as reaction occurred for 12 h. The flask and the ice bath were covered in aluminum foil to avoid decomposition of the N-bromosuccinimide due to light. After 12 h, the mixture was diluted by adding 150 ml of dichloromethane, the resulting organic phase was washed with a saturated solution of $NaHCO_3$ (3x150 ml) and was dried over anhydrous $MgSO_4$ and filtered. The organic phase was then evaporated. No purification was performed. Yield: dark yellow oil (38.94 g, 95%).

^{1}H NMR (400 MHz, $CDCl_3$): δ 6.86 (d, 1H$_f$), 6.56 (d, 1H$_e$), 2.77 (t, 2H$_d$), 1.66 (q, 2H$_c$), 1.34 (m, 6H$_b$), 0.93 (t, 3 H$_a$).

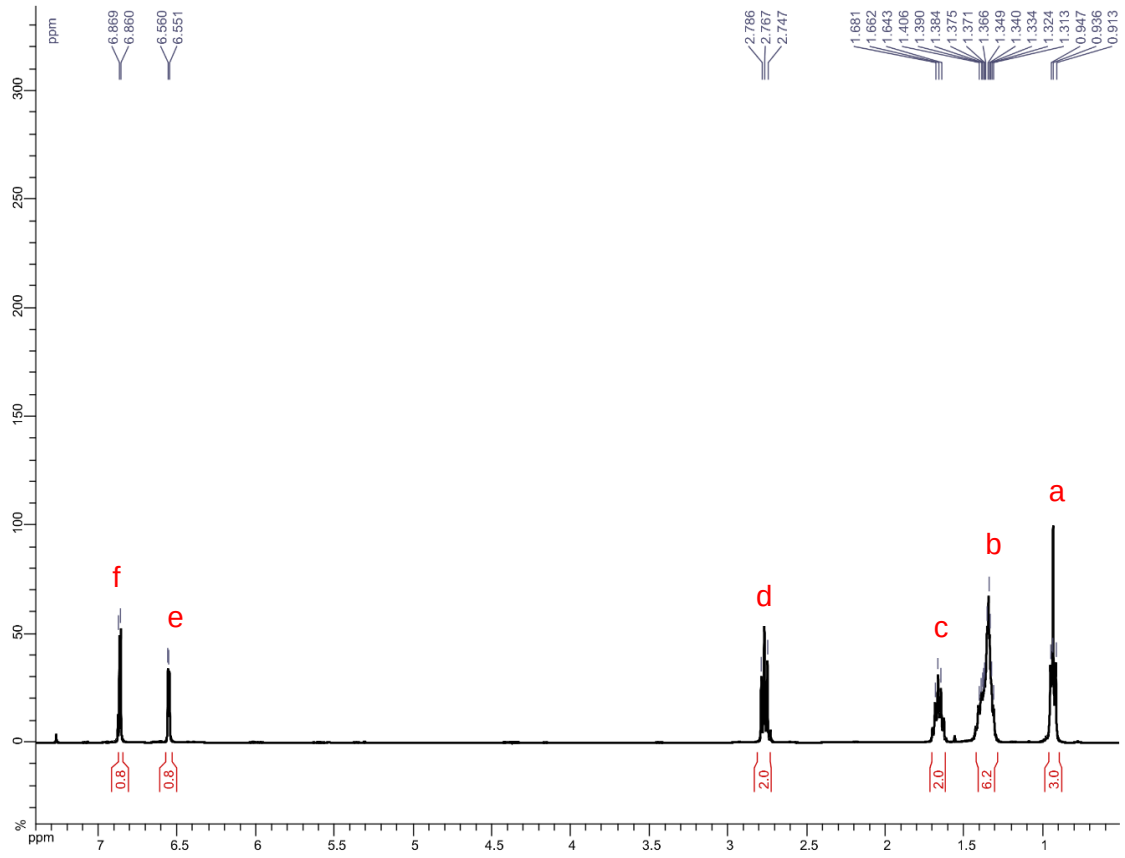

5-hexylthiophene-2-carbonitrile **(3)**

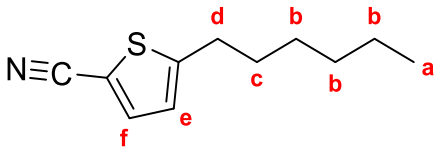

In a 3-neck round bottom flask under inert atmosphere, coupled with a reflux apparatus, 600 ml of dimethylsulfoxide were added along with a magnetic stirrer. The copper cyanide (265 mmol, 1.6 eq, 24.25 g) was then added to form a solution, which was then warmed up to 50 °C for 30 mins by using an oil bath to ensure the copper cyanide was dissolved. Then Compound **2** (166 mmol, 1 eq, 38.94 g) was added dropwise while the mixture was still at 50 °C and temperature was increased to 140 °C, allowing it to react overnight. Afterwards, reaction was allowed to cool down to room temperature and 200 ml of a 30% (w/w) ammonia solution were slowly added, since some bubbling and heating occurred. Mixture was so diluted with distilled water to a final volume of 1200 ml and a distinctive dark blue color solution was obtained. This solution was washed several times with ethyl acetate (300 ml per washing), until the ethyl acetate washing was not getting colored (from dark yellow in the first washing to slightly colorless in the last). The organic layers were combined and dried over anhydrous $MgSO_4$ and filtered, then the solvent was evaporated, and a dark brown oil remained. Purification was performed by Column Chromatography, using a mixture of cyclohexane: ethyl acetate (9:1) as the eluent. Yield: Dark yellow oil (16.25 g, 51%).

^{1}H NMR (400 MHz, $CDCl_3$): δ 7.44 (d, 1H_f), 6.79 (d, 1H_e), 2.84 (t, 2H_d), 1.68 (q, 2H_c), 1.31 (m, 6H_b), 0.89 (t, 3 H_a).

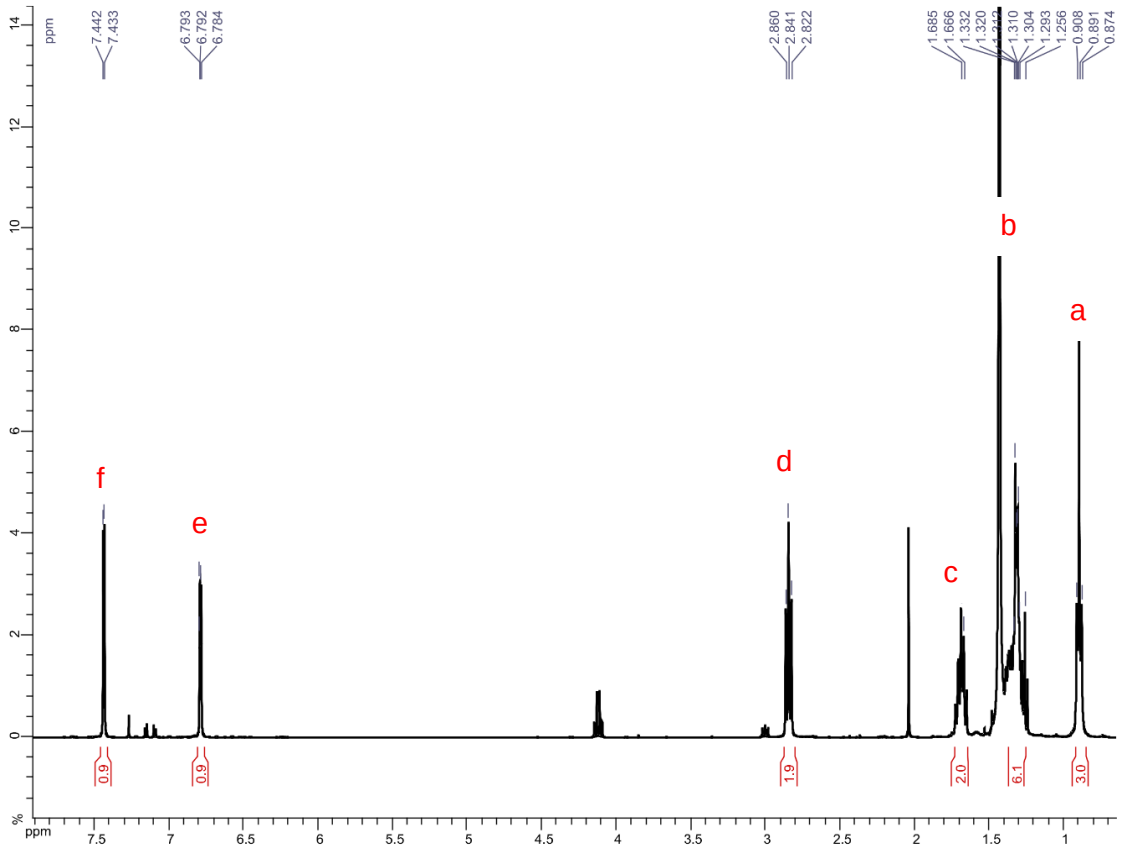

3,6-bis(5-hexylthiophen-2-yl)-2,5-dihydropyrrolo[3,4-c]pyrrole-1,4-dione (**4**)

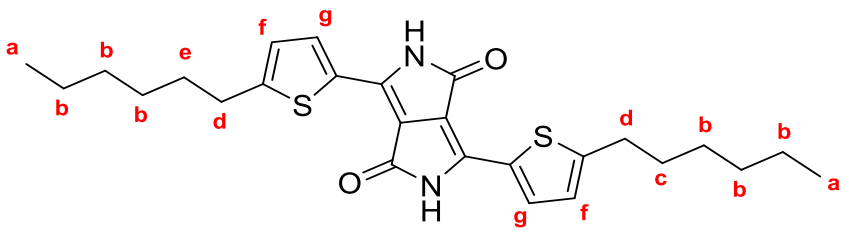

In a 3-neck round bottom flask under inert atmosphere, coupled with a reflux apparatus, the potassium t-Butoxide (92 mmol, 2.2 eq, 10.61 g), Compound **3** (84 mmol, 2 eq, 33.66 g) and 120 ml of t-amyl alcohol were added along with a magnetic stirrer. Mixture was stirred and warmed up to 120 °C for 30 mins by using an oil bath. Diethyl Succinate (42 mmol, 1 eq, 7.32 g) was added dropwise while the mixture was still at 120 °C, mixture became dark red in color upon addition of the diethyl succinate, reaction was carried overnight at 120 °C. Mixture was allowed to cool down to room temperature and 10 ml of acetic acid were used to neutralize the excess base, mixture turned dark purple. Purification was performed by filtering the mixture through a P16 fritted glass filter funnel and the solid product was put in the oven to dry overnight. Yield: Dark purple solid (14.24 g, 72%).

^{1}H NMR (400 MHz, DMSO-d_6): δ, 8.0 (d, *J* = 3.8 Hz, 2H$_f$), 7.02 (d, *J* = 3.8 Hz, 2H$_e$), 2.88 (t, J=7.6 Hz, 4H$_d$), 1.68 (quin, J= 7.2 Hz, 4H$_c$), 1.32-1.26 (m, 12H$_b$), 0.87 (ddt, J=7.1 Hz, 4.7 Hz, 6 H$_a$).

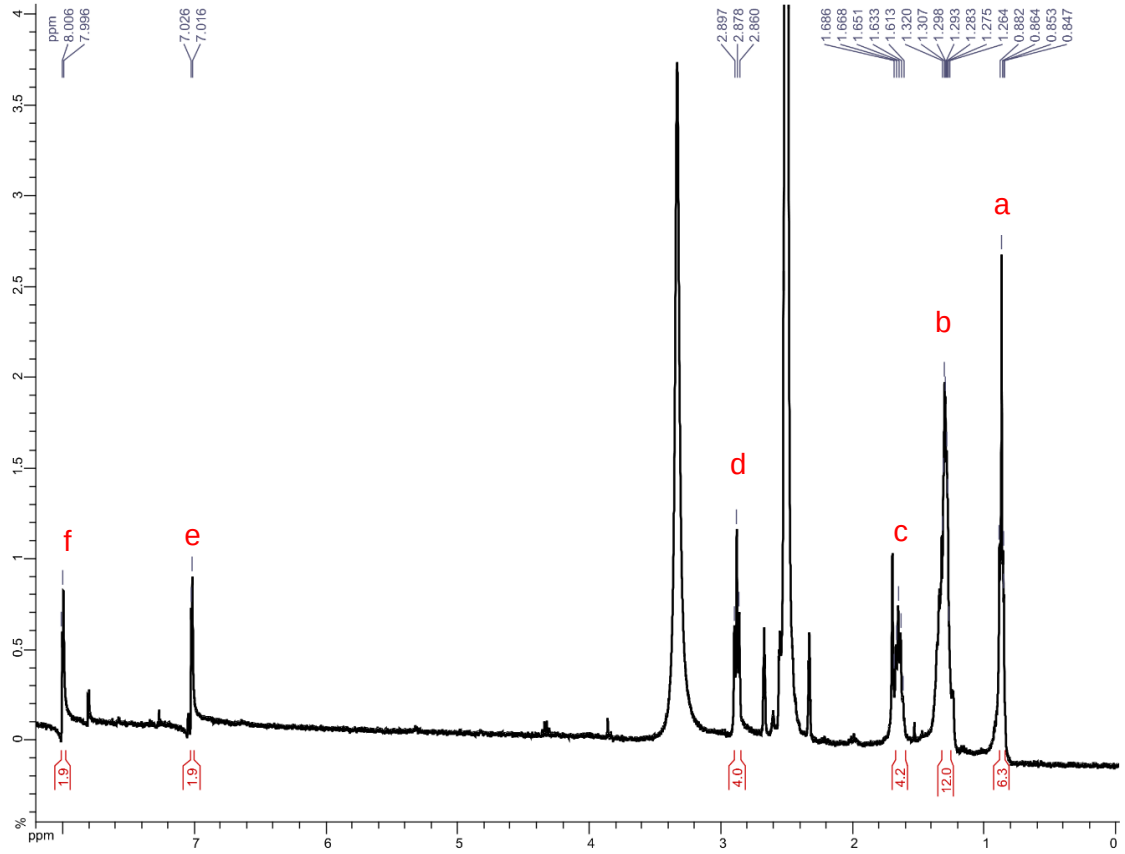

N-(5-hydroxypentyl)heptanamide

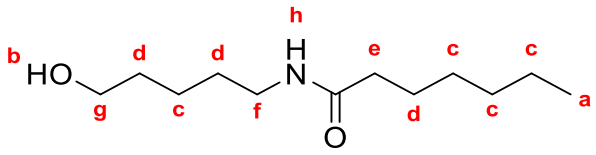

Heptanoyl chloride (4.1 mL, 26.5 mmol) dissolved in CH_2Cl_2 (50 mL) is added dropwise using an addition funnel to a solution of 5-amino-1-pentanol (3.1 mL, 27.1 mmol) in 0.2 M NaOH (50 mL). The reaction was vigorously stirred overnight. Next, the crude is extracted with $CHCl_3$ (3x 100 mL). Then, the organic layers were collected and washed with water (2x 50 mL) and saturated brine (50 mL). The organic layer was dried over $MgSO_4$ and the solvent evaporated under reduced pressure. The product is obtained as a white solid which is used in the next step without any further purification (5.4119 g, 91.0%).

^{1}H NMR (400 MHz, $CDCl_3$) δ[ppm]: 6.20 (t, J = 5.8 Hz, 1H$_h$), 3.56 (t, J = 6.4 Hz, 2H$_g$), 3.17 (td, J = 7.0, 5.7 Hz, 2H$_f$), 2.10 (t, J = 7.7 Hz, 2H$_e$), 1.63 – 1.41 (m, 6H$_d$), 1.40 – 1.14 (m, 8H$_c$), 0.87 – 0.75 (m, 3H$_a$).

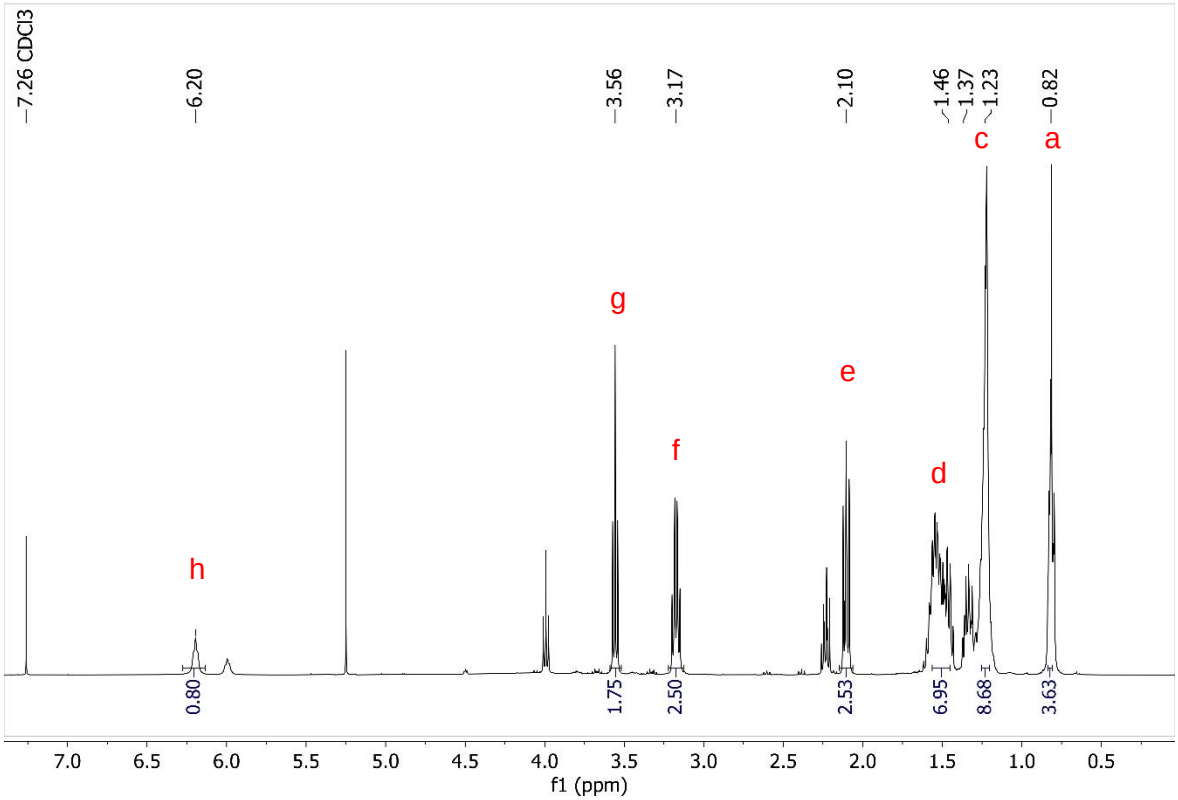

5-heptanamidopentyl methanesulfonate

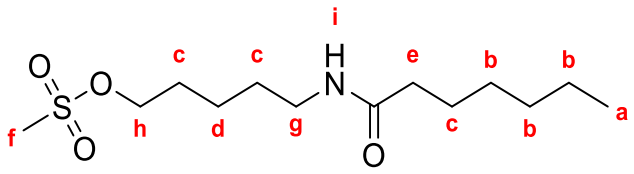

Mesyl chloride (1.1 mL, 14.2 mmol) was added dropwise to a solution of N-(5-hydroxypentyl)heptanamide (1.5540 g, 7.2 mmol), Et_3N (2.0 mL, 14.3 mmol) in dry THF (40 mL) at 0 °C. Then, the solution was let to reach room temperature and stirred for 3 h. After filtration, the solvent was vacuum evaporated, the crude dissolved in $CHCl_3$ (100 mL) and washed with water (2x 100 mL) and saturated brine (100 mL). The organic layer was dried over $MgSO_4$ and the solvent evaporated under reduced pressure. The crude product was purified by column chromatography using a cyclohexane-ethyl acetate (10 up to 100%) mixture. The desired product was obtained as a white solid (1.3103 g, 62.0%).

^{1}H NMR (400 MHz, $CDCl_3$) δ[ppm]: 5.52 (s, 1H$_i$), 4.22 (t, J = 6.4 Hz, 2H$_h$), 3.25 (td, J = 6.9, 5.9 Hz, 2H$_g$), 3.00 (s, 3H$_f$), 2.15 (t, J = 7.5 Hz, 2H$_e$), 1.83 – 1.72 (m, 2H$_d$), 1.67 – 1.38 (m, 6H$_c$), 1.37 – 1.21 (m, 6H$_b$), 0.87 (t, J = 7.0 Hz, 3H$_a$).

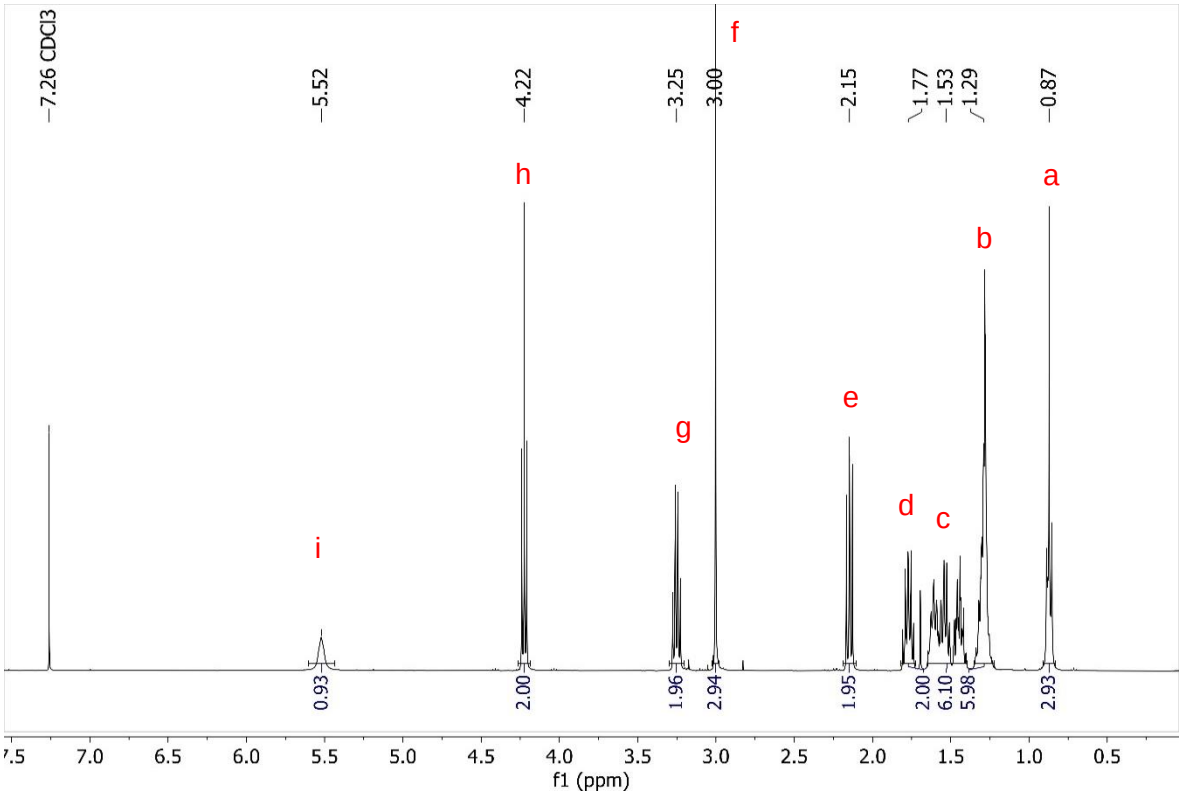

6,6'-(3,6-bis(5-hexylthiophen-2-yl)-1,4-dioxopyrrolo[3,4-c]pyrrole-2,5(1H,4H)-diyl)bis(N-hexylhexanamide) (**HDPPBA-C**)

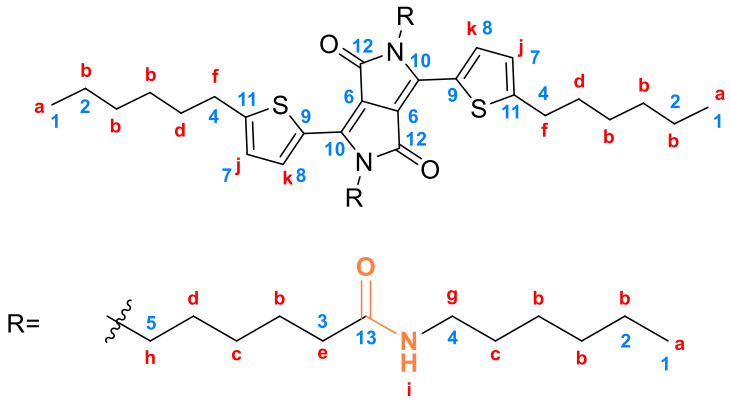

Cs_2CO_3 (0.8861 g, 2.7 mmol) was added to a suspension of **4** (0.5021 g, 1.1 mmol) in acetonitrile (40 mL) and stirred at 80 °C for one hour under argon atmosphere. Then, the C-centered amide chain (0.8861 g, 2.7 mmol) dissolved in acetonitrile (10 mL) was added dropwise during 20 min. The solution was stirred overnight at 80 °C. The reaction was allowed to cool to room temperature, the solvent was evaporated under vacuum. The residue was dissolved in $CHCl_3$ (70 mL) and washed with water (3x 100 mL). The organic phase was dried over $MgSO_4$ and filtered. Then, the solvent was vacuum evaporated. The crude product was purified by column chromatography using $CHCl_3$-Methanol (0 up to 10%) as eluent. Finally, the product was recrystallized in a $CHCl_3$-Methanol mixture to obtain HT**DPP**BA as purple flake-like solids (0.2868 g, 31.0%).

^{1}H NMR (400 MHz, $CDCl_3$) δ[ppm]: 8.72 (d, J = 3.9 Hz, $2H_k$), 6.96 (d, J = 4.0 Hz, $2H_j$), 5.47 (s, $2H_i$), 4.05 (t, J = 7.6 Hz, $4H_h$), 3.22 (dd, J = 7.3, 5.8 Hz, $4H_g$), 2.90 (t, J = 7.6 Hz, $4H_f$), 2.17 (t, J = 7.5 Hz, $4H_e$), 1.82 – 1.65 (m, $12H_d$), 1.51 – 1.35 (m, $12H_c$), 1.35 – 1.23 (m, $20H_b$), 0.91 – 0.85 (m, $12H_a$).

^{13}C NMR (101 MHz, $CDCl_3$) δ[ppm]: 172.78 ($2C_{13}$), 161.55 ($2C_{12}$), 153.06 ($2C_{11}$), 139.84 ($2C_{10}$), 135.71 ($2C_9$), 127.41 ($2C_9$), 126.25 ($2C_7$), 107.14 ($2C_6$), 41.90 ($2C_5$), 39.67 ($2C_4$), 36.77 ($2C_3$), 31.62, 31.59, 30.48, 29.79, 29.72, 28.93, 26.73, 26.53, 25.43, 22.70 ($4C_2$), 14.15 ($4C_1$).

Theoretical m/z: 862.5464, HR-MS (ESI-TOF): 885.5358 $[M+Na]^+$.

Elemental analysis for $C_{50}H_{78}N_4O_4S_2$: calculated: C, 69.56 %; H, 9.11 %; N, 6.49 %. Found: C, 69.03 %; H, 9.17 %; N, 6.49 %.

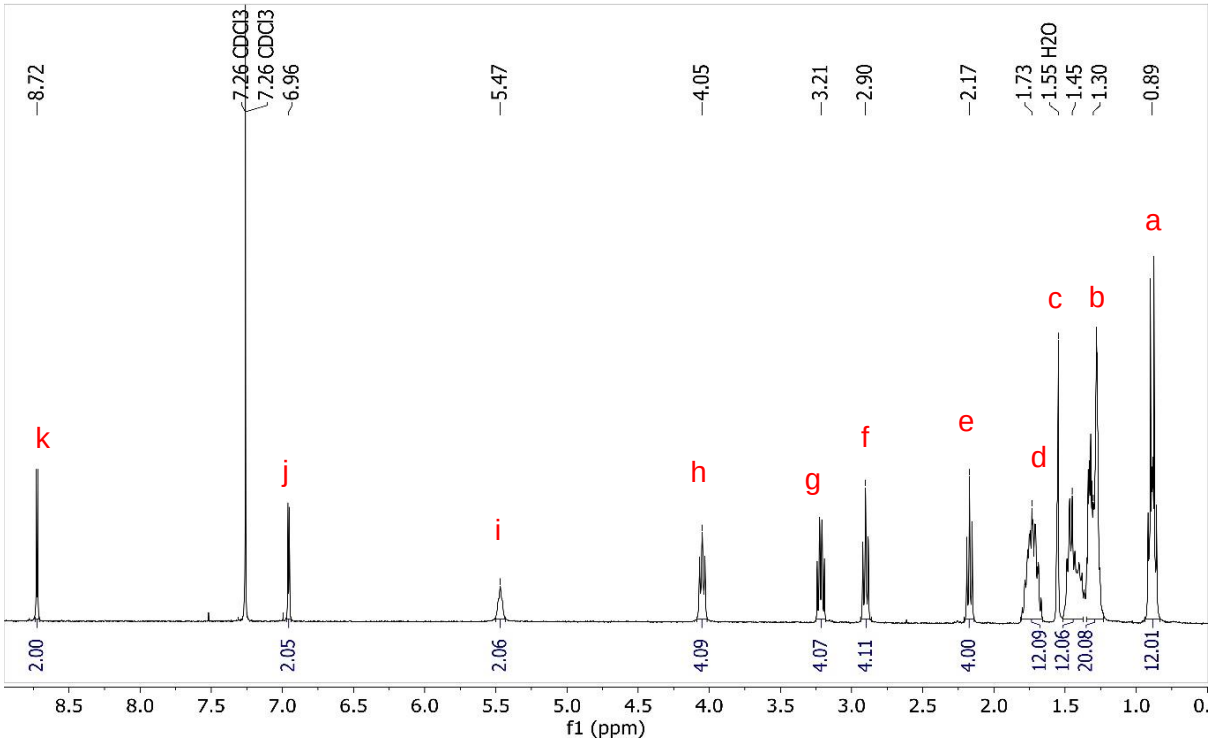

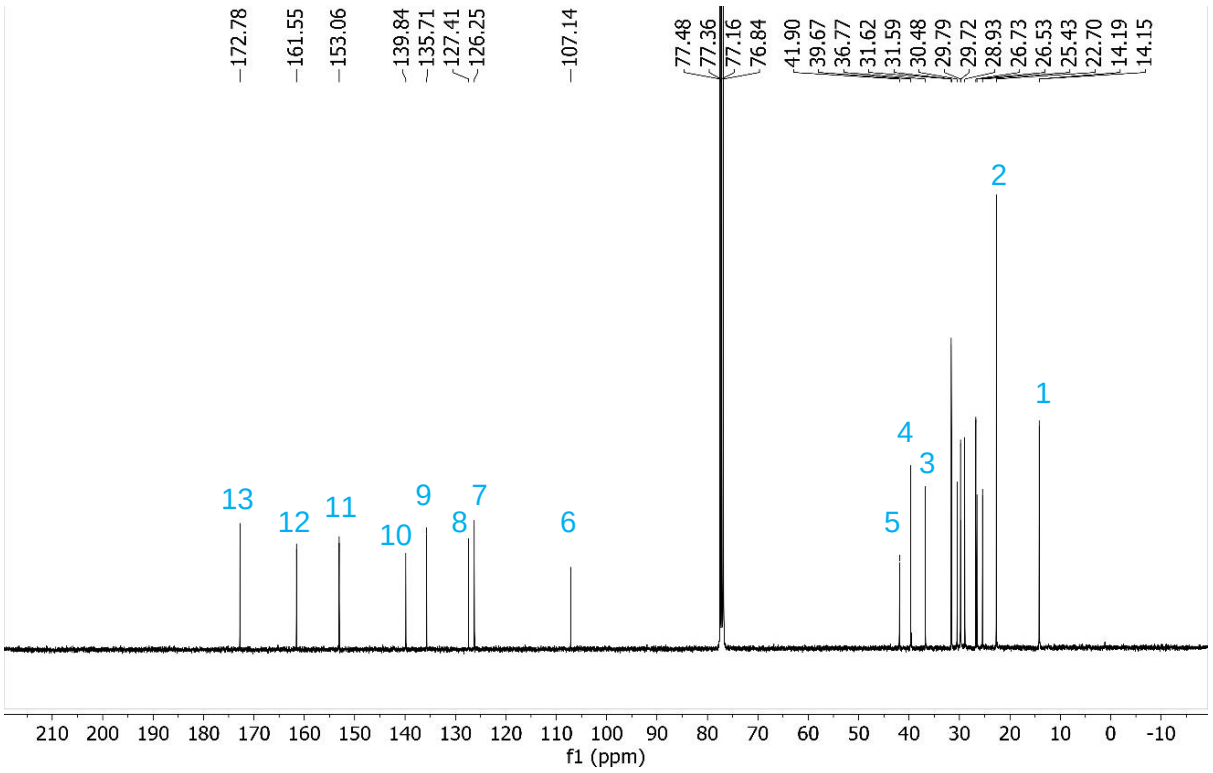

Mass Spectrum HR Report

Analysis Info

Analysis Name	D:\Data\SMasse\2020\09_Septembre 2020\F06794SK.d	Acquisition Date	9/23/2020 10:38:13 AM
Method	Tune_pos_Mid.m		
Sample Name	HTDPPBA	Operator	BDAL@DE
Comment		Instrument	micrOTOF II 8213750.1045 1

Acquisition Parameter

Source Type	ESI	Ion Polarity	Positive	Set Corrector Fill	52.4 V
n/a	n/a	n/a	n/a	n/a	n/a
Scan Begin	50 m/z	n/a	n/a	Set Reflector	1800.0 V
Scan End	3000 m/z	n/a	n/a	Set Flight Tube	8600.0 V
		n/a	n/a	Set Detector TOF	1985.0 V

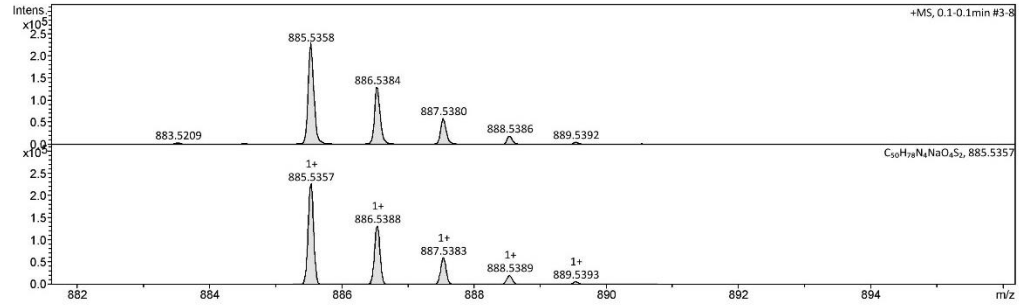

Meas. m/z	#	Ion Formula	m/z err [ppm]	Mean err [ppm]	rdb	N-Rule	e⁻ Conf	mSigma	Std I	Std Mean m/z	Std I	VarNorm	Std m/z Diff	Std Comb Dev
885.535834	1	C50H78N4NaO4S2	885.535670	-0.2	0.1	13.5	ok	even	6.6	7.0	n.a.	n.a.	n.a.	n.a.

Bruker Compass DataAnalysis 4.2 printed: 9/23/2020 3:36:29 PM Page 1 of 1

2,5-dihexyl-3,6-bis(5-hexylthiophen-2-yl)-2,5-dihydropyrrolo[3,4-c]pyrrole-1,4-dione (**HTDPPH**)

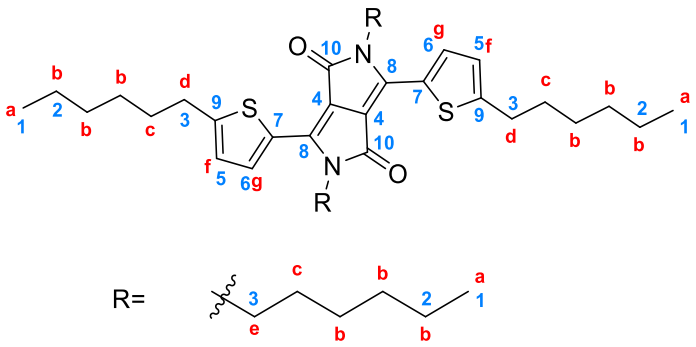

Cs_2CO_3 (0.7160 g, 2.1 mmol) was added to a suspension of **HTDPP** (0.4155 g, 0.9 mmol) in acetonitrile (25 mL) and stirred at 80 °C for one hour under argon atmosphere. Then, 1-bromohexane (0.3 mL, 2.1 mmol) was added dropwise during 20 min. The solution was stirred overnight at 80 °C. The reaction was allowed to cool to room temperature, the solvent was evaporated under vacuum. The residue was dissolved in $CHCl_3$ (70 mL) and washed with water (3x 100 mL). The organic phase was dried over $MgSO_4$ and filtered. Then, the solvent was vacuum evaporated. The crude product was purified by column chromatography using toluene as eluent. The desired product was obtained as a purple solid (0.1790 g, 33.7%).

^{1}H NMR (400 MHz, $CDCl_3$) δ[ppm]: 8.75 (d, J = 3.9 Hz, 2H$_g$), 6.95 (d, J = 3.9 Hz, 2H$_f$), 4.03 (t, J = 8.0 Hz, 4H$_e$), 2.90 (t, J = 7.6 Hz, 4H$_d$), 1.79 – 1.67 (m, 8H$_c$), 1.45 – 1.37 (m, 8H$_b$), 1.34 – 1.29 (m, 16H$_b$), 0.91 – 0.86 (m, 12H$_a$).

^{13}C NMR (101 MHz, $CDCl_3$) δ[ppm]: 161.53 (2C$_{10}$), 152.83 (2C$_9$), 139.85 (2C$_8$), 135.67 (2C$_7$), 127.57 (2C$_6$), 126.24 (2C$_5$), 107.19 (2C$_4$), 42.30 (4C$_3$), 31.65, 31.58, 31.57, 30.47, 30.03, 29.85, 28.90, 26.69, 22.69 (4C$_2$), 14.16 (4C$_1$).

Theoretical m/z: 636.3783, HR-MS (ESI-TOF): 636.3768 $[M]^+$.

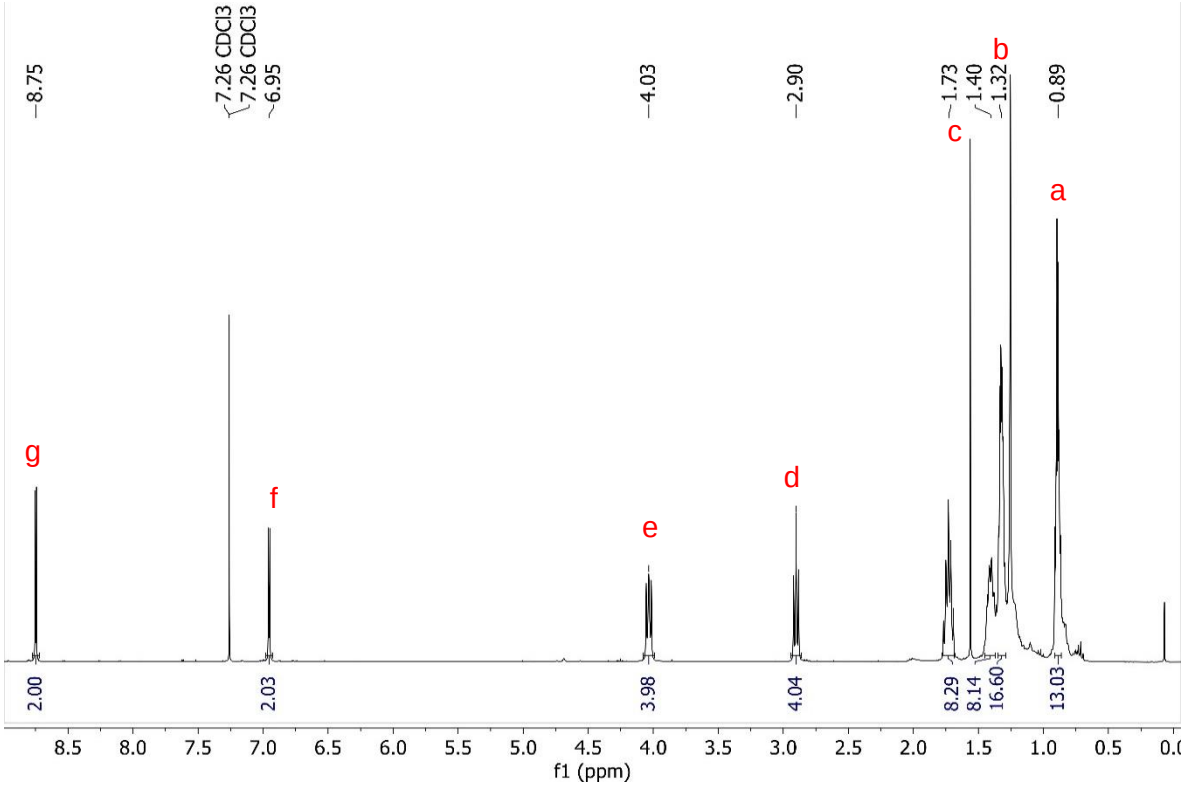
8.75
7.26 CDCl3
7.26 CDCl3
6.95
4.03
2.90
1.73
1.40
1.32
0.89
g
f
e
d
c
b
a
2.00
2.03
3.98
4.04
8.29
8.14
16.60
13.03
f1 (ppm)

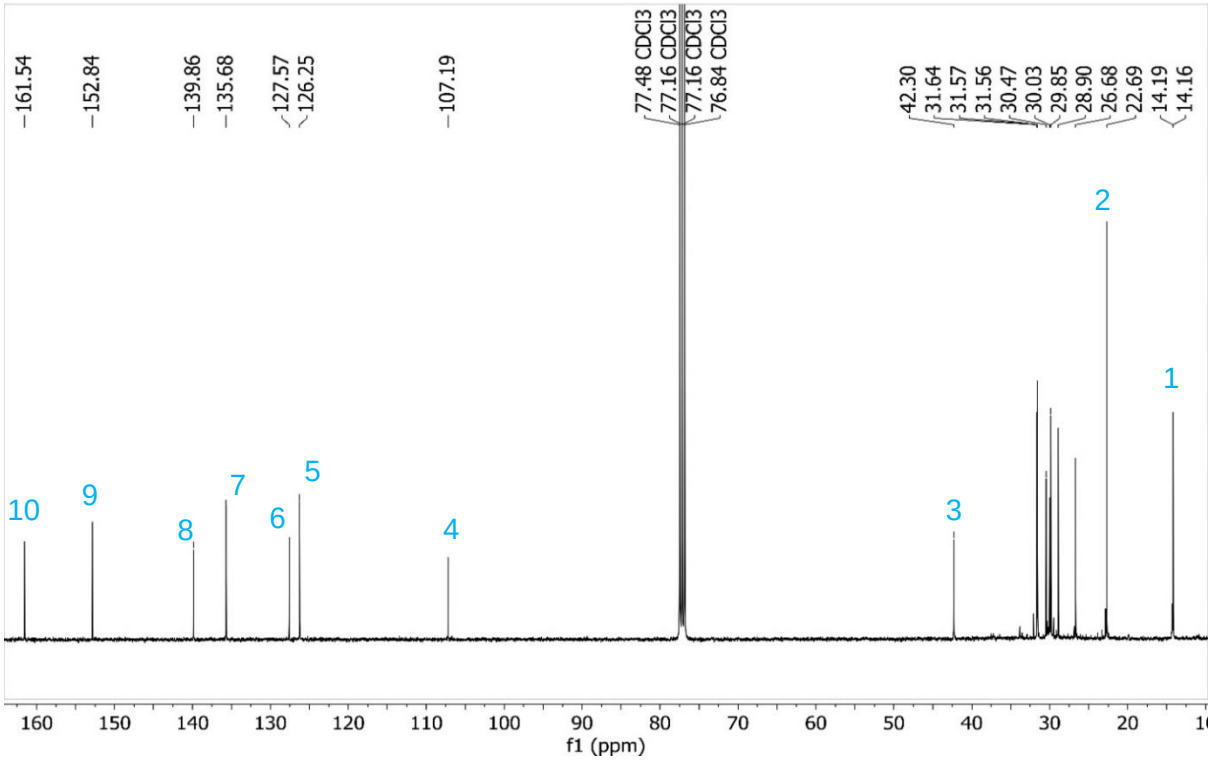
161.54
152.84
139.86
135.68
127.57
126.25
107.19
77.48 CDCl3
77.16 CDCl3
77.16 CDCl3
76.84 CDCl3
42.30
31.64
31.57
31.56
30.47
30.03
29.85
28.90
26.68
22.69
14.19
14.16
10
9
8
7
6
5
4
3
2
1
f1 (ppm)

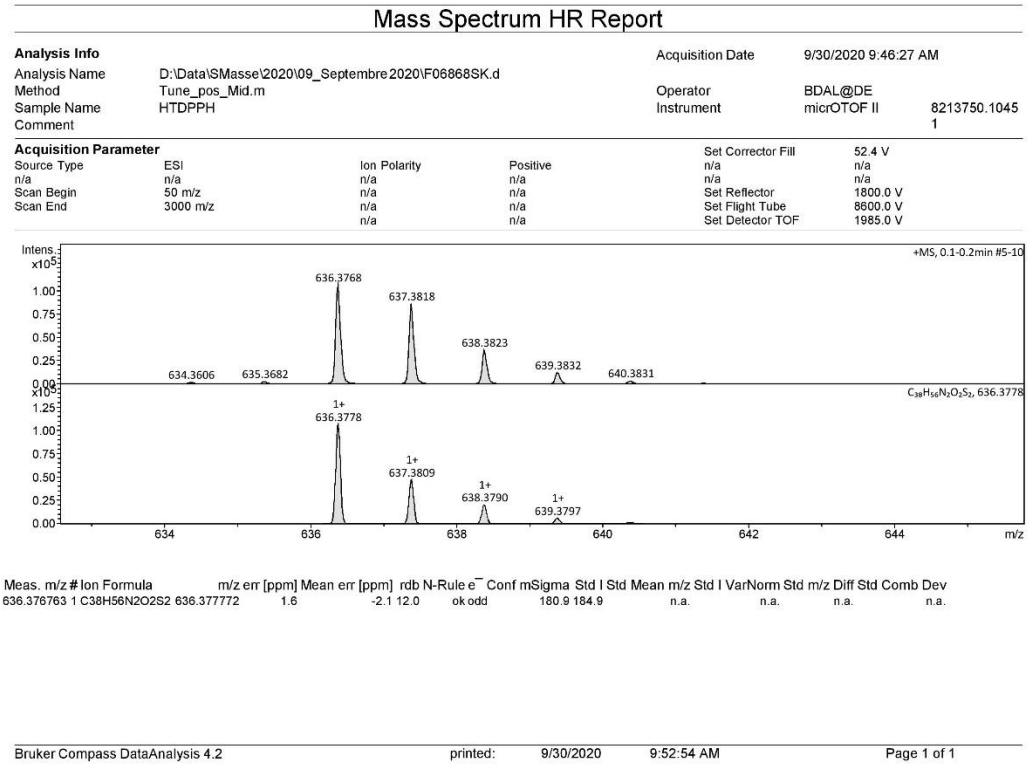

N,N'-((3,6-bis(5-hexylthiophen-2-yl)-1,4-dioxopyrrolo[3,4-c]pyrrole-2,5(1H,4H)-diyl)bis(pentane-5,1-diyl))diheptanamide (**HDPPBA-N**)

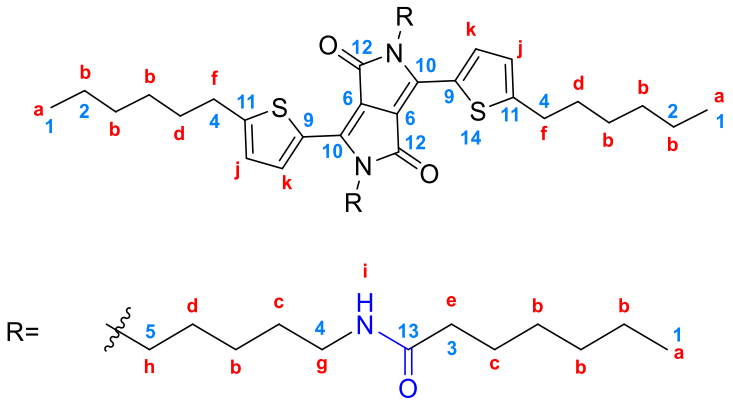

R=

Cs_2CO_3 (1.5077 g, 4.6 mmol) was added to a suspension of HT**DPP** (0.7103 g, 1.5 mmol) in acetonitrile (35 mL) and stirred at 80 °C for one hour under argon atmosphere. Then, the N-centered amide chain (1.1598 g, 4.0 mmol) dissolved in acetonitrile (10 mL) was added dropwise during 20 min. The solution was stirred overnight at 80 °C. The reaction was allowed to cool to room temperature, the solvent was evaporated under vacuum. The residue was dissolved in $CHCl_3$ (70 mL) and washed with water (3x 100 mL). The organic phase was dried over $MgSO_4$ and filtered. Then, the solvent was vacuum evaporated. The crude product was recrystallized in a $CHCl_3$-Methanol mixture to obtain the desired pure product as purple flake-like solids (0.2250 g, 17.2%).

^{1}H NMR (400 MHz, $CDCl_3$) δ[ppm]: 8.75 (d, J = 3.8 Hz, $2H_k$), 6.95 (d, J = 3.7 Hz, $2H_j$), 5.62 (s, $2H_i$), 4.06 (t, J = 7.1 Hz, $4H_h$), 3.25 (q, J = 6.4 Hz, $4H_g$), 2.90 (t, J = 7.6 Hz, $4H_f$), 2.12 (t, J = 7.5 Hz, $4H_e$), 1.82 – 1.66 (m, $8H_d$), 1.48 – 1.17 (m, $28H_b$ and $8H_c$), 0.92 – 0.83 (m, $12H_a$).

^{13}C NMR (101 MHz, $CDCl_3$) δ[ppm]: 173.32 ($2C_{13}$), 161.68 ($2C_{12}$), 153.23 ($2C_{11}$), 139.89 ($2C_{10}$), 135.86 ($2C_9$), 127.32 ($2C_8$), 126.27 ($2C_7$), 107.06 ($2C_6$), 41.60 ($2C_5$), 39.42 ($4C_4$), 36.95 ($2C_3$), 31.72, 31.62, 31.59, 30.47, 29.75, 29.11, 29.04, 28.93, 25.92, 24.11, 22.69 ($4C_2$), 14.19 ($4C_1$).

Theoretical m/z: 862.5464, HR-MS (ESI-TOF): 863.5537 $[M + H]^+$.

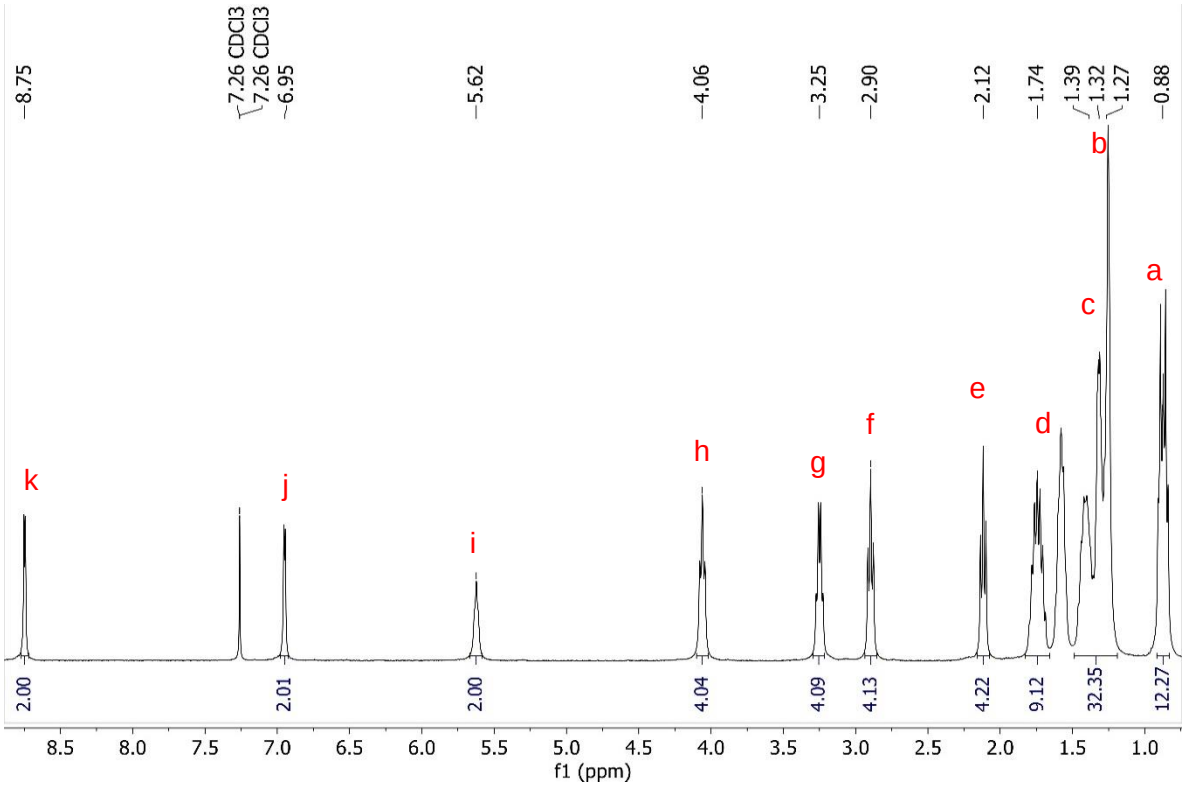

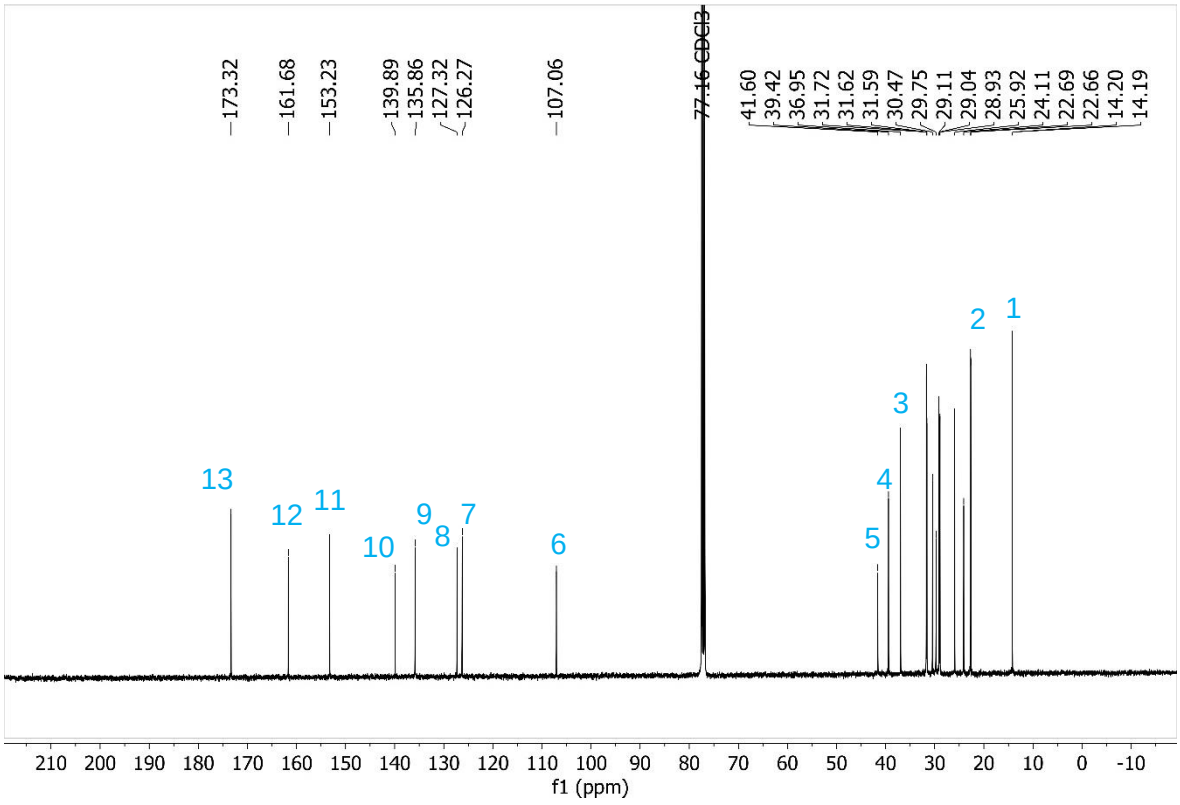

Mass Spectrum HR Report

Analysis Info

Analysis Name	D:\Data\SMasse\2021\01_Janvier 2021\F07714SK.d	Acquisition Date	1/18/2021 2:42:11 PM
Method	Tune_pos_Mid.m		
Sample Name	HTDPPBA Inverted	Operator	BDAL@DE
Comment		Instrument	micrOTOF II 8213750.1045 1

Acquisition Parameter

Source Type	ESI	Ion Polarity	Positive	Set Corrector Fill	52.4 V
n/a	n/a	n/a	n/a	n/a	n/a
Scan Begin	50 m/z	n/a	n/a	Set Reflector	1800.0 V
Scan End	3000 m/z	n/a	n/a	Set Flight Tube	8600.0 V
		n/a	n/a	Set Detector TOF	1985.0 V

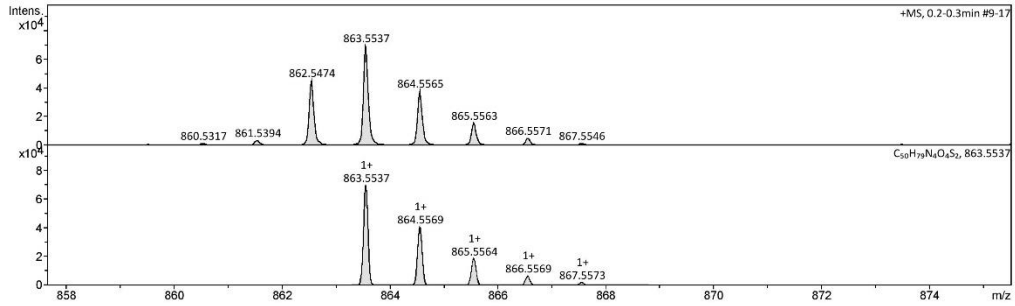

Meas. m/z	#	Ion Formula	m/z err [ppm]	Mean err [ppm]	rdb	N-Rule	e⁻ Conf	mSigma	Std I	Std Mean m/z	Std I	VarNorm Std m/z	Diff Std Comb	Dev
863.553660	1	C50H79N4O4S2	863.553725	0.1	0.5	13.5	ok	even	28.0	34.6	n.a.	n.a.	n.a.	n.a.

IV. References

[1] D. S. Philips, K. K. Kartha, A. T. Politi, T. Krüger, R. Q. Albuquerque, G. Fernández, *Angewandte Chemie International Edition* **2019**, *58*, 4732–4736.

[2] M. Wegner, D. Dudenko, D. Sebastiani, A. R. A. Palmans, T. F. A. de Greef, R. Graf, H. W. Spiess, *Chemical Science* **2011**, *2*, 2040–2049.

[3] G. M. Whitesides, *Science* **2002**, *295*, 2418–2421.

[4] C. Kulkarni, S. Balasubramanian, S. J. George, *ChemPhysChem* **2013**, *14*, 661–673.

[5] D. S. Philips, K. K. Kartha, A. T. Politi, T. Krüger, R. Q. Albuquerque, G. Fernández, *Angew. Chem. Int. Ed.* **2019**, *58*, 4732–4736.

[6] S. Militzer, N. Nishimura, N. R. Ávila-Rovelo, W. Matsuda, D. Schwaller, P. J. Mésini, S. Seki, A. Ruiz-Carretero, *Chem. Eur. J.* **2020**, chem.202001540.

[7] M. Kirkus, L. Wang, S. Mothy, D. Beljonne, J. Cornil, R. A. J. Janssen, S. C. J. Meskers, *J. Phys. Chem. A* **2012**, *116*, 7927–7936.

[8] W.-W. Tsai, I. D. Tevis, A. S. Tayi, H. Cui, S. I. Stupp, *J. Phys. Chem. B* **2010**, *114*, 14778–14786.

[9] Y. Zhou, C. X. Guzman, L. C. Helguero-Kelley, C. Liu, S. R. Peurifoy, B. Captain, A. B. Braunschweig, *Journal of Physical Organic Chemistry* **2016**, *29*, 689–699.

[10] S. Militzer, T. M. P. Tran, P. J. Mésini, A. Ruiz-Carretero, *ChemNanoMat* **2018**, *4*, 790–795.

EXPANDING THE BISAMIDE FAMILY:

Influence of amide position and topology

CHAPTER IV

I. Introduction and objectives

In this chapter, the main objective is to explore and evaluate the effect of the position of the H-bond within the main core. Apart from studying the influence of the position of the H-bond moiety, the topology of the amide was evaluated once again. In this new family, the position of the H-bonding units has been changed to the thiophene rings (Figure IV. 1). The thiophene rings on the **DPP** were functionalized with amide branches, while regular alkyl chains were placed in the lactam rings.

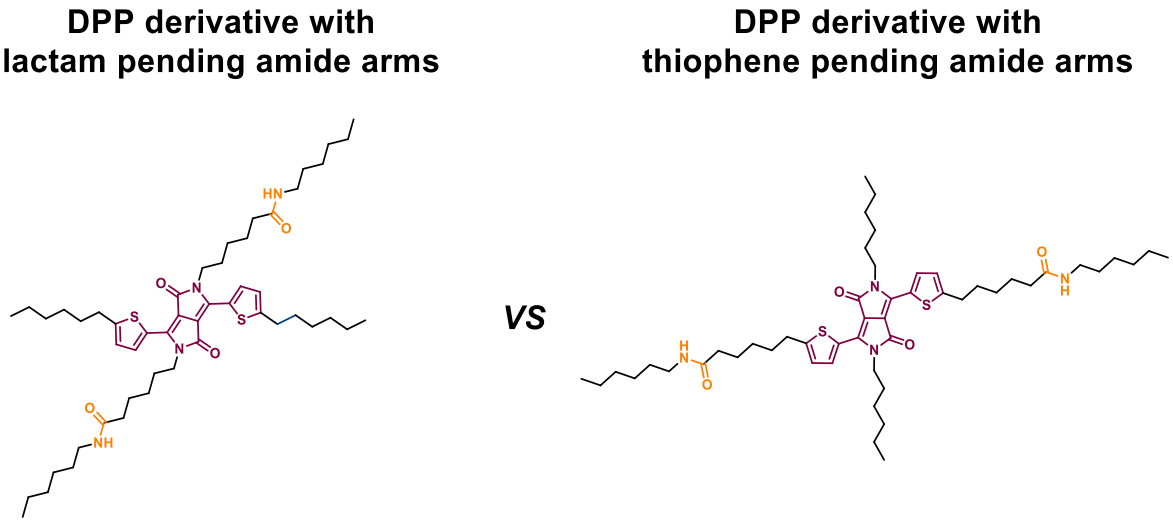

*Figure IV. 1 Structural comparison for the change in position of the amide group in **DPP** derivatives.*

In general, thiophene capped **DPP** derivatives are functionalized in the thiophenes to serve as the starting materials in Pd-catalyzed cross-coupling reactions. Grzybowski *et al* reviewed the synthesis and reactivities of **DPPs**, where they discussed the substitutions that can be performed on the thiophene units of **DPPs**, these include couplings such as Suzuki, Stille, Buchwald–Hartwig and Sonogashira.[1]

For instance, Suzuki and Stille couplings are employed most often for the synthesis of **DPP**-based π-conjugated polymers. Such an example is shown in Scheme IV. 1, where a brominated thiophene derivative was used along with tributyl-(4-dodecyl-thiophen-2-yl)-stannane under Stille conditions to extend the aromaticity of the **DPP** core and increase its solubility, to finally yield a polymer with ambipolar charge transport properties.[2]

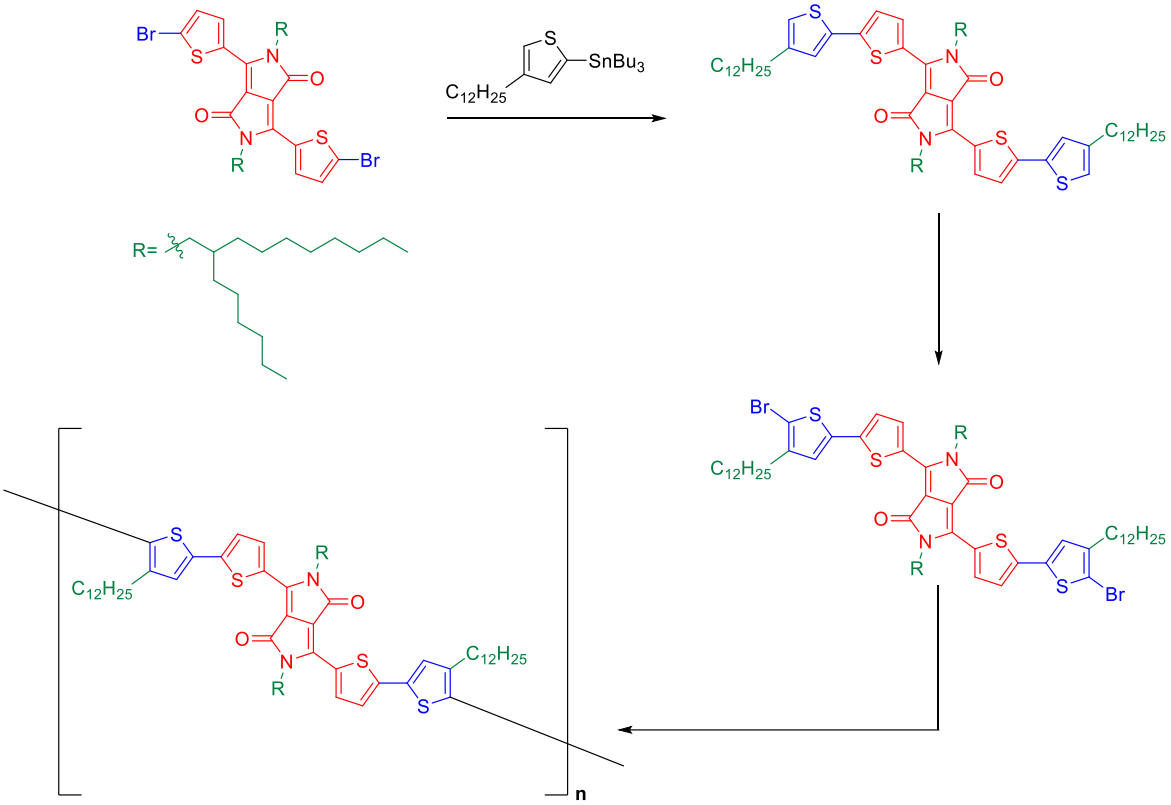

*Scheme IV. 1 Summarized synthetic approach of an alkylated bithiophene **DPP** polymer derivative.*

Another way the thiophene units on **DPPs** are functionalized is by creating oligomers, which is also done by Suzuki and Stille coupling. However, they have a major drawback: both reactions require the pre-activation of the substrates. For instance, the presence of reactive functional groups, such as bromine atoms in one of the species, and boronic or trialkyltin groups in the second component of the reaction.[3] While the introduction of bromine atoms is relatively easy, the synthesis of boronic acids/esters and organotin compounds is more troublesome.

An example with a **DPP** dimer was reported by Riaño *et al*, were they synthesized two dicyanovinylene-substituted **DPP**–oligothiophene semiconductors, **DPP-4T-2DCV** and **2DPP-6T-2DCV** (Figure IV. 2). In these materials, the combination of an extended oligothiophene conjugated skeleton with the strong electron-withdrawing **DPP**–dicyanovinylene groups results in semiconductors exhibiting ambipolar response with reasonably balanced electron and hole mobilities.[4]

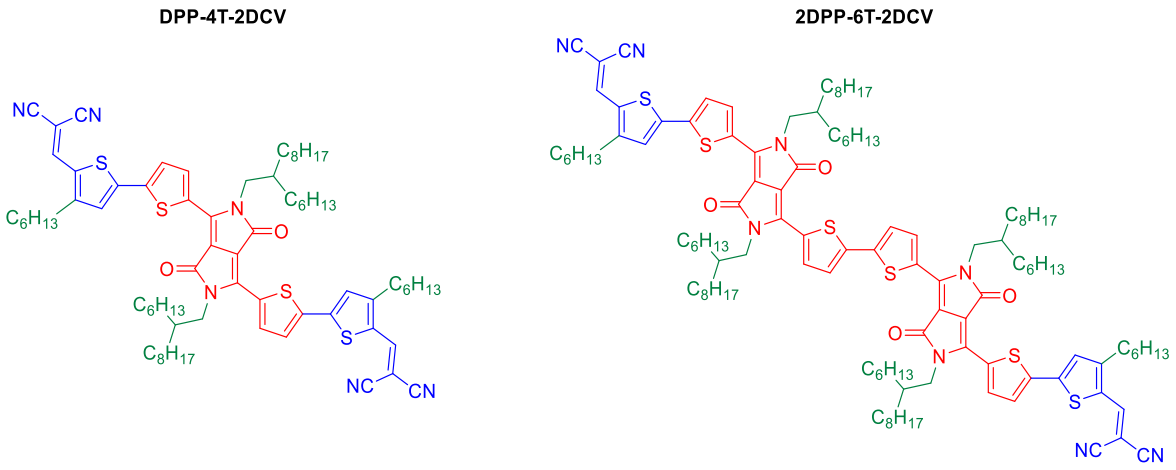

*Figure IV. 2 Molecular structures of semiconductors **DPP-4T-2DCV** and **2DPP-6T-2DCV**.*

The synthesis of compound **2DPP-6T-2DCV** is summarized in Scheme IV. 2. By using a monobromo **DPP** derivative and bis-tributyltin in refluxing toluene, a **DPP** dimer was obtained. They also discussed how this dimer can also be obtained by a Suzuki coupling reaction with bis-pinacolate diboron, but the yield was lower.

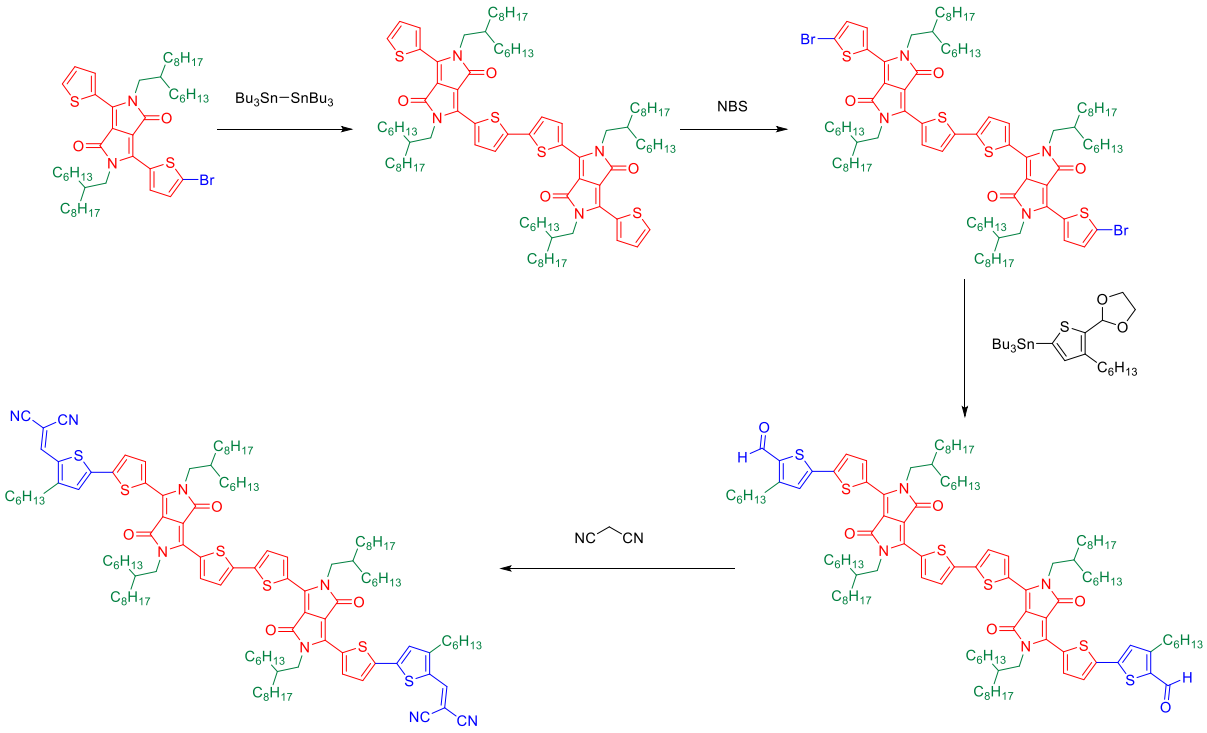

*Scheme IV. 2 Summarized synthetic approach of dimer **2DPP-6T-2DCV**.*

Subsequently, the bromination of the dimer was performed with NBS in $CHCl_3$, which was then followed by a Stille coupling with a thiophene stannyl derivative to afford an aldehyde **DPP** derivative after its respective hydrolysis in aqueous acid media. Subsequently, a Knoevenagel reaction with malononitrile yielded **2DPP-6T-2DCV**. Following the same methodology, compound **DPP-4T-2DCV** was also obtained.

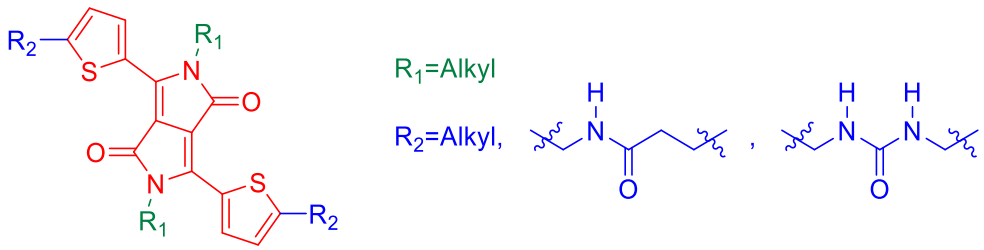

Figure IV. 3 Structure of a DPP core bearing functionalized alkylated chains directly attached to the thiophenes of the core.

It has been shown that examples including functionalization of the thiophenes in the **DPP** core exist in literature. Although, most of these approaches are generally used to extend the conjugated **DPP** core by adding more thiophene rings, while examples where the basic **DPP** core bears functionalized alkylated thiophenes (Figure IV. 3) are non-existent in the literature. Stas *et al* discussed and optimized several synthetic approaches to obtain **DPPs** bearing bithiophene moieties (Scheme IV. 3)[5], which are the closest structures to what we aimed to obtain. One of the pathways they discussed was a succinic cyclization approach that can be summarized as follows:

1) The synthesis of a carbonitrile bithiophene bearing alkyl chains by Stille coupling.
2) The use of the bithiophene in a reaction with diethyl succinate and sodium tert-amyl alkoxide to generate the **DPP** core.
3) The N-alkylation obtaining of the **DPP** core.

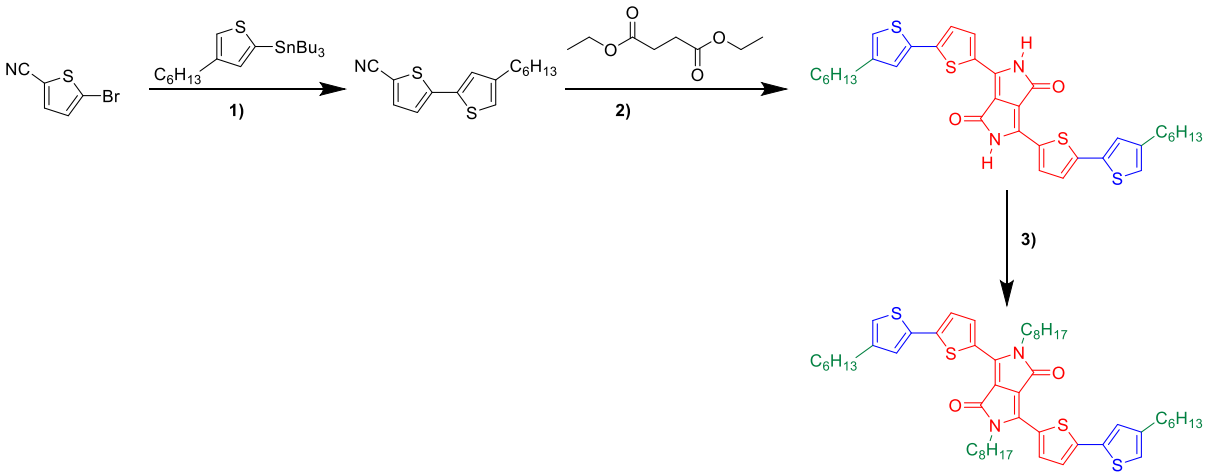

*Scheme IV. 3 Summarized synthetic succinic cyclization approach of an alkylated bithiophene **DPP** derivative.*

Yet, this is not the smallest thiophene alkylated **DPP** core that one can obtain and there is not a procedure describing such synthesis in the literature; furthermore, the previously discussed examples often contain unfunctionalized alkyl chains, which does not help in our quest of evaluating different flexible H-bonding groups pending on the thiophene.

Fortunately, in chapter III we presented that it is possible to synthesise **DPP** derivatives with pending alkyl chains on the thiophenes with a good yield. Therefore, we decided to perform the same succinic cyclization approach to synthesize a **DPP** bearing unfunctionalized alkyl chains on the lactam rings and with amide moieties pending from the thiophene rings.

Consequently, in this chapter a very detailed synthetic approach of two **DPP** derivatives with different topology and functionalized in the thiophene rings is presented. The synthesis of said derivatives was attempted by two different methods, the first one was inspired by the synthetic approach of Stas *et al*[5], while the second one is a more direct approach. It is convenient to mention and discuss all the difficulties encountered for achieving these products.

The self-assembly processes of the N- and C-centered amide-containing **DPP** derivatives were also followed with different spectroscopy and microscopy techniques. The results are compared to the derivatives described in the previous chapter.

Particularly, I focused on the synthesis of the C-centered amides, optimizing the synthetic method that was then applied for the N-centered analogue synthesized by another student of the group. The synthetic comparison between both compounds will still be done to have a better understanding of the results.

II. Results and Discussion

II.1) Synthesis

a) Succinic cyclization approach

At first, the direct alkylation of a thiophene molecule with an amide arm having a mesylate functionality was attempted, but this reaction did not yield the desired product (Scheme IV. 4). It seemed that the mesylate group was not a good leaving group for this coupling and we replaced it by an iodine (Scheme IV. 5).

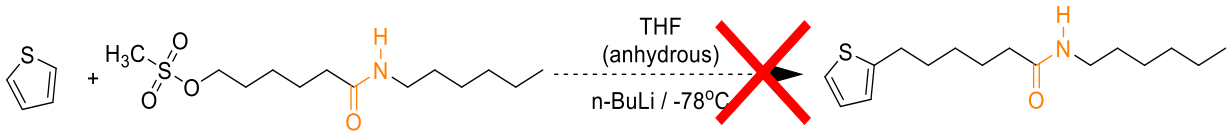

Scheme IV. 4 Failed attempt of a direct alkylation of a thiophene ring with amide arm.

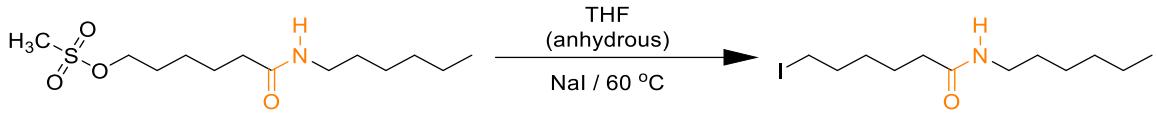

Scheme IV. 5 Replacement of the mesylate function by an Iodine.

Another alkylation reaction was attempted with this new amide arm, but again the desired product was not obtained. The amide functionality seemed to be undergoing another side reaction and therefore, the alkylation by this approach was discarded. An organometallic approach was also attempted, but the amide arm was also not suitable for this type of coupling.

Therefore, a retro-synthetic approach was made (Scheme IV. 6). On paper, this versatile pathway also allowed the synthesis of **DPP** derivatives with amide arms grafted to the thiophene rings with an inverted topology, the key precursor was compound **1** and the subsequent derivatives are shown in Scheme IV. 7. While the synthesis of the N-centered amide derivative had its own challenges, the C-centered amide derivative presented a major bottle neck on the synthetic step leading to compound **3-C**.

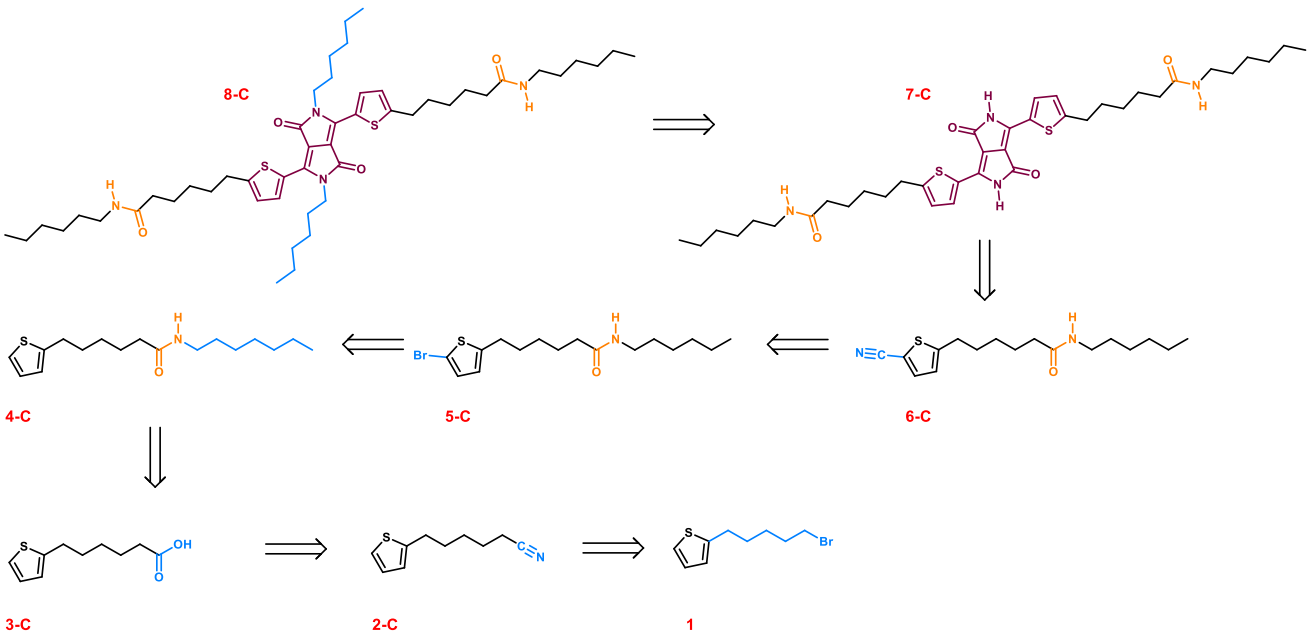

*Scheme IV. 6 Retro-synthetic approach for compound **8-C**.*

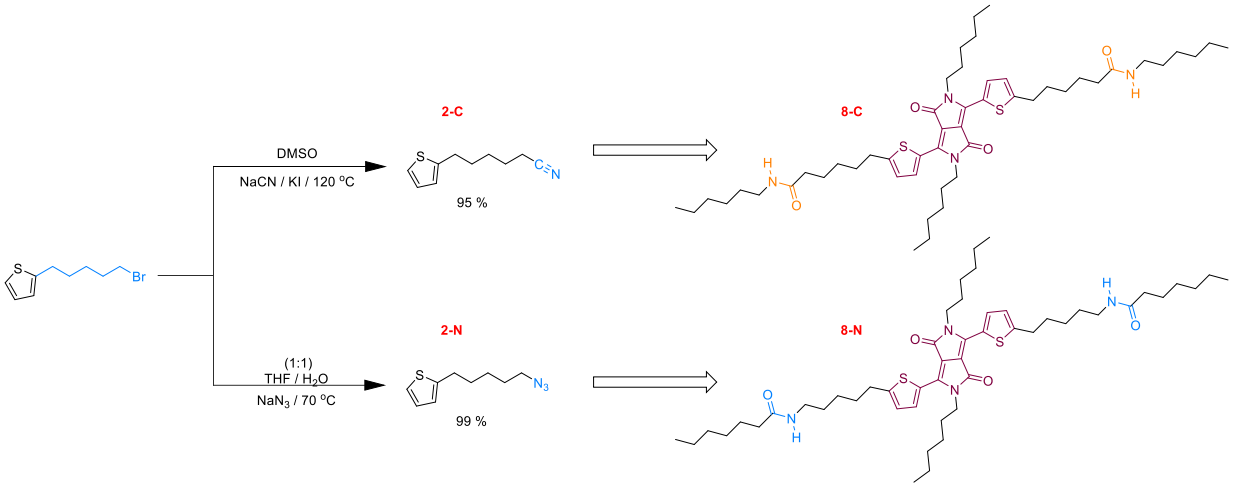

Scheme IV. 7 Precursors to obtain a **DPP** derivative with inverted amide topology.

The hydrolysis of the nitrile to a carboxylic acid seemed easy and straight on paper, however, it was very challenging. Acidic hydrolysis of nitriles has been extensively described in the literature[6], where strong acid and heat are sufficient to lead to a carboxylic acid with water as the solvent. However, the attempted reactions were unsuccessful.

Some protocols claim to have used few drops of concentrated sulfuric or hydrochloric acid, others use water/acid mixtures in a 1:1 ratio. Several attempts were performed but only the most relevant ones are commented.

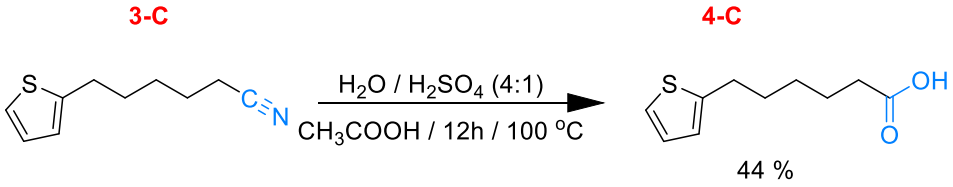

Scheme IV. 8 First successful attempt of the hydrolysis of compound **2-C**.

When water/acid mixtures in a 1:1 ratio were used, no reaction was occurring at room temperature, so the next step was to increase the temperature and see its impact. The reactions started to occur at temperatures above 40 ˚C for the mixture consisting of H_2O/H_2SO_4 (1:1), where the crude started to become black in color, and degradation of the starting material was confirmed by ^{1}H-NMR and TLC. For the H_2O/HCl (1:1) mixture, several attempts at different temperatures were performed but the hydrolysis was not occurring, and when the temperature was increased to 70 ˚C, the degradation reaction started.

Therefore, it was decided to play with the water/acid ratios, until finally, working conditions that led to the carboxylic acid were found. The first conditions that yielded compound **3-C** are shown in Scheme IV. 8, the major inconvenient of this approach was the solubilization of the starting material in the solvent mixture as it is insoluble in water, which ultimately impacted the yield. Later, this synthetic step was completely changed to a basic hydrolysis procedure[7] and

optimized, as can be seen in Scheme IV. 9. The yield was greatly improved, as solubility was better, especially as the temperature increased.

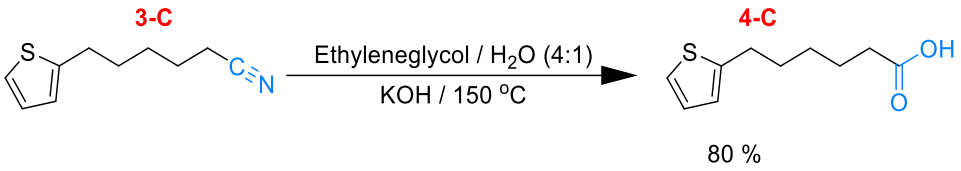

Scheme IV. 9 Optimized conditions for the hydrolysis of the nitrile into a carboxylic acid.

The synthesis of the precursors with different topologies was the same from **4-C** to **6-C** and **4-N** to **6-N**, in this case only the C-centered route is shown in Scheme IV. 10.

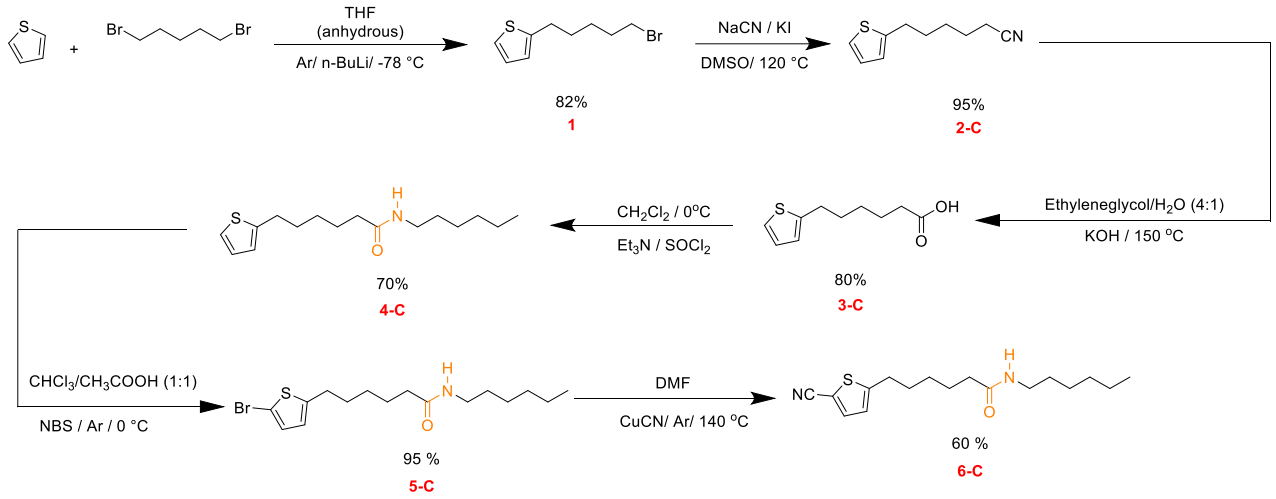

Scheme IV. 10 Synthetic route of the C-centered thiophene with the pending amide.

The next major issue of this approach was found on the cyclization reactions, where compounds **6-C** and **6-N** were involved, as the target molecules were not being obtained. For both compounds the reaction mixture became green in color upon addition of the base.

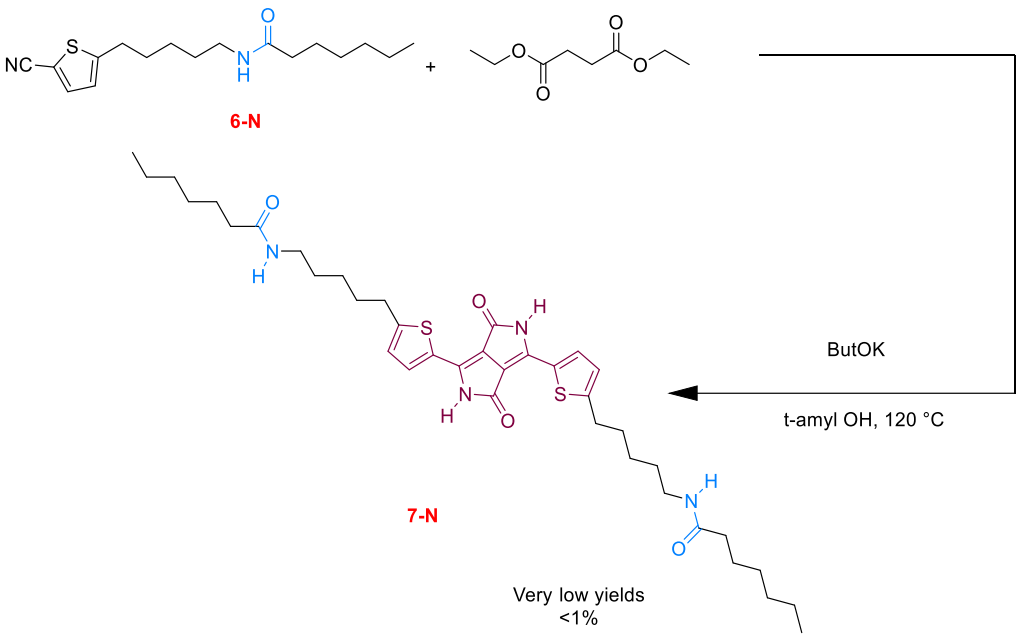

Scheme IV. 11 Cyclization reaction with compound **6-N**.

Several cyclization reactions (Scheme IV. 11) were done changing parameters such as the number of equivalents of potassium tert-butoxide, nitrile **6-N** and diethyl succinate, and the order of addition of the reagents. This was performed with N-centered derivatives by another PhD student, who will provide details on their synthesis in his manuscript.

In some trials with the C-centered derivative, the reaction mixture was getting the characteristic intense red color of **DPP** derivatives, but when trying to characterize the products from these reactions, the cyclization seemed to be more a parasitic reaction rather than the main one. The crude of this reaction was purified by column chromatography and used on an alkylation reaction, finally obtaining compound **8-C**, although the yield was low (Scheme IV. 12). Therefore, this approach was considered not suitable to obtain this type of products, leading to the proposal of alternative routes to obtain the **DPP** functionalized with an amide chain in the thiophene rings.

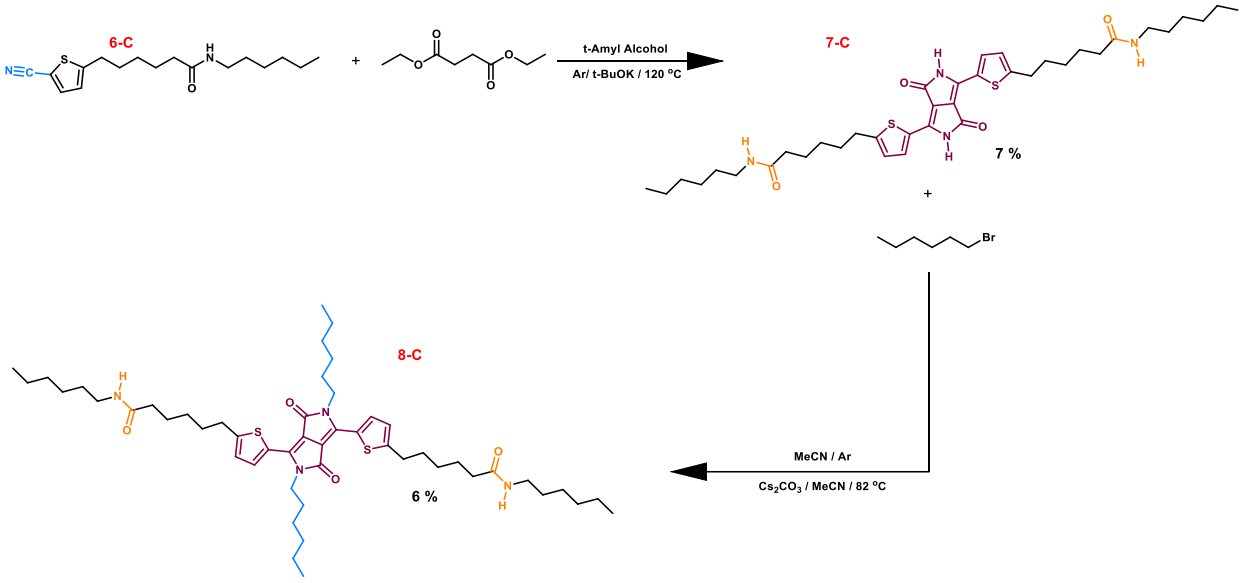

Scheme IV. 12 Final steps in the succinic cyclization synthesis approach of compound **8-C**.

First, the protection of the amide moieties was attempted with tert-butyloxycarbonyl (Boc), as displayed in Scheme IV. 13. This was done to avoid side reactions where the amides are involved during the cyclization, but as soon as the temperature was increased in the cyclization reaction, the mixture became green once again, indicating the deprotection of the amide.

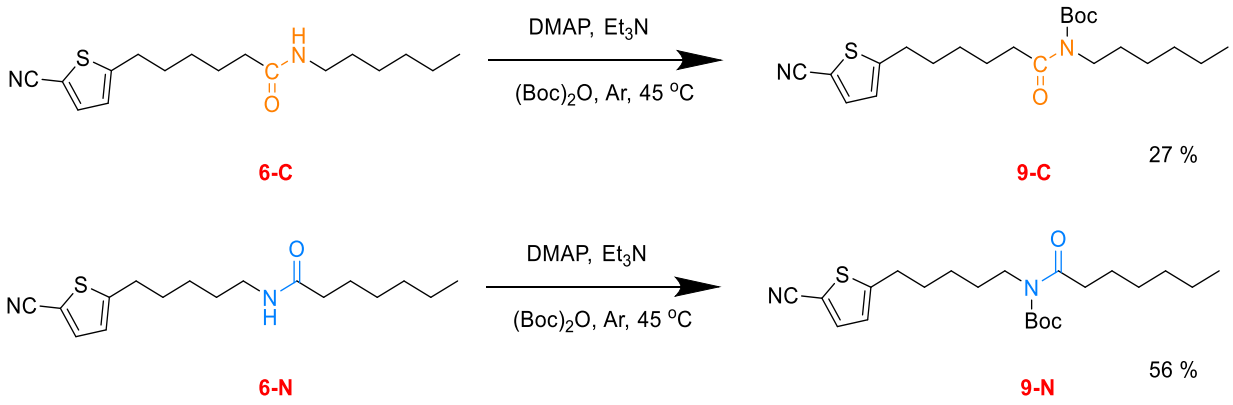

Scheme IV. 13 Protection of precursors with Boc**.**

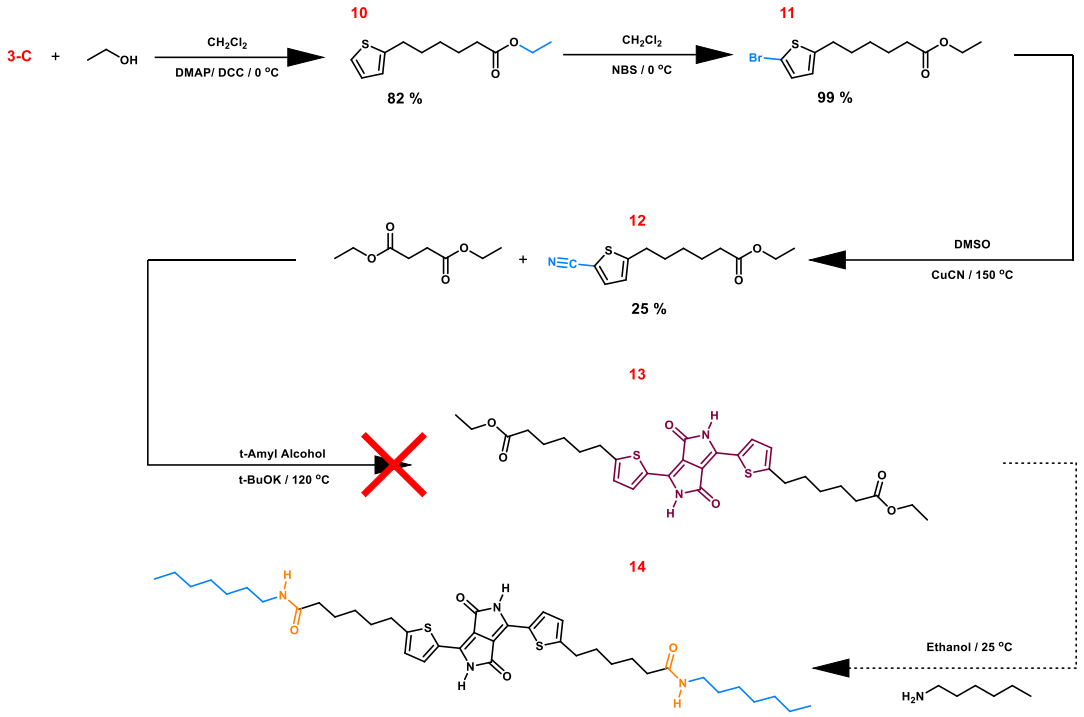

Scheme IV. 14 Ester thiophene derivative cyclization intended approach.

The amide moiety was considered the main issue in the failure of the cyclization and a new approach was envisioned (Scheme IV. 14). For this approach, instead of performing the cyclization on an amide functionalized thiophene, it was done on an ester that would later be converted into an amide. Nevertheless, the cyclization with compound **12** did not lead to a **DPP** cycle. It was inferred that the carbonyl group was undergoing a nucleophilic substitution and interfering in the cyclization mechanism.

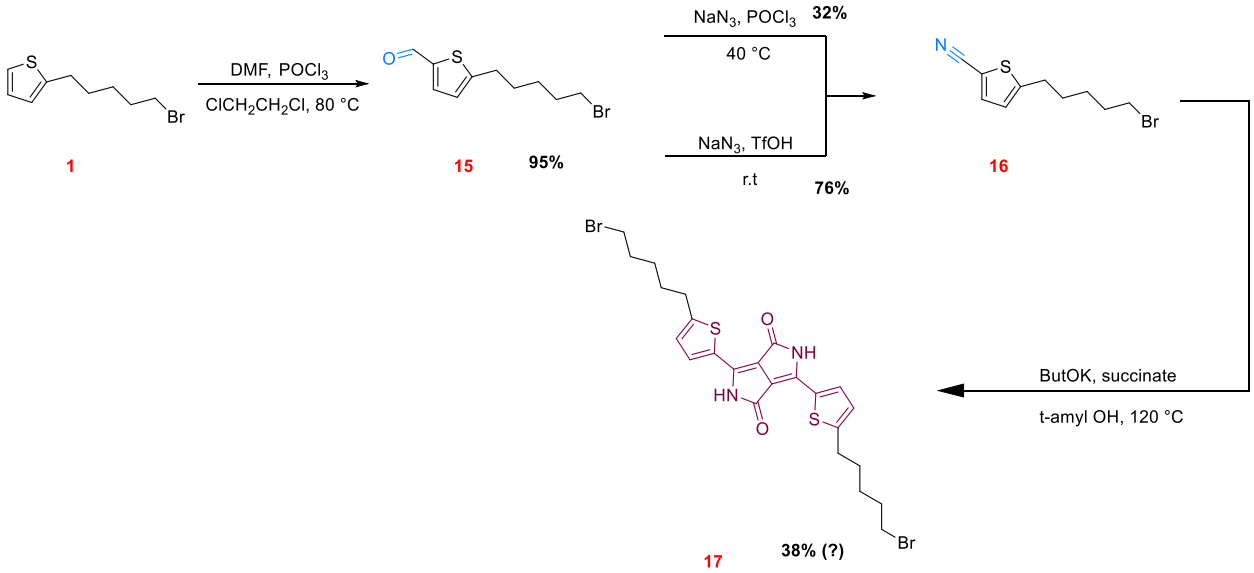

Scheme IV. 15 Cyclization reaction starting from a bromide-pending thiophene carbonitrile.

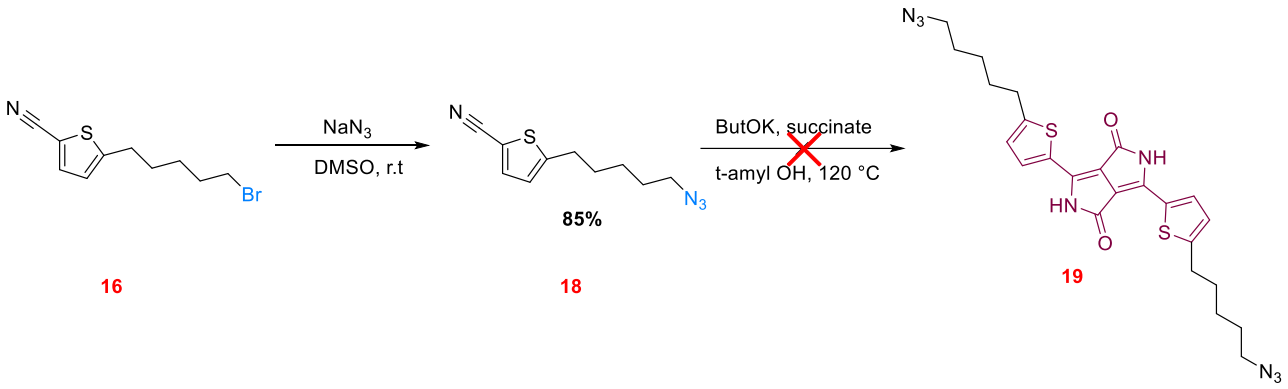

Scheme IV. 16 Alternative **DPP** cyclization using an azide pending thiophene precursor.

Consequently, another alternative was put into practice, consisting on the cyclization reactions with compounds **16** and **18** as shown in Scheme IV. 15 and Scheme IV. 16 respectively, but the reactions did not work again, concluding that this approach was not suitable for thiophenes that had functional groups at the end of the added alkyl chain, being halogens or azides in these cases.

The reaction using compound **18** gave a white solution with no trace of the targeted **DPP**. On the contrary, the cyclization reaction using compound **16** gave a violet solid which seemed like **DPP** and the obtained solid was used to synthesize compound **19** (Scheme IV. 17). This reaction was monitored by IR due to the low solubility of the product and a small signal around 2200 cm^{-1}, belonging to the azide group, was detected. The intensity of this signal did not increase with longer reaction times. At this point, we concluded the reaction had finished.

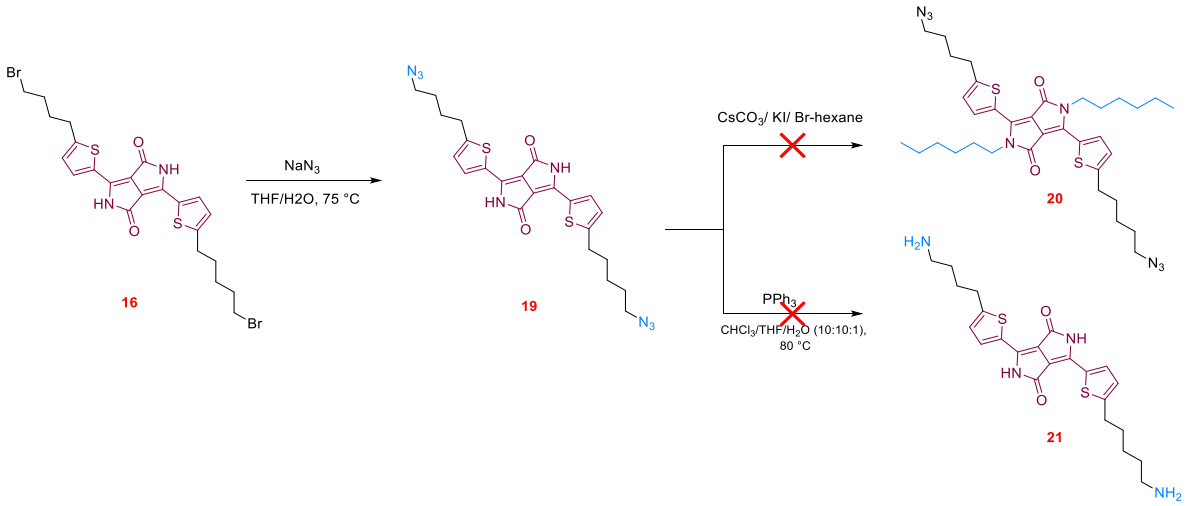

*Scheme IV. 17 Side chain functionalization of intermediate **DPP** compounds*.

Next, to increase the solubility of product **19**, an alkylation with 1-bromohexane was carried out. This reaction resulted in a red-brown solid, which was insoluble in common organic solvents like chloroform, tetrahydrofuran, methanol, cyclohexane (in which compound **20** should be at least partially soluble). It is possible that dimers or tetramers were being obtained by the reaction of the lactam nitrogen with the side chains in the thiophene containing either bromide or azide.

In a parallel reaction, reducing the azide groups in compound **19** was attempted to obtain compound **21**, bearing free amines (Scheme IV. 17). Nevertheless, it was not possible to isolate derivative **21**. Having exhausted this route, it was decided to change the synthetic strategy.

b) Direct approach

The possibility of performing a Sonogashira coupling to a **DPP**[8,9] was not yet explored and an attempt by using a dibrominated thiophene-capped **DPP** (compound **23**) as the starting material was performed (Scheme IV. 18). Compound **8-C** was obtained after hydrogenation at 60 °C using a mixture of solvents.

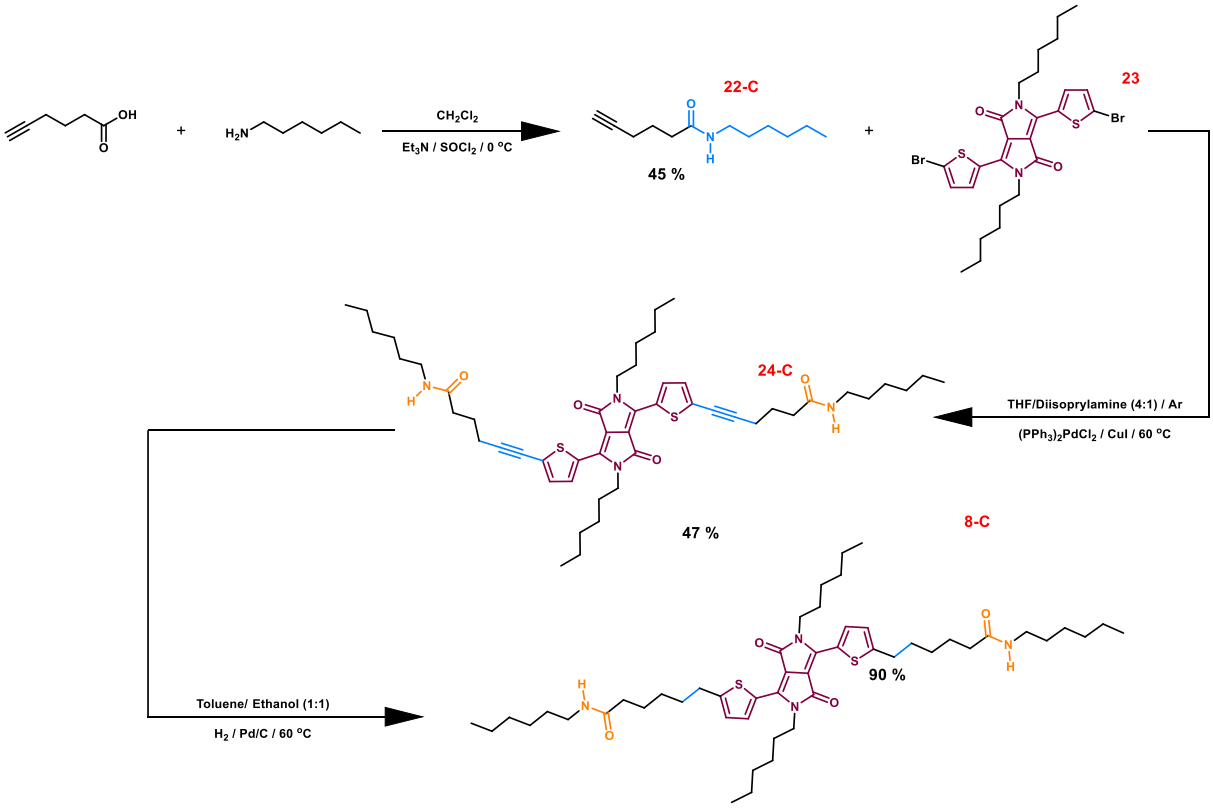

Scheme IV. 18 Final and reliable synthetic approach to obtain **8-C**.

Similarly, the N-centered amide analogue was obtained following the strategy shown in Scheme IV. 19. In this case, the amide branch **24** was synthesized starting with a Mitsunobu reaction to obtain compound **23**, followed by treatment with hydrazine and a coupling with heptanoyl chloride. In a next step, the amide branch (**22-N**) was coupled to compound **23** by Sonogashira coupling, yielding compound **24-N** that was subsequently hydrogenated to the final N-centered **DPP** amide derivative **8-N**.

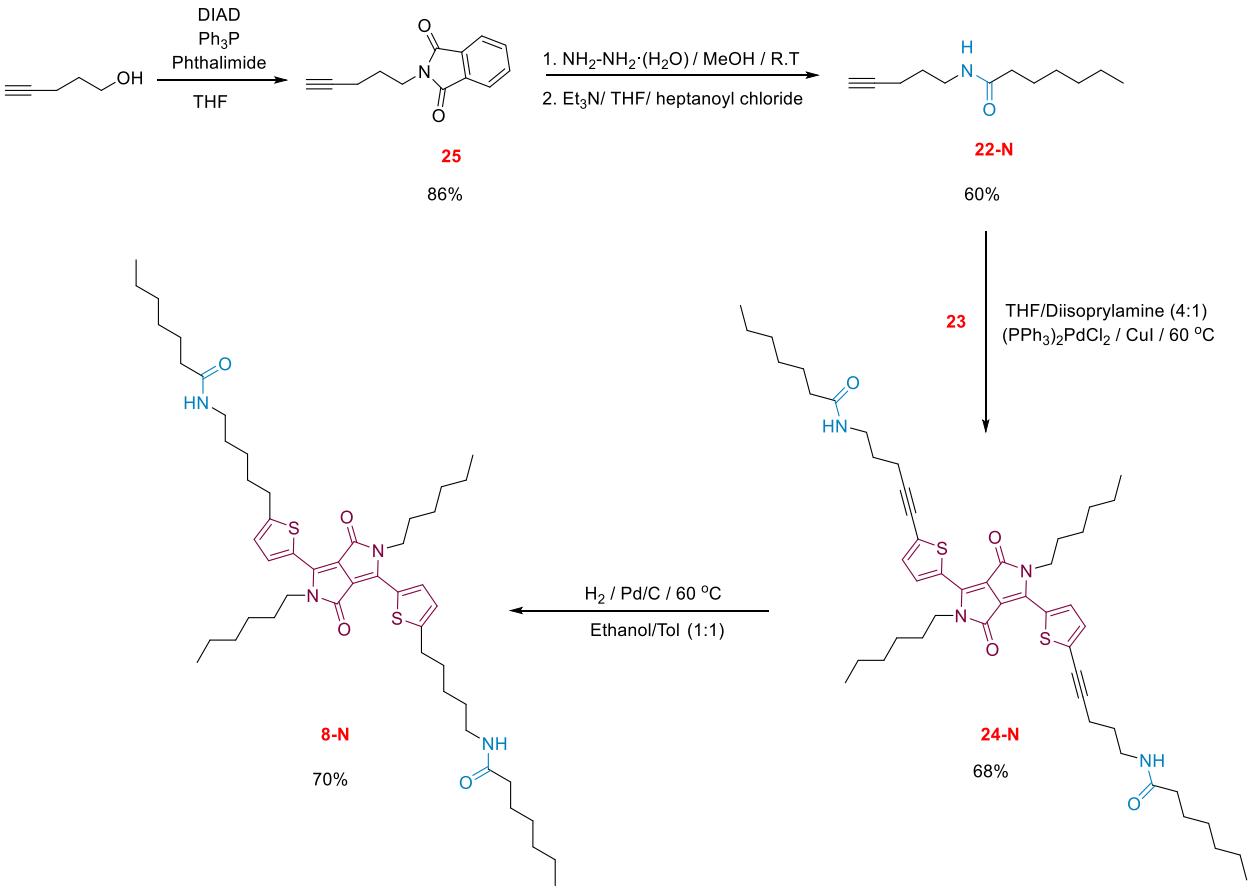

Scheme IV. 19 Synthetic route towards compound **8-N**.

This direct approach proved its versatility and will help in the synthesis of new **DPP** derivatives with functionalized alkyl chains pending from the thiophene rings.

II.2) Optical and self-assembly properties

The optical and self-assembly properties of **8-C** and **24-C** were followed with UV-Vis absorption in solution at variable temperature in different solvents and concentrations, and by FTIR. As usual with these derivatives, compound **8-C** displays broad absorption bands ranging from 400 to 600 nm at 20 °C in chloroform with absorption maxima at λ = 562 nm (Figure IV. 4); although it did not show any sign of aggregation in chloroform at 20 °C and the absorption bands did not change upon increasing the concentration (Figure IV. 5a). Additional absorption bands appeared at lower energy when **8-C** spectra were measured in different solvents, such

as chlorobenzene, toluene, and ethyl acetate. In chlorobenzene, the λ_{max} of this band was at 621 nm in toluene, at 622 nm in chlorobenzene, and at 629 nm in ethyl acetate (Figure IV. 4).

This band was attributed to the formation of J-type aggregates and its intensity decreased upon dilution and heating, like for the previously described families of H-bonded **DPPs** (Figure IV. 5b-d and Figure IV. 6, respectively); this was once again confirmed by measuring spectra upon the addition of methanol, finding the disappearance of the band in the same way as for the other H-bonded **DPPs** already described (Figure IV. 7).

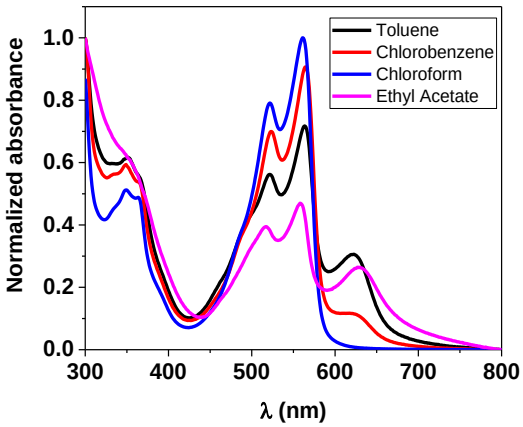

*Figure IV. 4 Absorption spectra of **8-C** at room temperature in different solvents. [**8-C**] = 0.5 mg/ml in all solvents.*

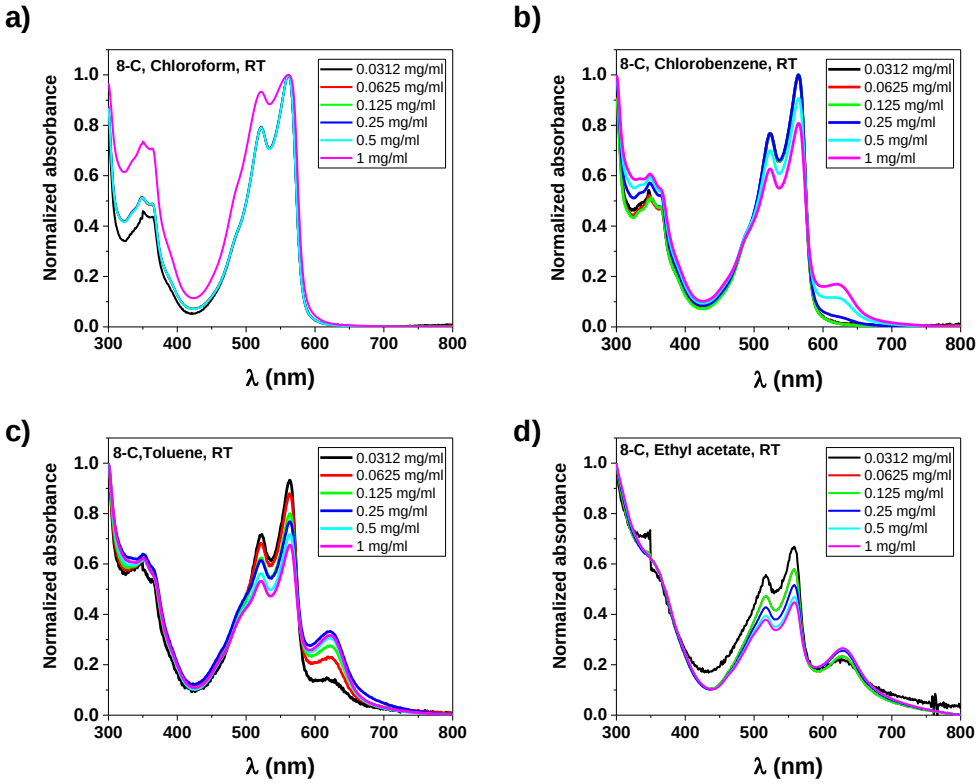

*Figure IV. 5 Absorption spectra of **8-C** at different concentrations, at room temperature in a) chloroform, b) chlorobenzene, c) toluene and d) ethyl acetate.*

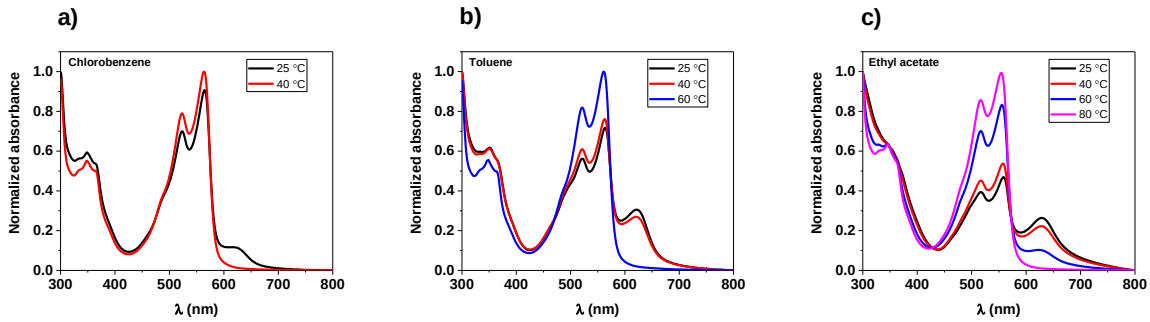

*Figure IV. 6 Absorption spectra of **8-C** showing the disappearance of the J-aggregate band upon heating in a) chlorobenzene, b) toluene and c) ethyl acetate. **[8-C]** = 0.5 mg/ml for all solvents.*

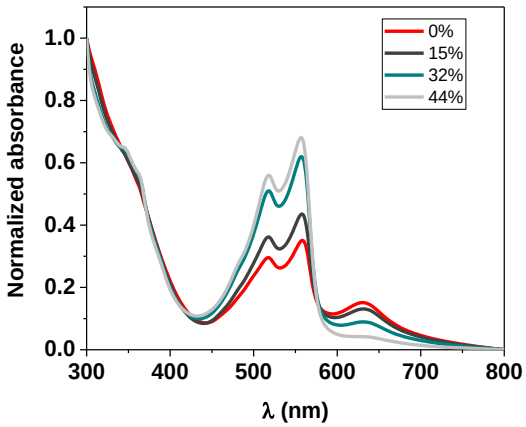

*Figure IV. 7 Absorption spectra for **8-C** showing disappearance of the J-aggregate band upon addition of methanol at room temperature. **[8-C]** = 2.5 mg/ml in ethyl acetate.*

The characterization of molecules **8-C** and **8-N** is still at a preliminary stage, but when comparing molecule **HDPPBA-C** (chapter III) with molecule **8-C**, the differences in the position of the amide bond within the molecular structure are evident. It has been found that they have different behavior in UV-Vis absorption as well as in morphology. While the optical properties of compound **8-C** follow similar trends as the rest of the H-bonded **DPP** studies, showing J-type aggregate bands in solvents such as chlorobenzene and toluene (Figure IV. 8, blue traces), it was found that **8-C** was more soluble than **HDPPBA-C** in all the solvents tested.

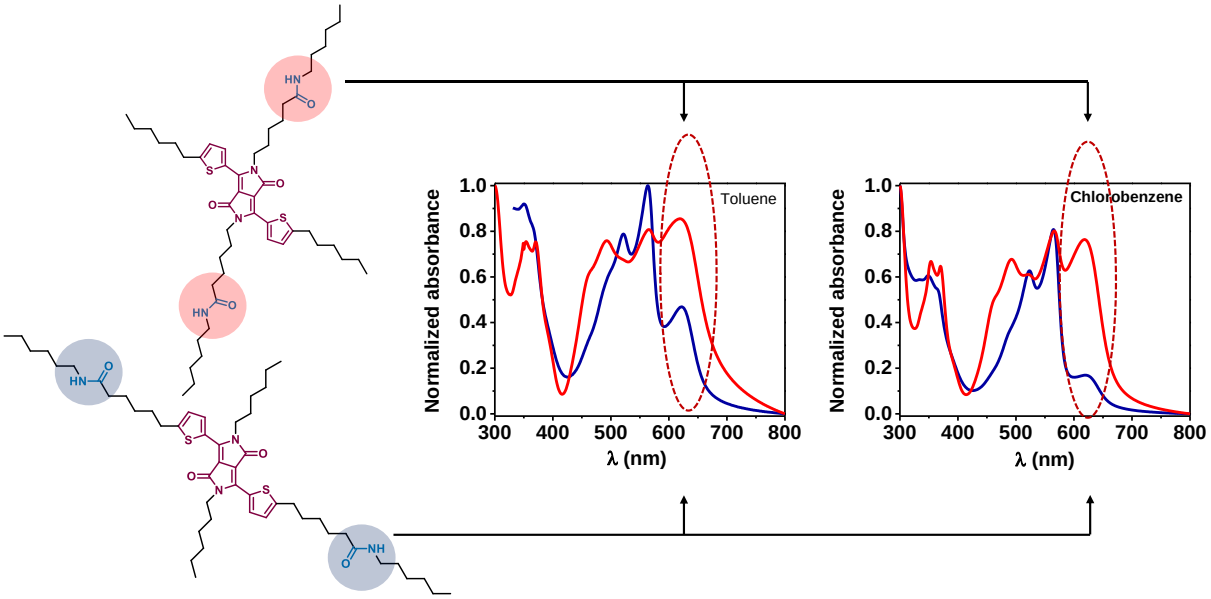

*Figure IV. 8 Absorption spectra of **HDPPBA-C** and **8-C** in toluene and chlorobenzene at the same concentration at room temperature.*

This behavior was reflected in the absorption spectra, which showed J-type aggregation bands much smaller than **HDPPBA-C** (Figure IV. 8) at the same concentration. When the morphology of the aggregates formed by **8-C** was studied (Figure IV. 9d-f), well-defined high-aspect ratio structures were not observed as in the case of **HDPPBA-C** (Figure IV. 9a-c), but instead there was amorphous material not assembled into well-defined structures. It seems that placing H-bonding groups in different positions dramatically changes the self-assembly processes and hence, the electronic properties.

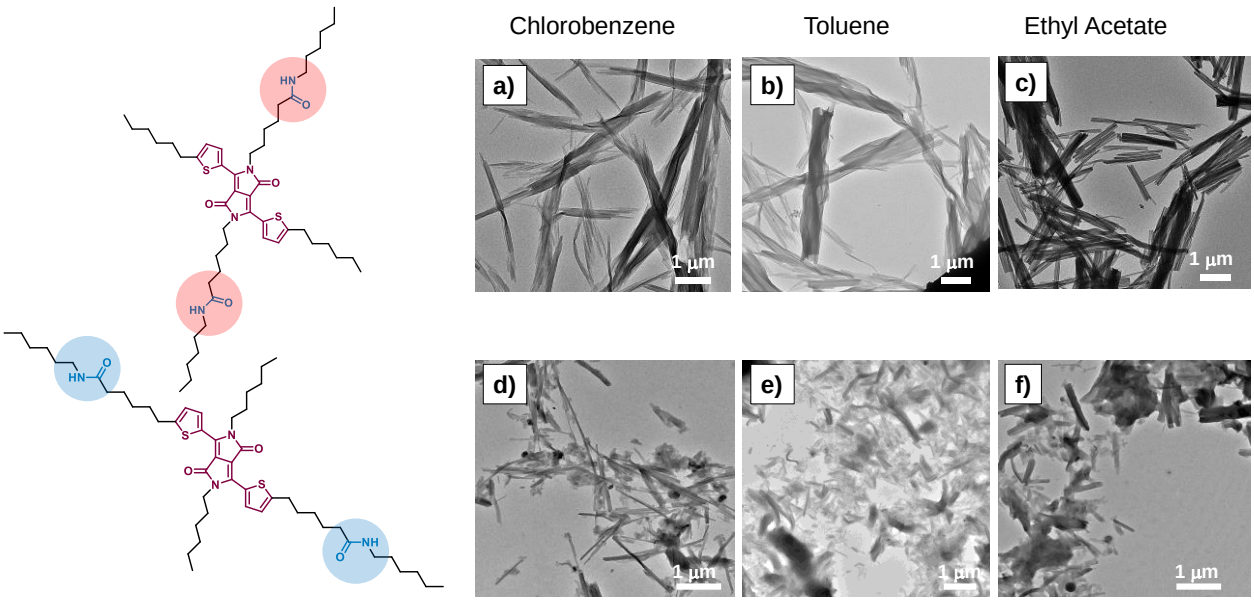

*Figure IV. 9 TEM images in different solvents of **HDPPBA-C** (a-c) and **8-C** (d-f).*

Furthermore, the alkyne precursors **24-C** and **24-N** are being investigated as well since the presence of the triple bond makes the self-assembly processes different despite having almost the same structure. Therefore, a comparison between compounds **8-C** and **24-C** was performed. For instance, when UV-Vis spectra of **24-C** were measured in $CHCl_3$, unlike for compound **8-C**, a band can be observed and remains even upon dilution (Figure IV. 10a), and likewise, the disappearance of this band was not observed upon heating (Figure IV. 10b). Moreover, the color of the solutions was different and for **24-C**, the spectra was red shifted and the additional band was observed at lower concentrations than in solutions of **8-C** in $CHCl_3$ where concentration was higher but the band was not present (Figure IV. 11). Finally, this band did not disappear upon addition of MeOH (Figure IV. 12). Ultimately, this signal is assumed to be a consequence of the extended conjugation of the **DPP** core, due to the triple bond next to the thiophene rings, which also gives a more rigid structure to the amide chain, inducing a planarization effect that might have an impact in π-π stacking, and creates stronger aggregates.

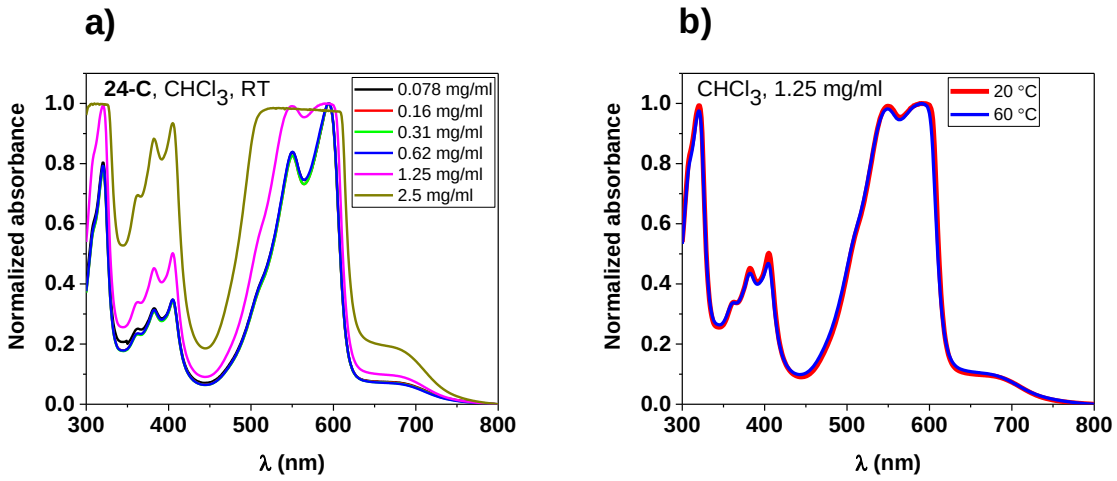

*Figure IV. 10 Absorption spectra for compound **24-C** in $CHCl_3$ at different a) concentrations and b) temperatures.*

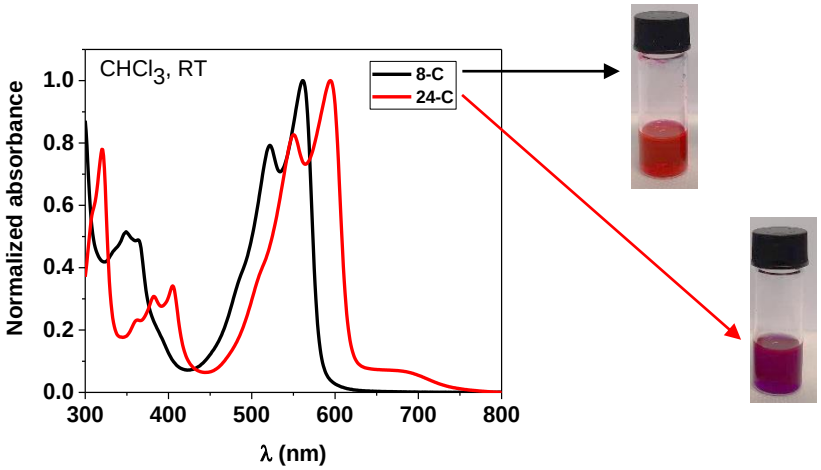

*Figure IV. 11 Spectra comparison between **8-C** and **24-C**. **[8-C]** = 0.5 mg/ml vs **[24-C]** = 0.31 mg/ml.*

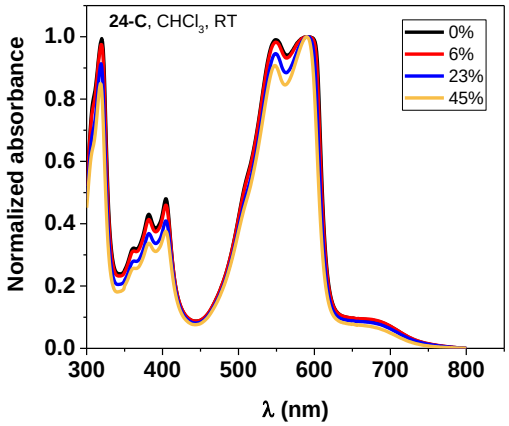

*Figure IV. 12 Absorption spectra for **24-C** upon addition of methanol at room temperature. **[24-C]** = 1.25 mg/ml in $CHCl_3$.*

FTIR spectra of powders at room temperature proved the existence of H-bonds in **8-C** and **24-C**. The first showed a band at 3295 cm^{-1} in the NH stretching area attributed to H-bonded amide bonds, whereas the latter showed it at 3299 cm^{-1} (Figure IV. 13a). In the region between 1600 cm^{-1} and 1700 cm^{-1}, both compounds show peaks at 1659 cm^{-1}, corresponding to the amide functions present in the lactam rings of the **DPP** core (Figure IV. 13b). Additional peaks at 1641 cm^{-1} and 1638 cm^{-1} for **8-C** and **24-C**, respectively were found in this area, corresponding to amide groups engaged in H-bonding like the peaks at 3295 cm^{-1} and at 3299 cm^{-1}. The difference of 3 cm^{-1} between the amide-containing derivatives indicates the subtle differences in aggregation. Furthermore, the IR also helped to confirm no traces of precursor remained, as the peak corresponding to the stretching of the disubstituted alkyne bond was observed at 2216 cm^{-1} only for **24-C** (Figure IV. 14).

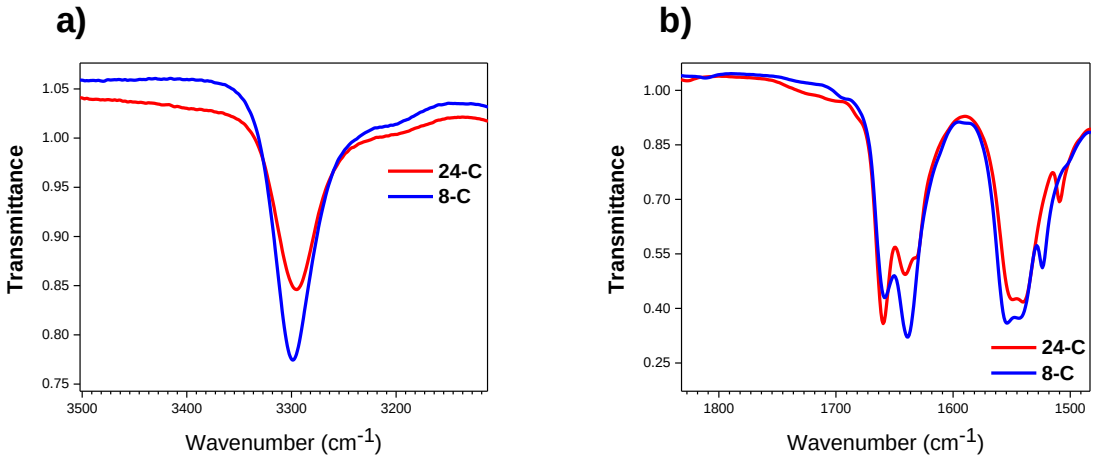

*Figure IV. 13 FTIR powder spectra of **8-C** and **24-C**.*

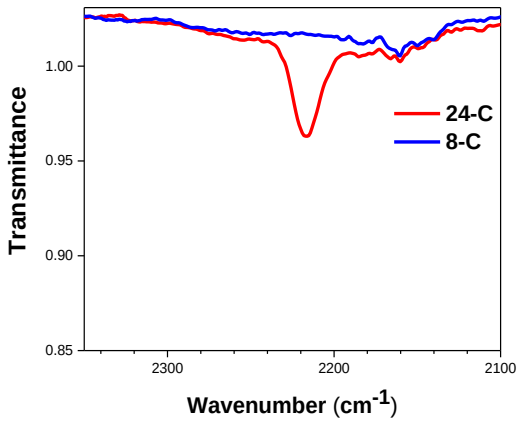

*Figure IV. 14 FTIR spectra showing the presence of the alkyne bond in **24-C** and its absence in **8-C**.*

A FTIR powder spectra comparison between **8-C** and **HDPPBA-C** was also performed, but no major differences were observed. The NH stretching signal attributed to H-bonded amide bonds was red-shifted by 3 cm^{-1} for **8-C**, 3303 cm^{-1} for **HDPPBA-C** *vs* 3299 cm^{-1} for **8-C** (Figure IV. 15a). In the region between 1600 cm^{-1} and 1700 cm^{-1}, both compounds show the corresponding peaks belonging to amide functions present in the lactam rings of the **DPP** core, this time blue shifted by 3 cm^{-1} (1655 cm^{-1} for **HDPPBA-C** and 1658 cm^{-1} for **8-C**), as well as those corresponding to amide groups engaged in H-bonding (Figure IV. 15b). These small shifts may ultimately explain the changes in self-assembly observed by TEM.

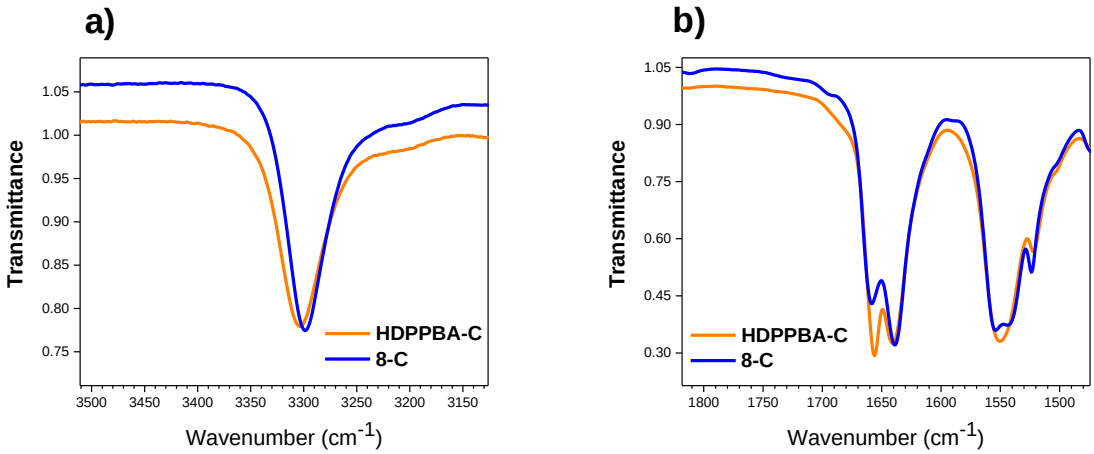

*Figure IV. 15 FTIR powder spectra of **8-C** and **HDPPBA-C**.*

Nevertheless, these results were obtained in powder samples where the differences in aggregation are not so evident. Currently, the comparison of these derivatives is being done in solution at different solvents and concentrations to obtain more detailed information about the self-assembly process.

II.3) Conclusions

In conclusion, a new family of **DPP** derivatives with amides pending from the thiophene, as well as bearing different amide topology, were synthesized and are being characterized. More importantly, to our knowledge, we obtained the first derivatives where the basic **DPP** core bears functionalized alkylated thiophenes.

Furthermore, new **DPP** derivatives bearing alkyne bonds were also obtained and are being characterized. Like the previously obtained families, some of these new derivatives also aggregate and form J-type aggregates where H-bonds are involved.

The succinic cyclization approach seems to be limited, as it works best for thiophene rings that have alkyl chains without moieties, whereas the direct approach proved its versatility and will help in the synthesis of new and different **DPP** derivatives.

In the case of morphology, placing H-bonding groups in different positions seems to dramatically change the self-assembly processes, as it was found that these new derivatives were more soluble than the ones described in chapter III. This behavior was also reflected in the absorption spectra, where they show much smaller intensity in the J-aggregation bands. The aggregates formed by **8-C** seem like amorphous material not assembled into well-defined structures, unlike **HDPPBA-C** which does present well-defined high-aspect ratio structures.

FTIR spectra of powders at room temperature also proved the existence of H-bonds in these new derivatives and provided further proof that there are small spectra shifts, that may ultimately explain the changes in self-assembly.

The complete characterization of this family will be very important, for instance, the photoconductivity measurements and a more complete comparison of the influence of topology, will provide crucial data on future molecular design and elucidate the impact of the position of the H-bond with respect to the conjugated core.

III. Experimental

III.1) Materials and methods

All reagents and solvents were obtained from commercial suppliers and purified or dried according to standard procedures. Column chromatography was performed on silica gel (VWR Silica 60, particle size 0.040–0.063 mm). Solvents for spectroscopic studies were of spectroscopic grade and used as received. Elemental analysis was performed on a Thermofischer Scientific Flash 2000. Matrix-assisted laser desorption/ionisation-time of filght (MALDI) was performed in a Bruker Daltonics. ^{1}H and ^{13}C spectra were recorded in $CDCl_3$ on a Bruker Avance 400 MHz spectrometer and/or Bruker Avance III HD 500 MHz spectrometer. UV–vis measurements were performed in a conventional quartz cell (light pass 1 mm) on a Cary 5000 UV-Vis-NIR spectrophotometer. TEM measurements were done with a Technai G2 (FEI) microscope with an accelerating voltage of 200 kV. 5 µL of the sample solution were deposited onto a freshly glow discharged carbon-covered grid (400 mesh). The suspension

was left for 2 min, and then, the grid was negatively stained with 5 µL of uranyl acetate (2% in water) for another 1 min and finally blotted using a filter paper.

FTIR spectra were recorded with a Vertex 70 from Bruker Optics, equipped with MCT detector and a black-body source. The spectra of the solids were measured by ATR on diamond. The solutions were studied in cells from Specac Pike with KBr NaCl windows. The spectra were measured with the built-in MCT detector of the Vertex 70. The spectra were compensated from CO_2 and moisture with OPUS from Bruker.

III.2) Synthetic procedure

*2-(5-bromopentyl)thiophene (Compound **1**).*

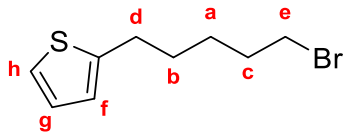

Reaction was performed in two batches to have enough product for the purification step (vacuum distillation). Each batch was prepared as follows: In a 2-neck round bottom flask under inert atmosphere, 50 ml of anhydrous Tetrahydrofuran were added along with a magnetic stirrer. The thiophene (125 mmol, 1 eq, 10.6 g) was then added to form a solution, which was then cooled down to -78 °C for 30 mins by using an isopropanol and dry ice bath. Mixture became white in color, then a 2.3 M solution of n-Buthyl Lithium in hexanes (138 mmol, 1.1 eq, 60 ml) was added dropwise while the mixture was still at -78 °C and it was allowed to react for 1h.

Finally, 1,5-dibromopentane (138 mmol, 1.1 eq, 31.7 g) was added dropwise and the mixture was allowed to gradually warm up to room temperature by changing to an ice bath that eventually warmed up to room temperature, since the reaction was allowed to occur for 24 h. The flask and the ice bath were covered in aluminum foil to avoid having decomposition products due to light (halides give the solution an orange color). After 24 h, the mixture was cooled down back to 0 °C, diluted and quenched by adding 50 ml of distilled water. Both crudes were then combined, and the extraction was performed by using diethyl ether (3x300 ml), the organic phase was then washed with 200 ml of a brine solution. The organic phase was then dried over anhydrous $MgSO_4$ and filtered.

Solvent was then evaporated, and a yellow oil remained as a mixture of 1,5-dibromopentane and the product. Purification was performed by vacuum distillation at 0.4 mbar, a first distillate was recovered at 110 °C, 1,5-dibromopentane, temperature was then increased to 150 °C and a second distillate was recovered, compound **1**. Yield: slightly yellow liquid (29.09 g, 50%).

^{1}H NMR (400 MHz, $CDCl_3$): δ 7.14 (dd, J=4.8 Hz, 1.2 Hz, 1H$_h$), 6.94 (t, J=4.6 Hz, 1H$_g$), 6.81 (dd, *J* = 3.6 Hz, 1.8 Hz, 1H$_f$), 3.43 (t, J=6.4 Hz, 2H$_e$), 2.87 (q, J=7.8 Hz, 2H$_d$), 1.92 (q, J=9.5 Hz, 2H$_c$), 1.73 (q, J=10.0 Hz, 2H$_b$), 1.54 (q, J=10.0 Hz, 2H$_a$).

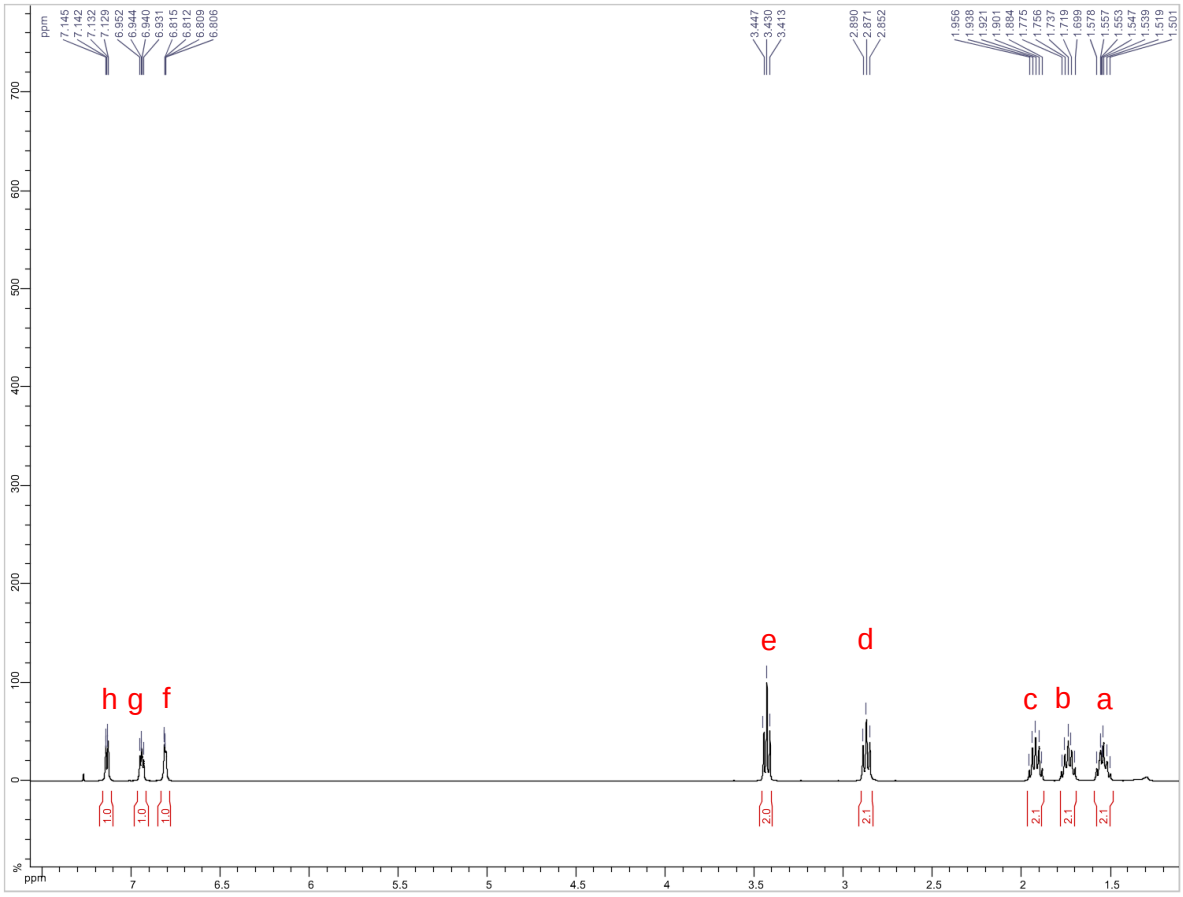

*6-(thiophen-2-yl)hexanenitrile (Compound **2-C**)*

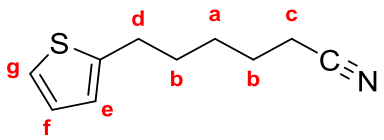

In a 2-neck round bottom flask, coupled with a reflux apparatus, 80 ml of DMSO were added along with a magnetic stirrer. The sodium cyanide (70.8 mmol, 1.1 eq, 3.58 g) and the potassium iodide (0.64 mmol, 0.01 eq, 0.11 g) were then added to form a solution, which was then warmed up to 50 °C for 30 mins by using an oil bath to ensure the salts were dissolved.

Compound **1** (64.3 mmol, 1 eq, 15.0 g) was so added dropwise while the mixture was still at 50 °C and then temperature was increased to 120 °C, allowing it to react overnight. Reaction was then allowed to cool down to room temperature, then diluted with distilled water to a final volume of 400 ml. Extraction was performed by using diethyl ether (3x300 ml), the organic phase was then dried over anhydrous $MgSO_4$ and filtered. Solvent was then evaporated and compound **2-C** was considered pure enough to follow with the next step. Yield: dark yellow oil (10.96 g, 95%).

^{1}H NMR (400 MHz, $CDCl_3$): δ 7.13 (dd, J=5.2 Hz, 1.0 Hz, 1H_g), 6.93 (dd, J=5.4 Hz, J=5.4 Hz, 1H_f), 6.80 (dt, *J* = 2.2 Hz, 1.8 Hz, 1H_e), 2.87 (t, J=7.4 Hz, 2H_d) , 2.35 (t, J=7.3 Hz, 2H_c), 1.72 (m, J=4.5 Hz, 4 H_b), 1.54 (m, J=7.6 Hz, 2 H_a).

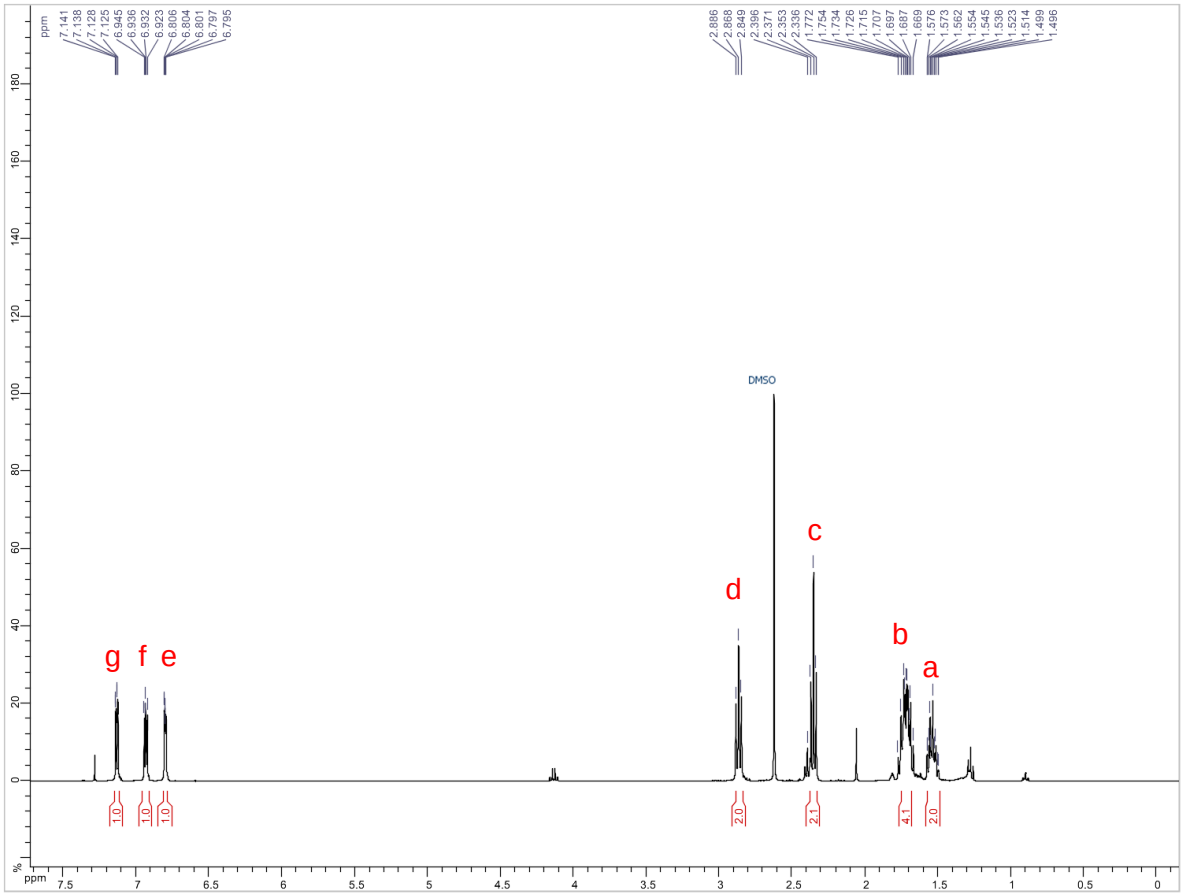

*6-(thiophen-2-yl)hexanoic acid (Compound **3-C**)*

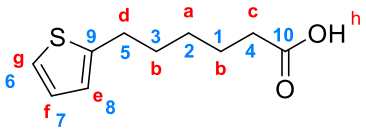

In a round bottom flask coupled with a reflux apparatus, potassium hydroxide (175.7 mmol, 5 eq, 11.6 g) and 100 ml of a mixture comprised of Ethylene glycol/H_2O (4:1) were added along with a magnetic stirrer to form a solution. Compound **2-C** (35.1 mmol, 1 eq, 6.3 g) was then added and mixture was then heated up to 150 °C for 16 h by using an oil bath. Afterwards, reaction was allowed to cool down to room temperature and diluted with distilled water to a final volume of 600 ml. Then, 17.2 ml of 37% (w/w) HCl were slowly added, to neutralize the base. This solution was washed with diethyl ether (3x200 ml) and the organic layers were combined and dried over anhydrous $MgSO_4$ and filtered, then the solvent was evaporated. A dark yellow oil remained, which became a waxy solid when left in the fume hood (during winter). Purification was performed by Column Chromatography, using chloroform as the

eluent. Yield: Slightly yellow oil/ wax (5.58 g, 80%). Product was confirmed by ^{1}H NMR and ^{13}C-NMR.

^{1}H NMR (400 MHz, $CDCl_3$): δ 11.49 (s, 1H_h), 7.12 (dd, J=5.1 Hz, J=1.1 Hz, 1H_g), 6.93 (t, J=4.3 Hz, 1H_f), 6.80 (dd, J=3.3 Hz, J=0.9 Hz, 1H_e), 2.85 (t, J=7.7 Hz, 2H_d), 2.37 (t, J=7.5 Hz, 2H_c), 1.70 (m, J=8.8 Hz, 4H_b), 1.44 (m, J=7.8 Hz, 2H_a).

^{13}C NMR δ 179.4 (1C_{10}), 145.3 (1C_9), 126.7 (1C_8), 124.1(1C_7), 122.9 (1C_6), 33.8 (1C_5), 31.4 (1C_4), 29.7 (1C_3), 28.5 (1C_2), 24.5 (1C_1).

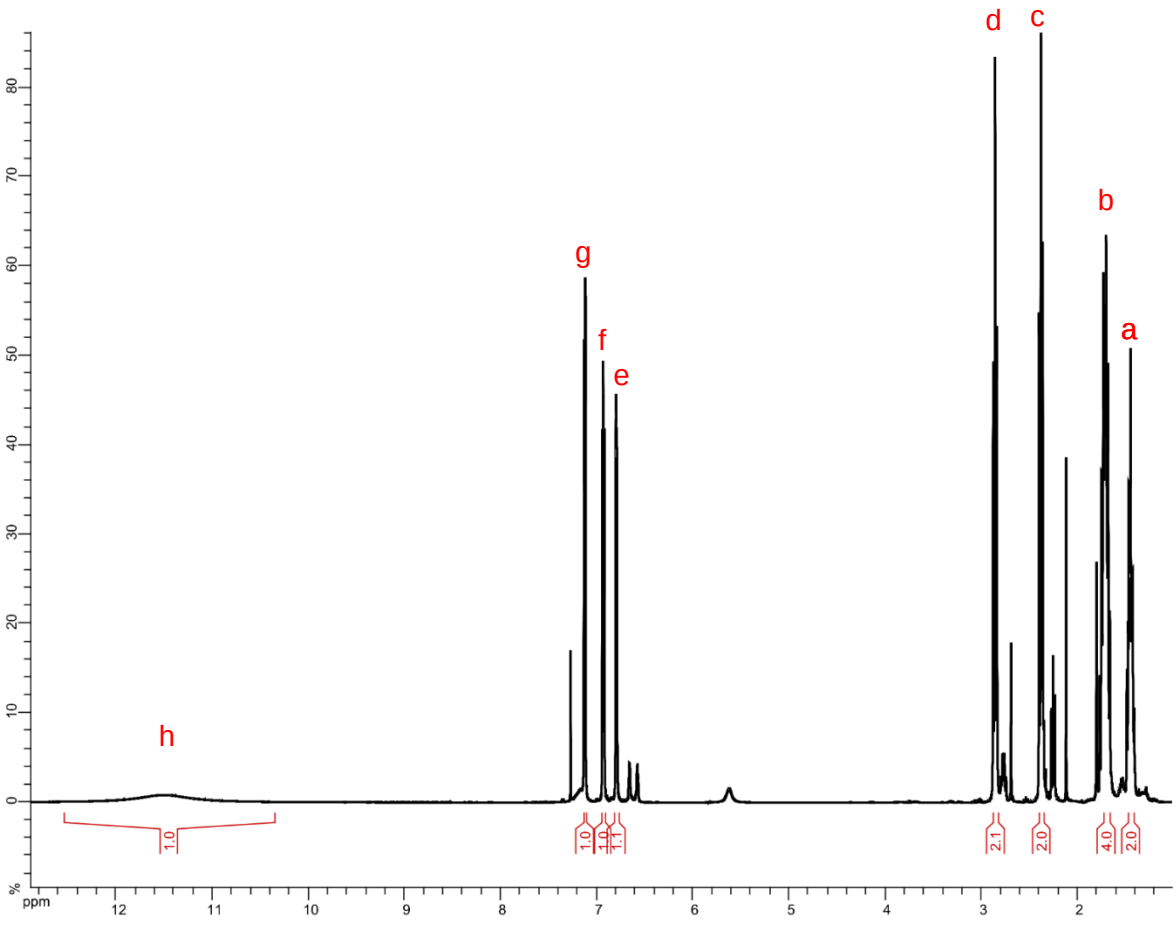

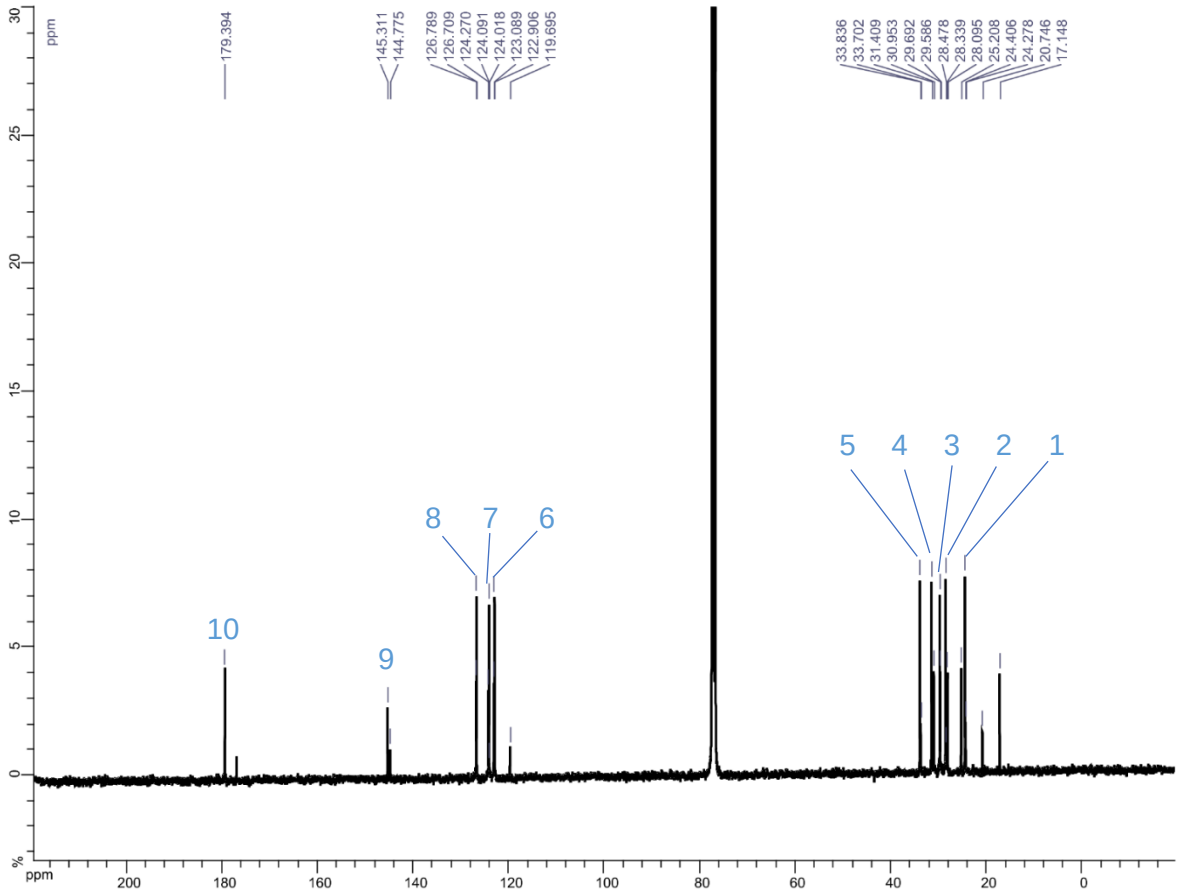

N-hexyl-6-(thiophen-2-yl)hexanamide (Compound **4-C**)

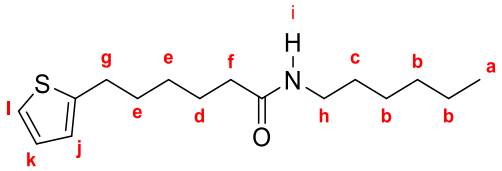

In a round bottom flask, 100 ml of CH_2Cl_2 were added along with a magnetic stirrer. Compound **3-C** (25.7 mmol, 1 eq, 5.1 g), hexyl amine (25.7 mmol, 1 eq, 3.4 g) and triethyl amine (77.2 mmol, 3 eq, 7.9 g) were then added and mixture was cooled down to 0 °C for 30 mins by using an ice/water bath. Afterwards, $SOCl_2$ (25.7 mmol, 1 eq, 3.1 g) was added dropwise to the mixture, which thickened and became yellow in color, gas was also released upon addition of each drop. Reaction was allowed to continue at room temperature for 1 h. Mixture was diluted with CH_2Cl_2 to a final volume of 200 ml and the organic phase was then washed as follows: first with 75 ml of a 1 mol/l solution of HCl, then with 75 ml of a 1 mol/l solution of NaOH and finally with 75 ml of a saturated brine solution. Organic phase was then dried over anhydrous $MgSO_4$ and filtered, then the solvent was evaporated. A yellow brownish solid remained. Purification was performed by Column Chromatography, using a mixture of Cyclohexane/Ethyl Acetate mixture (8:2) as the eluent. Yield: Slightly yellow solid (5.1 g, 70%).

^{1}H NMR (400 MHz, $CDCl_3$): δ 7.12 (dd, J=5.1 Hz, J=1.2 Hz, 1H$_l$), 6.93 (t, J=4.2 Hz, 1H$_k$), 6.79 (dd, J=2.8 Hz, J=1.0 Hz, 1H$_j$), 5.39 (s, 1H$_i$), 3.25 (q, J=6.9 Hz, 2H$_h$), 2.85 (t, J=7.8 Hz, 2H$_g$), 2.18 (t, J=7.6 Hz, 2H$_f$), 1.71 (m, J=10.2 Hz, 4H$_e$), 1.50 (t, J=6.5 Hz, 2H$_d$), 1.41 (q, J=5.8 Hz, 2H$_c$), 1.31 (m, 6H$_b$), 0.91 (t, J=6.2 Hz, 3H$_a$)

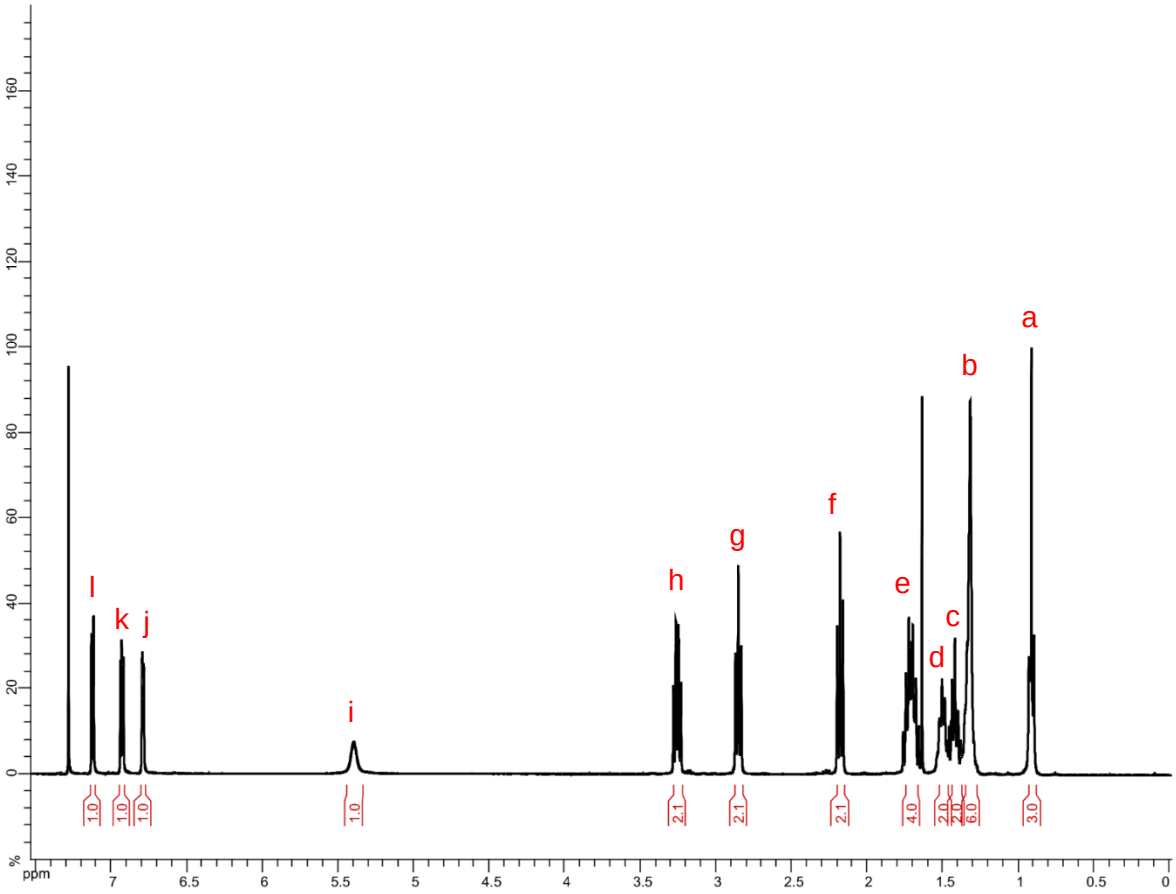

6-(5-bromothiophen-2-yl)-N-hexylhexanamide (Compound **5-C**)

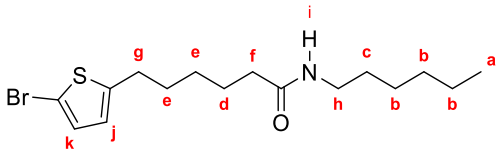

In a 2-neck round bottom flask under inert atmosphere, compound **4-C** (11.4 mmol, 1 eq, 3.21 g) and 40 ml of a mixture of chloroform and acetic acid (1:1, v/v) were added along with a magnetic stirrer, mixture was then cooled down to 0 °C for 30 mins by using an ice-cold water bath. N-bromosuccinimide (12.6 mmol, 1.1 eq, 2.28 g) was then added at once while the mixture was at 0 °C and it was allowed to gradually warm up to room temperature, as reaction

occurred for 12 h. The flask and the ice bath were covered in aluminum foil to avoid decomposition of the N-bromosuccinimide due to light.

After 12 h, the mixture was diluted with CH_2Cl_2 to a final volume of 300 ml, the resulting organic phase was washed with a saturated solution of $NaHCO_3$ (3x100 ml), extraction funnel was shaken carefully and properly vented, as gas is generated due to the neutralization of the acid. The organic phase was dried over anhydrous $MgSO_4$ and filtered, then solvent was evaporated. No purification was performed as not many impurities were seen in the NMR spectrum. Yield: light brown solid (3.91 g, 95%).

^{1}H NMR (400 MHz, $CDCl_3$): δ 6.84 (d, J=3.7 Hz, 1H$_k$), 6.53 (dt, J=3.5 Hz, J=0.6 Hz, 1H$_j$), 5.44 (s, 1H$_i$), 3.23 (dd, J=13.1 Hz, J=7.1 Hz, 2H$_h$), 2.75 (t, J=7.6 Hz, 2H$_g$), 2.15 (t, J=7.6 Hz, 2H$_f$), 1.65 (m, J=8.7 Hz, 4H$_e$), 1.48 (t, J=7.5 Hz, 2H$_d$), 1.38 (q, J=8.4 Hz, 2H$_c$), 1.29 (m, 6H$_b$), 0.89 (t, J=6.8 Hz, 3H$_a$)

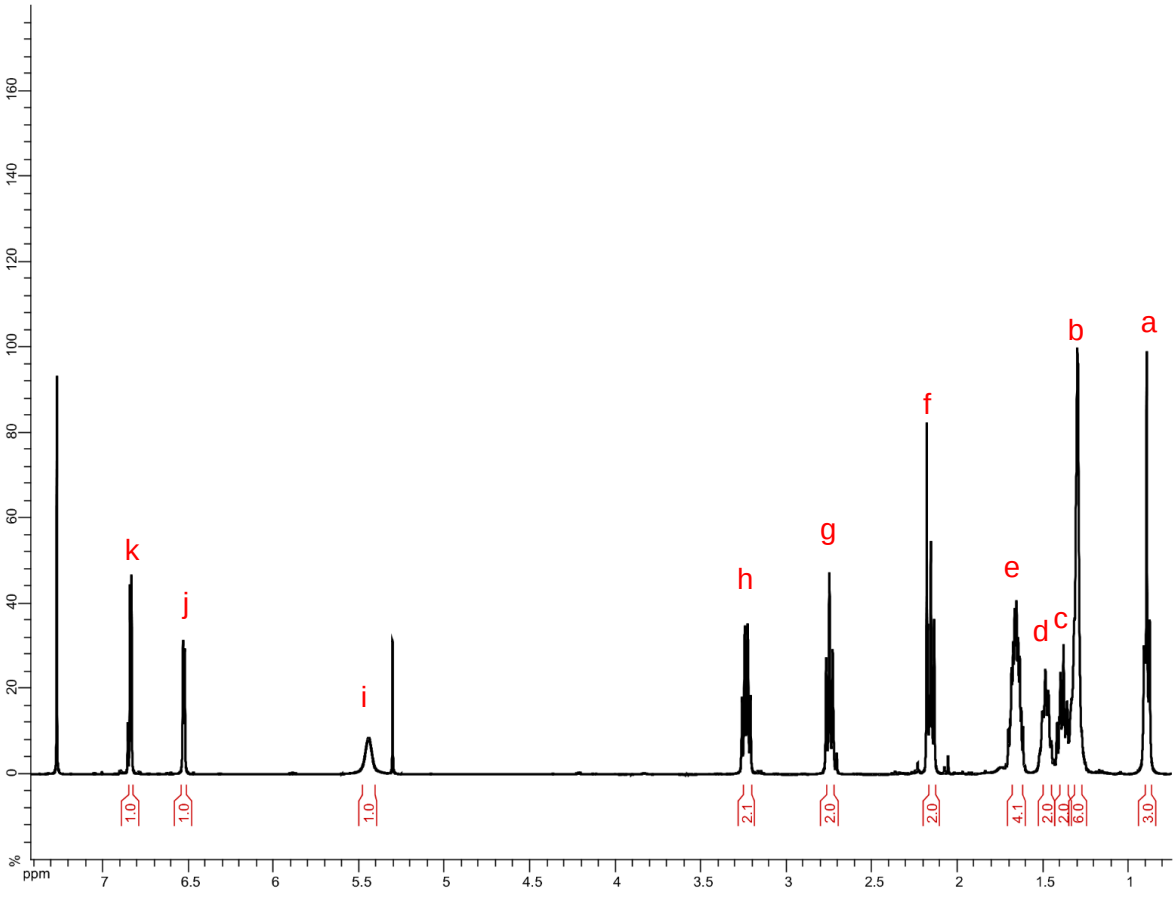

*6-(5-cyanothiophen-2-yl)-N-hexylhexanamide (Compound **6-C**)*

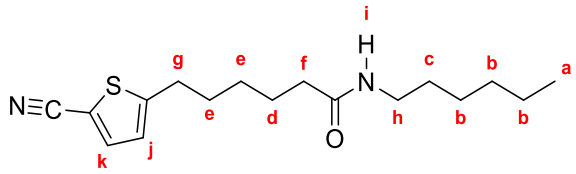

In a 3-neck round bottom flask under inert atmosphere, coupled with a reflux apparatus, 30 ml of DMSO were added along with a magnetic stirrer. The copper cyanide (16.1 mmol, 1.6 eq, 1.48 g) was then added to form a solution, which was then warmed up to 50 °C for 30 mins by using an oil bath to ensure the copper cyanide was dissolved. Then compound **6-C** (10.1 mmol, 1 eq, 2.84 g) was dissolved in 10 ml of DMSO and this solution was added dropwise while the mixture was still at 50 °C, temperature was increased to 150 °C afterwards, allowing it to react overnight.

Afterwards, reaction was allowed to cool down to room temperature and 38 ml of a 30% (w/w) ammonia solution were slowly added, since some bubbling and heating occurred. Mixture was so diluted with distilled water to a volume of 200 ml, this solution was further diluted with brine solution to a final volume of 500 ml to avoid having emulsification. This aqueous solution had a distinctive dark blue color. This solution was washed several times with diethyl ether (150 ml per washing), until the diethyl ether washing was not getting colored (from dark yellow in the first washing to slightly colorless in the last). The organic layers were combined and dried over anhydrous $MgSO_4$ and filtered, then the solvent was evaporated, and a dark oil remained. Purification was performed by Column Chromatography, using a gradual mixture of cyclohexane/ ethyl acetate (8:2) → (6:4) as the eluent. Yield: Dark yellow solid (1.88 g, 60 %).

^{1}H NMR (400 MHz, $CDCl_3$): δ 7.45 (d, J=3.8 Hz, 1H$_k$), 6.79 (dt, J=3.8 Hz, J=0.9 Hz, 1H$_j$), 5.42 (s, 1H$_i$), 3.24 (dd, J=13.7 Hz, J=6.3 Hz, 2H$_h$), 2.85 (t, J=7.6 Hz, 2H$_g$), 2.16 (t, J=7.4 Hz, 2H$_f$), 1.70 (m, J=10.8 Hz, 4H$_e$), 1.48 (t, J=7.9 Hz, 2H$_d$), 1.40 (q, J=7.9 Hz, 2H$_c$), 1.29 (m, 6H$_b$), 0.89 (t, J=6.9 Hz, 3H$_a$)

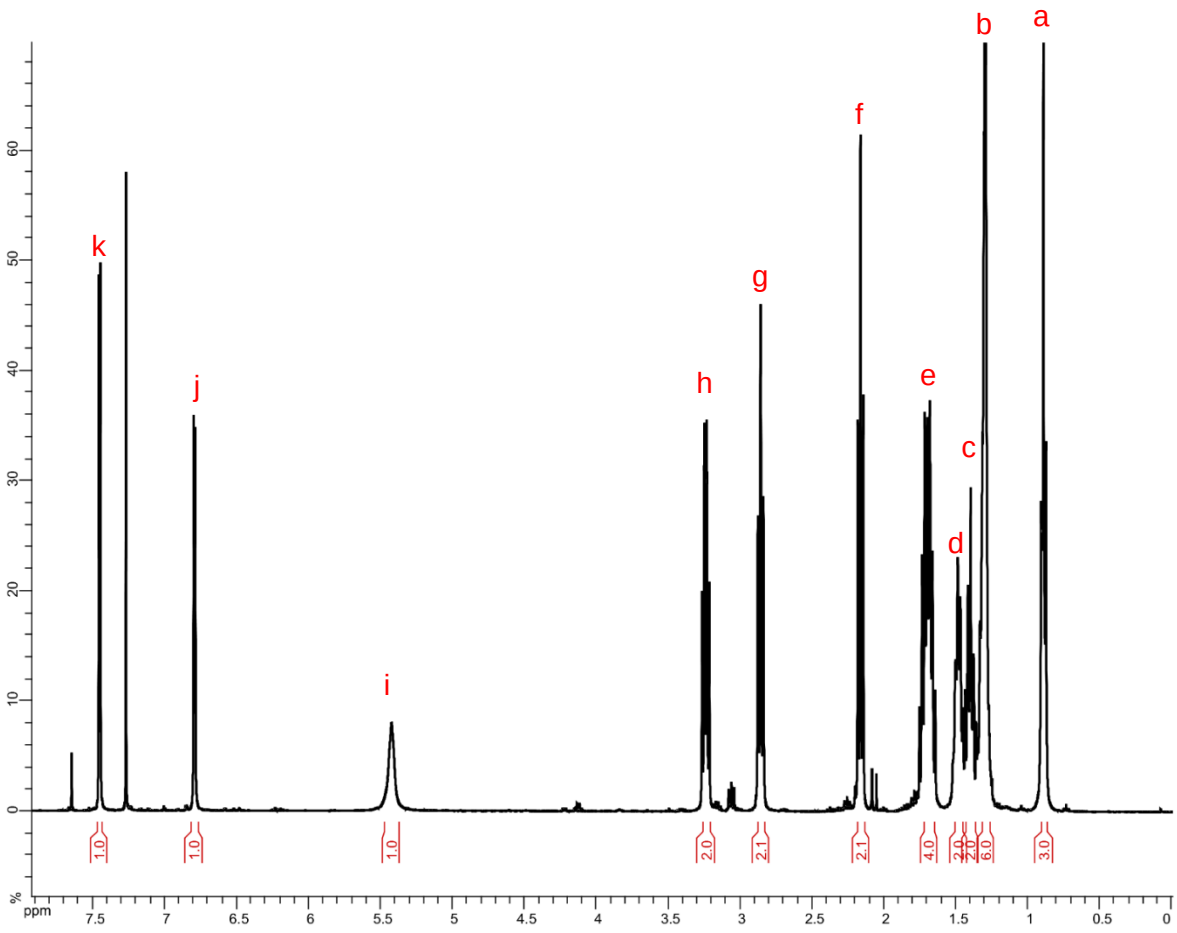

*6,6'-((3,6-dioxo-2,3,5,6-tetrahydropyrrolo[3,4-c]pyrrole-1,4-diyl)bis(thiophene-5,2-diyl))bis(N-hexylhexanamide) (Compound **7-C**)*

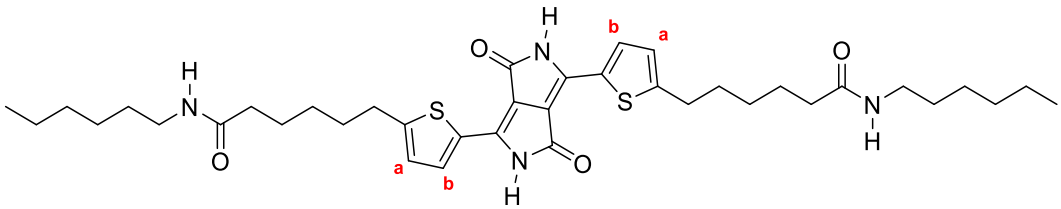

In a 2-neck round bottom flask coupled with a reflux apparatus, a solution of Compound **6-C** (4.2 mmol, 2 eq, 1.30 g) and potassium tert-butoxide (4.7 mmol, 2.2 eq, 0.53 g) was stirred under argon atmosphere in tert-amyl alcohol. Mixture was heated up for 1 hour to 120°C by using an oil bath. Diethyl succinate (2.1 mmol, 1 eq, 0.37 g) was then added dropwise while the mixture was at 120°C. Mixture became dark red in color after 1 h and the solution was stirred at 120 °C overnight, and then cooled down to room temperature. The base was neutralized with 5 ml of concentrated acetic acid, upon this addition mixture thickened and changed to a dark purple color. The mixture was vigorously stirred for 2 hours at room temperature. The crude was filtered through a type 4 fritted glass funnel and washed several times with ice cold MeOH and dried to afford a dark purple solid. Purification was attempted

by column chromatography using a $CHCl_3$/MeOH (98:2) mixture. A purple solid was obtained (0.10 g, 7 %) which was assumed to be the product by the ^1H NMR spectrum, as the expected aromatic signals from the protons in thiophenes could be observed. Product was used like this for the next step (despite the integration of signals in the aliphatic region of the spectrum did not match with what was expected).

^1H NMR (400 MHz, $CDCl_3$): δ 7.81 (d, J=3.8 Hz, $1H_b$), 6.94 (dt, J=3.8 Hz, J=0.9 Hz, $1H_a$)

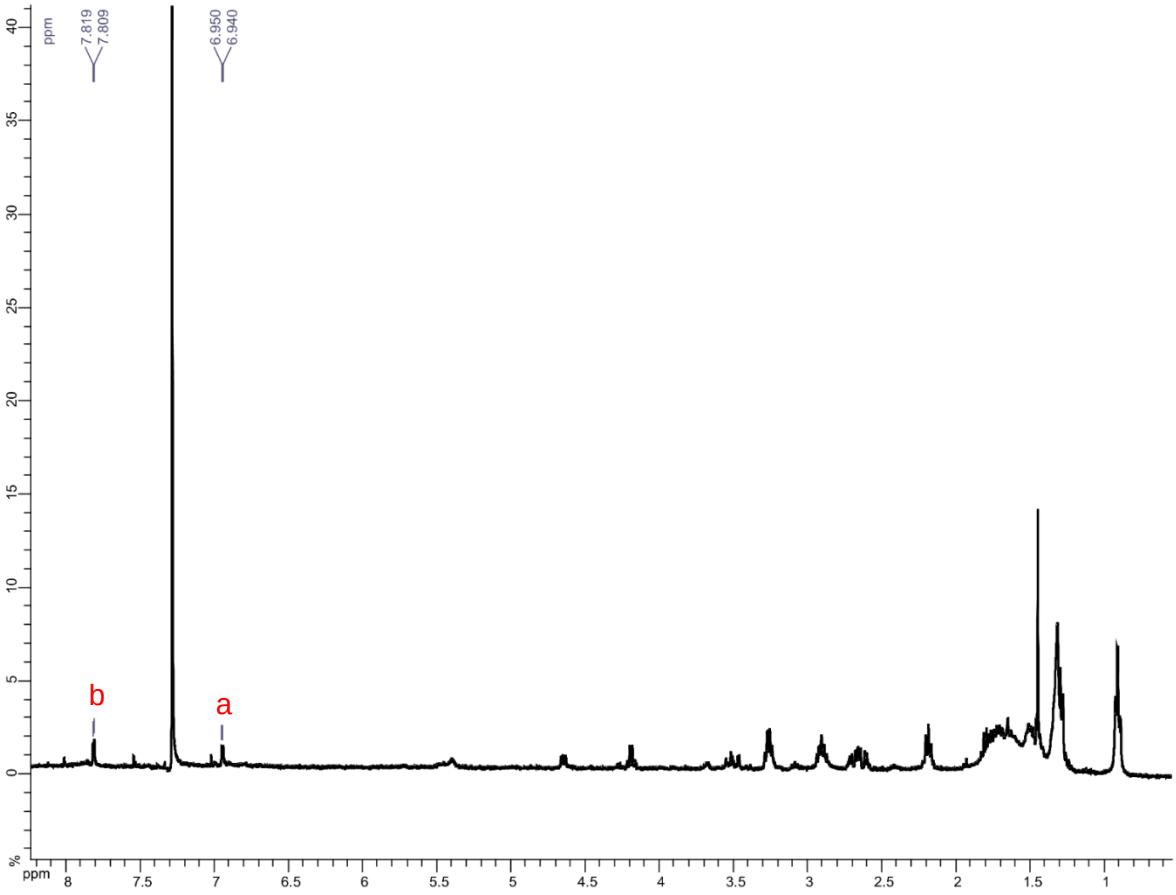

*Ethyl 6-(thiophen-2-yl)hexanoate (Compound **10**)*

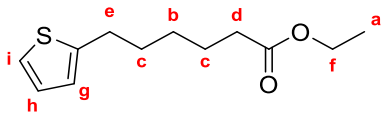

In a round bottom flask coupled with a magnetic stirrer, Compound **3-C** (6.8 mmol, 1 eq, 1.32 g), ethanol (13.7 mmol, 2 eq, 0.64 g) and 4-Dimethylaminopyridine (DMAP) (11.0 mmol, 1.6 eq, 1.3532 g) were dissolved in 30 ml of CH_2Cl_2. Mixture was then cooled down to 0 °C for 1 hour by using an ice-cold water bath, then a solution comprised of Dicyclohexylcarbodiimide (DCC) (15.1 mmol, 2.2 eq, 3.14 g) dissolved in 10 ml of CH_2Cl_2 was added dropwise at 0 °C.

Reaction was allowed to happen for 3h at room temperature. A white precipitate formed, which was removed by filtration; the filtrate was diluted with diethyl ether to a final volume of 100 ml. The organic phase was washed with 2 N HCl (1x50 ml), water (1x50 ml), and brine (1x50 ml) and was then dried over anhydrous $MgSO_4$ and filtered. After the solvent was removed, a slightly yellow powder remained. Purification was performed by Column Chromatography, using a mixture of Cyclohexane/Ethyl Acetate mixture (8:2) as the eluent. Yield: White powder with a faint yellow color (1.27 g, 82%).

^{1}H NMR (400 MHz, $CDCl_3$): δ 7.11 (dd, J=5.1 Hz, J=1.1 Hz, 1H$_i$), 6.92 (dd, J=5.2 Hz, J=3.4 Hz, 1H$_h$), 6.80 (dd, J=3.1 Hz, J=0.9 Hz, 1H$_g$), 4.13 (q, J=7.2 Hz, 2H$_f$), 2.84 (t, J=7.7 Hz, 2H$_e$), 2.31 (t, J=7.5 Hz, 2H$_d$), 1.67 (m, J=7.4 Hz, 4H$_c$), 1.42 (q, J=7.6 Hz, 2H$_b$), 1.25 (t, J=7.2 Hz, 3H$_a$).

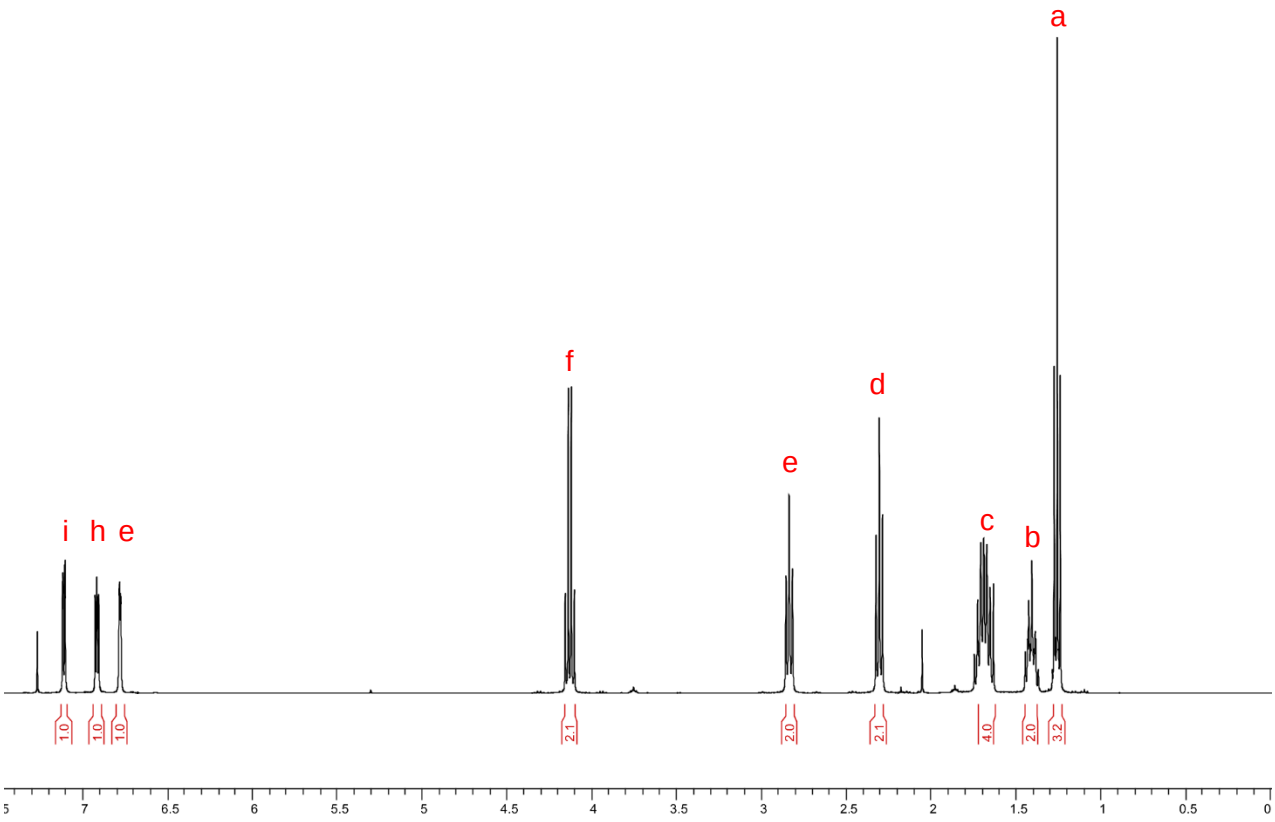

Ethyl 6-(5-bromothiophen-2-yl)hexanoate (Compound **11**)

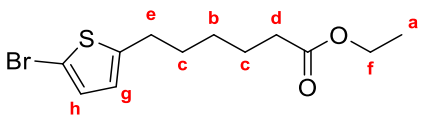

In a 2-neck round bottom flask under inert atmosphere, compound **10** (5.62 mmol, 1 eq, 1.27 g) and 20 ml of a mixture of chloroform and acetic acid (1:1, v/v) were added along with a magnetic stirrer, mixture was then cooled down to 0 °C for 30 mins by using an ice-cold water bath. NBS (6.18 mmol, 1.1 eq, 1.12 g) was then added at once while the mixture was at 0 °C and it was allowed to gradually warm up to room temperature, as reaction occurred for 12 h.

The flask and the ice bath were covered in aluminum foil to avoid decomposition of the N-bromosuccinimide due to light.

After 12 h, the mixture was diluted with CH_2Cl_2 to a final volume of 100 ml, the resulting organic phase was washed with a saturated solution of $NaHCO_3$ (3x50 ml), extraction funnel was shaken carefully and properly vented, as gas is generated due to the neutralization of the acid. The organic phase was dried over anhydrous $MgSO_4$ and filtered, then solvent was evaporated. No purification was performed as not many impurities were seen in the NMR spectrum. Yield: light brown solid (1.7 g, 99%).

^{1}H NMR (400 MHz, $CDCl_3$): δ 6.84 (d, J=3.7 Hz, 1H$_h$), 6.53 (dt, J=3.8 Hz, J=0.8 Hz, 1H$_g$), 4.13 (q, J=7.2 Hz, 2H$_f$), 2.74 (q, J=8.5 Hz, 2H$_e$), 2.30 (t, J=7.5 Hz, 2H$_d$), 1.65 (m, J=6.8 Hz, 4H$_c$), 1.38 (q, J=4.5 Hz, 2H$_b$), 1.26 (t, J=7.2 Hz, 3H$_a$).

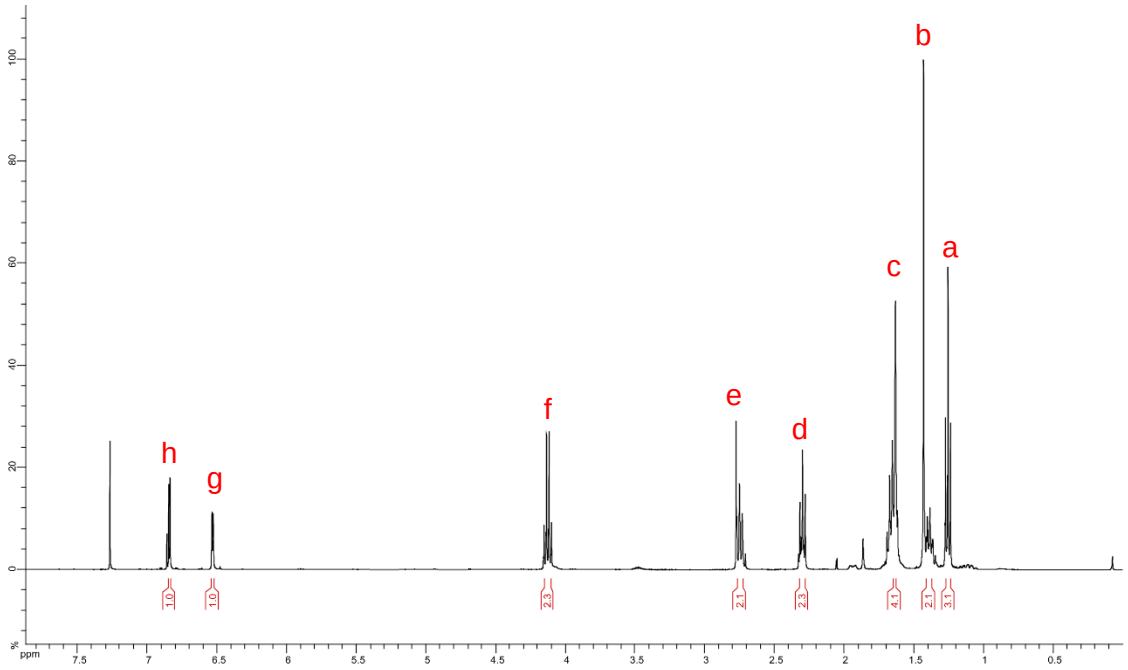

*Ethyl 6-(5-cyanothiophen-2-yl)hexanoate (Compound **12**)*

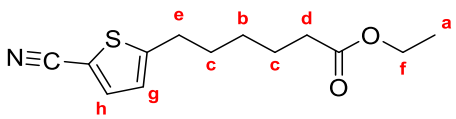

In a 3-neck round bottom flask under inert atmosphere, coupled with a reflux apparatus, 20 ml of DMSO were added along with a magnetic stirrer. The copper cyanide (16.1 mmol, 1.6 eq, 1.48 g) was then added to form a solution, which was then warmed up to 50 °C for 30 mins by using an oil bath to ensure the copper cyanide was dissolved. Then compound **11** (5.6 mmol, 1 eq, 2.84 g) was dissolved in 10 ml of DMSO and this solution was added dropwise while the

mixture was still at 50 °C, temperature was increased to 150 °C afterwards, allowing it to react overnight.

Afterwards, reaction was allowed to cool down to room temperature and 26 ml of a 30% (w/w) ammonia solution were slowly added, since some bubbling and heating occurred. Mixture was so diluted with distilled water to a volume of 200 ml, this solution was further diluted with brine solution to a final volume of 500 ml to avoid having emulsification. This aqueous solution had a distinctive dark blue color. This solution was washed several times with diethyl ether (150 ml per washing), until the diethyl ether washing was not getting colored (from dark yellow in the first washing to slightly colorless in the last). The organic layers were combined and dried over anhydrous $MgSO_4$ and filtered, then the solvent was evaporated, and a dark oil remained. Purification was performed by Column Chromatography, using a gradual mixture of cyclohexane/ ethyl acetate (8:2) → (6:4) as the eluent. Yield: Dark yellow solid (0.35 g, 25 %).

^{1}H NMR (400 MHz, $CDCl_3$): δ 7.48 (d, J=3.8 Hz, 1H_h), 6.82 (dt, J=3.7 Hz, J=0.9 Hz, 1H_g), 4.15 (q, J=7.1 Hz, 2H_f), 2.88 (t, J=7.6 Hz, 2H_e), 2.33 (t, J=7.4 Hz, 2H_d), 1.71 (m, J=8.7 Hz, 4H_c), 1.4 (q, J=3.7 Hz, 2H_b), 1.27 (t, J=7.1 Hz, 3H_a),

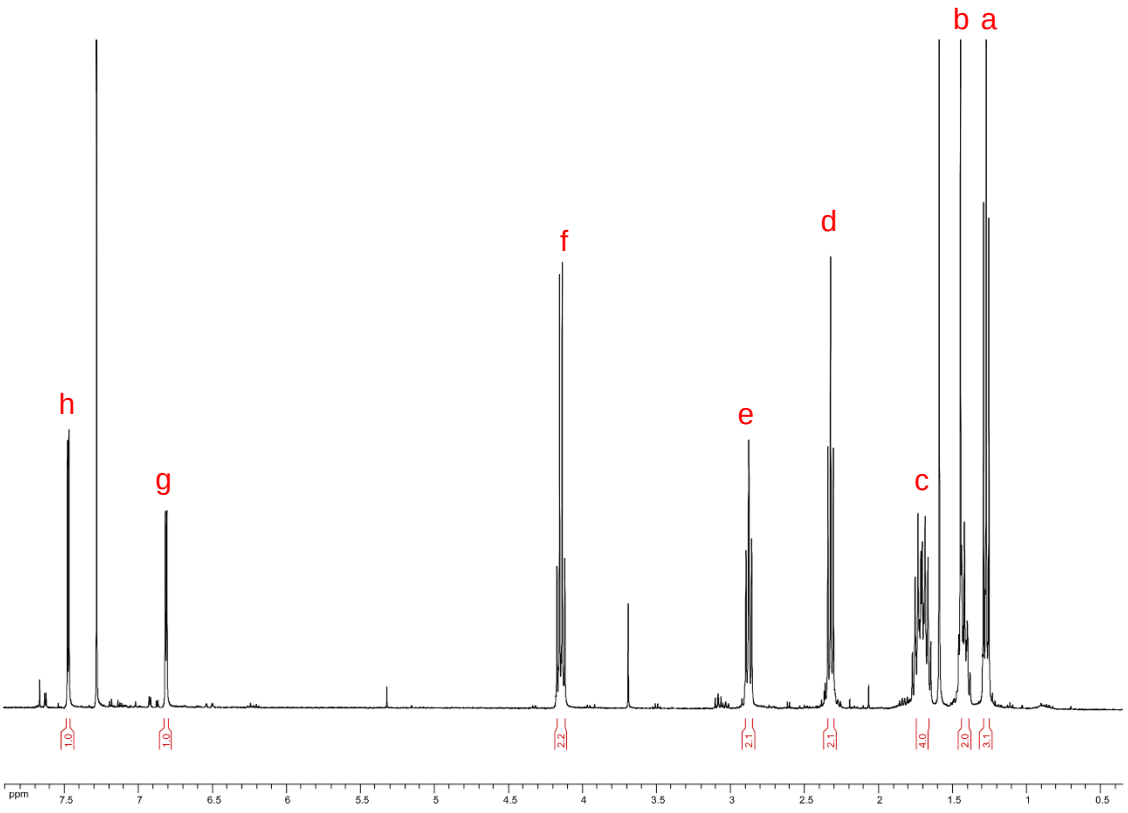

*N-hexylhex-5-ynamide (Compound **22-C**)*

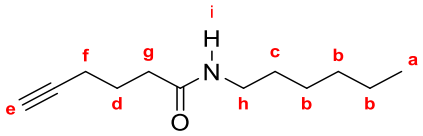

In a round bottom flask, 15 ml of CH_2Cl_2 were added along with a magnetic stirrer. Hex-5-ynoic acid (8.7 mmol, 1 eq, 5.1 g), hexyl amine (8.7 mmol, 1 eq, 3.4 g) and triethyl amine (26.1 mmol, 3 eq, 7.9 g) were then added and mixture was cooled down to 0 °C for 30 mins by using an ice/water bath. Afterwards, $SOCl_2$ (8.7 mmol, 1 eq, 3.1 g) was added dropwise to the mixture, which thickened and became yellow in color, gas was also released upon addition of each drop. Reaction was allowed to continue at room temperature for 1 h. Mixture was diluted with CH_2Cl_2 to a final volume of 100 ml and the organic phase was then washed as follows: first with 25 ml of a 1 mol/l solution of HCl, then with 25 ml of a 1 mol/l solution of NaOH and finally with 25 ml of a saturated brine solution. Organic phase was then dried over anhydrous MgSO4 and filtered, then the solvent was evaporated. A yellow brownish oil remained. Purification was performed by Column Chromatography, using a mixture of Cyclohexane/Ethyl Acetate mixture (1:1) as the eluent. Yield: Slightly yellow oil (0.77 g, 45%).

^{1}H NMR (400 MHz, $CDCl_3$): δ 5.64 (s, 1H$_i$), 3.23 (td, J=7.2 Hz, J=5.8 Hz, 2H$_h$), 2.29 (t, J=7.4 Hz, 2H$_g$), 2.25 (td, J=6.4 Hz, J=2.8 Hz, 2H$_f$), 1.96 (t, J=2.7 Hz, 1H$_e$), 1.85 (m, J=7.2 Hz, 2H$_d$), 1.48 (md, J=7.1 Hz, J=2.2 Hz, 2H$_c$), 1.32-1.25 (m, 6H$_b$), 0.87 (t, J=6.9 Hz, 3H$_a$).

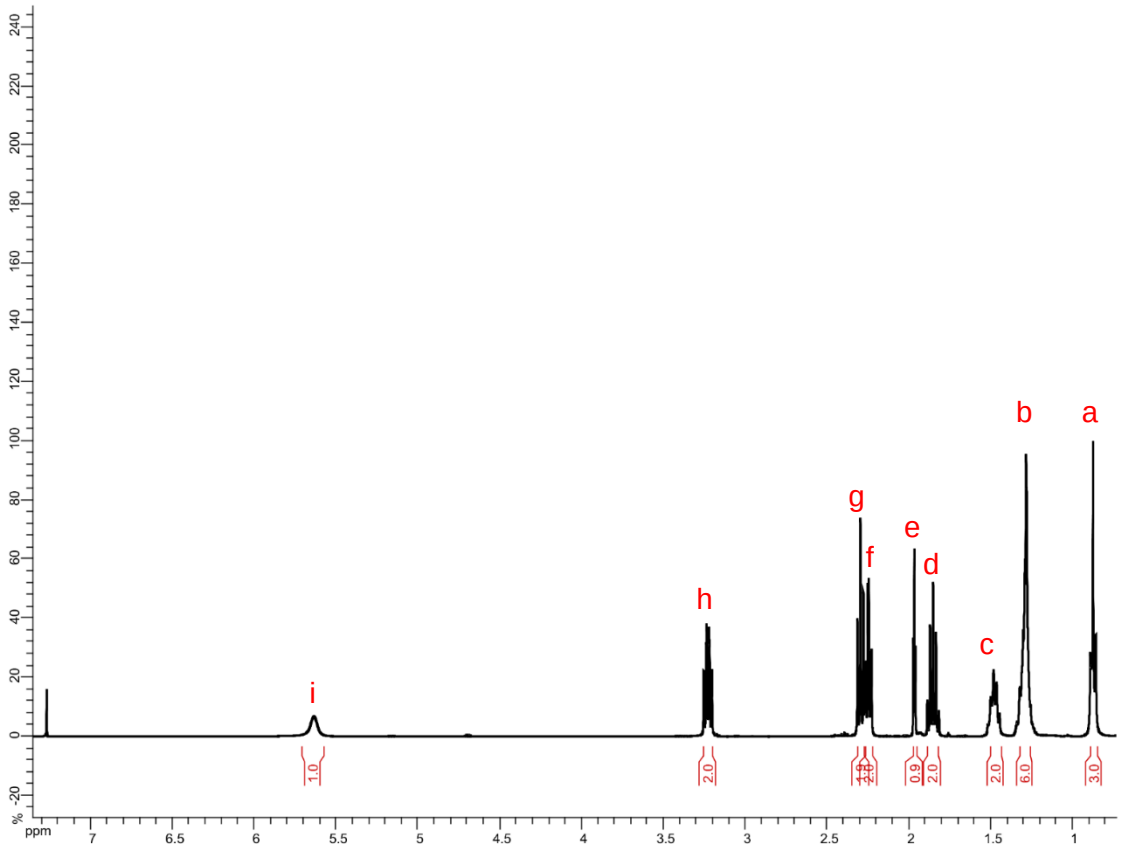

*6,6'-((2,5-dihexyl-3,6-dioxo-2,3,5,6-tetrahydropyrrolo[3,4-c]pyrrole-1,4-diyl)bis(thiophene-5,2-diyl))bis(N-hexylhex-5-ynamide) (Compound **24-C**)*

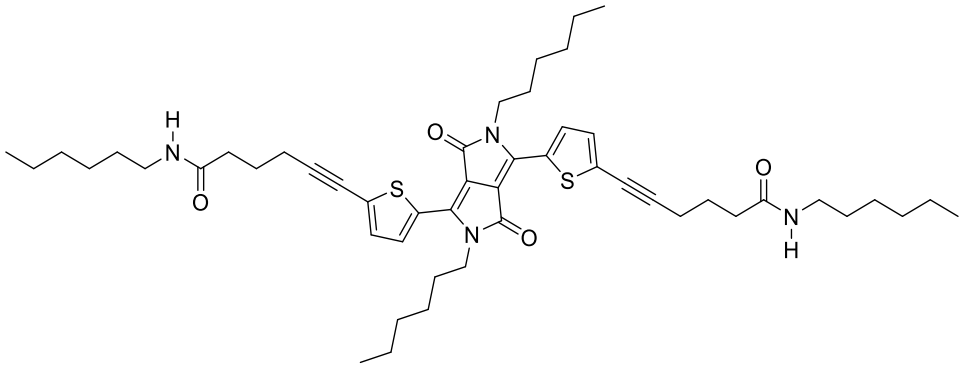

In a 2-neck round bottom flask coupled with a reflux apparatus, Compound **23** (0.16 mmol, 1 eq, 0.10 g), N-hexylhex-5-ynamide (0.33 mmol, 2.1 eq, 0.065 g), $(PPh_3)_2PdCl_2$ (0.02 mmol, 0.14 eq, 0.016 g) and CuI (0.01 mmol, 0.062 eq, 0.065 g), along with a magnetic stirrer, were dissolved in 10 ml of a mixture of THF/Diisopropylamine (4:1). Reaction was performed under argon atmosphere at 60°C. The mixture was stirred overnight and was then cooled down to room temperature. Mixture was diluted in 30 ml of distilled water and was then washed with $CHCl_3$ (3x50 ml) and the organic phase was dried over $MgSO_4$, filtered and the solvent was removed under vacuum. A dark bluish-purple solid remained, which was purified as follows: gradual column chromatography using $CHCl_3$ as the eluent, then polarity was increased using a mixture of $CHCl_3$/MeOH (99:1) as the eluent. The fractions containing what was suspected to be the product was kept apart, solvent was evaporated, and a dark bluish-purple solid remained. Upon ^{1}H-NMR product was confirmed but still had impurities, so a purification by precipitation was performed. Enough $CHCl_3$ was used to solubilize most of the solid and when a large excess of MeOH was added, a precipitate formed, suspension was left in the fridge overnight and the precipitate was filtered and dried, yielding a dark bluish-purple solid (64 mg, 47%).

^{1}H-NMR (400 MHz, $CDCl_3$) δ [ppm]: 8.85 (d, J = 4.1 Hz, $2H_m$); 7.25 (d, J = 4.2 Hz, $2H_l$), 5.47 (s, $2H_k$); 4.04 (t, J = 7.7Hz, $4H_j$); 3.27 (q, J = 6.7 Hz, $4H_i$); 2.58 (t, J = 6.9 Hz, $4H_h$); 2.36 (t, J = 7.4Hz, $4H_g$); 1.99 (quin, J = 7.0Hz, $4H_f$) 1.73 (quin, J=7.8 Hz, $4H_e$); 1.54-1.48 (t, J = 6.7Hz, $4H_d$), 1.46-1.40 (t, J = 7.7Hz, $4H_c$); 1.37-1.29 (m, J = 4.5Hz, $20H_b$); 0.89 (tq, J = 7.0 Hz, J=1.0 Hz, $12H_a$).

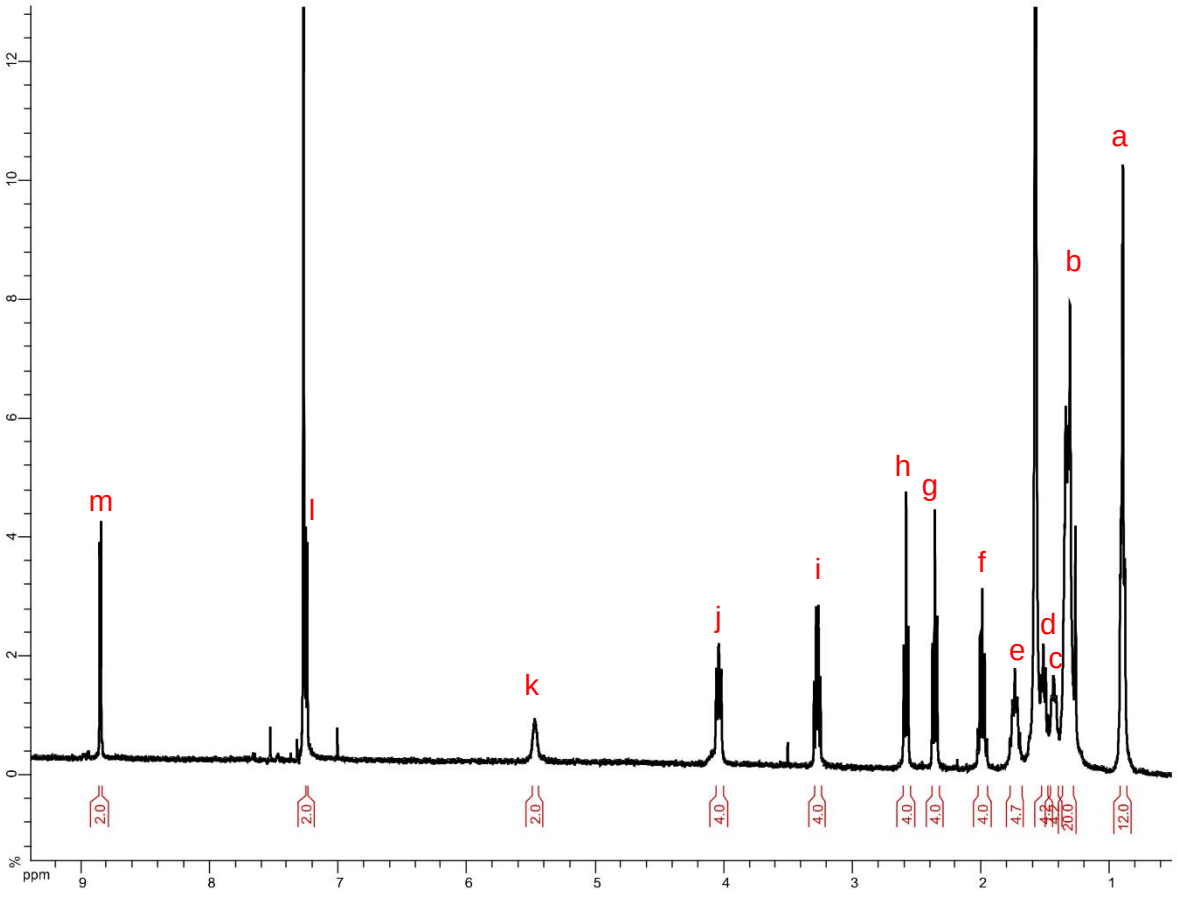

*6,6'-((2,5-dihexyl-3,6-dioxo-2,3,5,6-tetrahydropyrrolo[3,4-c]pyrrole-1,4-diyl)bis(thiophene-5,2-diyl))bis(N-hexylhexanamide) (Compound **8-C**)*

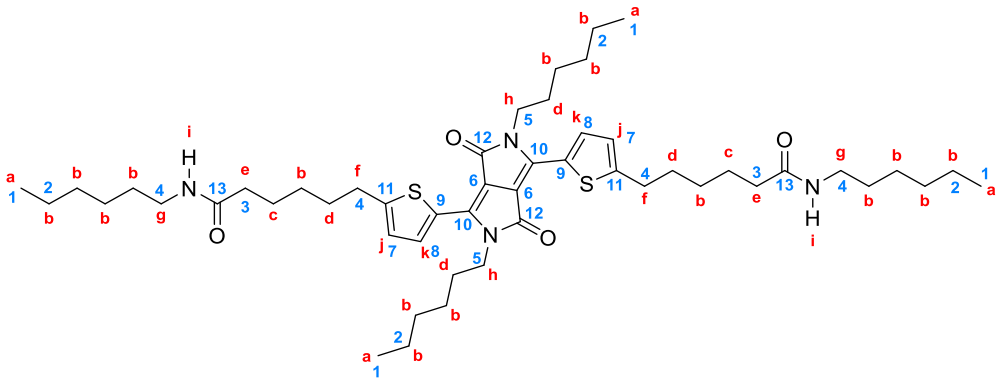

Succinic cyclization approach

In a 2-neck round bottom flask coupled with a reflux apparatus, a suspension of cesium carbonate (1.04 mmol, 3 eq, 0.35 g) and Compound **7-C** (0.35 mmol, 1 eq, 0.24 g) in 20 ml of acetonitrile was stirred under argon atmosphere at 82°C. The mixture was stirred for 1h at

82°C, then hexyl bromide (1.04 mmol, 3 eq, 0.18 g) was added dropwise. The solution was stirred overnight at 82°C and was then cooled down to room temperature. Solvent was evaporated from the crude, leaving a dark purple paste behind which was then dissolved in 200 ml of $CHCl_3$.

Mixture was washed with distilled water (3x75 ml) and the organic phase was dried over $MgSO_4$, filtered and the solvent was removed under vacuum. A dark purple solid remained, which was purified follows: column chromatography using a Toluene/MeOH (96:4) mixture as the eluent. The fraction containing what was suspected to be the product was kept apart, solvent was evaporated, and a dark purple solid remained. Upon ^{1}H-NMR product was confirmed but still had impurities, so a purification by precipitation was performed. Enough $CHCl_3$ was used to solubilize most of the solid and when a large excess of MeOH was added, a precipitate formed, suspension was left in the fridge overnight and the precipitate was filtered and dried, yielding a purple solid (17.4 mg, 6%).

Direct approach

In a 3-neck round bottom flask Compound **24-C** (0.05 mmol, 1 eq, 0.04 g) and 10% weight Pd/C (0.005 mmol, 0.1 eq, 0.005 g) were dissolved in 100 ml of a mixture consisting of Toluene/EtOH (1:1). Reaction was carried under hydrogen atmosphere at 60°C. The mixture was stirred for 2h at 60°C, and once it cooled down to room temperature, filtered through cotton with $CHCl_3$ to remove the catalyst. Solvent was evaporated from the crude, leaving a dark purple solid behind, which was purified by column chromatography using a mixture consisting of $CHCl_3$/EtOH (99:1) as the eluent. Product was recovered as a dark purple solid (48.4 mg, 90%).

^{1}H-NMR (400 MHz, $CDCl_3$) δ [ppm]: 8.68 (d, J = 3.9 Hz, 2H$_k$); 6.93 (d, J = 3.9 Hz, 2H$_j$); 5.38 (s, 2H$_i$); 4.00 (t, J = 7.9Hz, 4H$_h$); 3.21 (dt, J = 7.7 Hz, 6.1 Hz, 4H$_g$); 2.89 (t, J = 7.6 Hz, 4H$_f$); 2.14 (t, J = 7.6Hz, 4H$_e$); 1.76-1.65 (m, J=7.1 Hz, 8H$_d$); 1.45-1.42 (m, J = 3.6 Hz, 4H$_c$); 1.34-1.20 (m, J=8.1 Hz, 32H$_b$); 0.86 (t, J = 7.9Hz, 12H$_a$).

^{13}C NMR (101 MHz, $CDCl_3$) δ[ppm]: 172.8 (2C$_{13}$), 161.5 (2C$_{12}$), 152.4 (2C$_{11}$), 139.8 (2C$_{10}$), 135.5 (2C$_9$), 127.6 (2C$_8$), 126.25 (2C$_7$), 107.2 (2C$_6$), 42.3 (2C$_5$), 39.7 (4C$_4$), 36.8 (2C$_3$), 31.62, 31.59, 30.48, 29.79, 29.72, 28.93, 26.73, 26.53, 25.43, 22.70 (4C$_2$), 14.2 (4C$_1$).

Theoretical m/z: 862.5464, HR-MS (ESI-TOF) m/z 863.5522 $[M+H]^+$.

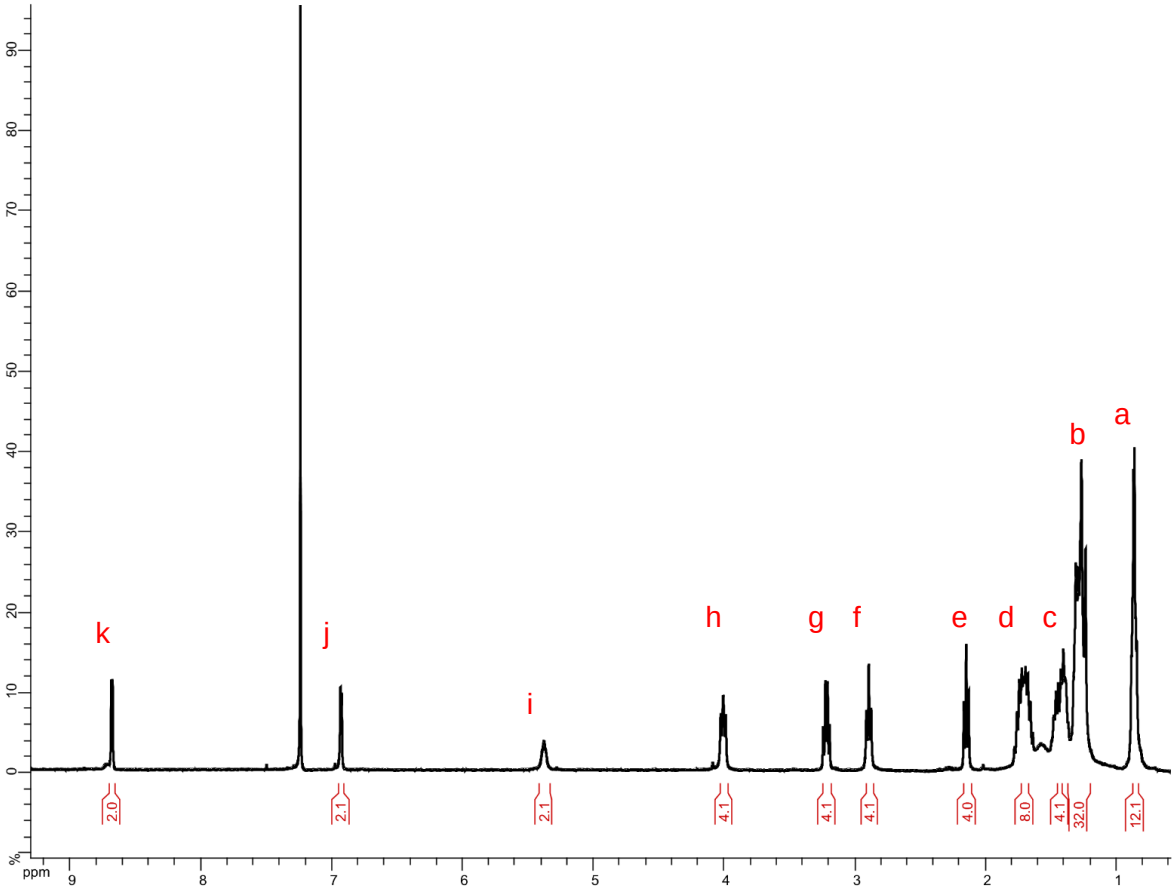
k
j
i
h
g
f
e
d
c
b
a
2.0
2.1
2.1
4.1
4.1
4.1
4.0
8.0
4.1
32.0
12.1
ppm
%

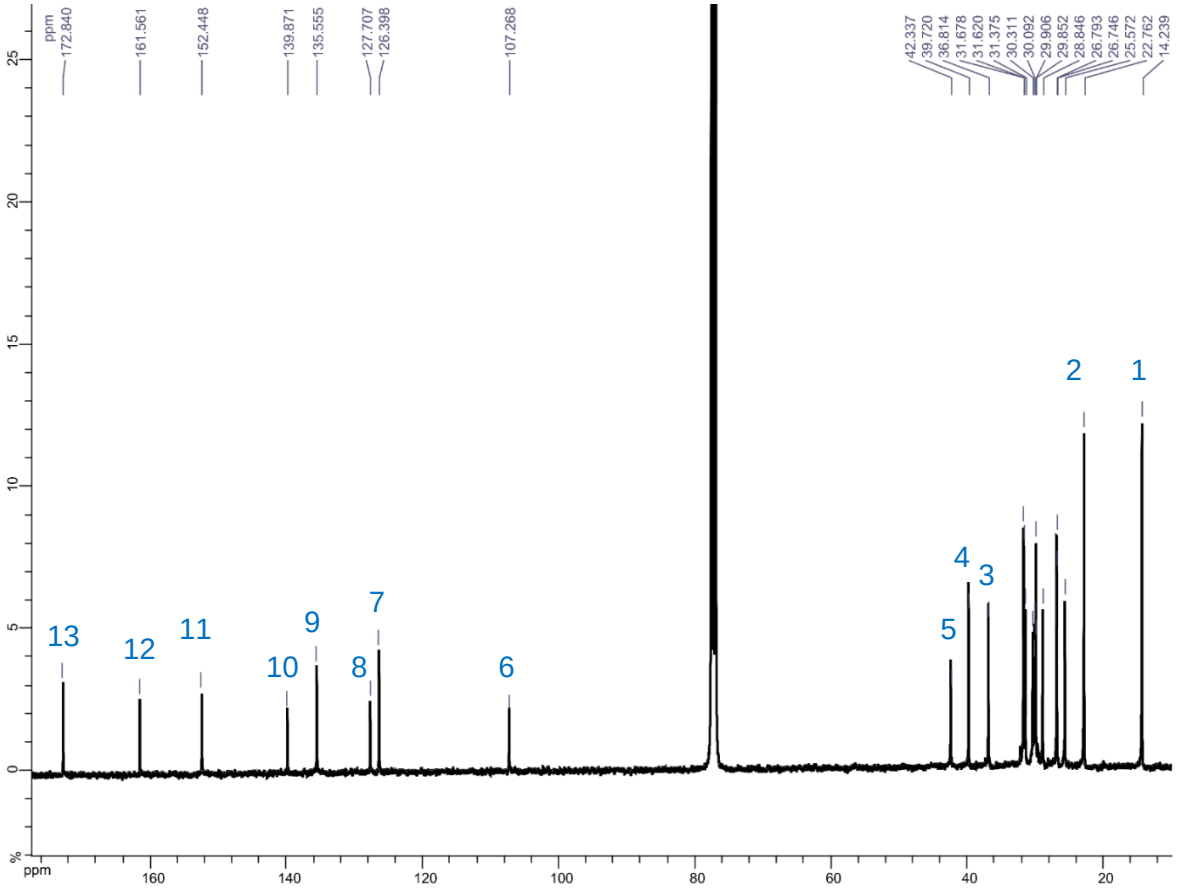
ppm
172.840
161.561
152.448
139.871
135.555
127.707
126.398
107.268
42.337
39.720
36.814
31.678
31.620
31.375
30.311
30.092
29.906
29.852
28.846
26.793
26.746
25.572
22.762
14.239
13
12
11
10
9
8
7
6
5
4
3
2
1
%
ppm
160
140
120
100
80
60
40
20

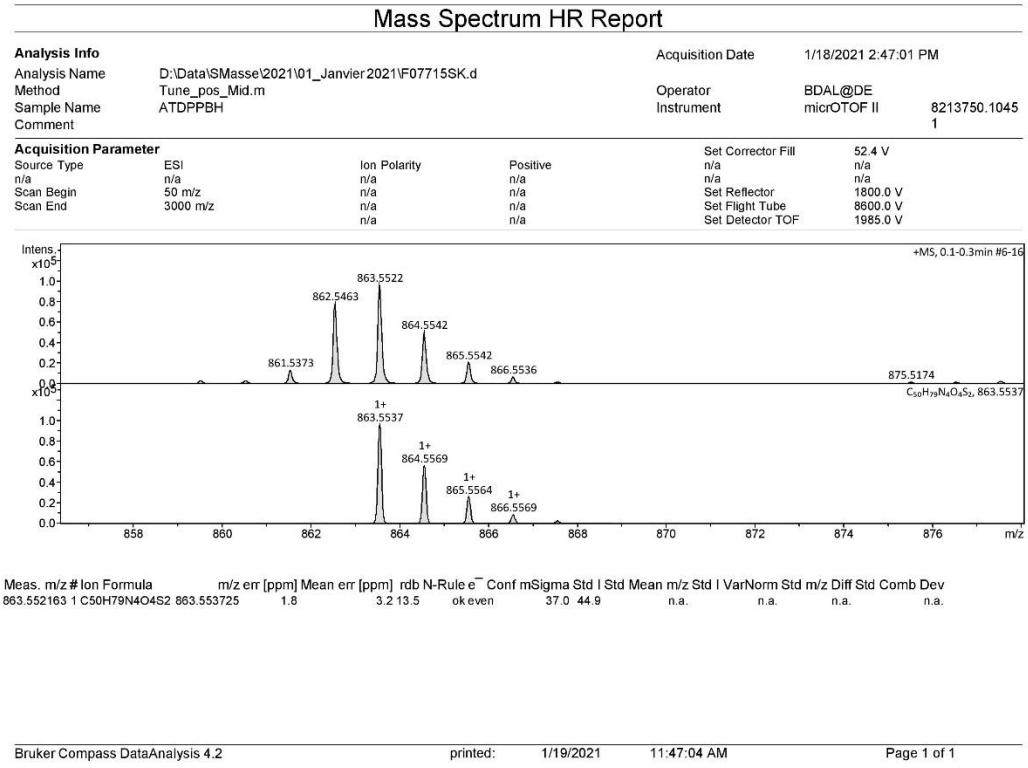

IV. References

[1] M. Grzybowski, D. T. Gryko, *Advanced Optical Materials* **2015**, *3*, 280–320.

[2] L. Bürgi, M. Turbiez, R. Pfeiffer, F. Bienewald, H.-J. Kirner, C. Winnewisser, *Adv. Mater.* **2008**, *20*, 2217–2224.

[3] G. P. McGlacken, L. M. Bateman, *Chemical Society Reviews* **2009**, *38*, 2447.

[4] A. Riaño, P. Mayorga Burrezo, M. J. Mancheño, A. Timalsina, J. Smith, A. Facchetti, T. J. Marks, J. T. López Navarrete, J. L. Segura, J. Casado, R. Ponce Ortiz, *J. Mater. Chem. C* **2014**, *2*, 6376.

[5] S. Stas, S. Sergeyev, Y. Geerts, *Tetrahedron* **2010**, *66*, 1837–1845.

[6] T. Řezanka, K. Sigler, *Eur. J. Org. Chem.* **2006**, *2006*, 4277–4284.

[7] C. B. Nielsen, T. Bjørnholm, *Org. Lett.* **2004**, *6*, 3381–3384.

[8] M. Takahashi, K. Masui, H. Sekiguchi, N. Kobayashi, A. Mori, M. Funahashi, N. Tamaoki, *J. Am. Chem. Soc.* **2006**, *128*, 10930–10933.

[9] Y.-Z. Wu, Y.-C. Zhang, J.-J. Chen, L.-J. Fan, *Chin J Polym Sci* **2019**, *37*, 1092–1098.

PERSPECTIVES:

Paving the way for real-time screening of organic electronic devices

CHAPTER V

I. Introduction and objectives

In the previous chapters we have shown the beginning of the comparative and systematic studies done on H-bonded π-conjugated materials based on **DPP**. These initial families are guiding us towards the next steps in the molecular design of new components. So far, we have found that even subtle differences in the molecular structure among **DPP** families and the different self-assembly processes can impact the optoelectronic properties. Furthermore, other parameters such as sample preparation, solvent chosen, concentration and temperature can influence the H-bonding ability, making the optimization process very complex. In this sense, we are starting to work on the *in-situ* control over the morphology and electric properties to gather as much information as possible and build up a screening protocol.

We have shown the different morphologies observed in the H-bonded **DPP** systems depend on the conditions. In addition, morphology transformations in solution as well as on thin films have been reported by other groups, as demonstrated in electroluminescent self-assembled systems,[1–3] opening a new platform to study morphology conversion in different types of devices. However, the use of H-bonds has been minimally employed in electronic devices despite the positive results found,[4–7] possibly due to the time consuming process needed to find first, the best supramolecular structures and second, the optimal device conditions. Therefore, the long-term goal of this project is to measure device efficiency in real time while simultaneously changing the morphology using stimuli such as solvent vapour (Figure V. 1).

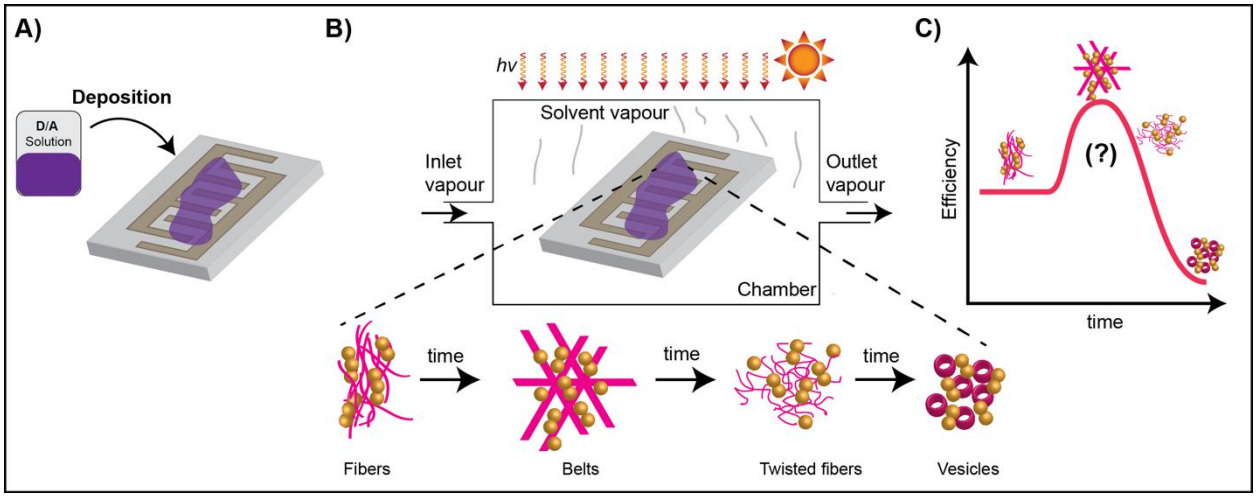

Figure V. 1 ***Real-time efficiency setup.*** *A) First the donor-acceptor solution is deposited; B) Next, the morphology is changed continuously using solvent vapour, while measuring the energy conversion efficiency in real-time. C) Expected efficiency vs time output that will be used to identify the most efficient morphology.*

The advantage of this approach over traditional device fabrication and testing cycles is that a great number of data points, such as efficiency vs. morphology, can be collected in a shorter time. Traditionally, many devices must be made, which is time consuming and only provides few scattered data points. This process can be even more tedious when testing completely new systems. In our case, the H-bonded groups will guide self-assembly into different

morphologies, forming nanostructures in solution that subsequently will be deposited to form thin films.

The resulting films will be exposed to different solvents to provoke a change in film morphology as has been observed in previously reported work.[8–10] Specifically, we intend to use substrates with interdigitated electrodes of cathode and anode and drop cast solutions of H-bonded molecules. In this way, we can characterize device performance, without applying a top electrode (Figure V. 1). We note that this will not be the best arrangement to optimize output characteristics, but at this stage our device structure is aimed at getting good correlations, not the best performance.

Practically, the substrate coated with the film consisting of nanostructures will be placed in a container with a gas inlet and outlet. After a defined period of time, the vapour pressure is reduced, and device performance is quantified. The process (i.e., vapour in → vapour out → measure) can be programmed and run dozens of times, resulting in high fidelity data. It will be interesting to see the device performance during a large morphological change, for instance, when going from vesicles to interconnected films or from nanobelts to twisted fibres.

At the moment, we have a similar setup in our group (made by Dr. Martin Brinkmann and Laurent Herrmann) that will allow us to observe in real time the morphology changes upon solvent vapor annealing and temperature (Figure V. 2).

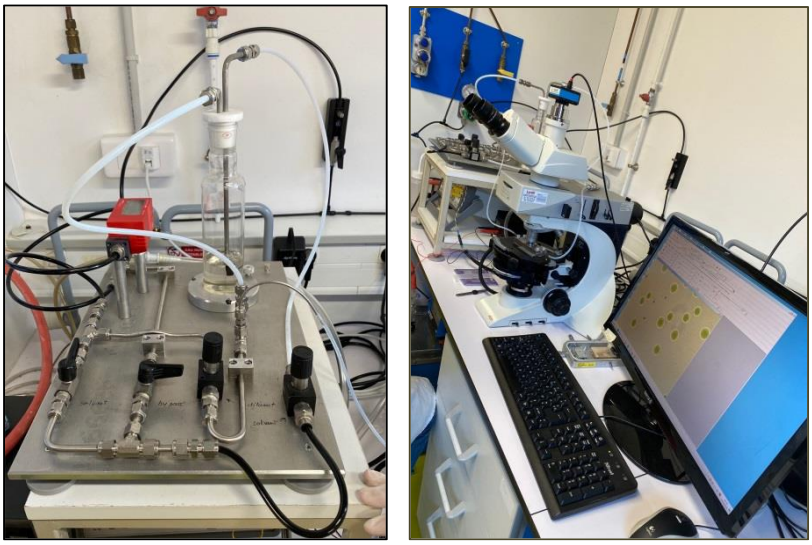

Figure V. 2 Solvent vapor annealing setup connected to an optical microscope and a Keithley machine.

This setup has been previously used by our team to control polymer crystallization on thin films using controlled solvent vapor annealing.[11] For instance, highly crystalline poly{[4,4-bis-alkyl-cyclopenta-(2,1-b;3,4-b′)dithiophen]-2,6-diyl-alt-(2,1,3-benzo-thiadiazole)-4,7-diyl} (**PCPDTBT**) films were prepared by exposing them to either chlorobenzene or carbon disulphide, in a controlled solvent vapor annealing protocol. Both, chlorobenzene and carbon disulphide annealing induced the formation of a polymorph of **PCPDTBT**, only differing in the

orientation of the polymer chains on the substrate. The electron diffraction patterns and the structural model of the polymorph did not give evidence for any efficient π-stacking and differed from the reflections reported in literature for films deposited by traditional device protocols.

These solvent-annealed films seemed to be quasi-equilibrated and were highly stable up to the melting point of the material. The difference in crystal structure was also reflected by the differing absorption spectra between the solvent-annealed and non-solvent annealed films. Furthermore, the potential of solvent vapor crystallization as an approach applicable to semicrystalline materials was highlighted. Lastly, the use of low boiling point solvents, demonstrated that it is possible to control the crystallization behaviour and to establish structure function relationships.

In this regard, our intention is to upgrade the setup by adding a properties analyser so we could choose an electronic parameter of interest. Nevertheless, before moving to our studies using this setup, we have studied several H-bonded **DPP** systems individually before and after exposure to solvent vapour and temperature. Particularly, we have explored the **DPP** derivatives presented in chapter III: **HDPPH**, **HDPPBA-C** and **HDPPBA-N** (Figure V. 3). The work shown in this chapter is the fruit of a collaboration with Dr. Martin Brinkmann from our group, an expert on alignment techniques and electron diffraction.

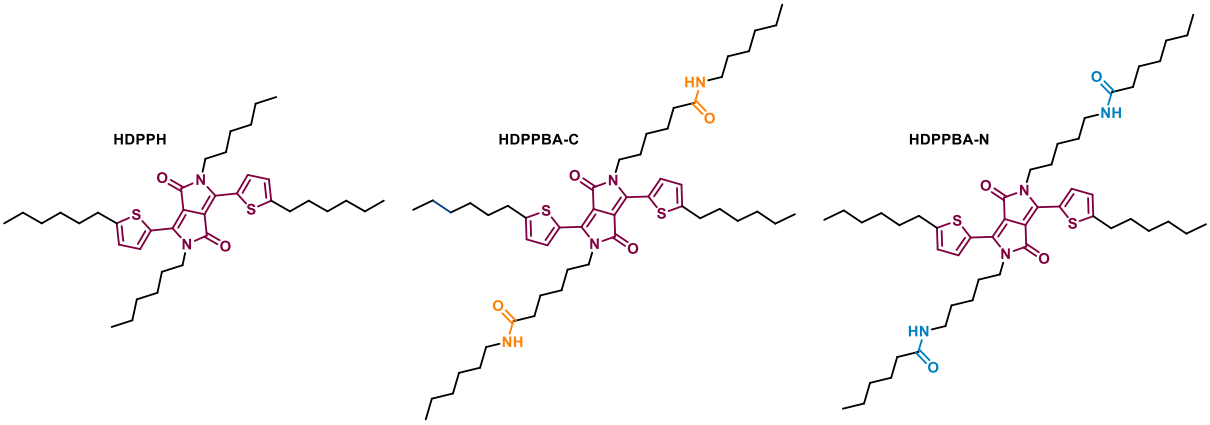

Figure V. 3 Chemical structure of the studied derivatives in this chapter.

II. Preliminary results and discussion

II.1) Thermal characterization

Our studies started by thermally characterizing the H-bonded **DPP** derivatives and the control molecule to know the degradation temperature and thermal stability of the derivatives. This way, we can evaluate the range of temperatures we could use during the thermal annealing processes. The thermogravimetric analysis (TGA), was performed by heating the samples from 25 °C to 300 °C at a rate of 5 °C/min under nitrogen atmosphere.

The results showed that **HDPPBA-C** (Figure V. 4a) and **HDPPBA-N** (Figure V. 4b) are thermally stable at this range of temperature, as they did not lose more than 1% of mass. On the other hand, **HDPPH** (Figure V. 4c) suffers a 2% weight loss by 230 °C and roughly a 10%

loss by 300 °C. This difference was attributed to the fact that **HDPPH** does not possess H-bonds and to the electron donating character of the alkyls chains. In fact, the introduction of hexyl chains to the nitrogen atoms breaks the planarity of the molecule, which upon heating causes easier defragmentation of the molecule.[12,13]

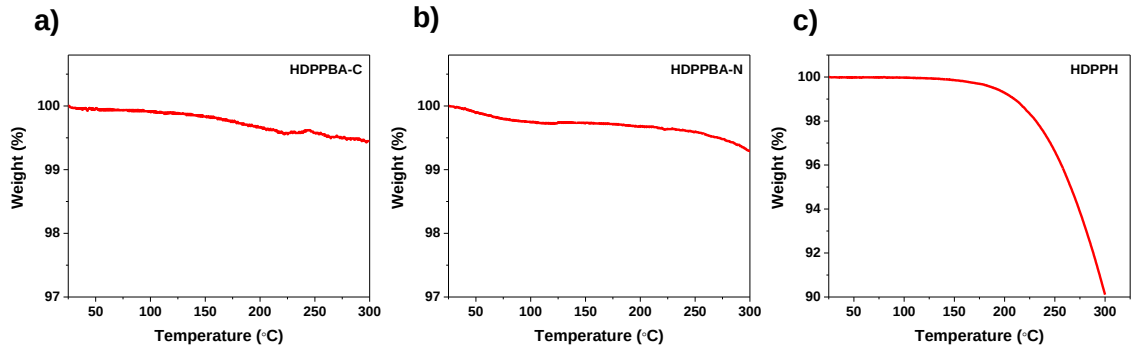

*Figure V. 4 TGA of a) **HDPPBA-C** b) **HDPPBA-N** and c) **HDPPH**.*

From the data collected from these experiments, it was possible to determine the conditions required to perform the differential scanning calorimetry (DSC). This measurement aimed to determine the melting behavior of these derivatives. The DSCs of **HDPPBA-C**, **HDPPBA-N** and **HDPPH** are shown in Figure V. 5, the first two compounds had melting points of 218 °C (Figure V. 5a) and 204 °C (Figure V. 5b) respectively, while the **HDPPH** had a substantially lower melting point of 159 °C (Figure V. 5c). Interestingly, there is a difference of 14 degrees in the melting temperature of the H-bonded derivatives, suggesting that the C-center derivative is more stable than the N-centered. It is probably due to the stronger aggregation character of **HDPPBA-C**, as we have shown in Chapter III. Once again, there was a big difference when comparing to the control molecule, attributed to the lack of H-bonds.

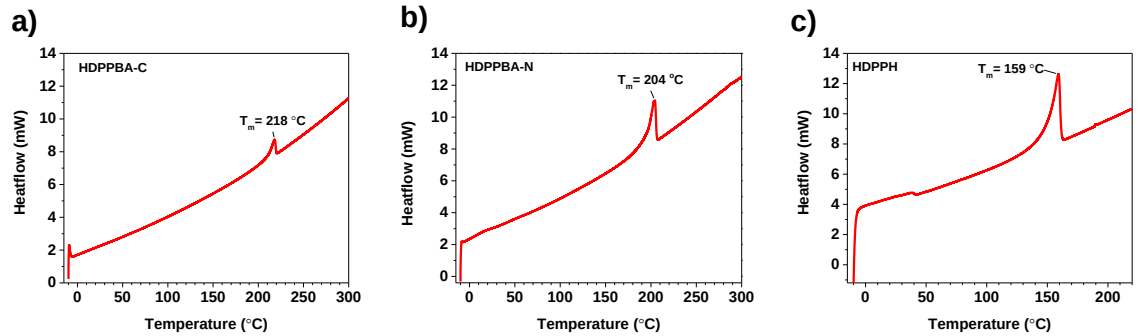

*Figure V. 5 DSC of a) **HDPPBA-C** b) **HDPPBA-N** and c) **HDPPH**.*

Additionally, these derivatives do not seem to display polymorphism since the DSC traces of the three compounds only show one peak, which is unusual as it has been reported that symmetrical **DPP** derivatives with long alkyl chains attached to the lactam ring have a tendency to form different crystalline forms, resulting in occurrence of multiple peaks in DSC.[13]

It is also possible that the **DPP** molecular skeleton has an influence on the alkyl chains via van der Waals interactions. In fact, the first carbons of an alkyl chain can be affected by the presence of a neighboring electron acceptor atom, having a great influence on the molecular

motion of the whole chain. On the other hand, it is possible that the molecular motion is influenced by the whole **DPP** skeleton, and the hexyl chain length is not long enough to overcome the electrostatic interactions between adjacent **DPP** molecules. In this sense, further measurements at slower cooling/heating rates (i.e., 1 °C/min), as well as starting the DSC measurements at lower temperature (i.e., -80 °C) could shed more light on possible crystalline forms.

These results lay the groundwork for the next measurements, as thin films of these derivatives were studied under melting conditions.

II.2) Oriented thin films study

To have a better understanding on the assemblies formed by these derivatives, thin films were studied. Particularly, the structural orientation of the self-assembled molecules was followed by electron diffraction (ED) preparing films on different substrates. The first set of experiments consisted of drop casting these derivatives from a chlorobenzene solution at a concentration of 2.5 mg/ml, the samples were casted onto carbon TEM grids and blotted to remove excess of solvent.

The first derivative that was analyzed was **HDPPBA-C**, finding that the stacking direction of the **DPP** molecules is parallel to the fiber axis (Figure V. 6). Additionally, it was observed that the molecules form columns and are tilted with respect to the fiber axis. The diffractogram shows the periodicity of H-bonded amides as the typical distance of 4.9 Angstroms (Å).

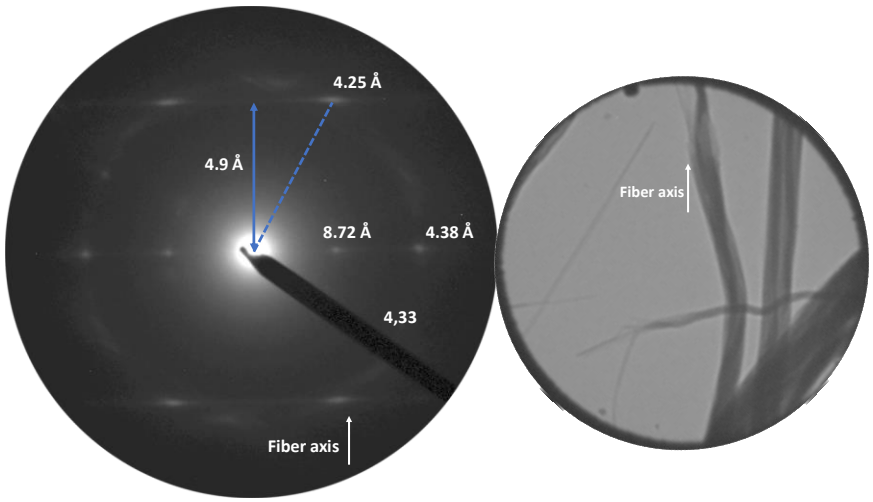

Figure V. 6 Left: ED pattern of a drop casted film from a chlorobenzene solution of ***HDPPBA-C*** *onto carbon TEM grids. Right: TEM image of the studied film.*

The next experiment that was performed aimed to see the impact that melting and recrystallization has on the orientation of the H-bonded aggregates. In this case the film was prepared on a polytetrafluoroethylene (PTFE) substrate by drop casting from solution and then

heating up the film to 240 °C during 1 min to ensure **HDPPBA-C** was melted. Next, the sample was cooled down to room temperature.

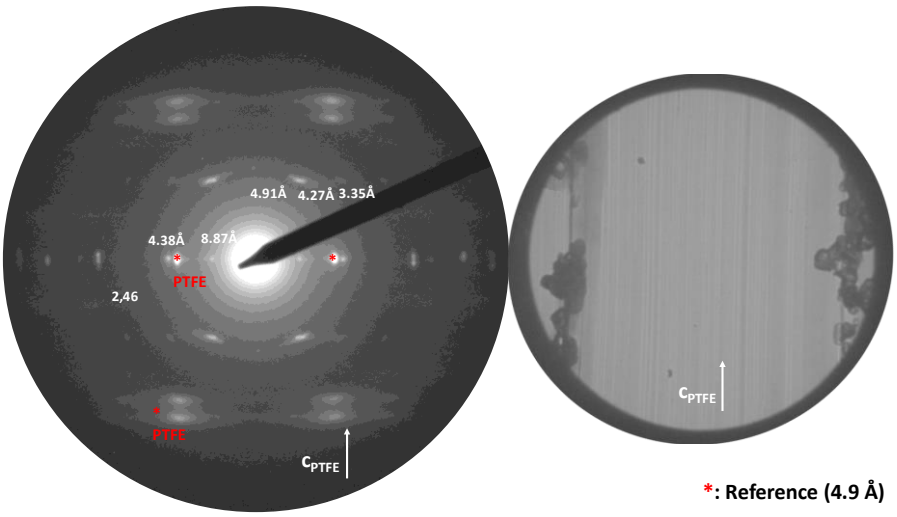

*Figure V. 7 Left: ED pattern of a melted and recrystallized film of **HDPPBA-C** in a PTFE substrate. Right: TEM image of the studied film.*

In this case, the electron diffractograms showed that the fibers had the same structure as the drop cast samples previously studied, but the crystallization was better as there are noticeable stronger reflections (Figure V. 7).

As it was observed that it is possible to control the orientation of these aggregates through melting, the impact of solvent vapor on the orientation was also evaluated. For this experiment, drop cast thin films were subjected to chloroform vapor annealing (SVA) for 1 hour. **HDPPBA-C** displayed the same structure as the drop cast samples, but the films showed stronger reflections as a sign of better crystallization and orientation, with no streaking of reflections (Figure V. 8).

Another ED pattern taken from the same sample shows additional reflections from crystals with different contact planes (Figure V. 9). In this case, more streaking is observed on the l=1 layer line, indicating some disorder in the arrangement of columns.

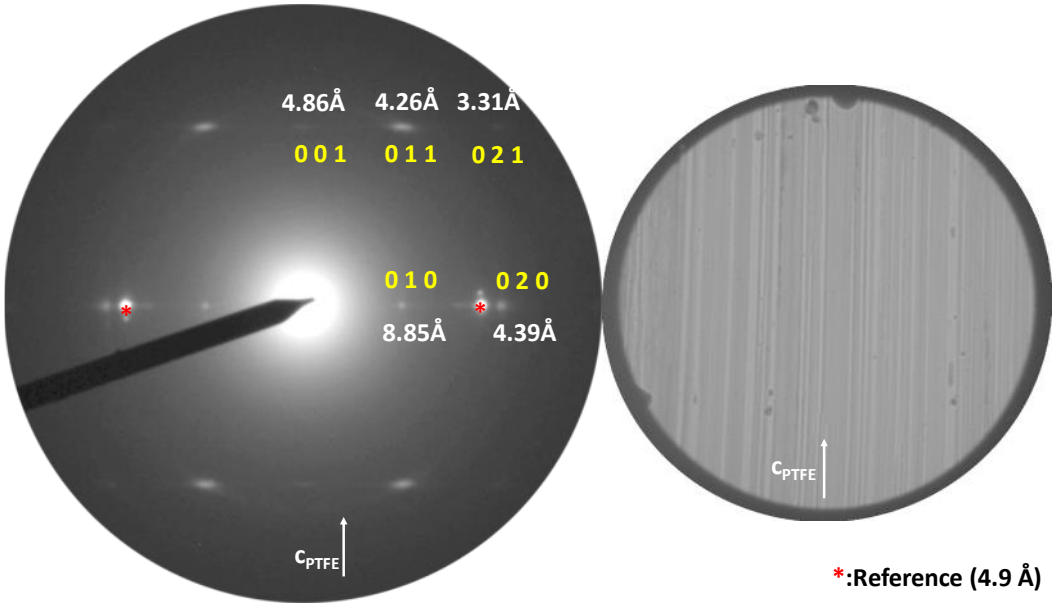

*Figure V. 8 Left: ED pattern of a film of **HDPPBA-C** that was annealed with vapor of chloroform in a PTFE substrate. Right: TEM image of the studied film.*

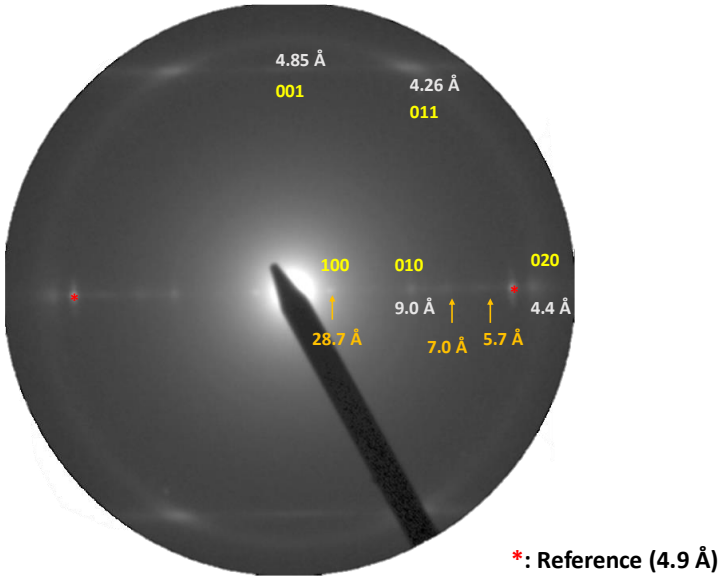

*Figure V. 9 A different ED pattern of **HDPPBA-C** showing additional reflections with different contact planes.*

With all the previously obtained ED patterns, it was possible to construct a very simple model of the structures formed by these aggregates (Figure V. 10). The reflections can be indexed based on a very simple orthorhombic unit cell.

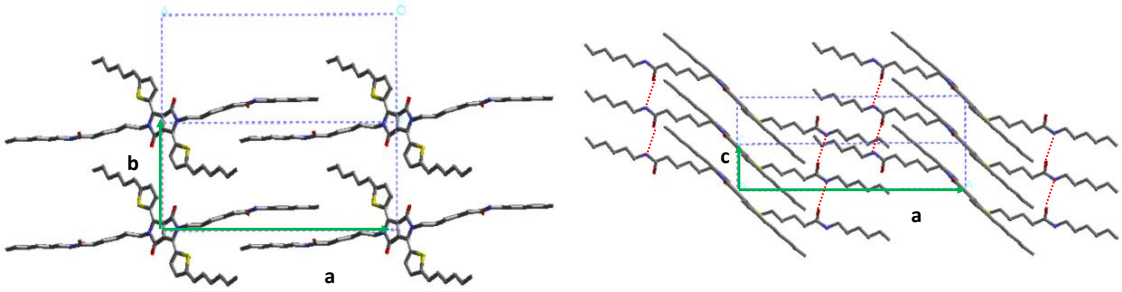

Figure V. 10 Modeling of the structure based on the obtained electron diffraction patterns.

The parameters of this model are as follows: a= 28.7 Å, b=8.9 Å and c=4.95 Å, $\alpha=\beta=\gamma$ =90°, where there is only one molecule per unit cell and possibly belonging to P-1 space group. The original ED pattern was further minimized in energy, but assuming the molecular conformation shown in Figure V. 10.

Interestingly, the minimization yielded a structure that is stable and shows nice H-bonds in the c-axis direction. This is fully consistent with the 4.9 Å periodicity along the stacking direction and explains why the **DPP** plane is tilted to the c-axis.

Furthermore, ED patterns for this model were calculated for planes [100] and [010] as depicted in Figure V. 11, which are in good agreement with the obtained experimental ED patterns.

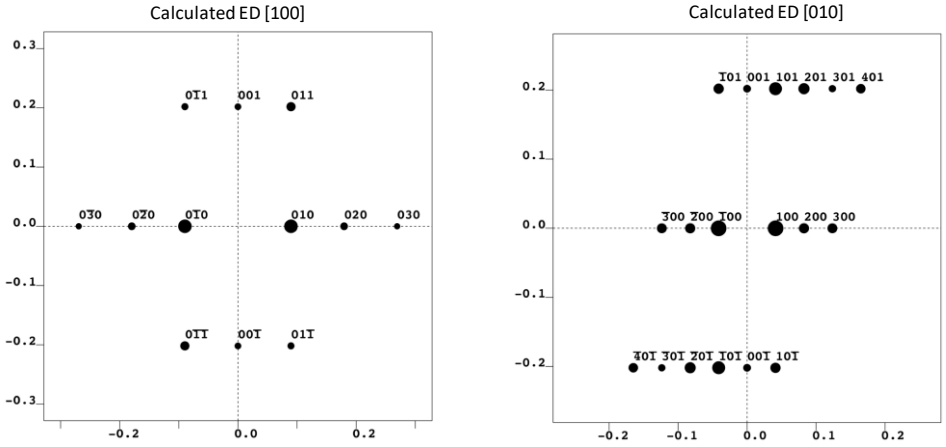

Figure V. 11 Calculated ED patterns for the proposed model of aggregation for planes [100] and [010].

The same sets of experiments were performed for **HDPPBA-N**, where the drop cast ED pattern shows the typical reflections as for its C-centered counterpart (Figure V. 12). The periodicity of H-bonded amides was observed once again. Additionally, ill-defined morphology of aggregates was observed in the film, with twisted lamellar objects and with very thin fibrils at extremities. These results agree with the morphology reported in chapter III for **HDPPBA-N**.

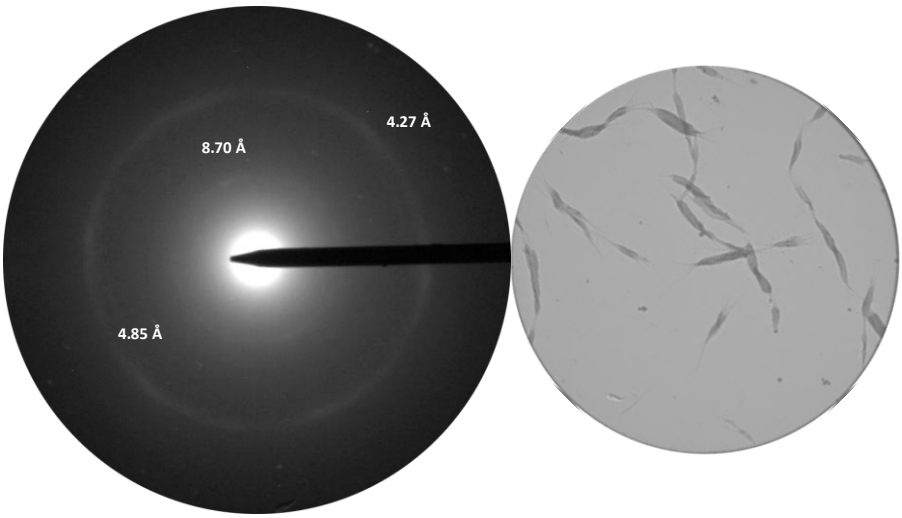

*Figure V. 12 Left: ED pattern of a drop casted film from a chlorobenzene solution of **HDPPBA-N** onto carbon TEM grids. Right: TEM image of the studied film.*

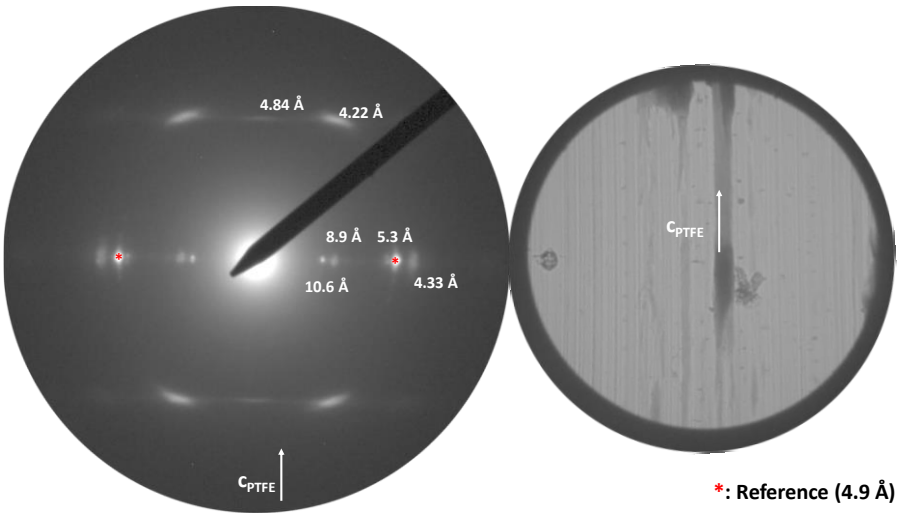

*Figure V. 13 Left: ED pattern of a melted and recrystallized film of **HDPPBA-N** in a PTFE substrate. Right: TEM image of the studied film.*

For the melted and recrystallized film experiment, the ED pattern of **HDPPBA-N** shows a unique orientation of crystals (edge-on) with (100) contact plane and it was observed that the c-axis of the aggregates formed by the **DPP** core are parallel to the c-axis of the oriented PTFE substrate (C_{DPP}//C_{PTFE}) (Figure V. 13). Additional reflections can be seen due to the presence of a few domains with slightly different orientation on the substrate plane. This may also indicate that the unit cell is slightly monoclinic.

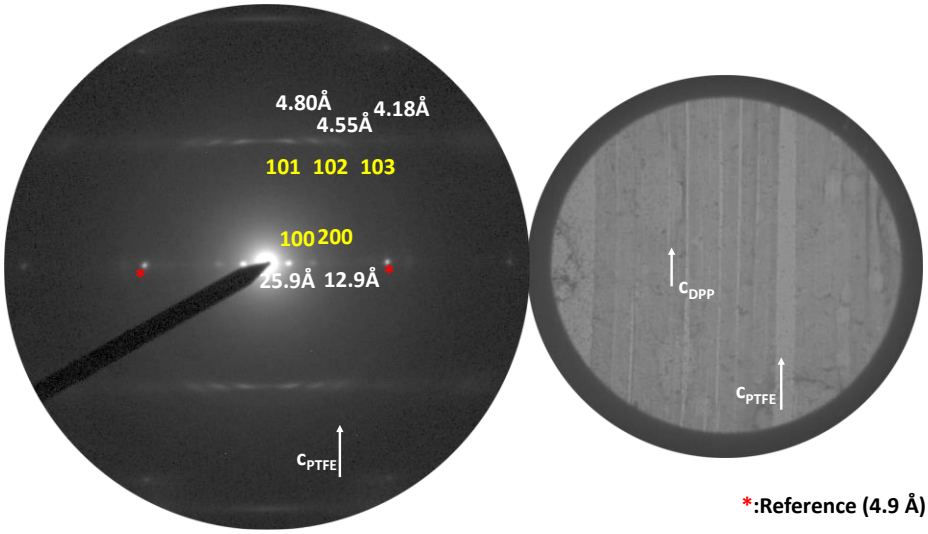

*Figure V. 14 Left: ED pattern of a film of **HDPPBA-N** that was annealed with vapor of chloroform in a PTFE substrate. Right: TEM image of the studied film.*

On the other hand, for the SVA experiment three different ED patterns were obtained. The first ED pattern is shown in Figure V. 14, where domains have a (010) contact plane and C_{DPP}//C_{PTFE}. Furthermore, the ED pattern is better defined and it is obvious that orientation was induced by epitaxy of the PTFE substrate because in this case the **HDPPBA-N** molecular columns run parallel to the PTFE chains.

The second ED pattern was taken from a sample where the stacking direction of molecules is perpendicular to the PTFE chain direction (Figure V. 15). This is a perfect example of 1D epitaxy induced by PTFE. A dominant (010) **DPP** contact plane on PTFE with a_{DPP} // c_{PTFE} was obtained.

In this case the epitaxial condition $(d_{001})_{DPP} \approx (d_{100})_{PTFE} \approx 4.9$ Å and the l=1 layer line show strong streaking, indicating disorder in the packing of adjacent columns of molecules.

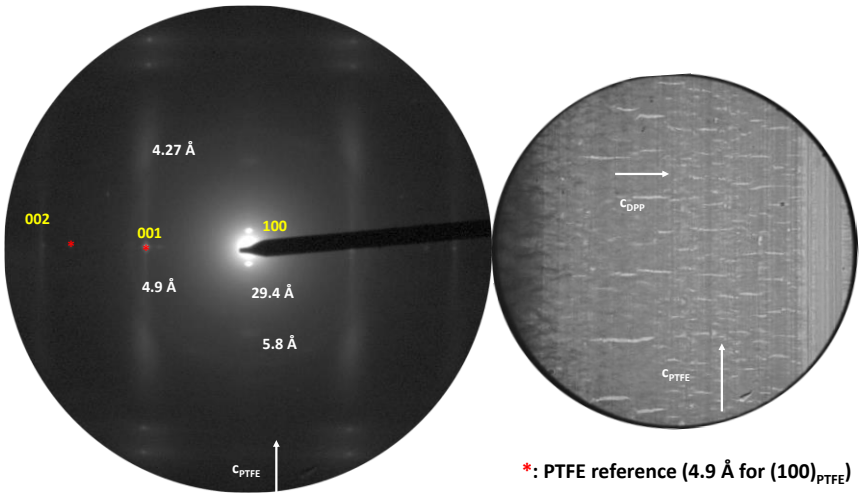

*Figure V. 15 Left: ED pattern of a SVA film of **HDPPBA-N** that has perpendicular orientation to C_{PTFE}. Right: TEM image of the studied film.*

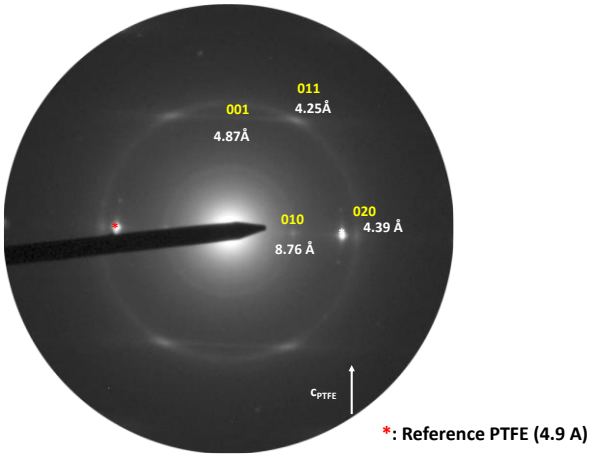

*Figure V. 16 A different ED pattern of **HDPPBA-N** showing Scherrer rings.*

In the third ED pattern, the stacking direction of molecules is parallel to the PTFE chain direction and the structure is very close to that of **HBDPPA-C** (Figure V. 16). Additionally, the presence of Scherrer rings indicates the presence of mis-oriented material.

The presence of a dominant (100) contact plane with $C_{DPP}//C_{PTFE}$ is somehow equivalent to edge-on orientation with respect to the substrate with the □-stacking in plane and the amide-side chains perpendicular to the substrate plane.

Lastly, **HDPPH** films were also studied, observing that crystals are formed and that the ED presents sharp reflections and high order (Figure V. 17), although no orientation was observed on the PTFE substrates. The diffraction pattern is similar to the H-bonded derivatives, and reticular distances are only slightly different. The ED pattern corresponds to edge-on crystals with side-chains normal to the substrate (100) contact plane. The similarity of ED with amides suggests that the packing is essentially driven by van der Waals interactions.

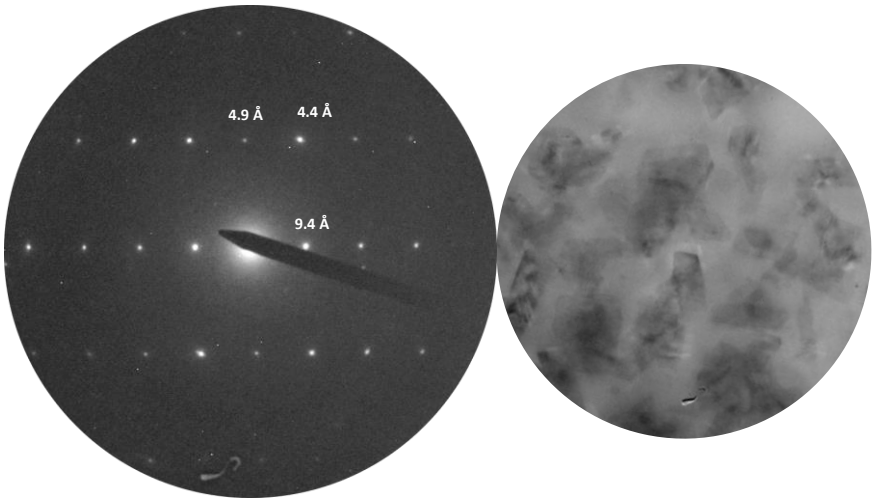

*Figure V. 17 Left: ED pattern of a melted and recrystallized film of **HDPPH** in a PTFE substrate. Right: TEM image of the studied film.*

In a next step, the orientation of the aggregates on thin film was evaluated placing the films under the polarized optical microscope (POM). The preparation protocol for the samples is described in (Figure V. 18).

The procedure consisted of two steps, first an isotropic solution of the **DPP** molecules in a given solvent was spread between the PTFE/glass substrate and a cover slip by capillarity. In this step it is important to make sure the molecules are completely solubilized; hence, the solution was heated above the isotropic temperature to reach dissolution of all aggregates. Lastly, the sample was moved to a colder surface to initiate the growth by reaching supersaturation, where heterogeneous nucleation occurs on the PTFE substrate and the orientation of **DPP** occurs.

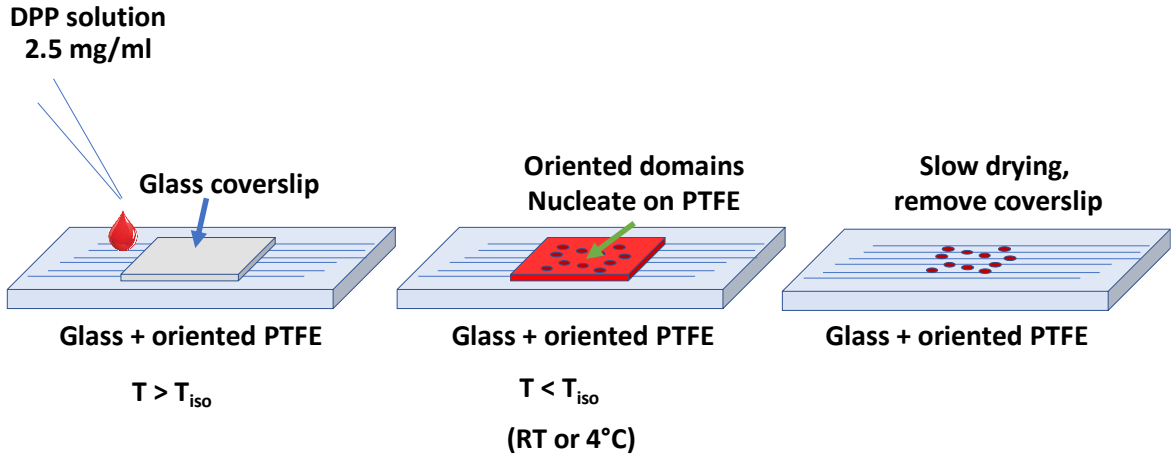

*Figure V. 18 Protocol to prepare oriented self-assembled **DPP** systems on PTFE substrates.*

All three derivatives were used to prepare films on PTFE substrates, samples for **HDPPBA-C** and **HDPPBA-N** were prepared departing from a 2.5 mg/ml solution in chlorobenzene.

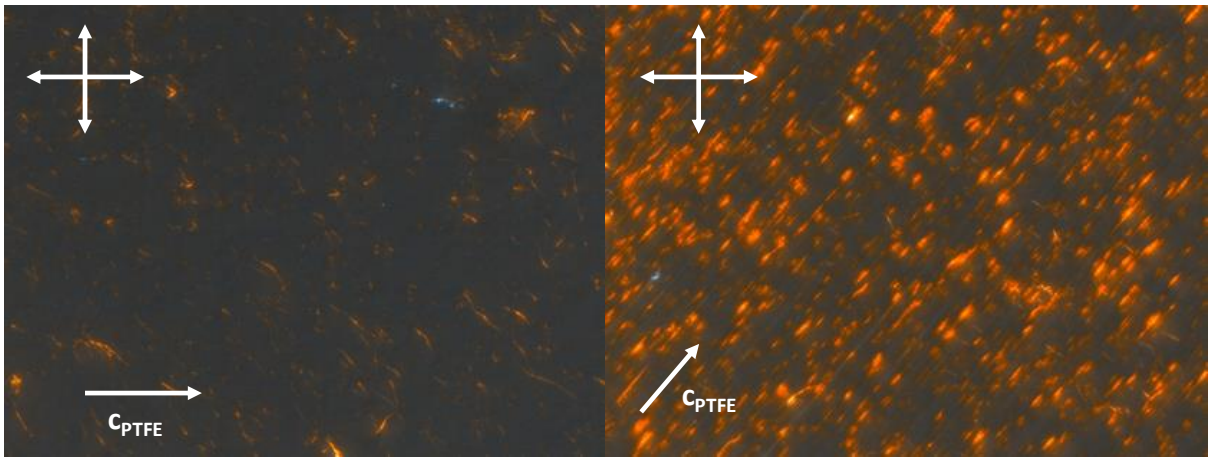

*Figure V. 19 Oriented **HDPPBA-N** on PTFE observed in the POM under crossed polarizers.*

For the films prepared with the N-centered derivative, birefringent domains appeared upon cooling when observing the film by POM under crossed polarizers (Figure V. 19). They correspond to oriented aggregates of **HDPPBA-N** nucleated on PTFE substrates, although the films were not yet continuous, and it is estimated that higher concentrations (10 mg/ml) are necessary to improve the continuity of the films.

To understand this behavior, UV-vis measurements of the thin films with parallel and perpendicular orientation to the C_{PTFE} axis were performed. The first experiment aimed to evaluate what happens when the aggregates grow from solution at room temperature. **HDPPBA-N** was deposited in the PTFE substrate at 70°C and allowed to cool down to room temperature and left for nucleation/growth, then UV-vis measurements were performed (Figure V. 20).

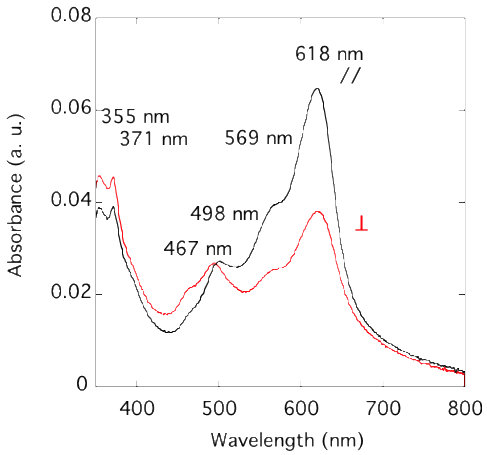

*Figure V. 20 UV-vis of a film of **HDPPBA-N** grown from solution in chlorobenzene at room temperature, black trace: parallel orientation, red trace: perpendicular orientation.*

The dichroic ratio (DR) value was 1.7 at 618 nm and it can be seen that not all features are equally polarized, for instance at 467 nm components are less polarized. Its contribution may add with the component at 618nm, hence reducing the apparent DR value. Nevertheless, low DR does not mean poor alignment. The transition dipole is certainly tilted to the stacking axis and this is why DR is small, similar to form beta of phthalocyanines.

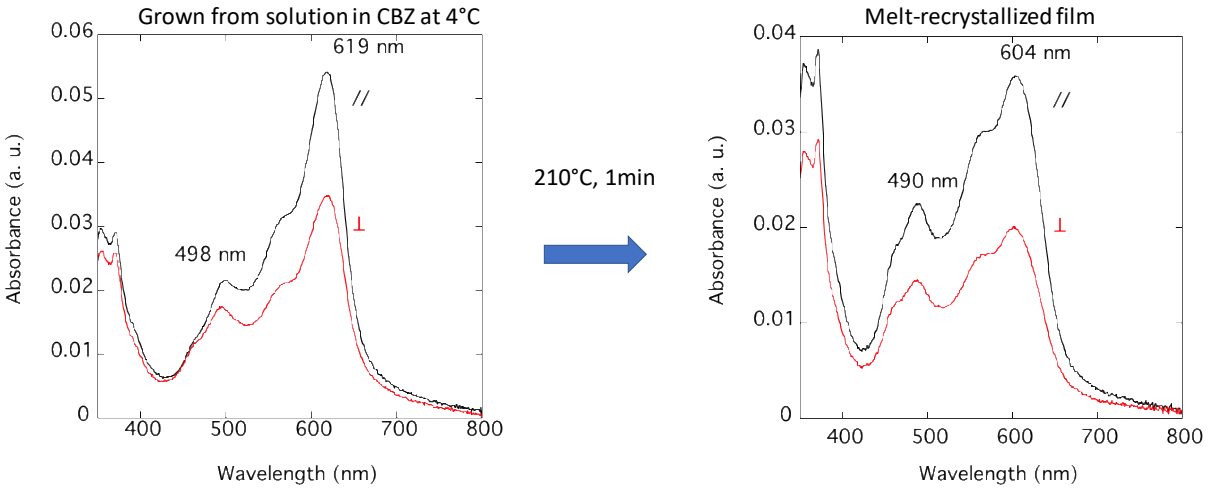

*Figure V. 21 UV-vis comparison of a film of **HDPPBA-N** grown at 4 °C and upon melting and recrystallizing of the film.*

Another film was measured by depositing **HDPPBA-N** from solution on a PTFE substrate at 70°C and cooled down to 4 °C. Absorption spectra were taken and then the film was melted by heating it up at 210 ºC for 1 min. Then recrystallization was allowed by cooling the film to room temperature, taking UV-vis spectra subsequently (Figure V. 21). It was observed that the melting-recrystallization process modifies the vibronic structure of the spectra. In this case, the 0-0 becomes weaker than the 0-1 and shifts to the blue from 619 nm to 604 nm, although the alignment was almost not affected (Figure V. 21).

The films were then studied by ED at 4 °C and after the melting-recrystallization process. When the film was grown on PTFE at 4°C, the ED pattern shows very narrow (010) diffraction, indicating very high in-plane alignment (Figure V. 22). Additionally, the films show oriented tapes or fibers along the PTFE chain direction, meaning that the stacking direction of **HDPPBA-N** is parallel to C_{PTFE}. The ED pattern also shows that the (011) is strongly streaked and overlaps with the (001). The streaking in l=1 layer indicates disorder between adjacent molecular columns.

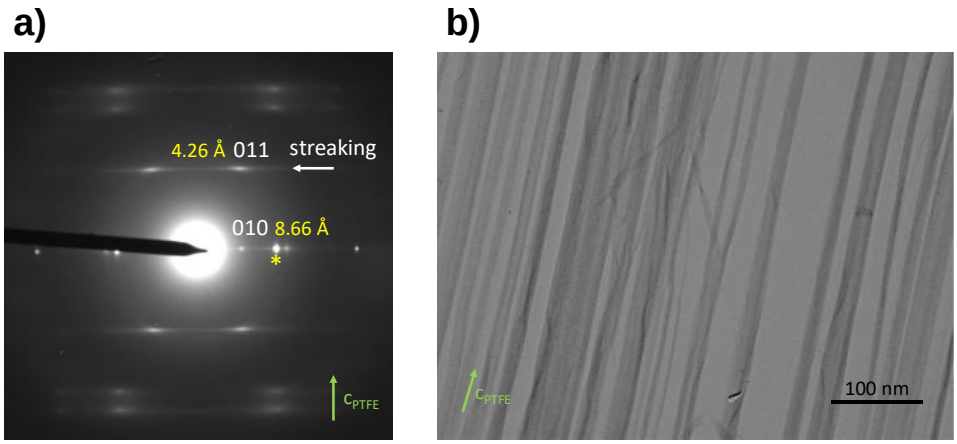

*Figure V. 22 a) ED pattern of **HDPPBA-N** film grown on PTFE at 4°C and b) TEM image of the studied film.*

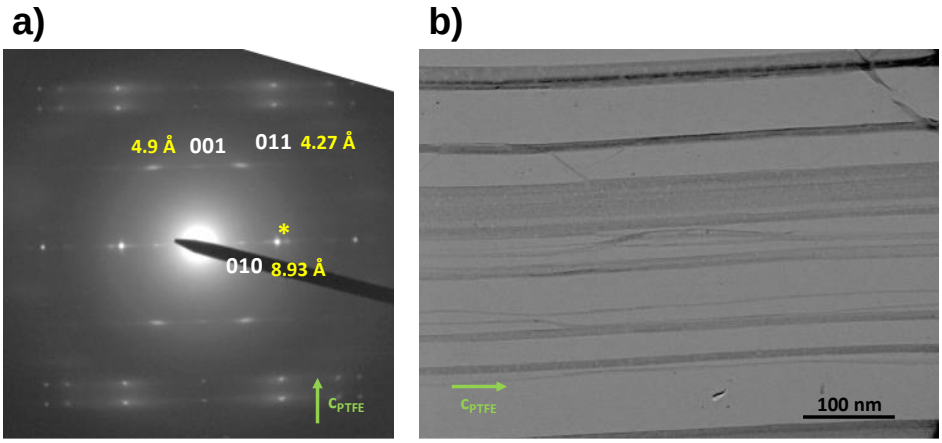

*Figure V. 23 a) ED pattern of **HDPPBA-N** film after thermal annealing and b) TEM image of the studied film.*

After thermal annealing (melt-recrystallization), the orientation is maintained, and no change of contact plane was observed (Figure V. 23). The streaking in the l=1 layer line is strongly reduced after annealing. Moreover, sharper reflections can be observed, which implies ordering of the adjacent molecular columns and explains the change in the UV-vis spectra.

The same sequence of experiments was then performed for **HDPPBA-C**. Thin films of this derivative showed some birefringence when observed by POM, but much smaller as compared to **HDPPBA-N** (Figure V. 24).

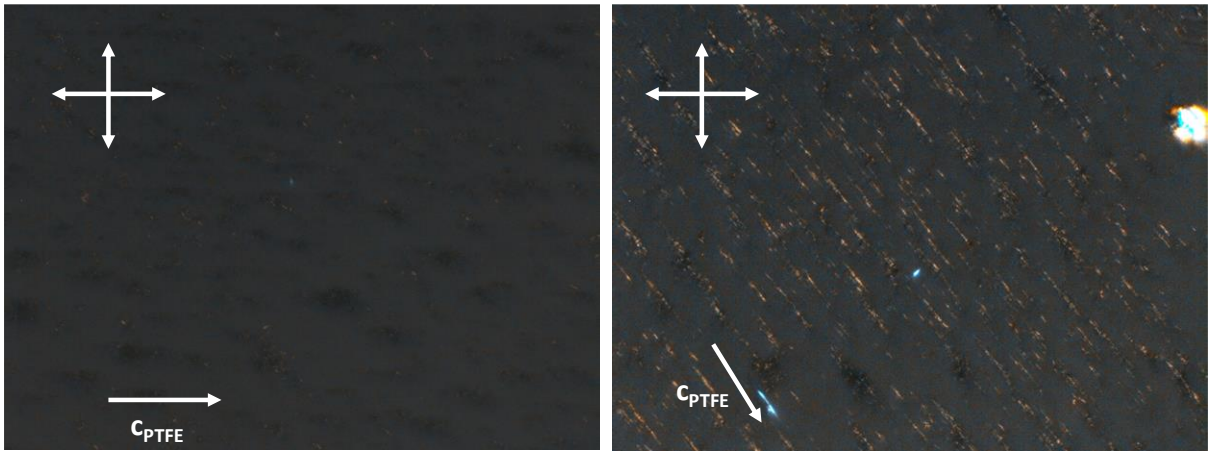

*Figure V. 24 Oriented **HDPPBA-C** on PTFE observed in the POM under crossed polarizers.*

Next, the UV-vis measurements of films cooled down to 4 °C and after thermal annealing were performed (Figure V. 25). No clear anisotropy in UV-vis was seen in the first part of the experiment, whereas upon thermal annealing an improvement of alignment was observed. In fact, there was no change in the positions of the bands, contrary to what happened with **HDPPBA-N**. The vibronic structure was maintained, as well as the relative intensities of the

0-0 and 0-1 transitions, meaning there is apparently no important structural changes after the thermal annealing of **HDPPBA-C**.

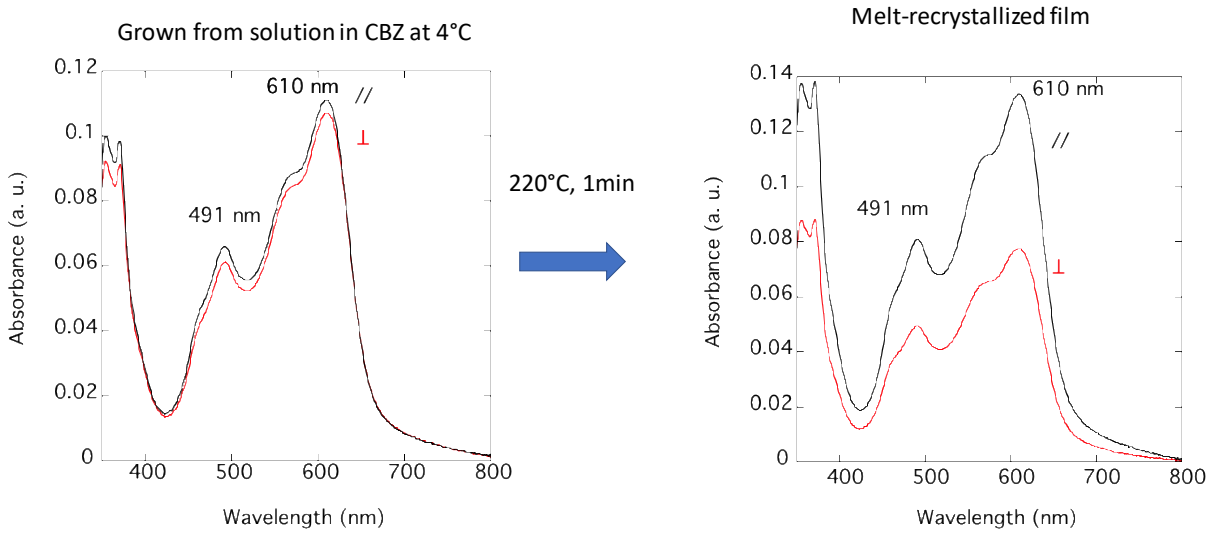

*Figure V. 25 UV-vis comparison of a film of **HDPPBA-C** grown at 4 °C and upon thermal annealing of the film.*

The corresponding ED pattern of the film grown at 4 °C is shown in Figure V. 26. It can be seen that most of the film is not oriented due to the presence of the Scherrer ring. Some domains are aligned and give sharper reflections that are indexed in the same way as for **HDPPBA-N**. Upon thermal annealing, additional Scherrer rings are visible as well as no sign of improved orientation (Figure V. 27). It appears that **HDPPBA-C** does not orient on PTFE unlike its N-centered counterpart. Once again, the subtle changes in the molecular design show important changes in aggregation and orientation, yielding very important information at the time of choosing a given compound for any specific application.

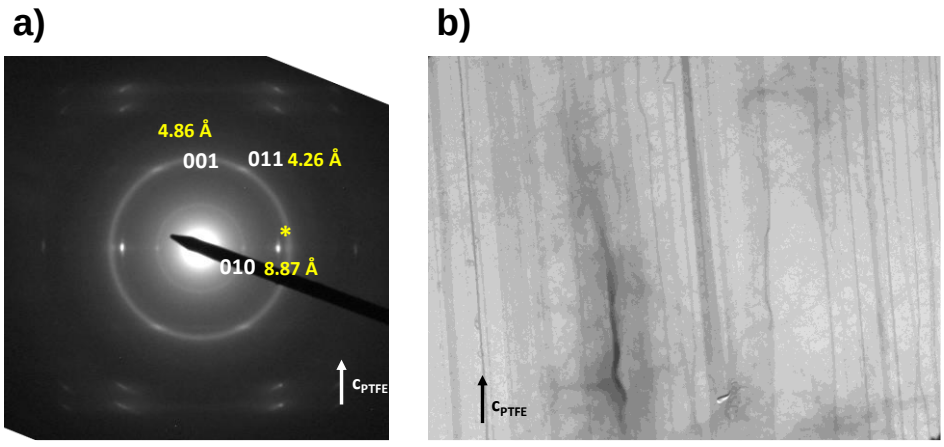

*Figure V. 26 a) ED pattern of **HDPPBA-C** film grown on PTFE at 4°C and b) TEM image of the studied film.*

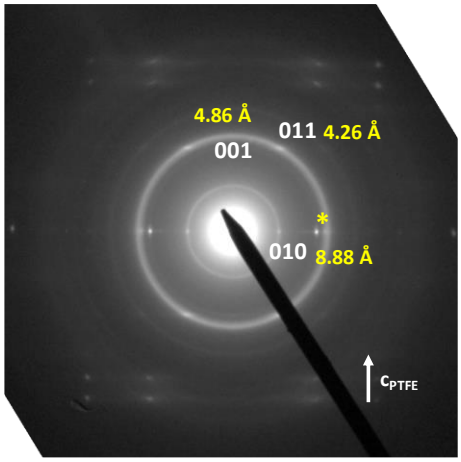

*Figure V. 27 ED pattern of **HDPPBA-C** film after thermal annealing.*

Finally, **HDPPH** was studied by using a 2.5 mg/ml solution in chloroform. The sample was doctor bladed on PTFE and the substrate was thermally annealed by heating at 165 °C, allowing it to recrystallize by cooling down to room temperature.

The PO micrograph shows some alignment of **HDPPH** crystals, but most importantly there is a clear change of color with light polarization (Figure V. 28). When the substrate is in parallel to the source of polarized light crystals have blue color, whereas upon perpendicular exposure they become orange.

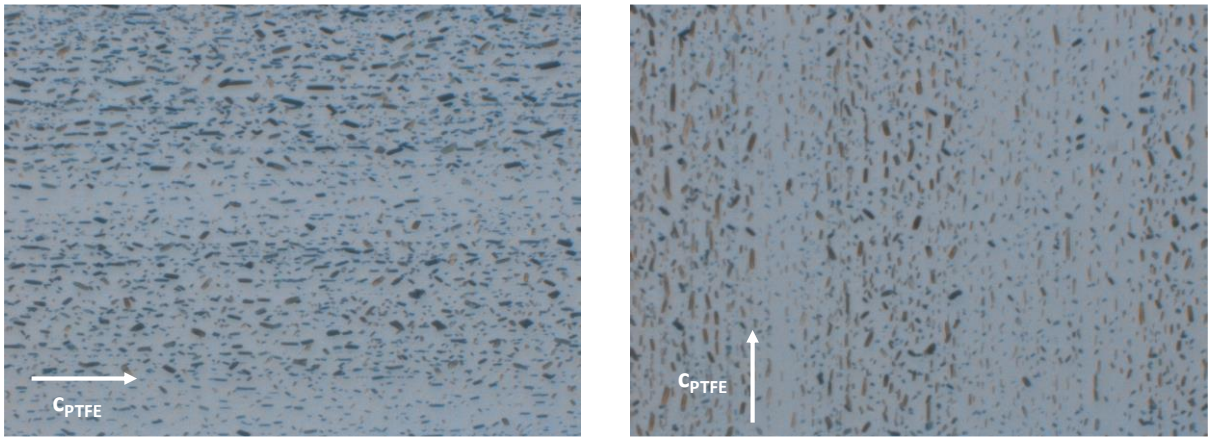

*Figure V. 28 Oriented **HDPPH** on PTFE observed in the POM under crossed polarizers.*

When the sample was subjected to SVA with chloroform, larger needle-like crystals grew as shown in Figure V. 29.

Figure V. 29 Needle type crystals of HDPPD grown upon exposure to vapor of chloroform.

UV-vis measurements were also performed for thermally annealed films (Figure V. 30), in this case a change in the relative absorbance of the 637 nm band *vs* 497 nm band is observed, which explains the change in color when exposed to polarized light. This situation is similar to other **DPPs** studied by Genevaz *et al*.[14]

In this case, it is assumed that the J-aggregate band at 637 nm is mostly polarized parallel to the PTFE chains and in strong contrast, the H-like band at 497 nm is weakly polarized along the PTFE, highlighting the fact that the two bands must have a different electronic origin.

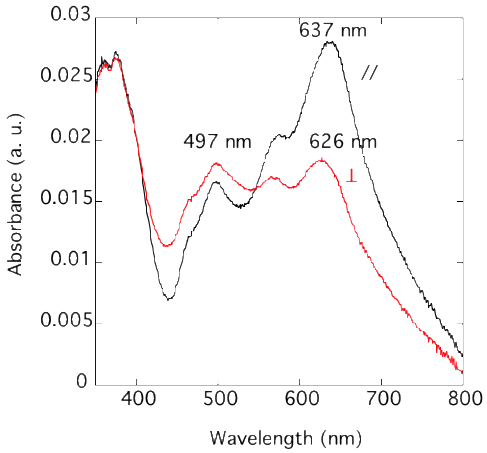

*Figure V. 30 UV-vis spectrum of **HDPPH** upon thermal annealing.*

Lastly, the ED pattern of the thermally annealed sample of **HDPPH** is almost identical to the amide-containing molecules (Figure V. 31). Dominant reflections are observed at 4.96 Å, 4.26Å and 9.46Å. The angle α^*=85° corresponds to a slightly monoclinic (or triclinic) crystalline lattice, where c* is along the crystal long axis (stacking direction) and one population of **HDPPH** crystals is defined by C_{HDPPH} // C_{PTFE}.

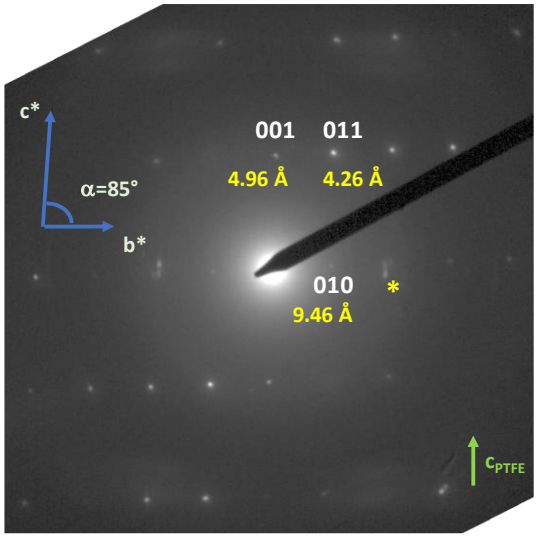

*Figure V. 31 ED pattern of a **HDPPH** film after thermal annealing.*

Subsequently, a comparison of the UV-vis spectra of the three derivatives was performed for films grown from solution on PTFE without any type of treatment (Figure V. 32). **HDPPH** the most red-shifted signal at 637 nm, followed by **HDPPBA-N** at 619 nm and lastly **HDPPBA-C** at 610 nm. This difference between the H-bonded derivatives and the control was attributed to the extended low-energy tail of **HDPPH**.

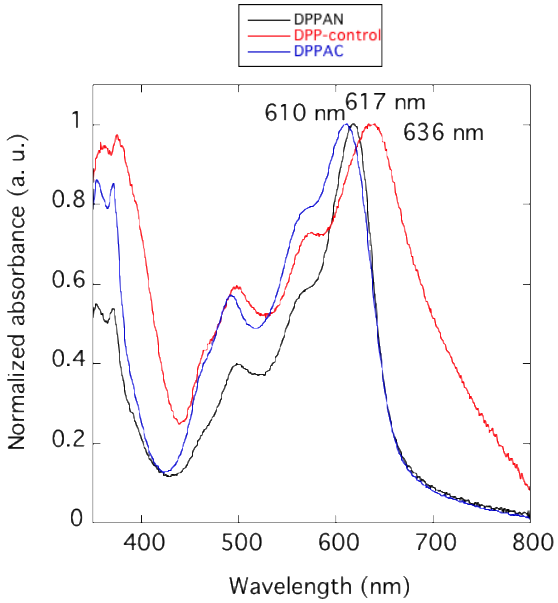

Figure V. 32 Comparison of the UV-vis spectra of all three derivatives.

A summary containing the main observations about the lattice parameters before and after thermal annealing is presented in Table V. 1.

Table V. 1 Summary of the observed lattice parameters for the three derivatives.

Plane	HDPPBA-N		HDPPBA-C		HDPPH Annealed (Å)
	Before annealing (Å)	After annealing (Å)	Before annealing (Å)	After annealing (Å)	
010	8.66	8.93	8.87	8.88	9.46
011	4.26	4.27	4.26	4.26	4.26
001	-	4.90	4.86	4.86	4.96

Lattice parameters for 010, 011 and 001 are similar for the three molecules, suggesting quite similar packing, despite the presence of amides for **HDPPBA-N** and **HDPPBA-C**.

In fact, only **HDPPBA-N** presents a significant change in the parameters, especially of d_{010} after thermal annealing, where it goes from 8.66 Å to 8.93 Å. This is consistent with the changes in UV-vis spectra with a shift of the 0-0 from 619 nm to 604 nm after thermal annealing.

This means the **DPP** packing is more robust compared against the H-bonding packing of amides in the side chains. Finally**, HDPPH** shows the largest value of d_{010}=9.46 Å, hinting that this parameter seems to be affected by the molecular structure, in other words, by the presence of the amide group.

III. Conclusions and perspectives

We have reported the first successful orientation of a self-assembled molecule on PTFE from solution, which provides evidence for oriented growth and heterogeneous nucleation on PTFE. Moreover, a clear difference in the orientation between **HDPPBA-N** and **HDPPBA-C** on PTFE was observed. For instance, excellent alignment was obtained for **HDPPBA-N**, whereas **HDPPBA-C** does not tend to orient on PTFE.

The change in color from blue (when exposure is done in parallel to C_{PTFE}) to orange (when the exposure es perpendicular to C_{PTFE}) of the polarized UV-vis spectra is due to the balance of absorbance between 610-620 nm *vs* 500 nm, as the band at 500 nm is less polarized.

The UV-vis spectra of the three derivatives when samples were annealed are quite similar, although differences between grown and annealed films were observed for **HDPPBA-N**, which is the one that orients on PTFE. The TEM ED patterns showed that annealing of **HDPPBA-N** improves ordering between columns as there was loss of streaking. This means that the aggregates could be undergoing a transformation from columnar 1D order to more 3D order. This results in a shift of the 0-0 absorption band and lattice expansion along the b axis. On the other hand, films made of **HDPPBA-C** do not seem to change much their structure between solution-grown and melt-recrystallized. This indicates the less dynamic character of the aggregates formed by this derivative, as evidenced in chapter III.

In order to complement and expand these studies, thicker films for **HDPPBA-N** could be grown, to have more continuous thin films. This can be done by preparing films from solutions

at a higher concentration, such as 10 mg/ml, which might also be used to do inverted OFETs on the oriented films and help us with the first experiments on the in-situ morphology control setup presented in the introduction of this chapter.

Furthermore, atomic force microscopy measurements of oriented **HDPPBA-N** films must be performed to check the morphology of the fibers before and after melt-crystallization. Additionally, to get out-of-plane structural information, grazing-incidence wide-angle X-ray scattering can be performed.

Moreover, adapting the protocol for the oriented growth on PTFE of **HDPPBA-N** from solution to other solvents, such as toluene and ethyl acetate, would help to evaluate the impact of different solvents.

Finally, performing the same type of experiments and analysis to the thiophene functionalized **DPP** derivatives that were described in Chapter IV would also help and complement these results, which will ultimately pave the way for real-time screening of organic electronic devices.

IV. Experimental

IV.1) Materials and methods

TGA was performed by using a TGA 2 Mettler Toledo instrument, the sample was heated from 25 °C to 300 °C at a rate of 5 °C/min under nitrogen atmosphere at a flowrate of 20 ml/min. DSC was performed by using a DSC 8500 Perkin Elmer instrument, a first heating-cooling cycle was performed to remove any potential thermal history, then a second cycle was performed to measure the properties of each sample. The samples were heated from -10 °C to 300 °C at a rate of 5 °C/min under nitrogen atmosphere at a flowrate of 20 ml/min, and the cooling down was performed under the same rates and conditions. The film orientation was investigated by using a LEICA DM-2700 P microscope. The films were studied in bright field and diffraction modes with a 120 kV Philips CM12 electron microscope equipped with a MVIII charge-coupled device camera. UV–vis measurements were performed on a Cary 5000 UV-Vis-NIR spectrophotometer.

V. References

[1] Y.-T. Tsai, K.-P. Tseng, Y.-F. Chen, C.-C. Wu, G.-L. Fan, K.-T. Wong, G. Wantz, L. Hirsch, G. Raffy, A. Del Guerzo, D. M. Bassani, *ACS Nano* **2016**, *10*, 998–1006.

[2] M.-C. Kuo, H.-F. Chen, J.-J. Shyue, D. M. Bassani, K.-T. Wong, *Chemical Communications* **2012**, *48*, 8051.

[3] K.-P. Tseng, Y.-T. Tsai, J.-J. Shyue, G. Raffy, A. Del Guerzo, K.-T. Wong, D. M. Bassani, *Chemical Physics Letters* **2017**, *683*, 43–48.

[4] A. Ruiz-Carretero, T. Aytun, C. J. Bruns, C. J. Newcomb, W.-W. Tsai, S. I. Stupp, *Journal of Materials Chemistry A* **2013**, *1*, 11674.

[5] T. Aytun, L. Barreda, A. Ruiz-Carretero, J. A. Lehrman, S. I. Stupp, *Chemistry of Materials* **2015**, *27*, 1201–1209.

[6] R. J. Kumar, J. Subbiah, A. B. Holmes, *Beilstein Journal of Organic Chemistry* **2013**, *9*, 1102–1110.

[7] C.-H. Huang, N. D. McClenaghan, A. Kuhn, J. W. Hofstraat, D. M. Bassani, *Organic letters* **2005**, *7*, 3409–3412.
[8] S. K. P. Velu, M. Yan, K.-P. Tseng, K.-T. Wong, D. M. Bassani, P. Terech, *Macromolecules* **2013**, *46*, 1591–1598.
[9] S. Militzer, T. M. P. Tran, P. J. Mésini, A. Ruiz-Carretero, *ChemNanoMat* **2018**, *4*, 790–795.
[10] S. Militzer, N. Nishimura, N. R. Ávila-Rovelo, W. Matsuda, D. Schwaller, P. J. Mésini, S. Seki, A. Ruiz-Carretero, *Chem. Eur. J.* **2020**, *26*, 9998–10004.
[11] F. S. U. Fischer, D. Trefz, J. Back, N. Kayunkid, B. Tornow, S. Albrecht, K. G. Yager, G. Singh, A. Karim, D. Neher, M. Brinkmann, S. Ludwigs, *Adv. Mater.* **2015**, *27*, 1223–1228.
[12] M. Vala, M. Weiter, J. Vyňuchal, P. Toman, S. Luňák, *J Fluoresc* **2008**, *18*, 1181.
[13] J. David, M. Weiter, M. Vala, J. Vyňuchal, J. Kučerík, *Dyes and Pigments* **2011**, *89*, 137–143.
[14] N. Genevaz, P. Chávez, V. Untilova, A. Boeglin, C. Bailly, L. Karmazin, L. Biniek, *J. Mater. Chem. C* **2018**, *6*, 9140–9151.

SUMMARY AND GENERAL CONCLUSIONS

In summary, in my thesis I have expanded the library of **DPP** molecules for the systematic and comparative studies based on **DPP** as a model (Figure 38, highlighting in light blue the families I have directly worked on). Parameters such as solubility, chirality, topology and position of the H-bonding functionality with respect to the **DPP** core were also investigated.

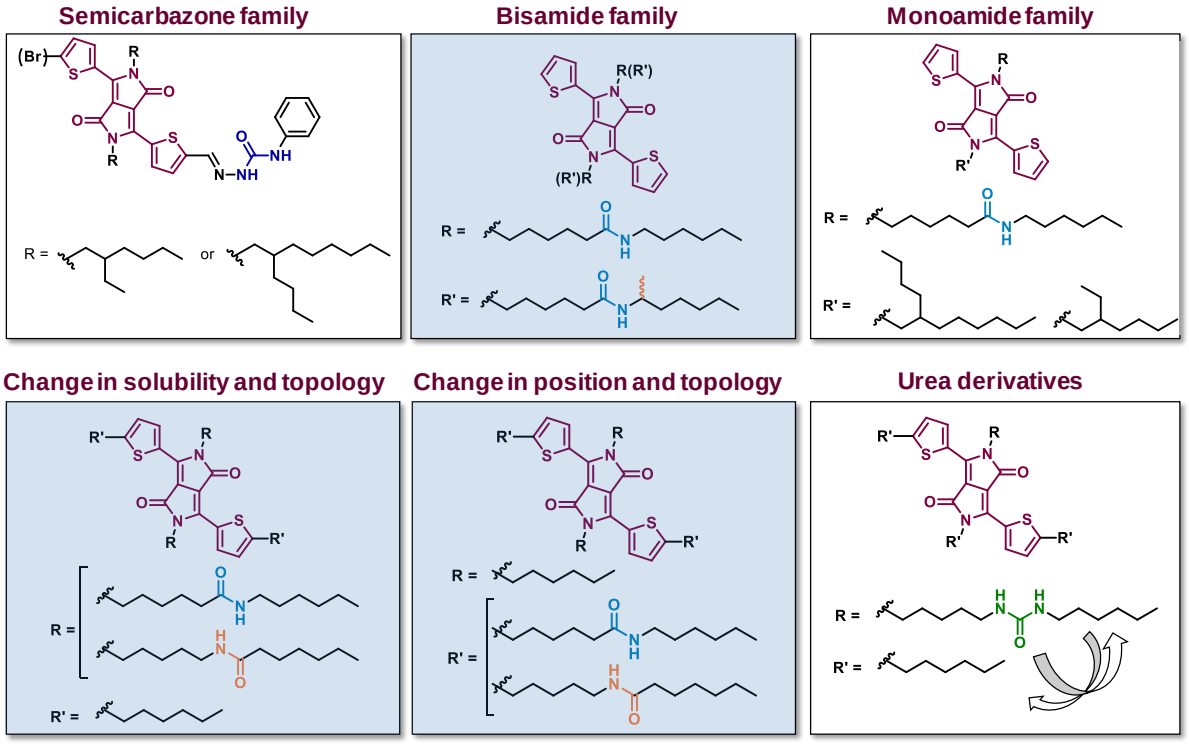

*Figure 38 H-bonded **DPP** families synthesized so far in the **DPP** model system study, the families studied in this thesis are highlighted in light blue.*

Several characterization techniques were used to have a better understanding on the behaviour and properties of these molecules. For instance, UV-visible spectra revealed the formation of aggregates, usually attributed to J-type aggregates, depending on the nature of the solvent, concentration and temperature. Moreover, experiments were MeOH was added, and FTIR spectra confirmed the formation of H-bonds and their involvement in the aggregate formation.

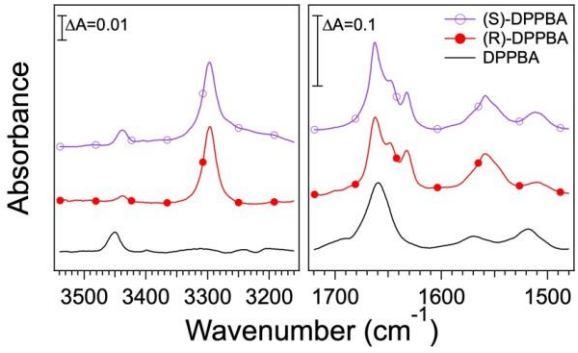

*Figure 39 FTIR spectra in deuterated chloroform at room temperature of **(S)-DPPBA**, **(R)-DPPBA** and **DPPBA**.*

In the case of the amide containing **DPP** derivatives presented in chapter II, all three derivatives aggregate and form J-type aggregates, where H-bonds are involved (Figure 39). The aggregation is particularly strong in the chiral derivatives, which show aggregate signals in solvents where the achiral **DPP** is fully dissociated.

The photoconductivity measurements performed using FP-TRMC indicate that the achiral derivative has superior values of photoconductivity as well as slower recombination of the charge carriers.

As for the derivatives presented in chapter III, despite having mostly the same structure, but different amide topology and increased solubility, it was observed that the recombination of charge carriers and the photoconductivity values are comparable to the previously studied families.

Remarkably, the recombination of charge carriers for chiral **DPP** derivatives is in the same order of magnitude as for the control molecule **HDPPH**, containing no H-bonds in its structure, which indicates how important is to finely-tune the molecular design of H-bonded π-conjugated materials, since the most subtle change can dramatically impact the electronic properties.

Slight differences were observed for changes in topology, the C-centered derivative presents a bathochromic shift in all the solvents compared to N-centered derivative, and the J-aggregate is more pronounced in all the solvents tested, presumably as a sign of stronger aggregation.

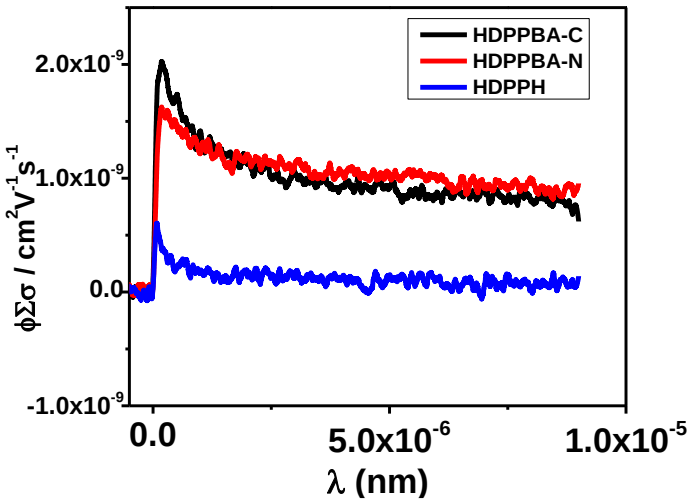

*Figure 40 Kinetic traces of photoconductivity transients of **HDPPBA-C**, **HDPPBA-N** and **HDPPH** cast from chloroform/toluene solutions.*

The photoconductivities of **HDPPBA-C** and **HDPPBA-N** are very similar, but clearly larger than the value found for **HDPPH**, highlighting the beneficial role of H-bonding in this family and in extension, to the rest of the families explored so far (Figure 40).

The family of **DPP** derivatives described in chapter IV is to our knowledge, the first derivatives where the basic **DPP** core bears functionalized alkylated thiophenes. The succinic cyclization approach seems to be limited, as it works best for thiophene rings that have alkyl chains

without moieties, whereas the direct approach proved its versatility and will help in the synthesis of new and different **DPP** derivatives (Figure 41).

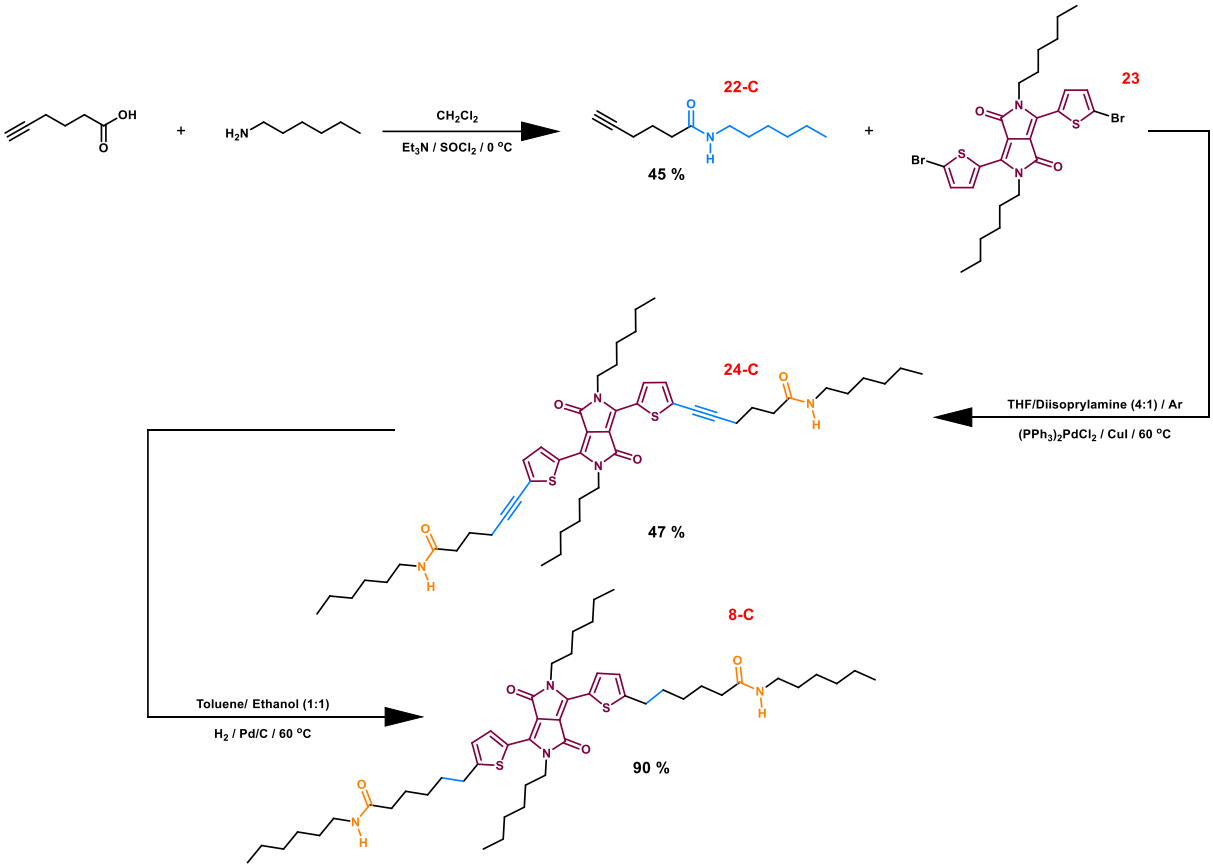

Figure 41 Final and reliable synthetic approach to obtain **8-C**.

In the case of morphology, placing H-bonding groups in different positions seems to dramatically change the self-assembly processes. This behavior was also reflected in the absorption spectra, where they show smaller bands in the J-aggregate regions.

FTIR spectra of powders at room temperature also proved the existence of H-bonds in these new derivatives and provided further proof that there are small spectra shifts, that may ultimately explain the changes in self-assembly.

The complete characterization of this family will be very important, as it will provide crucial data on future molecular design and elucidate the impact of the position of the H-bond with respect to the conjugated core.

In chapter V, we have reported the first successful orientation of a self-assembled molecule on PTFE from solution. Additionally, from the obtained diffraction patterns, it was possible to construct a very simple model of the structures formed by these aggregates (Figure 42).

However, more studies such as AFM or GIWAXS are needed to complement and expand the scope of the results. Moreover, preparing thicker and continuous films might also be done to

produce inverted OFETs that will help us with the first experiments on the in-situ morphology control.

In this sense, the results presented in this thesis will help in the development of the *in-situ* control over the morphology and electric properties of H-bonded organic electronic materials, ultimately gathering as much information as possible and helping to build a screening protocol.

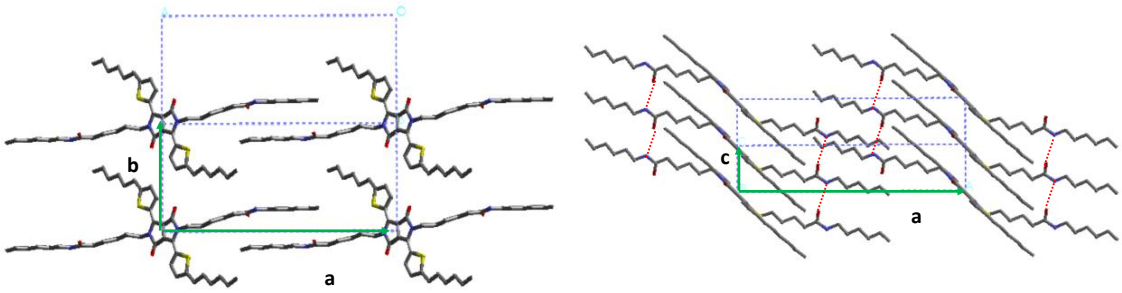

Figure 42 Modeling of the structure based on the obtained electron diffraction patterns.

Nelson Ricardo ÁVILA ROVELO

Vers une vision globale des liaisons hydrogène dans l'organique électronique : le dicétopyrrolopyrrole comme système modèle

Résumé

Les semi-conducteurs organiques combinent les avantages électroniques des matériaux semi-conducteurs avec les bénéfices chimiques et mécaniques de composés organiques. En outre, lorsque des interactions non covalentes telles que les liaisons hydrogène sont présentes, certaines études démontrent qu'elles améliorent l'efficacité des différents dispositifs électroniques ; tandis que d'autres travaux démontrent qu'elles sont désavantageuses. Cela a conduit à un manque de consensus par rapport à l'incorporation des liaisons hydrogène dans les semi-conducteurs. L'objectif de cette thèse est d'élucider l'impact de ces liaisons sur les propriétés des semi-conducteurs organiques, ainsi que de cribler les conditions nécessaires pour fabriquer des dispositifs électroniques efficaces. Pour cette raison, des études systématiques et comparatives ont été faites en utilisant une molécule conjuguée comme un système modèle, plus précisément, le dicétopyrrolopyrrole (DPP). Trois familles différentes basées sur le DPP ont été étudiées et l'effet de la variation de certains paramètres comme la fonctionnalité, la topologie et la position des liaisons hydrogène a été évalué. Ces études ont apporté plus d'informations sur le rôle des liaisons hydrogène dans l'organique électronique et serviront de base pour le bon développement de procédés pour obtenir des dispositifs organiques électroniques de haute performance dans le futur.

Mots clés : Dicétopyrrolopyrrole, semi-conducteurs organiques, liaisons hydrogène.

Summary

Organic semiconductors combine the electronic advantages of semiconducting materials with the chemical and mechanical benefits of organic compounds. When non-covalent interactions such as hydrogen bonds (H-bonds) are added, some studies have demonstrated they improve efficiency in different electronic devices; while others report they are detrimental. This has led to a lack of consensus regarding the incorporation of H-bonds in semiconductors. The aim of this PhD is to elucidate their impact in the optoelectronic properties of organic semiconductors, as well as screening the required conditions needed to fabricate efficient electronic devices. For this purpose, systematic and comparative studies have been done using a conjugated molecule as a model system, more precisely, diketopyrrolopyrrole (DPP). Three different DPP families were studied, evaluating the effect of varying parameters such as functionality, topology, and position of the H-bonds. These studies have brought more light on the role of H-bonds in organic electronics and will serve as a basis to successfully develop processing techniques to obtain high performing organic electronic devices in the future.

Key words: Diketopyrrolopyrrole, organic semiconductors, hydrogen bonds.